

Vibration Control

edited by

Dr. Mickaël Lallart

SCIYO

Vibration Control

Edited by Dr. Mickaël Lallart

Published by Sciyo

Janeza Trdine 9, 51000 Rijeka, Croatia

Copyright © 2010 Sciyo

All chapters are Open Access articles distributed under the Creative Commons Non Commercial Share Alike Attribution 3.0 license, which permits to copy, distribute, transmit, and adapt the work in any medium, so long as the original work is properly cited. After this work has been published by Sciyo, authors have the right to republish it, in whole or part, in any publication of which they are the author, and to make other personal use of the work. Any republication, referencing or personal use of the work must explicitly identify the original source.

Statements and opinions expressed in the chapters are these of the individual contributors and not necessarily those of the editors or publisher. No responsibility is accepted for the accuracy of information contained in the published articles. The publisher assumes no responsibility for any damage or injury to persons or property arising out of the use of any materials, instructions, methods or ideas contained in the book.

Publishing Process Manager Ana Nikolic

Technical Editor Teodora Smiljanic

Cover Designer Martina Sirotic

Image Copyright SaferTim, 2010. Used under license from Shutterstock.com

First published September 2010

Printed in India

A free online edition of this book is available at www.sciyo.com

Additional hard copies can be obtained from publication@sciyo.com

Vibration Control, Edited by Dr. Mickaël Lallart

p. cm.

ISBN 978-953-307-117-6

SCIYO.COM
WHERE KNOWLEDGE IS FREE

free online editions of Sciyo
Books, Journals and Videos can
be found at **www.sciyo.com**

Contents

Preface IX

- Chapter 1 **Electromechanical Dampers for Vibration Control of Structures and Rotors 1**
Andrea Tonoli, Nicola Amati and Mario Silvagni
- Chapter 2 **The Foundation of Electromagnets Based Active Vibration Control 33**
Ramón Ferreiro García, Manuel Haro Casado and F. Javier Perez Castelo
- Chapter 3 **A Magnetorheological Damper with Embedded Piezoelectric Force Sensor: Experiment and Modeling 55**
Y. Q. Ni and Z. H. Chen
- Chapter 4 **Vibration Isolation System Using Negative Stiffness 79**
Taksehi Mizuno
- Chapter 5 **Mass Inertia Effect based Vibration Control Systems for Civil Engineering Structure and Infrastructure 105**
Chunwei Zhang and Jinping Ou
- Chapter 6 **AVC Using a Backstepping Design Technique 159**
R. Ferreiro García, F. Fragueta Diaz, A. De Miguel Catoira
- Chapter 7 **Model Independent Vibration Control 187**
Jing Yuan
- Chapter 8 **Active Vibration Control for a Nonlinear Mechanical System using On-line Algebraic Identification 201**
Francisco Beltrán, Gerardo Silva, Andrés Blanco and Esteban Chávez
- Chapter 9 **A Self-Organizing Fuzzy Controller for the Active Vibration Control of a Smart Truss Structure 215**
Gustavo Luiz C. M. Abreu, Vicente Lopes Jr. and Michael J. Brennan
- Chapter 10 **Semi-active Vibration Control Based on Switched Piezoelectric Transducers 235**
Hongli Ji, Jinhao Qiu and Pinqi Xia

- Chapter 11 **Self-Powered and Low-Power Piezoelectric Vibration Control Using Nonlinear Approaches** 265
Mickaël Lallart and Daniel Guyomar
- Chapter 12 **Active Vibration Control of Rotor-Bearing Systems** 293
Andrés Blanco, Gerardo Silva, Francisco Beltrán and Gerardo Vela
- Chapter 13 **Automotive Applications of Active Vibration Control** 303
Ferdinand Svaricek, Tobias Fueger, Hans-Juergen Karkosch, Peter Marienfeld and Christian Bohn
- Chapter 14 **Neural Network Control of Non-linear Full Vehicle Model Vibrations** 319
Rahmi Guclu and Kayhan Gulez
- Chapter 15 **Robust Active Vibration Control of Flexible Stewart Isolators** 335
Liu Lei, Wang Pingping, Kong Xianren and Wang Benli
- Chapter 16 **Vibration Control** 355
Ass. Prof. Dr. Mostafa Tantawy Mohamed

Preface

Vibrations are a part of our environment and daily life. Many of them are useful and are needed for many purposes, one of the best example being the hearing system. Nevertheless, vibrations are often undesirable and have to be suppressed or reduced, as they may be harmful to structures by generating damages (possibly leading to dramatic and spectacular accidents such as the case of the Aloha 243 flight or the bridge of Tacoma Narrows) or compromise the comfort of users through noise generation of mechanical wave transmission to the body.

Vibration control and limitation is an exciting field in the research community and raises challenging issues in industrial applications. This topic involves multidisciplinary approaches and multi-physic coupling, from mechanical to thermal, and possibly through electrical or magnetic fields, the basic idea being the dissipation of the mechanical energy into heat or preventing mechanical energy from entering into the structures.

Two strategies are typically used for limiting vibrations. The mechanical energy may be directly dissipated into heat through the use of viscoelastic layers or the use of additional stiffeners can prevent energy from entering in the system, but the performance of such approaches is limited, especially in the case of low-frequency vibrations.

In order to dispose of efficient systems, the second method consists of using intermediate energy conversion media, such as electromagnets or piezoelectric actuators. When using multiphysic coupling, mechanical energy is first transferred into another form (electrical, magnetic...) before being dissipated. Energy conversion systems may also be used to ensure that the input force spectrum does not overlap the frequency response function of the structure to ensure that no energy goes into the device.

To limit the vibrations of a system, many methods have been proposed, which can be classified into several families. Although the classification of vibration control schemes can be done in several ways, an interesting one lies in the analysis of the energy used for the control, leading to the following classes:

- **Passive control schemes** where no energy is injected into the system, and no particular control is performed. This class comprises purely mechanical devices (e.g., viscoelastic layers), but also includes approaches featuring energy conversion materials (such as piezoelectric and magnetic transducers) that are not subjected to a particular control (for example, resistive shunted electroactive materials fall into this category).
- **Semi-passive techniques** where no energy is used in the energy conversion system, but are necessary for the command law. This includes switched systems. As such techniques are used when the amount of required energy is a critical constraint, the command laws are usually quite simple.

- **Semi-active techniques** that consist of an extension of semi-passive systems. In the case of semi-active approaches, a small amount of energy is given to the energy conversion systems in order to enhance the vibration limitation abilities of the device.
- **Active control schemes** which include a full feedback loop (sensors, controller, amplifier, actuator), and require large amounts of energy. Because energy is not critical in this case, the command law of active control scheme may be complex.

In terms of applications, the choice of the vibration control technique is not only motivated by the efficiency of the method, but several constraints may have to be taken into account as well. Apart from vibration suppression performance, the most usual constraints lie in the energy required by the technique and the size of the vibration control system. Hence, the design of vibration limitation techniques involves a lot of parameters, and each approach presents its own trade-off between performance, energy requirements and size (and possibly other considerations). Typically, semi-passive and semi-active techniques have low energy consumption and can be easily embedded to the structure, while active approaches provide higher vibration damping performance.

Therefore, the purpose of this book is to present basic and advanced methods for efficiently controlling the vibrations and limiting their effects. Open-access publishing is an extraordinary opportunity for a wide dissemination of high quality research. This book is not an exception to this, and I am proud to introduce the works performed by experts from all over the world. I would also like to take this opportunity to thank all the authors for their high quality contributions, as well as the Sciyo publishing team (and especially the book manager Ms. Ana Nikolic) for their outstanding support.

The book is organised as follows. Chapters 1 to 3 aim at introducing some actuator architectures and principles for their application to vibration control purposes. Then, efficient active control schemes will be exposed in chapters 4-9. The next two chapters (10-11) present semi-passive and semi-active techniques. Finally chapters 12-16 present some typical application examples of vibration control techniques.

July 2010

Editor

Dr. Mickaël Lallart,
INSA Lyon, Villeurbanne

Electromechanical Dampers for Vibration Control of Structures and Rotors

Andrea Tonoli, Nicola Amati and Mario Silvagni
*Mechanics Department, Mechatronics Laboratory - Politecnico di Torino
Italy*

To the memory of Pietro, a model student, a first-class engineer, a hero

1. Introduction

Viscoelastic and fluid film dampers are the main two categories of damping devices used for the vibration suppression in machines and mechanical structures. Although cost effective and of small size and weight, they are affected by several drawbacks: the need of elaborate tuning to compensate the effects of temperature and frequency, the ageing of the material and their passive nature that does not allow to modify their characteristics with the operating conditions. Active or semi-active electro-hydraulic systems have been developed to allow some forms of online tuning or adaptive behavior. More recently, electrorheological, (Ahn et al., 2002), (Vance & Ying, 2000) and magnetorheological (Vance & Ying, 2000) semi-active damping systems have shown attractive potentialities for the adaptation of the damping force to the operating conditions. However, electro-hydraulic, electrorheological, and magnetorheological devices cannot avoid some drawbacks related to the ageing of the fluid and to the tuning required for the compensation of the temperature and frequency effects.

Electromechanical dampers seem to be a valid alternative to viscoelastic and hydraulic ones due to, among the others: a) the absence of all fatigue and tribology issues motivated by the absence of contact, b) the small sensitivity to the operating conditions, c) the wide possibility of tuning even during operation, and d) the predictability of the behavior. The attractive potentialities of electromechanical damping systems have motivated a considerable research effort during the past decade. The target applications range from the field of rotating machines to that of vehicle suspensions.

Passive or semi-active eddy current dampers have a simpler architecture compared to active closed loop devices, thanks to the absence of power electronics and position sensors and are intrinsically not affected by instability problems due to the absence of a fast feedback loop. The simplified architecture guarantees more reliability and lower cost, but allows less flexibility and adaptability to the operating conditions. The working principle of eddy current dampers is based on the magnetic interaction generated by a magnetic flux linkage's variation in a conductor (Crandall et al., 1968), (Meisel, 1984). Such a variation may be generated using two different strategies:

- moving a conductor in a stationary magnetic field that is variable along the direction of the motion;
- changing the reluctance of a magnetic circuit whose flux is linked to the conductor.

In the first case, the eddy currents in the conductor interact with the magnetic field and generate Lorentz forces proportional to the relative velocity of the conductor itself. In (Graves et al., 2000) this kind of damper are defined as “motional” or “Lorentz” type. In the second case, the variation of the reluctance of the magnetic circuit produces a time variation of the magnetic flux. The flux variation induces a current in the voltage driven coil and, therefore, a dissipation of energy. This kind of dampers is defined in (Nagaya, 1984) as “transformer”, or “reluctance” type.

The literature on eddy current dampers is mainly focused on the analysis of “motional” devices. Nagaya in (Nagaya, 1984) and (Nagaya & Karube, 1989) introduces an analytical approach to describe how damping forces can be exploited using monolithic plane conductors of various shapes. Karnopp and Margolis in (Karnopp, 1989) and (Karnopp et al., 1990) describe how “Lorentz” type eddy current dampers could be adopted as semi-active shock absorbers in automotive suspensions. The application of the same type of eddy current damper in the field of rotordynamics is described in (Kligerman & Gottlieb, 1998) and (Kligerman et al., 1998).

Being usually less efficient than “Lorentz” type, “transformer” eddy current dampers are less common in industrial applications. However they may be preferred in some areas for their flexibility and construction simplicity. If driven with a constant voltage they operate in passive mode while if current driven they become force actuators to be used in active configurations. A promising application of the “transformer” eddy current dampers seems to be their use in aero-engines as a non rotating damping device in series to a conventional rolling bearing that is connected to the main frame with a mechanical compliant support. Similarly to a squeeze film damper, the device acts on the non rotating part of the bearing. As it is not rotating, there are no eddy currents in it due to its rotation but just to its whirling. The coupling effects between the whirling motion and the torsional behavior of the rotor can be considered negligible in balanced rotors (Genta, 2004).

In principle the behaviour of Active Magnetic Dampers (AMDs) is similar to that of Active Magnetic Bearings (AMBs), with the only difference that the force generated by the actuator is not aimed to support the rotor but just to supply damping. The main advantages are that in the case of AMDs the actuators are smaller and the system is stable even in open-loop (Genta et al., 2006),(Genta et al., 2008),(Tonoli et al., 2008). This is true if the mechanical stiffness in parallel to the electromagnets is large enough to compensate the negative stiffness induced by the electromagnets.

Classical AMDs work according to the following principle: the gap between the rotor and the stator is measured by means of position sensors and this information is then used by the controller to regulate the current of the power amplifiers driving the magnet coils. Self-sensing AMDs can be classified as a particular case of magnetic dampers that allows to achieve the control of the system without the introduction of the position sensors. The information about the position is obtained by exploiting the reversibility of the electromechanical interaction between the stator and the rotor, which allows to obtain mechanical variables from electrical ones.

The sensorless configuration leads to many advantages during the design phase and during the practical realization of the device. The intrinsic punctual collocation of the not present sensor avoids the inversion of modal phase from actuator to sensor, with the related loss of

the zero/pole alternation and the consequent problems of stabilization that may affect a sensed solution. Additionally, getting rid of the sensors leads to a reduction of the costs, the reduction of the cabling and of the overall weight.

The aim of the present work is to present the experience of the authors in developing and testing several electromagnetic damping devices to be used for the vibration control.

A brief theoretical background on the basic principles of electromagnetic actuator, based on a simplified energy approach is provided. This allow a better understanding of the application of the electromagnetic theory to control the vibration of machines and mechanical structures. According to the theory basis, the modelling of the damping devices is proposed and the evidences of two dedicated test rigs are described.

2. Description and modelling of electromechanical dampers

2.1 Electromagnetic actuator basics

Electromagnetic actuators suitable to develop active/semi-active/passive damping efforts can be classified in two main categories: Maxwell devices and Lorentz devices.

For the first, the force is generated due to the variation of the reluctance of the magnetic circuit that produces a time variation of the magnetic flux linkage. In the second, the damping force derives from the interaction between the eddy currents generated in a conductor moving in a constant magnetic field.

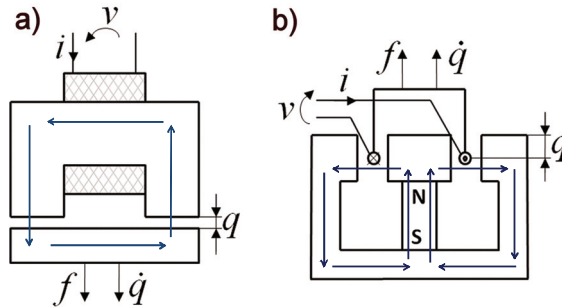


Fig. 1. Sketch of a) Maxwell magnetic actuator and b) Lorentz magnetic actuator.

For both (Figure 1), the energy stored in the electromagnetic circuit can be expressed by:

$$E = \int_{t_0}^{t_1} (P_{\text{electrical}} + P_{\text{mechanical}}) dt = \int_{t_0}^{t_1} (v(t)i(t) + f(t)\dot{q}(t)) dt \quad (1)$$

Where the electrical power ($P_{\text{electrical}}$) is the product of the voltage ($v(t)$) and the current ($i(t)$) flowing in the coil, and the mechanical power is the product of the force ($f(t)$) and speed ($\dot{q}(t)$) of the moving part of the actuator.

Considering the voltage ($v(t)$) as the time derivative of the magnetic flux linkage ($\lambda(t)$), eq.(1) can be written as:

$$E = \int_{t_0}^{t_1} \left(\frac{d\lambda(t)}{dt} i(t) + f(t)\dot{q}(t) \right) dt = \int_{\lambda_0}^{\lambda_1} i(t) d\lambda + \int_{q_0}^{q_1} f(t) dq = E_{\lambda} + E_q \quad (2)$$

In the following steps, the two terms of the energy E will be written in explicit form. With reference to Maxwell Actuator, Figure 1a, the Ampère law is:

$$H_a l_a + H_{fe} l_{fe} = Ni \quad (3)$$

where H_a and H_{fe} indicate the magnetic induction in the airgap and in the iron core while l_a and l_{fe} specify the length of the magnetic circuit flux lines in the airgap in the same circuit. The product Ni is the total current linking the magnetic flux (N indicates the number of turns while i is the current flowing in each wire section). If the magnetic circuit is designed to avoid saturation into the iron, the magnetic flux density B can be related to magnetic induction by the following expression:

$$B = \mu_0 H \quad , \quad B = \mu_0 \mu_{fe} H_{fe} . \quad (4)$$

Considering that ($\mu_{fe} \gg \mu_0$) and noting that the total length of the magnetic flux lines in the airgap is twice q , eq.(3) can be simply written as:

$$\frac{2Bq}{\mu_0} = Ni . \quad (5)$$

The expressions of the magnetic flux linking a single turn and the total number of turns in the coil are respectively:

$$\varphi = BS_{airgap} \quad (6)$$

$$\lambda = N\varphi = NBS_{airgap} = \mu_0 \frac{N^2 S_{airgap}}{2q} i \quad (7)$$

Hence, knowing the expression (eq.(7)) of the total magnetic flux leakage, the E_λ of eq. (1) for a generic flux linkage λ and air q , can be computed as:

$$E_\lambda = \int_{\lambda_0}^{\lambda_1} i(t) d\lambda = \frac{\lambda^2 q}{\mu_0 N^2 S_{airgap}} \quad (8)$$

Note that this is the total contribution to the energy (E) if no external active force is applied to the moving part.

Finally, the force generated by the actuator and the current flowing into the coil can be computed as:

$$f = \frac{\partial E}{\partial q} = \frac{\lambda^2}{\mu_0 N^2 S_{airgap}} , \quad (9)$$

$$i = \frac{\partial E}{\partial \lambda} = \frac{2q\lambda}{\mu_0 N^2 S_{airgap}} . \quad (10)$$

Then, the force relative to the current can be obtained by substituting eq.(10) into eq.(9):

$$f = \frac{\mu_0 N^2 S_{airgap} i^2}{4q^2} . \quad (11)$$

Considering the **Lorentz actuator** (Figure 1 b), if the coil movement q is driven while the same coil is in open circuit configuration so that no current flows in the coil, the energy (E) is zero as both the integrals in eq. (1) are null. In the case the coil is in a constant position and the current flow in it varies from zero to a certain value, the contribution of the integral leading to (E_q) is null as the displacement of the anchor (q) is constant while the integral leading to (E_λ) can be computed considering the total flux leakage.

$$\lambda = 2\pi RqB + Li = \lambda_0 + Li \quad (12)$$

The first term is the contribution of the magnetic circuit (R is the radius of the coil, q is the part of the coil in the magnetic field), while the second term is the contribution to the flux of the current flowing into the coil. Current can be obtained from eq.(12) as:

$$i = \frac{\lambda - \lambda_0}{L} \quad (13)$$

Hence, from the expression of eq.(13), the E_λ term, that is equal to the total energy, can be computed as:

$$E_\lambda = \int_{\lambda_0}^{\lambda_1} i(t) d\lambda = \int_{\lambda_0}^{\lambda_1} \frac{\lambda - \lambda_0}{L} d\lambda = \frac{1}{2L} (\lambda - \lambda_0)^2 = \frac{1}{2L} (\lambda - 2\pi RqB)^2 \quad (14)$$

Finally computing the derivative with respect to the displacement and to the flux, the force generated by the actuator and the current flowing into the coil can be computed:

$$f = \frac{\partial E}{\partial q} = \frac{-2\pi RB}{L} (\lambda - \lambda_0) \quad (15)$$

$$i = \frac{\partial E}{\partial \lambda} = \frac{1}{L} (\lambda - \lambda_0) \quad (16)$$

The expression of the force relative to the current can be obtained by substituting eq.(16) into eq.(15)

$$f = -2\pi RBi . \quad (17)$$

The equations above mentioned represent the basis to understand the behaviour of electromagnetic actuators adopted to damp the vibration of structures and machines.

2.2 Classification of electromagnetic dampers

Figure 2 shows a sketch representing the application of a Maxwell type and a Lorentz type actuator. In the field of damping systems the former is named transformer damper while the latter is called motional damper. The transformer type dampers can operate in active mode if current driven or in passive mode if voltage driven. The drawings evidence a compliant

supporting device working in parallel to the damper. In the specific its role is to support the weight of the rotor and supply the requested compliance to exploit the performance of the damper (Genta, 2004). Note that the sketches are referred to an application for rotating systems. The aim in this case is to damp the lateral vibration of the rotating part but the concept can be extended to any vibrating device. In fact, the damper interacts with the non rotating raceway of the bearing that is subject only to radial vibration motion.

2.3 Motional eddy current dampers

The present section is devoted to describe the equations governing the behavior of the motional eddy current dampers. A torsional device is used as reference being the linear ones a subset. The reference scheme (Kamerbeek, 1973) is a simplified induction motor with one magnetic pole pair (Figure 3a).

The rotor is made by two windings 1,1' and 2,2' installed in orthogonal planes. It is crossed by the constant magnetic field (flux density B_s) generated by the stator. The analysis is performed under the following assumptions:

- the two rotor coils have the same electric parameters and are shorted.
- The reluctance of the magnetic circuit is constant. The analysis is therefore only applicable to motional eddy current devices and not to transformer ones (Graves et al., 2009), (Tonoli et al., 2008).

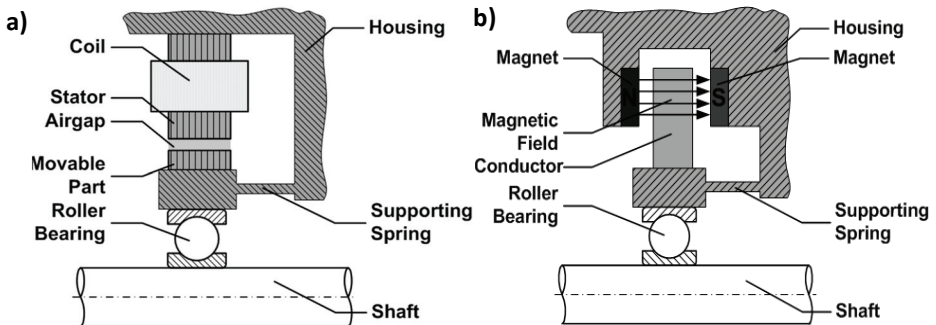


Fig. 2. Sketch of a transformer (a) and a motional damper (b).

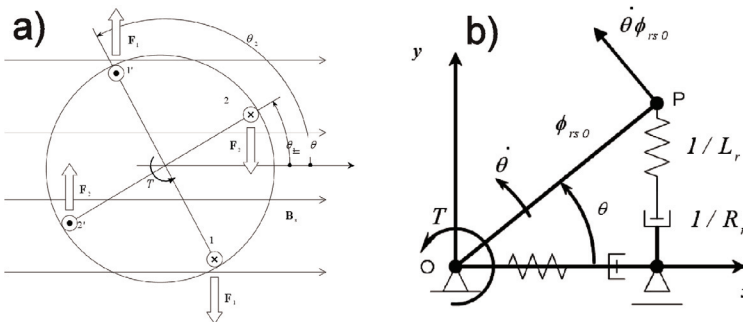


Fig. 3. a) Sketch of the induction machine b) Mechanical analogue. The torque T is balanced by the force applied to point P by the spring-damper assemblies.

- The magnetic flux generated by the stator is constant as if it were produced by permanent magnets or by current driven electromagnets.
- The stator is assumed to be fixed. This is equivalent to describe the system in a reference frame rigidly connected to it.
- All quantities are assumed to be independent from the axial coordinate.
- Each of the electric parameter is assumed to be lumped.

Angle $\theta(t)$ between the plane of winding 2 and the direction of the magnetic field indicates the angular position of the rotor relative to the stator. When currents i_{r1} and i_{r2} flow in the windings, they interact with the magnetic field of the stator and generate a pair of Lorentz forces ($F_{1,2}$ in Figure 3a). Each force is perpendicular to both the magnetic field and to the axis of the conductors. They are expressed as:

$$F_1 = Nl_r i_{r1} B_s, \quad F_2 = Nl_r i_{r2} B_s \quad (18)$$

where N and l_r indicate the number of turns in each winding and their axial length. The resulting electromagnetic torques T_1 and T_2 applied to the rotor of diameter d_r are:

$$T_1 = F_1 d_r \sin \theta = \phi_{rs0} \sin \theta i_{r1}, \quad T_2 = F_2 d_r \cos \theta = \phi_{rs0} \cos \theta i_{r2} \quad (19)$$

where $\phi_{rs0} = Nl_r d_r B_s$ is the magnetic flux linked with each coil when its normal is aligned with the magnetic field \mathbf{B}_s . It represents the maximum magnetic flux. The total torque acting on the rotor is:

$$T = T_1 + T_2 = \phi_{rs0} (\sin \theta i_{r1} + \cos \theta i_{r2}) \quad (20)$$

Note that the positive orientation of the currents indicated in Figure 3a has been assumed arbitrarily, the results are not affected by this choice.

From the mechanical point of view the eddy current damper behaves then as a crank of radius ϕ_{rs0} whose end is connected to two spring/damper series acting along orthogonal directions. Even if the very concept of mechanical analogue is usually a matter of elementary physics textbooks, the mechanical analogue of a torsional eddy current device is not common in the literature. It has been reported here due to its practical relevance. Springs and viscous dampers can in fact be easily assembled in most mechanical simulation environments. The mechanical analogue in Figure 3b allows to model the effect of the eddy current damper without needing a multi-domain simulation tool.

The model of an eddy current device with p pole pairs can be obtained by considering that each pair involves two windings electrically excited with 90° phase shift. For a one pole pair device, each pair is associated with a rotor angle of 2π rad; a complete revolution of the rotor induces one electric excitation cycle of its two windings. Similarly, for a p pole pairs device, each pair is associated to a $2\pi/p$ rad angle, a complete revolution of the rotor induces then p excitation cycles on each winding ($\theta_r = p\theta$).

The orthogonality between the two windings allows adopting a complex flux linkage variable

$$\phi_r = \phi_{r1} + j\phi_{r2} \quad (21)$$

where j is the imaginary unit. Similarly, also the current flowing in the windings can be written as $i_r = i_{r1} + j i_{r2}$. The total magnetic flux ϕ_r linked by each coil is contributed by the

currents i_r through the self inductance L_r and the flux generated by the stator and linked to the rotor

$$\phi_r = L_r i_r + \frac{\phi_{rs0}}{p} e^{-j\theta_e}. \quad (22)$$

The differential equation governing the complex flux linkage ϕ_r is obtained by substituting eq.(22) in the Kirchoff's voltage law

$$\frac{d\phi_r}{dt} + R_r i_r = 0. \quad (23)$$

It is therefore expressed as

$$\dot{\phi}_r + \omega_p \phi_r = j\dot{\theta} \phi_{rs0} e^{-j\theta_e} \quad (24)$$

where ω_p is the is the electrical pole of each winding

$$\omega_p = \frac{R_r}{L_r}. \quad (25)$$

The electromagnetic torque of eq.(20) results to be p times that of a single pole pair

$$T = p \frac{\phi_{rs0}}{L_r} \text{Im}(\phi_r e^{j\theta_e}). \quad (26)$$

The model holds under rather general input angular speed. The mechanical torque will be determined for the following operating conditions:

- coupler: the angular speed is constant: $\dot{\theta} = \Omega = \text{const}$,
- damper: the rotor is subject to a small amplitude torsional vibration relative to the stator.

Coupler

For constant rotating speed ($\dot{\theta}(t) = \Omega$, $\theta(t) = \Omega t$), the steady state solution of eq.(24) is

$$\phi_r = \phi_{r0} e^{-jp\Omega t}; \quad \phi_{r0} = \frac{j\Omega \phi_{rs0}}{\omega_p - jp\Omega} \quad (27)$$

The torque (T) to speed (Ω) characteristic is found by substituting eq.(27) into eq.(26). The result is the familiar torque to slip speed expression of an induction machine running at constant speed

$$T(\Omega) = \frac{c_0}{1 + (p\Omega)^2 / \omega_p^2} \Omega, \quad \text{where } c_0 = \frac{p\phi_{rs0}^2}{R_r}. \quad (28)$$

A simple understanding of this characteristic can be obtained by referring to the mechanical analogue of Figure 3b. At speeds such that the excitation frequency is lower than the pole ($p\Omega \ll \omega_p$), the main contribution to the deformation is that of the dampers, while the

springs behave as rigid bodies. The resultant force vector acting on point P is due to the dampers and acts perpendicularly to the crank ϕ_{rs0} , this produces a counteracting torque

$$T = c_0 \Omega \quad (29)$$

By converse, at speeds such that $p\Omega \gg \omega_p$ the main contribution to the deformation is that of the springs, while the dampers behave as rigid bodies. The resultant force vector on point P is due to the springs. It is oriented along the crank ϕ_{rs0} and generates a null torque.

Damper

If the rotor oscillates ($\theta(t) = \theta_0 \Re(e^{j\omega t}) + \theta_m$) with small amplitude about a given angular position θ_m , the state eq.(24) can be linearized resorting to the small angle assumption

$$\dot{\phi}_r + \omega_p \phi_r = j\dot{\theta} \phi_{rs0} e^{-jp\theta_m} \quad (30)$$

The solution is found in terms of the transfer function between the rotor flux $\phi_r(s)$ and the input speed $\dot{\theta}(s)$

$$\frac{\phi_r(s)}{\dot{\theta}(s)} = \frac{j\phi_{rs0} e^{-jp\theta_m}}{s + \omega_p}, \quad (31)$$

where s is the Laplace variable. The mechanical impedance $Z_m(s)$, i.e. the torque to speed transfer function is found by substituting eq.(31) into Eq.(26)

$$Z_m(s) = \frac{T(s)}{\dot{\theta}(s)} = \frac{c_{em}}{1 + s / \omega_p} = \frac{c_{em}}{1 + s(k_{em} / c_{em})}. \quad (32)$$

This impedance is that of the series connection of a torsional damper and a torsional spring with viscous damping and spring stiffness given by

$$c_{em} = \frac{p\phi_{rs0}^2}{R_r}, \quad k_{em} = \frac{p\phi_{rs0}^2}{L_r} \quad (33)$$

that are constant parameters. At low frequency ($s \ll \omega_p$), the device behaves as a pure viscous damper with coefficient c_{em} . This is the term that is taken into account in the widespread reactive model. At high frequency ($s \gg \omega_p$) it behaves as a mechanical linear spring with stiffness k_{em} . This term on the contrary is commonly neglected in all the models presented in the literature (Graves et al., 2009), (Nagaya, 1984), (Nagaya & Karube, 1989). The bandwidth of the mechanical impedance (Figure 4b) is due to the electrical circuit resistance and inductance. It must be taken into account for the design of eddy current dampers. The assumption of neglecting the inductance is valid only for frequency lower than the electric pole ($s \ll \omega_p$). The behavior of the mechanical impedance has effects also on the operation of an eddy current coupler. Due to the bandwidth limitations, it behaves as a low pass filter for each frequency higher than the electric pole.

To correlated the torque to speed characteristic of eq.(28) and the mechanical impedance of eq. (32), it should be analyzed that the slope c_0 of the torque to speed characteristic at zero or low speed ($\Omega = p\omega_p$) is equal to the mechanical impedance at zero or low frequency ($s = \omega_p$):

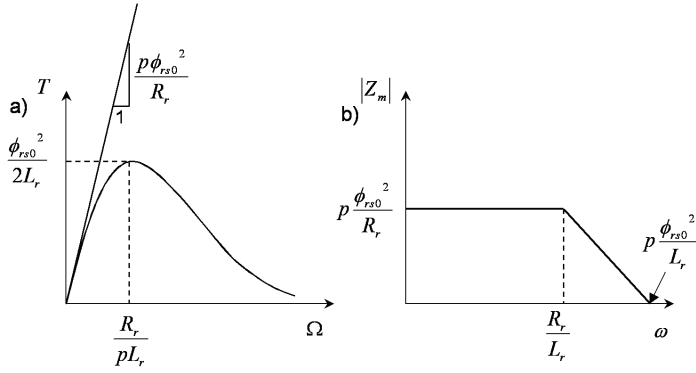


Fig. 4. a) Static characteristic of an axial-symmetric induction machine b) Representation of its mechanical impedance (magnitude in logarithmic scales).

$$c_0 = c_{em} = \frac{p\phi_{rs0}^2}{R_r}. \quad (34)$$

Additionally, the maximum torque (T_{\max}) at steady state is related to the high frequency mechanical impedance ($Z_m(s)$)

$$T_{\max} = \frac{\phi_{rs0}^2}{2L_r}, k_{em} = \frac{p\phi_{rs0}^2}{L_r} \quad (35)$$

The relationship between T_{\max} and $Z_m(s)$ at high frequency is therefore

$$\Omega_{T_{\max}} = \frac{\omega_p}{p}, \quad T_{\max} = \frac{c_{em}\omega_p}{2p} = \frac{k_{em}}{2p} \quad (36)$$

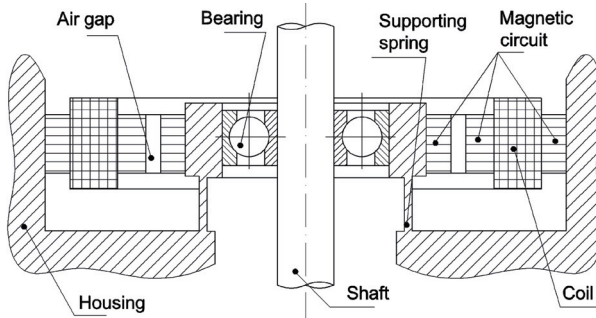


Fig. 5. Sketch of an Active Magnetic Damper in conjunction with a mechanical spring. They both act on the non rotating part of the bearing.

A graphical representation of the relationships between eqs.(35) and (36) is given in Figure 4. They allow to obtain the mechanical impedance and/or the state space model valid under general operating condition, eq.(24), from the torque to speed characteristic. This is of

interest because numerical tools performing constant speed analysis are far more common and consolidated than those dealing with transient analysis. Vice versa, the steady state torque to speed characteristic can be simply obtained identifying by vibration tests the parameters c_{em} and k_{em} (or ω_p).

It's worth to note that eqs.(28), (32) and Eqs.(35), (36) hold in general for eddy current devices with one or more pole pairs. They can be applied also to linear electric machines provided that the rotational degree of freedom is transformed into a linear one.

2.4 Transformer dampers in active mode (AMD)

Transformer dampers can be used in active mode. Active Magnetic Dampers (Figure 5) work in the same way as active magnetic bearings, with the only difference that in this case the force generated by the actuator is not aimed to support the rotor but, in the simplest control strategy, it may be designed just to supply damping; this doesn't exclude the possibility to develop any more complex control strategy. An AMD can be integrated into one of the supports of the rotor. In this concept, a rolling element bearing is supported in the housing via mechanical springs providing the required stiffness. Both the spring and the damper act on the non-rotating part of the support. The stiffness and the load bearing capacity is then provided by the mechanical device while the AMD is used to control the vibrations, adding damping, in its simplest form. It is important to note that the stiffness of the springs can be used to compensate the open loop negative stiffness of a typical Maxwell actuator. This allows to relieve the active control of the task to guarantee the static stability of the system. A proportional-derivative feedback loop based on the measurement of the support displacements may be enough to control the rotor vibrations. Sensors and a controller are then required to this end. Under the assumption of typical Maxwell actuators, the force that each coil of the actuator exerts on the moving part is computed by eq.(11), that can be used to design the actuators once its maximum control force is specified. It's worth to note that such damping devices can be applied to any vibrating system.

2.5 Transformer dampers in active mode and self-sensing operation

The reversibility of the electromechanical interaction induces an electrical effect when the two parts of an electromagnet are subject to relative motion (back electromotive force). This effect can be exploited to estimate mechanical variables from the measurement of electrical ones. This leads to the so-called self-sensing configuration that consists in using the electromagnet either as an actuator and a sensor. This configuration permits lower costs and shorter shafts (and thus higher bending frequencies) than classical configurations provided with sensors and non-collocation issues are avoided. In practice, voltage and current are used to estimate the airgap. To do so, the two main approaches are: the state-space observer approach (Vischer & Bleuler, 1990), (Vischer & Bleuler, 1993) and the airgap estimation using the current ripple (Noh & Maslen, 1997), (Schammass et al., 2005). The former is based on the electromechanical model of the system. As the resulting model is fully observable and controllable, the position and the velocity of the mechanical part can be estimated and fed back to control the vibrations of the system. This approach is applicable for voltage-controlled (Mizuno et al., 1996) and current-controlled (Mizuno et al., 1996) electromagnets. The second approach takes advantage from the current ripple due to the switching amplifiers to compute in real-time the inductance, and thus the airgap. The airgap-estimation can be based on the ripple slope (PWM driven amplifiers, (Okada et al., 1992)) or

on the ripple frequency (hysteresis amplifiers, (Mizuno et al., 1998)). So far in the literature, self-sensing configurations have been mainly used to achieve the complete suspension of the rotor. The poor robustness of the state-space approach greatly limited its adoption for industrial applications. As a matter of fact, the use of a not well tuned model results in the system instability (Mizuno et al., 1996) , (Thibeault & Smith 2002). Instead, the direct airgap estimation approach seems to be more promising in terms of robustness (Maslen et al., 2006).

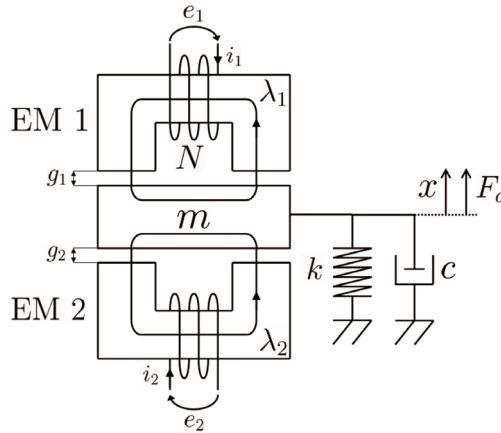


Fig. 6. Schematic model of electromagnets pair to be used for self-sensing modelling.

Here below is described a one degree of freedom mass-spring oscillator actuated by two opposite electromagnets (Figure 6). Parameters m , k and c are the mass, stiffness and viscous damping coefficient of the mechanical system. The electromagnets are assumed to be identical, and the coupling between the two electromagnetic circuits is neglected. The aim of the mechanical stiffness is to compensate the negative stiffness due to the electromagnets.

Owing to Newton's law in the mechanical domain, the Faraday and Kirchoff laws in the electrical domain, the dynamics equations of the system are:

$$\begin{aligned} m\ddot{x} + c\dot{x} + kx + F_1 + F_2 &= F_d \\ \dot{\lambda}_1 + Ri_1 &= v_1 \\ \dot{\lambda}_2 + Ri_2 &= v_2 \end{aligned} \quad (37)$$

where R is the coils resistance and v_j is the voltage applied to electromagnet j . F_d is the disturbance force applied to the mass, while F_1 and F_2 are the forces generated by the coils as in eq. (9).

The system dynamics is linearized around a working point corresponding to a bias voltage v_0 imposed to both the electromagnets:

$$\begin{aligned} i_j &= i_0 \pm i_c \\ v_j &= v_0 \pm v_c, j = 1, 2 \\ F_j(i_j, x) &= \pm F_0 + \Delta F_j \end{aligned} \quad (38)$$

where F_0 is the initial force generated by the electromagnets due to the current $i_0 = v_0 / R$, and ΔF_j is the small variation of the electromagnets' forces. As the electromagnets are identical, $(i_1 - i_0) = -(i_2 - i_0) = i_c$. Therefore, a three-state-space model is used to study the four-state system dynamics described in eq.(37) (Vischer & Bleuler, 1990). The resulting linearized state-space model is:

$$\begin{aligned} \dot{X} &= AX + Bu \\ y &= CX \end{aligned} \quad (39)$$

where A , B and C are the dynamic, action and output matrices respectively defined as:

$$A = \begin{bmatrix} 0 & 1 & 0 \\ -\frac{k+2k_x}{m} & -\frac{c}{m} & \frac{2k_i}{m} \\ 0 & -\frac{k_m}{L_0} & -\frac{R}{L_0} \end{bmatrix}, \quad (40)$$

$$B = \begin{bmatrix} 0 & 0 \\ \frac{1}{m} & 0 \\ 0 & \frac{1}{L_0} \end{bmatrix}, C = [0 \quad 0 \quad 1],$$

with the associated state, input and output vectors $X = \{x, \dot{x}, i_c\}^T$, $u = \{F_d, v_c\}^T$ $y = i_c$.

The terms in the matrices derive from the linearization of the non-linear functions defined in eq. (7) and eq. (9):

$$\begin{aligned} L_0 &= \frac{\Gamma}{x_0}, & k_m &= L_0 \frac{i_0}{x_0}, \\ k_i &= L_0 \frac{i_0}{x_0}, & k_x &= -k_m \frac{i_0}{x_0} \end{aligned} \quad (41)$$

where $\Gamma = \mu_0 N^2 S / 2$ is the characteristic factor of the electromagnets, L_0 , k_i , k_m and k_x are the inductance, the current-force factor, the back-electromotive force factor, and the so-called negative stiffness of one electromagnet, respectively. The open-loop system is stable as long as the mechanical stiffness is larger than the total negative stiffness, i.e. $k + 2k_x > 0$. As eq.(39) describes the open-loop dynamics of the system for small variations of the variables, and the system stability is insured, the various coefficients of A can be identified experimentally.

Due to the strong nonlinearity of the electromagnetic force as a function of the displacement and the applied voltage, and to the presence of end stops that limit the travel of the moving

mass, the linear approach may seem to be questionable. Nevertheless, the presence of a mechanical stiffness large enough to overcome the negative stiffness of the electromagnets makes the linearization point stable, and compels the system to oscillate about it. The selection of a suitable value of the stiffness k is a trade-off issue deriving from the application requirements. However, as far as the linearization is concerned, the larger is the stiffness k relative to $|k_x|$, the more negligible the nonlinear effects become.

2.5.1 Control design

The aim of the present section is to describe the design strategy of the controller that has been used to introduce active magnetic damping into the system. The control is based on the Luenberger observer approach (Vischer & Bleuler, 1993), (Mizuno et al., 1996). The adoption of this approach was motivated by the relatively low level of noise affecting the current measurement. It consists in estimating in real time the unmeasured states (in our case, displacement and velocity) from the processing of the measurable states (the current). The observer is based on the linearized model presented previously, and therefore the higher frequency modes of the mechanical system have not been taken into account. Afterwards, the same model is used for the design of the state-feedback controller.

2.5.2 State observer

The observer dynamics is expressed as (Luenberger, 1971):

$$\dot{\hat{X}} = A\hat{X} + Bu + L\left(y - \hat{y}\right) \quad (42)$$

where \hat{X} and \hat{y} are the estimations of the system state and output, respectively. Matrix L is commonly referred to as the gain matrix of the observer. Eq.(42) shows that the inputs of the observer are the measurement of the current (y) and the control voltage imposed to the electromagnets (u).

The dynamics of the estimation error ε are obtained combining eq. (39) and eq. (42):

$$\dot{\varepsilon} = (A - LC)\varepsilon \quad (43)$$

where $\varepsilon = X - \hat{X}$. Eq. (43) emphasizes the role of L in the observer convergence. The location of the eigenvalues of matrix $(A - LC)$ on the complex plane determines the estimation time constants of the observer: the deeper they are in the left-half part of the complex plane, the faster will be the observer. It is well known that the observer tuning is a trade-off between the convergence speed and the noise rejection (Luenberger, 1971). A fast observer is desirable to increase the frequency bandwidth of the controller action. Nevertheless, this configuration corresponds to high values of L gains, which would result in the amplification of the unavoidable measurement noise y , and its transmission into the state estimation. This issue is especially relevant when switching amplifiers are used. Moreover, the transfer function that results from a fast observer requires large sampling frequencies, which is not always compatible with low cost applications.

2.5.3 State-feedback controller

A state-feedback control is used to introduce damping into the system. The control voltage is computed as a linear combination of the states estimated by the observer, with K as the control gain matrix. Owing to the separation principle, the state-feedback controller is designed considering the eigenvalues of matrix $(A-BK)$.

Similarly to the observer, a pole placement technique has been used to compute the gains of K , so as to maintain the mechanical frequency constant. By doing so, the power consumption for damping is minimized, as the controller does not work against the mechanical stiffness. The idea of the design was to increase damping by shifting the complex poles closer to the real axis while keeping constant their distance to the origin ($|p_1| = |p_2| = \text{constant}$).

2.6 Semi-active transformer damper

Figure 7 shows the sketch of a “transformer” eddy current damper including two electromagnets. The coils are supplied with a constant voltage and generate the magnetic field linked to the moving element (anchor). The displacement with speed \dot{q} of the anchor changes the reluctance of the magnetic circuit and produces a variation of the flux linkage. According to Faraday’s law, the time variation of the flux generates a back electromotive force. Eddy currents are thus generated in the coils. The current in the coils is then given by two contributions: a fixed one due to the voltage supply and a variable one induced by the back electromotive force. The first contribution generates a force that increases with the decreasing of the air-gap. It is then responsible of a negative stiffness. The damping force is generated by the second contribution that acts against the speed of the moving element.

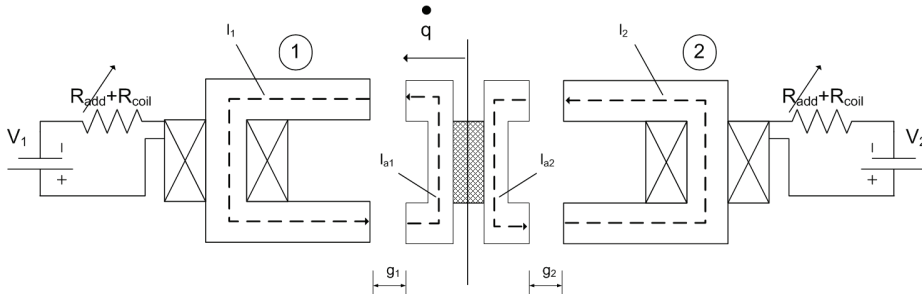


Fig. 7. Sketch of a two electromagnet Semi Active Magnetic Damper (the elastic support is omitted).

According to eq. (9), considering the two magnetic flux linkages λ_1 and λ_2 of both counteracting magnetic circuits, the total force acting on the anchor of the system is:

$$f = \frac{\lambda_2^2 - \lambda_1^2}{\mu_0 N^2 S_{\text{airgap}}} \quad (44)$$

The state equation relative to the electric circuit can be derived considering a constant voltage supply common for both the circuits that drive the derivative of the flux leakage and the voltage drop on the total resistance of each circuit $R = R_{\text{coil}} + R_{\text{add}}$ (coil resistance and additional resistance used to tune the electrical circuit pole as:

$$\begin{aligned}\dot{\lambda}_1 + \alpha R(g_0 - q)\lambda_1 &= V \\ \dot{\lambda}_2 + \alpha R(g_0 + q)\lambda_2 &= V\end{aligned}\quad (45)$$

Where g_0 is the nominal airgap and $\alpha = 2 / (\mu_0 N^2 A)$.

Eqs.(44) and (45) are linearized for small displacements about the centered position of the anchor ($q = 0$) to understand the system behavior in terms of poles and zero structure

$$\begin{aligned}\dot{q} &= v, \\ \dot{\lambda}_1 &= -\alpha R(g_0 \lambda_1' - \lambda_0 q), \\ \dot{\lambda}_2 &= -\alpha R(g_0 \lambda_2' + \lambda_0 q),\end{aligned}\quad (46)$$

$$F_{em} = \alpha \lambda_0 (\lambda_2' - \lambda_1'). \quad (47)$$

The term $\lambda_0 = V / (\alpha g_0 R)$ represents the magnetic flux linkage in the two electromagnets at steady state in the centered position as obtained from eq.(45) while λ_1' and λ_2' indicate the variation of the magnetic flux linkages relative to λ_0 .

The transfer function between the speed \dot{q} and the electromagnetic force F shows a first order dynamic with the pole (ω_{RL}) due to the R-L nature of the circuits

$$\begin{aligned}\frac{F_{em}}{\dot{q}} &= \frac{1}{s} \frac{K_{em}}{(1 + s / \omega_{RL})}, \\ \left(K_{em} &= -\frac{2V^2 / R}{g_0^2 \omega_{RL}}, \quad \omega_{RL} = \frac{R}{L_0}, \quad L_0 = \frac{\mu_0 N^2 A}{2g_0} \right).\end{aligned}\quad (48)$$

L_0 indicates the inductance of each electromagnet at nominal airgap.

The mechanical impedance is a band limited negative stiffness. This is due to the factor $1/s$ and the negative value of K_{em} that is proportional to the electrical power ($K_m \geq -K_{em}$) dissipated at steady state by the electromagnet.

The mechanical impedance and the pole frequency are functions of the voltage supply V and the resistance R whenever the turns of the windings (N), the air gap area (A) and the airgap (g_0) have been defined. The negative stiffness prevents the use of the electromagnet as support of a mechanical structure unless the excitation voltage is driven by an active feedback that compensates it. This is the principle at the base of active magnetic suspensions.

A very simple alternative to the active feedback is to put a mechanical spring in parallel to the electromagnet. In order to avoid the static instability, the stiffness K_m of the added spring has to be larger than the negative electromechanical stiffness of the damper ($K_m \geq -K_{em}$). The mechanical stiffness could be that of the structure in the case of an already supported structure. Alternatively, if the structure is supported by the dampers themselves, the springs have to be installed in parallel to them. As a matter of fact, the mechanical spring in parallel to the transformer damper can be considered as part of the damper.

Due to the essential role of that spring, the impedance of eq.(48) is not very helpful in understanding the behavior of the damper. Instead, a better insight can be obtained by studying the mechanical impedance of the damper in parallel to the mechanical spring:

$$\frac{F_{em}}{v} = \frac{1}{s} \left(\frac{K_{em}}{(1+s/\omega_{RL})} + K_m \right) = \frac{K_{eq}}{s} \frac{1+s/\omega_z}{1+s/\omega_{RL}} \quad (49)$$

where $K_{eq} = K_m + K_{em}$; $\omega_z = \omega_{RL} \frac{K_{eq}}{K_m}$.

Apart from the pole at null frequency, the impedance shows a zero-pole behavior. To ensure stability ($0 < -K_{em} < K_m$), the zero frequency (ω_z) results to be smaller than the pole frequency ($0 < \omega_z < \omega_{RL}$).

Figure 8a underlines that it is possible to identify three different frequency ranges:

1. Equivalent stiffness range ($\omega \ll \omega_z < \omega_{RL}$): the system behaves as a spring of stiffness $K_{eq} > 0$.
2. Damping range ($\omega_z < \omega < \omega_{RL}$): the system behaves as a viscous damper of coefficient

$$C = \frac{K_m}{\omega_{RL}} \quad (50)$$

3. Mechanical stiffness range ($\omega_z < \omega_{RL} \ll \omega$): the transformer damper contribution vanishes and the only contribution is that of the mechanical spring (K_m) in series to it.

A purely mechanical equivalent of the damper is shown in Figure 8b where a spring of stiffness K_{eq} is in parallel to the series of a viscous damper of coefficient C and a spring of stiffness $-K_{em}$. Due to the negative value of the electromagnetic stiffness, $-K_{em}$ is positive. It is interesting to note that the resulting model is the same as Maxwell's model of viscoelastic materials. At low frequency the system is dominated by the spring K_{eq} while the lower branch of the parallel connection does not contribute. At high frequency the viscous damper "locks" and the stiffnesses of the two springs add. The viscous damping dominates in the intermediate frequency range.

Eq. (50) shows that the product of the damping coefficient C and the pole frequency ω_{RL} is equal to the mechanical spring stiffness K_m . A sort of constant gain-bandwidth product therefore characterizes the damping range of the electromechanical damper. This product is just a function of the spring stiffness included in the damper. The constant gain-bandwidth means that for a given electromagnet, an increment of the added resistance leads to a higher pole frequency (eq. (48)) but reduces the damping coefficient of the same amount. Another interesting feature of the mechanical impedance of eq. (49) is that the only parameters affected by the supply voltage V are the equivalent stiffness (K_{eq}) and the zero-frequency (ω_z). The damping coefficient (C) and the pole frequency (ω_{RL}) are independent of it.

The substitution of the electromechanical stiffness K_{em} of eq. (48) into eq. (49) gives the zero frequency as function of the excitation voltage

$$\omega_z = \omega_{RL} \left(1 - \frac{2V^2/R}{g_0^2 \omega_{RL} K_m} \right). \quad (51)$$

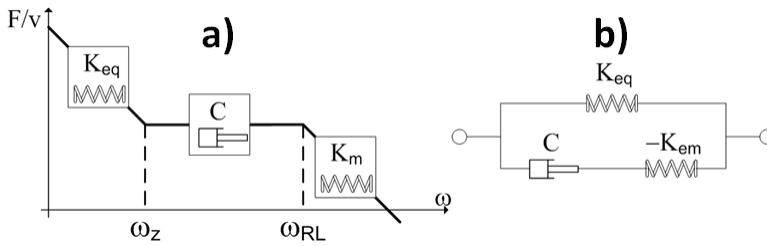


Fig. 8. a) mechanical impedance of a transformer eddy current damper in parallel to a spring of stiffness K_m . b) Mechanical equivalent.

The larger the supply voltage the smaller the zero frequency and the larger the width of the damping region. If $V=0$, there are no electromagnetic forces and the damper reduces to the mechanical spring. The outcome on the mechanical impedance of a null voltage is that the zero and the pole frequency become equal. By converse, the largest amplitude of the damping region is obtained in the limit case when $K_m = -K_{em}$, i.e. when the mechanical stiffness is equal to the negative stiffness of the electromagnet. In this case the equivalent stiffness and therefore the zero frequency are null. As a matter of fact, this last case is of little or no practical relevance as the system becomes marginally stable.

The equations governing the damping coefficient, the zero and electric pole (eq. (49) - eq. (51)) outline a design procedure of the damper for a given mechanical structure. Starting from the specifications, the procedure allows to compute the main parameters of the damper.

2.6.1 Specifications

The knowledge of (a) the resonant frequencies at which the dampers should be effective and (b) the maximum acceptable response allows to specify the needed value of the damping coefficient (C). The pole and zero frequencies (ω_{RL}, ω_z) have been decided so as the relevant resonant frequencies fall within the damping range of the damper. Additionally, tolerance and construction technology considerations impose the nominal airgap thickness g_0 . Electrical power supply considerations lead to the selection of the excitation voltage V .

2.6.2 Definition of the SAMD parameters

The mechanical stiffness K_m can be obtained from eq. (50) once the pole frequency (ω_{RL}) and the damping coefficient (C) are given by the specifications.

The electromechanical parameters of the damper: i.e. the electromechanical constant N^2A , and the total resistance R can be determined as follows:

- the required electrical power V^2/R is obtained from eq. (51). The knowledge of the available voltage V allows then to determine the resistance R .
- The electromechanical constant N^2A is then found from eq. (48).

3. Experimental results

The present section is devoted to the experimental validation of the models described in section 2. Two different test benches were used. The former is devoted to validate the

models of the motional eddy current dampers while the latter is used to perform experimental tests on the transformer dampers in active mode (both in sensor and sensorless configuration), and semi-active mode.

3.1 Experimental validation of the motional eddy current dampers

The aim of the present section is to validate experimentally the model of the eddy current damper presented in section 2.3; in detail, the experimental work is addressed

- to confirm that the mechanical impedance ($Z_m(s)$) of a motional eddy current damper is given by the series of a viscous damper with damping coefficient c_{em} and a linear spring with stiffness k_{em} ,
- c. to validate experimentally that the torque to constant speed characteristic ($T(\Omega)$) of a torsional damper operating as coupler or brake is described by the same parameters c_{em} , k_{em} and k_{em} characterizing the mechanical impedance ($Z_m(s)$).
- to validate the correlation between the torque to speed characteristic and the mechanical impedance.

3.1.1 Induction machine used for the experimental tests

A four pole pairs ($p = 4$) axial flux induction machine has been realized for the steady state (Figure 9) and vibration tests (Figure 10). The magnetic flux is generated by permanent magnets while energy is dissipated in a solid conductive disk. The first array of 8 circular permanent magnets is bonded on the iron disk (1) with alternate axial magnetization. The second array is bonded on the disk (2) with the same criterion. Three calibrated pins (9) are used to face the two iron disk - permanent magnet assemblies ensuring a 1 mm airgap between the conductor and the magnet arrays. They are circumferentially oriented so that the magnets with opposite magnetization are faced to each other. In the following such an assembly is named "stator". The conductor disk (4) is placed in between the two arrays of magnets and is fixed to the shaft (6). It can rotate relative to the stator by means of two ball bearings installed in the hub (7 in Figure 10). Table 1 collects the main features of the induction machine.

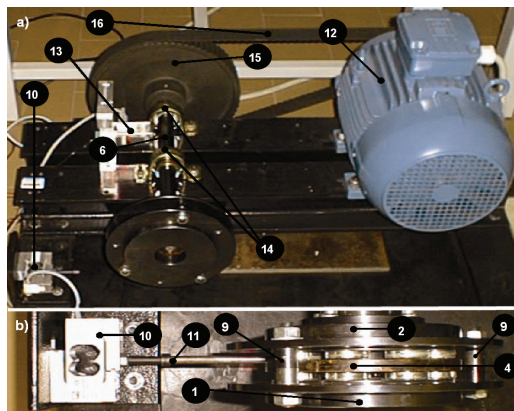


Fig. 9. Test rig used for the identification of the motional eddy current machine operating at steady state. a) View of the test rig. b) Zoom in the induction machine.

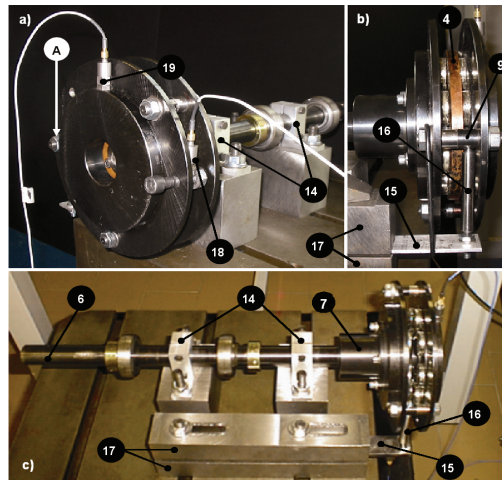


Fig. 10. Test rig configured for the vibration tests. a) Front, side view zoomed in the induction machine. The impulse hammer force is applied at Point A. b) Lateral view of the induction machine. c) Top view of the whole test rig.

Feature	Unit	Value
Number of pole pairs	--	4
Diameter of the magnets	Mm	30
Thickness of the magnets	Mm	6
Magnets geometry	--	Circular
Magnets material	--	Nd-Fe-B (N45)
Residual magnetization of the magnets	T	1.22
Thickness of conductor	Mm	7
Conductivity of conductor (Cu)	$\Omega^{-1}\text{m}^{-1}$	5.7×10^7
Air gap	Mm	1

Table 1. Main features of the induction machine used for the tests.

3.1.2 Experimental characterization at steady state

The experimental tests at steady state were carried out to identify the slope c_0 of the torque to speed characteristic at zero or low speed and the pole frequency ω_p . Three type of tests, defined as "run up", "constant speed" and "quasi - static" have been carried out to this end.

Test rig set up (Figure 9). The electric motor (12 - asynchronous induction motor with rated power = 2.2 kW) drives the shaft (6) through the timing belt (16). The conductor disk (4) rotates with the shaft (6) being rigidly connected to it. The rotation of the stator is constrained by the bar (11) which connects one of the three pins of the stator to the load cell fixed to the basement. The tests at steady state are carried out by measuring the torque generated at different slip speeds Ω . The torque is obtained from the measurement of the tangential force while the slip speed Ω is measured using the pick up (13).

Run up tests. They are related to a set of speed ramps performed with constant acceleration. The ramp slopes have been chosen to ensure the steady state condition (a), the minimum temperature drift (b) and an enough time interval to acquire a significant amount of data (c). The rated power of the electric motor (12) limits the slip speed to 405 rpm that does not correspond to the maximum torque velocity ($\Omega_{T_{max}}$). Nevertheless, the inductive effects are evidenced allowing the identification of the electric pole ω_p (see Figure 11).
Constant Speed Tests. A second set of tests was carried out by measuring the counteracting torque with the induction machine rotating at a predefined constant slip speed. The aim is to increase the number of the data at low velocities where the run ups have not supplied enough points and to confirm the results acquired with the run up procedure.

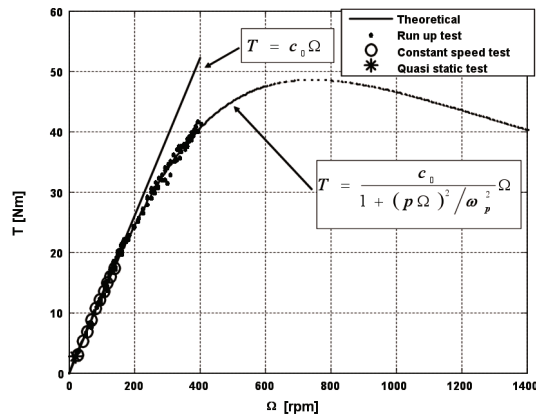


Fig. 11. Experimental results of the induction machine characterization at steady state.

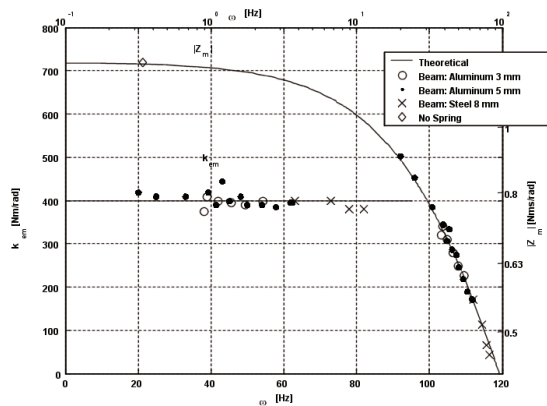


Fig. 12. Identified values of k_{em} in the frequency range 20–80 Hz. Full line, k_{em} mean value obtained as best fit of the experimental points. The experimental points of Z_m are plotted with reference to the top-right scale. Full line, Z_m plotted using $c_{em}=c_0$ and $k_{em} = \bar{k}_{em}$.

The results of the constant speed tests are plotted in the graph of Figure 11 with circle marks. Each point represents the average value of a set of 5 tests. The results are consistent with the expected trend and allow to get more experimental points at low speeds.

Quasi-Static Tests. The aim of the quasi static tests is to characterize the slope c_0 of the torque to speed curve at very low speed where eq.(28) reduces to $T = c_0\Omega$ (eq. (29)).

A motor driven test is not adequate for an accurate identification of c_0 as the inverter cannot control the electric motor at rotational speeds lower than 40 rpm. The test set up was then modified locking the rotation of the shaft (6) connected to the conductor disk and enabling the rotation of the stator assembly. The driving torque was generated by a weight force (mg) acting tangentially on the stator. This is realized using a ballast (mass m) connected to a thread wound about the hub (7).

Under the assumption of low constant speed, the slope c_0 can be expressed as

$$c_0 = \frac{mg\Delta t}{\Delta x} r^2 \quad (52)$$

where Δt indicates the time interval required for the force mg to perform the work $L = mg\Delta x$ while r represents the radius of the hub ($m = 0.495 \text{ kg}$, $\Delta x = 1.54 \text{ m}$, $r = 32 \text{ mm}$). The tests have been carried out by measuring the time interval the ballast needs to cover the distance Δx . A set of 5 tests leads to an average slope $c_0 = 1.24 \text{ Nms/rad}$ (max deviation = 5%). The corresponding torque ($T_{quasi_static} = 2.67 \text{ Nm}$ and speed ($\Omega_{quasi_static} = 20.5 \text{ rpm}$) are reported as the lowest experimental point (asterisk mark *) in the torque to speed curve of Figure 11. It agrees with the trend of the experimental data obtained at low speed during the motor driven tests.

Results of the Characterization at Steady State. The electric pole ω_p was identified as best fit of the experimental points reported in the graph of Figure 11 with the model of eq.(28). Being c_0 already known from the quasi static tests, the identified value of ω_p is

$$\omega_p = 51.1 \text{ Hz}, \quad (c_0 = 1.24 \text{ Nms/rad}). \quad (53)$$

The full line curve plotted in Figure 11 was obtained using the identified values of c_0 and ω_p . The good correlation between the identified model and the experimental results can be considered as a proof of the validity of the steady state model in the investigated speed range. It derives that the maximum torque and the relative speed that characterize the induction machine operating at steady state are

$$T_{\max} = \frac{c_0\omega_p}{2p} = 49.8 \text{ Nm}, \quad \Omega_{T_{\max}} = \frac{\omega_p}{p} = 766 \text{ rpm}. \quad (54)$$

3.1.3 Vibration tests

The aim of the vibration tests is to validate experimentally the mechanical impedance of eq.(32) using the same induction machine adopted for the constant speed experimental characterization presented in section 3.1.2.

Test Rig set up. The test rig used for the steady state characterization was modified to realize a resonant system. The objective is to identify the parameters c_{em} and k_{em} from the response at the resonant frequency. To this end the rotation of the conductor disk (4 - Figure

10) was constrained by two rigid clamps (14) connected to the basement (a 300 kg seismic mass). The torsional spring is realized by a cantilever beam acting tangentially on the stator. Its free end is connected to one of the pins (9) by the axially rigid bar (16) while the constrained one is clamped by two steel blocks (17) bolted to the basement. The beam stiffness can be modified by varying its free length. This is obtained by sliding the blocks (17) relative to it. A set of three beams with different Young modulus and thickness (aluminum 3 and 5 mm, steel 8 mm) were used to cover the frequency range spanning from 20 Hz to 80 Hz. It's worth to note that the expected pole $\omega_p = 52$ Hz falls in the frequency range.

Impact tests using an instrumented hammer and two piezoelectric accelerometers were adopted to measure the frequency response between the tangential force (input) and the tangential accelerations (outputs), both applied and measured on the stator. Instrumented hammer and accelerometer signals are acquired and processed by a digital signal analyzer.

Identification Procedure. The identification of the electromechanical model parameters was carried out by the comparison of the numerical and experimental transfer function $T(s) / \hat{\theta}(s)$. The procedure leads to identify the damping coefficient c_{em} and the electrical pole ω_p (or the spring stiffness k_{em} being $\omega_p = k_{em} / c_{em}$) of the spring-damper series model of eq.(32). The value of the electromechanical damping obtained from the steady state characterization ($c_0 = 1.24$ Nms / rad) is assumed to be valid also in dynamic vibration conditions ($c_{em} = c_0$). Even if this choice blends data coming from the static and the dynamic tests, it does not compromise the validity of the identification procedure and has been adopted to reduce the number of unknown parameters. Additionally it allows to perform the dynamic characterization by means of impact tests only. As a matter of fact, the best sensitivity for the identification of c_{em} could be obtained by setting the resonant frequency very low compared to the electrical pole (e.g. in the range of $\omega_p / 10$). The values of the static damping, combined with low stiffness required in this case would imply a nearly critical damping of the resonant mode. This would make the impact test very unsuitable to excite the system.

The model used for the identification is characterized by a single degree of freedom torsional vibration system whose inertia is that of the stator ($J = 0.033$ kgm²). The contribution of the cantilever beam and of the electromagnetic interaction are taken into account by a mechanical spring with structural damping $k_m(1 + i\eta)$ in parallel to the spring-viscous damper series of electromagnetic stiffness k_{em} and electromagnetic damping c_{em} .

The procedure adopted for the identification is the following:

- Impact test without conductor disk to identify the mechanical spring stiffness k_m and the related structural damping η . This test is repeated for each resonance which is intended to be investigated.
- Assembly of the conductor disk. This step is carried out without modifying the set up of the bending spring whose stiffness k_m and damping η have been identified at the previous step.
- Impact test with conductor disk.
- Identification of the electromechanical stiffness k_{em} that allows the best fit between the numerical and experimental transfer function.

The procedure is repeated for 23 resonances in the frequency range 20-80 Hz. Figure 13 shows the comparison between the measured FRF and the transfer function of the identified model in the case of undamped (a) and damped (b) configuration at a resonance of 34 Hz.

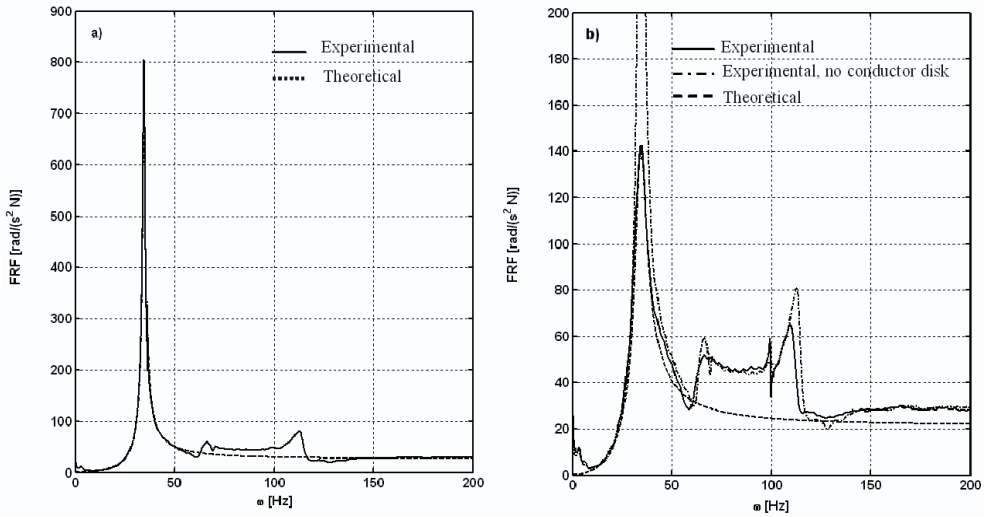


Fig. 13. Example of numerical and experimental FRF comparison. a) Identification of the torsional stiffness k_m and of the structural damping η b) Identification of k_{em} using for c_{em} the value obtained by the weight-driven tests ($c_{em}=1.24$ Nms/rad).

The close fit between the model and the experiments indicates that:

- the dynamic model and the relative identification procedure are satisfactory for the purpose of the present analysis.
- the differential setup adopted for the measurement (accelerations) eliminates the contribution of the flexural modes from the output response.
- the higher order dynamics (in the range 60 - 120 Hz for the resonance at 34 Hz) are probably due to a residual coupling that does not affect the identification of k_{em} . The comparison of the experimental curves in Figure 13b) highlights how the not modeled vibration motion influences the test with and without conductor disk in the same manner.

Figure 12 shows the results of the identification procedure. The values of the stiffness k_{emr} as identified in each test, are plotted as function of the relevant resonant frequency. Its mean value is

$$\bar{k}_{em} = 399.8 \text{ Nm/rad} \quad (55)$$

and is plotted as a full line. A standard deviation of 15.24 Nm/rad (3.8% of the mean value \bar{k}_{em}) is considered as a proof of the validity of the mechanical impedance model described by eq.(32). Adopting for c_{em} the damping obtained from the weight - driven test ($c_{em} = c_0 = 1.24$ Nms/rad) and for k_{em} the values identified by each vibration tests, the experimental points of Z_m , as reported in Figure 12, are obtained. The full line in the same graph refers to eq.(32) in which are adopted for c_{em} and k_{em} the following parameter: $c_{em} = c_0 = 1.24$ Nms/rad and $k_{em} = \bar{k}_{em} = 399.8$ Nm/rad. From that values it follows that the pole ω_p is

$$\omega_p = \bar{k}_{em} / c_{em} = 51.2 \text{ Hz} \quad (56)$$

The comparison proves the validity of the models. The small scattering of the experimental points about the mean value confirm the high predictability of the eddy current dampers and couplers with the operating conditions.

3.2 Experimental validation of the transformer dampers

Figure 14a shows the test rig used for the experimental characterization of the Transformer dampers in active (sensor feedback (AMD) and self-sensing (SSAMD)) and semiactive (SAMD) configuration. It reproduces a single mechanical degree of freedom. A stiff aluminium arm is hinged to one end while the other end is connected to the moving part of the damper. The geometry adopted for the damper is the same of a heteropolar magnetic bearing. This leads to negligible stray fluxes, and makes the one-dimensional approximation acceptable for the analysis of the circuit.

The mechanical stiffness required to avoid instability is provided by additional springs. Two sets of three cylindrical coil springs are used to provide the arm with the required stiffness. They are preloaded with two screws that allow to adjust the equilibrium position of the arm. Attention has been paid to limit as much as possible to the friction in the hinge and between the springs and the base plates. To this end the hinge is realized with two roller bearings while the contact between the adjustment screws and the base plates is realized by means of steel balls. Mechanical stops limit to ± 5 degrees the oscillation of the arm relative to the centred position.

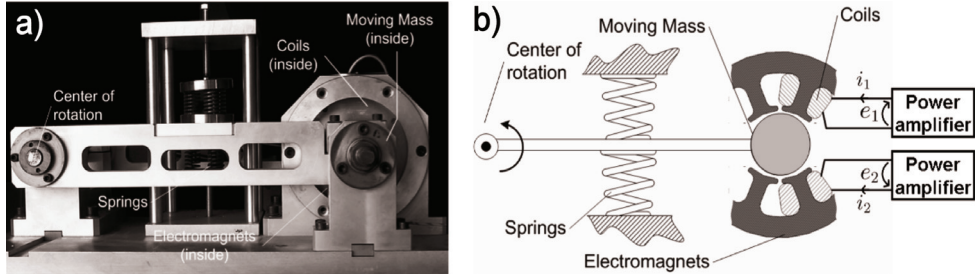


Fig. 14. a) Picture of the test rig b) Test rig scheme.

As shown in Figure 14b, the actuator coils are connected to the power amplifier. If it is simply a voltage supply, the system works in semi active mode while, when the power amplifier drives the coils as a current sink, the active configuration is obtained. If the current value is computed starting from the information of the position sensor, the damper works in sensor mode, otherwise, if the movement is estimated by using a technique as that described in section 2.5, the self-sensing operation is obtained.

3.2.1 Active Magnetic Damper (AMD)

When the Transformer damper is configured to operate in AMD mode, the position of the moving part is measured by means of an eddy current position sensors. Referring to Figure 15 the control system layout is completely decentralized.

Feature	Unit	Value
Damper- hinge distance	mm	320
Spring stiffness	N/m	6x30000
Hinge-spring system axis distance	mm	160
Magnetic circuit laminations	--	8 caves/4 electromagnets
Number of turns/electromagnet	--	142
Nominal air gap	mm	0.5
Air gap active area	mm ²	420
Coil Resistance	Ω	0.4
Additional Resistance	Ω	1.0
Coil inductance at nominal air gap	mH	10.2

Table 2. Main features of the Transformer damper test bench.

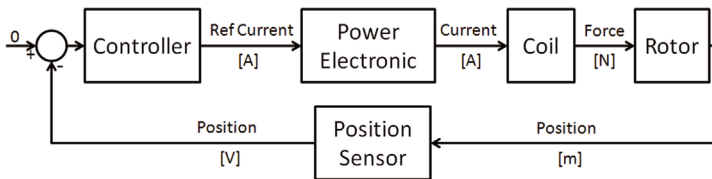


Fig. 15. Scheme of the complete control loop used in the AMD configuration.

The position signal is fed back into the corresponding controller and acts on the collocated electromagnet. The controller transfer function, capable to provide the required damping (by a simple PD control loop), is:

$$\frac{\text{Ref Current}}{\text{Position}} = \frac{1.22 \cdot 10^8 (s + 13.25)}{(s + 383.3)(s + 1339)} \left[\frac{A}{m} \right] \quad (57)$$

The controller output is fed in the power electronic (full H-bridge switching) which current control loop assures an unitary gain and bandwidth@-3dB of about 1kHz.

The AMD and current loops are implemented on a DSP based electronic board.

The damping performances are evaluated comparing the time response of the closed-loop with the open-loop system when an impulse excitation is applied to the system. The impulse excitation is obtained by hitting the system with a hammer. In Figure 16, the open-loop system response (dashed line) is compared to the closed-loop one when the feedback controller, reported in eq.(57), is activated.

3.2.2 Self-Sensing Active Magnetic Damper (SSAMD)

The validation of the damper in self-sensing configuration was carried out by implementing in the DSP based electronic board used for AMD, the observer-controller described in section 2.5. The current flowing into the coils is measured by means of a hall current sensor and is fed back into the corresponding observer-controller. The controller output acts on the collocated electromagnet. Observer and controllers parameters (poles) are reported in Table 3.

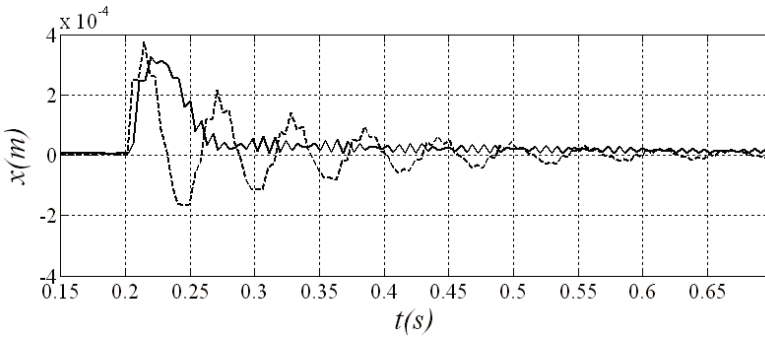


Fig. 16. Time response of the test rig to an impulse excitation. The time response of the system in two different configurations is plotted as follows: open-loop (dashed line) and closed-loop based with the AMD controller (solid line).

	Poles
Open Loop System	$p_1 = -3.32 + 113.35j$
	$p_2 = -3.32 - 113.35j$
	$p_2 = -62.6$
Observer $eig(A - LC)$	$p_1 = -99.74 + 113.35j$
	$p_1 = -99.74 - 113.35j$
	$p_2 = -626.09$
State-feedback controller $eig(A - BK)$	$p_1 = -29.92 + 109.38j$
	$p_1 = -29.92 - 109.38j$
	$p_2 = -500.87$

Table 3. Main features of the Transformer damping in different control configuration.

The open-loop voltage-to-displacement transfer function obtained from the model and the experimental tests are compared in Figure 17a. The correspondence between the two plots is considered a good validation of the model. The same transfer functions in closed-loop operation with the controller designed in section 2.5 are compared in Figure 17b. Also in this case, the correspondence is quite good. This is a proof of the self sensing control strategy validity. The damping performances are evaluated by analyzing the time response of the closed-loop system when an impulse excitation is applied to the system.

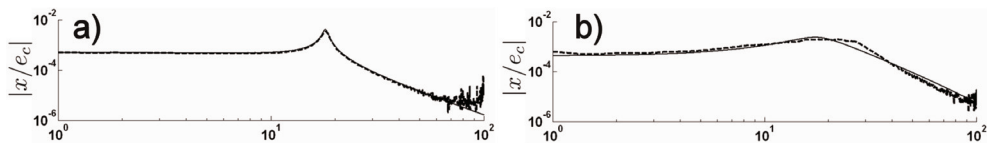


Fig. 17. Frequency response of the test rig in (a) open-loop and (b) closed-loop configuration compared to the model. Solid and dashed lines are the model and the plant frequency responses, respectively.

The impulse excitation is obtained by hitting the system with a hammer. In Figure 18, the open-loop system response (dashed line) is compared to the closed-loop one when the observer and state-feedback controller are designed from a model based on the nominal value of the system parameters. This result is worthy, as it shows that good damping can be achieved for active magnetic dampers obtained with the simplified model. Furthermore, this controller does not destabilize the system, as it is the case for full suspension self-sensing configurations.

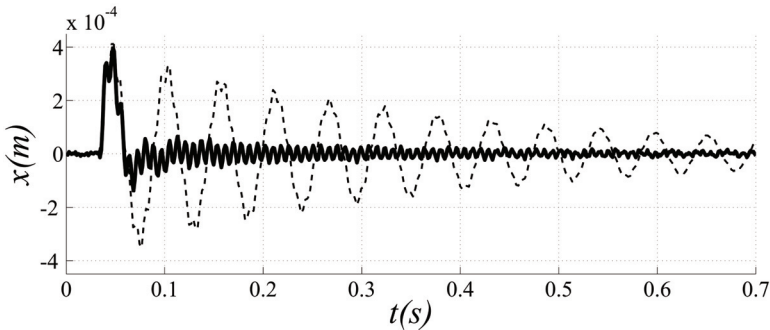


Fig. 18. Time response of the test rig to an impulse excitation. The time response of the system in two different configurations open-loop (dashed line) and closed-loop based on the identified model (solid line) is plotted.

3.2.3 Semi Active Magnetic Damper (SAMD)

As shown in the Figure 14b, the electrical terminals of each electromagnet are driven by a voltage power supply and (not shown) are connected in series to an additional resistance. The value of the additional resistance can be modified to tune the electrical pole frequency. The natural frequency of the mechanical system can be modified selecting coil spring with appropriate stiffness. During tests the mechanical frequency was set at 19 Hz and the electrical pole at 22.3 Hz. The main numerical parameters of the experimental set up are collected in Table 2.

The validation was performed by comparing the transfer function (FRF) between the input force and the output acceleration obtained from the experimental tests and that obtained from the model. The input force was actuated by means of an instrumented hammer; the acceleration was measured using an accelerometer. The impact point and the accelerometer are close to the end of the rigid arm. A first series of tests was performed with null excitation voltage.

The transfer functions obtained from the model are then compared in Figure 19a to the experimental ones for various excitation voltages.

Solid thick lines in the figure indicate the results from the model while the thin lines refer to the experimental results. The correlation between the numerical and experimental results confirms the validity of the adopted modelling approach and of the underlying assumptions.

As predicted by the model, increasing the voltage supply increases the damping range of the transformer damper. The modal damping is increased of a factor of about 20 from 0.0073

to 0.153 with a power expense of 1.4 W. Even if the damping is increased at the cost of a reduction of the resonant frequency, the large added damping demonstrates the effectiveness of the SAMDs. From the point of view of the required power the results obtained from the single degrees of freedom test bench demonstrates the need of electromagnets with small airgap and optimised geometry.

The non linear effects are also investigated. The system has been excited with impulse forces of increasing intensity and leaving constant the voltage supply. Impulse intensities are chosen so that the amplitude of the oscillation at the beginning of the transient are in a range 0.1-0.6 of the available airgap. The free oscillations due to different initial airgaps are reported in Figure 19b (voltage supply equal to 0.75 V). Higher displacements are not allowed due to the attractive force of the electromagnets that makes the system unstable.

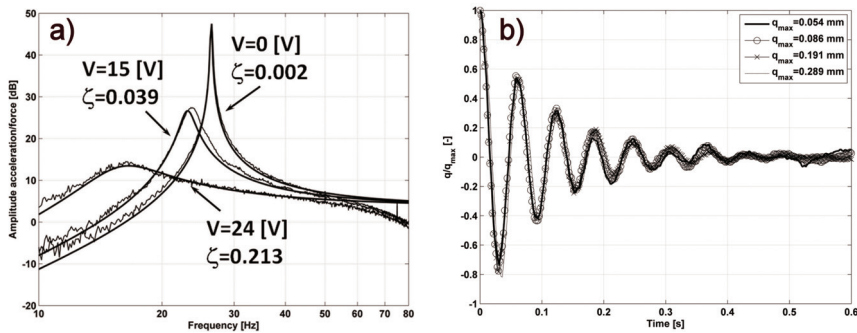


Fig. 19. a) Frequency response with various supply voltage for the SAMD b) Time response with various electromagnets airgaps for the SAMD.

4. Conclusions

The chapter describes the modelling and the experimental validation of different types of electromagnetic actuators used to damp the vibration in mechanical structures and machines. The first section describes the theoretical background based on an energetic approach. Section 2 is devoted to the description and analysis of possible configurations of electromagnetic actuators. The analysis is supported by the modelling of the different configurations. In section 3 the experimental validation is presented for four different types of damping devices: motional eddy current, transformer active based on sensor signal feedback, transformer active based on self sensing feedback and transformer semi-active.

The analyses described in the present chapter lead to the following results:

- the vibration response of a motiona eddy current damper can be modeled as the series connection of a linear mechanical spring and a viscous damper. In general an eddy current machine behaves as a crank whose end is connected to two spring/damper series acting along orthogonal directions.
- The mechanical impedance is a band limited function affected by the pole of the electric circuit. The band limitation can be usefully exploited in vibration isolation systems addressed either to reduce the vibration at the fundamental resonant frequency and to

- minimize the transmissibility of higher excitation frequency. This feature is of interest also for eddy current couplers. A proper positioning of the electric pole allows to drive a load with a continuous torque filtering out the torque irregularities.
- The parameters describing the behavior of a motional eddy current damper are related to that of the same device operating at constant speed according to the "conversion rules" presented section 2.3.
 - The technology of magnetic bearings can be adopted as damping systems if a mechanical element is introduced to stabilize statically the system. The static stability of the system allows the adoption of self sensing techniques to feedback the state of the structure to be damped. It has been shown that the damping performance of the Luenberger observer based approach are comparable to the control strategies based on the position sensor feedback.
 - Electromagnets as that adopted for magnetic bearings can be adopted also as passive or semi-active damping systems if a constant voltage is supplied to them. In section 1.6 it was shown that a mechanical impedance of a transformer damper parallel to a mechanical spring is characterized by a zero and a pole. At frequencies lower than the zero and higher than the pole, the device behaves as a mechanical spring. Between the zero and the pole, it operates as a pure viscous damper. The frequency of the pole can be tuned by adding an external resistance in series to the coil resistance.

5. References

- Ahn, Y. K., Yang, B-S. & Morishita S. (2002). Directional Controllable Squeeze Film Damper Using Electro-Rheological Fluid, *ASME Journal of Vibration and Acoustics*, Vol. 124, pp. 105-109.
- Crandall, S. H., Karnopp, D., Kurtz, E. F, Pridmore-Brown, E. C. (1968), *Dynamics of Mechanical and Electromechanical Systems*, New York: McGraw-Hill.
- Genta, G. (2004), *Dynamics of Rotating Systems*, Springer Verlag.
- Genta, G., Festini, A., De Lépine, X. (2008) From oil to magnetic fields: active and passive vibration control, *Acta mechanica et automatica*, 2(2), pp. 11-20.
- Genta, G., Tonoli, A., Amati, N., Macchi, P., Silvagni, M., and Carabelli, S. (2006), More electric aeroengines: tradeoff between different electromagnetic dampers and supports, *Tenth International Symposium on Magnetic bearings*, EPFL, 21-23 Aug., Martigny, Switzerland.
- Graves, K. E., Toncich, D., Iovenitti, P. G. (2000), Theoretical Comparison of the Motional and Transformer EMF Device Damping Efficiency, *Journal of Sound and Vibration*, Vol. 233, No. 3, pp 441-453.
- Kamerbeek, E. M. H. (1973), *Electric motors*¹, Philips tech. Rev., vol. 33, pp. 215--234.
- Karnopp, D. (1989), Permanent Magnets Linear Motors used as Variable Mechanical Damper for Vehicle Suspension, *Vehicle System Dynamics*, Vol. 18, pp. 1 87-200.
- Karnopp, D., Margolis, D. L., Rosenberg, R. C. (1990), *System Dynamics: a Unified Approach*, J. Wiley & Sons.
- Kligerman, Y. , Gottlieb, O. (1998), Dynamics of a Rotating System with a Nonlinear Eddy-Current Damper, *ASME Journal of Vibration and Acoustics*, Vol. 120, pp. 848-853.

- Kligerman, Y., Grushkevich, A., Darlow, M. S. (1998), Analytical and Experimental Evaluation of Instability in Rotordynamics System with Electromagnetic Eddy-Current Damper, *ASME Journal of Vibration and Acoustics*, Vol. 120, pp. 272-278.
- Luenberger, D. G. (1971), An introduction to observers, *IEEE Trans. Autom. Contr.*, AC-16(6), pp. 596-602.
- Maslen, E. H., Montie, D., T., Iwasaki, T. (2006), Robustness limitations in self-sensing magnetic bearings, *Journal of Dynamic Systems, Measurement and Control*, 128, pp. 197-203.
- Meisel, J. (1984), *Principles of Electromechanical Energy Conversion*, Robert Krieger, Malabar, Florida.
- Mizuno, T., Araki, K., Bleuler, H., (1996), Stability analysis of self-sensing magnetic bearing controllers, *IEEE Transaction of Control System and Technology*, 4(5), pp. 572-579.
- Mizuno, T., Namiki, H., Araki, K., (1996), Self-sensing operations of frequency-feedback magnetic bearings, *Fifth International Symposium on Magnetic Bearings*, 29-30 Aug., Kanazawa, Japan, pp. 119-123.
- Mizuno, T., Ishii, T., Araki, K. (1998), Self-sensing magnetic suspension using hysteresis amplifier, *Cont. Eng. Pract.*, 6, pp. 1133-1140.
- Nagaya, K. (1984), On a Magnetic Damper Consisting of a Circular Magnetic Flux and a Conductor of Arbitrary Shape. Part I: Derivation of the Damping Coefficients, *Journal of Dynamic Systems, Measurement and Control*, Vol. 106, pp. 46-51.
- Nagaya, K., Karube, Y. (1989), A Rotary Magnetic Damper or Brake Consisting of a Number of Sector Magnets and a Circular Conductor, *Journal of Dynamic Systems, Measurement and Control*, Vol. 111, pp. 97-104.
- Noh, M. D., Maslen, E. H. (1997), Self-sensing magnetic bearings using parameter estimation, *IEEE Transaction of Instruments and Measurements*, 46(1), pp. 45-50.
- Okada, Y., Matsuda, K., Nagai, B. (1992), Sensorless magnetic levitation control by measuring the PWM carrier frequency component, *Third International Symposium on Magnetic Bearings*, 21-31 July, Radisson Hotel, Alexandria, VA.
- Schammas, A., Herzog, R., Buhler, P., Bleuler, H. (2005), New results for self-sensing active magnetic bearings using modulation approach, *IEEE Transaction of Control System and Technology*, 13(4), pp. 509-516.
- Thibeault, N. M., Smith, R. (2002), Magnetic bearing measurement configurations and associated robustness and performance limitations, *Journal of Dynamic Systems, Measurement and Control*, 124, pp. 589-598.
- Tonoli, A., Amati, N., Silvagni, M. (2008), Transformer eddy current dampers for the vibration control, *Journal of Dynamic Systems, Measurement and Control*, Vol. 130, pp. 031010-1 - 031010-9.
- Vance, J. M. & Ying, D. (2000), Experimental Measurements of Actively Controlled Bearing Damping with an Electrorheological fluid, *ASME Journal of Engineering for Gas Turbines and Power*, Vol. 122, pp 337 - 344.
- Vischer, D., and Bleuler, H. (1990), A new approach to sensorless and voltage controlled AMBs based on network theory concepts, *Second International Symposium on Magnetic bearings*, 12-14 July, Tokyo, Japan, pp. 301-306.

-
- Vischer, D., Bleuler, H. (1993), Self-sensing magnetic levitation, *IEEE Transaction on Magnetics*, 29(2), pp. 1276-1281.
- Tonoli A., Amati N., Bonfitto A., Silvagni M, Staples B., Karpenko E., (2010) - Design of Electromagnetic Dampers for Aero-Engine Applications, *Accepted for Journal of Engineering for Gas Turbines and Power*, ISSN: 0742-4795

The Foundation of Electromagnets Based Active Vibration Control

Ramón Ferreiro García, Manuel Haro Casado* and F. Javier Perez Castelo
*University of A Coruña, University of Cadiz**
Spain

1. Introduction

Turbines, pumps, compressors, blowers and all rotating machinery in general, is commonly used in process industry, including machining tools, power generation, as well as aircraft and marine propulsion among the most important industrial applications. Mass imbalance is commonly responsible for rotating machinery vibration. When the principal axis of inertia of the rotor is not coincident with its geometric axis imbalance occurs. Nevertheless there are some more causes for rotating machinery vibration such as operation near resonant frequencies, critical speeds and so on. Higher speeds cause much greater centrifugal imbalance forces, and the current trend of rotating equipment toward higher power density clearly leads to higher operational speeds. For instance, speeds approaching 35,000 rpm are common in machining applications. Therefore, vibration control is essential in improving machining surface finish; achieving longer bearing, spindle, and tool life in high-speed machining; and reducing the number of unscheduled shutdowns. A great cost savings for high-speed turbines, compressors, and other turbomachinery used in petrochemical and power generation industries can be realized using vibration control technology.

Passive and active vibration control (AVC) techniques of rotating machinery are being used. It is well established that the vibration of rotating machinery can be reduced by introducing passive or active devices into the system. Although an active control system is usually more complicated than a passive vibration control scheme, an AVC technique has many advantages over a passive vibration control technique.

In (Fuller et al., 1996) it is shown that AVC is more effective than passive vibration control in general. Furthermore, the passive vibration control is of limited use if several vibration modes are excited. Finally, because the active actuation device can be adjusted according to the vibration characteristic during the operation, the active vibration technique is much more flexible than passive vibration control.

There are two major categories in AVC techniques for rotating machinery:

- Direct active vibration control (DAVC) techniques in which directly apply a lateral control force to the rotor.
- Active balancing techniques which adjust the mass distribution of a mass redistribution actuator. Active balancing isn't under the scope of this chapter.

The control variable in DAVC techniques is a lateral force generated by a force actuator based on a magnetic bearing. The advantage of DAVC techniques is that the input control force to the system can be changed according to vibration characteristics.

By applying a fast changing lateral force to the rotating machinery, the total vibration, including the synchronous vibration, the transient free vibration, and other nonsynchronous vibration modes of the rotating machinery, can be attenuated or suppressed. The limitation of most force actuators is the maximum force they can provide. In high rotating speed, the imbalance-induced force could reach a very high level. As most force actuators cannot provide sufficient force to compensate for this imbalance-induced force, active balancing methods are well justified. Although active balancing methods can eliminate imbalance-induced synchronous vibration, they cannot suppress transient vibration and other nonsynchronous vibration.

In this chapter DAVC techniques are introduced. Since the mathematical model is the foundation of any AVC technique, a description of dynamic modelling techniques applied on rotating machinery is included.

1.1 Dynamic modeling of a planar rotor

The simplest rotor model the planar one. Only the motion in the plane, which is perpendicular to the rotating shaft, is considered. The geometric setup of the planar rotor model is shown in figure 1.

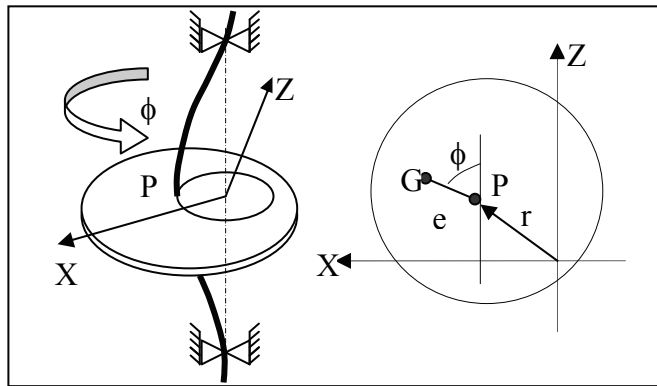


Fig. 1. Planar rotor

In this model, the imbalance-induced vibration is described by the particle motion of the geometric center of the disk. P is the geometric center of the disk, and G is the mass center of the disk. The motion is represented by the vector r . According to (Childs, 1993) the governing equation of motion is

$$\begin{aligned} m\ddot{r}_x + c\dot{r}_x + kr_x &= ma_x\dot{\phi}^2 + ma_z\ddot{\phi} \\ m\ddot{r}_z + c\dot{r}_z + kr_z &= ma_z\dot{\phi}^2 - ma_x\ddot{\phi} \end{aligned} \quad (1)$$

where m , c , and k are the mass, the viscous damping coefficient, and the shaft-stiffness coefficient, respectively. $[a_x, a_z]$ is the vector from P to G , expressed in the stationary coordinate system. ϕ is the rotating angle of the rotor. For a constant rotating speed, $\dot{\phi}$ is zero. The planar rotor can be used to study the basic phenomena in rotor dynamics such as critical speed, the effect of damping as well as its associated phenomena.

The planar rotor model is a special case of the model given by (Jeffcott, H. H., 1919), (J.M Vance, 1987). In the Jeffcott model, the rotor was modelled as a rigid disk supported by a

massless elastic shaft that was mounted on fixed rigid bearings. This model is also equivalent to a rigid shaft supported by elastic bearings. The major improvement over the simple planar rotor model is that the motion of the rotor is depicted by rigid body motion instead of by particle motion. Although this model is a single rigid body model, it can be shown the basic phenomena in the motion of the rotor, including the forward and backward whirling under imbalance force, critical speeds and the gyroscopic effect.

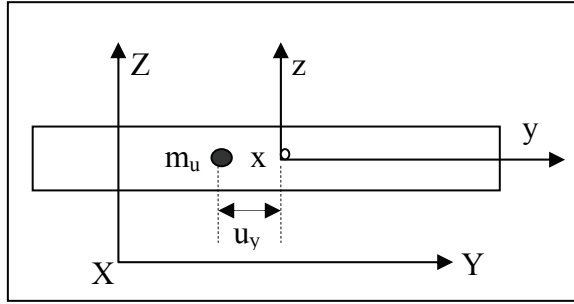


Fig. 2. Rigid Rotor Model

Due to the fact that the natural frequency is a function of the rotating speed, it can also be predicted by this model. The geometric setup of this model is shown in figure 2.

In this setup, bearings are modelled as isotropic linear spring and damper. The imbalance is modelled as concentrated mass on the rigid shaft. Two coordinate systems are used: the body-fixed coordinate $oxyz$ and the inertial coordinate $OXYZ$. The body-fixed y -axis is the rotating axis of the shaft, and x and z axes are defined by the other two principal inertia axes of the rotor. The origin of xyz is selected as the geometric centre of the shaft. The XYZ coordinate system is the stationary coordinate which is coincident with the xyz coordinate system under body rest condition. The transverse motion of the rotor is described by the position of the geometric centre $[RX RZ]$ and by the orientation of the rigid shaft with respect to the X and Z axes $[\phi, \psi]$. A simplified state space governing equation is shown in (2) (Zhou & Shi, 2000):

$$\frac{d}{dt} \begin{bmatrix} R_x \\ R_z \\ \Theta \\ \Psi \\ \dot{R}_x \\ \dot{R}_z \\ \dot{\Theta} \\ \dot{\Psi} \end{bmatrix} = \begin{bmatrix} 0 & 0 & 0 & 0 & 1 & 0 & 0 & 0 \\ 0 & 0 & 0 & 0 & 0 & 1 & 0 & 0 \\ 0 & 0 & 0 & 0 & 0 & 0 & 1 & 0 \\ 0 & 0 & 0 & 0 & 0 & 0 & 0 & 1 \\ -\frac{2k}{m} & 0 & 0 & 0 & -\frac{2c}{m} & 0 & 0 & 0 \\ 0 & -\frac{2k}{m} & 0 & 0 & 0 & -\frac{2c}{m} & 0 & 0 \\ 0 & 0 & -\frac{kL^2}{2I_t} & \frac{I_p \ddot{\phi}}{I_t} & 0 & 0 & -\frac{cL^2}{2I_t} & \frac{I_p \dot{\phi}}{I_t} \\ 0 & 0 & -\frac{I_p \ddot{\phi}}{I_t} & -\frac{kL^2}{1I_t} & 0 & 0 & -\frac{I_p \dot{\phi}}{I_t} & \frac{cL^2}{2I_t} \end{bmatrix} + \begin{bmatrix} R_x \\ R_z \\ \Theta \\ \Psi \\ \dot{R}_x \\ \dot{R}_z \\ \dot{\Theta} \\ \dot{\Psi} \end{bmatrix} + \begin{bmatrix} 0 & 0 \\ 0 & 0 \\ 0 & 0 \\ \frac{-m_u u_z}{m} & \frac{m_u u_x}{m} \\ \frac{m_u u_x}{m} & \frac{m_u u_z}{m} \\ \frac{m_u u_z u_y}{I_t} & \frac{m_u u_y u_z}{I_t} \\ \frac{m_u u_y u_z}{I_t} & \frac{-m_u u_x u_y}{I_t} \end{bmatrix} \begin{bmatrix} f_1 \\ f_2 \end{bmatrix} \quad (2)$$

where L is the length of the shaft; I_p and I_t are the polar and the diametric moments of inertia of the shaft, respectively; mu , ux , uy , uz are the mass and the position of the imbalance in body-fixed coordinate. Exciting forces are defined as:

$$f_1 = \ddot{\phi} \cos(\dot{\phi}^2) \cdot \sin(\phi), \quad f_2 = \ddot{\phi} \sin(\dot{\phi}^2) \cdot \cos(\phi) \quad (3)$$

The model given by (2) can be used on most of the shafts provided that the rigidity of the shaft is high compared to the supporting bearing. For analysis, simulation and control objectives the proposed model is considered sufficiently accurate

When flexible rotor models are applied, more complicated rotor system models must be developed. Such models allows for the elastic deformation of the rotor when in rotation. Consequently, it is more accurate than the rigid rotor model. A complicated rotor system is divided into several kinds of basic elements: rigid disk, bearing, flexible shaft segments, couplings, squeeze-film dampers, and other needed accessories. The equations of motion for each of these components can be developed using the appropriate force-displacement and force-velocity relations and the momentum principles as well as other equivalent dynamic relations. From the above review on rotor dynamics, it is concluded that many powerful tools for the linear system and frequency response are available. However, most of these techniques are targeted at the rotor design analysis.

It has been mentioned that for an efficient AVC system synthesis, a suitable analytical model must be used which is simple in comparison to the overall system equations, while still providing the essential dynamic characteristics.

(Maslen & Bielk, 1992) presented a stability model for flexible rotors with magnetic bearings. Besides the flexible rotor model itself, their model included the dynamics of the magnetic bearing and the sensor-actuator noncollocation. This model can be used for stability analysis and active vibration synthesis.

Most recently, an analytical imbalance response of the Jeffcott rotor with constant acceleration was developed by (Zhou & Shi, 2001). They concluded that a satisfactory solution quantitatively shows that the motion consists of three parts:

- the transient vibration at damped natural frequency,
- the synchronous vibration with the frequency of instantaneous rotating speed,
- and a suddenly occurring vibration at damped natural frequency.

Such mentioned technique provides physical insight into the imbalance-induced vibration of the rotor during acceleration. For this reason it can be used for the synthesis of AVC schemes.

For the synthesis of DAVC techniques, most it is common to use simplified low-order finite element models of the rotor system. Although the techniques developed can be extended to a high-order system theoretically, the computational load and consequently the signal-to-noise ratio will have to be higher. The DAVC techniques can be difficult to implement for the high-order system. Therefore, it is conveniently to use a reduced order models to approximate the high-order system models. Applied model reduction techniques have a specific impact on the performance of the DAVC schemes that must be considered if expected performance cannot be achieved.

1.2 DAVC for rotating machinery

AVC for rotating machinery is considered a special case of AVC for a flexible structure. The general topic regarding AVC was discussed by (Inman and Simonis, 1987) and (Meirovitch,

1990). The difference between rotating machinery and other flexible structures is that the dynamics of the rotor changes with the rotating speed of the shaft. Best control performance could be achieved if control gains vary with rotating speed. Also, because the shaft is a moving part, a noncontact actuator is used to apply the control force to the rotating shaft. There are many types of actuators for direct AVC, including electromagnetic, hydraulic and piezoelectric as the most important ones. The active magnetic bearing (AMB) is an established industrial technology with a rapidly growing number of applications. A good example of the application of magnetic bearings in the machine tool industry can be found in (Bleuler et al., 1994).

AMB can be used to apply a synchronous force to the shaft to control the imbalance response, either to cancel the force transmitted to the base or to compensate for the vibration displacement of the shaft. In (Knospe et al., 1996; Knospe et al., 1995; Knospe, Tamer, & Fittro, 1997; Knospe, Tamer, & Fedigan, 1997) presented an adaptive open-loop control method for the imbalance displacement vibration control using AMBs. A synchronous force that consists of sinusoids that are tied to the shaft angular position via a key phasor signal was generated and applied to the rotor through the magnetic supporting bearings. The magnitude and phase of these sinusoids were periodically adjusted so as to minimize the rotor unbalance response. The magnetic bearings were used to emulate the imbalance-induced force to offset the force induced by the system imbalance.

Therefore, Knospe and colleagues' methods are called "active balancing" methods rather than "DAVC" methods. Other researchers such as (Herzog et al., 1996) and (Lum et al., 1996) published their work on the imbalance transmitted force controlled by magnetic bearings.

The basic idea is to use a notch filter to blind the control system of the supporting magnetic bearing to the imbalance induced response. Therefore, no synchronous forces can be generated by the magnetic bearings. The rotor will then rotate about its own principal inertia axis provided that the gap between the shaft and the bearing is large enough. (Fan et al., 1992) presented a vibration control scheme for an asymmetrical rigid rotor using magnetic bearings.

Other researchers working in DAVC for rotating machinery adopted a state space representation of a rotor system. The control inputs are lateral forces. (Balas, 1978) pointed out that for a feedback control system for flexible systems, the control and observation spill-over due to the residual (uncontrolled) modes could lead to potential instabilities.

In (Stanway & Burrows, 1981), the dynamic model of the flexible rotor was written in the state space format and the controllability and observability of the model were studied. Stanway and Burrows concluded that the lateral motion of the rotor can, under certain conditions, be stabilized by the application of a single control input to a stationary component. (Ulsoy, 1984) studied the characteristics of rotating or translating elastic system vibration problems that are significant for the design of active controllers. The basic conclusions of his research were that a controller gain matrix that is a function of the rotating speed is required to maintain a desired closed-loop eigenstructure and that a residue model spill-over should be handled carefully by the active controller to avoid instability.

(Firoozian & Stanway, 1988) adopted a full-state observer technique to design a feedback AVC system.

The stability of the closed-loop system was also studied. To build an AVC system for flexible structures, the sensor/actuator deployment is an interesting topic. The issue of

actuator/sensor placement for control of flexible structures is an active research area. This problem is often formulated as a constraint optimization problem. The constraints of this optimization problem are the limited available locations for the actuators and sensors. The objective function of this optimization problem is closely related to the control algorithm used for the flexible structure.

The main possible optimal cost functions for sensor and actuator placement are for system identification, state estimation (which is represented by the observability) and indirect control performance (which is represented by the controllability), and direct control performance (e.g., the transient response, stability).

1.3 Discussion about DAVC

Since rotating machinery is widely used in industry, the AVC of the rotating machinery is an important engineering problem for both industry and academia. In this introductory section, a review of the direct vibration control for rotating machinery was conducted.

The major problem faced by the AVC scheme is the use of a limited number of actuators to control an infinite number of vibration modes. To design an active control scheme, a reduced-order model should be used and the effect of the spill-over of higher vibration modes assessed. Although the available techniques developed for dynamic analysis and active real-time vibration control can be extended to high-order systems theoretically, the computational load will be heavier and the signal-to-noise ratio of the vibration measurement will have to be higher. Hence, the available techniques could be difficult to implement in high-order systems. Consequently, it is necessary to use a model reduced system to approximate the high-order system.

In most of AVC methods, the imbalance estimation is coupled with the control strategy. So far, there are no systematic methods available to show the relationship between the estimation and the control strategy. A control action is preferable if it can obtain small imbalance-induced vibration and excite the system to obtain the good imbalance estimation at the same time.

Thus, coupling effects should be investigated by considering the estimation algorithm, the system dynamics, and the control performance. This research can also lay a scientific foundation for the design of an efficient and reliable generic adaptive control system.

It is clear that the active balancing can improve product quality and improve the fatigue life of the machine and cutting tools and, hence, reduce the system cost. However, the installation and maintenance of an active vibration system for rotating machinery will increase the system cost. How to assess the AVC system from a cost-effective point of view and on a higher process level is not well studied in the literature. More than two decades of experience demonstrates that this is an interesting and important problem in the AVC of rotating machinery.

2. AVC with magnetic actuators

2.1 Introduction

Unbalance response is a common vibration problem associated with rotating machinery. During several years, researchers have demonstrated that this vibration could be greatly alleviated for machines using active magnetic bearings through active magnetic control. Many of the control strategies employed fall into a class which the authors have termed *adaptive open loop control*.

Active magnetic bearings provide a number of advantages over conventional bearings for a variety of practical industrial applications. These include elimination of the lubrication system, friction free operation, decreased power consumption, operation at temperature extremes, and vibration control.

Recently there has been a great deal of interest in digital control of magnetic bearing systems. Digital control offers several major benefits for magnetic bearing supported rotors:

- quick tuning of a magnetic bearing system during installation
- implementation of some simple but powerful control strategies, such as gain scheduling
- application of fault tolerant controller architectures
- built-in monitoring and diagnostic capabilities

As the results shown along a couple of years indicate, digital control provides capabilities for adaptive control which can be used to greatly alleviate the unbalance vibration of rotating machinery. This is often the worst vibration problem encountered during operation. The source of this vibration is the discrepancy between the geometric axis of the rotor and its inertial axis. When the rotor is spinning, this imbalance results in a centrifugal force which causes synchronous vibration throughout the machine. This problem is managed on conventional machinery through mechanical balancing by means of the addition or removal of a small amount of mass from the shaft to reduce the residual imbalance. Rotor balancing in the field, unfortunately, is usually time consuming and costly. The down-time incurred can also be very expensive in terms of lost production. Also for some machines where the imbalance changes often during operation, such as centrifuges, mechanical balancing will have a limited benefit.

Magnetic bearings, being active devices, offer the capability to establish new and beneficial relationships between rotor and casing vibration and applied bearing force.

This capability has been employed by a considerable number of researchers investigating the control of unbalance response. One method to achieve unbalance response attenuation is through design of the feedback compensation. This has been achieved via the addition of filters to stabilizing controllers (Habermann & M. Brunet, 1994), (Larsonneur & R. Herzog, 1994) or through the addition of pseudo-states in observer based controllers (T. Higuchi, T. Mizuno, & M. Tsukamoto, 1990), (F. Matsumura, M. Fujita, & K. Okawa, 1990). Other researchers (C.R. Burrows & M.N. Sahinkaya, 1983), (C.R. Burrows, M.N. Sahinkaya, & S. Clements, 1989), (T. Higuchi et al., 1990), (R. Larsonneur, 1988), (Larsonneur & R. Herzog, 1994), (B. Shafai et al., 1994), (C.R. Knospe et al., 1993), have employed methods which the authors refer to as *adaptive open loop control*. These methods, as pointed out by (R. Larsonneur, 1988), (Larsonneur & R. Herzog, 1994) and Shafai et al., 1994), have the advantage that they may be added to feedback controllers that have been designed for optimum transient response without altering system stability or performance. These methods were first employed on a magnetic bearing supported rotor by (C.R. Burrows & M.N. Sahinkaya, 1983) who solved a least-squares-balancing problem for the proper forces to apply using an off-line theoretical model. They later extended this work to obtain an estimate of an influence coefficient matrix through trial forces and the use of a recursive control law (C.R. Burrows, M.N. Sahinkaya, & S. Clements, 1989). (Higuchi et al., 1990) applied an adaptive open loop method (*periodic learning control*) employing an estimate of the inverse transfer function in a recursive procedure. This method can only be applied on systems with square influence coefficient matrices (number of actuators equals number of

vibration sensors). Following references (C.R. Burrows, M.N. Sahinkaya, & S. Clements, 1989), (Higuchi et. al., 1990) are very similar to the convergent control algorithm presented by Knospe et al., 1993) which uses a look-up table of influence coefficients obtained through off-line testing. Shafai et al., 1994) apply a distinct method of adapting the open loop forces to cancel a synchronous signal. In such a method, only one Fourier coefficient of the open loop signal is changed per adaptation cycle in such a mode as to decrease the residual error. This method, originally developed for SISO systems, was extended to square MIMO systems. Stability and performance robustness of this method (convergence to optimal open loop control) is ensured. This is in contrast to most of the model-based methods where stability and performance robustness is being studied now. The transient performance of the adaptive open loop algorithms to changes in imbalance or rotor speed has to be considered because of its practical importance

2.2 The test environment

This section presents the test environment for active vibration control of rotating machinery. The principal idea is to control bending vibrations of a flexible rotor, supported by AMBs based on two sets of non-contacting electromagnetic actuators located at both shaft ends as shown in figure 3.

The test environment is composed of the following parts; a rotor test rig, two sets of magnetic actuators assembled to operate as both electromagnetic actuators and AMBs, and a programmable control unit (C.R. Fuller, S.J. Elliot, & P.A. Nelson, 1996), (C.R. Knospe, et al., 1997), (S.J. Elliot, 2001) to be applied on vibration attenuation or vibration suppression by means of feedback control applied to decrease the dynamic response of the rotor assumed as active magnetic dynamic damping. The main studies to be carried out on the described test rig deals with the dynamic response in the range of velocities of interest, especially near the resonant frequency region which can be reduced with a conventional velocity-feedback controller, or alternatively feedback filtering based control (K. Tammi (a), 2003), (K. Tammi (b), 2003).

The feedback force is derived from the displacement measurements, obtained from the eddy current transducers approximately collocated with the actuators as shown in figure 3 and 4. The use of a velocity feedback controller decreases the response of the rotor significantly. The active control brings the possibility to run the rotor across the critical speed. A feedforward system, based on an adaptive finite-impulse-response filter (K. Tammi (b), 2003), may also be designed to compensate disturbances caused by the mass imbalance if a reliable model of imbalance is available.

As shown in figure 4, every degree of freedom to be controlled requires a feedback control loop. The control system applies the force commands to attenuate shaft vibration while keeping the shaft into the radial position centre. The implementation of a shaft end vibration and position control scheme is shown in figure 5. It consists in an Agilent Technologies based hardware programmed under Matlab-Simulink V.9(a).

Every shaft end should be equipped with a control system comprising at least the parts shown in figure 6. It consists in two independent closed loop controllers to attenuate or suppress the shaft vibration in the normal plane of the shaft. The other shaft end should be equipped with a similar system.

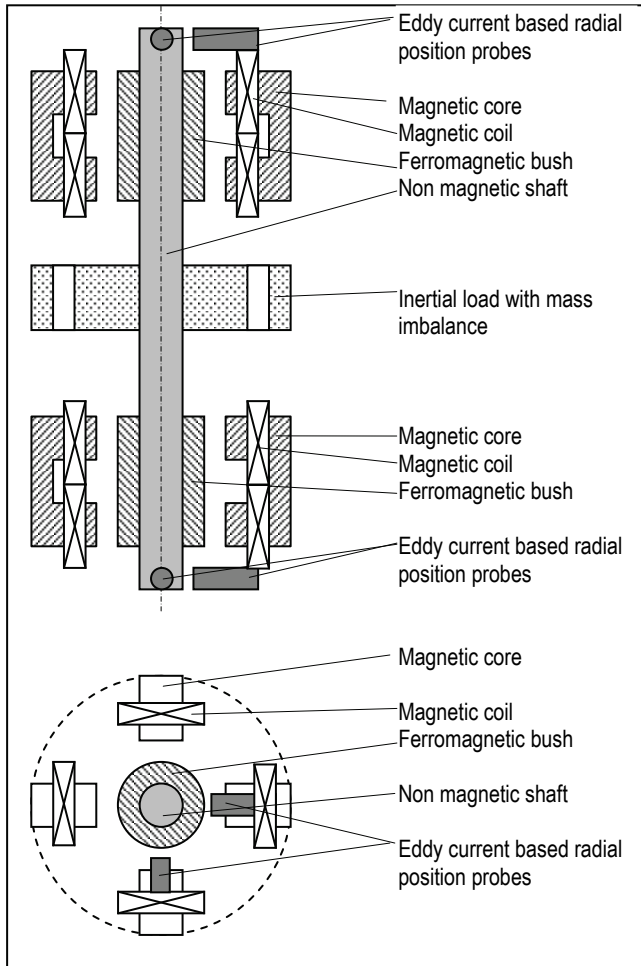


Fig. 3. The rotor-actuator system in two planes which must be controlled by two control loops because of the two degrees of freedom.

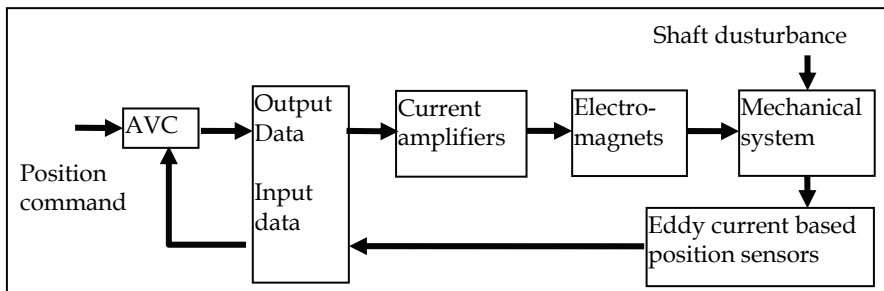


Fig. 4. Basic control loop.

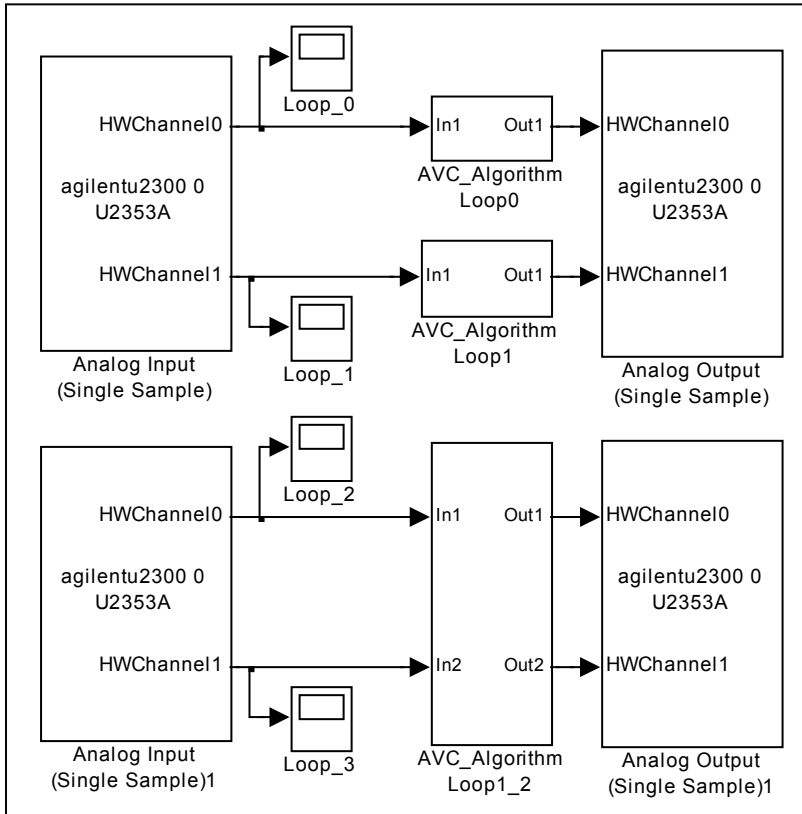


Fig. 5. Control loops implementation for a shaft end, using Matlab_Simulink: (a), with independent control algorithms. (b), with coupled control algorithms.

2.3 Control loop hardware

Control loops accessories such as data acquisition and final control elements or actuation devices are implemented with specifically designed hardware based components.

2.3.1 Data acquisition system

Radial displacement is sensed by means of a data acquisition system which is based on a set of Eddy current probes. Axial displacement is measured under the same technology. Eddy Current Probe (ECP) systems are integral components, which typically consists of a non-contacting probe, an extension cable and a driver. An ECP typically senses mechanical movement and converts this movement (displacement) into a usable electrical signal. As shown in figure 7, the signal can be sent to a monitor system for condition monitoring, analysis and/or alarm protection as well as control applications.

2.3.2 Final control elements

The final control elements composed by the magnetic field coils demand a large amount of current, which must be supplied by means of a Voltage Controlled Current Source (VCCS).

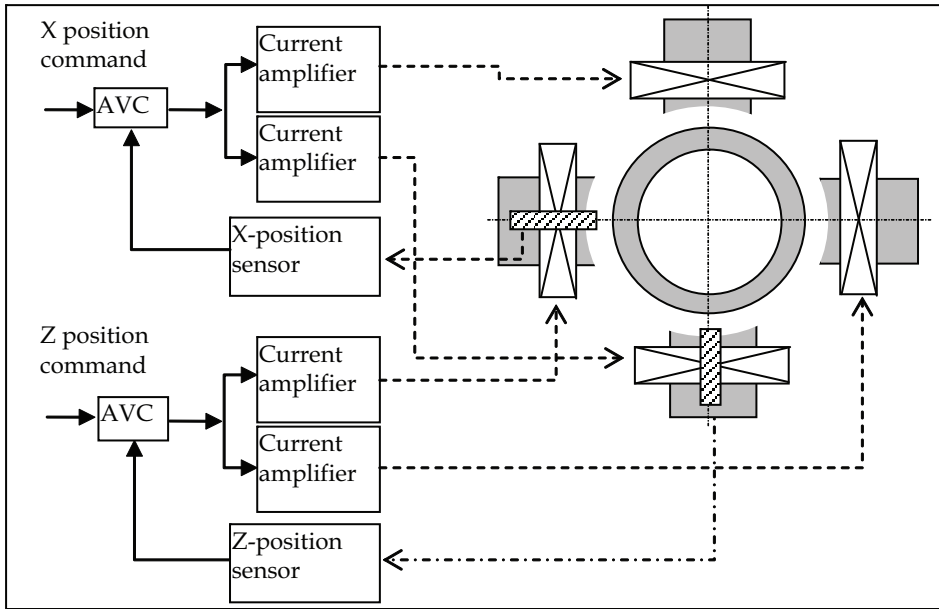


Fig. 6. Control structure for a shaft end.

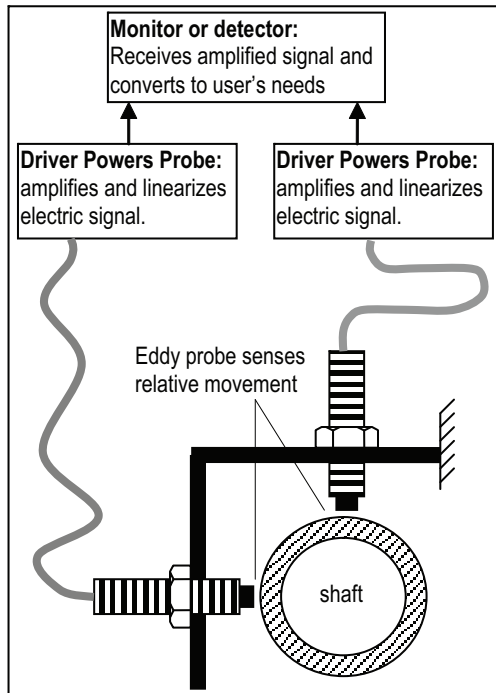


Fig. 7. Data acquisition hardware

The figure 8 shows the current amplifiers structure for a set of two opposite coils, capable for perform control forces in a single degree of freedom. The controller output provides a voltage based signal. Voltage to current conversion is performed by means of a VCCS. The VCCS can be useful for applications such as active loads for use in torque or force control servomotors. Force control is simplified since force is a direct function of current in an inductive load, such the applied coils. Figure 8 illustrates the basic circuit of a VCCS for a floating load. The load is actually in the feedback path. R1 and R2 are current sense resistors that develops a voltage proportional to load current.

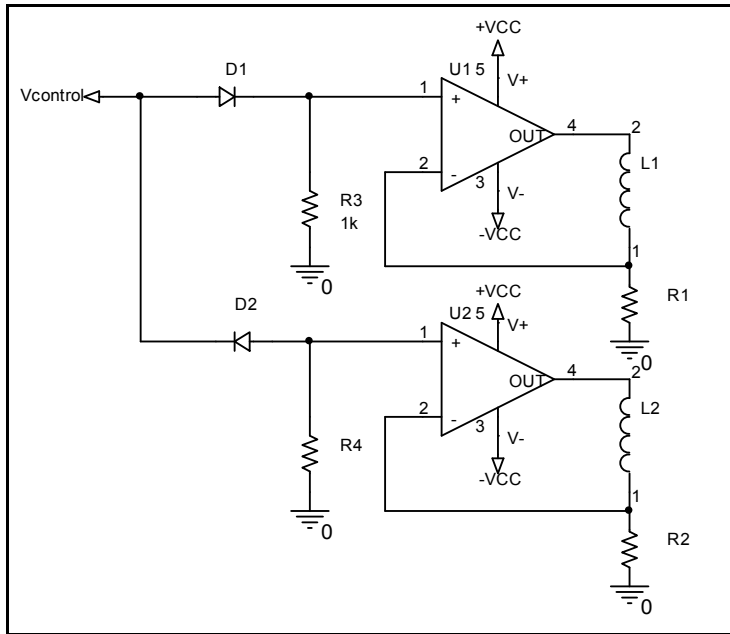


Fig. 8. The current amplifiers structure for two opposite coils

2.4 Force current model for electromagnet based actuators

A magnetic attraction based magnetic bearing comprises a set of radially positioned electromagnets positioned in opposing pairs around a permanent magnetic bearing journal. For instance, for a magnetic bearing with four electromagnets there is one opposing pair for each perpendicular axis. Each electromagnet consists of a laminated core and one or more coil windings. The force produced by a single two pole electromagnet can be shown to be given by the following equation where I is the total current in the magnet coils, z is the gap distance, μ_0 is the permeability of free space, A is the pole face area, and N is the number of coil turns:

$$F = \frac{\mu_0 AN^2 I^2}{4 z^2} \quad (4)$$

The force in (9) is repulsive and increases as the gap decreases. This repulsive force produces a stable system for an open loop magnetic bearing configuration. The net force, F_n

produced by an opposing pair of identical two-pole electromagnets on a single axis is the sum of the forces produced by each electromagnet; taking account of the sign convention, the net repulsive force equation is given as follows:

$$F_n = \frac{\mu_0 AN^2}{4} \left[\frac{I_2^2}{z_2^2} - \frac{I_1^2}{z_1^2} \right] \tag{5}$$

I_j is the current in magnet j , and z_j is the gap distance for magnet j .

A dynamical mathematical model for the HMB is shown in figure 9, where disturbances and external forces can be established as follows:

$$m\ddot{x} = \frac{\mu_0 AN^2}{4} \left[\left(\frac{I_2}{X_0 - x} \right)^2 - \left(\frac{I_1}{X_0 + x} \right)^2 \right] - F_D \tag{6}$$

where

- z_2 $X_0 - x$ air gap 2 (m);
- z_1 $X_0 + x$ air gap 1 (m);
- m rotor mass (kg);
- x rotor displacement (m);
- X_0 nominal air gap (m); the gap at centered rest position
- μ_0 permeability of free space (H/m);
- A total pole-face area of each electromagnet (m²);
- N number of turns on each electromagnet coil;
- I_1, I_2 opposing electromagnets coil currents (A);
- F_D some unknown force acting on the rotor (N);

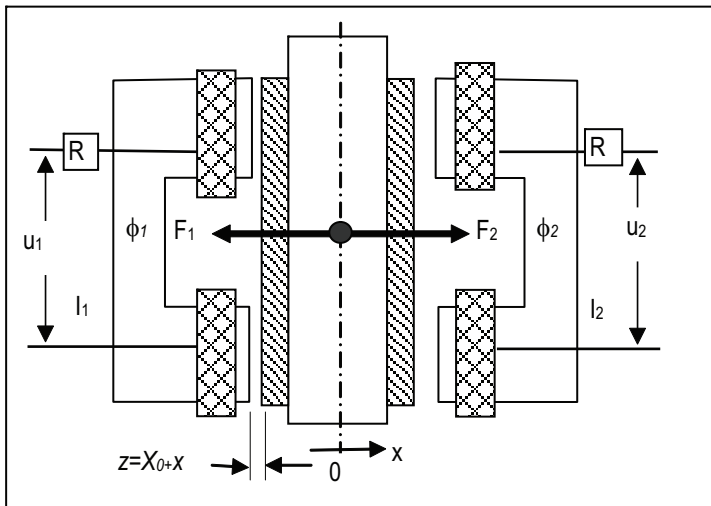


Fig. 9. Electromagnet based actuator structure

Previously, the equations were given for the static force produced by a magnetic bearing along a single axis. That force is affected dynamically by the rate limit at which current

changes in the coils, called the current slew rate limit, which is dependent on the voltage limit, of the power supply and the coil inductance, L .

The general nonlinear electromechanical model of the one degree-of-freedom (DOF) actuator system, for a number of electromagnet coils, can be subdivided into the mechanical subsystem dynamics, the magnetic force equation, and the electrical subsystem dynamics. The mechanical subsystem is governed by

$$m\ddot{x} = \sum_{i=1}^2 F_i(\Phi_i) - \sum F_D \quad (7)$$

where m is the rotor mass, x represents the position of the rotor centre, Φ_i is the magnetic flux in the i_{th} electromagnet, F_i denotes the force produced by the electromagnet, given by

$$F_i = \frac{(-1)^{i+1} \Phi_i^2}{\mu_0 A}, \quad i = 1, 2 \quad (8)$$

The electrical subsystem is governed by the equations

$$N\dot{\Phi}_i + R_i I_i = v_i, \quad i = 1, 2 \quad (9)$$

where u is the input control voltage of the i_{th} electromagnet, I_i is the current in the i_{th} electromagnet which is related to the flux.

$$I_i = \frac{2(X_0 + (-1)^i x)\Phi_i}{\mu_0 AN}, \quad i = 1, 2 \quad (10)$$

and X_0 is the nominal air gap in a disturbance free steady state.

2.5 Field-current models

The measurement of the real time currents feeding the coils supposes a reliable method to attenuate or suppress AMB vibration. Not only in steady state operating conditions but in transient operation modes, the actual current is compared with nominal current specified by the master feedback controller output yielding the manipulated variable as the squared current feeding the coils. Such varying currents have its origin in the loads exerted on parts of the shaft, rotor, turbine or impeller.

In the following analysis it is assumed that iron is infinitely more permeable than air. Also it is assumed that the bearing gap does not change its regular shape when the rotor moves back and forth. Furthermore, leakage and fringing are neglected.

Assuming that the reluctance of the iron can be neglected, the magnetic flux is

$$\phi = \frac{\mu_0 AN^2}{2z} \quad (11)$$

and if u is the voltage applied across the coils having a resistance of R , then

$$u = Ri + N \frac{d\phi}{dt} \quad (12)$$

Once assumed the previously cited restrictions, then follows that

$$\phi = \phi(z, i) \rightarrow \frac{d\phi}{dt} = \frac{\partial\phi}{\partial z} \frac{dz}{dt} + \frac{\partial\phi}{\partial i} \frac{di}{dt} \quad (13)$$

where dz/dt is the radial displacement velocity of the rotor. Applying partial differentiation on expression (13) with respect to d and i , yields

$$\frac{\partial\phi}{\partial z} = -\frac{\mu_0 AN^2 i}{2z^2} \quad (14)$$

$$\frac{\partial\phi}{\partial i} = \frac{\mu_0 AN^2}{2z} = L \quad (15)$$

Substituting (13) and (14) in (12), and assuming the air gap z as (X_0+x) , the expression (10) yields for the voltage

$$u = Ri - \frac{\mu_0 AN^2 i}{2z^2} \frac{dx}{dt} + \frac{\mu_0 AN^2}{2z} \frac{di}{dt} \quad (16)$$

Expression (15) is generally applicable any magnetodynamic circuit under radial displacement or translational and/or rotational degrees of freedom. Taking into account that the air gap for every coil set is defined by

$$\begin{aligned} z_2 &= X_0 - x \\ z_1 &= X_0 + x \end{aligned} \quad (17)$$

yields the following two equations

$$\begin{aligned} u_2 &= Ri_2 - \frac{\mu_0 AN^2}{2(X_0 - x)^2} i_2 \frac{dx}{dt} + \frac{\mu_0 AN^2}{2(X_0 + x)} \frac{di_2}{dt} \\ u_1 &= Ri_1 - \frac{\mu_0 AN^2}{2(X_0 + x)^2} i_1 \frac{dx}{dt} + \frac{\mu_0 AN^2}{2(X_0 - x)} \frac{di_1}{dt} \end{aligned} \quad (18)$$

Defining a constant parameter as $k = 0.5\mu_0 AN^2$, then follows that

$$\begin{aligned} u_2 &= Ri_2 - \frac{k}{(X_0 - x)^2} i_2 \frac{dx}{dt} + \frac{k}{(X_0 + x)} \frac{di_2}{dt} \\ u_1 &= Ri_1 - \frac{k}{(X_0 + x)^2} i_1 \frac{dx}{dt} + \frac{k}{(X_0 - x)} \frac{di_1}{dt} \end{aligned} \quad (19)$$

As can be seen from (19), both expressions relating input voltages are functions of measured variables (real-time currents and air gap).

3. The AVC under unbalance influences

To initiate the discussion, it is appropriate to consider the traditional diagram of a Jeffcott rotor as shown in figure 10 (a).

At very low speeds, unbalance forces are negligible. The shaft turns around the bearing centreline and all rotating elements are concentric. This condition is depicted in the detail (b) of figure 10. As rotor speed increases, the straight shaft will deflect into the predictable mode shape shown in figure 11.

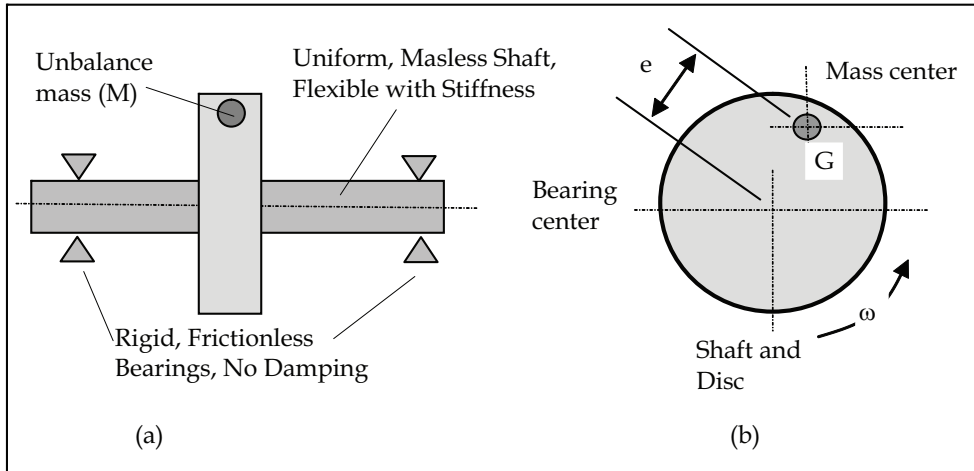


Fig. 10. The Jeffcott rotor diagram

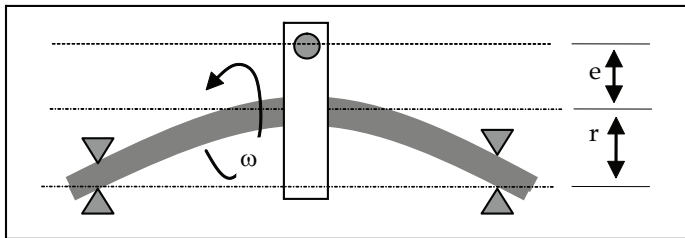


Fig. 11. Shaft deflection mode under centrifugal forces

The only driving force in the system is the centrifugal force due to the unbalance mass M . The maximum bending deflection of the shaft is identified by r and the mass eccentricity by e . Furthermore, the rotational speed is indicated by ω . By inspection of the figure 11 it can be seen that the shaft and disk are rotating at the operating speed ω . Simultaneously, the deflected shaft is whirling in the magnetic bearings at this speed. The mechanism driving this whirl is the centrifugal force generated by the eccentric mass on the disc. As rotor speed increases, the outward force increases in accordance with the normal centrifugal force F_c equation

$$F_c = M \cdot (r + e) \cdot \omega^2 \quad (20)$$

With regard to expression (20), the total radius of the mass unbalance M is composed of the shaft bending r , and the eccentricity of the mass with respect to the shaft centreline e . Such

centrifugal forces will be compensated as much as possible by the active magnetic forces developed by the control algorithm. Since the shaft speed is squared in expression (20), the shaft rotational speed has a strong influence on the AVC algorithm. Nevertheless, such influence is attenuated due to the inertial effect of the rotor which causes the response magnitude to decrease as rotational speed increases. The developed test rig has been subjected to experimental validation where a feedback control action provided by a PID is implemented. Several controller gains have been applied so that the time response is achieved for variable rotational speeds. As shown in figure 11 a vibration control test is performed under variable rotational speed. The rotating speed is varying from zero at the start point to 16 rad/sec. in about 50 seconds. At same time, different controller gains have been applied. As consequence, after three tests with different controller gains given as $K_p=3, 5$ and 7 respectively, three time responses are achieved and shown in figure 12. As depicted in figure 12, analytical or theoretical prediction of the optimum controller gain K_p , is not trivial. Instead, the selection of a controller gain K_p such that for a known rotating speed the response be acceptable, appears to be a satisfactory solution.

Generally, for very low rotating speeds, a low gain value is better than a high one. As rotational speed increase the effect of varying the controller gain is decreasing. This means that for high frequency vibration the variation of the AVC algorithm gain is not effective at all. An interesting topic to be taken into account with regard to the vibration attenuation is

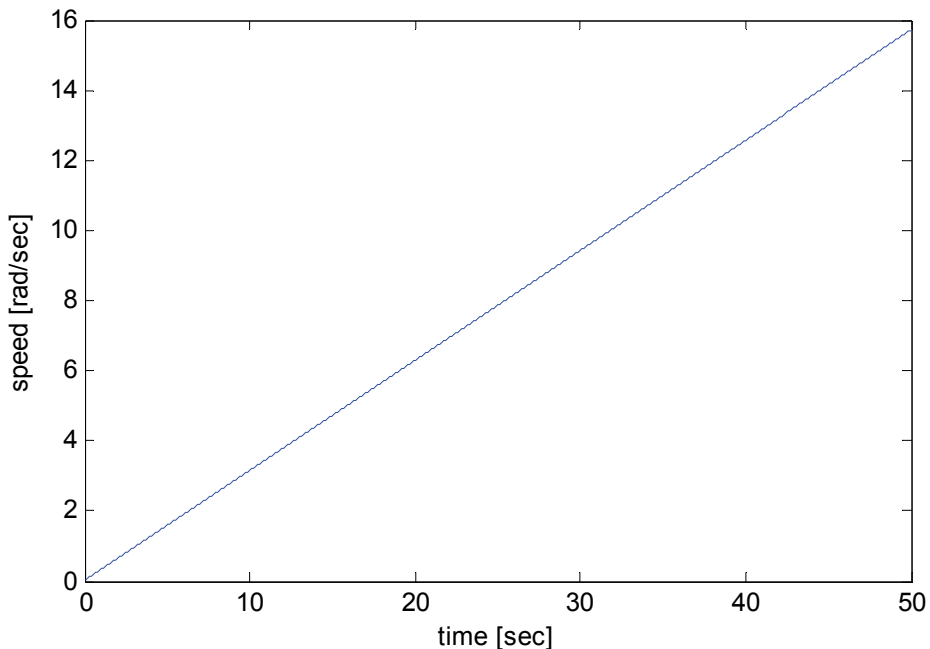


Fig. 12. Rotational speed (Rad/sec) as function of time

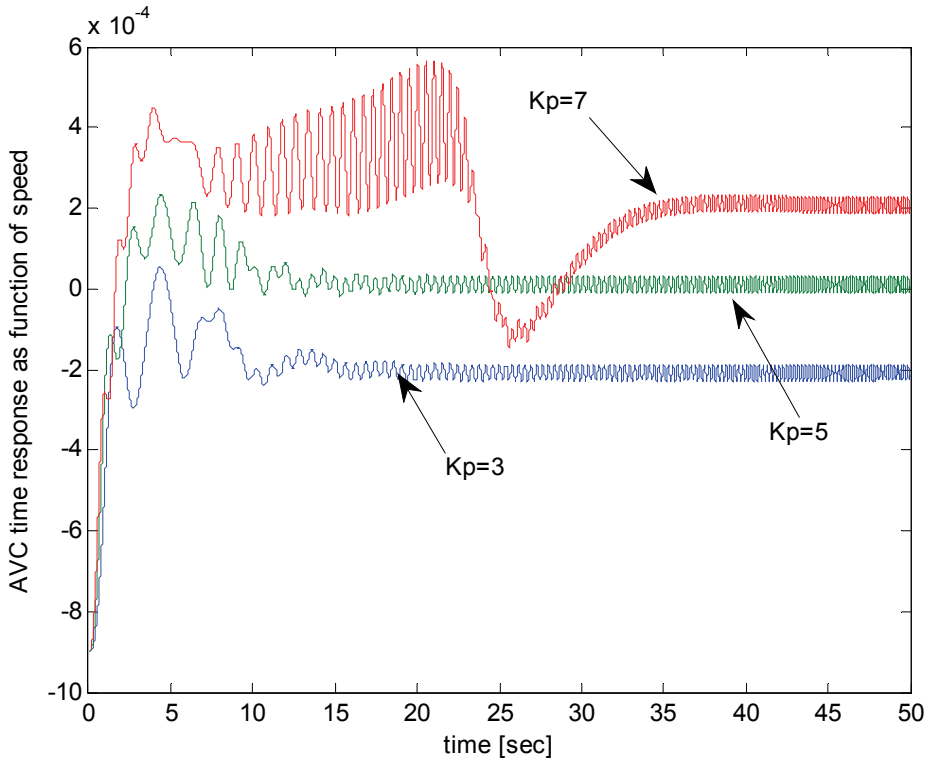


Fig. 13. Time response of the AVC as function of rotation speed.

the vibration effect of the shaft on the shaft support rig. If the rotor mass insignificant with respect to the bedplate mass, then vibration attenuation may be considered effective. On the other hand, shaft vibration is transmitted to the bedplate, with dramatic consequences.

4. Discussion and conclusions

The basics of active vibration control have been introduced. The vibration damages or harmful effects of unbalance-induced vibration cause significant productivity and precision reductions in a variety of industrial processes. A direct consequence rely on the implementation of next generation technology such as high-speed machining that has been delayed and restricted because of unbalance issues.

Standard off-line balancing techniques cannot address many of these unbalance problems because of the transient nature of both residual unbalance and machinery dynamics in operation.

Active balancing techniques promise solution to many of these problems and lead to significant economic benefits through increased reliability of machinery and the enabling of emerging advanced technologies.

Previous state-of-the-art non-adaptive active balancing control methods required extensive *a priori* modelling of system dynamics. Existing adaptive control methods for active balancing were not able to take advantage of the most recent data fast enough to ensure good performance and stability in the event of time-varying or nonlinear dynamics. This means that it is necessary a great research effort on this field, which must be associated to efficient and sophisticated test rigs to accurately improve and verify results.

A couple of basic and advanced control algorithms have been applied along the last three decades. The most simple is velocity feedback control.

Vibrations around the critical can be efficiently damped by velocity feedback control. It provided a possibility to run the rotor at critical speed by virtue of increased damping. It also provided smoother phase characteristics, which made feedforward compensation easier.

Control algorithms based on velocity feedback are one of the most simple examples for active vibration control in general. An important reason for this is the characteristically low damping of mechanical systems; a significant reduction in response can be achieved by a simple controller acting against vibration velocity. According to the literature review, the control method has also been applied to rotors. It has been shown experimentally that the reduction is significant in the resonance region for a rotor with low external damping.

The resonance can also be shifted with the control system by implementing a control force proportional to the displacement of the rotor. A load-carrying function is thus applied. This was briefly tested and found to work in the test environment. However, this was out of focus, because very large forces would be required in heavy rotating machines.

Velocity feedback control can also be successfully associated to feedforward control. Feedforward compensation converges at low frequencies, and outside the range of resonant frequencies, but diverges when the resonance frequencies are approached.

As mentioned, advanced control techniques and algorithms are being applied in order to render efficient productivity under the increasing industrial demands.

A variety of sophisticated control algorithms using the most efficient techniques to identify and estimate plant parameters, observer design, and advanced filtering is being applied, including predictive control and nonlinear Backstepping, optimal control and so on. Nevertheless the AVC continues being an active research area of interest.

5. Acknowledgments

This work has been partially supported by the XUNTA DE GALICIA under the grant DPI 1 IN825N cod_web:772.

6. References

- B. Shafai, S. Beale, P. LaRocca, and E. Cusson, (1994), "Magnetic Bearing Control Systems and Adaptive Forced Balancing", *IEEE Control Systems*, Volume 14, No. 2, pp. 4-13.
- Balas, M. J., (1978), "Feedback Control of Flexible Systems," *IEEE Transactions on Automatic Control*, Vol. AC-23, 673-679.

- Bleuler, H., Cahler, C., Herzog, R., Larssonneur, R., Mizuno, T., Siegart, R., and Woo, S., (1994), "Application of Digital Signal Processors for Industrial Magnetic Bearings," *IEEE Transactions on Control Systems Technology*, Vol. 2, 280-289.
- C.R. Burrows and M.N. Sahinkaya, (1983), "Vibration Control of Multi-Mode Rotor-Bearing Systems", *Proceedings of the Royal Society of London*, Vol. 386, pp. 77-94.
- C.R. Burrows, M.N. Sahinkaya, and S. Clements, (1989) "Active Vibration Control of Flexible Rotors: an Experimental and Theoretical Study", *Proceedings of the Royal Society of London*, Vol. 422, pp. 123-146.
- Childs, D., (1993), *Turbomachinery Dynamics*, John Wiley & Sons, New York.
- Fan, Y. H., Chen, S. T., and Lee, A., (1992), "Active Control of an Asymmetrical Rigid Rotor Supported by Magnetic Bearings," *Journal of the Franklin Institute*, Vol. 329, 1153-1178.
- F. Matsumura, M. Fujita, and K. Okawa, (1990), "Modeling and Control of Magnetic Bearing Systems Achieving a Rotation Around the Axis of Inertia", *Proceedings of the 2nd International Symposium on Magnetic Bearings*, July 12-14, 1990, Tokyo, Japan.
- Firoozian, R., and Stanway, R., (1988), "Modeling and Control of Turbomachinery Vibrations," *ASME Transactions, Journal of Vibration, Acoustics, Stress, and Reliability in Design*, Vol. 110, 521-527.
- Fuller, C. R., Elliott, S. J., and Nelson, P. A., (1996), *Active Control of Vibration*, Academic Press, New York.
- H. Habermann and M. Brunet, (1984), "The Active Magnetic Bearing Enables Optimum Damping of Flexible Rotors", *ASME Paper 84-GT-117*, 1984.
- Herzog, R., Buhler, P., Gahler, C., and Larssonneur, R., (1996), "Unbalance Compensation Using Generalized Notch Filters in the Multivariable Feedback of Magnetic Bearings," *IEEE Transactions on Control Systems Technology*, Vol. 4, 580-586.
- Inman, D. J., and Simonis, J. C., eds., (1987), *Vibration Control and Active Vibration Suppression*. Boston, MA, pp. 201-217. The ASME, (New York, N.Y. (345 E. 47th St., New York 10017)
- Jeffcott, H. H., (1919), "Lateral Vibration of Loaded Shafts in the Neighbourhood of a Whirling Speed -The Effect of Want of Balance," *Philosophical Magazine*, Vol. 37, 304-314.
- J.M. Vance, *Rotordynamics of Turbomachinery*, John Wiley & Sons, Inc., USA (1987).
- K. Tammi (a) (2003), *Active Vibration Control of Rotor in Desktop Test Environment*, VTT - Technical Research Centre of Finland, VTT Publications series 498, Espoo, Finland 2003.
- K. Tammi (b) (2003), *Mass imbalance compensation of rotor with adaptive finite-impulse-response filter and convergent control*, VTT Industrial Systems, Espoo 2003, p.23, Research report BTUO57-031122.
- Knospe C. R., R.W. Hope, S.J. Fedigan, and R.D. Williams, (1993), "Adaptive On-Line Rotor Balancing Using Digital Control", *Proceedings of MAG '93 Magnetic Bearings, Magnetic Drives, and Dry Gas Seals Conference*, Technomic Publishing, Lancaster, PA, July 1993.

- Knospe, C. R., Hope, R. W., Fedigan, S., and Williams, R., (1995), "Experiments in the Control of Unbalance Response Using Magnetic Bearings," *Mechanics*, Vol. 5, 385-400.
- Knospe, C. R., Hope, R. W., Tamer, S. M., and Fedigan, S. J., (1996), "Robustness of Adaptive Unbalance Control of Rotors with Magnetic Bearings," *Journal of Vibration and Control*, Vol. 2, 33-52.
- Knospe, C. R., Tamer, S. M., and Fittro, R., (1997), "Rotor Synchronous Response Control: Approaches for Addressing Speed Dependence," *Journal of Vibration and Control*, Vol. 3, 435-458.
- Knospe, C. R., Tamer, S. M., and Fedigan, S. J., (1997), "Robustness of Adaptive Rotor Vibration Control to Structured Uncertainty," *ASME*
- Knospe, C. R., J. Fedigan, R.W. Hope, R.D. Williams, (1997), "A multitasking DSP implementation of adaptive magnetic bearing control", *IEEE Transactions on Control Systems Technology*, Vol.5, No.2, March 1997, pp.230-238.
- Lum, K. Y., Coppola, V. T., and Bernstein, D., (1996), "Adaptive Autocentering Control for an Active Magnetic Bearing Supporting a Rotor with Unknown Mass Imbalance," *IEEE Transactions on Control Systems Technology*, Vol. 4, 587-597.
- Maslen, E. H., and Bielik, J. R., (1992), "A Stability Model for Flexible Rotors with Magnetic Bearings," *ASME Transactions, Journal of Dynamic Systems, Measurement, and Control*, Vol. 114, 172-175.
- Meirovitch, L., (1990), *Dynamics and Control of Structures*, John Wiley & Sons, New York.
- R. Larssonneur and R. Herzog, (1994), "Feedforward compensation of Unbalance: New Results", IUTAM Symposium, Bath, UK, September 1994.
- R. Larssonneur, (1998), "Design and Control of Active Magnetic Bearing Systems for High Speed Rotation", PhD Thesis, Swiss Federal Institute of Technology, ETH Zurich, Switzerland, June, 1998.
- S.J. Elliot, (2001), *Signal Processing for Active Control (Signal Processing and its Applications)* Ed. Stephen Elliot, Academic Press, London.
- Stanway, R., and Burrows, C. R., (1981), "Active Vibration Control of a Flexible Rotor on Flexibly-Mounted Journal Bearings," *ASME Transactions, Journal of Vibration, Acoustics, Stress, and Reliability in Design*, Vol. 103, 383-388.
- T. Higuchi, M. Otsuka, T. Mizuno, and T. Ide, (1990), "Application of Periodic Learning Control with Inverse Transfer Function Compensation in Totally Active Magnetic Bearings", *Proceedings of the 2nd International Symposium on Magnetic Bearings*, July 12-14, 1990, Tokyo, Japan.
- T. Higuchi, T. Mizuno, and M. Tsukamoto, (1990), "Digital Control System for Magnetic Bearings with Automatic Balancing", *Proceedings of the 2nd International Symposium on Magnetic Bearings*, July 12-14, 1990, Tokyo, Japan.
- Ulsoy, A. G., (1984), "Vibration Control in Rotating or Translating Elastic Systems," *ASME Transactions, Journal of Dynamic Systems, Measurement, and Control*, Vol. 106, 6-14.

-
- Zhou, S., and Shi, J., (2000), "Active Balancing and Vibration Control of Rotating Machinery: A Survey", Sage Publications, *The Shock and Vibration Digest*, Vol. 33, No. 4, 361-371
- Zhou, S., and Shi, J., (2001), "The Analytical Unbalance Response of Jeffcott Rotor during Acceleration," *ASME Transactions, Journal of Manufacturing Science and Engineering*, 123(2): 299-302.

A Magnetorheological Damper with Embedded Piezoelectric Force Sensor: Experiment and Modeling

Y. Q. Ni and Z. H. Chen

*Department of Civil and Structural Engineering, The Hong Kong Polytechnic University
Hong Kong, China*

1. Introduction

Semiactive control systems that offer the reliability of passive control systems as well as the versatility and adaptability of active control systems have received significant attention for structural vibration control (Jung et al., 2004). Magnetorheological (MR) fluid dampers have emerged as such a class of semiactive damping devices. By activating the MR fluid contained in the device through magnetic field, it can reversibly change from liquid to semisolid in milliseconds, which results in a continuously controllable device with high bandwidth. Moreover, MR dampers require minute power for the field activation and are insensitive to impurity penetration such as are commonly encountered during manufacture and usage (Carlson et al., 1996). More importantly, they are inherently fail-safe devices in that they can still operate as passive dampers once the control hardware fails. Recognizing the attractive characteristics and promising potential of the MR-based damping technique, numerous researchers and engineers have investigated the feasibility and application of the MR dampers in a wide variety of areas, such as seismic protection of building and bridge structures (Dyke et al., 1996; Gordaninejad et al., 2002; Loh et al., 2007), vibration control of bridge cables (Johnson et al., 2000; Ko et al., 2002; Ni et al., 2002; Duan et al., 2005; Weber et al., 2005b; Li et al., 2007), vibration damping of suspension systems of trains and vehicles (Liao and Wang, 2003; Song et al., 2005; Choi et al., 2009), and stability augmentation of helicopters (Gandhi et al., 2001; Hu & Wereley, 2008).

While possessing controllable damping capability, the existing MR dampers are incapable of monitoring structural vibrations or excitations exerted on structures, and require extra sensors for implementing closed-loop semiactive control. As a consequence, the MR dampers are usually used as adjustable passive dampers in an open-loop mode in the current practices of civil structural control, like in vibration control of bridge cables (Chen et al., 2004; Weber et al., 2005a), which hinders full utilization of their controllable damping capability. Recently, a self-sensing MR damper embedded with a piezoelectric force sensor has been developed to possess dual functionality of force sensing and controllable damping; thus it has the potential to facilitate real-time closed-loop control in a relatively simple and cost-effective manner (Or et al., 2008).

One of the important tasks to fully exploit the potential of an MR damper in control implementation is to establish an accurate model that can characterize its intrinsic highly

nonlinear properties, particularly hysteresis and force saturation. On the other hand, in well recognizing the fact that the force generated by the MR damper cannot be controlled directly and only the current applied to the MR damper can be commanded, it is essential and beneficial to build a model for describing the inverse dynamics of the MR damper. The inverse dynamic model will be incorporated into the control system to produce currents for the MR damper to track the desired optimal control forces implementable by the damper.

Since the last decade, considerable research efforts have been devoted to representing the forward dynamics of MR dampers and a variety of models have been documented in the literature. They can be classified as parametric and nonparametric models. Among several parametric models described in terms of analogous mechanical elements (Kamath & Wereley, 1997; Wereley et al., 1998; Spencer et al., 1997; Jiménez & Álvarez-Icaza, 2005; Ikhouane & Dyke, 2007), a phenomenological model on the basis of the Bouc-Wen hysteresis model proposed by Spencer et al. (1997) is regarded as the “state-of-the-art” semi-physical model of an MR damper. This model can accurately represent the nonlinear hysteresis of a typical MR damper over a wide range of operating conditions. However, it includes fourteen parameters in need to be adapted; identification of them requires sophisticated searching algorithms and is computationally intense. Also, a high integration-step rate in the order of kHz has to be used to ensure numerical stability in solving the nonlinear differential equations, which limits the model’s application in real-time control.

An alternative representation of forward dynamics of MR dampers is by using nonparametric methods, especially black-box modeling techniques, due to their considerable flexibility and effectiveness in system modeling as well as few physical insights necessary for developing a model. These black-box techniques include adaptive neuro-fuzzy inference system (Schurter & Rochke, 2000), polynomial NARX (nonlinear autoregressive with exogenous inputs) modeling (Leva & Piroddi, 2002), wavelets-based identification technique and ridgelet network optimization approach (Jin et al., 2005), and artificial neural networks (Chang & Roschke, 1998; Wang & Liao, 2001; Du et al., 2006; Cao et al., 2008). Despite the widespread use of the black-box techniques in MR damper modeling, only a few models were developed and evaluated based on real measurement data of MR dampers and using numerical simulation data instead. Moreover, it is commonly believed that neural networks are prone to overfitting, which occurs when a neural network only memorizes the superficial details of training data rather than learns the true relationship underlying the data. Hence, generalization capability is a critical concern in constructing a neural network for estimation or prediction on novel situations. However, few of the previous works addressed the overfitting or generalization issue when using neural networks to identify the dynamics of MR dampers, which might give rise to reliability problem in the control applications with the overfitted black-box models.

Likewise, due to the highly nonlinear properties of an MR damper, a linear forward parametric model invertible for determining command current to be input into the MR damper is not available; and what is more, it is challenging to formulate a nonlinear parametric model for the inverse dynamics similar to a forward one. Tsang et al. (2006) developed simplified inverse dynamics (SID) models for MR dampers with respect to the Bingham plasticity model and the Bouc-Wen hysteresis model (Spencer et al., 1997) using a piston velocity feedback algorithm and a damper force feedback algorithm for each model. The effectiveness of the SID models was demonstrated in terms of force tracking accuracy through numerical simulations, while errors exist in the pre-yielding phase when the damper piston velocity is small. More recently, attention has been attracted to modeling of

the inverse dynamics of MR dampers with the employment of black-box techniques, such as neural networks (Wang & Liao, 2001; Chang & Zhou, 2002; Xia, 2003; Du et al., 2006; Cao et al., 2008), neuro-fuzzy methods (Schurter & Roschke, 2001) and fuzzy logic methods (Zhou et al., 2003; Du & Zhang, 2008).

This chapter describes configuration, fabrication as well as calibration and performance tests of the devised self-sensing MR damper firstly. Then, a black-box identification approach for modeling the forward and inverse dynamics of the self-sensing MR damper is presented, which is developed with the synthesis of NARX model and neural network within a Bayesian inference framework to have the ability of enhancing generalization.

2. Self-sensing MR damper

As illustrated in Fig. 1, the configuration of a self-sensing MR damper is composed of damper and sensor parts. The damper part originates from an actuation-only MR damper. It comprises a cylinder with MR fluid, an electromagnet, a diaphragm, an accumulator and a piston housed inside, as well as a pair of electrical wires extended from the electromagnet and through the piston. The body diameter of the damper is 41 mm. It is 208 mm and 155 mm long in fully extended and compressed positions, respectively, and hence can provide a stroke of ± 25 mm. The magnetic field inside the device can be varied externally by monitoring the input current supplied to the device. The maximum input currents are 1 A and 2 A for continuous and intermittent working situations, respectively.

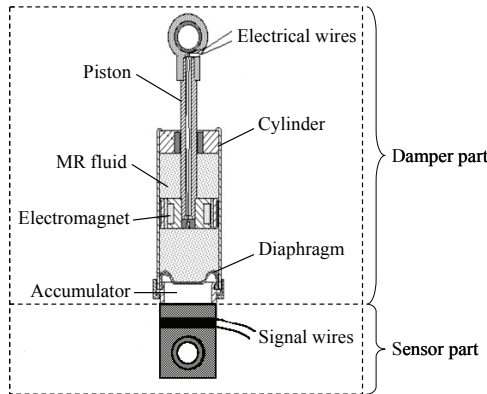


Fig. 1. Schematic diagram of self-sensing MR damper

The sensor part is essentially a prestress-type piezoelectric force sensor attached axially to the damper part, the detailed configuration of which is shown in Fig. 2. Components of the piezoelectric force sensor include a piezoelectric wafer, two electrode wafers, two insulating wafers, two adaptors, a pair of signal wires and a threaded bolt. A lead zirconate titanate (PZT) piezoceramic ring (Ferroperm Pz28), having an outer diameter of 38 mm, an inner diameter of 13 mm and a thickness of 2 mm, is selected as the piezoelectric wafer. Fired silver layers are coated on the two surfaces of the piezoelectric wafer perpendicular to its thickness, and electric polarization is induced along the thickness direction using these electrode surfaces. The electrode wafers are made of a beryllium-copper (Be-Cu) alloy sheet and positioned on either side of the piezoelectric wafer to provide external connections with

the sensor signal wires. The insulating wafers made of polyimide are also in a ring shape with an outer diameter of 40 mm, an inner diameter of 10 mm and a thickness of 0.1 mm. Each of them is inserted between the electrode wafer and the metal adaptor to prevent short-circuiting of the piezoelectric wafer and the whole sensor. These sensor components are sandwiched centrally in a stack between two steel adaptors and assembled by using a standard M10 threaded bolt according to the arrangement in Fig. 2. The bolt is insulated using a plastic band from the electrode wafers and the piezoelectric wafer.

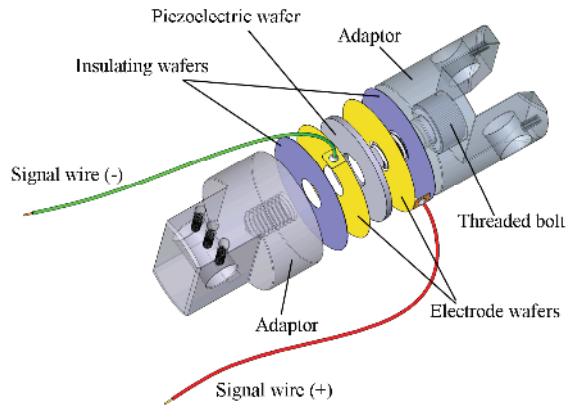


Fig. 2. Assembly diagram of piezoelectric force sensor

Since the piezoelectric force sensor works properly only under compression, the technique of mechanical prestressing is performed on the sensor so that tension forces can be measured while the piezoelectric element remains in compression during operation. A torque driver (BRITTOOL), calibrated with the compression stress of 18 MPa on the piezoelectric wafer for a torque of 30 N·m, is employed to exert torque slowly to the bolt until it is overloaded. During the prestressing, the positive and negative electrodes are connected to form a short-circuit condition to avoid accumulation of charges on the surfaces of the piezoelectric wafer. The assembled sensor is evaluated (to be reported in the next section) and then embedded with the damper part with the configuration of Fig. 1. Fig. 3 shows the photograph of the self-sensing MR damper prototype. In operation, the embedded piezoelectric force sensor senses the variation of force imposed on the damper during structural vibration. The sensed signals are then used to assist in adjusting the current input to the damper through an appropriate control strategy and thereby the commanded damping force. The self-sensing MR damper thus has the dual function of force sensing while controllable damping.

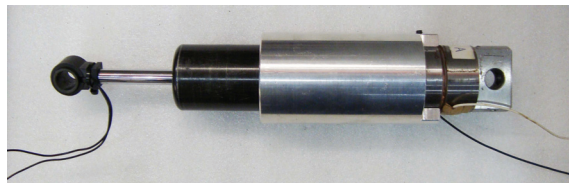


Fig. 3. Photograph of self-sensing MR damper prototype

3. Experiments of self-sensing MR damper

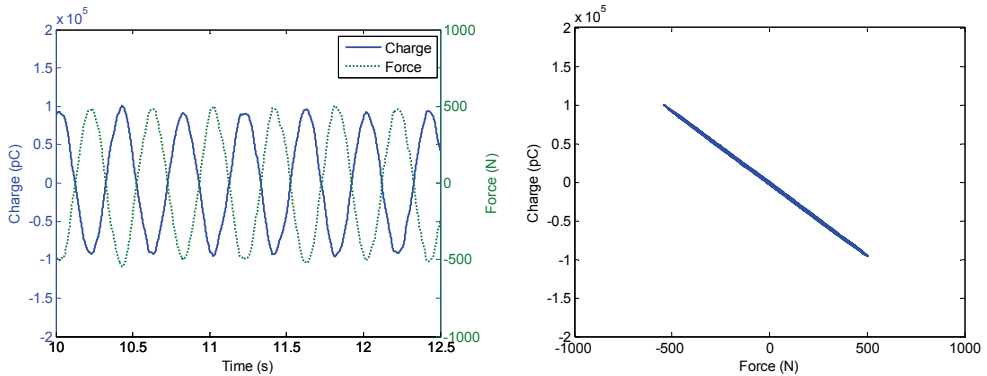
Calibration tests of the piezoelectric force sensor are conducted prior to embedding it with the damper. Then, performance tests are carried out to investigate sensing capability and damping behaviors of the self-sensing MR damper. All the tests are performed on a servohydraulic material testing system (MTS 810). The MTS is operated in force-controlled mode for the calibration tests and in displacement-controlled mode for the performance tests using harmonic excitations with a wide spectrum of frequency and amplitude. The output charge signals generated by the piezoelectric force sensor are measured through a charge meter (Kistler 5015). The charge, force and displacement signals are sampled and recorded by a computer-controlled data acquisition system. The displacement and force excitations exerted to the damper by the MTS are also acquired with the data acquisition unit incorporated in the MTS for further data analysis.

3.1 Calibration

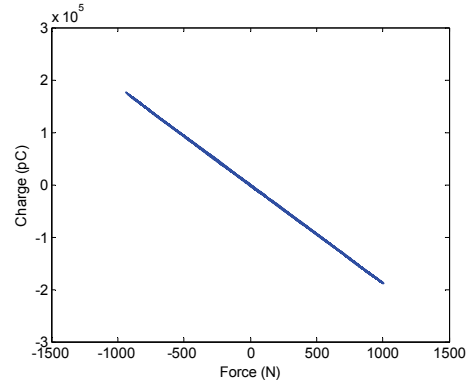
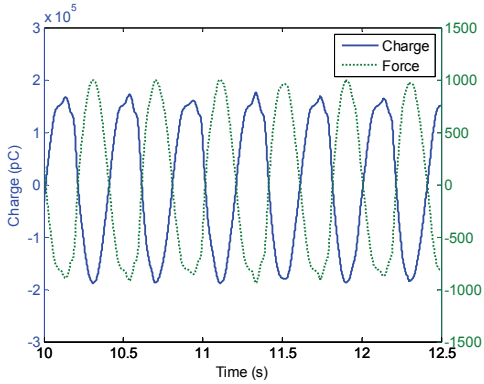
For calibration of the piezoelectric force sensor, force-controlled tests are conducted using sinusoidal excitations with frequencies of 0.5, 1.0, 2.5, 5.0 and 10.0 Hz and amplitudes of 500, 750, 1000, 1250, 1500, 1750 and 2000 N, as well as ramp excitations with frequencies of 0.5, 1.0, 5.0 and 10.0 Hz and amplitudes of 500, 1000, 1500 and 2000 N. Experimental data are used to investigate the relationship between the MTS driving force exerted on the piezoelectric sensor and the output charge from the piezoelectric sensor. Fig. 4 shows the time domain signals of the driving force and the output charge, as well as relationship plots of force versus charge for the selected calibration cases under the sinusoidal force excitations with a frequency of 2.5 Hz and amplitudes of 500 to 2000 N. It is observed that for each case there is always a phase difference of 90° between the output charge and the input force. The relationship between the charge and the force is linear, and the slopes of charge versus force obtained under different excitation conditions are almost identical.

A sensitivity coefficient for the piezoelectric force sensor, quantified as the ratio of charge to force (k), can be derived from the linear relationship between the charge (Q) and the force (F), and is calculated by

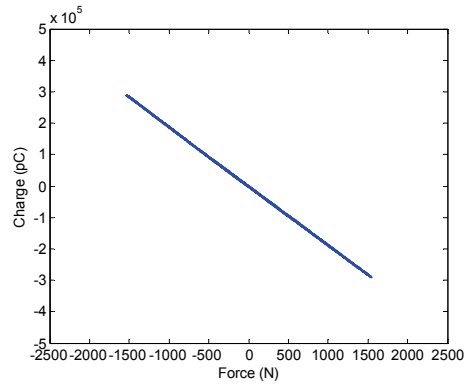
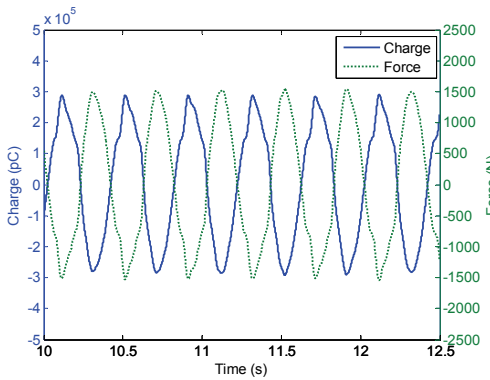
$$k = \frac{\sum_{i=1}^n Q_i^2}{\sum_{i=1}^n (Q_i F_i)} \tag{1}$$



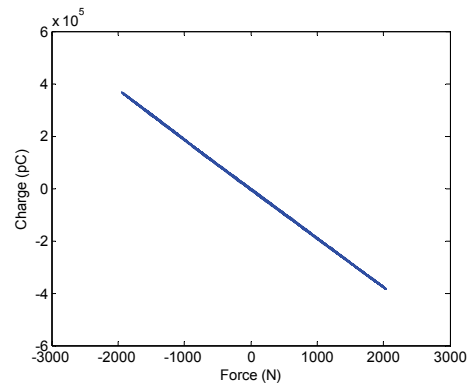
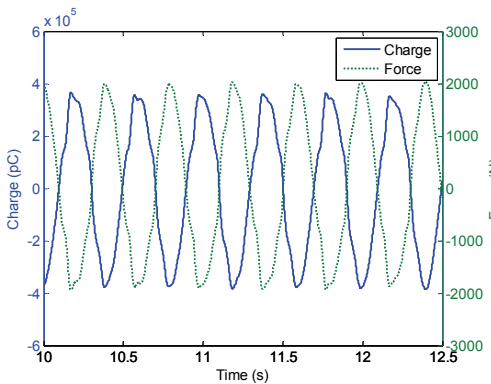
(a) 2.5 Hz, 500 N



(b) 2.5 Hz, 1000 N



(c) 2.5 Hz, 1500 N



(d) 2.5 Hz, 2000 N

Fig. 4. Calibration of piezoelectric force sensor under force-controlled sinusoidal excitations

where n is the total number of the data samples used for the calibration. In addition, a normalized standard deviation

$$\delta_1 = \sqrt{\frac{1}{n} \sum_{i=1}^n \left(F_i - \frac{Q_i}{k} \right)^2} \bigg/ \sqrt{\frac{1}{n} \sum_{i=1}^n (F_i - \bar{F})^2} \quad (2)$$

is defined to evaluate the accuracy of the sensitivity k , where \bar{F} is the mean of the force. The values of the sensitivity coefficient k and the corresponding normalized standard deviations δ_1 are calculated for each calibration case (with different combinations of frequencies from 0.5 to 10.0 Hz and excitation amplitudes from 500 to 2000 N). It is found that the sensitivity coefficients obtained from all the calibration cases are almost identical, and the corresponding normalized standard deviations are all less than 0.07. Finally, the sensitivity coefficient for the piezoelectric force sensor is averaged from the results of all the calibration cases to be $\bar{k} = -187.874$ pC/N with a normalized standard deviation of 0.0102. As a result, the force sensed by the piezoelectric force sensor is expressed as

$$F_{PZT} = Q/\bar{k} \quad (3)$$

3.2 Performance

The sensing capability of the self-sensing MR damper is evaluated by the degree of agreement between the force signals from the piezoelectric force sensor and from the MTS transducer, which is defined by a normalized root mean squared residual of

$$\delta_2 = \sqrt{\frac{1}{m} \sum_{j=1}^m (F_{MTS}|_j - F_{PZT}|_j)^2} \bigg/ \sqrt{\frac{1}{m} \sum_{j=1}^m F_{MTS}|_j^2} \quad (4)$$

in which m is the total number of the data samples used in the calculation.

Experimental data are obtained under displacement-controlled excitations of different frequencies and amplitudes and with currents (I) supplied to the damper of 0, 0.25, 0.5, 0.75 and 1.0 A, respectively. Fig. 5 shows a comparison of the force signals from the embedded piezoelectric force sensor and from the MTS transducer for the sinusoidal excitation with a frequency of 5 Hz and an amplitude of 5 mm while the input currents are from 0 to 1.0 A, and Table 1 gives the corresponding values of δ_2 . A good agreement between the two force signals is observed, verifying the good sensing capability of the self-sensing MR damper.

Fig. 6 shows force-displacement and force-velocity hysteresis loops of the self-sensing MR damper under displacement-controlled sinusoidal excitations with a frequency of 5 Hz and an amplitude of 5 mm for various currents from 0 to 1.0 A. It is clear that the magnitude of the damper force increases with the increment of the applied current, but the increase slows down when the current approaches to 1.0 A due to the magnetic saturation. Also, the areas enclosed by the force-displacement and force-velocity hysteresis loops enlarge with the increasing current, indicating the enhanced capability of dissipating vibration energy.

Current (A)	0	0.25	0.5	0.75	1.0
δ_2	0.0410	0.0387	0.0396	0.0390	0.0386

Table 1. Normalized root mean squared residuals of force signals

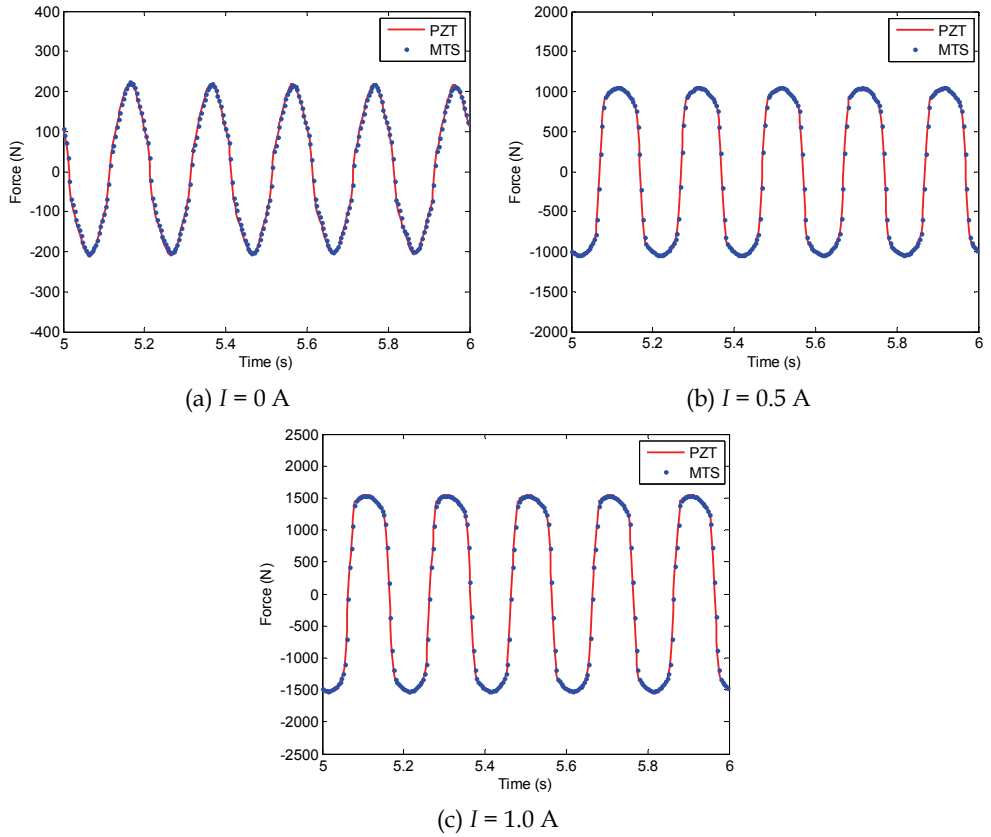


Fig. 5. Comparison between force signals obtained from piezoelectric force sensor and MTS transducer

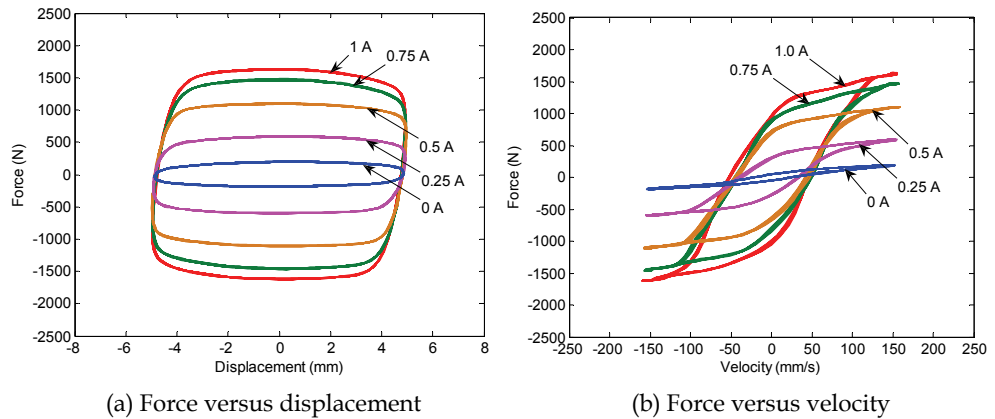


Fig. 6. Hysteresis behavior of self-sensing MR damper

4. Modeling of self-sensing MR damper

Due to the inherent nonlinearity of the self-sensing MR damper, the modeling of its dynamics is a nontrivial task. In order to build effective and versatile models for the damper, a black-box modeling method is developed by synthesizing NARX model and neural network from a Bayesian inference perspective.

4.1 Methodology

4.1.1 NARX network

NARX model is a very general and powerful black-box model structure due to both its capability of capturing a wide variety of nonlinear dynamic behaviors and the availability of identification algorithms with a reasonable computational cost (Chen et al., 1990). It has been indicated, under mild assumptions, that any finite-dimensional nonlinear system admits an input-output NARX representation, at least locally (Levin & Narendra, 1996). An NARX model is formulated as a discrete time input-output recursive equation of

$$y(t) = f(y(t-1), \dots, y(t-n_y), u(t), u(t-1), \dots, u(t-n_u); \theta) + e(t) \quad (5)$$

where $u(t)$ and $y(t)$ denote model input and output variables at time t ; the integers n_u and n_y are the respective maximum lags of the input and the output; $e(t)$ is the model error between the target and the prediction; and $f(\cdot, \theta)$ is a nonlinear mapping function of its arguments depending on a vector of parameters θ . In order to ensure a good approximation to the real system, $f(\cdot, \theta)$ should be a universal approximating function.

The multi-layer perceptron (MLP) is an artificial neural network that can realize an overall input-output black-box mapping. It consists of multiple layers of computational neurons interconnected with connection weights in a feedforward way. An MLP with one hidden layer has been theoretically proved to be a universal approximator in the sense that it can approximate any continuous nonlinear function to arbitrary accuracy provided the number of neurons in the hidden layer is adequate and the network weights and biases are adjusted appropriately (Hornik et al., 1989; Leshno et al., 1993). By applying a single-hidden-layer MLP to emulate the multiple-input-single-output NARX model (5), it can be expressed as

$$\hat{y}(t) = g_2 \left(\sum_{j=1}^{n_h} w_j^o g_1 \left(\sum_{i=1}^{n_i} w_{ji}^h z_i(t) + b_j^h \right) + b^o \right) \quad (6)$$

where $z(t) = [y(t-1), \dots, y(t-n_y), u(t), u(t-1), \dots, u(t-n_u)]$ is the input vector fed into the network; z_i is the i th variable of $z(t)$; n_i ($= n_y + n_u + 1$) denotes the number of input neurons; w_{ji}^h is the connection weight from the i th input neuron to the j th hidden neuron; b_j^h is the bias for the j th hidden neuron; n_h is the total number of hidden neurons; w_j^o is the weight connecting the only neuron in the output layer to the j th hidden neuron; b^o is the bias for the output neuron; $g_1(\cdot)$ and $g_2(\cdot)$ are activation functions for the hidden and output layers, respectively; $\hat{y}(t)$ is the network output at time t . By expressing the function $f(\cdot, \theta)$ in Eq. (5) using Eq. (6) with the real valued weights w ($= \{w_{ji}^h, w_j^o\}^T$) and biases b ($= \{b_j^h, b^o\}^T$), which together make up the model parameter vector θ , the resulting system is named an NARX network. This synthesis results in a powerful model structure that is able to represent complex nonlinear behaviors such as chaos, hysteresis, saturation effects, or combinations of several nonlinear phenomena (Suykens et al., 1996).

4.1.2 Bayesian learning

From the statistical point of view, the concept of maximum likelihood, like back-propagation algorithms, is typically employed in the training procedure of MLP models for the parameter estimation. It attempts to search a single set of network parameters from a sequence of training data D with N samples through the minimization of an error function, the sum of squares error between the network prediction and the corresponding target

$$E_D = \sum_{t=1}^N (\hat{y}(t) - y(t))^2 \quad (7)$$

However, during such searching (training) process, MLP models based on the maximum likelihood approach are easily led to complex topologies, which may overfit the training data. As a result, such overfitted models will deteriorate the generalization performance and be unable to make predictions as well for unseen input data as for the training case.

One of the feasible procedures to improve generalization is weight decay, which modifies the error function (7) by involving a penalty term to

$$S(\theta) = \beta E_D + \alpha E_\theta \quad (8)$$

where the regularizing term $E_\theta = \sum_{i=1}^M \theta_i^2$ is the sum of squares of the M network parameters

(weights and biases), which constrains the complexity of the network by limiting the growth of the network parameters; and α and β are regularization parameters, which serve to balance the trade-off between the prediction accuracy and the model complexity. MacKay (1992a, b) has made extensive investigations on the application of a Bayesian inference technique to adapt the weights and biases through network training and meanwhile to optimize the regularization parameters in an automated fashion.

Unlike the maximum likelihood approach, the Bayesian inference technique considers a probability distribution over the network parameters, which represents the relative degree of belief in different parameter values and is described by a prior distribution $P(\theta | \alpha)$ in the absence of any data. Once the data set D is taken, the posterior probability distribution for the network parameters can be expressed using the Bayes' theorem as

$$P(\theta | D, \alpha, \beta) = \frac{P(D | \theta, \beta) P(\theta | \alpha)}{P(D | \alpha, \beta)} \quad (9)$$

where $P(D | \theta, \beta)$ is the likelihood of the data that accounts for the network accuracy on the training data; and $P(D | \alpha, \beta)$ is a normalization factor which ensures that the posterior gives unity when integrated over the parameter space.

By assuming a zero-mean Gaussian noise in the training data D and Gaussian priors for the network parameters θ , the likelihood of the data and the prior probability of the parameters can be written respectively as

$$P(D | \theta, \beta) = \frac{1}{Z_D(\beta)} \exp(-\beta E_D), \quad P(\theta | \alpha) = \frac{1}{Z_\theta(\alpha)} \exp(-\alpha E_\theta) \quad (10a, b)$$

where $Z_D(\beta) = (\pi/\beta)^{N/2}$ and $Z_\theta(\alpha) = (\pi/\alpha)^{M/2}$.

Substitution of Eq. (10) into Eq. (9) obtains the posterior probability distribution as

$$P(\theta | D, \alpha, \beta) = \frac{1}{Z_s(\alpha, \beta)} \exp(-S(\theta)) \quad (11)$$

where $S(\theta)$ is given by Eq. (8) and $Z_s(\alpha, \beta) = \int \exp(-S(\theta)) d\theta$.

Accordingly, the network parameters corresponding to the maximum posterior distribution or the most plausible network parameters θ^{MP} can be found by minimizing the negative logarithm of Eq. (11) with respect to the network parameters. Since the normalizing factor $Z_s(\alpha, \beta)$ is independent of the network parameters, this is equivalent to minimizing the regularized error function $S(\theta)$ given by Eq. (8). Therefore, by solving the parameter optimization problem to minimize the objective function of Eq. (8), the maximum posterior network parameters can be inferred during the network learning procedure.

The other crucial inference step in the Bayesian learning technique is the optimization of the regularization parameters α and β . By applying the Bayes' theorem, the posterior probability for these two parameters given the data D is represented as

$$P(\alpha, \beta | D) = \frac{P(D | \alpha, \beta) P(\alpha, \beta)}{P(D)} \quad (12)$$

The prior $P(D | \alpha, \beta)$ is assumed to be chosen as very insensitive to the values of α and β . Since $P(D)$ is independent of α and β , the maximum posterior values for the regularization parameters are found by maximizing the likelihood term $P(D | \alpha, \beta)$, which is the normalization factor in Eq. (9). Using Eqs. (9) to (11), the likelihood is derived as

$$P(D | \alpha, \beta) = \frac{P(D | \theta, \beta) P(\theta | \alpha)}{P(\theta | D, \alpha, \beta)} = \frac{Z_s(\alpha, \beta)}{Z_D(\beta) Z_\theta(\alpha)} \quad (13)$$

If the Gaussian approximation is made for the posterior distribution of the network parameters, then Z_s is given by (MacKay, 1992a)

$$Z_s \approx (2\pi)^{M/2} |H^{\text{MP}}|^{-1/2} \exp(-S(\theta^{\text{MP}})) \quad (14)$$

where H^{MP} is the Hessian matrix H of the regularized objective function $S(\theta)$ evaluated at θ^{MP} . Introducing Eq. (14) into Eq. (13) and taking the derivatives of the logarithm of the likelihood respectively with respect to α and β yield

$$\alpha^{\text{MP}} = \frac{\gamma}{2E_\theta^{\text{MP}}}, \quad \beta^{\text{MP}} = \frac{N - \gamma}{2E_D^{\text{MP}}} \quad (15a, b)$$

where $\gamma = M - 2\alpha^{\text{MP}} \text{trace}((H^{\text{MP}})^{-1})$ measures the number of network parameters that are effectively involved in reducing the objective function.

In this study, the Levenberg-Marquardt (LM) algorithm (Marquardt, 1963; Hagan and Menhaj, 1994) is employed to find the most plausible network parameters θ^{MP} to minimize the objective function Eq. (8), due to its efficient and stable convergence for moderate-sized neural networks that contain up to a few hundred weights. The costly computation of the

Hessian matrix can also be solved by making a Gauss-Newton approximation to it using the LM algorithm. As γ depends on α , the values of α and β are re-estimated iteratively using Eq. (15), which is carried out during the training process.

In practical implementation of the Bayesian learning technique, it is suggested that all data sets be normalized into the range of $[-1, 1]$ to avoid that some network parameters will be trained to be extremely large or small to accommodate different scales of input and target variables. In addition, the procedure of multiple random initializations of network parameters is used to retrain the network to assure that the optimal solution, instead of local minima, has been reached.

4.2 Forward dynamic model

4.2.1 Model formulation

In terms of Eq. (5), an NARX network model for describing the forward dynamics of the devised self-sensing MR damper can be expressed as

$$\hat{F}(t) = \mathcal{N}_{fwd}(x(t), \dots, x(t-n_x), \dot{x}(t), \dots, \dot{x}(t-n_{\dot{x}}), I(t), \dots, I(t-n_I), F(t-1), \dots, F(t-n_F)) \quad (16)$$

where x , \dot{x} , I and F are displacement, velocity of the damper piston, current input and damper force, respectively; n_x , $n_{\dot{x}}$, n_I and n_F denote the respective maximum lags of the displacement, velocity, current and damper force; and $\mathcal{N}_{fwd}(\cdot)$ represents the forward input-output mapping identified by an MLP. In Eq. (16), present and past values of the piston displacement, velocity, current together with past values of the sensed damper force, which contain dynamic physical information of the damper, are chosen as possible network input variables to describe its forward dynamics and predict the one-step-ahead damper force.

To assess the prediction performance of the formulated NARX network model, the root mean square error (RMSE) between the measured damper force and the prediction from the model is adopted and evaluated, which is given by

$$\text{RMSE} = \sqrt{\frac{1}{T} \sum_{t=1}^T [F(t) - \hat{F}(t)]^2} \quad (17)$$

4.2.2 Model architecture design

The NARX network employed in this study is configured to consist of three successive layers, which are an input layer, a hidden layer and an output layer, and is formulated as Eq. (6). The activation functions for the hidden and output layers are chosen as a hyperbolic tangent sigmoid function and a linear function, respectively, and expressed as

$$g_1(a) = \tanh(a) = \frac{1 - e^{-2a}}{1 + e^{-2a}}, \quad g_2(a) = a \quad (18a, b)$$

The experimental data from the displacement-controlled tests are used to train, design and evaluate the NARX network model for the self-sensing MR damper. The modeling process is divided into two stages. In the first stage, a training set and a validation set are built up with the acquired experimental data. The training set is used to adapt the network parameters through the Bayesian learning, while the validation set is used for designing

model architecture. In the second stage, the well-trained model is evaluated using a novel test set uninvolved in the first stage to examine its generalization performance. Table 2 lists information of different sinusoidal excitations and input current levels for generating the training, validation and test sets.

Data set	Sinusoidal excitation		Current
	Amplitude	Frequency	
Training	1 mm	1 Hz	0:0.25:1.0 A
	5 mm	5 Hz	0:0.25:1.0 A
	1 mm	5 Hz	0:0.5:1.0 A
	5 mm	1 Hz	0:0.5:1.0 A
Validation	1 mm	1 Hz	0.5 A
	5 mm	5 Hz	0.5 A
	1 mm	5 Hz	0.25, 0.75 A
	5 mm	1 Hz	0.25, 0.75 A
Test	5 mm	2.5 Hz	0:0.25:1.0 A

Table 2. Experimental cases for generation of training, validation and test sets

In designing the NARX network architecture, three important issues are addressed with the purpose of realizing superior modeling performance and enhancing generalization capability. These issues include selection of an optimal combination of input variables, choice of the required numbers of input lags and determination of the optimal number of neurons in the hidden layer.

From the physical behaviors of the self-sensing MR damper shown in Fig. 6 and the model formulation (16), the damper piston displacement (x) and velocity (\dot{x}), the current input to the damper (I), and the past values of the damper force (F) can be chosen as the NARX network inputs. However, to reduce redundant information and obtain a simple network topology for improving model performance, the optimal combination of input variables is identified for the NARX network. In terms of the RMSE index in Eq. (17) evaluated on the validation set in Table 2, Fig. 7 compares the model performance with different input combinations among the input variables x , \dot{x} , I and F . Here the input lags $n_x = n_{\dot{x}} = n_I = 0$ and $n_F = 1$ are taken and the number of hidden neurons (n_h) is equally set to be 15 for each network configuration. It evidences from Fig. 7 that as the combination of either (x , I , F) or (x , \dot{x} , I) is used, poor model performance is obtained, which reveals that the use of both the velocity \dot{x} and the past damper force F is important and essential for enhancing the model prediction quality. The involvement of the current I is also necessary in that it affects the damper force significantly, which is verified by comparing the results with the inputs of (x , \dot{x} , F) and (x , \dot{x} , I , F). Moreover, if all the three variables of \dot{x} , I and F are taken, the role played by the displacement x is negligible.

Fig. 8 shows the network performance over various input combinations, numbers of input lags ($n_x = n_{\dot{x}} = n_I = n_F = 1, 2, 3$) and numbers of hidden neurons ($n_h = 5, 10, 15, 20$). By further comparing the results on different input combinations in Fig. 8, the significance of involving \dot{x} , I and F into the network inputs is again confirmed. The RMSE values of the combination (\dot{x} , I , F) are comparable to those of the combination (x , \dot{x} , I , F) in the same case of input lag. Thereby, from the view of model simplicity, the velocity \dot{x} , the current I and the past damper force F are finally selected as the input variables for the forward model.

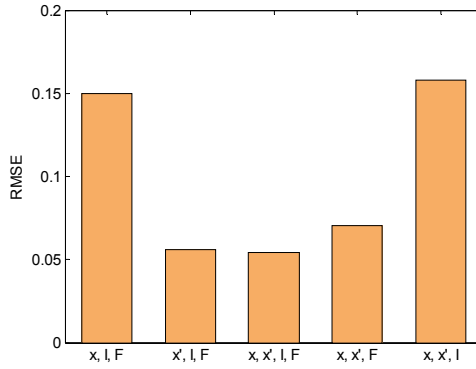


Fig. 7. RMSE analysis for different input combinations ($n_x = n_{\dot{x}} = n_I = 0, n_F = 1, n_h = 15$)

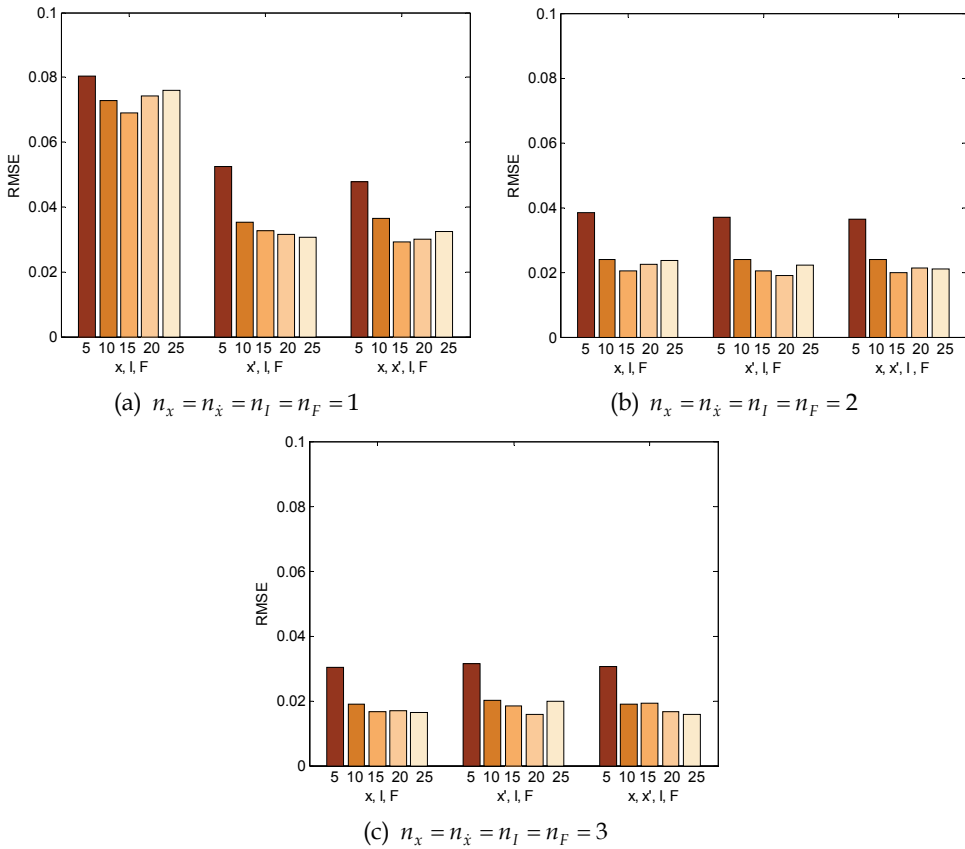


Fig. 8. RMSE analysis for different input lags

On the other hand, effects of the input lags can be observed from Figs. 7 and 8. The RMSE of validation for each network configuration decrease with the increment of the input lag. The

rate of decrease becomes less as larger input lag is used. Especially, for models with inputs of (\dot{x}, I, F) and enough hidden neuron number, larger input lags ($n_x = n_{\dot{x}} = n_I = n_F = 3$) has a relatively small effect on further enhancing the model performance in comparison with the case of $n_x = n_{\dot{x}} = n_I = n_F = 2$. Consequently, the input lag for each input variable is chosen to be two to achieve a compact network topology and its resulting training efficiency.

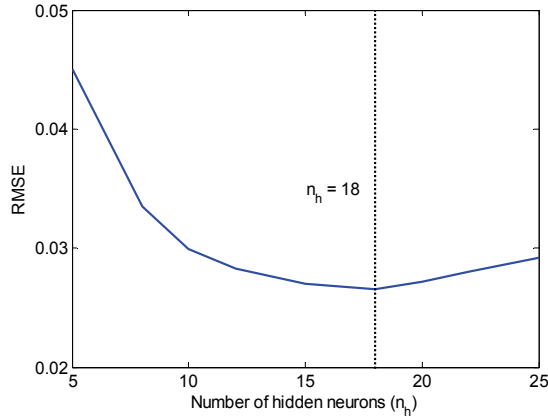


Fig. 9. RMSE analysis for different numbers of hidden neurons ($n_x = n_{\dot{x}} = n_I = n_F = 2$)

Once the input variables and the number of input lags are determined, it is simple to decide the number of hidden neurons (n_h) using a trial and error procedure by extending it from 5 to 25. Fig. 9 displays the RMSE index (evaluated on the validation set) as a function of the number of hidden neurons (n_h). The optimal number of hidden neurons is determined to be 18, in which the minimal RMSE of validation is reached.

With a comprehensive consideration of topology simplicity and model accuracy, an NARX network, configured with 8 input neurons, 18 neurons in one-hidden-layer and 1 output neuron, is designed for modeling the forward dynamics of the self-sensing MR damper.

4.2.3 Model prediction capability under harmonic excitations

Generalization performance of the configured Bayesian NARX network is examined using the test set given in Table 2. The test set is acquired under 2.5 Hz sinusoidal displacement excitations with an amplitude of 5 mm and current inputs ranging from 0 A to 1.0 A, which has not been involved in the stage of training and is new for the model assessment. The one-step-ahead damper force is produced from the model once it is exposed to the test data. The RMSE between the predicted and measured damper forces is less than 0.04 for each case of input current in the test set, as shown in Table 3, which demonstrates that the model generalizes well. Fig. 10 plots the hysteresis loops of force-displacement and force-velocity of the damper obtained from the predicted results of the model and from the experimentally recorded data. A comparison between the predicted and measured results indicates that the NARX network model accurately describes the hysteretic behaviors of the self-sensing MR damper. It also well learns the saturation effects of the damper, verifying the learning ability of the Bayesian NARX network technique.

Current (A)	0	0.25	0.5	0.75	1.0
RMSE	0.0269	0.0132	0.0173	0.0238	0.0312

Table 3. RMSE results for test set

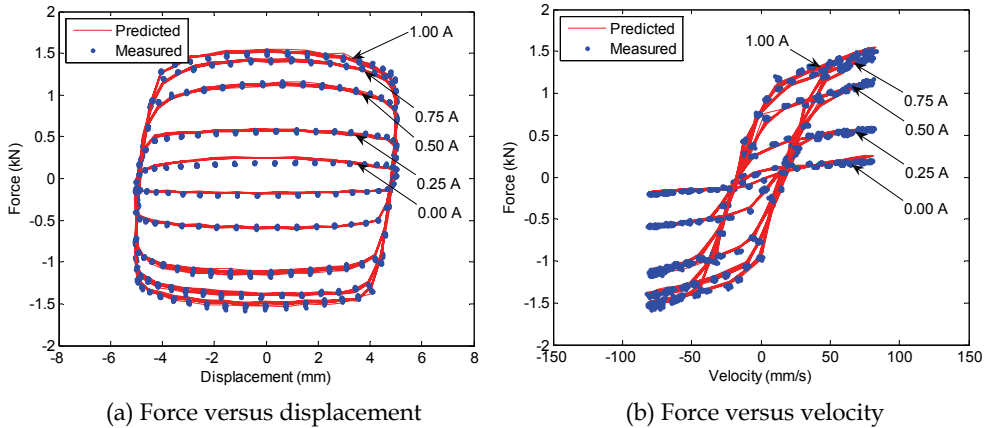


Fig. 10. Comparison of predicted and measured force-displacement and force-velocity loops under 5 mm, 2.5 Hz harmonic excitation

4.2.4 Model prediction capability under random excitations

All of the data examined previously for the Bayesian NARX network modeling have been based on the responses of the self-sensing MR damper subjected to harmonic displacement-controlled excitations and commanded by currents held at constant levels. However, an important requirement for system modeling is a set of representative data containing abundant system information. To ensure generalization and robustness of the damper models in practical control circumstances, multiple harmonic excitations are often insufficient due to the limited amount of information included within them. Therefore, random displacement-controlled excitations and current inputs are more appropriate for activating the dynamic behaviors of the self-sensing MR damper and acquiring the random data for training the NARX network models. In this subsection, performance of the Bayesian NARX network model with random excitations and input commands will be examined.

For acquiring random responses, the self-sensing MR damper is installed with a steel-frame structure mounted on a shaking table, as shown in Fig. 11. The structure consists of a stack of steel plates weighing 655.8 kg as the floor mass and four steel columns with 75 mm × 10 mm rectangular cross-sections. The damper is connected between the mass and a support in the height of 745 mm. The support for fixing one end of the damper is designed to be rigid enough to assume this end is unmovable. The structural system is excited by band-limited white noise ground motions produced by the shaking table, while the damper is controlled by varying current commands. The real-time data acquisition for a variety of structural responses, which include ground acceleration, floor displacement, damper piston displacement, current and damper force, is accomplished by a dSPACE system by setting the sampling rate to be 250 Hz. Velocity of the damper piston is calculated from the measured piston displacement using a finite difference approximation.

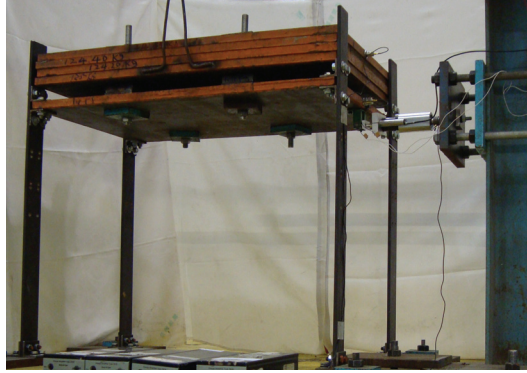


Fig. 11. Experimental setup for random vibration testing of self-sensing MR damper

With the purpose of assessing its prediction capability under random loadings, the previous optimal Bayesian NARX network model is retrained using the random response data of the self-sensing MR damper, which are acquired when the structural system subjected to narrow-band white noise excitations with amplitude of about 8 m/s^2 and frequency within $0.8\text{-}10 \text{ Hz}$. The damper is controlled by random current with amplitude ranging from 0 A to 1.85 A and frequency within $0\text{-}10 \text{ Hz}$. Fig. 12 illustrates the damper piston velocity, current and damper force signals for network training within a time window of 10 s . After training, another three sets of measured data unseen during the training phase are used for verification of the trained model. As listed in Table 4, these test sets are obtained when the structure is excited by ground motions with different frequency and amplitude ranges, while the damper is prescribed with three types of currents, including constant current held at 0.97 A , chirp current with amplitude between $0\text{-}1.85 \text{ A}$ and frequency range of $0.1\text{-}10 \text{ Hz}$, as well as random current with amplitude between $0\text{-}1.85 \text{ A}$ and frequency within $0\text{-}5 \text{ Hz}$.

Fig. 13 shows time histories of the damper forces predicted by the Bayesian NARX network model based on the test sets shown in Table 4 together with the measured damper forces, in which the prediction residuals are also superposed. Through comparisons, the forward

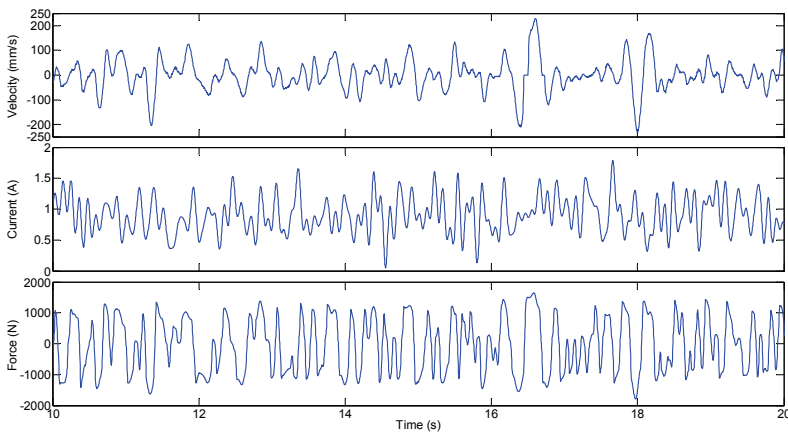


Fig. 12. Random signals for network training

Data set	Ground acceleration excitation		Current		
	Amplitude	Frequency	Type	Amplitude	Frequency
Training	-7.7~8.1 m/s ²	0.8-10 Hz	Random	0-1.85 A	0-10 Hz
Test I	-5.6~5.9 m/s ²	0.8-5 Hz	Constant	0.97 A	--
Test II	-5.3~5.2 m/s ²	0.5-10 Hz	Chirp	0-1.85 A	0.1-10 Hz
Test III	-8.2~8.0 m/s ²	0.5-10 Hz	Random	0-1.85 A	0-5 Hz

Table 4. Information of excitations for generation of training and test sets

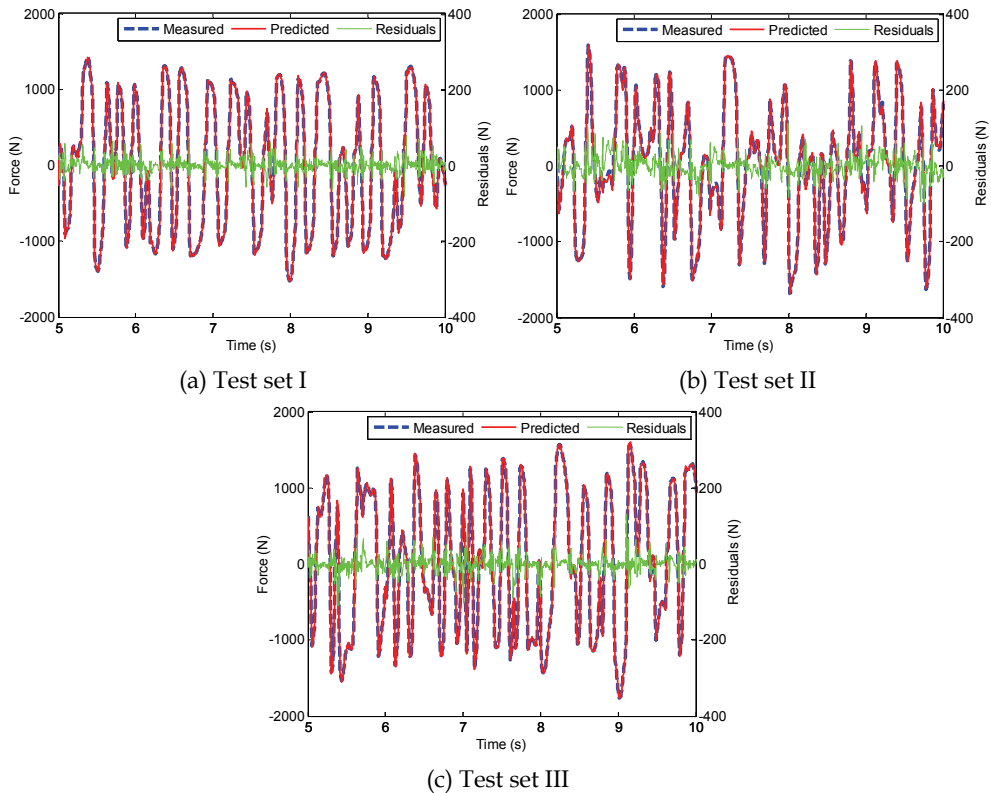


Fig. 13. Comparison between predicted and measured damper forces and their residuals

model effectively predicts the damper forces with the RMSE values of 19.20 N, 27.30 N and 23.01 N for test sets I, II and III, respectively, which are all lower than 5% of the norm values of their corresponding target forces. Hence, the Bayesian NARX network model generalizes well to the random situations.

4.3 Inverse dynamic model

In control application of the self-sensing MR damper, similar to the conventional MR dampers, current is the only physical quantity that can be directly controlled to render the

damper to track the optimal control force calculated by a certain active control algorithm. Dyke et al. (1996) proposed a clipped optimal control algorithm for commanding the current or voltage which, however, only switches at either the minimum or the maximum achievable level. To avoid the damper working in such a bang-bang manner, which requires very fast dynamic responses of a current driver and the damper, it is beneficial and essential to develop an inverse dynamic model for the self-sensing MR damper to produce continuously varying current signals. However, it is still a difficult task to build such an inverse model for the highly nonlinear damper. Due to the success of the Bayesian NARX network in modeling the forward dynamics of the self-sensing MR damper, the feasibility of applying this technique to emulate the inverse dynamics of the self-sensing MR damper is explored.

According to Eqs. (5) and (16), an NARX network model for the inverse dynamics of the self-sensing MR damper can be represented as

$$\hat{I}(t) = \mathcal{N}_{inv}(x(t), \dots, x(t-n_x), \dot{x}(t), \dots, \dot{x}(t-n_{\dot{x}}), F(t), \dots, F(t-n_F), I(t-1), \dots, I(t-n_I)) \quad (19)$$

where $\mathcal{N}_{inv}(\cdot)$ denotes an MLP trained to approximate the inverse input-output relationship of the damper. Present and past values of the damper piston displacement, velocity and the desired damper force together with past values of the applied current are taken as possible input variables for the inverse model to decide the required current $\hat{I}(t)$ for the damper to produce the instant value of the desired control force $F(t)$.

Similar to the forward model, the input variables for the inverse model are also determined to be the damper piston velocity \dot{x} , the desired damper force F and the past current I with input lags of $n_{\dot{x}} = n_F = n_I = 2$. The network structure is the same as Eq. (6), and consists of three sequential layers assigned with 8 input neurons, 18 hidden neurons and 1 output neuron, respectively. Transfer functions for the hidden layer and the output layer are taken as a hyperbolic tangent sigmoid function and a linear function, respectively, in the forms given by Eq. (18).

The envisaged inverse NARX network model is then trained by employing the Bayesian learning algorithm. The training data are the same as the random signals employed for building the forward model, as shown in Fig. 12 and Table 4. Subsequently, test sets defined in Table 4 are presented to the inverse model to evaluate the prediction performance. Fig. 14 illustrates the predicted currents from the well trained Bayesian NARX network model in comparison with the measured ones, as well as their residuals. It is seen that the predicted currents in the constant, chirp and random cases agree well with the measured currents applied to the damper. The RMSE values of predictions for test sets I, II and III are 0.016, 0.018 and 0.008 A, respectively. These verification results demonstrate that the developed Bayesian NARX network model satisfactorily emulates the inverse dynamics of the self-sensing MR damper and is adequate for control applications.

5. Conclusions

A self-sensing MR damper with embedded piezoelectric force sensor was devised, calibrated and characterized. Experimental results have shown reliable force sensing and controllable damping capabilities, as well as nonlinear hysteresis and saturation behaviors of the self-sensing MR damper. The attractive sensing-while-damping function renders the

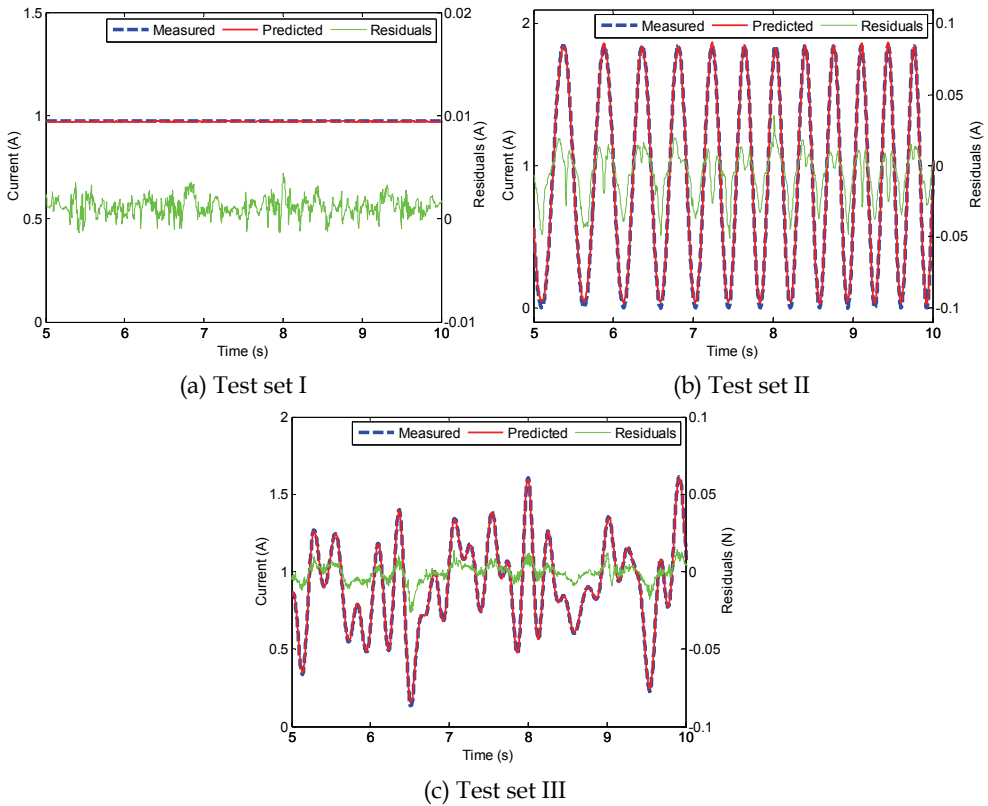


Fig. 14. Comparison between predicted and measured currents and their residuals

devised damper promising for real-time closed-loop control of structural vibration in a relatively simple and cost-effective manner.

In order to formulate the inherently nonlinear dynamics of the self-sensing MR damper for its control application, a black-box modeling method has been developed by synthesizing NARX model and neural network within a Bayesian inference framework. Verification results based on experimental data have demonstrated that the formulated Bayesian NARX network models with an appropriate architecture can accurately emulate the forward and inverse dynamic behaviors of the self-sensing MR damper. Also, they exhibit good generalization capability when exposed to different test scenarios, due to the effect of the automated regularization of the Bayesian learning technique during the training phase. As a result, the developed models can be further integrated with semiactive control algorithms to achieve real-time structural vibration control using the self-sensing MR damper.

6. Acknowledgements

The work described in this chapter was supported in part by a grant from the Research Grants Council of the Hong Kong Special Administrative Region, China (Project No. PolyU 5252/07E), and partially by a grant from The Hong Kong Polytechnic University through

the Development of Niche Areas Programme (Project No. 1-BB95). These supports are gratefully acknowledged.

7. References

- Cao, M.; Wang, K. W. & Lee, K. Y. (2008). Scalable and invertible PMNN model for magneto-rheological fluid dampers. *Journal of Vibration and Control*, Vol. 14, No. 5, (May 2008) 731-751, ISSN 1077-5463
- Carlson, J. D.; Catanzarite, D. M. & Clair, K. A. St. (1996). Commercial magneto-rheological fluid devices. *International Journal of Modern Physics B*, Vol. 10, No. 23-24, (October 1996) 2857-2865, ISSN 0217-9792
- Chang, C.-C. & Roschke, P. N. (1998). Neural network modeling of a magnetorheological damper. *Journal of Intelligent Material Systems and Structures*, Vol. 9, No. 9, (September 1998) 755-764, ISSN 1045-389X
- Chang, C.-C. & Zhou, L. (2002). Neural network emulation of inverse dynamics for a magnetorheological damper. *Journal of Structural Engineering*, Vol. 128, No. 2, (February 2002) 231-239, ISSN 0733-9445
- Chen, S.; Billings, S. A. & Grant, P. M. (1990). Non-linear system identification using neural networks. *International Journal of Control*, Vol. 51, No. 6, (January 1990) 1191-1214, ISSN 0020-7179
- Chen, Z. Q.; Wang, X. Y.; Ko, J. M.; Ni, Y. Q.; Spencer, B. F.; Yang, G. & Hu, J. H. (2004). MR damping system for mitigating wind-rain induced vibration on Dongting Lake Cable-Stayed Bridge. *Wind and Structures*, Vol. 7, No. 5, (September 2004) 293-304, ISSN 1226-6116
- Choi, S.-B.; Seong, M.-S. & Ha, S.-H. (2009). Vibration control of an MR vehicle suspension system considering both hysteretic behavior and parameter variation. *Smart Materials and Structures*, Vol. 18, No. 12, (December 2009) 125010, ISSN 0964-1726
- Du, H.; Lam, J. & Zhang, N. (2006). Modelling of a magneto-rheological damper by evolving radial basis function networks. *Engineering Applications of Artificial Intelligence*, Vol. 19, No. 8, (December 2006) 869-881, ISSN 0952-1976
- Du, H. & Zhang, N. (2008). Application of evolving Takagi-Sugeno fuzzy model to nonlinear system identification. *Applied Soft Computing*, Vol. 8, No. 1, (January 2008) 676-686, ISSN 1568-4946
- Duan, Y. F.; Ni, Y. Q. & Ko, J. M. (2005). State-derivative feedback control of cable vibration using semiactive magnetorheological dampers. *Computer-Aided Civil and Infrastructure Engineering*, Vol. 20, No. 6, (November 2005) 431-449, ISSN 1093-9687
- Dyke, S. J.; Spencer, B. F. Jr.; Sain, M. K. & Carlson, J. D. (1996). Modeling and control of magnetorheological dampers for seismic response reduction. *Smart Materials and Structures*, Vol. 5, No. 5, (October 1996) 565-575, ISSN 0964-1726
- Gandhi, F.; Wang, K. W. & Xia, L. (2001). Magnetorheological fluid damper feedback linearization control for helicopter rotor application. *Smart Materials and Structures*, Vol. 10, No. 1, (February 2001) 96-103, ISSN 0964-1726
- Gordaninejad, F.; Saiidi, M.; Hansen, B. C.; Ericksen, E. O. & Chang, F.-K. (2002). Magneto-rheological fluid dampers for control of bridges. *Journal of Intelligent Material Systems and Structures*, Vol. 13, No. 2-3, (February 2002) 167-180, ISSN 1045-389X

- Hagan, M. T. & Menhaj, M. B. (1994). Training feedforward networks with the Marquardt algorithm. *IEEE Transactions on Neural Networks*, Vol. 5, No. 6, (November 1994) 989-993, ISSN 1045-9227
- Hornik, K.; Stinchcombe, M. & White, H. (1989). Multilayer feedforward networks are universal approximators. *Neural Networks*, Vol. 2, No. 5, (July 1989) 359-366, ISSN 0893-6080
- Hu, W. & Wereley, N. M. (2008). Hybrid magnetorheological fluid-elastomeric lag dampers for helicopter stability augmentation. *Smart Materials and Structures*, Vol. 17, No. 4, (August 2008) 045021, ISSN 0964-1726
- Ikhouane, F. & Dyke S. J. (2007). Modeling and identification of a shear mode magnetorheological damper. *Smart Materials and Structures*, Vol. 16, No. 3, (June 2007) 605-616, ISSN 0964-1726
- Jiménez, R. & Álvarez-Icaza, L. (2005). LuGre friction model for a magnetorheological damper. *Structural Control and Health Monitoring*, Vol. 12, No. 1, (October 2004) 91-116, ISSN 1545-2255
- Jin, G.; Sain, M. K. & Spencer, B. F. Jr. (2005). Nonlinear blackbox modeling of MR-dampers for civil structural control. *IEEE Transactions on Control Systems Technology*, Vol. 13, No. 3, (May 2005) 345-355, ISSN 1063-6536
- Johnson, E. A.; Baker, G. A.; Spencer, B. F. Jr. & Fujino, Y. (2000). Mitigating stay cable oscillation using semiactive damping, *Proceedings of SPIE, Smart Structures and Materials 2000: Smart Systems for Bridges, Structures, and Highways*, Vol. 3988, pp. 207-216, ISBN 0-8194-3606-2, Newport Beach, CA, USA, March 2000, SPIE, Bellingham
- Jung, H.-J.; Spencer, B. F. Jr.; Ni, Y. Q. & Lee, I.-W. (2004). State-of-the-art of semiactive control systems using MR fluid dampers in civil engineering applications. *Structural Engineering and Mechanics*, Vol. 17, No. 3, (March 2004) 493-526, ISSN 1225-4568
- Kamath, G. M. & Wereley, N. M. (1997). A nonlinear viscoelastic-plastic model for electrorheological fluids. *Smart Materials and Structures*, Vol. 6, No. 3, (June 1997) 351-359, ISSN 0964-1726
- Ko, J. M.; Ni, Y. Q.; Chen, Z. Q. & Spencer, B. F. Jr. (2002). Implementation of magnetorheological dampers to Dongting Lake Bridge for cable vibration mitigation, *Proceedings of the Third World Conference on Structural Control*, Vol. 3, pp. 777-786, ISBN 0-4744-8980-8, Como, Italy, April 2002, John Wiley & Sons, Chichester
- Leshno, M.; Lin, V. Y.; Pinkus, A. & Schocken, S. (1993). Multilayer feedforward networks with a nonpolynomial activation function can approximate any function. *Neural Networks*, Vol. 6, No. 6, (August 1993) 861-867, ISSN 0893-6080
- Leva, A. & Piroddi, L. (2002). NARX-based technique for the modelling of magnetorheological damping devices. *Smart Materials and Structures*, Vol. 11, No. 1, (February 2002) 79-88, ISSN 0964-1726
- Levin, A. U. & Narendra, K. S. (1996). Control of nonlinear dynamical systems using neural networks - part II: observability, identification, and control. *IEEE Transactions on Neural Networks*, Vol. 7, No. 1, (January 1996) 30-42, ISSN 1045-9227
- Li, H.; Liu, M.; Li, J.; Guan, X. & Ou, J. (2007). Vibration control of stay cables of the Shandong Binzhou Yellow River Highway Bridge using magnetorheological fluid

- dampers. *Journal of Bridge Engineering*, Vol. 12, No. 4, (July/August 2007) 401-409, ISSN 1084-0702
- Liao, W. H. & Wang, D. H. (2003). Semiactive vibration control of train suspension systems via magnetorheological dampers. *Journal of Intelligent Material Systems and Structures*, Vol. 14, No. 3, (March 2003) 161-172, ISSN 1045-389X
- Loh, C.-H.; Lynch, J. P.; Lu, K.-C. & Wang, Y. (2007). Experimental verification of a wireless sensing and control system for structural control using MR dampers. *Earthquake Engineering and Structural Dynamics*, Vol. 36, No. 10, (August 2007) 1303-1328, ISSN 0098-8847
- MacKay, D. J. C. (1992a). A practical Bayesian framework for backprop networks. *Neural Computation*, Vol. 4, No. 3, (May 1992) 448-472, ISSN 0899-7667
- MacKay, D. J. C. (1992b). Bayesian interpolation. *Neural Computation*, Vol. 4, No. 3, (May 1992) 415-447, ISSN 0899-7667
- Marquardt, D. W. (1963). An algorithm for least-squares estimation of nonlinear parameters. *Journal of the Society for Industrial and Applied Mathematics*, Vol. 11, No. 2, (June 1993) 431-441, ISSN 0368-4245
- Ni, Y. Q.; Chen, Y.; Ko, J.M. & Cao, D.Q. (2002). Neuro-control of cable vibration using semi-active magneto-rheological dampers. *Engineering Structures*, Vol. 24, No. 3, (March 2002) 295-307, ISSN 0141-0296
- Or, S. W.; Duan, Y. F.; Ni, Y. Q.; Chen, Z. H. & Lam, K. H. (2008). Development of magnetorheological dampers with embedded piezoelectric sensors for structural vibration control. *Journal of Intelligent Material Systems and Structures*, Vol. 19, No. 11, (November 2008) 1327-1338, ISSN 1045-389X
- Schurter, K. C. & Roschke, P. N. (2000). Fuzzy modeling of a magnetorheological damper using ANFIS. *Proceedings of the Ninth IEEE International Conference on Fuzzy Systems*, Vol. 1, pp. 122-127, ISBN 0-7803-5877-5, San Antonio, TX, May 2000, IEEE, Piscataway
- Schurter, K. C. & Roschke, P. N. (2001). Neuro-fuzzy control of structures using acceleration feedback. *Smart Materials and Structures*, Vol. 10, No. 4, (August 2001) 770-779, ISSN 0964-1726
- Song, X.; Ahmadian, M.; Southward, S. & Miller, L. R. (2005). An adaptive semiactive control algorithm for magnetorheological suspension systems. *Journal of Vibration and Acoustics*, Vol. 127, No. 5, (October 2005) 493-502, ISSN 1048-9002
- Spencer, B. F. Jr.; Dyke, S. J.; Sain, M. K. & Carlson, J. D. (1997). Phenomenological model for magnetorheological dampers. *Journal of Engineering Mechanics*, Vol. 123, No. 3, (March 1997) 230-238, ISSN 0733-9399
- Suykens, J. A. K., Vandewalle, J. P. L. & De Moor, B. L. R. (1996). *Artificial Neural Networks for Modeling and Control of Non-linear Systems*, Kluwer Academic, ISBN 0-7923-9678-2, Boston
- Tsang, H. H.; Su, R. K. L. & Chandler, A. M. (2006). Simplified inverse dynamics models for MR fluid dampers. *Engineering Structures*, Vol. 28, No. 3, (February 2006) 327-341, ISSN 0141-0296
- Wang, D.-H. & Liao, W.-H. (2001). Neural network modeling and controllers for magnetorheological fluid dampers, *Proceedings of the 10th IEEE International Conference on Fuzzy Systems*, pp. 1323-1326, ISBN 0-7803-7293-X, Melbourne, Australia, December 2001, IEEE, Piscataway.

- Weber, F.; Distl, H.; Feltrin, G. & Motavalli, M. (2005a). Evaluation procedure of decay measurements of a cable with passive-on operating MR damper, *Proceedings of the Sixth International Symposium on Cable Dynamics*, pp. 143-150, Charleston, USA, September 2005, AIM, Liège
- Weber, F.; Distl, H.; Feltrin, G. & Motavalli, M. (2005b). Simplified approach of velocity feedback for MR dampers on real cable-stayed bridges, *Proceedings of the Sixth International Symposium on Cable Dynamics*, pp. 107-114, Charleston, USA, September 2005, AIM, Liège
- Wereley, N. M.; Pang, L. & Kamath G. M. (1998). Idealized hysteresis modeling of electrorheological and magnetorheological dampers. *Journal of Intelligent Material Systems and Structures*, Vol. 9, No. 8, (August 1998) 642-649, ISSN 1045-389X
- Xia, P.-Q. (2003). An inverse model of MR damper using optimal neural network and system identification. *Journal of Sound and Vibration*, Vol. 266, No. 5, (October 2003) 1009-1023, ISSN 0022-460X
- Zhou, L.; Chang, C.-C. & Wang, L.-X. (2003). Adaptive fuzzy control for nonlinear building-magnetorheological damper system. *Journal of Structural Engineering*, Vol. 129, No. 7, (July 2003) 905-913, ISSN 0970-0137

Vibration Isolation System Using Negative Stiffness

Taksehi Mizuno
Saitama University
Japan

1. Introduction

Vibration isolation plays an important role in the operation of many advanced production and measurement systems such as semiconductor manufacturing and high-precision measuring. Rapid technological developments in these fields have increased the need for higher-performance vibration isolation systems.

There are two kinds of vibration that must be reduced by a vibration isolation system:

1. vibration transmitted from the ground through the suspension (ground vibration),
2. vibration caused by disturbances acting on an isolation table (direct disturbance).

A suspension with less stiffness is better for reducing the former because dynamic coupling between the vibration source and the isolation table is weakened; thus, zero stiffness is ideal. However, higher stiffness is better for suppressing the latter because it reduces displacement of the isolation table from its desired position; thus, infinite stiffness is ideal. In conventional passive-type vibration isolation systems, a trade-off between lower and higher stiffness is inevitable, so that performance is limited.

In contrast, active-type vibration isolation systems do not suffer from such performance limitations (Rivin, 2003). In particular, the performance limitations of passive-type vibration isolation systems can be effectively overcome by two-degrees-of-freedom control (Yasuda *et al.*, 1996). There are also various control methods applied according to required performance and acceptable cost. One of the fundamental control strategies is to provide feedback regarding the absolute velocity of the isolation table, which is often referred to as skyhook damping (Fuller *et al.*, 1996). State feedback (Miyazaki *et al.*, 1994), feedforward (Mohamed *et al.*, 2005) and active acceleration control (Zhu *et al.*, 2006) have also been applied. Meanwhile, most active vibration isolation systems use high-performance sensors, such as servo-type accelerometers, to detect the vibration of an isolation table with high sensitivity in a low-frequency domain. Since these sensors are costly, active systems are more expensive than passive systems, sometimes by a factor of ten, which represents a critical obstacle to expanding their fields of application.

This chapter presents a novel solution to the problem of vibration isolation (Mizuno *et al.*, 2006a). It uses suspension with negative stiffness. Infinite stiffness against direct disturbances acting on the isolation table can be achieved by combining the suspension with a normal spring. As a result, direct vibration is suppressed while system vibration transmitted from the ground is reduced. Suspension with negative stiffness can be achieved by using only relative-displacement sensors, which cost far less than servo-type

accelerometers. This chapter describes the principles of vibration isolation system using negative stiffness and the control methods of realizing negative stiffness.

The application of negative stiffness to vibration isolation was previously reported by Platus (1999) and Trimboli *et al.* (1994). In their work, a negative spring was used in *parallel* with a positive spring to lower the stiffness of suspension. In our approach, by contrast, *serial* connection of a negative spring and a positive spring is applied to vibration isolation system.

2. Principles of vibration isolation system using negative stiffness

2.1 Basic configuration

The concept of the proposed vibration isolation is illustrated by using Fig.2.1. When two springs with spring constants k_1 and k_2 are connected in series, the total stiffness k_c is given by (Mizuno *et al.*, 2006a)

$$k_c = \frac{k_1 k_2}{k_1 + k_2} . \quad (2.1)$$

This equation shows that when normal springs are connected the total stiffness becomes lower than the stiffness of each spring. However, if one of the springs has negative stiffness

$$k_1 = -k_2 , \quad (2.2)$$

the resultant stiffness becomes infinite:

$$|k_c| = \infty . \quad (2.3)$$

This principle of generating high stiffness is applied to vibration isolation system to counteract direct disturbances acting on the isolation table.

Figure 2.2 shows a conceptual model of the proposed vibration isolation system (Mizuno *et al.*, 2003a). A middle mass m_1 is supported by a spring k_1 with positive stiffness (*positive spring*) and a damper c_1 ; they work like a passive suspension. A linear actuator fixed on the middle mass supports a isolation table m_2 . The actuator is controlled to have negative stiffness $-k_n$ as shown in Fig.2.3. In the initial steady states (Fig.2.3a), the distance between the table m and the base is kept to be L . When downward force ΔF is applied to the table, the distance increases by ΔL as shown in Fig.2.3b. The displacement of the table is in the direction opposite to the added force so that the static stiffness of the suspension is given by

$$-\frac{\Delta F}{\Delta L} (\equiv -k_n) . \quad (2.4)$$

This system can reduce vibration transmitted from ground by making k_1 small because the dynamic coupling between the vibration source (ground) and the isolation table *via the middle mass* is weakened. At the same time, infinite stiffness can be produced to counteract direct disturbances by setting the amplitude of negative stiffness k_n equal to k_1 . To explain such action more concretely, it is assumed that the table is subject to a downward force. The distance between the middle mass and the table becomes larger because of the *negative stiffness*; *that is*, the table would move upwards if the middle mass were fixed. Meanwhile,

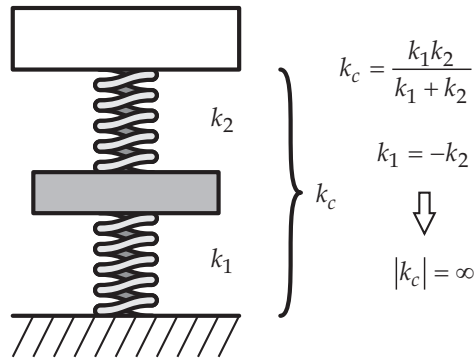


Fig. 2.1. Series connection of two springs

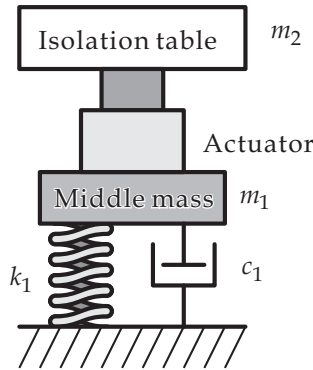


Fig. 2.2. Basic structure of vibration isolation system

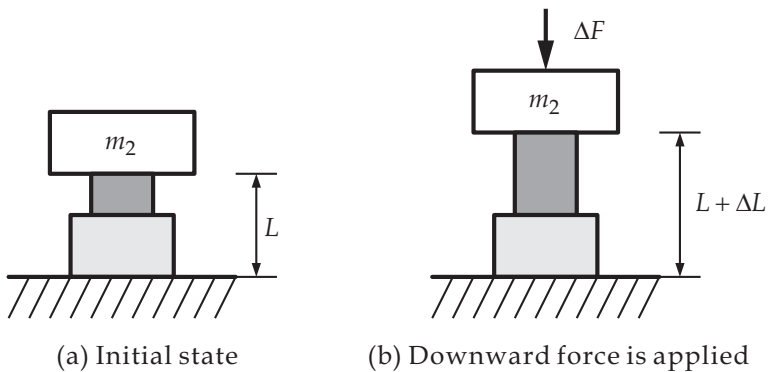


Fig. 2.3. Negative stiffness achieved by the actuator

the middle mass moves downwards because of *positive* stiffness. The increase in the distance is cancelled by the downward displacement of the middle mass due to the above-mentioned setting. Thus, the isolation table is maintained at the same position as before.

It is to be mentioned that suspension with negative stiffness can be achieved by using only relative-displacement sensors, which cost far less than servo-type accelerometers.

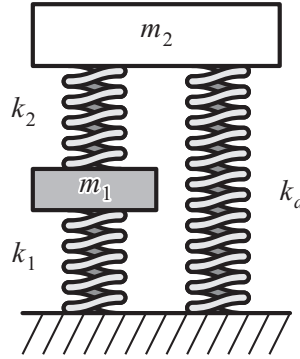


Fig. 2.4. Introduction of a parallel spring

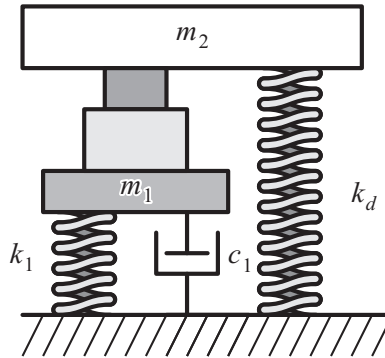


Fig. 2.5. Vibration isolation system with a weight support mechanism

2.2 Introduction of weight support mechanism

In the system shown by Fig.2.2, the entire weight of the isolation table is supported by the linear actuator. When the isolation table is large, therefore, high-power actuators are needed to suspend its weight, which will raise the cost of system. Such problem can be overcome by introducing an auxiliary suspension for supporting the weight of the isolation table, as explained in Fig.2.4 (Mizuno *et al.*, 2006a). A spring k_d is added in parallel with the serial connection of the positive and negative springs. The total stiffness \tilde{k}_c is given by

$$\tilde{k}_c = \frac{k_1 k_2}{k_1 + k_2} + k_d. \quad (2.5)$$

When Eq. (2.2) is satisfied, the resultant stiffness becomes infinite for any finite value of k_d .

$$|\tilde{k}_c| = \infty. \quad (2.6)$$

Figure 2.5 shows the configuration of one of the proposed vibration isolation systems. A spring k_d is inserted between the isolation table and the base. The spring is set to reduce the suspension force produced by the actuator in the equilibrium state. It should be noted that isolation from ground vibration can be maintained by using a soft spring as k_d .

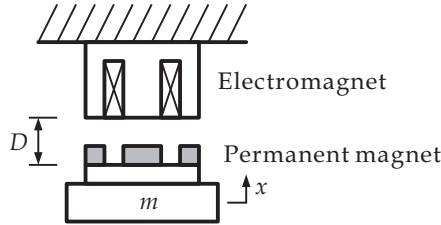


Fig. 3.1. Basic model of zero-power magnetic suspension system

3. Realization of negative stiffness

3.1 Zero-power control

Controller design. To maintain stability, suspension with negative stiffness is realized by using active control. The original system has used zero-power magnetic suspension. Due to its power-saving properties, zero-power control has been used in magnetic suspension systems such as momentum wheels for spacecraft stabilization (Sabnis *et al.*, 1975) and carrier systems in clean rooms (Morishita *et al.*, 1989). In this form of control, a hybrid magnet consisting of an electromagnet and a permanent magnet is used. Control of the electromagnet makes steady deviation of the coil current converge to zero. As a result, the air-gap length is maintained so that the attractive force generated by the permanent magnet balances the other, static forces acting on the suspended object.

Figure 3.1 shows a single-degree-of-freedom-of-motion model for analysis (Mizuno & Takemori, 2002). A hybrid magnet consisting of a permanent magnet and a pair of electromagnets is used for generating suspension force. The suspended object with a mass of m is assumed to move only in the vertical direction translationally. The equation of motion is given by

$$m\ddot{x}(t) = k_s x(t) + k_i i(t) + f_d(t), \quad (3.1)$$

where x is the displacement of the suspended object, k_s and k_i are, respectively, the gap-force and current-force coefficients, i is the control current, and f_d is the disturbance force acting on the suspended object. The transfer function representation of the dynamics described by Eq. (3.1) becomes

$$X(s) = \frac{1}{t_o(s)} (b_0 I(s) + d_0 F_d(s)), \quad (3.2)$$

in which each Laplace-transformed variable is denoted by its capital, and

$$t_o(s) = s^2 - a_0, \quad (3.3)$$

$$a_0 = \frac{k_s}{m}, \quad b_0 = \frac{k_i}{m}, \quad d_0 = \frac{1}{m}. \quad (3.4)$$

The zero-power control operates to accomplish

$$\lim_{t \rightarrow \infty} i(t) = 0 \text{ for stepwise disturbances,} \quad (3.5)$$

In discussing the zero-power control, therefore, disturbance should be considered to be stepwise.

$$F_d(s) = \frac{F_0}{s} \quad (F_0 : \text{const}), \quad (3.6)$$

Considering linear output feedback control, the control input can be represented as

$$I(s) = -\frac{h(s)}{g(s)} X(s), \quad (3.7)$$

where $g(s)$ and $h(s)$ are coprime polynomials in s . They are selected for the closed-loop system to be stable.

Substituting Eq. (3.7) into Eq. (3.2) gives

$$X(s) = \frac{g(s)}{t(s)} d_0 F_d(s), \quad (3.8)$$

where

$$t(s) = (s^2 - a_{21})g(s) + a_{23}h(s). \quad (3.9)$$

Substituting Eqs. (3.6) and (3.8) into Eq. (3.7) gives

$$I(s) = -\frac{h(s)}{t(s)} d_0 \cdot \frac{F_0}{s}. \quad (3.10)$$

To achieve the control object described by Eq. (3.5), $h(s)$ must satisfy

$$h(s) = \tilde{s}h(s), \quad (3.11)$$

where $\tilde{h}(s)$ is an appropriate polynomial. Therefore, the control input achieving zero-power control is represented by

$$I(s) = -\frac{\tilde{s}\tilde{h}(s)}{g(s)} X(s). \quad (3.12)$$

Figure 3.2(a) shows a general form of zero-power controller (Mizuno & Takemori, 2002). Since velocity is the time derivative of displacement, it indicates that an approach for achieving the zero-power control is

[Approach 1] Feeding back the velocity of the suspended object.

Substituting Eq.(3.12) into Eq.(3.7) and transforming it gives

$$I(s) = -\frac{\tilde{s}\tilde{h}(s)}{g(s)} X(s) = -\frac{1}{1 - \frac{\tau}{s}} \cdot \frac{(s - \tau)\tilde{h}(s)}{g(s)} X(s). \quad (3.13)$$

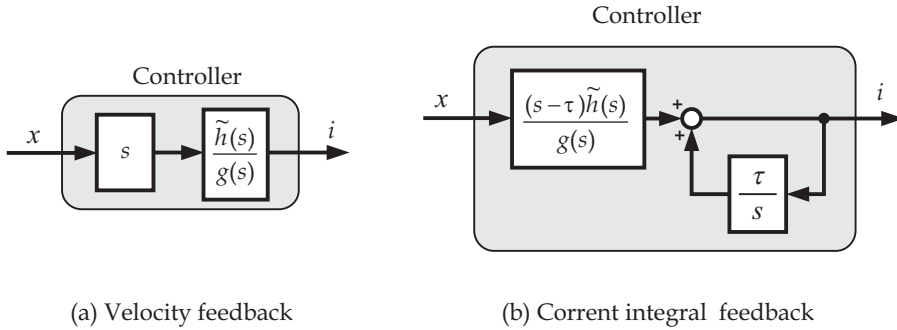


Fig. 3.2. General forms of zero-power controller

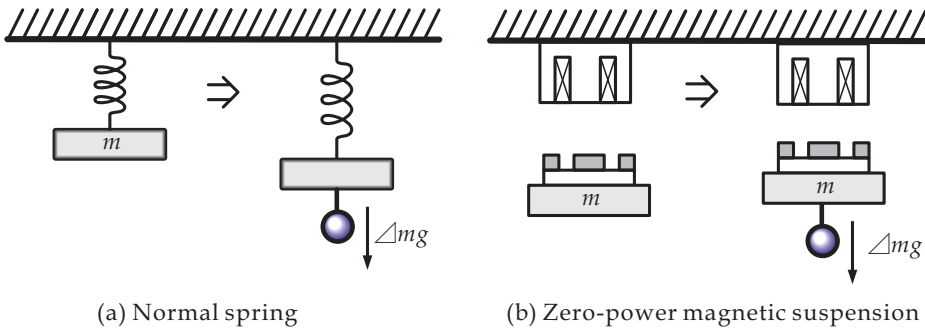


Fig. 3.3. Comparison of zero-power magnetic suspension with a normal spring

where τ is a parameter introduced for the transformation. Figure 3.2(b) shows the transformed block diagram. It indicates another approach for achieving virtually zero-power control:

[Approach 2] Introducing a minor feedback of the integral of current.

In actual implementation, this configuration is more often used which is combined with PD control as mentioned in Section 4.1.

Negative Stiffness. A unique characteristic of the zero-power control system is that it behaves as if it has negative stiffness. When an external force is applied to the mass in a common mass-spring system, the mass moves to the direction of the applied force, as shown in Fig.3.3a. In the system controlled by zero-power, the suspended object moves to a new equilibrium position located in the direction opposite to the applied force, as shown in Fig.3.3b. This characteristic is shown analytically in the following.

At steady state, the suspended object is maintained at a position such that

$$0 = k_s x(\infty) + k_i i(\infty) + F_0 . \tag{3.14}$$

In the zero-power control system, the coil current is controlled to converge to zero, that is

$$i(\infty) = 0 . \tag{3.15}$$

Therefore,

$$x(\infty) = -\frac{F_0}{k_s}. \quad (3.16)$$

The negative sign on the right-hand side indicates that the new equilibrium position is in a direction opposite to the applied force.

3.2 Stiffness control (linear actuators)

In the zero-power magnetic suspension system, however, the magnitude of negative stiffness is a function of the gap between the electromagnet and the suspended object. When the mass on the isolation table changes, therefore, the negative stiffness varies from the nominal value so that the stiffness against disturbances acting on the isolation table becomes lower (Mizuno *et al.*, 2006a).

Suspension with negative stiffness can be also realized with other linear actuators such as voice coil motor and pneumatic cylinder. The actuator is controlled to behave as shown by Fig.2.3. In this section, the design of control system for realizing negative stiffness is described. A voice coil motor (VCM) is adopted as an actuator (Mizuno *et al.*, 2003a).

Figure 3.4 shows a single-degree-of-freedom model used in analysis. The equation of motion is

$$m\ddot{x} + c_a\dot{x} + k_ax = f_a + f_d, \quad (3.17)$$

where m : mass of the table, x : displacement from the equilibrium point, k_a : stiffness of supporting spring, c_a : damping coefficient of support, f_a : force generated by the actuator, f_d : direct disturbance acting on the table. Since the force generated by the actuator is proportional to the coil current i , f_a is given by

$$f_a = k_i i, \quad (3.18)$$

where k_i : current-force coefficient. From Eqs.(3.17) and (3.18), we get a transfer representation of the dynamics:

$$X(s) = \frac{1}{s^2 + a_1s + a_0} (b_0I(s) + d_0F_d(s)), \quad (3.19)$$

where

$$a_0 = \frac{k_a}{m}, \quad a_1 = \frac{c_a}{m}, \quad b_0 = \frac{k_i}{m}, \quad d_0 = \frac{1}{m} \dots \quad (3.20)$$

The displacement of the table is treated as an output signal here. When linear control law is applied, therefore, the control input is generally represented as

$$I(s) = -\frac{h(s)}{g(s)} X(s). \quad (3.21)$$

When the transfer function of the controller is proper, the polynomials are represented as

$$g(s) = s^n + \sum_{k=0}^{n-1} g_k s^k, \quad (3.22)$$

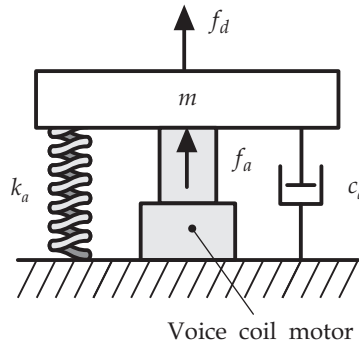


Fig. 3.4. Basic model with voice coil motor

$$h(s) = \sum_{k=0}^n h_k s^k . \quad (3.23)$$

Substituting Eq.(3.21) into Eq.(3.19) leads to

$$X(s) = \frac{g(s)}{(s^2 + a_1 s + a_0)g(s) + b_0 h(s)} d_0 F_d(s) . \quad (3.24)$$

The disturbance is assumed to be stepwise so that it is represented as Eq.(3.6). It is assumed that the controller is selected to stabilize the closed loop system. The steady-state displacement $x(\infty)$ is given by

$$\frac{x(\infty)}{F_0} = \lim_{s \rightarrow 0} \frac{g(s)}{(s^2 + a_1 s + a_0)g(s) + b_0 h(s)} d_0 = \frac{d_0 g_0}{a_0 g_0 + b_0 h_0} . \quad (3.25)$$

For the system to have negative stiffness with a magnitude of k_n , the following equation must be satisfied

$$\frac{d_0 g_0}{a_0 g_0 + b_0 h_0} = -\frac{1}{k_n} . \quad (3.26)$$

For assigning the closed-loop poles arbitrarily, second- or higher-order compensators are necessary. When a second-order compensator is used, the characteristic polynomial of the closed-loop system becomes

$$t_c(s) = s^4 + (a_1 + g_1)s^3 + (a_0 + g_0 + a_1 g_1 + b_0 h_2)s^2 + (a_0 g_1 + a_1 g_0 + b_0 h_1)s + (a_0 g_0 + b_0 h_0) . \quad (3.27)$$

To obtain a system with a characteristic equation of the form

$$t_d(s) = s^4 + e_3 s^3 + e_2 s^2 + e_1 s + e_0 , \quad (3.28)$$

we can match coefficients to obtain

$$g_0 = -\frac{e_0}{d_0 k_n} = -e_0 \frac{m}{k_n}, \quad (3.29)$$

$$g_1 = e_3 - a_1, \quad (3.30)$$

$$h_0 = \frac{1}{b_0} (e_0 - a_0 g_0), \quad (3.31)$$

$$h_1 = \frac{1}{b_0} (e_1 - a_0 g_1 - a_1 g_0), \quad (3.32)$$

$$h_2 = \frac{1}{b_0} (e_2 - a_0 - g_0 - a_1 g_1). \quad (3.33)$$

It is to be mentioned that the zero-power controller can be designed in a similar way (Mizuno & Takemori 2002).

4. Vibration isolation systems using zero-power magnetic suspension

There are a variety of configurations of system for vibration isolation using negative stiffness. This section treats vibration isolation systems using zero-power magnetic suspension for achieving negative stiffness.

4.1 Single-axis system

Basic Structure. Figure 4.1 shows a basic configuration of vibration isolation system using zero-power magnetic suspension. A middle mass is connected to the base through a spring k_1 and a damper c_1 , which together work as a conventional vibration isolator. An electromagnet for zero-power magnetic suspension is fixed to the middle mass. The part of an isolation table facing the electromagnet is made of a soft iron material for confining the magnetic fields produced by the permanent magnets for zero-power control. This is referred to as the reaction part (Mizuno *et al.*, 2006a).

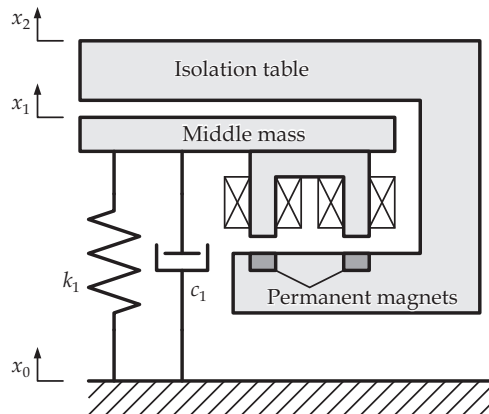


Fig. 4.1. Basic structure of vibration isolation system using zero-power magnetic suspension

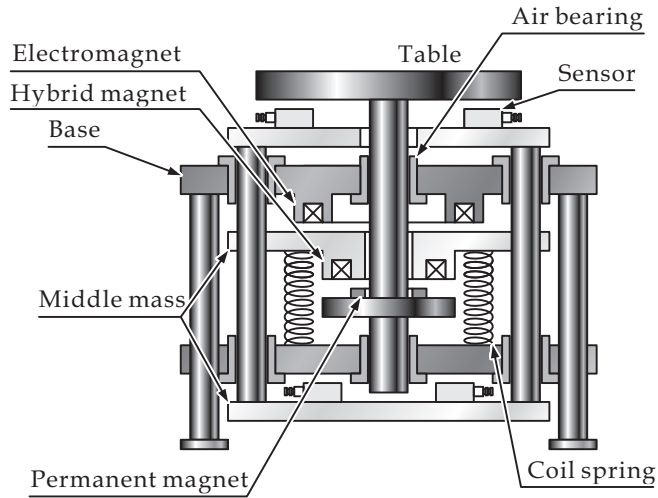


Fig. 4.2. Schematic drawing of experimental apparatus

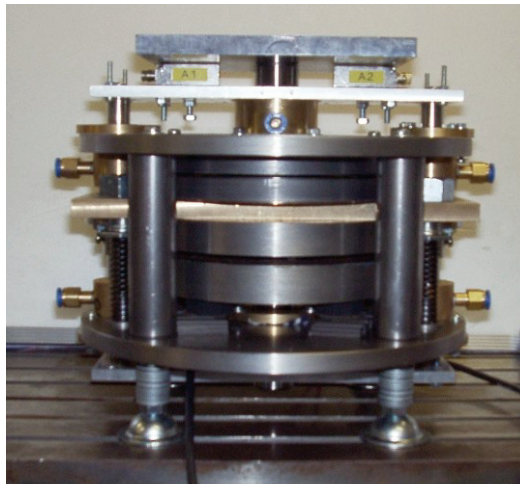


Fig. 4.3. Photo of experimental apparatus

Apparatus. Figures 4.2 and 4.3 are a schematic diagram and a photograph of a single-axis apparatus that was built for experimental study. The height, diameter, and mass of the apparatus are 200 mm, 226 mm and 18 kg, respectively. The isolation table and the middle mass weigh 3.5 kg and 5 kg, respectively, and are guided to move translationally in the vertical direction by linear air bearings. A ring-shape electromagnet with a 448-turn coil is fixed to the middle mass; its inner and outer diameters are 68 and 138 mm, respectively. Ten $10 \times 10 \times 5$ -mm permanent magnets made of NdFeB provide bias flux. These magnets, rather than the electromagnet, are built in the reaction part of the isolation table. The nominal gap between the electromagnet and the permanent magnets is about 3mm. The middle mass is suspended by four mechanical springs. An electromagnet for adjusting the positive stiffness

k_1 and the damping c_1 is installed on the base, and its reaction part is built in the middle mass. The electromagnet is referred to as an auxiliary electromagnet and is used to equalize the positive stiffness and the amplitude of the negative stiffness in the following experiment. The relative displacement of the middle mass to the base and that of the isolation table to the middle mass are detected by eddy-current gap sensors.

In the experiments, we use a zero-power controller in the form of

$$i = -(p_d + p_v \frac{d}{dt})(x_2 - x_1) + p_i \int idt . \quad (4.1)$$

This is a combination of PD (proportional-derivative) control and a local integral feedback of current (Mizuno & Takemori, 2002). Equation (4.1) states that

$$I(s) = -\frac{s(p_d + p_v s)}{s - p_i}(X_2(s) - X_1(s)) = -c_2(s)(X_2(s) - X_1(s)) , \quad (4.2)$$

The designed control algorithm is implemented with a digital controller. The control period is $100\mu\text{s}$. The feedback gains p_d , p_v , and p_i are tuned by trial and error.

Experiments. To estimate the *negative* stiffness of the zero-power magnetic suspension, its force-displacement characteristics are measured when the middle mass is fixed; downward force is produced by placing weights on the isolation table. Figure 4.4 presents the measurement results. The *upward* displacement of the isolation table is plotted against the *downward* force produced by the weights. As shown in the figure, the direction of the displacement is opposite to that of the applied force so that the stiffness is negative. Figure 4.5 shows the magnitude of negative stiffness versus the applied force, which is calculated based on the measurement results shown in Fig.4.4. As the downward force increases, the gap between the electromagnet and the reaction part decreases so that the gap-displacement coefficient k_s becomes larger. As a result, the amplitude of negative stiffness also becomes larger. However, it will be assumed to be constant in the following experiments, in which the zero-power magnetic suspension system is combined with a suspension mechanism with positive stiffness. The average value of k_s is 14.3 kN/m in the range of force 0 to 9 N, which is treated as a nominal value (Mizuno *et al.*, 2006a).

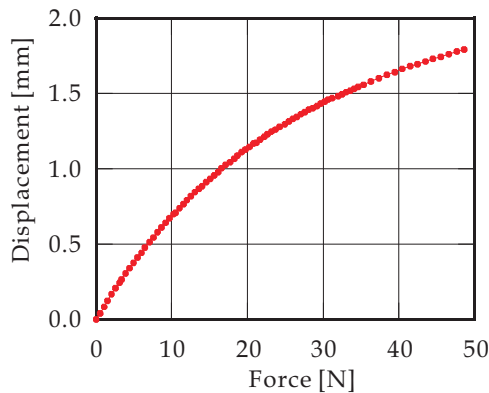


Fig. 4.4. Force-displacement characteristics of the zero-power magnetic suspension

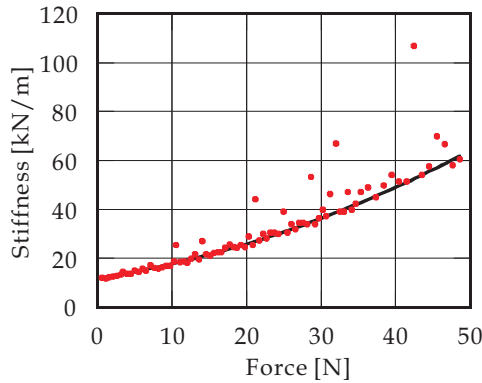


Fig. 4.5. Amplitude of the negative stiffness of the zero-power magnetic suspension system

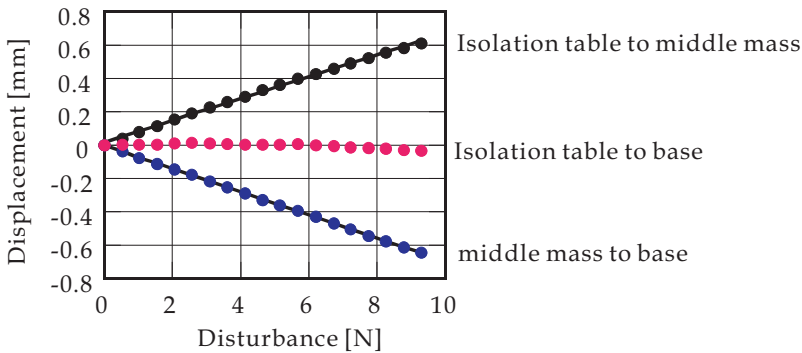


Fig. 4.6. Displacements of the isolation table and the middle mass

In the second experiment, the middle mass is released so that it is supported by the springs, and weights are again added onto the isolation table as a direct disturbance. Since the positive stiffness by the springs is 12.5 kN/m, it is adjusted to equal the nominal value 14.3 kN/m by the auxiliary electromagnet. It should be noted that this type of adjustment can be achieved by changing the springs.

Figure 4.6 shows the displacement of the isolation table to the base, that of the isolation table to the middle mass, and that of the middle mass to the base. The figure shows that the position of the table is maintained at the same position while the position of the middle mass changes proportionally to the force applied to the isolation table. The estimated stiffness between the isolation table and the base is 892 kN/m in this region, which is about 63 times k_1 and k_s (14.3 kN/m). This result demonstrates well that combining a zero-power magnetic suspension with a normal spring can generate high stiffness against a static direct disturbance acting on the isolation table.

Since the magnitude of negative stiffness is a function of the gap between the electromagnet and the reaction part, the stiffness against the direct disturbance will decrease when the amplitude of the disturbance exceeds a certain level. Three approaches are proposed for resolving this problem. One is to apply a nonlinear compensation to the zero-power controller (Hoque *et al.*, 2006b). Another is to use a linear actuator instead of the hybrid

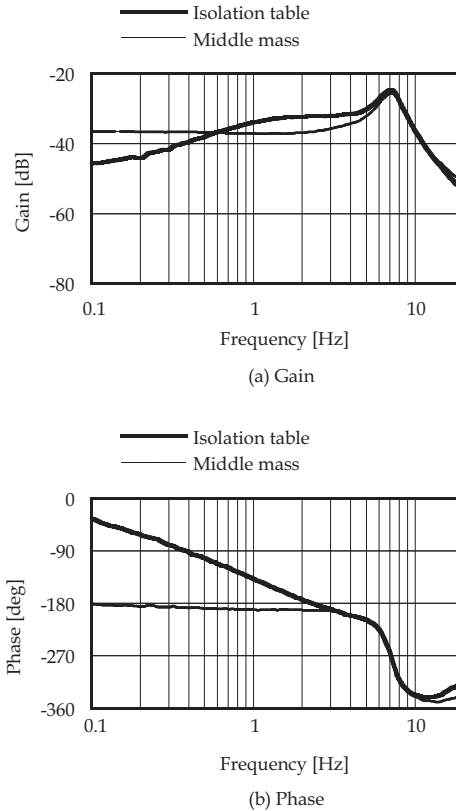


Fig. 4.7. Frequency response of the vibration isolation system to direct disturbance

magnet to produce negative stiffness as treated in Section 5 (Mizuno *et al.*, 2003a). The other is to use a nonlinear spring to produce positive stiffness (Mizuno *et al.*, 2003b).

Figure 4.7 shows a frequency response of the system to direct disturbance. A sinusoidal disturbance was produced by an electromagnet, which was installed over the isolation table for measurement. The command signal inputted to the amplifier was treated as an input signal while the displacement of the isolation table to the base and that of the middle mass to the base were treated as output signals. As can be seen in the figure, the displacement of the isolation table is reduced at a frequency range lower than 1 Hz. This result also supports the conclusion that the proposed system can generate high stiffness against a static direct disturbance acting on the isolation table.

The dynamic performances of the system, i.e., its responses to sinusoidal and stepwise direct disturbances, depend on the control performance. In this work, the controller was tuned by trial and error, as mentioned above. To improve more effectively the dynamic performance of the system, further intensive study on the applications of advanced-control design methods will be necessary. Since the performances of the system also depends on physical parameters such as k_1 , c_1 and m_2 , the integrated design of mechanism and control using optimization techniques offers a promising approach to optimizing performance.

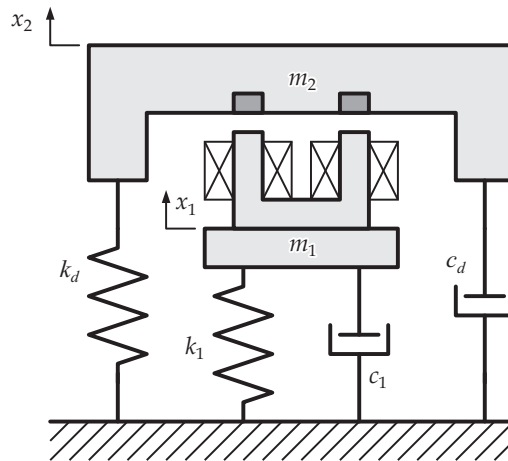


Fig. 4.8. Vibration isolation system with a weight support mechanism

4.2 Single-axis system with a weight support mechanism

Basic Structure. The systems using zero-power magnetic suspension have several problems. One of them is that the whole weight of the isolation table is supported by zero-power magnetic suspension; when the isolation table is large, it is necessary to use a lot of permanent magnets. Another problem is that a ferromagnetic part of the isolation table must be under the middle table, because zero-power magnetic suspension can produce only attractive force. It makes the structure of vibration isolation system rather complex. These problems can be overcome by introducing a weight support mechanism as mentioned in Section 2.2 (Mizuno *et al.*, 2006a).

A basic structure of a modified vibration isolation system is shown in Fig.4.8. This configuration is possible when an upward force produced by the parallel spring k_d can be made larger than gravitational force. This structure is simpler than the original one so that it will be better in manufacturing.

Apparatus. Figure 4.9 shows a schematic diagram of a single-axis apparatus fabricated for experimental study (Mizuno *et al.*, 2006b). The isolation table is supported by four coil springs and a pair of plate springs, which operate as k_d in Fig.4.8. The middle table is also supported by four coil springs and a pair of plate springs, which operate as k_1 in Fig.4.8. The plate springs restrict the motion of the isolation table and the middle table to one translational motion in the vertical direction. An electromagnet is on the middle table, and permanent magnets are on the isolation table. The zero-power control is realized by this hybrid magnet to produce negative stiffness. An auxiliary electromagnet for adjusting the positive stiffness and adding damping is set on the base. Figure 4.10 shows a photograph of the experimental apparatus.

Experiments. First, zero-power control was realized when the middle table was fixed. Then the middle table was released. In order to satisfy $k_1 = k_n$, the springs for weight support mechanism and the auxiliary electromagnet were adjusted. The experimental results for static characteristics of the isolation table are shown in Fig.4.11. When the load is between 0 to 10 [N], the displacement of the isolation table is quite small so that high stiffness is achieved. When the load is over 10 [N], the isolation table moves upward because the

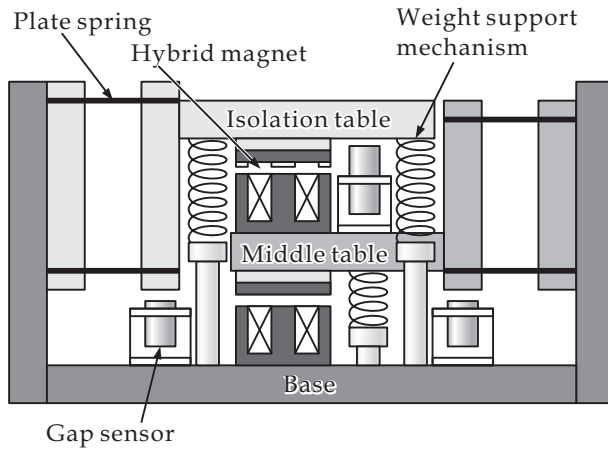


Fig. 4.9. Schematic drawing of experimental apparatus with a weight support mechanism

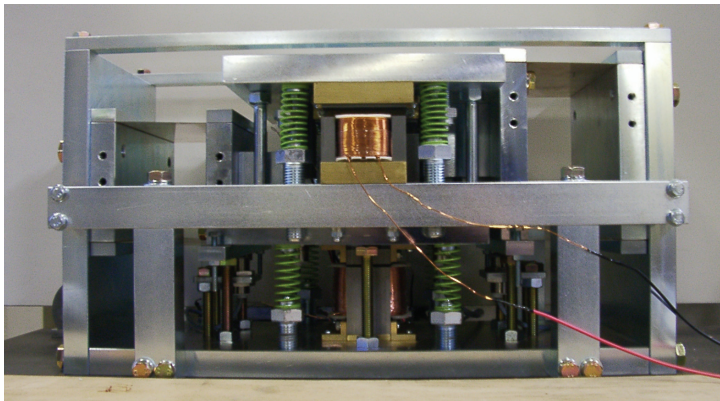


Fig. 4.10. Photo of experimental apparatus

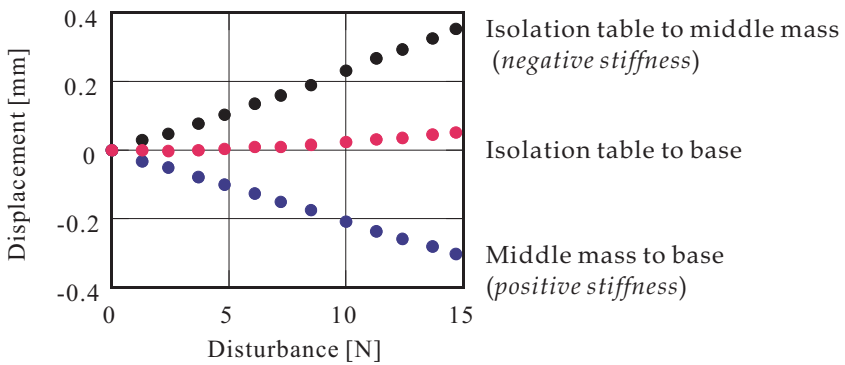


Fig. 4.11. Response to static direct disturbance

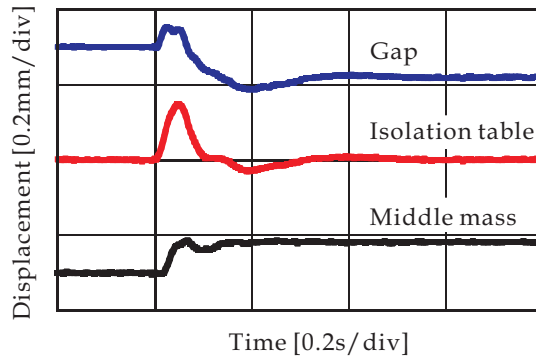


Fig. 4.12. Response to a stepwise direct disturbance

negative stiffness produced by zero-power control becomes lower. This is caused by non linear characteristics of magnets.

Figure 4.12 shows a response to a stepwise direct disturbance that was produced by the electromagnet over the isolation table. An upward force applied to the isolation table initially was quickly removed by making the coil current zero. The middle mass begins to move downward and stay at a position that is lower than the initial position. The relative displacement of the isolation table to the middle mass is negative just after the applied force is removed and then positive at steady state. The former displacement is cancelled by the latter one so that the position of the isolation table returns to its initial position at steady state.

4.3 Six-axis system with weight support mechanism

Apparatus. For studying multi-axis vibration control, three-axis and six-axis vibration isolation systems have been developed (Hoque *et al.*, 2006a and 2007). The latter is treated here. Figures 4.13 and 4.14 show a photo and a schematic drawing. It consisted of a rectangular isolation table, middle table and base. The height, length, width and mass of the apparatus were 300 mm, 740 mm, 590 mm and 400 kg respectively. The isolation and middle tables weighed 88 kg and 158 kg respectively. The middle table was supported by four pair of coil springs and dampers, and the isolation table was supported by another four coil springs, as *weight support springs*, in addition to the zero-power control system by four sets of hybrid magnets. The sensor and hybrid magnet positions for controlling vertical and horizontal modes are shown in Fig. 4.15. The actuators (1 to 4) were used for table levitation as well as for controlling the three-degree-of-freedom motions (z , roll and pitch) of the table in the vertical direction. Each set of hybrid magnet for zero-power suspension consisted of five square-shaped permanent magnets and five 585-turn electromagnets. The permanent magnet is made of NdFeB materials. The stiffness of each normal spring was 12.1 N/mm and that of weight support spring was 25.5 N/mm. There was flexibility to change the position of the weight support springs to make it compatible for designing stable zero-power controlled magnetic suspension system.

The relative displacements of the isolation table to the middle table and those of the middle table to the base were detected by eight eddy-current gap sensors. The displacements of the isolation table from base were measured by another four gap sensors.

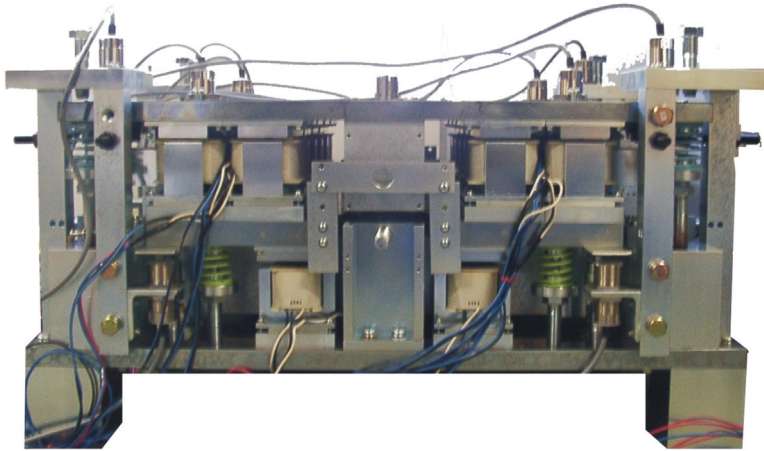


Fig. 4.13. Photo of 6-axis vibration isolation system with weight support mechanism

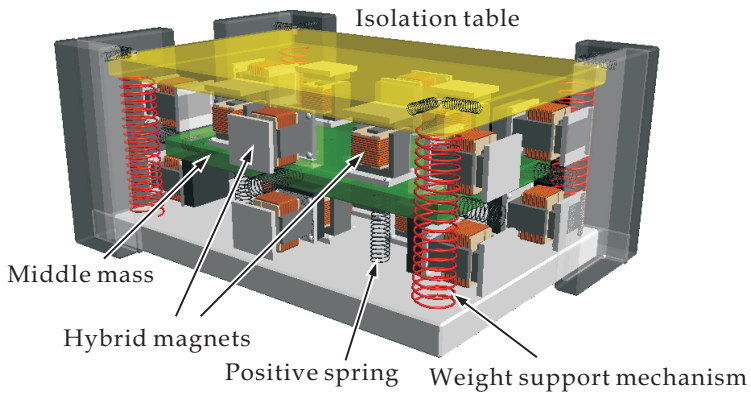


Fig. 4.14. Schematic drawing of the 6-axis vibration isolation system

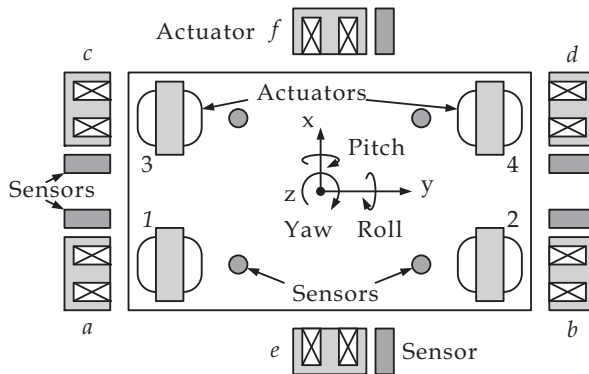


Fig. 4.15. Layout of actuators for 6-DOF motion control

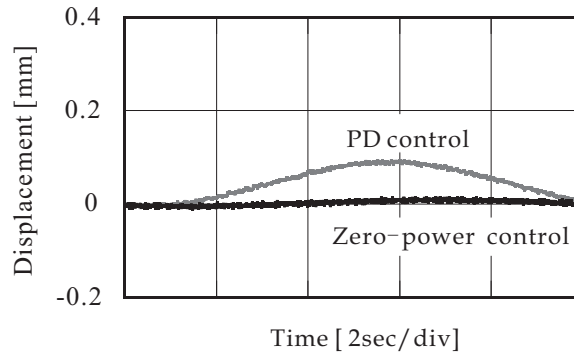


Fig. 4.16. Response to a sinusoidal direct disturbance

The isolation table was also supported by several normal springs and hybrid magnets for controlling other three-degree-of-freedom motions (x , y and yaw) in the horizontal directions. The layout of actuators (a to f) for controlling the horizontal modes is also shown in Fig.4.15. Two pairs of hybrid magnets were used in the y -direction and one pairs in the x -direction between isolation table to middle table. Similarly six pairs of normal springs and actively controlled electromagnets (two pairs in the x -direction and four pairs in the y -direction) were used between base to middle table to adjust the positive stiffness. The isolation table was also supported by four pairs of normal springs from base, as weight support spring for the horizontal directions. Hence the isolation table was also capable to control the other three modes in the horizontal directions. One pair of displacement sensors were used in the x -direction and two pairs in the y -direction to measure the relative displacement between isolation table to middle table for horizontal displacements. Similarly six pairs of sensors were used to measure the relative displacement between middle table to base.

Experiments. Figure 4.16 shows the response in the vertical direction to a sinusoidal direct disturbance with a frequency of 0.015Hz. When PD control is applied to control by the hybrid magnets, the isolation behaves as if it is suspended by conventional spring and damper. Thus, it moves due to the direct disturbance. In contrast, the table does not move when the zero-power control is applied because high stiffness is achieved according to Eq.(2.2).

5. Vibration isolation system using pneumatic actuator

In the zero-power magnetic suspension system, the magnitude of negative stiffness is a function of the gap between the electromagnet and the suspended object. When the mass on the isolation table changes, therefore, the negative stiffness varies from the nominal value so that the stiffness against disturbances acting on the isolation table becomes lower (Mizuno *et al.*, 2006a). In this paper, we propose to use a linear actuator instead of an electromagnet for generating a suspension system with negative stiffness. It enables the vibration isolation system to keep high stiffness for a wider range of operation than the original system.

5.1 Single-axis system

A pneumatic cylinder of diaphragm type is fabricated for the realization of suspension with negative stiffness (Mizuno *et al.*, 2005). Figure 5.1 and 5.2 show its schematic drawing and photograph. This type of cylinder is characterized by short stroke and small friction.

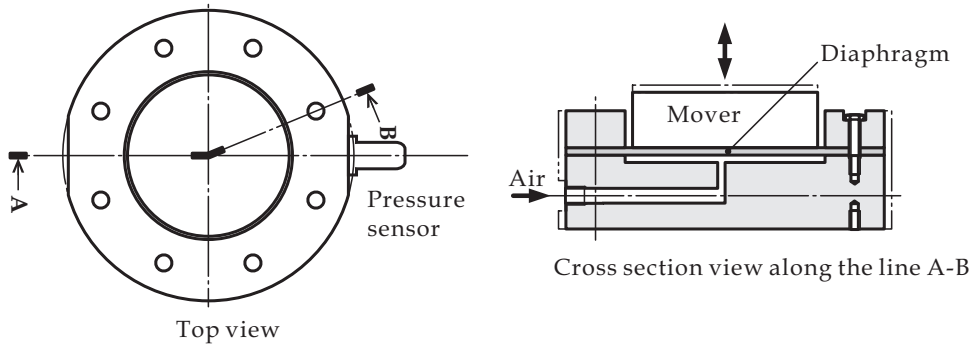


Fig. 5.1. Schematic drawing of pneumatic cylinder

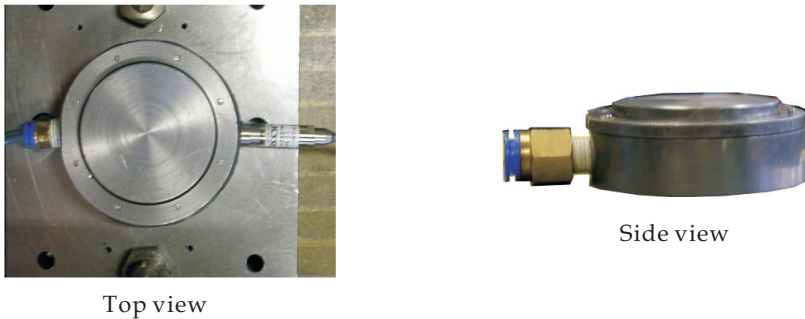


Fig. 5.2. Photo of pneumatic cylinder

The treatment of the dynamics of this cylinder is similar to that of VCM described in Section 3.2. The stiffness of the suspension system using this cylinder can be set arbitrary theoretically (Mizuno *et al.*, 2005).

Figure 5.3 shows a schematic drawing of the developed experimental apparatus with four cylinders. Each cylinder has a diaphragm made of rubber with a thickness of 2 mm. Its effective sectional area is 50cm^2 so that the generated force is approximately 500N when the gauge pressure of supply air is 0.1MPa. To reduce the mass of the apparatus, therefore, two cylinders are operated in a differential mode, which are referred to as a dual-cylinder.

One dual-cylinder suspends the middle mass and operates as a suspension with positive stiffness. Another dual-cylinder fixed on the middle mass suspends the isolation table and operates as a suspension with negative stiffness. These cylinders are controlled with flow control valves.

The middle mass and the isolation table are guided to be in translation by plate springs. The relative displacement of the middle mass to the base and that of the isolation table to the middle mass are detected by eddy-current gap sensors with a resolution of 1mm. Designed control algorithms are implemented with a DSP-based digital controller.

First, suspension with prescribed negative stiffness is realized by the pneumatic actuator was estimated. The middle mass is clamped in this experiment. The amplitude of negative stiffness is set to be

(a) $k_n = 300$ [kN/m], (b) $k_n = 400$ [kN/m], (c) $k_n = 500$ [kN/m].

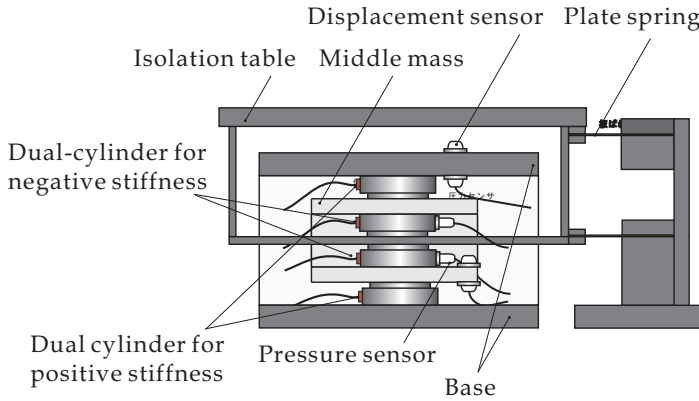


Fig. 5.3. Experimental apparatus

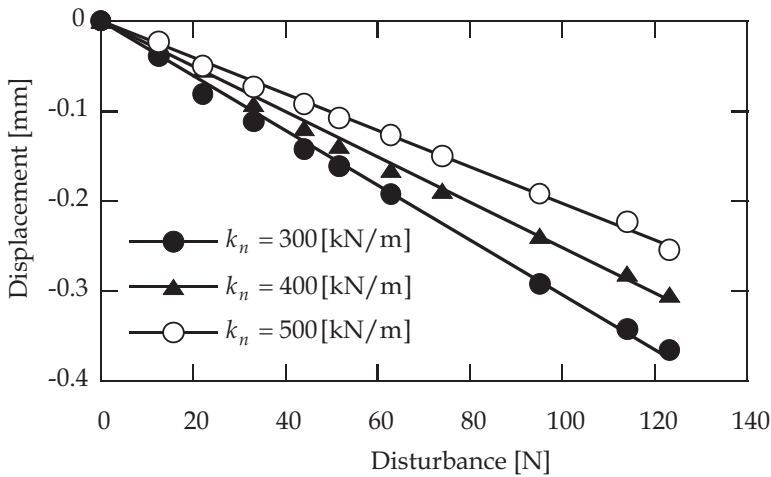


Fig. 5.4. Realization of suspension with negative stiffness

Figure 5.4 shows the measurement results. The estimated amplitude of stiffness is (a) $k_n = 328$ [kN/m], (b) $k_n = 398$ [kN/m], (c) $k_n = 493$ [kN/m].

The differences between the prescribed and experimental values are within 5%. The difference is small when the amplitude of stiffness is large.

In the second experiment, the clamp of the middle mass is released. The two dual-cylinders are designed to have static stiffness of ± 1000 [kN/m]. Figure 5.5 shows the displacement of the isolation table to the base, that of the isolation table to the middle mass and that of the middle mass to the base. It is observed that the position of the isolation table is maintained at the same position while the position of the middle mass changes proportion to direct disturbance. The estimated stiffness between the isolation table and the base is 8.8×10^5 [kN/m], which is about 90 times the stiffness of each suspension. This result demonstrates that the compliance between the isolation table and the base is made very small by the proposed mechanism (Mizuno *et al.*, 2005).

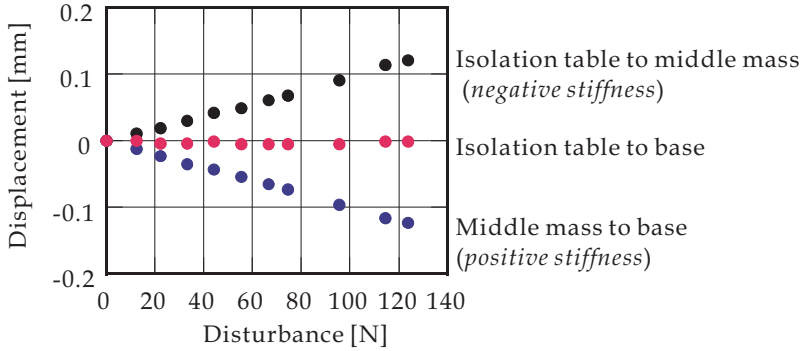


Fig. 5.5. Series connection of positive stiffness and negative stiffness

5.2 Three-axis system using pneumatic actuators

Apparatus. Figure 5.6 shows a photograph of a manufactured experimental apparatus with six cylinders (Mizuno *et al.*, 2005). Its schematic diagram is presented by Fig.5.7. The diameter and height is 200mm and 600mm, respectively. It has a circular isolation table and a circular middle table corresponding to the middle mass. The isolation and middle tables weigh 65kg and 75kg, respectively.

The middle table is suspended by three cylinders for positive stiffness and damping. They are located at the vertices of an equilateral triangle on the base. The isolation table is suspended by three cylinders for negative stiffness, which are fixed to the middle table. Each cylinder for negative stiffness is aligned with a cylinder for positive stiffness vertically. Hence, the three-degree-of-freedom motions of the isolation table can be controlled. They are one translational motion in the vertical direction (z) and two rotational motions, pitch (ξ) and roll (η).

The displacements of the isolation table are detected by three eddy-current sensors, which located at the vertices of an equilateral triangle on the base. The displacement of the middle table is detected similarly. The detected places are at the middle between the actuation positions (not collocated). The displacement at the position of each cylinder, and the displacement of each motion are calculated from these detected signals.

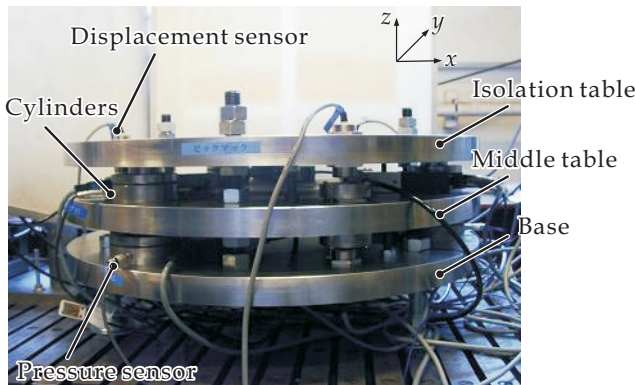


Fig. 5.6. Photo of 3-axis vibration isolation system with pneumatic actuators

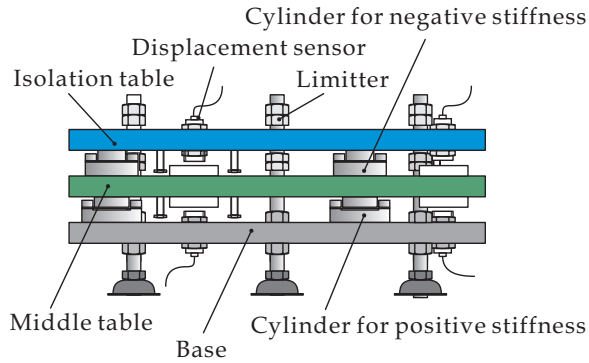


Fig. 5.7. Schematic drawing of the apparatus

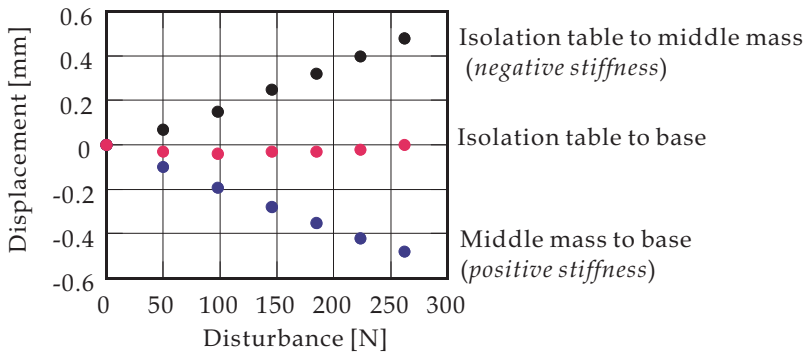


Fig. 5.8. Force-displacement characteristics of the isolation system in the vertical direction

For multi-channel control systems, there are two approaches to constructing the controller:

- local control (decentralized control)
- mode control (centralized control).

In the first controller, each actuator is controlled based on the local information, which is the displacement at the position in this case. In the second controller, a compensator is built for each mode. This work adopts the first approach.

Each controller is designed based on the pole-assignment approach as described 3.2. The order of the desired characteristic polynomial corresponding to Eq.(3.28) is six in this case (Mizuno *et al.*, 2005). It is represented by

$$t_d(s) = \prod_{n=1}^3 (s^2 + 2\zeta_n \omega_n s + \omega_n^2) \tag{5.1}$$

Figure 5.8 shows the vertical displacement of the isolation table to the base. Each cylinder is controlled to have static stiffness of ± 250 [kN/m]. It is observed that the position of the isolation table is maintained at the same position while the position of the middle mass changes proportion to direct disturbance. Such performance was also achieved in the other two modes. The ratio of the total stiffness to the individual stiffness is

- (a) 68 (translation), (b) 12 (pitch), (c) 12 (yaw)

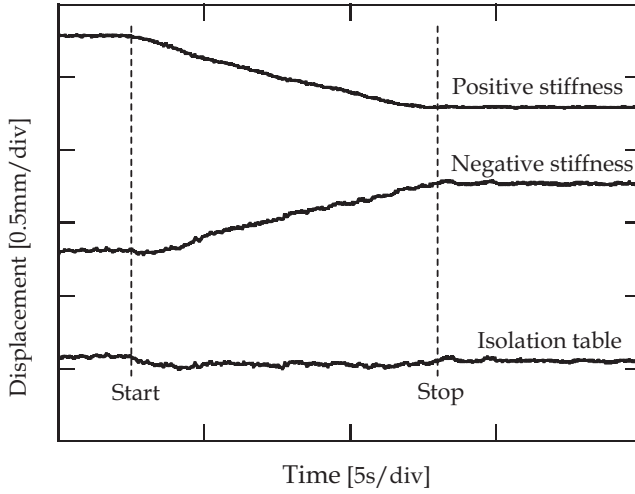


Fig. 5.9. Response to a moving mass on the table

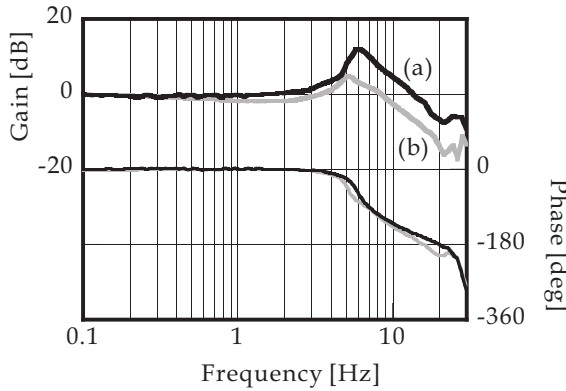


Fig. 5.10. Frequency responses to floor vibration.

This result demonstrates that the equalization of the amplitude of negative and positive stiffness enables the system to have virtually zero compliance to direct disturbance.

Figure 5.9 shows the response when a weight with a mass of 12kg moves on the isolation table, which is a typical source of direct disturbance. The velocity of the movement is approximately 45mm/s. It demonstrates that the position and attitudes of the isolation table are kept constant even with a presence of such a dynamic direct disturbance.

To study on the vibration isolation performance, frequency response to floor vibration was measured as shown by Fig.5.10 (Mizuno *et al.*, 2005). The parameters in designing the controllers are selected as

- amplitude of stiffness: 500 kN/m
- desired characteristic polynomial

- suspension with positive stiffness* (a) $\omega_1 = \omega_2 = \omega_3 = 2\pi \times 12$ [rad/s], $\zeta_1 = \zeta_2 = \zeta_3 = 0.7$.
 (b) $\omega_1 = \omega_2 = \omega_3 = 2\pi \times 5$ [rad/s], $\zeta_1 = \zeta_2 = \zeta_3 = 1.2$.
suspension with negative stiffness (a) $\omega_1 = \omega_2 = \omega_3 = 2\pi \times 12$ [rad/s], $\zeta_1 = \zeta_2 = \zeta_3 = 0.7$.
 (b) $\omega_1 = \omega_2 = \omega_3 = 2\pi \times 12$ [rad/s], $\zeta_1 = \zeta_2 = \zeta_3 = 1.0$.

It demonstrates that the vibration isolation performance can be adjusted by the selection of the target characteristic polynomial in designing each suspension.

To improve the vibration isolation performance more, the amplitude of each stiffness should be decreased. In the fabricated system, however, the behavior of suspension became rather unstable mainly because displacement caused by direct disturbance increased when stiffness is set to be smaller. Such a problem can be solved by modifying the design of pneumatic cylinder and controller.

6. Conclusion

Active vibration isolation systems using negative stiffness were presented. Connecting a negative-stiffness suspension with a normal spring in series can generate infinite stiffness against disturbances acting on the isolation table. This property is maintained even if a suspension to support the weight of the isolation table is introduced in parallel with the serial combination. The principles and fundamental characteristics of the systems were described in an analytical form together with experimental apparatuses developed for experimental study and experimental results. It was experimentally confirmed that combining a negative-stiffness suspension with a normal spring in series generates high stiffness against static direct disturbance acting on an isolation table.

Vibration isolation using negative stiffness is a quite unique approach. Very high (*theoretically infinite*) stiffness to direct vibration is achieved with low-cost sensors while system vibration transmitted from the ground is reduced. Since negative stiffness can be achieved by any linear actuator including electromagnetic actuator (zero-power magnetic suspension), various types of system are possible. Active research and development has been and will be continued to industrial applications (Mizuno *et al.*, 2007 & 2008).

7. References

- Fuller, C. R., Elliott, S. J. & Nelson, P. A. (1996). *Active Control of Vibration*. Academic Press, pp.213-220.
- Hoque, Md. E., Takasaki, M., Ishino, Y. & Mizuno, T. (2006a). Development of a Three-Axis Active Vibration Isolator Using Zero-Power Control, *IEEE/ASME Transactions on Mechatronics*, Vol.11, No.4, pp.462-470.
- Hoque, Md. E., Mizuno, T., Takasaki, M. & Ishino, Y. (2006b). A Nonlinear Compensator of Zero-Power Magnetic Suspension for Zero-Compliance to Direct Disturbance, *Trans. the Society of Instrument and Control Engineering*, Vol.42, No.9, pp.1008-1016.
- Hoque, Md. E., Mizuno, T., Takasaki, M. & Ishino, Y. (2007). Horizontal Motion Control in a Six-Axis Hybrid Vibration Isolation System using Zero-Power Control, *Proc. Asia-Pacific Vibration Conference 2007*, G16-1-4.
- Hoque, Md., E., Mizuno, T., Ishino, Y., & Takasaki, M. (2010). A Six-Axis Hybrid Vibration Isolation System Using Active Zero-Power Control Supported by Passive Weight Support Mechanism, *Journal of Sound and Vibration*, Vol.329, Issue 17, pp.3417-3430.

- Miyazaki, T., Mizuno, K., Kawatani, R. & Hamada, H. (1994). Consideration about Feedback Feedforward Hybrid Control for Active Control of Micro-Vibration Control, *Proc. Second International Conference on Motion and Vibration Control*, pp.29-34.
- Mizuno, T. & Takemori, Y. (2002). A Transfer-Function Approach to the Analysis and Design of Zero-Power Controllers for Magnetic Suspension System, *Electrical Engineering in Japan*, Vol.141, No.2, pp.67-75.
- Mizuno, T., Toumiya, T. & Takasaki, M. (2003a). Vibration Isolation System Using Negative Stiffness, *JSME International Journal, Series C*, Vol.46, No.3, pp.807-812.
- Mizuno, T., Iwashita, S., Takasaki, M. and Ishino, Y. (2003b): Vibration Isolation System Combining Zero-Power Magnetic Suspension with a Magnetic Spring, *Proc. Asia-Pacific Vibration Conference 2003*, pp.469-474.
- Mizuno, T., Murashita, M., Takasaki, M., & Ishino, Y. (2005). Pneumatic Active Vibration Isolation Systems Using Negative Stiffness, *Trans. SICE*, Vol.41, No.8, pp 676-684 (in Japanese).
- Mizuno, T., Takasaki, M., Kishita, D. & Hirakawa, K. (2006a). Vibration Isolation System Combining Zero-Power Magnetic Suspension with Springs, *Control Engineering Practice*, Vol.15, No.2, pp 187-196.
- Mizuno, T., Kishita, D., Takasaki, M. & Ishino, Y. (2006b). Vibration Isolation System Using Zero-Power Magnetic Suspension (2nd report: Introduction of Weight Support Mechanism), *Trans. JSME, Series C*, Vol.72, No.715, pp. 714-722 (in Japanese).
- Mizuno, T., Unno, Y., Takasaki, M. & Ishino, Y. (2007). Vibration Isolation Unit Combining a Air Spring with a Voice Coil Motor for Negative Stiffness, *Proc. European Control Conference 2007*, WeC02.2, pp.3153-3158.
- Mizuno, T., Kawachi, Y., Ishino, Y. & Takasaki, M. (2008). Vibration Isolation Unit Using Zero-Power Magnetic Suspension with a Weight Support Mechanism, *Proc. 9th International Conference on Motion and Vibration Control*, AV4-1298.
- Morishita, M., Azukizawa, T., Kanda, S., Tamura, N. & Yokoyama, T. (1989). A New Maglev System for Magnetically Levitated Carrier System. *IEEE Trans. Vehicular Technology*, Vol.38, No.4, pp.230-236.
- Mohamed, Z., Martins, J.M., Tokhi, M.O., Sá da Costa, J. & Botto, M.A. (2005). Vibration Control of a Very Flexible Manipulator System, *Control Engineering Practice*, Vol.13, Issue 3, pp.267-277.
- Platus, D. L. (1999). Negative-Stiffness-Mechanism Vibration Isolation Systems. *Proceedings of the SPIE-The International Society for Optical Engineering*, Vol.3786, pp.98-105.
- Rivin, E. I. (2003). *Passive Vibration Isolation*. ASME Press, New York, ix-xv.
- Sabnis, A.V., J.B. Dendy, and F.M. Schmitt (1975). A Magnetically Suspended Large Momentum Wheel. *J. Spacecraft*, Vol.12, pp.420-427.
- Trimboli, M.S., Wimmel, R. and Breitbach, E. (1994). A Quasi-Active Approach to Vibration Isolation Using Magnetic Springs. *Proceedings of the SPIE-The International Society for Optical Engineering*, Vol.2193, pp.73-83.
- Yasuda, M., Osaka, T. & Ikeda, M. (1996). Feedforward Control of a Vibration Isolation System for Disturbance Suppression. *Proc. 35th Conference on Decision and Control*, pp.1229-1233.
- Zhu, W.H., Tryggvason, B. & Piedboeuf, J.C. (2006). On Active Acceleration Control of Vibration Isolation Systems, *Control Engineering Practice*, Vol.14, Issue 8, pp.863-873.

Mass Inertia Effect based Vibration Control Systems for Civil Engineering Structure and Infrastructure

Chunwei Zhang and Jinping Ou

*Harbin Institute of Technology, Harbin, Dalian University of Technology, Dalian,
P.R.China*

1. Introduction

In 1972, J.T.P. Yao introduced the modern control theory into vibration control of civil structures (Yao, 1972), which started the new era of research on structural active control in civil engineering field. During the development of nearly 40 years, Active Mass Driver/Damper (AMD) control, with the better control effect and cheaper control cost, has taken the lead in various active control occasions, becoming the most extensively used and researched control systems in lots of practical applications (Soong, 1990; Housner *et al.*, 1997; Spencer *et al.*, 1997; Ou, 2003). Several important journals in civil engineering field, such as ASCE Journal of Engineering Mechanics (issue 4th, in 2004), ASCE Journal of Structural Engineering (issue 7th, in 2003), Earthquake Engineering and Structural Dynamics (issue 11th, in 2001 and issue 11th, in 1998), reviewed the-state-of-the-art in research and engineering applications of semi-active control and active control, especially AMD control. In addition, Spencer and Nagarajaiah (2003) systematically overviewed the applications of active control in civil engineering. Up to date, more than 50 high-rising buildings, television towers and about 15 large-scale bridge towers have been equipped with AMD control systems for reducing wind-induced vibration or earthquake-induced vibration of the structures.

Besides, there are quite a number of successful applications with passive Tuned Mass Damper (TMD) control system, from wind induced vibration control of long-span bridge towers and building structures, to chimneys and mast structures; from the first applications of the collapsed World Trade Center towers and coetaneous John Hancock building etc., which were built in 1960s, to recently built highest structures in the world, *e.g.* Twin towers in Kulua- Lumpur in Malaysia, 101 skyscraper in Taipei city and Guangzhou New TV tower in China etc. It can be seen from these applications, the implementation of incorporating Mass Driver/Damper based vibration control systems for protection of Civil Engineering structures and infrastructures against wind and earthquake excitations, have already been widely accepted by the field researchers as well as engineer societies.

2. EMD control systems

Zhang (2005) made a systematically comparison for different control schemes under the background of the Benchmark control problem, and disclosed that the AMD control was the

best control scheme due to these merits, such as the best ratio of control effect over control effort, simple and easy to be implemented etc. Moreover, through analysis of typical important large-scale structures subjected to different excitations, the effectiveness and feasibility of employing AMD control for civil structures has been successfully proven (Ou, 2003; Zhang, 2005), where wind and earthquake induced vibration control of high-rising buildings and bridge towers, ice induced vibration control of offshore platforms, wind-wave-current coupling excited control of deep sea platforms are all studied. Usually, an AMD control system is composed of a mass piece, an actuator, stiffness component (coil spring is commonly used), a damper, a stroke limiting device, a brake protector, sensors, a data acquisition and processing system, computerized real-time control software and hardware system (Dyke *et al.*, 1994, 1996; Quast *et al.*, 1995; Spencer *et al.*, 1997). In addition, a power supplying system is needed for operating all the electrical devices mentioned above. In traditional AMD system, the mostly used actuators are hydraulic cylinders or electrical servo motors, which may have the following disadvantages, such as large in system volume, complicated in construction, time delay, slow to response, and limited mass stroke etc. Aiming at this, several new special devices were put forward to replace the traditional actuators (Haertling, 1994, 1997; Nerves, 1996; Scruggs, 2003). Learning from the motion control principle of magnetic suspended vehicle, the electromagnetic mass damper (subsequently called the “EMD”) control system, as an innovative active control system, was proposed for structural vibration control (Zhang, 2005), which uses the driving technology of linear electric machines, transforming the electric energy directly into mechanical energy of EMD system, for example, the kinetic energy of EMD mass. Figure 1(a) shows the conception sketch of hydraulic actuated AMD system and its implementation illustration in a typical structural model, as shown in figure 1(b). By comparison, figure 2(a) and 2(b) shows the corresponding sketch and implementation sketch of the EMD control system.

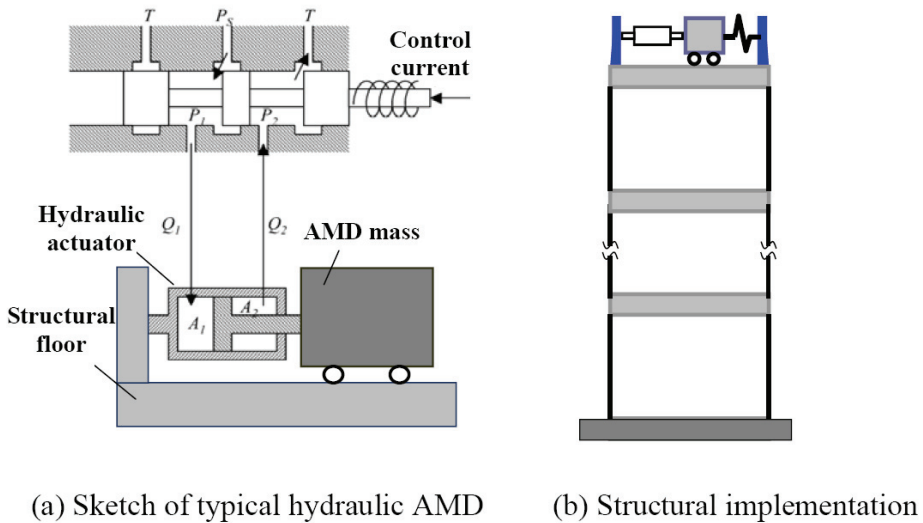


Fig. 1. Sketch of structure with hydraulic actuated AMD control System

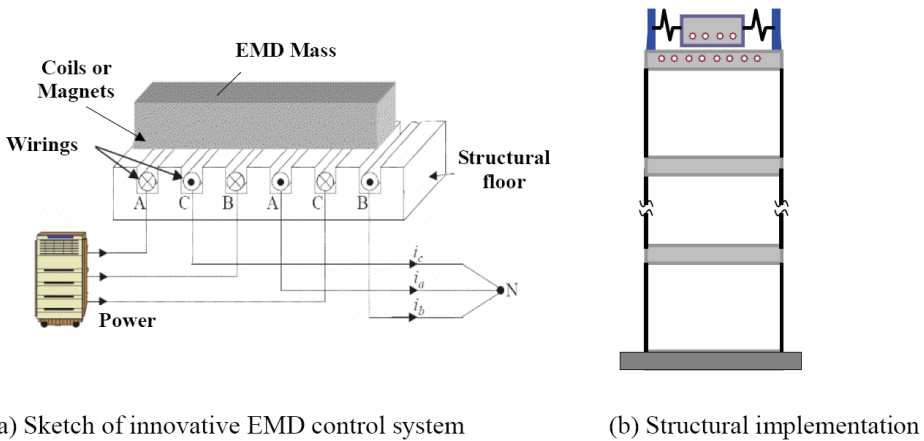


Fig. 2. Sketch of structure with Electromagnetic Mass Damper (EMD) control system

2.1 Miniature EMD control system

The miniature experimental EMD control system is composed of a mass piece (direct current excitation coils encapsulated in high-strength engineering plastics, with mounting holes on its surface), a permanent magnet rod made of high energy rare earth material, linear sliding bearings and the system chassis. In addition, in order to form a closed-loop EMD system, an optical scale and an accelerometer are integrated into the EMD system to measure the stroke and absolute acceleration of the mass, respectively. Photo of the whole integrated system is shown in figure 3.

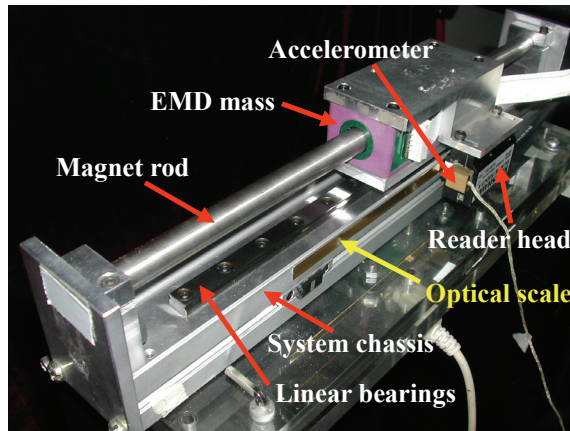


Fig. 3. Integrated photo of the EMD actuator

The excitation coil in the sealed mass package is 87mm long, made by Copley Controls Inc., and the whole mass piece weighs 186 grams. The permanent magnet rod is 332mm long with the diameter of 11mm. The main electrical specifications of this EMD system are: peak force constant is 5.74N/A, root mean square (RMS) force constant is 8.12N/A, back electro-

motive force (EMF) constant is $6.63 \text{ V} \cdot \text{s/m}$, the coil resistance at 25°C is 5.35Ω , and the coil inductance is 1.73mH . The mass stroke of EMD system is measured using a Renishaw optical scale, which is pasted onto the system chassis as shown in the photo above, while the reading head is fixed on the side wall of EMD mass. The reading head model is RGH24 with the resolution of 2-micro-meter, and the scale is 220mm long. In addition, one tiny accelerometer (type DH201-050) is installed on the prolonging side-wall of the EMD mass with the measuring range of $\pm 50\text{g}$. This accelerometer is very compact indeed, with a weight of only two grams and a volume of $10\text{mm} \times 10\text{mm} \times 5\text{mm}$, and it can be conveniently attached to any part of the mass piece without influencing the operation of the whole system.

2.1.1 System mathematical models

From the aspect of circuit calculation, the armature of EMD system consists of three parts: motor coil which is capable of outputting mechanical force or energy, coil inductance and coil resistance. According to the Kirchhoff's first principle, the relationship of the circuit voltage and current can be written as

$$L_m \frac{di(t)}{dt} + R_m i(t) + \varepsilon(t) = V_m(t) \quad (1)$$

Where L_m is the coil inductance, R_m is the coil resistance, $V_m(t)$ is the input voltage, $\varepsilon(t)$ is the inducted back EMF constant, $i(t)$ is the current intensity in the coil.

Defining the following two electric indices of linear motors, $K_f = \frac{F_{\text{EMD}}}{I}$ standing for force constant which means electromagnetic force generated by unit current input, and $K_m = \frac{\varepsilon}{v}$ standing for the back EMF constant which means back EMF generated by unit velocity, then the following relationships are reached,

$$i(t) = F_{\text{EMD}} / K_f; \quad \varepsilon(t) = K_m v \quad (2)$$

Substituting equation (2) into equation (1) gives

$$L_m \frac{dF(t)}{dt} \frac{1}{K_f} + \frac{R_m}{K_f} F(t) + K_m v(t) = V_m(t) \quad (3)$$

After proper transformation, equation (3) can be rewritten as,

$$F(t) = \frac{K_f}{R_m} V_m(t) - \frac{K_f K_m}{R_m} \dot{x}_a(t) - \frac{L_m}{R_m} \frac{dF(t)}{dt} \quad (4)$$

Where \dot{x}_a is the relative velocity of EMD mass, and $F(t)$ is the controllable electromagnetic force.

2.1.2 System dynamic tests

During dynamical tests, the EMD system is fixed on the shaking table, and the system coil is powered with the ASP-055-18 servo amplifier, with a DC current output of 0~10A and voltage of 0~55V. The power supply is the HB17600SL series regulator module. A series of

sine position based tests under Position-velocity control of large mass strokes and low frequencies are conducted.

For example, figure 4 shows the hysteresis loops of control force versus velocity and circuit current, respectively. From the force-current relationship, fine linear relationship again indicates the EMD system to be a linear actuator under low operating frequencies, with high ability in dissipating energy at the same time.

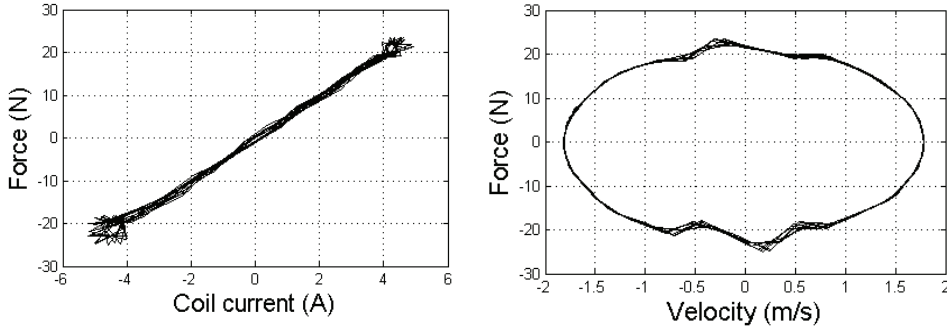


Fig. 4. Force hysteresis loops of EMD system

2.1.3 Experimental implementation of structural model

The test structural model employed in this part is a two-story shearing type structure, called the Bench-scale structure, manufactured by Quanser Inc., which has been designed to study critical aspects of structural control implementations and widely used in education or research of civil engineering and earthquake engineering throughout the world (Battaini, 2000; Quanser, 2002). The column of the test structure is made of thin steel plate, 2mm thick, and the floors are made of plastic, 13mm thick, and the inter-storey height of the structure is 490mm. Shaker-II table, made by Quanser Inc., is employed here for generating earthquake excitations as well as other excitations to be exerted onto the test structure. Through sine sweep test, the natural frequencies of the structure are found to be 1.27Hz and 4.625Hz corresponding to the first two dominant vibration modes respectively, where the mass of the EMD system is fixed on the top floor, named as uncontrolled case. The photo of the whole experimental system and its calculation sketch are shown in figure 5.

In the current experimental setup, two accelerometers are installed under each floor and another accelerometer is installed on the shaking table surface to measure structural response and input excitation respectively. The acceleration transducers are the type of Kistler K-Beam 8034A with the measuring range being $\pm 2.0g$ and the sensitivity gain being 1024mV/g. Two laser displacement sensors, type of Keyence LK-2501/2503, are employed to measure the absolute displacement of each floor of the structure, which both work under the long distance mode, and the measuring range is $\pm 250mm$ with the gain being 200mV/cm. Here the displacement measurement is used only for verification purpose, while not for feedback.

In this section, shaking table tests of structural seismic response control employing the EMD system were conducted, where three benchmark earthquake waves were used as input to examine the control effectiveness of such an innovative active control system, and typical results under Kobe earthquake wave (NS, January 17, 1995) input will be shown in the

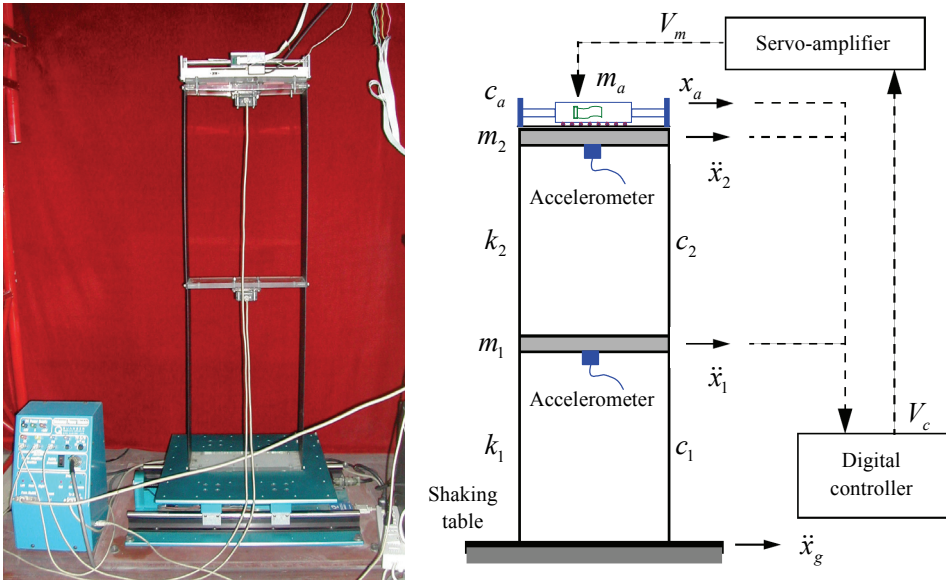
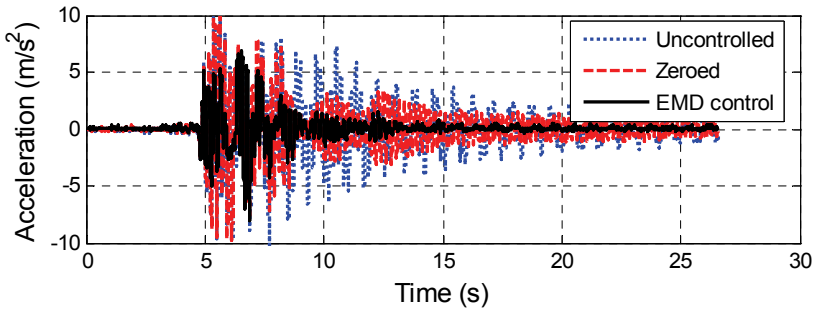
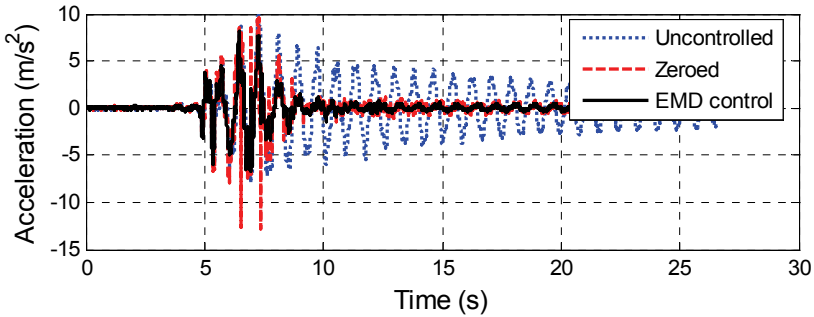


Fig. 5. Photo and calculation sketch of whole system

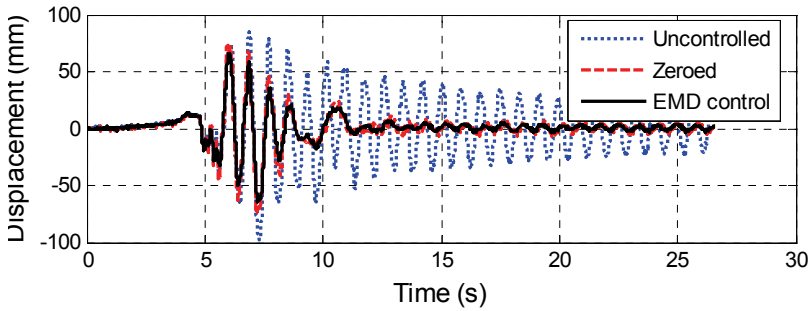


(a) Absolute acceleration of the first floor

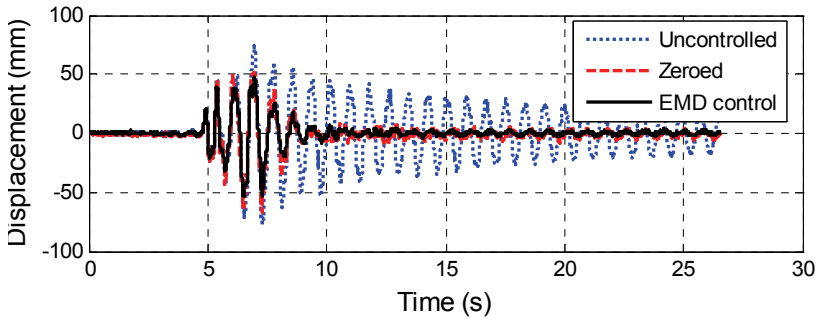


(b) Absolute acceleration of the top floor

Fig. 6. Experimental structural acceleration under Kobe wave excitation



(a) Absolute displacement of the first floor



(b) Inter-drift of the top floor

Fig. 7. Experimental structural displacement under Kobe wave excitation

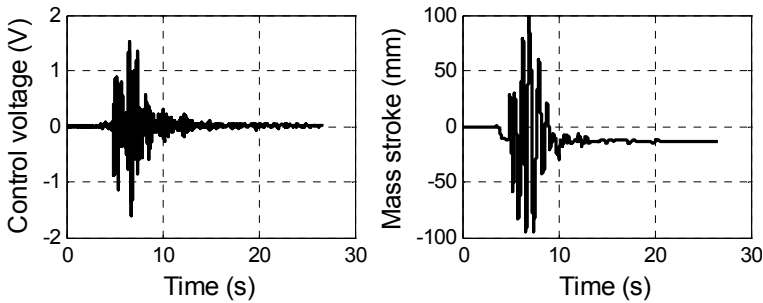


Fig. 8. Time history of control voltage and mass stroke of EMD system under Kobe wave excitation

following part. During the experiment, laser transducers are used to measure the absolute displacements of each floor of the test structure, and the inter-storey deformation can be calculated through subtraction of displacements of adjacent floors.

Figure 6 and figure 7 show the comparison of the structural absolute acceleration and floor displacement and inter-drift under three cases, Uncontrolled, Zeroed and EMD active control respectively. From the results, the EMD control is shown to be the most effective in suppressing structural vibrations. In addition, time histories of control voltage and mass stroke of the EMD system are also shown in figure 8.

In the above, theoretical modeling, dynamical testing, shaking table tests have been systematically carried out for the miniature EMD control to investigate its feasibility for using in structural vibration control. All the results show it to be a promising active control system for civil engineering.

2.2 Benchmark scale EMD control system

The existing linear motor products are already getting so close to rotatory motors in velocity regulation area, and the products are mostly low power motors to drive the AMD mass (Zong et al., 2002). Requested performances of AMD system used for vibration control of civil engineering structures are high power, heavy load and high response ability to frequency, however control accuracy is not necessarily requested. Sometimes the servo motor power may exceed hundreds or thousands of Kilowatts. One of the possible means to solve the problems is to use simple tri-phase asynchronous linear motors in the design of full scale AMD control system.

An approach of setting up the high power linear electrical motor servo system is studied in this part. To build the high power position servo system, normal frequency transducer is used to drive an asynchronous linear motor. Because the mathematical model of asynchronous motor is not easy to set up, a new controller design method based on the step response of the closed-loop system is introduced, and series of numerical simulations and experimental verifications were carried out. Experimental results showed that good control performance can be achieved using the designed controller for the physical system.

2.2.1 Principles of position control for asynchronous linear motor

Constitution of traditional rotatory position servo systems is shown in figure 9. In the traditional structure, rotatory machines and ball bearing screw are used, and the mass load is driven to perform linear motion. Due to the avoidless clearance between screw and load, transmission accuracy gets declined and the servo rigidity is affected. Linear motors are taken in to drive the load in the linear electric motor position servo system shown in figure 10. Without transmission components and movement transform, higher transmission accuracy and servo rigidity are achieved from asynchronous motors. At the same time, higher accuracy and dependability are achieved from whole position closed-loop system with raster ruler instead of rotatory encoder than half closed-loop system.

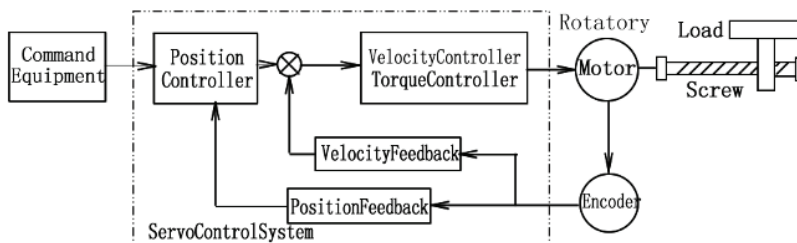


Fig. 9. Sketch of Rotary Servo System for Position Control

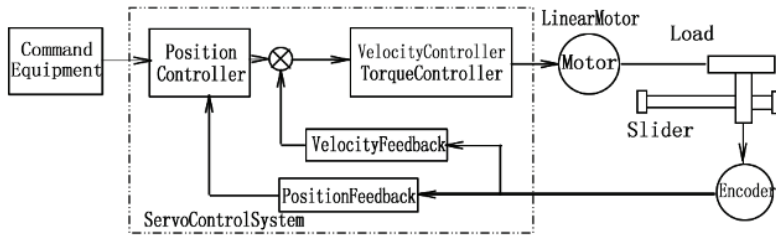


Fig. 10. Sketch of Linear Servo System for Position Control

Applications of linear motors focus on low power situations such as disk reader, printer, and numerical machine tools, so high power linear motion servo driver equipments can't be purchased. All the correlative hardware equipments have to be designed independently (Ye, 2003). This part takes vector alternating frequency transducer driver and asynchronous linear motor instead of position servo system, and makes use of computer servo control card to perform the controller's function, then builds the integrated servo system with asynchronous linear motor. The frame of the whole system is shown in figure 11.

From figure 11, functions of the components are shown: Control computer plays the role of servo controller. The position command signal is generated in MatLab/Simulink. Position error is calculated out from position command and position feedback from raster ruler, then velocity command signal is calculated, at last velocity voltage is produced from real-time control software WinCon and servo control card to frequency transducer. The linear motor is driven by the frequency transducer to run at the assigned speed according to the velocity command. The load is driven by the linear motor to perform linear motion displacement following the position command.

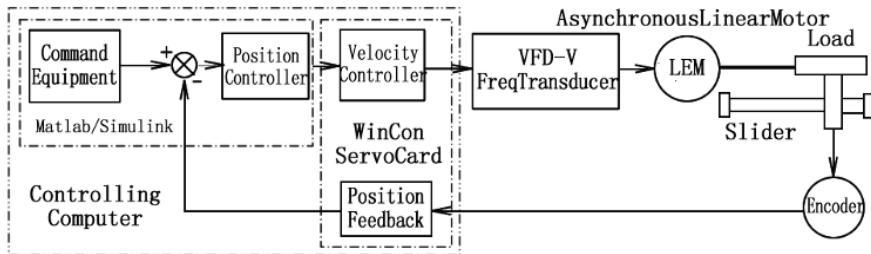


Fig. 11. Position Control of Asynchronous Linear Motor

Based on the structure shown in figure 11, equipments are chosen according to the power requirement. A tri-phase asynchronous linear motor with the power 4.5 kW, synchronous speed 4.5 m/s (50 Hz) is ordered, and a speed slip of 0.05 (5%) is estimated from experiments. The linear motor driver is Delta VFD-V model, high performance vector tri-phase alternating frequency transducer, with driving power of 5.5 kW. Position feedback tache is the most important component of the whole system, so a raster ruler produced by Renishaw Co. is chosen. Model of the ruler reader is RGS20, and minimal resolving power of the raster is 20 um. MultiQ-3 servo control card produced by Quanser Co. is setup in the control computer, with software of WinCon3.2 and Matlab 6.0. Structure of the whole

asynchronous linear electric motor is shown in figure 12. Figure 13 shows the picture of the experiment equipment and the software runtime is shown in figure 14.

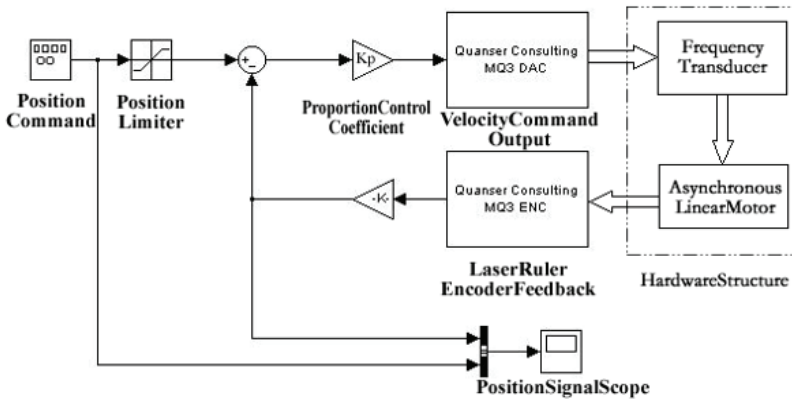


Fig. 12. Structure of the Position Control System

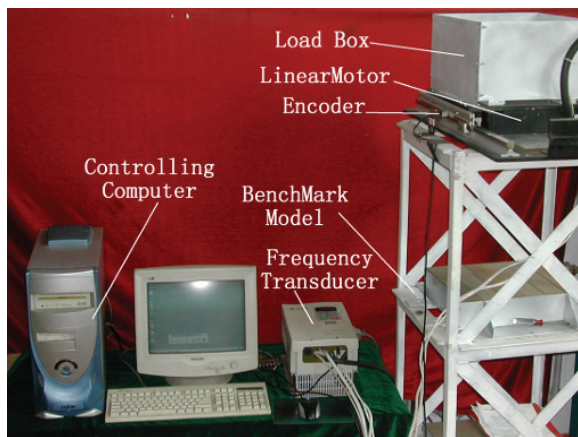


Fig. 13. Picture of the Control System

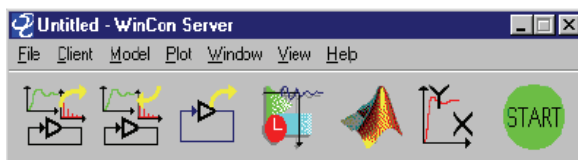


Fig. 14. Picture of the running WinCon

2.2.2 System model and position controller design

Traditional control method and controller design is commonly based on mathematics model of the object under control, and the controller is calculated according to required performance. Generally, mathematics model of the system is obtained by the method of analyze or system

identify, estimating model from the input and output experimental data. For the mathematic expression of asynchronous linear motor is so complex and parameters the manufacturer offered is not enough to build the model from analyze. At the same time, experiment situation of linear motor is limited by dimensions of the platform, so experiments can't be implemented to get enough data system identify required, which makes design of the controller much more difficult. In the engineering problem design process, simplification of the mathematics model usually makes the controller difficult to actualize or get awful performance. So a simple and facile approach that fits the engineering application is necessary.

This part analyzes and summarizes most of the design methods and tries a new design method. Reference to the design method of Extraction of Features of Object's Response, briefly EFOR, an approach to design the Lag-Lead compensator based on the experimental step response of the closed-loop system is implemented and good performances is achieved. Basic idea of quondam EFOR method is described as below: closed-loop simulation is carried out to a series of "Normal Object", to get the step response, and then some main time characteristic parameters are read out, and the controller is designed according to the parameters. The "Normal Object" is provided with some special characters: transfer function is strict proper rational point expression or proper rational point expression; minimum phase; at most one layer integral calculus; magnitude-frequency character is monotonous reduced function to the frequency (Wu et al., 2003).

Experiments showed that the asynchronous linear motor system couldn't satisfy all the requirement of the "Normal Object", especially the magnitude-frequency character is not monotonous reduced function to the frequency. But the step response of closed-loop system is similar to the attenuation oscillatory of the second-order system, so the EFOR method could be attempted to design the controller. So reference to the EFOR design method, a new method of Lag-Lead compensator design based on the experimental test is tried to accomplish the controller design. Detailed design process is shown below:

- a. Step response experiment is carried out, especially the curve of high oscillatory with similar amplitudes, and attenuation oscillatory periods T_d is obtained, and then the frequency of system attenuation oscillatory $\omega_d = 2\pi / T_d$ is calculated, at last the critical attenuation oscillatory ω_p is estimated; The experimental method is especially fit for some systems which only perform movement within limited displacement such as linear electric motors. These systems have only limit experiment situation and can't perform long time experiments. The curve of high oscillatory with similar amplitudes when the proportion control coefficient is $K_p=15$ from the experiments is shown in figure 15. Parameters below are obtained:

$$T_d = 2.926 - 1.702 = 1.224s \tag{5}$$

$$\omega_p \approx \omega_d = 2\pi / T_d = 5.133rad / s \tag{6}$$

The Lag-Lead compensator is designed according to equivalence oscillatory frequency. Structure of the lead compensator is shown below:

$$K_h(s) = \frac{\frac{s}{\omega_m / \lambda} + 1}{\frac{s}{\lambda \omega_m} + 1} = \lambda^2 \frac{s + \frac{\omega_m}{\lambda}}{s + \lambda \omega_m} \quad (\lambda > 1) \tag{7}$$

Design of the lead compensator is mainly the chosen of parameters λ and ω_m .

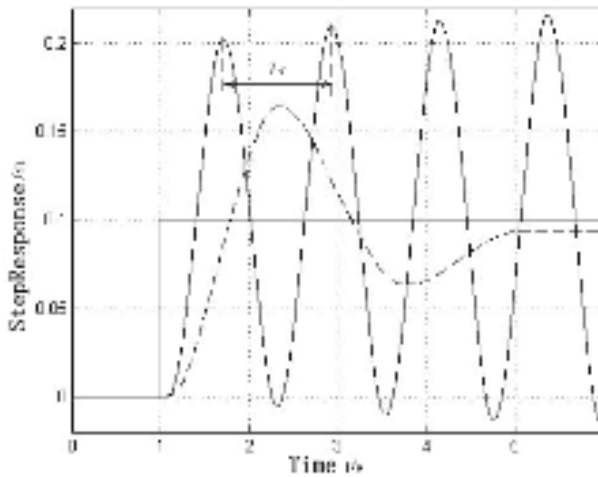


Fig. 15. Curve of Critical Oscillating System from Experiments

Parameter λ is named compensator strength. Larger λ produces plus phase excursion and better performance; too larger λ produces phase excursion increased not evidently, but makes the higher frequency gain so large that the high frequency noise is enlarged. So the λ should be selected based on the exceed quantity λ , usually from the empirical formula

$$\lambda = \begin{cases} 1.2 + 4\sigma & (\sigma \leq 0.6) \\ 3.6 & (\sigma > 0.6) \end{cases} \quad (8)$$

So the compensator strength for the current system is $\lambda = 3.6$.

The compensator mid-frequency ω_m should be a little higher than ω_p . For the second-order system, usually from the empirical formula $\omega_m = \sqrt{\lambda} \omega_p$, so

$$\begin{aligned} \omega_m &= \sqrt{\lambda} \omega_p = \sqrt{3.6} \times 5.133 \\ &= 9.740 \text{ rad / s} \end{aligned} \quad (9)$$

Thereby the lead compensator is achieved:

$$K_h(s) = \frac{\frac{s}{\omega_m / \lambda} + 1}{\frac{s}{\lambda \omega_m} + 1} = \frac{0.37s + 1}{0.0285s + 1} \quad (10)$$

- b. The main purpose of the lag compensator is to reduce the stable error, but phase will usually be reduced, too, so the lag compensator parameters should be determined by the steady error after the lead compensator added. For the system that the error fits the requirement, a lag compensator is not necessary. Usually structure of the lag compensator is like this:

$$K_l(s) = \frac{s + \omega_1}{s + \rho\omega_1} \quad (11)$$

In the expression, the compensator strength is $0 < \rho < 1$. ω_1 is the seamed frequency of the lag compensator, so it must be lower than magnitude crossing frequency ω_c and not close to ω_c , to reduce the effect to mid-frequency performance. Usually $\omega_1 \approx (0.1 \sim 0.2)\omega_c$, $\rho = 1/n$, so that the steady error could be reduced to $1/n$. Accordingly, the position controller is designed for the system. The perfect proportion control coefficient is $Kp=8$. Figure 16 shows the controller structure.



Fig. 16. Structure of Lag-Lead Controller

2.2.3 Simulation and experimental results

The lag-lead compensator based on the step response is $K_h(s) = (0.37s + 1) / (0.0285s + 1)$, and the perfect proportion control coefficient is $Kp=8$. With the method of getting controller coefficient from test-run, the best perfect coefficient for only proportion controller is $Kp=8$, and the best perfect coefficient for proportion differential controller is $Kp=8, Kd=0.4$. The coefficients are applied in the simulations and the experiments below.

By analyzing parameters of the lag-lead compensator and some conclusion from system identification, a simplification model was estimated to test the performance of the controllers. Simulations using different controllers such as lag-lead compensator, proportion controller, or proportion differential controller were carried out with the help of Matlab software. Simulation result with different controllers is shown in figure 17.

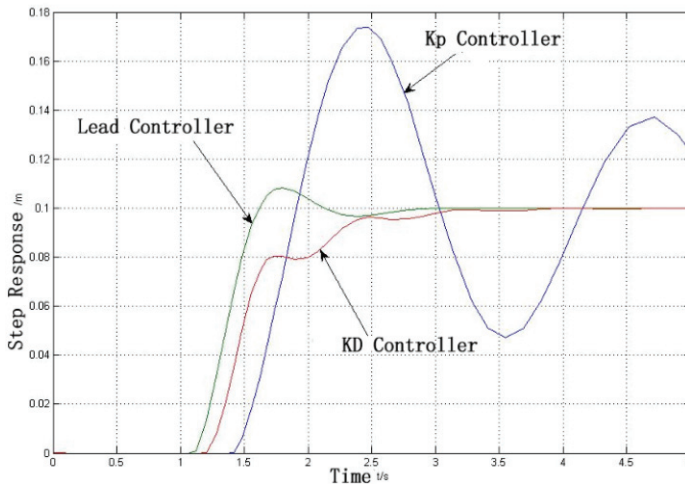


Fig. 17. Results of the Simulations using three different controllers

The figure shows that the lead compensator and the proportion differential controller make great improvement to the object under control. Compared with simple proportion controller, the response speed and the position control error are reduced a lot.

Some experiments were performed on the mechanic equipments. Figure 18 shows the performance of the lead compensator while adjusting the proportion coefficient near $K_p=8$. The performance of following ability test under the lead compensator is shown in figure 19. Obvious following effect to the sine position command with magnitude 50mm and frequency 1Hz is obtained.

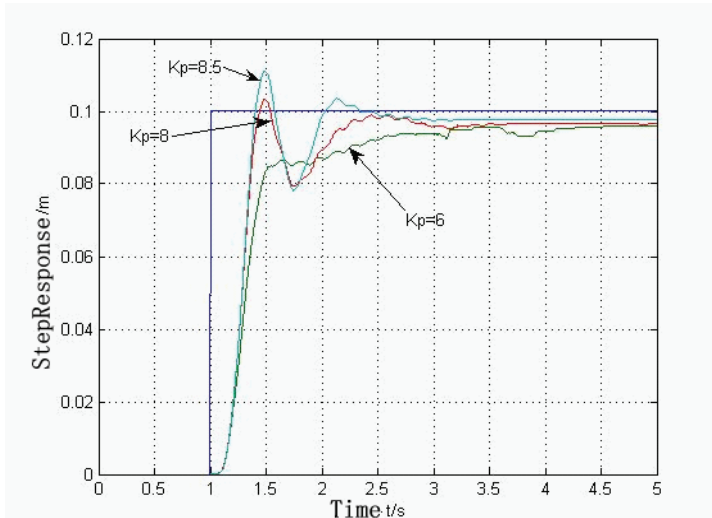


Fig. 18. Experiment Results using different K_p

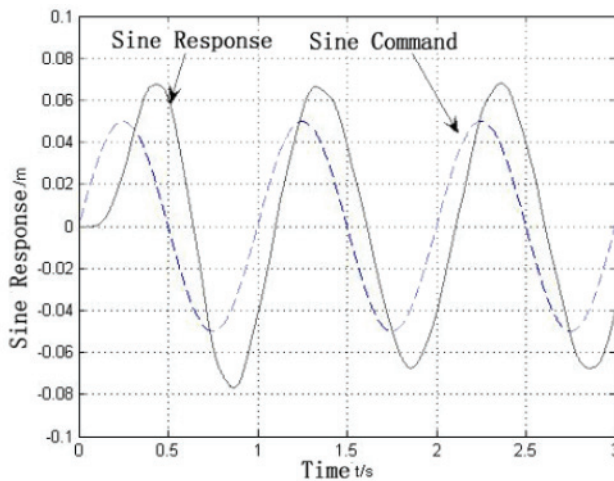


Fig. 19. Experiments Curve of Sine Signal Response

Based on the experiments, the performances of the three different controllers are shown in figure 20.

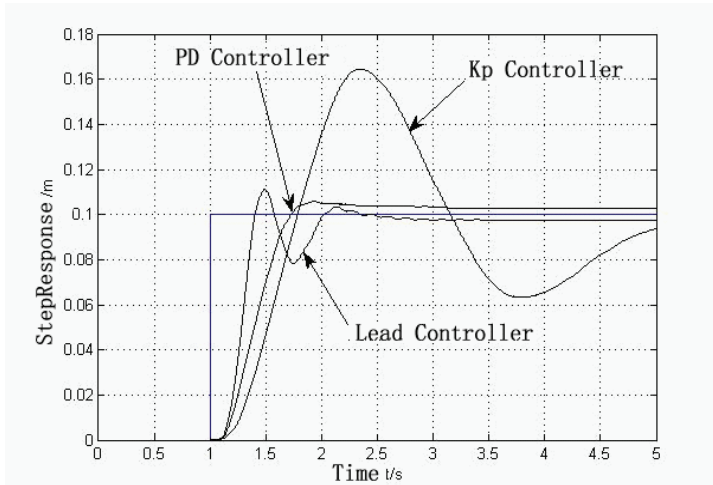


Fig. 20. Comparison of the Experiment results using three different controllers

The following function parameters based on step response are obtained from figure 20.

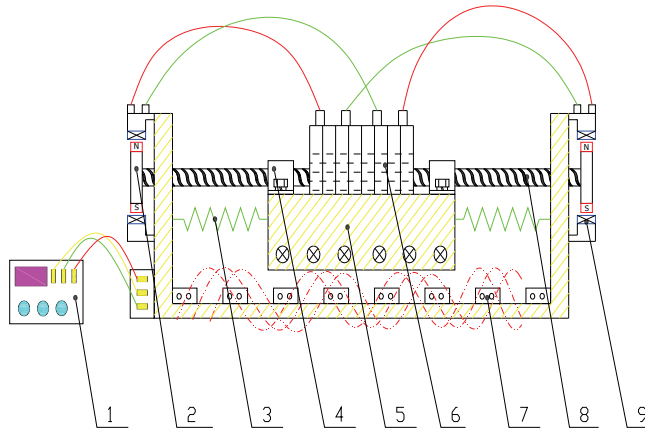
System Function Value	ising Time/s	ransit Time/s	Surpass Amounts	teady Error	Oscillation Number
LagLeadcontroller	.37	.96	11.5%	%	2
KD Controller	.62	.97	6%	%	1
Kp Controller	.73	.9	64%	%	3

Table 1. Comparison of Function Values from Experiments using three different controllers

The functional parameters shows that the controller designed by the method based on the experimental step response of the closed-loop system improves the system performance a lot, even much better than the proportion differential controller, while the design process is far simple than the design of PD controller.

2.3 Energy harvest EHMD control system

In the following figure 21, the main parts of the innovative EHMD system and their relations were illustrated, respectively. The EHMD system can be divided into the following parts: TMD subsystem with energy dissipating and recycling functions, power module which can preserve and release electrical energy, EMD subsystem which is directly driven by electro-magnetic force. To be specific, TMD damper is replaced by coils embedded fly-wheels combined with high-power batteries, EMD active force is realized using soft magnetic material actuator and high-power capacitor; besides, the standard DSP module is incorporated to make up a real-time control system. The fly-wheels is composed of wheel body, reducer or accelerator using gear boxes, energy generating and dissipating coils, high power storage battery and capacitor, electronic and electrical regulator, as well as mechanical couplings and attachments etc. Considering the fly-wheel battery is relatively a matured technique, here the EHMD should be focused on solving its control strategies to realize a reasonable energy preserving-releasing process for structural active control.



(Note: 1-digital controller, 2-fly-wheel(s), 3-spring element, 4-mechanical couplings, 5-system mass (embedded coils), 6-energy-storing battery, 7-excitation coils, 8-bearings and system rails, 9-permanent magnets)

Fig. 21. Structural integration photos of EHMD system

In the following figure 22, analysis and design procedure of the EHMD system is proposed. First, aiming at the requirement of the specific structure to be controlled, optimal mass ratio, stiffness and damping coefficients, maximum mass stroke and peak control force were calculated, which were set as the hardware standard parameters of the moderate scale EHMD system. Second, applying relevant research results, such as linear motor technique in magneto suspension trains and energy accumulation technologies in fly-wheel batteries etc, key parts of energy recycling, preserving and utilizing for driving EHMD system would be developed. At last, integrating DSP based data acquisition, processing and real-time control modules, the whole experimental EHMD system are fabricated and integrated.

When the structure vibrates, the mass moves driving the couplings rotating which transforms linear motion into rotation, and the embedded coil cut the magnetic field and generates induction currents and stored in the batteries which will be utilized at a

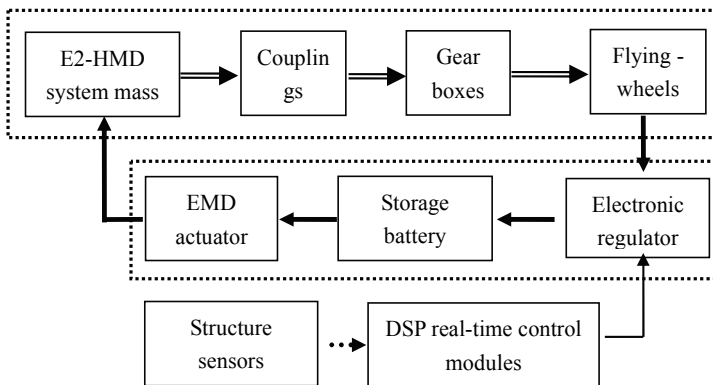


Fig. 22. Structural construction sketch of EHMD system

reasonable occasion. If reducer or accelerator is incorporated into the system, then the efficiency of generating electrical power can be greatly improved, through calculations the optimal gear ratio and damping coefficient can be achieved.

In the following, feasibility of utilizing such kind of EHMD system for suppressing structural vibrations will be considered. Basically, the main problems will be focused on the electrical loops of the system, because the other two major parts will be benefited from AMD and TMD control techniques. Currently, a high-power capacitor can be stored with energy of up to 3MJ, where its energy density will be 1.35kJ / kg and about 1.5kJ / dm³, thus the mass will be about 2m³ and the weight will be 2tons or so, which can power the EMD actuator in continuous working mode for more than 200 seconds. From the data, the EHMD for protection of structural seismic response is absolutely feasible.

3. DDVC based AMD control system

This DDVC based active mass driver control system is proposed for low frequency vibration and motion control, *e.g.* wave induced motion control of offshore platform structures. DDVC (Direct Drive Volume Control) technology comes from the hydraulic industry, which utilizes integrated pump and motor to replace servo valve from traditional hydro cylinders, and to realize such functions as pressure control, speed control and changing working directions etc. DDVC control is also called as valve-less control, which uses servo AC motors driving fixed displacement pumps. DDVC is operated based on regulating rotary speed of pumps rather than changing its flow, and to control actuating speed of actuators. DDVC has been widely researched by institutions from Japan, USA, German, Sweden and China. The most common applications are used in such industries as high-precision forging machinery, ship helms, heavy load casting machineries, printing machines, 6-DOF platforms and rotary tables, 2500 ton inner high pressure shaping machine, operating switch for floodgates etc. Besides, some applications have been proposed for aerospace engineering (also called EHA, Electrical Hydro Actuator) recently because the most attracting advantages of compact volumes, high energy saving efficiencies etc.

Figure 23 shows the photo of one typical DDVC system fabricated by 1st Japan Electric Corporation. DDVC-AMD is an innovative replacement of actuator from traditional hydro cylindrical AMD control system, and figure 24 shows the working principles of such DDVC actuated AMD control system.



Fig. 23. Photo of DDVC driver

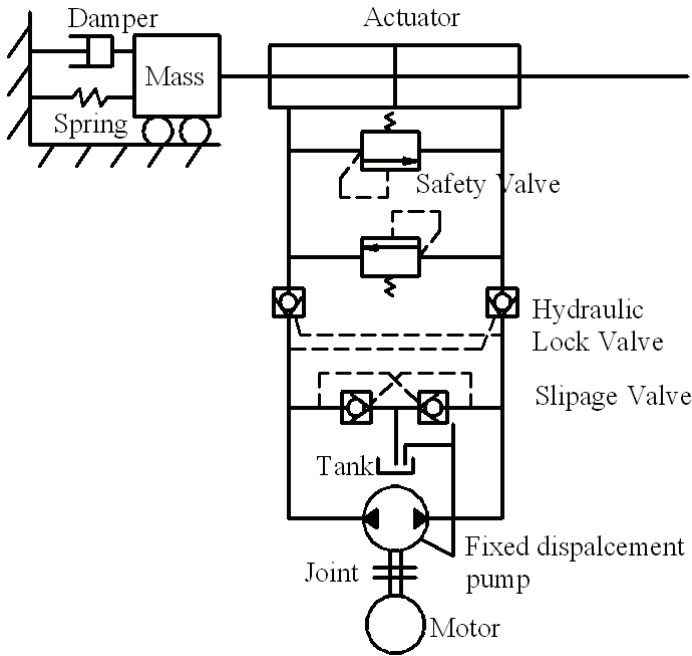


Fig. 24. Principle chart of DDVC-AMD system

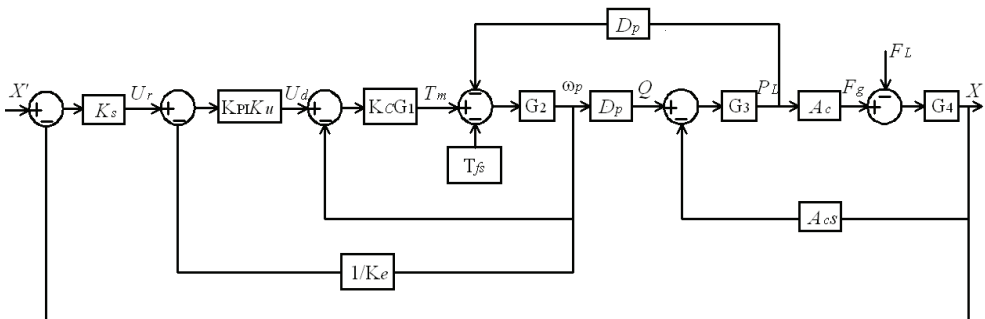


Fig. 25. Simulation block diagram for DDVC-AMD control system

The following section established the formulations for DDVC based AMD control system. Motor control loop, hydraulic power plant and actuation part were studied and numerically validated. As shown in figure 25, Simulink simulation block diagram was used to perform numerical simulations and comparisons on the force-displacement hysteresis loops are given in figure 26. Furthermore, structural seismic response control using DDVC-AMD are numerically studied. Figures 27 to 28 show some preliminary results under Kobe and Hachinohe earthquake excitations, which indicates the feasibility and effectiveness of such system for structural vibration mitigation.

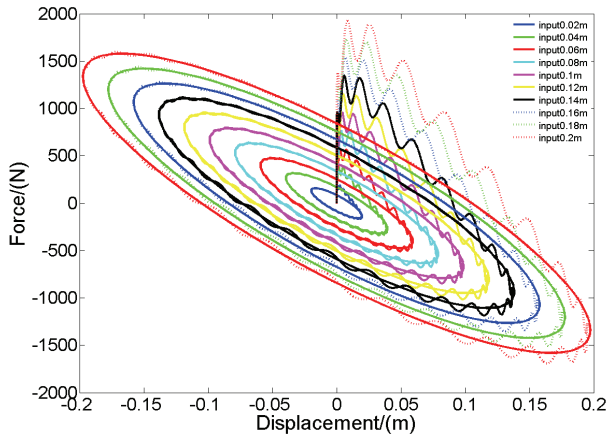


Fig. 26. Hysteresis loops of DDVC-AMD under different loading amplitudes

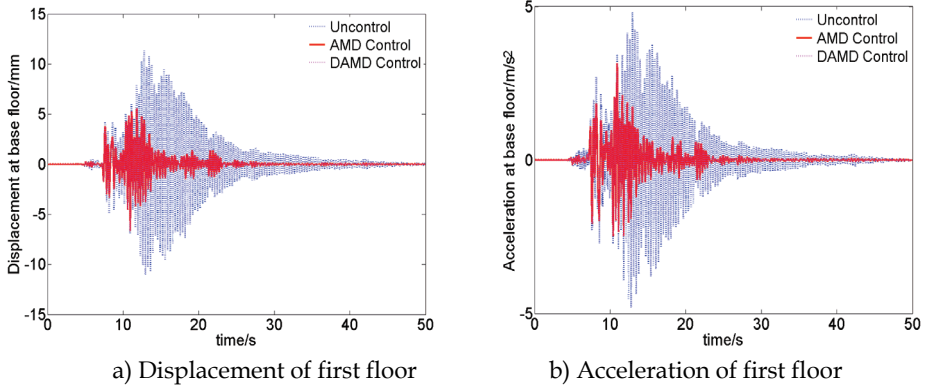


Fig. 27. Kobe earthquake excitation

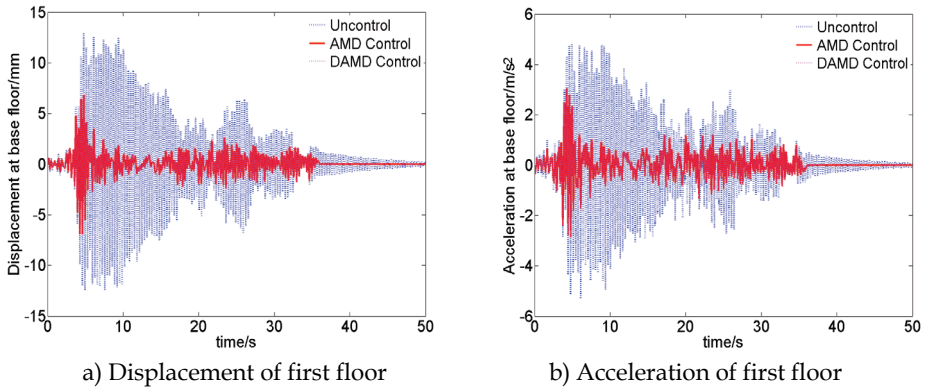


Fig. 28. Hachinohe earthquake excitation

4. Structural swinging motion and vibration control

Vessel-mounted cranes of heavy lifting and pipeline paving ships are used to construct large scale offshore structures, such as steel jacket platforms and oil-gas transporting pipeline systems etc. Owing to the complicated conditions of ocean environment, the wave-induced ship motion, sometimes wind-wave-current coupling excitations of the crane ship produces large pendulation of hook structure, which causes normal operations of the ship to be suspended and results in economic losses. For example, when the wind speed exceeds 6 degree, the probability of suspended operations will be about 50%, which greatly affects the construction progress.

Based on a large amount of observations on the hook vibration, the pendulation can be divided into two types: in-plane motion and rotary motion with respect to certain axis (namely gyrus motion). After thorough numerical simulations and experimental verifications, the control solution corresponding to each type of the motion is found to be absolutely different.

In the followings, the modeling of two motion modes and the methods of suppressing different types of pendulation of hook structure will be discussed respectively, and eventually be experimentally verified on a scale model structure.

4.1 Theoretical modeling

The calculation sketch of the crane ship can be simplified as a SDOF system, which is represented using a basket model as shown in figure 29, and a passive TMD (Tuned Mass Damper) control system is attached onto the structure. Based on the measurement of the motion of the suspended hook structure, the pendulation could be classified into two modes owing to different relation between suspension points and motion direction as shown in figure 29, where SP stands for "suspension points".

After thorough theoretical analysis and numerical simulations, the two types of motion is found to be absolute different, and the Lagrange's equation is introduced to model each motion mode respectively. As shown in figure 30, to quantity compare the differences, the hook is simplified as a bar with two masses on each end, besides the TMD system is simplified as a spring-mass second system. Using x stands for mass strokes of TMD system,

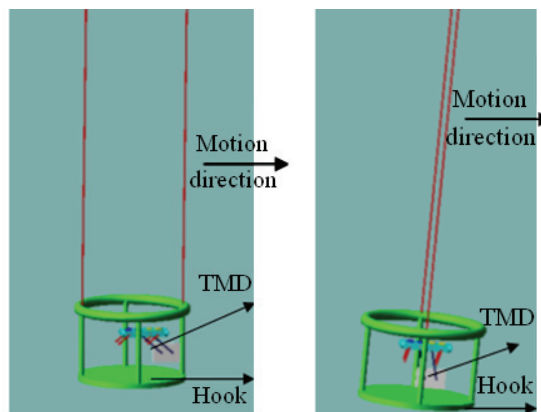
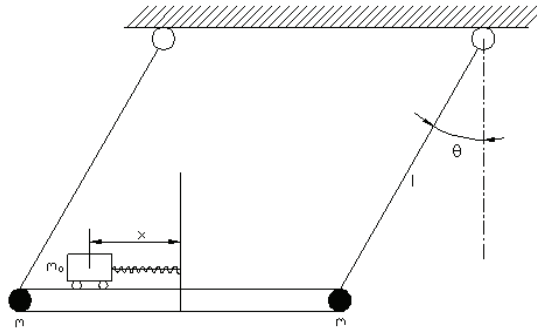
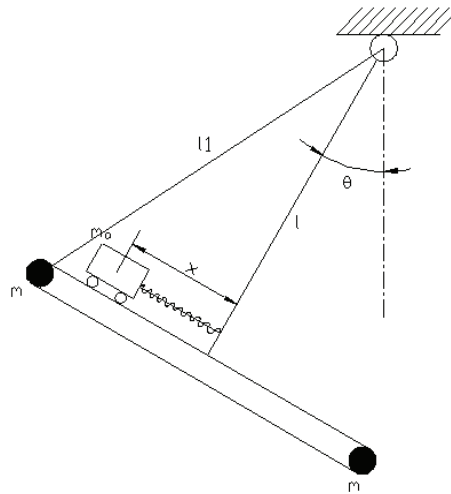


Fig. 29. Suspension points and motion directions



(a) In-plane motion



(b) Rotary motion

Fig. 30. Typical motion modes

l stands for the length of suspension cable, θ stands for pendulation angle with respect to vertical direction, m stands for one half of the mass of hook structure, m_a stands for mass of TMD control system.

The whole system shown in figure 30(a) has the following kinetic energy and potential energy expressions:

$$T = ml\dot{\theta}^2 + \frac{1}{2}m_a l\dot{\theta}^2 + \frac{1}{2}m_a \dot{x}^2 + m_a l\dot{x}\dot{\theta} \cos\theta \quad (12)$$

$$V = 2mgl(1 - \cos\theta) + m_a gl(1 - \cos\theta) + \frac{1}{2}kx^2 \quad (13)$$

Using Lagrange's formulation, $L = T - V$, $\frac{d}{dt}\left(\frac{\partial L}{\partial \dot{x}}\right) - \frac{\partial L}{\partial x} = 0$ and $\frac{d}{dt}\left(\frac{\partial L}{\partial \dot{\theta}}\right) - \frac{\partial L}{\partial \theta} = 0$, we have

$$\ddot{x} + \frac{k}{m_a}x = l\dot{\theta}^2 \sin \theta - l\ddot{\theta} \cos \theta \quad (14)$$

$$2ml^2\ddot{\theta} + m_a l^2 \ddot{\theta} + m_a l \dot{x} \cos \theta + 2mgl \sin \theta + m_a gl \sin \theta = 0 \quad (15)$$

Equation (14) gives the solution of TMD mass strokes relative to the main structure, and equation (15) is the standard formula of simple pendulum structure.

For comparison, the kinetic energy and potential energy of the system shown in figure 30(b) has the following expressions:

$$T = ml_1^2 \dot{\theta}^2 + \frac{1}{2} m_a \dot{x}^2 + \frac{1}{2} m_a (l^2 + x^2) \dot{\theta}^2 + m_a x l \dot{\theta} \quad (16)$$

$$V = 2mgl(1 - \cos \theta) + m_a g(l - l \cos \theta + x \sin \theta) + \frac{1}{2} kx^2 \quad (17)$$

Where l_1 is the distance between suspension point and concentrated mass of the suspended structure. Similarly, using Lagrange's formulation, the equation of motion can be achieved as

$$\ddot{x} + \frac{k}{m_a}x = x\dot{\theta}^2 - l\ddot{\theta} - g \sin \theta \quad (18)$$

$$2ml_1^2\ddot{\theta} + m_a(l^2 + x^2)\ddot{\theta} + 2m_a x \dot{x} \dot{\theta} + m_a l \dot{x} + 2mgl \sin \theta + m_a gl \sin \theta + m_a gx \cos \theta = 0 \quad (19)$$

4.2 Numerical simulation

Assuming the system parameters are $m=5\text{kg}$, $m_a=0.5\text{kg}$ and $l=10\text{m}$, imposing an initial kinetic energy on the suspended structure shown in figure 30(a) and the dynamical response of the system is listed in the figure 31.

Here assuming there is no damping existed in the TMD system, thus the vibration of the system will not be suppressed, and energy exchanges between the TMD control system and the main structure, as shown in figure 31(a) and 31(b). In figure 31, the unified force is defined as the sum of the two items in the right hand side of equation (14). From the definition we can see that such kind of unified force is independent of mass strokes x , which was also verified by the simulation results shown above. From both the figures and the equations, we can see that the unified force of the TMD system is proportional to the vibration amplitude of the structure, which is equals to the control force which is imposed onto the main structure. Thus the TMD system behaves like a closed-loop feedback control system of the structure (Zhang *et al.*, 2006).

On the other hand, equation (18) gives the equation of TMD mass in the second suspension case, where the last two items are the ideal motion equation of the simple pendulum system. The control force of TMD system is shown to be dependent on the product of x times angular velocity. After a lot of simulations, the mass stroke is shown to be very small, which can not provides sufficient control force to suppress the structural vibrations. Moreover, the

control effectiveness is also affected by the initial phase lags between TMD mass and the hook displacement. As a result, traditional TMD system will lose its effects during the rotary motion mode.

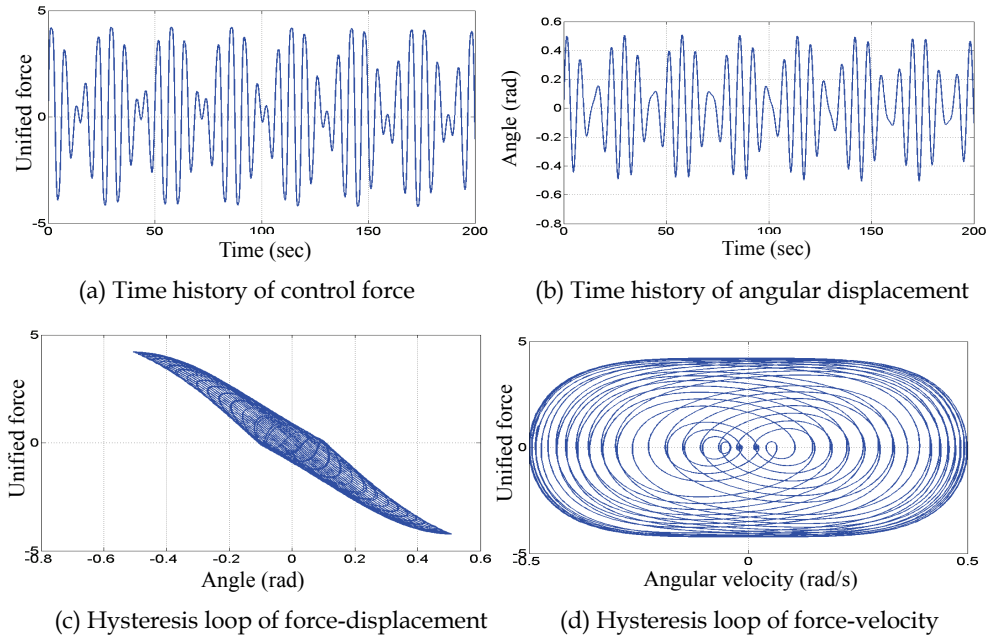


Fig. 31. Numerical simulation responses of in-plane vibration mode

4.3 Solutions for rotary and swinging motion control

For the rotary motion mode, which is exactly similar to the gyrus motion or swing vibration of a simple pendulum, the gravity acceleration plays both as disturbance force and restoring force at the same time, thus the ability of the traditional in-plane control device is of no effect any longer, and innovative mechanism or special device, which can exert control torques to suppress such gyrus motion should be developed.

Taking a simple pendulum system for example, the suspended structure and the gyrus motion control system is shown in figure 32, where m_0 is the mass of hook structure, l_0 is the length of suspension cable, r is the radius of fly-wheel, for simplification, m is the representative value of half mass of the fly-wheel, θ and φ are angle of wheel rotation and vertical direction respectively.

Kinetic and potential energy of the simple pendulum and rotary control system shown in figure 32 are given below, where k_t is the stiffness coefficient of torsion spring.

$$T = \frac{1}{2}(m_0 + m_a)l_0^2\dot{\varphi}^2 + m_a r^2 \dot{\theta}^2 \quad (20)$$

$$V = (m_0 + 2m_a)gl_0(1 - \cos\varphi) + \frac{1}{2}k_t(\theta - \varphi)^2 \quad (21)$$

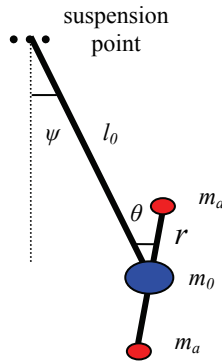


Fig. 32. Computational sketch of rotary motion

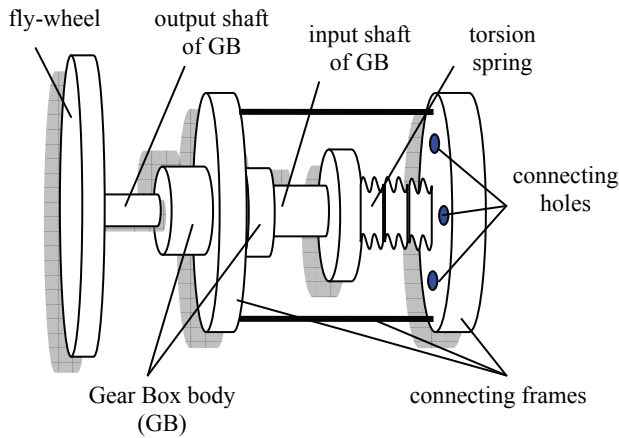


Fig. 33. Numerical simulation responses of in-plane vibration mode

Using Lagrange’s principal, the system equations of motion can be achieved as

$$(m_0 + 2m_a)l_0^2\ddot{\phi} + (m_0 + 2m_a)gl_0 \sin \phi - k_t(\phi - \theta) = 0 \tag{22}$$

$$2m_a r^2 \ddot{\theta} + k_t(\theta - \phi) = 0 \tag{23}$$

In order to control the rotary motion, the control system must be able to rotate relative to the pendulation of the hook structure. The innovative tuned torsion inertia damper system is composed of torsion spring element, fly-wheel, gear boxes and necessary connecting accessories is developed and its main structure is shown in figure 33. If the reducer gear box is introduced, then the volume of the whole rotary control system can be greatly reduced, and the rotation inertia of the control system can be increased by i^2 times, where i is the gear ratio. The intrinsic characteristic of such an innovative rotary control system is to use high rotation speed to make up for the smaller physical rotation inertia indeed. After incorporating gear box device, equations (22) and (23) can be rewritten as

$$\ddot{\phi} = \frac{1}{(m_0 + m_1 + m_2)l_0^2} [-(m_0 + m_1 + m_2)gl_0 \sin \varphi + k_t(\theta - \varphi)] \quad (24)$$

$$\ddot{\theta} = \frac{1}{(m_1 r_1^2 + i^2 m_2 r_2^2)} [-k_t(\theta - \varphi)] \quad (25)$$

Where m_1 is mass of the input shaft (low speed end) of reducer GB box and r_1 is the rotation inertia radius of m_1 , m_2 is the mass of output shaft (high speed end) of reducer GB box and r_1 is the corresponding rotation inertia radius.

4.4 Innovative TRID control system

TRID system, as shown in figure 34, was composed of a torsion spring, with the stiffness k_t , and a cricoid mass, with the mass m and the radius r , so the rotation inertia can be expressed as $J_a = mr^2$.

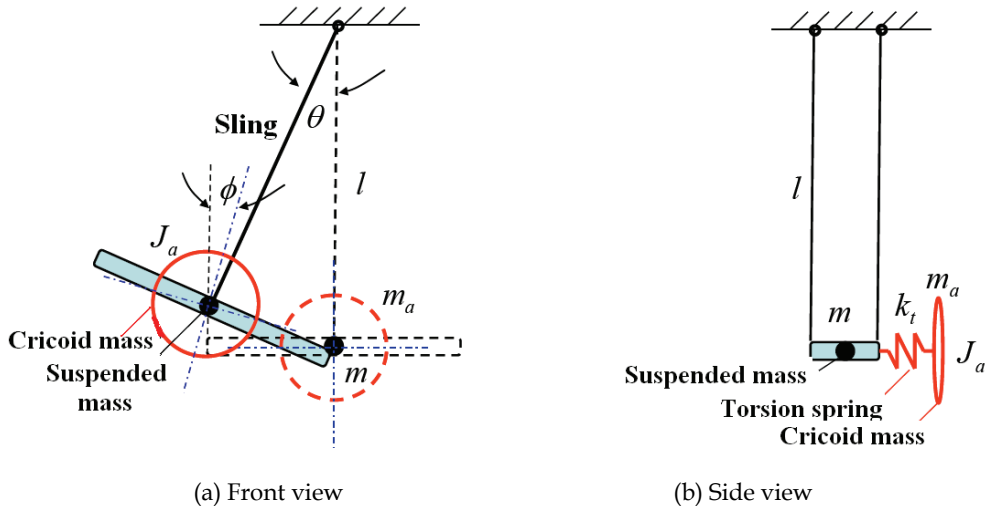


Fig. 34. Pendulum-TRID system

Based on the Lagrange principle, the differential equation of free pendular vibration with TRID system is:

$$\begin{cases} (m + m_a)l^2\ddot{\theta} + (m + m_a)gl \sin \theta - c_t(\dot{\phi} - \dot{\theta}) - k_t(\phi - \theta) = 0 \\ J_a\ddot{\phi} + c_t(\dot{\phi} - \dot{\theta}) + k_t(\phi - \theta) = 0 \end{cases}$$

Where: θ denotes the angle of the pendulum, ϕ denotes the angle of the torsion spring. The following are some primary simulation results:

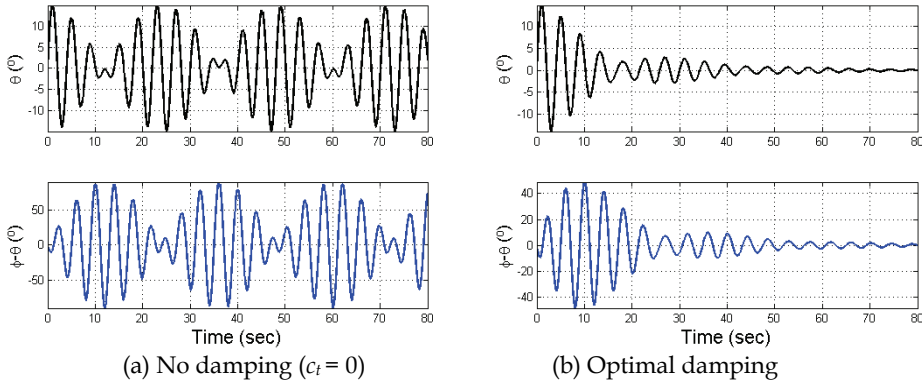


Fig. 35. Free pendular vibration controlled with TRID system

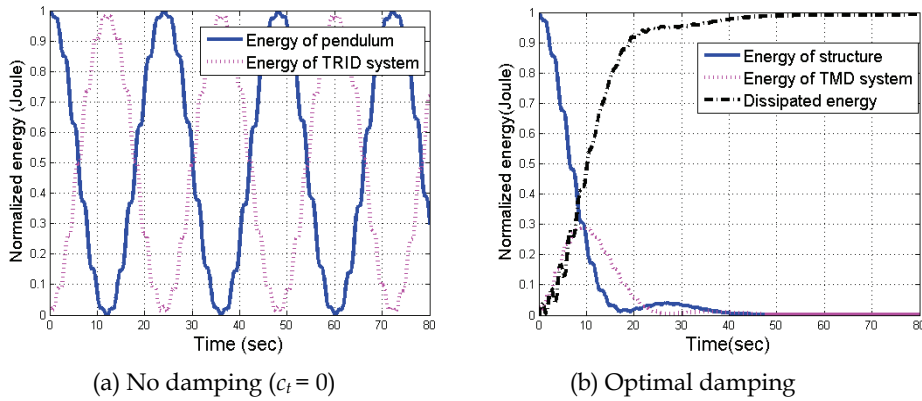


Fig. 36. Energy transmission and dissipation of pendulum-TRID system

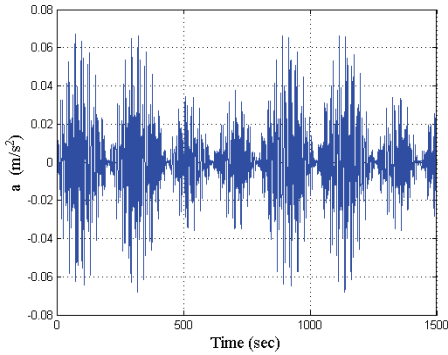
Figure 35 shows that the TRID control system was effective for the control of free pendular vibration. And figure 36(a) shows the energy transmission between the pendulum and the TRID system without damping in the TRID system. If there is an appropriate damping in the TRID system, the energy transmitted to the TRID system will be dissipated gradually. Thus, the total energy of the pendulum-TRID system decays and the pendular vibration is controlled finally.

4.4.1 Forced pendular vibration control

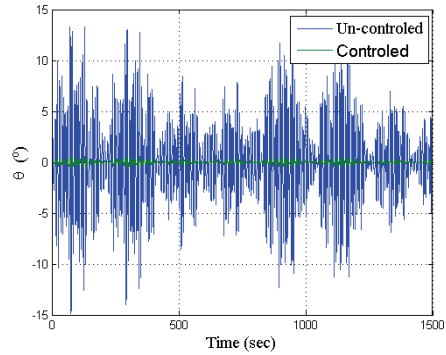
For excited pendular vibration with displacement excitation at the suspended points, the differential equation is:

$$\begin{cases} (m + m_a)l^2\ddot{\theta} + (m + m_a)gl\sin\theta - c_t(\dot{\phi} - \dot{\theta}) - k_t(\phi - \theta) = -(m + m_a)l\ddot{x}\cos\theta \\ J_a\ddot{\phi} + c_t(\dot{\phi} - \dot{\theta}) + k_t(\phi - \theta) = 0 \end{cases}$$

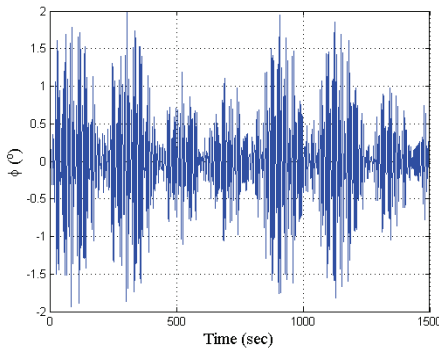
Where: \ddot{x} denotes the acceleration of the moving suspended point of the structure.
 And some numerical results of excited pendular vibration control are given in figure 37.



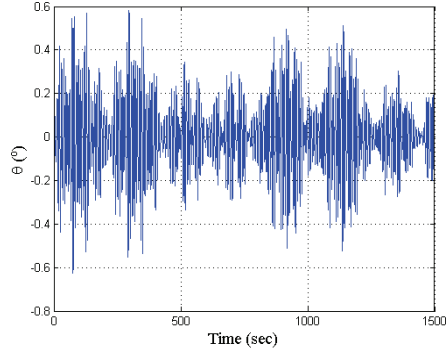
(a) The acceleration of the upper point: \ddot{x}



(b) The angle of the pendular vibration



(c) The angle of the inertia



(d) The angle of the controlled pendular vibration

Fig. 37. Forced pendular vibration controlled with TRID system

4.4.2 Experimental investigations

A series of experiments of both free pendular vibration and harmonic excited pendular vibration with TRID system were carried out. The experimental setup and some results are shown in figure 38 and figure 39, respectively.

From figure 39, the test results as well as the simulation results show that the TRID system is effective in suppressing the pendular vibration of both free and forced vibrations.

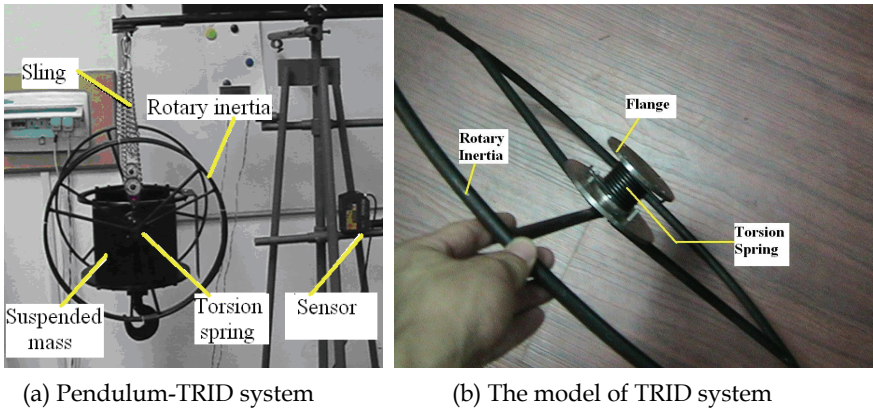


Fig. 38. The equipments of the experiments

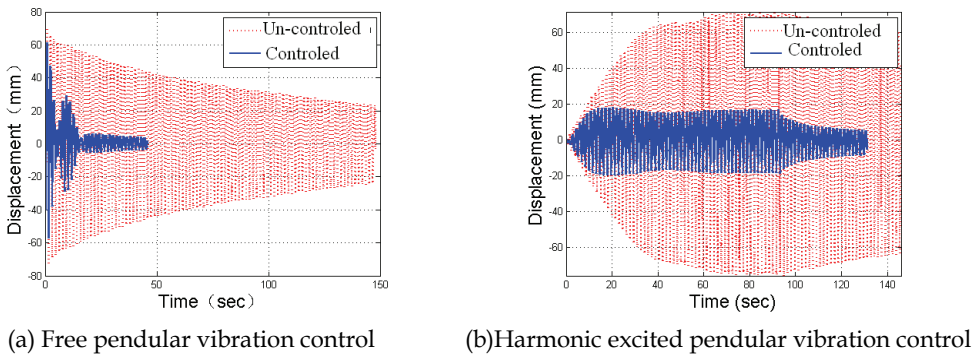


Fig. 39. Pendular vibration controlled with TRID system

4.4.3 Parameter optimization of TRID control system

The effect of TRID system mainly depends on its frequency tuning ratio and damping ratio. Based on a lot of numerical simulations, the following results were obtained:

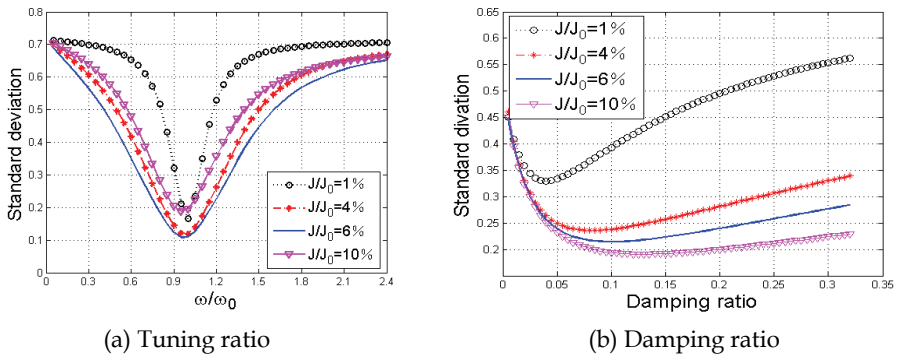


Fig. 40. Impact of the main parameters of TRID control system

Figure 40(a) shows that the TRID system have the best performance when the frequency ratio is set to 1.0 or so. Beyond that range, the TRID system loses its effectiveness quickly.

Figure 40(b) shows the damping ratio impact of TRID system under different inertia ratios. The simulation results indicate that when the design of TRID system is being considered, the intersect influence of parameters must be addressed.

4.5 Preliminary results on TRID control system

This part studies an innovative passive control system for rotary motion control of suspended hook structures, and main conclusions are achieved as:

1. Gravity acceleration is the disturbance effect on the in-plane motion of the suspension hook structure, on the other hand, it plays as disturbance as well as restoring force in the rotation mode of the structure.
2. According to different motion types, traditional TMD system can be used to control the in-plane motion, however, only the tuned torsion inertia damper is shown to be feasible for reducing the rotary (gyrus) motion.
3. For the miniaturization of the innovative rotary control system, the reducer gear box is introduced, which compensates system rotation inertias at the cost of high rotation speed. Through model test, the control system is proven to be feasible and effective.

5. Force characteristics of AMD control system

5.1 Background

The wind-induced vibration control problem of the Melbourne Benchmark building has attracted much research concern in the past eight years, and a lot of control schemes either in control algorithms or in physical control systems have been proposed by researchers all over the world (Yang *et al.*, 1998, 2004; Ricciardelli *et al.*, 2003; Samali *et al.*, 2004). Ou studied the structural interbedded active control scheme for the Benchmark problem, where the active control force of the actuators were found to be possessing the damping force behavior (Ou, 2003), which indicated that all the active actuators can be replaced by semi-active devices or even passive viscous damping devices. As a comparison, after a lot of numerical analysis, Zhang *et al.* (Zhang *et al.*, 2004) disclosed that the active force of AMD control system doesn't possess damping behavior, which resulted in the actuators of AMD control system can not be replaced by any semi-active devices. On the other hand, after the more than 30 years development of structural active control research (Ou, 2003), the Active Mass Driver/Damper (AMD) control, with the better control effect and cheaper control cost, has taken the lead in various active control occasions, becoming the most extensively used and researched control method in practical applications (Soong, 1990; Housner *et al.*, 1997; Spencer *et al.*, 1997; Ou, 2003). Besides, several important journals in civil engineering field, such as ASCE Journal of Engineering Mechanics (issue 4th, in 2004), ASCE Journal of Structural Engineering (issue 7th, in 2003), Earthquake Engineering and Structural Dynamics (issue 11th, in 2001 and issue 11th, in 1998), reviewed the-state-of-the-art in research and engineering applications of semi-active control and active control, especially AMD control. In addition, Spencer and Nagarajaiah (2003) systematically overviewed the applications of active control in civil engineering. Up to date, more than 50 high-rising buildings, television towers and about 15 large-scale bridge towers have been equipped with AMD control systems for reducing wind-induced vibration or earthquake-induced vibration of the structure. As a result, aiming at the above problem, some researchers have

made some studies on the intrinsic characteristic of active control force of different schemes (Horvat *et al.*, 1983; Mita *et al.*, 1992; Pinkaew *et al.*, 2001; Ou *et al.*, 2004; Zhang *et al.*, 2004). As a continued study, this part is focused on making a systematical comparison for different control schemes under the background of the Benchmark control problem, in order to disclose what are the intrinsic differences for each control scheme and relative advantages as well as restrictions of each control scheme. However the present standard solution of AMD control proposed by Yang *et al.* (2004) has already been widely accepted from all over the world, which is based on a reduced order of structural model, some changes must be conducted to the existing control scheme first in order to achieve at the same level for comparison of different active control schemes.

5.2 Comparisons on analysis of AMD control

Yang *et al.* (2004) proposed the AMD control scheme, where the mass is 500 ton, which accounts for nearly 0.32% of the total structural weight. Besides, a standard program based on Matlab was also incorporated. Under the input of first 900 seconds of the wind load acquired by wind tunnel test (Samali *et al.*, 2004), the results of standard solution are given in table 2.

Items	Peak reduction (%)		RMS reduction (%)		Control cost	
	Displacement	Acceleration	Displacement	Acceleration	Control force (kN)	Mass stroke (cm)
Values	28.3	49	42.2	49.7	118	73.3

Table 2. Standard solution of AMD control for the wind-excited Benchmark problem

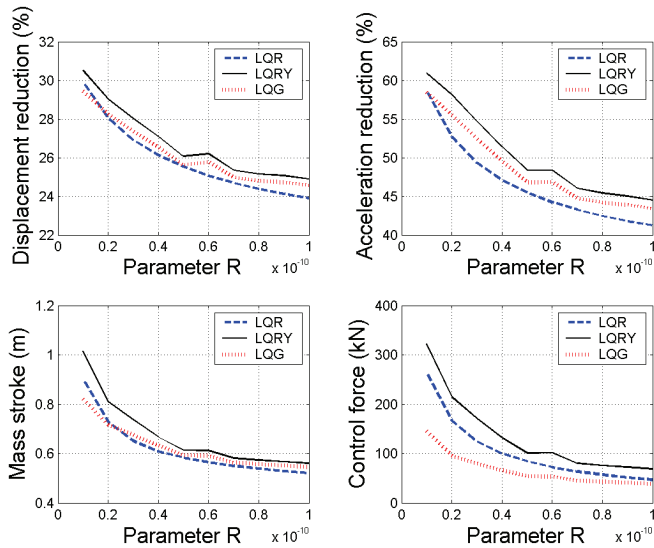


Fig. 41. Comparison of AMD control effect based on non-reduced model under three control algorithms

Here the control analysis was conducted on a reduced order structural model, however, in this part all the three control schemes should be compared on a same model, after a thorough comparison on the impact of order reduction on the Benchmark control problem, the non-reduced model, 76DOFs structure, is found to be the most appropriate (Zhang, 2005). In order to exclude the possible influence caused by control algorithms and their weight parameters, the proposed AMD control scheme deals with three independent control algorithms respectively, classical Linear Quadratic Regulator (LQR), output based optimal control (named as LQRY) and Linear Quadratic Gauss (LQG) control. Figure 41 shows the peak response of the top structural floor under the three algorithms, where all weight parameters in Q matrix of LQR are set to be unit, except parameters corresponding to the state of mass are set to be zero.

In addition, quantitative results of the proposed AMD control scheme are given in the following table, which are comparative with the standard Benchmark solution.

Items	Peak reduction (%)		RMS reduction (%)		Control cost	
	Displacement	Acceleration	Displacement	Acceleration	Control force (kN)	Mass stroke (cm)
Control results	24~30	42~58	36~44	47~60	50~270	55~90

(RMS: root mean square value.)

Table 3. Solution of AMD control based on non-reduced order structure

5.3 Structural interbedded active control

Structural interbedded active control (STI) is to add actuators into the adjacent structural inter-storeys, such as active brace systems (ABS) or active tendon systems (ATS), where active force is being directly exerted onto the structural floors or column-beam joints. However, for numerical analysis purpose, the control force and its counter force should be both considered at the same time from the equation of motion of the system. Furthermore, if every actuator takes the same value, then owing to the quits effect, the ultimate situation is equal to add two forces with opposite direction, one at the bottom and the other at the top, which equals to the effect of an active moment. On the other hand, AMD control system utilizes the mass as supporting point for the counter force, so it is absolutely different from STI control during calculation. Figure 42 shows the conception comparison between those two control schemes.

5.3.1 Comparison between STI control and AMD control

The optimization placement of actuators for STI control scheme is not the concerned question here, so we assume that the structure be controlled by placing actuators at each floor throughout the building. Zhang *et al.* (2005) have made a thorough comparison on control algorithms as well as impact of weight parameters, and here a representative case is chosen with its settings of control parameters based on LQR algorithm given in table 4, which is going to be used for comparison with AMD control scheme.

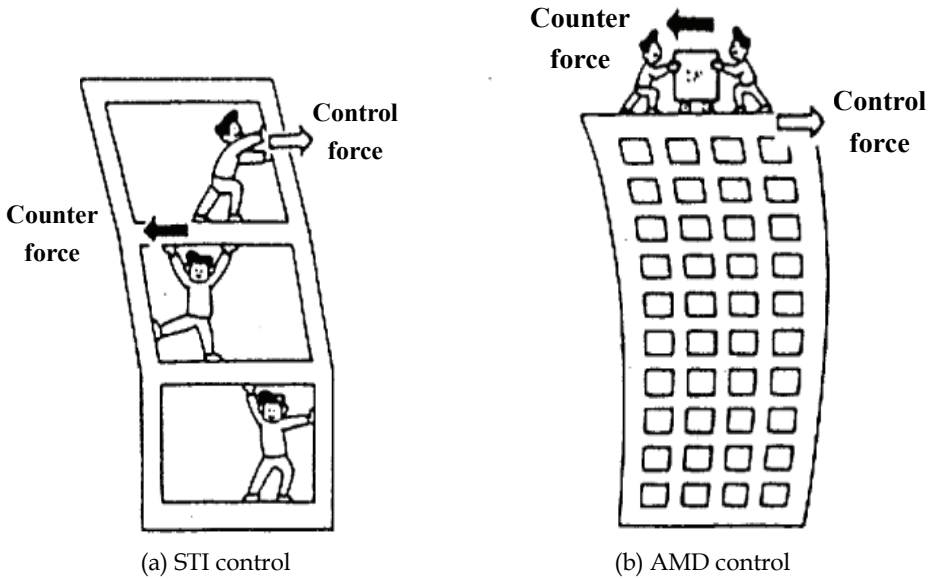


Fig. 42. Sketch of control force and counter force between active control system and structure

Parameter	AMD control	STI control
Q matrix	$\begin{bmatrix} [I]_{76 \times 76} & & & \\ & 0 & & \\ & & [I]_{76 \times 76} & \\ & & & 0 \end{bmatrix}$	$[I]_{152 \times 152}$
R matrix	$r = 1 \times 10^{-11}$	$1 \times 10^{-13} \times [I]_{76 \times 76} \times \sqrt{\Phi_1}$

(Note: Φ_1 is the first column vector of the structural flexibility matrix; $[I]_{n \times n}$ is a unit matrix with the dimension of $n \times n$.)

Table 4. Parameters of LQR control algorithm for AMD and STI control schemes

Under the above settings, the structural response is calculated to be controlled within the same range for the two control schemes as shown in figure 43.

Figure 44 shows the control forces corresponding to the above two schemes. First the left two figures show two time histories of control force for comparison, the upper is the STI control force at the 60th floor and the lower is the AMD control force. Besides, the right figure shows the peak and RMS control force of each floor of the STI control scheme, where the peak values falls between 400kN to 500kN, and the RMS values all exceed 100kN. Basically we can find that STI control is achieving the comparative control performance at the cost of tens times of the AMD control. The specific results for the two control schemes are: 1) For AMD control, the peak value is 265kN and the RMS value is 63.5kN; 2) For the STI control, it needs 76 actuators, and the peak forces range from 372kN to 527kN with the average is 438kN, besides, the average RMS force is 125kN. As a result, the STI control is

shown to be at the cost of 125~150 times of AMD control to get the similar performance, therefore the AMD control scheme is shown to be economical and advantageous for the Benchmark problem.

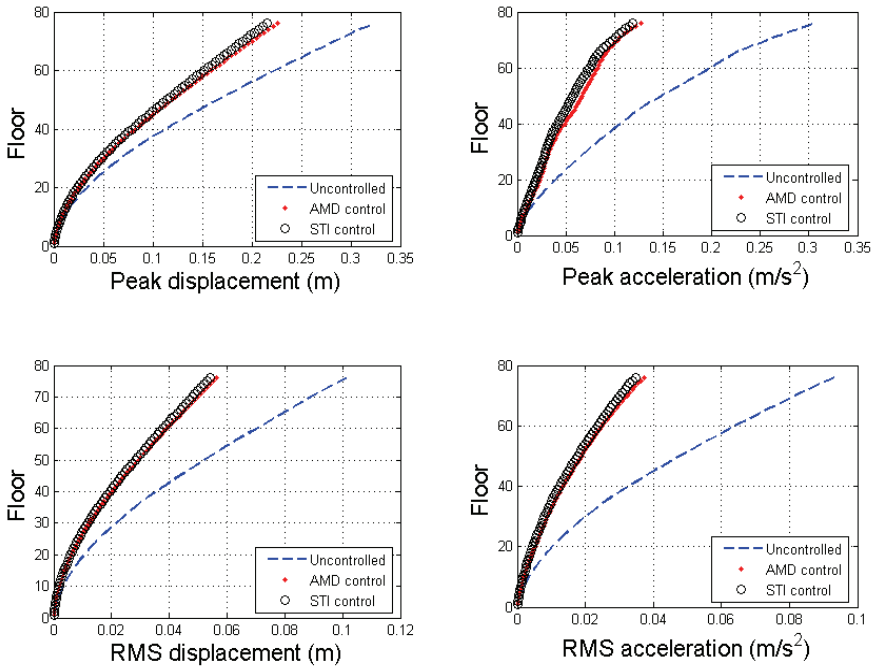


Fig. 43. Controlled response of the structure under AMD control and STI control

In addition, Ou (2003) has put forward another STI control scheme, where 20 actuators are employed and they were placed at every other 3 floors from the bottom floor to the top floor. If the control goal was chosen for 33.5% reduction in peak structural displacement and 46.8% reduction in acceleration, then the corresponding control forces of each actuator should be from 100kN to 1500kN. In the following table, the results of the above two STI control schemes as well as AMD control scheme are summarized.

Control results	Reduction of displacement (%)		Reduction of acceleration (%)		Actuator devices	
	Peak value	RMS value	Peak value	RMS value	Peak force (kN)	Quantity
AMD control	30.0	43.3	58.7	59.9	265	1
STI control (in this part)	33.2	46.5	61.3	62.7	372~527	76
STI control (Ou, 2003)	33.5	-	46.8	-	110~1500	20

Table 5. Comparison of AMD control scheme with STI control scheme

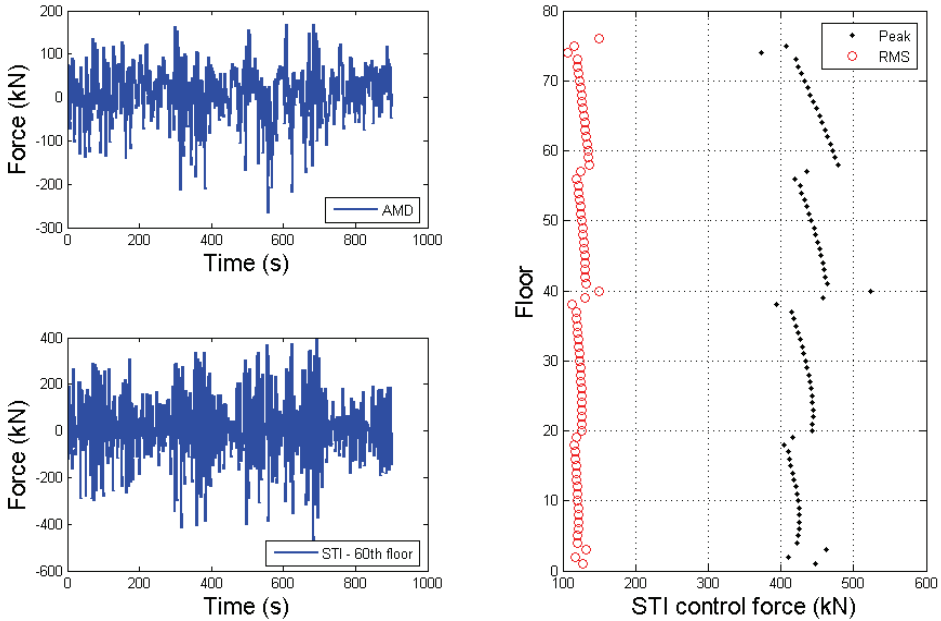


Fig. 44. Comparison of STI control force with AMD control force

From the results above, the AMD control is shown to be more superior and economical than STI control for the Benchmark building.

5.3.2 Characteristic of control force of STI control scheme

So far, the STI control is shown to be more consumptive than AMD control, for example the total control force is about 125 times of that of AMD control, while achieving at the comparative performance. The reason mainly comes from the quits effect between control force and counter force as shown in figure 42, therefore, it is not effective to place pure active actuators at inter-storeys for vibration control of the structure.

Then what are the advantages for STI control, the following sections will focus on the analysis of characteristic of active force, which will show that the active force is purely damping force and can be replaced by semi-active devices completely.

Ou (2003) put forward a set of indices denoting the relationship between control force and relative velocity of actuator. For supplementation, the following three sets of indices are defined as

Index of relationship between active force and relative velocity

$$u_i^*(t) = -\text{sgn}(\dot{x}_i u_i) |u_i(t)| \tag{26}$$

$$\gamma_{1,i} = \frac{\int_0^T H(-\dot{x}_i u_i) u_i^*(t) dt}{\int_0^T |u_i(t)| dt} \tag{27}$$

Where i is the number of floor on which the actuator is being installed, u_i is the control force of the corresponding actuator, \dot{x}_i is the interbedded velocity, T is the time duration, for example the total length of time for analysis; $\text{sgn}(\cdot)$ and $H(\cdot)$ are sign function and unit step function respectively.

$$\text{sgn}(x) = \begin{cases} 1 & x \geq 0 \\ -1 & x < 0 \end{cases}; H(x) = \begin{cases} 1 & x \geq 0 \\ 0 & x < 0 \end{cases} \quad (28)$$

Equation (26) defines a virtual time history of the active control force, where positive values of $u_i^*(t_j)$ stand for the force $u_i(t_j)$ being opposite to actuator velocity $\dot{x}_i(t_j)$ at time t_j , whereas, negative values stand for the force being in the same direction with velocity. Therefore, equation (27) defines the proportional factor of how much active force is being opposite to the relative velocity of actuator. Figure 45 shows the time history of virtual control force at 60th floor corresponding to equation (26).

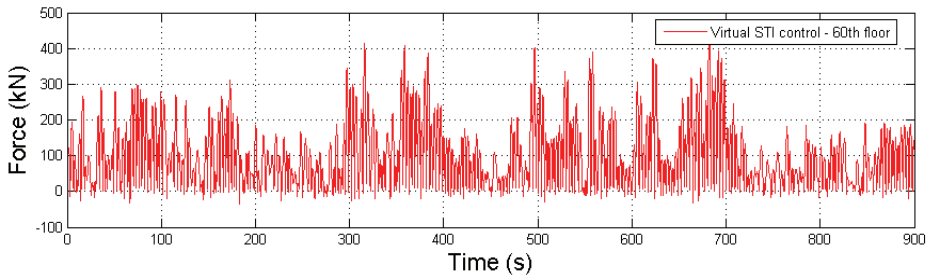


Fig. 45. Virtual time history of STI control force

It can be seen from figure 45 that a large amount of interbedded active control force is being in opposite direction with velocity. For comparison, figure 46 shows the time history of AMD control force after similar transformation, where the direction characteristic of force can't be easily seen. As a result, the two types of forces are different from each other for AMD control and STI control.

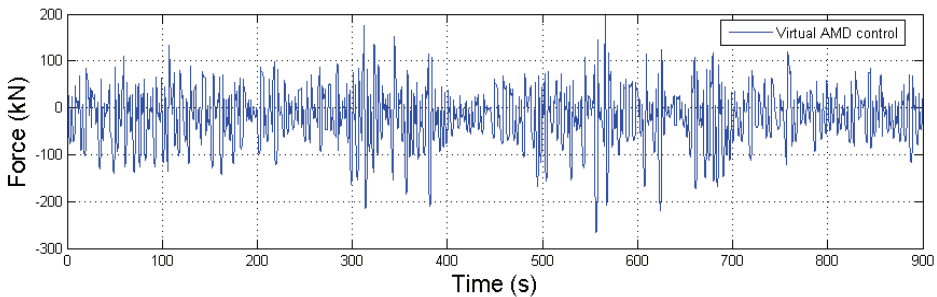


Fig. 46. Virtual time history of AMD control force

Index of relationship between active force with velocity and displacement

$$u_i^{**}(t) = -H(x_i \dot{x}_i) \text{sgn}(\dot{x}_i u_i) |u_i(t)| \quad (29)$$

$$\gamma_{2,i} = \frac{\int_0^T H(-\dot{x}_i u_i) u_i^{**}(t) dt}{\int_0^T |u_i(t)| dt} \tag{30}$$

Where x_i is the interbedded displacement of i th floor.

Here equation (29) defines a virtual time history of active control force, where positive values of $u_i^{**}(t_j)$ stand for the force $u_i(t_j)$ being opposite to its velocity $\dot{x}_i(t_j)$ during the actuator vibrating against its equilibrium position. Accordingly, equation (30) defines the proportional factor of how much active force is being opposite to its relative velocity during that period.

Index of vibration characteristic of actuator device

$$\gamma_{opp,i} = \frac{\int_0^T H(x_i \dot{x}_i) dt}{\int_0^T 1 dt} \tag{31}$$

Equation (31) defines the proportional factor of how much velocity is in the same direction with displacement for the structural floor during the vibration.

5.3.3 Analysis of direction characteristic of STI control force

In the following, quantitative results of the indices defined above will be given to show the directional characteristic of active forces in the STI control scheme. From figure 47, the first index of each floor is found to be $\gamma_{1,i} \geq 90\%$ for $i = 1, 2, \dots, 76$, which indicates that control force is being opposite to velocity at the possibility of more than 90%. Besides, the second index is $\gamma_{2,i} \cong 50\%$ for $i = 1, 2, \dots, 76$, which means the active force is opposite to its velocity at the possibility of 50% during it vibrates against the equilibrium position. At last, the third index is found to be $\gamma_{opp,i} \cong 0.5$, which means the vibration of each actuator is almost balanced, nearly 50% against the equilibrium position and 50% towards the equilibrium position. Figure 48 shows the results of decomposing active control force into damping force and stiffness force, where the damping component is shown to be dominant, and this conclusion tally well with the results of another STI control scheme (Ou, 2003), where 20 actuators were employed and the resulting changes are 0.06% in the first modal frequency and 2.17% in the corresponding damping ratio.

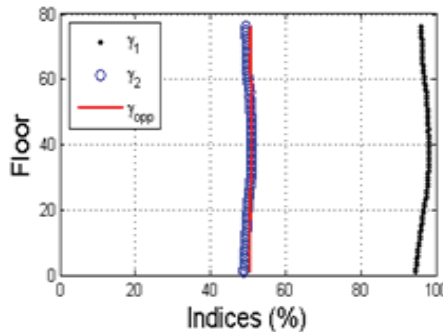


Fig. 47. Characteristic indices of active control force of STI control scheme

In the following, hysteresis loops of STI control force versus displacement and velocity are given in figure 49 and hysteresis loops of AMD control force are given in figure 50 for comparison. Here big difference can easily be seen between the two control schemes, where the STI control force is obviously some kind of damping force behavior.

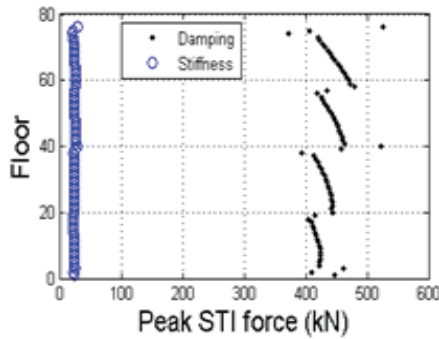


Fig. 48. Decomposing of active control force of STI control scheme

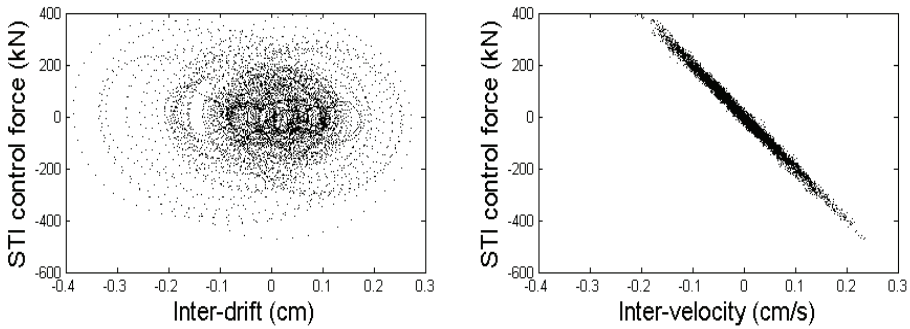


Fig. 49. Hysteresis loops of active control force of STI control scheme

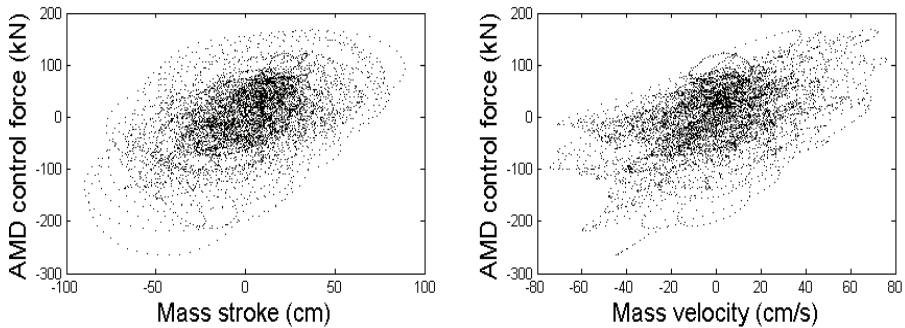


Fig. 50. Hysteresis loops of active control force of AMD control scheme

5.3.4 Energy characteristic of STI control force

In section 5.3.2, index γ_1 defines the direction characteristic of active control force, which stands for the ratio of area of virtual force defined in equation (26), which is the area of positive values divided by total areas. However, it is merely a measurement from the aspect of force magnitude, which does not take the effect of corresponding velocity into consideration. Noticing that there is such a relation exists between energy and force as $W = F \times v$, thus to improve equation (27), the proportional factor describing energy characteristic of control force can be defined as

$$\gamma_{Eopp} = \frac{\int_0^T \text{H}[-\dot{x}_i(t) \cdot u_i(t)] \cdot |\dot{x}_i(t) \cdot u_i(t)| dt}{\int_0^T |\dot{x}_i(t) \cdot u_i(t)| dt} = \frac{E_{opposite}}{E_{total}} \quad (32)$$

Where $E_{opposite}$ stands for the energy of active control when the force is opposite to its velocity, and E_{total} stands for the total energy consumed by active control.

Figure 51 shows the energy indices distributed all through the entire structure of STI control scheme, where the maximum value of γ_{Eopp} is found to be 99.9977% and the minimum is 99.9492%, besides, the average value is 99.987%. Therefore, the result shows that nearly 100% control energy is distributed during the vibration course of force being opposite to velocity, which indicates that the force be damping control behavior.

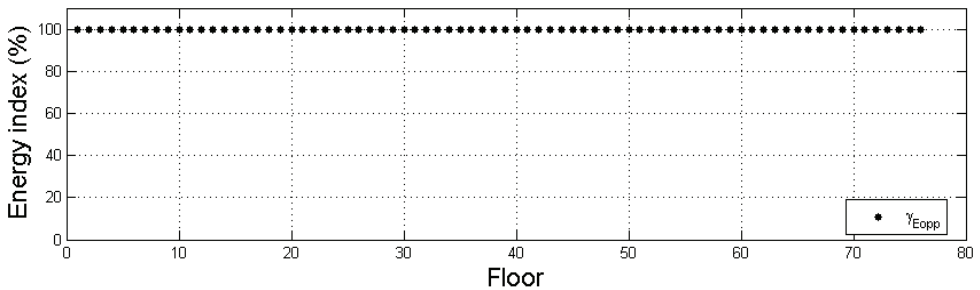


Fig. 51. Energy indexes of STI control force

So far, the active force of STI control scheme is proven to be intrinsically damping force, thus, it is feasible to replace active actuators in this scheme by semi-active or even passive devices to achieve comparative pure active control performance. On the other hand, the force of AMD control doesn't possess the damping behavior, thus it can't be replaced by any semi-active device.

5.4 Structural adjacent wall active control

The reason of wasteful control cost of STI control scheme is owing to the existing of quits effect between control force and counter force for the adjacent structural floors. How to eliminate the disadvantageous is challenging. However, for the purpose of simulation, imagining a stiffen wall is placed beside the structure to be controlled, on which counter force of each actuator will be exerted, where the quits effect can be successfully excluded and we call such a scheme as structural adjacent wall (abbreviated as STA) active control.

Figure 52 shows the conception sketch of STA control. Although similar in name to adjacent-structures or coupled-structures control (Ying, 2004), they are absolutely different from the nature. In addition, STA control can be used to study the difference between AMD control and STI control from the aspect of function of actuators.

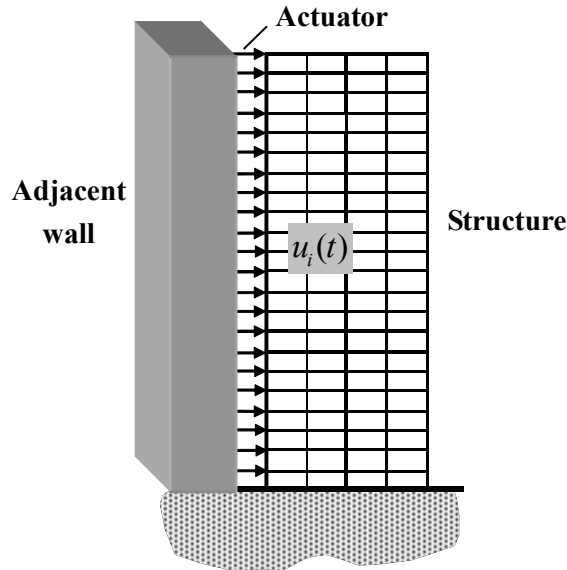


Fig. 52. Sketch of structural vibration control using STA control scheme

5.4.1 Comparison between STA control and AMD control

Similar approaches used in the above analysis of STI control will be introduced here to make a comparison between STA control and AMD control. Besides, for the purpose of analytical comparison, three control algorithms LQR, LQRY and LQG are all used again in order to exclude the possible differences caused by control algorithms and their parameters. In the following, table 6 gives the weight parameters of each control algorithm.

Control algorithms	LQR	LQRY, LQG
Q matrix	$[I]_{152 \times 152}$	$[I]_{228 \times 228}$
R matrix	$3 \times 10^{-10} \times [I]_{76 \times 76} \times \Phi_1$	

Table 6. Weight parameters of STA control scheme

According to the above settings, peak and RMS response of structural displacement and acceleration are shown in figure 53, where the control object is set to achieve comparative performance with AMD control.

Figure 54 shows the control force of each actuator corresponding to the above three control algorithms in STA scheme, where LQR control is shown to be the lowest in requirement of control force.

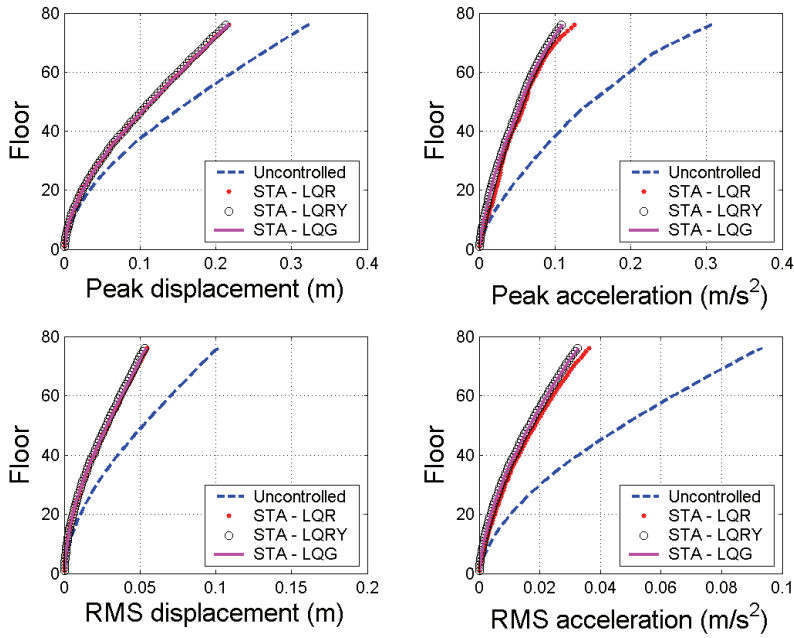


Fig. 53. Peak and RMS response of structure under STA control

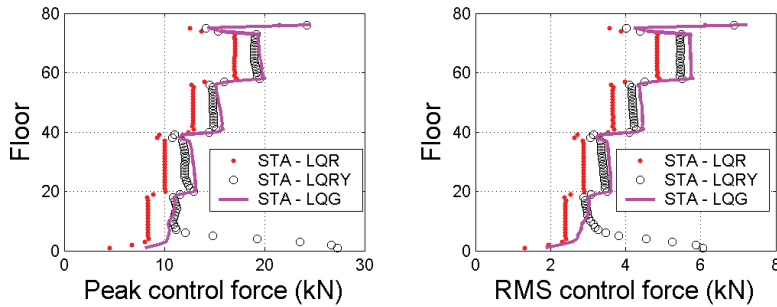


Fig. 54. Comparison of active force under three algorithms of STA control

Control scheme	Sum of control force(kN)		Reduction in displacement (%)		Reduction in acceleration (%)	
	Peak values	RMS values	Peak values	RMS values	Peak values	RMS values
AMD control	265	63.5	30.0	43.3	58.7	59.9
STI control	33288 (range: 527~372)	9500	33.2	46.5	61.3	62.7
STA control	905.7 (range: 4.6~21.5)	258.4	32.7	45.9	59.1	64.2

Table 7. Control forces and structural response results of three control schemes

So far, the results of structural response under three control schemes are studied respectively, and they were summarized in table 7. From the results, AMD control is shown to be the highest efficiency from the aspect of control effect over control effort, and STA control is inferior, whereas STI control is the lowest in control efficiency.

5.4.2 Analysis of characteristic of STA control force

Similar to indices defined in section 5.3.2, here the corresponding indices should be modified according to the changes of the coordinator system. Equation (27), (30) and (31) should be rewritten as

$$\begin{aligned}\gamma_{1,i}^s &= \frac{\int_0^T H(-u_i \dot{y}_i) \operatorname{sgn}(-u_i \dot{y}_i) |u_i(t)| dt}{\int_0^T |u_i(t)| dt} \\ &= \frac{\int_0^T H(-u_i \dot{y}_i) |u_i(t)| dt}{\int_0^T |u_i(t)| dt}\end{aligned}\quad (33)$$

$$\begin{aligned}\gamma_{2,i}^s &= \frac{\int_0^T H(-u_i \dot{y}_i) H(y_i \dot{y}_i) \operatorname{sgn}(-u_i \dot{y}_i) |u_i(t)| dt}{\int_0^T |u_i(t)| dt} \\ &= \frac{\int_0^T H(-u_i \dot{y}_i) H(y_i \dot{y}_i) |u_i(t)| dt}{\int_0^T |u_i(t)| dt}\end{aligned}\quad (34)$$

$$\gamma_{opp,i}^s = \frac{\int_0^T H(y_i \dot{y}_i) dt}{\int_0^T 1 dt}\quad (35)$$

Where y_i and \dot{y}_i are displacement and velocity of the i th floor relative to the ground, and the other symbols take the meanings as defined before.

In addition, the energy index of equation (32) can be rewritten as

$$\gamma_{Eopp}^s = \frac{\int_0^T H[-\dot{y}_i(t) \cdot u_i(t)] \cdot |\dot{y}_i(t) \cdot u_i(t)| dt}{\int_0^T |\dot{y}_i(t) \cdot u_i(t)| dt}\quad (36)$$

Figure 55 shows the indices corresponding to equation (33) ~ equation (36), where the control force is found to be almost opposite to velocity from the results of γ_1^s , especially from energy index γ_{Eopp}^s , and results of the other two indices are similar as before. Besides, figure 56 shows the results of decomposing active control force into damping force and stiffness force, where the damping component is shown to be dominant again. Figure 57 shows the hysteresis loops between control force and displacement as well as velocity for STA control. From the results, the force is obviously shown to be some kind of damping force behavior.

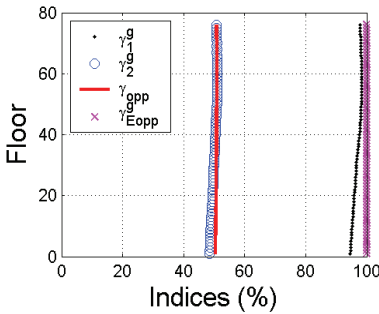


Fig. 55. characteristic indexes of control force of STA control scheme

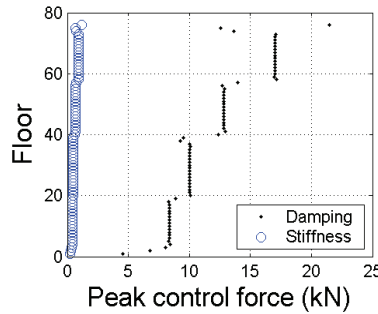


Fig. 56. decomposing of control force of STA control scheme

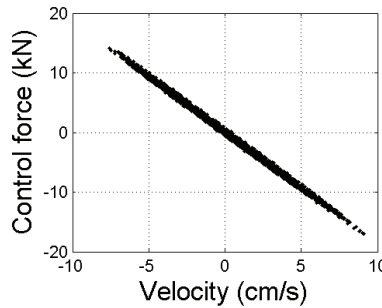
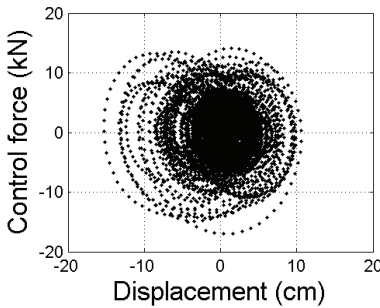


Fig. 57. Hysteresis loop of control force of STA control scheme

5.5 Discussions on similarity between AMD control and STA control

In the above two sections, three control schemes were compared from control effect to control cost, and the results show that AMD control is the best one compared with the other two schemes. Besides, STA control is shown to be rather better than SII control, and there must be some kind of relationship between AMD control and STA control. In the following, the numerical comparison between AMD control and STA control will be conducted to investigate their similarities as well as differences.

As shown in figure 53 and figure 54, three control algorithms of STA scheme are achieving almost at the same control results while at different cost, especially very large control forces are needed for the lower floors of structure in LQRY and LQG control case. This result indicate that forces at lower floors are ineffective for suppressing structural vibration, therefore, it would be better to place limited control devices onto higher floors as much as possible, and with the increase of height the control effectiveness will be enhanced. To the extreme situation, all actuators are concentrated onto the top floor, then the STA control is equal to AMD control, where both of the two control schemes use additional mass or wall other than the structure itself to provide supporting point for the counter force.

In the following, two special control cases, one is STA control with only one actuator at the top floor and the other is pure AMD control without damper and spring, are designed to

investigate the similarity between them. For the purpose of analytical comparison, the LQR control algorithm is being chosen, and the corresponding weight parameters are listed in the following table.

LQR algorithm	AMD control	STA control
Q matrix	$\begin{bmatrix} [I]_{76 \times 76} & & & \\ & 0 & & \\ & & [I]_{76 \times 76} & \\ & & & 0 \end{bmatrix}$	$[I]_{152 \times 152}$
R matrix	$r = 1 \times 10^{-11}$	

Table 8. Parameters of LQR control algorithm for AMD control and STA control

Figure 58 shows the comparison of AMD force versus STA force, where two forces are exactly the same, which indicates that under the above settings the two schemes have achieved at the same result as exerting control force onto the structure.

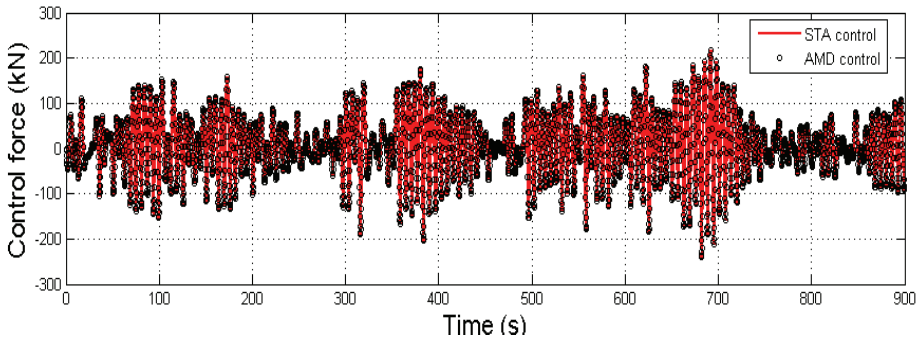


Fig. 58. Comparison of time history of control forces between AMD control and STA control

Except for the same control force, there are some other differences as well as similarity exist between the two control schemes. For AMD control, the force is generated by the actuator and the counter force is absorbed by mass, which oscillates on the top floor of the structure; Whereas for STA control, the stiffen wall is assumed to be infinity in stiffness, therefore stroke of the actuator is equal to the relative displacement of the top floor of the structure. Supposing that the mass of AMD increases to a certain amount until the mass stroke equals to that of STA actuator, then AMD control will be completely equivalent with STA control. This means we don't necessarily need a real "stiffen" wall, in fact a relative large mass will do, as well as no need for an adjacent wall, and a moving mass will do.

In order to validate the above assumption, the following analysis of mass ratio impact on characteristic of control force will be conducted. Here the variation range of mass ratio is chosen to be from 0.1% to 10%, which covers the range of interest.

As shown in figure 59, AMD-1 stands for the AMD control system with damper and spring element, and AMD-2 stands for the system without damper and spring, namely pure actuator based AMD control system. Besides, for comparison, the energy index of control force in STA scheme corresponding to equation (36) is also shown in figure 59 denoted with circle markers, and the exact value is 99.9993%.

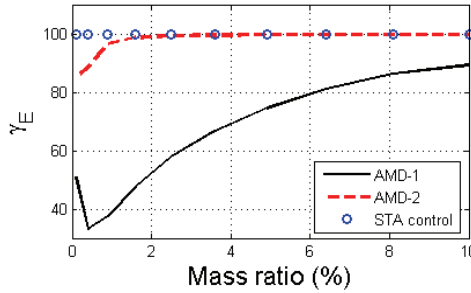


Fig. 59. Energy indexes of control force between AMD control and STA control

From the results, when mass ratio increases to 2% and thereafter, energy index of active force of AMD-2 system will be the same as STA control, which indicate that not only the envelope of force, as shown in figure 58, but also the intrinsic behavior is the same for AMD control and STA control. So far, AMD control is shown to be consistent with STA control under certain conditions, and we can come to the extension conclusions: 1) The effect of mass in the AMD system is equal to the wall in STA control scheme, which provides support point for the counter force; 2) AMD control is the simplest realization of STA control with smaller attached mass needed, and it is rather easier to be implemented than setting up an adjacent wall.

On the other hand, for AMD-1 system, the active force is affected by spring and damper element, thus the characteristic indices shown in figure 59 change differently with respect to mass ratio. Moreover, the effect of damper and spring on control performance is shown in figure 60

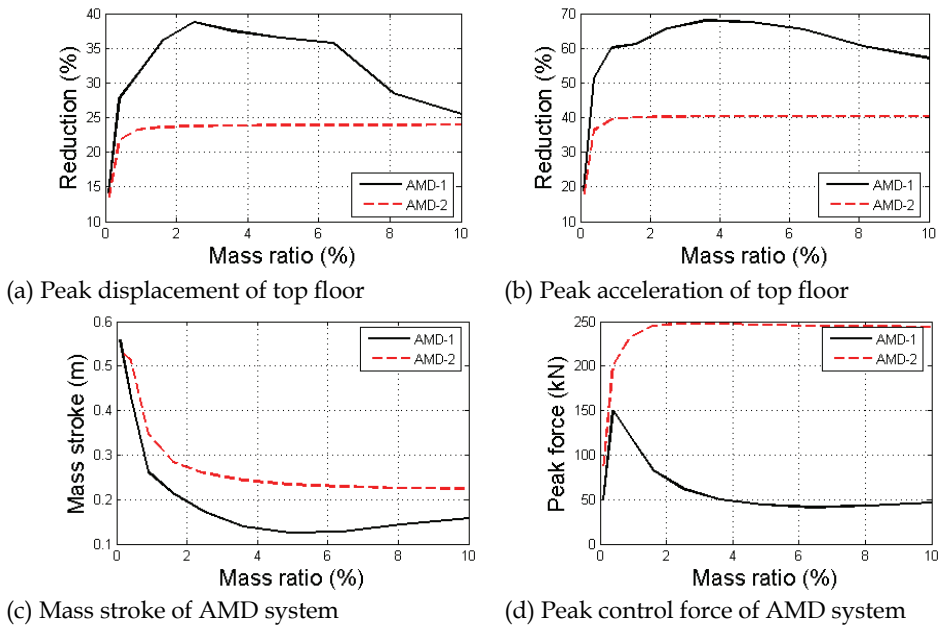


Fig. 60. Influence of mass ratio for AMD control scheme

From figure 60, the effect of mass in AMD-2 system is well demonstrated again, after the mass ratio increases to 2% as explained above, AMD control is equal to STA control, which will have no influence on control performance with increasing in mass weight. By comparison, owing to the interaction effect among actuator, damper and spring element, the ultimate control result of AMD-1 system is better than that of pure AMD system, besides the control cost, such as mass stroke and control force, is also reduced, which indicates that the complete construction of AMD control is better than STA control.

5.6 Summary on intrinsic mechanism of AMD control

In this section, three active control schemes, AMD control, STI control and STA control, have been studied under the background of wind-induced vibration control problem of the Benchmark 76-storey building structure, and main conclusions are achieved as follows:

1. Through comparison of control effect over control effort of the three control schemes, AMD control, with comparative control performance meanwhile at the minimum control cost, is shown to be most superior and economical. On the other hand, STA control is inferior and STI control is the worst one.
2. Indices denoting the direction and energy relationship between active force with velocity and displacement are developed to study the intrinsic behavior of control force in each control scheme. Through numerical analysis, quantitative results show that active force of STI control and STA control are damping force essentially, therefore it is feasible to replace active actuators in those schemes by semi-active or even passive control systems to achieve comparative performance of pure active control. However, the behavior of AMD control force is absolutely different, thus the actuator can't be replaced by any semi-active device.
3. Through similarity study between AMD control and STA control, the results well disclose the effect of mass piece in AMD system, which is similar to the wall in STA control scheme as providing supporting point for working of actuator, thus AMD control can be viewed as the simplest realization of STA control. Besides, the effect of mass as well as spring and damper in AMD control system is studied from a new aspect, and all the results show that AMD control is the most effective scheme for suppressing wind-induced vibration of the Benchmark building.

6. Application of AMD Control system

Based on the vibration analysis of the Guangzhou New TV Tower structure, the scheme of hybrid mass driver & variable damper (HMVD) is advanced to modify the common control systems. To choose the nodes at which the accelerations are measured to be used in Kalman estimator, the approach is proposed and adopted via the principle of modal superposition. Then the performance of the control system under T-year return periods is analyzed. And the control effectiveness is analyzed considering the variation of the damper-structure frequency tuning ratio.

6.1 Analytical model of the tower structure

The tower, as shown in figure 61, locates at the intersection of Guangzhou city new mid-axis and south bank of Zhujiang River, where is to be the central district of the city. The tower is designed for broadcasting, sightseeing, exhibiting purpose, etc. It will become the landmark

of Guangzhou City. Thus, it is obviously very important. The tower is 610m high, composed of a 454m high main tower and a 156m high antenna. The building is very slender, with the first natural period of 10.02 seconds. It is so slender and very sensitive to wind excitations. Therefore, studying the vibration control of the tower is remarkably significant.

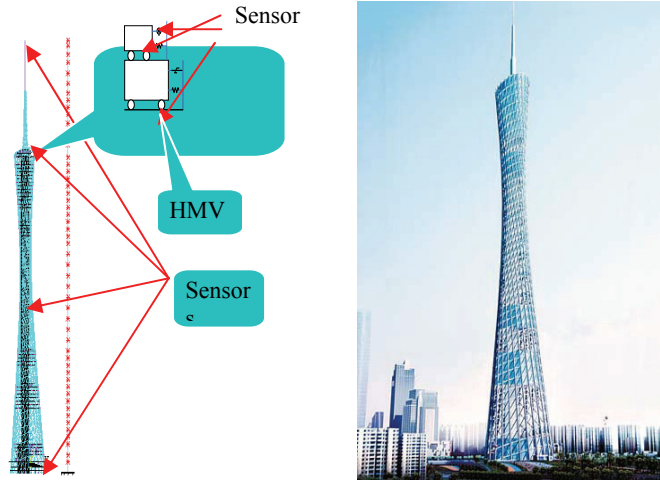


Fig. 61. Guangzhou New TV Tower structure

The wind reference pressure at the structure location is 0.55 KN/m^2 assuming a 100-year return period. The sort of the terrain roughness is C.

The main tower is a shear-flexural structure, composed of inner RC core tower and the steel frame outside, where the steel frame is composed of inclining columns of concrete filled steel tube, steel ring beams, and steel braces. To simplify the analytical model, the tower is discretized with a simple 106-degree-of-freedom lump mass model considering 53 concentrated mass nodes with two orthogonal lateral displacement DOF. The physical parameters, mass matrix M_s and stiffness matrix K_s , are obtained based on the FEM model using SAP2000. According to the Structural Preliminary Design Report, the damping ratios of its first two modes are 1.5%, respectively. And the Rayleigh damping matrix C_s is contributed. The dynamic properties of the 106 DOF model and the FEM model are compared and summarized in table 9.

Table 9 indicates that the 106 DOF model has almost the same dynamic characteristic with the FEM model. So it is appropriate for further analysis using the 106 DOF model.

Both time domain approaches and frequency domain approaches can be adopted to analyze the response and vibration control of the tower under wind excitation. The statistical characteristics of the response can be obtained through frequency domain approach. However, the necessary constraints, such as the peak value of the damper stroke and the control force, can not be explicitly considered in frequency domain method. Thus in this part, the linear elastic dynamic time-history analysis of the structure under random wind excitation is conducted.

Based on the Davenport spectrum, gust wind load time-histories are sampled. And three representative time histories are chosen for further analysis. Table 10 listed some responses at the top of the uncontrolled tower under these three wind samples.

Order of the modes	Natural period (s)			Descriptions of mode shapes	
	FEM model In SAP2000	106 DOF model	Relative error		
1	10.0135	9.9661	0.47 %	Global translational motion shape of 1 st order	Along weak axis
2	6.9324	6.8978	0.51 %		Along strong axis
3	2.9074	2.8950	0.43 %	Coupled mode Hape of main tower's 2 nd order and antenna's 1 st order	Along weak axis
4	2.4611	2.4626	0.06 %		Along strong axis

Table 9. Dynamic characters of the MDOF model and the FEM model

Analytical model	Load case	Displacement(m)		Acceleration(m/s ²)	
		MAX	RMS	MAX	RMS
106 DOFmodel	Case1	0.890	0.3250	0.4182	0.1348
	Case2	0.900	0.3020	0.4316	0.1326
	Cas 3	0.876	0.3272	0.4024	0.1378

Table 10. Response at the top of the uncontrolled main tower under 100-year return period wind cases

6.2 Analysis and design of the control system

Previous studies have shown the advantages and the disadvantages of common control systems, such as viscous damper, tuned mass damper (TMD), active mass driver/damper (AMD), and hybrid mass damper (HMD). The conclusion is none of them could be used in this project directly. Further research proposed the scheme of hybrid mass driver & variable damper, which is abbreviated as HMVD. Figure 62 shows the main idea of the HMVD system to be introduced into this project. To avoid additional load and cost, the two 600-ton water tanks are taken as the mass in the passive part. It is proven effective and economical. Each tank is supported by three bilateral track supports along the two orthogonal axes. The steel-plate-laminated-rubber-bearing isolator is introduced to provide stiffness for the control system. Linear motor is introduced to drive the active subsystem, considering the requirement of the long stroke and the limitation of the installation space.

Computation results show that the stroke of the water tank along the strong axis of the tower can not exceed the limitation. So the control system is briefly designed as a TMD system along the strong axis.

6.2.1 Control analysis

The equation of motion of the 106 DOF model controlled with the HMVD is expressed by Eq. (37).

$$M_h \ddot{x} + C_h(t) \dot{x} + K_h x = F_w(t) + u_a(t) \quad (37)$$

Where, $x = [x_1, \dots, x_n, y_1, \dots, y_n, x_t, y_t, x_a]^T$; M_h , C_h and K_h are the mass matrix, damping matrix and the stiffness matrix of the tower-HMVD system respectively; $F_w(t)$ denotes the

wind load time-history; $u_a(t)$ denotes the driving force of the linear motor in the AMD subsystem.

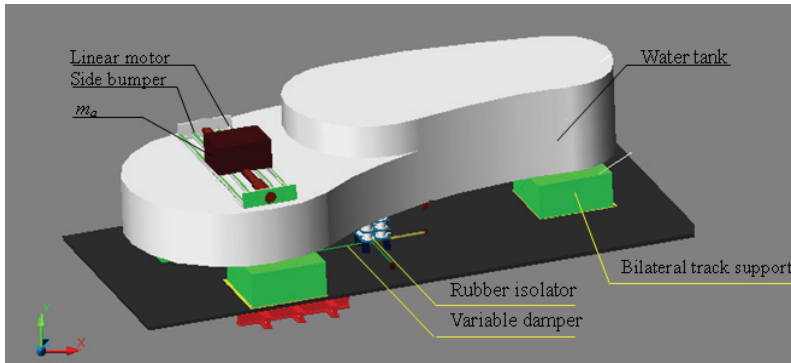


Fig. 62. Sketch of the HMVD system used in Guangzhou New TV Tower

The additional damping force provided by the additional damping Δc is considered as an external input force $F_{\Delta c}(t)$. Then the damping coefficient matrix C_h is invariable. And the equation of motion becomes:

$$M_h \ddot{x} + C_h \dot{x} + K_h x = F_w(t) + u_a(t) + F_{\Delta c}(t) \tag{38}$$

Where, $F_{\Delta c}(t) = \Delta c \times \Delta v(t)$, Δc is the additional damping coefficient, $\Delta v(t)$ denotes the relative velocity between the water tank and the floor on which the control system is installed.

The displacements, velocities, accelerations can be obtained via solving the Eq.(38).

6.2.2 Variable damper

There are two ways to design the damping coefficient for the traditional tuned mass damper control system. The first one is to set the damping ratio to the optimal case. With optimal damping, the control system can reduce the response of the tower under the regular wind load. But the stroke of the water tank will exceed the installation constraint under strong winds. Table 11 shows the stroke of the water tank with optimal damping under T -year return period wind loads.

Return period (year)	3	5	10	20	30	50	80	100	200	
W_0 (KN/m ²)	0.14	0.19	0.26	0.34	0.38	0.45	0.52	0.55	0.66	
stroke (m)	Case 1	0.42	0.56	0.77	0.99	1.14	1.34	1.54	1.62	1.96
	Case 2	0.35	0.47	0.65	0.84	0.96	1.12	1.29	1.37	1.64
	Case 3	0.57	0.77	1.06	1.37	1.57	1.83	2.12	2.23	2.69

Table 11. Stroke of control system with optimal damping

The stroke of the water tank is limited to 1.2m by the installation space. However, as safety is considered, the stroke should not exceed 0.8m under 100-year return period wind excitations.

Another way to design the damping coefficient is to insure that the stroke of the water tanks will not exceed 0.8m under 100-year return period wind load. The damping coefficient designed in this way will be a big one, and will lead to much loss of effectiveness of the control system.

6.2.3 Role of the variable damper

After thorough analysis, a variable damper is introduced to reduce the stroke of the water tanks without much loss of the effectiveness under strong wind excitation. Considering the feasibility and reliability, the adopted variable damper scheme can be described as followings:

When the stroke is less than ±0.5m (phase A shown in figure 63), the damper is set to be the optimal damping coefficient c_{opt} ;

When the stroke is greater than ±0.5m, and the water tank is moving away from the equilibrium point (phase B shown in figure 63), the damper is set to be a much higher damping coefficient $c' = c_{opt} + \Delta c$, where Δc is the additional damping coefficient;

When the stroke is greater than ±0.5m, and the water tank is moving back to the equilibrium point (phase C shown in figure 63), the damper is set to be the optimal damping coefficient c_{opt} again.

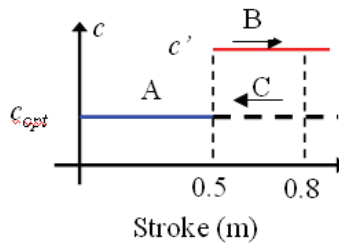


Fig. 63. Rule of the variable damper

6.2.4 Optimal damping coefficient

The optimal damping ratio of the control system is $\xi_{opt} = 0.08$. As the AMD system is fixed to the water tank except during few strong winds, the mass of the system should be considered as: $m_{ht} = m_t + m_a = 1200 + 100 = 1300$ t. So the optimal damping coefficient is:

$$c_{opt} = 2m_{ht}\omega_1\xi_{opt} = 2 \times 1300 \times 0.6305 \times 0.08 = 131.14 \text{KN} \cdot \text{s} \cdot \text{m}^{-1}$$

6.2.5 Additional damping coefficient Δc

Figure 64 shows the relationship between the additional damping coefficient Δc and the maximum stroke of the water tank under 100-year return period wind load. The maximum stroke reduces as the additional damping coefficient Δc increases. To limit the stroke of the water tank to 0.8m under 100-year return period, the additional damping coefficient Δc should be no less than 1800 $\text{KN} \cdot \text{s} \cdot \text{m}^{-1}$. So the bigger damping coefficient in figure 63 taken as: $c' = c_{opt} + \Delta c = 131 + 1800 = 1931 \text{KN} \cdot \text{s} \cdot \text{m}^{-1}$. The following analysis is based on these parameters.

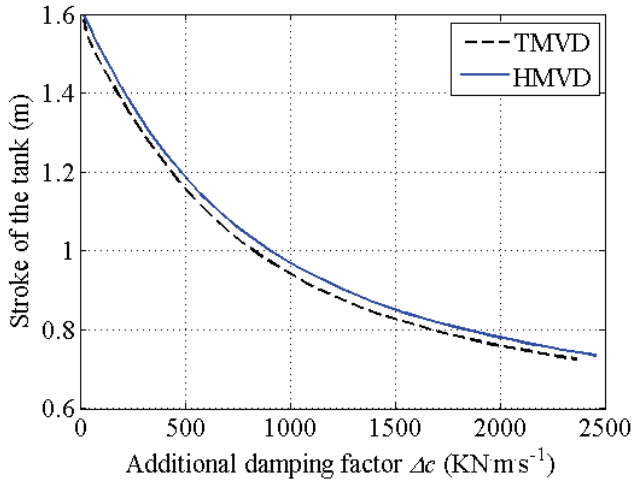
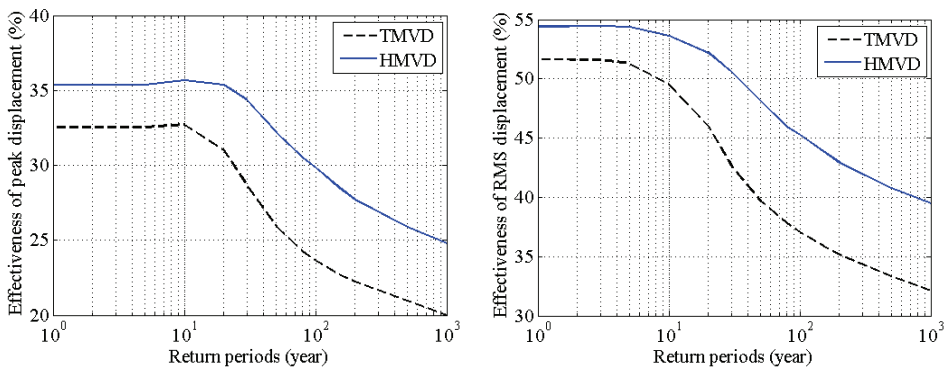


Fig. 64. Relationship between the maximum stroke and the additional damping ratio

6.3 Effectiveness of the control system

For uncontrolled case, TMVD control case and HMVD control case, the response at the top of the main tower is computed under T - year return periods wind loads. The control effectiveness of the displacement response and the acceleration response, besides the parameters of the TMVD system and the HMVD system are given in figure 65.



(a) Control effectiveness of peak displacement (b) Control effectiveness of RMS displacement

Fig. 65. Comparison on performance of passive and hybrid control system

Figure 65 shows that, the effectiveness is highest when the frequency tuning ratio is about 0.9 under 100-year return period. When the frequency tuning ratio varies, the effectiveness of the HMVD system varies on an even level, while the effectiveness of the TMVD system decrease drastically. That means the HMVD system is rather insensitive to the variation of the damper-structure frequency tuning ratio.

Based on the former comparison analysis of vibration control schemes for Guangzhou New TV Tower structure, the hybrid mass driver & variable damper (HMVD) control scheme is proposed and numerically studied in this section. Main conclusions can be achieved as: 1) The strategies to choose the measuring nodes for MDOF system is proposed based on the principle of modal superposition. According to this approach, the characteristic nodes of the main modes of the system are chosen, where the corresponding accelerations are measured to estimate the full states of the system. 2) The driving force of the AMD subsystem is calculated based on the LQG algorithm with Kalman estimator. 3) By introducing the variable damper, the optimal effectiveness of the control system is about 35%~50% with acceptable stroke under regular wind load. Under extreme strong winds (with bigger return period), the control system works in the active-passive hybrid mode. In this case, the stroke of the control system can be limited within the installation constraint range, keeping the remarkable effectiveness of 30%~45%. Thus the HMVD system is shown to be adaptive to the winds with different intensities. 4) The water tanks of the super-tall buildings are usually used as the mass of the tuning control system. While the mass of water may vary from time to time, leading to the variation of the optimal frequency tuning ratio of the damper and the decreased effectiveness of the control system. Further analysis indicates that the HMVD system is more robust to the damper-structure frequency tuning ratio. And this feature is especially beneficial for achieving better effectiveness of the HMVD control system.

7. Chapter summary

This chapter introduces some recent research works carried out in the Blast Resistance and Protective Engineering laboratory of Harbin Institute of Technology (HIT-BRPE) during the past few years. The EMD control system is shown to be effective and feasible for vibration control of civil engineering structures subjected to, such as earthquake, excitations. The DDVC based AMD control system is suitable for low frequency vibration and motion control. The innovative passive TRID system is applicable for rotation and swing motion control, whereas linear TMD system is shown to be invalid for structural swinging motion. All of the control systems mentioned in this chapter, whatever active or passive or hybrid, have a common characteristic, which is to utilize the mass inertia effect either to provide counter force support for functioning of actuator, *e.g.* AMD subsystem, or to provide gyros or rotary inertia for anti swinging motion of suspended structure. Traditionally, these systems have been called Active Mass Damper/Driver (AMD) or Tuned Mass Damper (TMD), herein we want to emphasize the mass inertia effect and its functions. The basic is to be a necessary component of a control system, and more important is its way of working in the subsystem.

8. Acknowledgements

These researches are supported by the National Natural Science Foundation of China under grant No. 50608026 and 90815027, and the National Key Technology R&D Program under grant No. 2006BAJ03B06, and the National Major Fundamental Program under grant No. 2007CB714204. Associate Professor Li Jilong, Dr. Li Luyu, Dr. Liu Junlong, Mr. Xu Huaibing, Mr. Wu Zhiwu, Mr. Liu Chuan during their postgraduate studies in the Blast Resistance and Protective Engineering laboratory of Harbin Institute of Technology (HIT-BRPE Lab.), are acknowledged for their efforts in carrying out relevant experiments and analysis. Besides, the authors would like to give their sincere thanks to colleagues from Guangzhou

University and HIT-Shenzhen Graduate School for their effort and cooperation in application of control systems in the Guangzhou New TV tower project.

9. References

- [1] Abdel-Rohman M. and Leipholz H.H.E. Structural Control by Pole Assignment Method. *ASCE Journal of Engineering Mechanics*, 1978, 104: 1157~1175.
- [2] Battaini M., Yang G. and Spencer B. F. Jr. Bench-Scale Experiment for Structural Control. *ASCE Journal of Engineering Mechanics*. 2000, 126(2): 140~148.
- [3] Brock J E. A Note on the Damped Vibration Absorbers. *Journal of Applied Mechanics*. 1946,13(4), A-284.
- [4] Chu S.Y., Soong T.T., Reinhorn A.M. Real-time active control verification via a structural simulator. *Engineering Structures*, 2002, 24(3), 343~353.
- [5] Den Hartog J.P. *Mechanical Vibrations*, 4th Ed, McGraw-Hill, 1956.
- [6] Dyke S. J., Spencer B. F., Belknap A. E., Ferrell K. J., Quast P., and Sain M. K. Absolute Acceleration Feedback Control Strategies for the Active Mass Driver. Proc. First World Conference on Structural Control, Pasadena, California. 1994, 2, TP1: 51~TP1: 60.
- [7] Dyke S. J., Spencer B.F.Jr., Quast P., Kaspari D.C. Jr. and Sain M. K. Implementation of an Active Mass Driver Using Acceleration Feedback Control, *Microcomputers in Civil Engineering: Special Issue on Active and Hybrid Structural Control*. 1996, 11, 305~323.
- [8] Haertling G. H. Rainbow Actuators and Sensors: A New Smart Technology. *Proceedings of SPIE*. 1997, 3040, 81~92.
- [9] Haertling G. H. Rainbows-a New Type of Ultra-High Displacement Actuators. *Am. Ceram. Soc. Bull.* 1994, 73~96.
- [10] Housner G. W., Bergman L. A., Caughey T. K., Chassiakos A. G., Claus R. O., Masri S. F., Skelton R. E., Soong T. T., Spencer B. F. and Yao J. T. P.. *Structural Control: Past, Present, and Future*. *J Engng Mech*, ASCE. 1997, 123(9): 897~971.
- [11] Kuo B. C. *Automatic Control Systems*. 7th Edition, Prentice-Hall, 1995.
- [12] Lee D. J. Use of Accelerometer in Precision Motion Control Systems Design and Its Applications to Linear Motors. Ph.D Dissertation of California at Berkeley. (Supervised by Prof. M. Tomizuka), 2002.
- [13] Liu Junlong, Zhang Chunwei, Ou Jinping. Modeling and numerical analysis on direct driving active mass driver control system for structural vibrations, *Journal of Vibration Engineering*, v 21, n 4, p 323-328, August 2008 Language: Chinese.
- [14] Mita A., Kaneko M. Hybrid versus tuned or active mass dampers for response control of tall buildings. The 1st international conference on motion and vibration control, Yokohama, Japan, 304-309, 1992.
- [15] Nerves A.C., Krishnan R. A strategy for active control of tall civil structures using regenerative electric actuators. Proc., 11th ASCE Eng. Mech. Spec. Conf., Ft. Lauderdale, FL, 1996, 503-506.
- [16] Ou J. P. *Structural vibration control - active, semi-active and smart control*, science press, 2003
- [17] Ou Jinping, Zhang Chunwei. Modeling and dynamical testing of an innovative electromagnetic active mass driver control system for structural vibration, *Chinese High Technology Letters*, v 17, n 4, p 382-388, April 2007 Language: Chinese.
- [18] PMAC motion servo controller, user's manual (CD-ROM), 2003.
- [19] Quanser Consulting Inc. *Active Mass Damper - Two-Floor (AMD-2)*, User Manual, 2002.

- [20] Quast P., Sain M.K., Spencer B.F. Jr. and Dyke S.J. Microcomputer Implementations of Digital Control Strategies for Structural Response Reduction. *Microcomputers in Civil Engineering: Special Issue on New Directions in Computer Aided Structural System Analysis, Design and Optimization*, 1995, Vol. 10, pp. 1325.
- [21] Rana R., Soong T.T. Parametric Study and Simplified Design of Tuned Mass Dampers. *Engineering Structures*, 1998, 20(3), 193-204.
- [22] Ricciardelli F., Pizzimenti A. D., Mattei M. Passive and active mass damper control of the response of tall buildings to wind gustiness. *Engineering structures*, 2003, 25, 1199-1209.
- [23] Schmitendorf W E, Faryar J and Yang J N. Robust Control Techniques for Building under Earthquake Excitation[J]. *Earthquake Engineering and Structural Dynamics*, 1994,23: 539-552.
- [24] Scruggs J. T. and Iwan W. D. Control of a Civil Structure Using an Electric Machine with Semiactive Capability. *ASCE Journal of Structural Engineering*, 2003, 129(7): 951~959.
- [25] Soong T. T.. *Active Structure Control Theory and Practice*. Longman Scientific & Technical. New York, USA. 1990.
- [26] Spencer B. F. Jr, Dyke S J and Deoskar H S. Benchmark Problems in Structural Control: Part I - Active Mass Driver System. *Earthquake Engineering and Structural Dynamics*. 1998, 27(11), 1127~1139.
- [27] Spencer B. F. Jr. and Sain M. K., *Controlling Buildings: A New Frontier in Feedback*, IEEE Control Systems Magazine: Special Issue on Emerging Technologies (Tariq Samad Guest Ed.). 1997, 17(6): 19~35.
- [28] Spencer B. F.Jr. and Nagarajaiah S. State of the Art of Structural Control. *ASCE Journal of Structural Engineering*. 2003, 129(7): 845-856.
- [29] Warburton G.B. Optimal Absorber Parameters for Various Combination of Response and Excitation parameters. *Earthquake Engineering and Structural Dynamics*, 1982, 10, 381-401.
- [30] Warburton G.B., Ayorinde E.O. Optimum Absorber Parameters for Simple Systems. *Earthquake Engineering and Structural Dynamics*. 1980, 8, 197-217.
- [31] Wu Zhiwu.(2008). Modeling and control scheme analysis on spatial planar-rotational-coupling motions of suspensory structures. Master thesis of Harbin Institute of Technology,2008. Language: Chinese.
- [32] Xue D. Y. Design and analysis of feedback control system - the application of MATLAB. Tsinghua University press, 2000.
- [33] Yang G. Large-Scale Magnetorheological Fluid Damper for Vibration Mitigation: Modeling, Testing and Control, Ph.D dissertation, University of Notre Dame. 2001.
- [34] Yang G., Spencer B. F.Jr., Carlson J. D. and Sain M. K. Large-Scale MR Fluid Dampers: Modeling and Dynamic Performance Considerations, *Engineering Structures*. 2002, 24(3): 309~323.
- [35] Yao J. T. P. Concept of Structure Control. *Journal of Structure Division*, ASCE 1972, 98(ST7): 1567~1574.
- [36] Yie Y.Y. Principles and applications of linear motors. Mechanical industrial press, Beijing, 2000.
- [37] Yoshida I., Kurose H., Fukui S., Iemura H. Parameter identification on active control of a structural model. *Smart Materials and Structures*, 1995, 4(1A), A82~A90.
- [38] Zhang Chunwei, Li Luyu, Ou Jinping. Swinging motion control of suspended structures: Principles and applications, *International Journal of Structural Control and Health Monitoring*, 2009 (published online 10.1002/stc.331).

- [39] Zhang Chunwei, Ou Jinping. Analysis of active mass driver control against wind-wave coupled excitations for deep-water fixed jacket platform structures, *Journal of Harbin Institute of Technology*, v 37, n SUPPL. 1, p 198-201, May 2005 Language: Chinese.
- [40] Zhang Chunwei, Ou Jinping. Characteristic indices and analysis of active control forces in active mass driver control system for structural vibration, *Engineering Mechanics*, v 24, n 5, p 1-9, May 2007 Language: Chinese.
- [41] Zhang Chunwei, Ou Jinping. Characteristic of Control Force in Structure- Active Mass Driver Control System, *Journal of Vibration Engineering*, 2010, 23(1), 1-6. Language: Chinese
- [42] Zhang Chunwei, Ou Jinping. Characteristics of Active Forces in Structural Hybrid Mass Damper Control Systems, 2004 ANCER Annual Meeting Networking of Young Earthquake Engineering Researchers and Professionals, July 28-30, 2004, Honolulu, Hawaii, USA.
- [43] Zhang Chunwei, Ou Jinping. Closed-loop control strategies and dynamical tests of the electromagnetic mass damper control system, *Journal of Vibration Engineering*, v 20, n 3, p 213-218, June 2007 Language: Chinese.
- [44] Zhang Chunwei, Ou Jinping. Control strategies and experimental verifications of the electromagnetic mass damper system for structural vibration control, *Earthquake Engineering and Engineering Vibration*, 2008, 7(2), 181-192.
- [45] Zhang Chunwei, Ou Jinping. Control Strategies and Experiments of the Electromagnetic Mass Damper Control System for Structural Vibration, *Journal of Sound and Vibration Control*, 2006, 26(5), 9-13. (in Chinese)
- [46] Zhang Chunwei, Ou Jinping. Control Structure Interaction of Electromagnetic Mass Damper System for Structural Vibration Control, *ASCE Journal of Engineering Mechanics*, 2008, 134(5), 428-437
- [47] Zhang Chunwei, Ou Jinping. Evaluation Indices and Numerical Analysis on Characteristic of Active Control Force in Structural Active Mass Driver Control System, *Pacific Science Review*, 2007, 9(1), 115-122.
- [48] Zhang Chunwei, Ou Jinping. Intrinsic Behavior Analysis of Active Force in HMD Systems, the Eighth International Symposium on Network and Center-Based Research for Smart Structures Technologies and Earthquake Engineering, July 6-9, 2004, Osaka, Japan.
- [49] Zhang Chunwei, Ou Jinping. Modeling and testing for electromagnetic mass damper and structure coupled system, *Journal of Vibration Engineering*, v 19, n 3, p 289-295, September 2006 Language: Chinese.
- [50] Zhang Chunwei, Ou Jinping. Shaking table tests of electromagnetic mass damper system for control of structural seismic response, *Journal of Earthquake Engineering and Engineering Vibration*, 2006, 26(2), 104-110. (in Chinese)
- [51] Zhang Chunwei, Xu Huaibing, Li Luyu, Ou Jinping. Parametric impact analysis and experimental verifications of TRID system for structural pendular vibration control, I Parametric impact analysis and Bench-scale experimental verifications, *Journal of Control Theory and Application*, CCTA090432, 2010 in press. Language: Chinese
- [52] Zhang Chunwei. Electromagnetic AMD systems and their relevant theory and experiments for structural vibration control. Ph.D thesis of Harbin Institute of Technology, 2005.
- [53] Zhang Chunwei. Some problems on blast resisting, anti-shocking and vibration control of structures. Postdoctoral Research Report of Harbin Institute of Technology, 2007
- [54] Zhang Y.F., Iwan W.D. Active interaction control of civil structures. Part 2: MDOF systems. *Earthquake Engineering and Structural Dynamics*, 2002, 31(1), 179~194.

AVC Using a Backstepping Design Technique

R. Ferreiro García, F. Fraguera Diaz, A. De Miguel Catoira
University of A Coruna
Spain

1. Introduction

This chapter deals with the vibration attenuation or vibration suppression by means of feedback control techniques applied to decrease the dynamic response of a rotor assumed as active magnetic dynamic damping which is common in rotating machinery supported by active magnetic bearings. Position control systems applied on active magnetic bearings are using sometimes nonlinear robust control techniques. Backstepping control algorithms have been successfully applied to control active magnetic bearings in recent industrial applications. Consequently, when such an algorithm is being applied to control the radial shaft position, active vibration control should be performed taking advantage of the use of the same control algorithm. In the proposed methodology it is applied the Backstepping algorithm in cascade with a master conventional PID controller. The main functions of the cascade strategy are summarized as, desired radial shaft trajectory and radial position generation, rotor stabilization and vibration attenuation. Backstepping methodology provides a rather straightforward way to design the slave or cascade controller suitable for an unstable nonlinear system such as a magnetic bearing. Stabilization of the closed-loop system is achieved by incorporating appropriate Lyapunov functions which are inherent to the Backstepping algorithm. The global asymptotic stability is ensured when the derivative of the Lyapunov function is rendered negative definite by the control law. The closed loop damping or vibration attenuation is achieved according requirements by on-line determining and selecting the appropriate gains and parameters for the implemented control strategy as function of the fundamental vibration characteristics.

The aim to continue with research activities on this technologic field after more then three decades of intensive work, obeys to the fact that some modern machines require the characteristics and advantages of applying such technology (Gerhard Schweitzer, Eric H. Maslen Editors, 2009). The main characteristics of AMB based machines where the rotor is supported by radial active magnetic bearings are summarized as follows:

The *unbalance compensation*.- The most relevant characteristic of an AMB deals with the active compensation of shaft disturbances, such vibration due to residual unbalance which can be effectively measured and identified by the AMB control system. The signal is used to either generate counteracting and compensating bearing forces or to shift the rotor axis in such way that the rotor is rotating force-free.

The *positioning precision*.- The radial precision with which the position of the rotor can be controlled, is mainly determined by the precision or quality of the measurement signal within the control loop. Conventional inductive sensors, (eddy current based sensors) for example, have a measurement resolution of about 1/100 to 1/1000 of a millimetre.

Diagnostics.- On the basis of acquired data inherent to the position and vibration suppression control, diagnostics are readily performed, as the states and dynamic condition of the rotor are measured for the operation of the AMB anyway, and this information can be used to monitor and check operating conditions and performance. Even active diagnostics are feasible, by using the AMB as actuators in model analysis mode for generating well defined test signals simultaneously with their bearing function. The results of the design technique are evaluated on a vertical test rig where real-time data is analysed and compared with conventional control results.

1.1 The backstepping based AVC background

Active vibration control (AVC) applied on rotating machinery continues being after more than three decades of intensive research an area of primary interest (Tao Yang et al., 2009). AVC applied on active magnetic bearings (AMB) continues also being an important and active research area motivated by the demand of efficiency in the industrial production system. It deals essentially with nonlinear systems and nonlinear control theory, where among a vast range of applied nonlinear control strategies and algorithms, backstepping theory can definitely contribute positively to AVC of AMB.

Nonlinear control theory has been the subject of very strong development during the last two decades (Hassan K. Khalil, 2002), (Krstic, M., I. Kanellakopoulos, & P. Kokotovic, 1995). The existing problems with regard to the control of unstable nonlinear systems, has been the amount of difficulties encountered in achieving a systematic way to ensure closed loop stability (Krstic M., & H. Deng, 1998). The tools developed in this area suddenly made the design and implementation of controllers to be applied on nonlinear systems, significantly more structured and rather straightforward with the incorporation of Backstepping theory. One of the concepts, which are well known today to overcome some of the mentioned difficulties with nonlinear control algorithms, is Backstepping theory. Some interesting applications to AVC have recently been reported. Hence, in (Guang Lia & Amir Khajepour, 2005) a robust controller is developed to regulate both flexural vibrations and rigid body motion of a hydraulically driven flexible arm. The proposed controller combines backstepping, sliding mode, and pole placement techniques to arrive at a controller capable of dealing with a nonlinear system with uncertainties. The sliding mode technique is used to achieve an asymptotic joint angle and vibration regulation. (Qinglei Hu, 2009) proposes an angular velocity bounded robust adaptive control design for attitude maneuver and vibration reduction in the presence of external disturbances and uncertainties in the inertia matrix. (V. Mañosa, F. Ikhouane, J. Rodellar, 2005) presents a backstepping-based adaptive control designed for a class of one degree-of-freedom uncertain non-linear systems. The efficiency of the approach has been tested by numerical simulations on Duffing oscillators and systems with non-linear and hysteretic stiffness under external loads. In (Francesc Pozo et al., 2006) it is used an adaptive backstepping approach for vibration control of a hybrid seismic control system. (In Tao Yang et al., 2009), a backstepping control approach is applied to solve the active vibration isolation problem using a Stewart platform. They demonstrated that the controller can effectively attenuate low frequency vibrations in six degrees of freedom achieving satisfactory vibration isolation performance.

The work presented in this chapter is focused on the successfully application of the Backstepping theory on a typical unstable nonlinear system such as the active vibration control (vibration attenuation but not vibration suppression) on AMB's.

1.2 The backstepping background

The backstepping algorithm can be applied on control problems where a strict feedback state space model of the plant or process is available. The application presented in this chapter is one of those nonlinear systems, which have been subject to intensive studies in order to find fully stabilizing controllers. The Backstepping theory provides a tool for the recursive design of the control law based on the Lyapunov theory for stabilizing the controlled system (Hassan K. Khalil, 2002) and (Krstic, M., I. Kanellakopoulos, & P. Kokotovic, 1995). Control systems have one main goal to achieve, and that is the stability of the controlled system. An important topic with regard to the stability of dynamical systems concerns to the stability of equilibrium points, which is verified by Lyapunov Stability and LaSalle-Yoshizawa theorems (LaSalle J. P., 1960), (LaSalle, J.P., 1966), (Sontag E. D., A, 1989), (Yoshizawa, T., 1968).

The stability of nonlinear systems is verified by means of the following analytical background:

Theorem 1 (LaSalle-Yoshizawa)

Assuming the system

$$\dot{x} = f(x(t)) \quad (1)$$

with the initial condition $x(0)$, let $x=0$ be an equilibrium point for (1); let $V(x)$ be a scalar, continuously differentiable function of the state x such that

- $V(x)$ is positive definite
- $V(x)$ is radially unbounded
- $\dot{V}(x) = V_x(x)f(x) \leq -W(x)$, where $W(x)$ is positive semi-definite

Then, all solutions of (1) satisfy

$$\lim_{t \rightarrow \infty} W(x(t)) = 0$$

Furthermore, if $W(x)$ is positive definite, then the equilibrium $x = 0$ is globally uniformly asymptotically stable (GUAS). For proof, see (Hassan K. Khalil, 2002) and (Krstic, M., I. Kanellakopoulos, & P. Kokotovic, 1995) and (LaSalle J. P., 1960), (LaSalle, J.P., 1968), (Sontag E. D., A, 1989), (Sontag E.D., & Sussman, 1998), (Yoshizawa, T, 1966), (Yoshizawa, T., 1968).

Note that any equilibrium under investigation can be mapped to the origin by substituting x with $z = x - x_e$. Therefore, there is no loss of generality in standardizing results for the zero solution $z \equiv 0$. But demanding \dot{V} to be negative definite, in order to claim stability, may not perform successfully.

Now that it is stated the foundation of Lyapunov stability, the main question arising is how to find these functions. The theorems above do not provide any systematic method of finding these functions. In the case of electrical or mechanical systems there are natural Lyapunov function candidates like total energy functions. In other cases, it is basically a matter of trial and error.

The Backstepping approach is so far the only systematic and recursive method for constructing a Lyapunov function, along the design of the stabilizing control law. Yet, the system must have a lower triangular structure in order to apply the method. Before we can explore this state-of-the-art technique in control of nonlinear systems, it is convenient extend the systems handled so far to those including a control input.

1.3 Control Lyapunov Functions (CLF)

Since an objective is to develop closed-loop systems with desirably stability properties, let us now add a control input to the considered system

$$\dot{x} = f(x, u), \quad x \in R^n, \quad u \in R, \quad f(0,0) = 0 \quad (2)$$

It is necessary to introduce an extension of the Lyapunov function concept, the CLF. Given the stability results from the previous section, the objective is to find a control law $u = \alpha(x)$ such that the desired state of the closed-loop system $\dot{x} = f(x, \alpha(x))$ be Globally Asymptotic Stable (GAS) equilibrium point. Once again it is considered the origin to be the goal state for simplicity. It can be chosen a function $V(x)$ as a Lyapunov candidate, and require that its derivative along the solutions of (2) satisfy $\dot{V}(x) \leq -W(x)$, where $W(x)$ is positive definite function. Then closed-loop stability follows from Theorem (1). It is necessary therefore to find $\alpha(x)$ to guarantee that for all $x \in R^n$.

$$\dot{V}(x) = \frac{\partial V}{\partial x}(x) f(x, \alpha(x)) \leq -W(x) \quad (3)$$

The pair V and W must be chosen carefully otherwise (4) will not be solvable. This motivates the following definition, which can be found in (Krstic, M., I. Kanellakopoulos, & P. Kokotovic, 1995).

Definition 1.(CLF)

A smooth positive definite and radially unbounded function $V: R^n \rightarrow R$ is a CLF if for(2) and every $x \neq 0$

$$\dot{V}(x) = V_x(x) f(x, u) < 0 \quad \forall x \neq 0 \text{ and for some } u \quad (4)$$

The significance of this definition concerns to the fact that, the existence of a globally asymptotic stabilizing control law is equivalent to the existence of a CLF. If exists a CLF for the system, then it is certainly possible to find a globally stabilizing control law. The reverse is also true. This is known as Artstein's theorem and can be found in (Sontag E. D., 1989). Now that the concept CLF is defined, it is necessary to move on and explore the Backstepping theory, which is the main tool we must deal with.

1.4 The backstepping algorithm

The main drawback of the CLF concept as a design tool is that for most nonlinear systems the proper CLF is not known. The task of finding an appropriate CLF may be complex as well as that of designing a stabilizing feedback law. The Backstepping procedure solves both problems simultaneously. The standard procedure can be found in (Hassan K. Khalil, 2002), (Krstic, M., I. Kanellakopoulos, & P. Kokotovic, 1995). To spare the reader from the effort to understand the main ideas of Backstepping by a theorem, it helps more by starting from the description of the general procedure, which will clarify such concepts

1.5 General backstepping procedure

Given a SISO nonlinear, non-minimum phase process described under a state feedback state space model, and assuming Y_r to be a tracking reference trajectory, the following sequence is to be performed under a systematic procedure according the generic following steps:

Step 1:

Error step 1:

$$Z_1 = Y_r - X_1 \quad (5a)$$

Lyapunov Function 1st step:

$$V_1 = \frac{1}{2} Z_1^2 \quad (5b)$$

Derivative of V_1 :

$$\dot{V}_1 = Z_1 \dot{Z}_1 = Z_1 (\dot{Y}_r - \dot{X}_1) \quad (5c)$$

Stabilizing function 1st step:

$$\alpha_1 = X_{2d} = \dot{Y}_r - P_1 Z_1 \quad (5d)$$

with $P_1 > 0$

Step 2:

Error step 2

$$Z_2 = X_2 - X_{2d} = X_2 - \alpha_1 \quad (5e)$$

Lyapunov Function 2^d step:

$$V_2 = \frac{1}{2} Z_1^2 + \frac{1}{2} Z_2^2 \quad (5f)$$

With

$$\dot{Z}_1 = \dot{Y}_r - \dot{X}_1 = \dot{Y}_r - X_2 = P_1 Z_1 - Z_2 \quad (5g)$$

Derivative of V_2 :

$$\dot{V}_2 = P_1 Z_1^2 - Z_2 (Z_1 + \dot{X}_2 - \dot{\alpha}_1) \quad (5h)$$

$$\dot{V}_2 = P_1 Z_1^2 - Z_2 \left[(1 - P_1^2) Z_1 + P_1 Z_2 + X_3 - \ddot{Y}_r \right] \quad (5i)$$

Stabilizing function 2^d step:

$$\alpha_2 = X_{3d} = (P_1^2 - 1) Z_1 - (P_1 + P_2) Z_2 + \ddot{Y}_r \quad (5j)$$

with $P_2 > 0$

Step i:

Error step i

$$Z_i = X_i - X_{id} = X_i - \alpha_{i-1} \quad (5k)$$

Lyapunov Function i^{th} step:

$$V_i = \frac{1}{2} \sum_{j=1}^i Z_j^2 \quad (5l)$$

With

$$\dot{Z}_{i-1} = Z_i - P_{i-1}Z_{i-1} - Z_{i-2} \tag{5m}$$

Derivative of V_i :

$$\dot{V}_i = -\sum_{j=1}^{i-1} P_j Z_j^2 + Z_i [Z_{i-1} + \dot{X}_i - \dot{\alpha}_{i-1}] \tag{5n}$$

Stabilizing function i^{th} step:

$$\alpha_i = X_{i+1} = -P_i Z_i - Z_{i-1} + \dot{\alpha}_{i-1} \tag{5o}$$

where $P_i > 0$, are positive constants.

The corresponding notation is shown in figure 1, in which it is illustrated a generic process state space representation corrected with stabilizing functions by means of Backstepping procedure.

In order to avoid static control errors for systems type 0, an integrator must be added in series with the plant model. Then, at the end of the design procedure, this integrator is moved from the plant model to the control equation (Hassan K. Khalil, 2002), (Krstic, M., I. Kanellakopoulos, & P. Kokotovic, 1995). An alternative to such generalized technique consists in adding a cascade Backstepping algorithm following the setpoint generated by a feedback conventional controller.

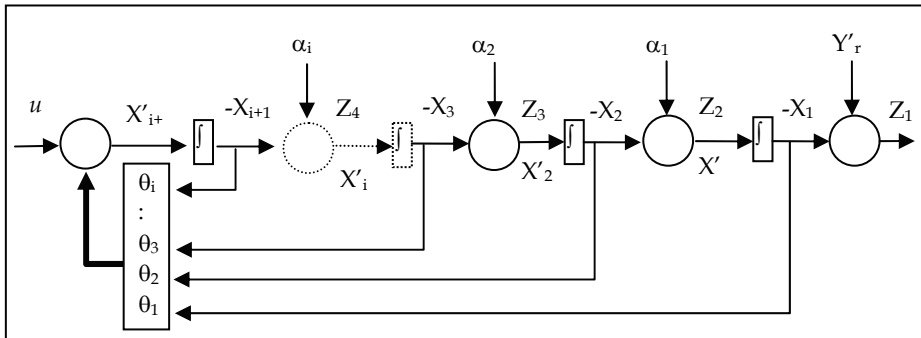


Fig. 1. General process representation stabilized by means of the Backstepping procedure

Assumption 1.

Assuming the system

$$\dot{x} = f(x) + g(x)u, \quad f(0) = 0, \tag{6}$$

where $x \in R^n$ is the state and $u \in R^n$ is the control input, there exists a continuous differentiable feedback control law

$$u = \alpha(x), \quad \alpha(0) = 0, \tag{7}$$

and a smooth, positive definite, radially unbounded function $V: R^n \rightarrow R$ such that

$$\frac{\partial V}{\partial x} [f(x) + g(x)\alpha(x)] \leq -W(x) \leq 0, \quad \forall x \in R \tag{8}$$

where $W: R^n \rightarrow R$ is positive semi-definite.

By means of this assumption, the control (7) applied to the system (6) guarantees global boundedness of $x(t)$.

Let the system (6) be augmented by an integrator according the expression

$$\begin{aligned} \dot{x} &= f(x) + g(x)\xi \\ \dot{\xi} &= u \end{aligned} \tag{9}$$

and suppose that satisfies the above assumption with $\xi \in \mathbb{R}^n$ as its control variable.

Lemma 1

Being $V(x)$ positive definite, then

$$V_a(x, \xi) = V(x) + \frac{1}{2}[\xi - \alpha(x)]^2 \tag{10}$$

is a CLF for the complete system (9). That means, there exists a feedback control $u = \alpha_a(x, \xi)$ which renders $(x, \xi) = (0, 0)$ the GAS equilibrium of (9). Such control results in

$$u = -c(\xi - \alpha(x)) + \frac{\partial \alpha}{\partial x} [f(x) + g(x)\xi] - \frac{\partial V}{\partial x} g(x), ; c > 0 \tag{11}$$

Up to now it has been introduced the methodology and tools to design a stabilizing control law and determine its stability properties. In the next section a brief description of active magnetic bearings is presented.

2. The AMB control environment

2.1 Background

From a control viewpoint, an AMB is a nonlinear unstable process. The simplest model is represented with figure 2. The application of AMB's is based upon the principle that an electromagnet will attract ferromagnetic material. A ferromagnetic rotor can thus be supported in a magnetic field generated in the bearing electromagnet stator, as shown in the figure 2.

Since the natural tendency of the stator is to attract the rotor until it makes contact, some control action is required to modulate the magnetic field and maintain the rotor in the desired position. The most common type of control involves the feedback of shaft position. This information is then used by the control system to modulate the magnetic field through power amplifiers, so that the desired rotor position is maintained even under changing shaft load conditions. An active magnetic bearing system consists of electromagnet bearing actuators, position sensors, a control system and power amplifiers. The bearing actuators and sensors are located in the machine, while the control system and amplifiers are generally located remotely.

A typical system consists of two radial bearings and a thrust bearing. Each radial bearing has a stator and sensor system mounted over a ferromagnetic rotor installed on the shaft. The rotor consists of a stack of lamination rings mounted on a sleeve that fits onto the shaft. Laminations are used to reduce eddy current losses and to improve the response of the bearing. The stator is made of a stack of lamination rings with poles on the internal diameter. Coils are wound around each pole so that the bearing is divided into four

quadrants. The coils in each quadrant are wound in series making each quadrant function as one electromagnet. Typically on horizontal machines, the quadrants are aligned 45 degrees from vertical. Opposing quadrants constitute an axis and therefore each radial bearing can be described by two axes. A set of sensors that measure shaft position are mounted as close to the bearing as possible.

As the results shown along a couple of years indicate, digital control provides capabilities for adaptive control which can be used to greatly alleviate the unbalance vibration of rotating machinery. This is often the worst vibration problem encountered during operation. The source of this vibration is the discrepancy between the geometric axis of the rotor and its inertial axis. When the rotor is spinning, this imbalance results in a centrifugal force which causes synchronous vibration throughout the machine. This problem is managed on conventional machinery through mechanical balancing by means of the addition or removal of a small amount of mass from the shaft to reduce the residual imbalance. Rotor balancing in the field, unfortunately, is usually time consuming and costly. The down-time incurred can also be very expensive in terms of lost production. Also for some machines where the imbalance changes often during operation, such as centrifuges, mechanical balancing will have a limited benefit.

Magnetic bearings, being active devices, offer the capability to establish new and beneficial relationships between rotor and casing vibration and applied bearing force. This capability has been employed by a considerable number of researchers investigating the control of unbalance response. One method to achieve unbalance response attenuation is through design of the feedback compensation. This has been achieved via the addition of filters to stabilizing controllers (Habermann & M. Brunet, 1994), (Larsonneur & R. Herzog, 1994) or through the addition of pseudo-states in observer based controllers (T. Higuchi, T. Mizuno, & M. Tsukamoto, 1990), (F. Matsumura, M. Fujita, & K. Okawa, 1990). Other researchers (C.R. Burrows & M.N. Sahinkaya, 1983), (C.R. Burrows, M.N. Sahinkaya, & S. Clements, 1989), (T. Higuchi et al., 1990), (R. Larsonneur, 1988), (Larsonneur & R. Herzog, 1994), (B. Shafai et al., 1994), (C.R. Knospe et al., 1993), have employed methods which the authors refer to as *adaptive open loop control*. These methods, as pointed out by (R. Larsonneur, 1988), (Larsonneur & R. Herzog, 1994) and Shafai et al., 1994), have the advantage that they may be added to feedback controllers that have been designed for optimum transient response without altering system stability or performance. These methods were first employed on a magnetic bearing supported rotor by (C.R. Burrows & M.N. Sahinkaya, 1983) who solved a least-squares-balancing problem for the proper forces to apply using an off-line theoretical model. They later extended this work to obtain an estimate of an influence coefficient matrix through trial forces and the use of a recursive control law (C.R. Burrows, M.N. Sahinkaya, & S. Clements, 1989). (Higuchi et al., 1990) applied an adaptive open loop method (*periodic learning control*) employing an estimate of the inverse transfer function in a recursive procedure. This method can only be applied on systems with square influence coefficient matrices (number of actuators equals number of vibration sensors). Following references (C.R. Burrows, M.N. Sahinkaya, & S. Clements, 1989), (Higuchi et al., 1990) are very similar to the convergent control algorithm presented by Knospe et al., 1993) which uses a look-up table of influence coefficients obtained through off-line testing. (Shafai et al., 1994) apply a distinct method of adapting the open loop forces to cancel a synchronous signal. In such a method, only one Fourier coefficient of the open loop signal is changed per adaptation cycle in such a mode as to decrease the residual error. This method, originally developed for SISO systems, was extended to square MIMO systems. Stability and performance robustness of

this method (convergence to optimal open loop control) is ensured. This is in contrast to most of the model-based methods where stability and performance robustness is being studied now. The transient performance of the adaptive open loop algorithms to changes in imbalance or rotor speed has to be considered because of its practical importance.

2.2 Modeling a generic AMB

A typical magnetic bearing comprises a set of radially positioned electromagnets located in opposing pairs around a laminated magnetic bearing journal. For instance, for a magnetic bearing with four electromagnets as depicted in figure 2, there is one opposing pair for each perpendicular axis. Each electromagnet consists of a laminated core and one or more coil windings. The force produced by a single two pole electromagnet can be shown to be given by the following equation:

$$F = \frac{\mu_0 AN^2}{4} \frac{I^2}{z^2} \tag{12}$$

where I is the total current in the magnet coils, z is the gap distance, μ_0 is the permeability of free space, A is the pole face area, and N is the number of coil turns
 The force in (8) is attractive and increases as the gap decreases. This attractive force produces an unstable system for an open loop magnetic bearing configuration. The net force, F_n produced by an opposing pair of identical two-pole electromagnets on a single shaft is the sum of the forces produced by each electromagnet. Taking account of the sign convention (see Fig. 2), the net force equation is given by:

$$F_n = \frac{\mu_0 AN^2}{4} \left[\frac{I_2^2}{z_2^2} - \frac{I_1^2}{z_1^2} \right] \tag{13}$$

I_j is the current in magnet j , and z_i is the gap distance for magnet j .
 A dynamical mathematical model for the AMB is shown in Fig. 2, where disturbances and external forces can be established as follows:

$$m\ddot{x} = \frac{\mu_0 AN^2}{4} \left[\left(\frac{I_2}{X_0 - x} \right)^2 - \left(\frac{I_1}{X_0 + x} \right)^2 \right] + F \tag{14}$$

where

- z_2 $X_0 - x$ air gap 2
- z_1 $X_0 + x$ air gap 1
- m mass of the rotor (kg);
- x position displacement of the rotor (m);
- X_0 nominal air gap (m);
- μ_0 permeability of free space H/m;
- A total pole-face area of each electromagnet (m²);
- N number of turns on each electromagnet coil;
- I_1, I_2 electromagnet coil currents (A);
- F some known force acting on the rotor such as load disturbances and/or the rotor weight (N).
- mg the rotor weight

Previously, the equations were given for the static force produced by a magnetic bearing along a single axis. That force is affected dynamically by the rate limit at which current changes in the coils, called the current slew rate limit, which is dependent on the voltage limit, of the power supply and the coil inductance, L .

The general nonlinear electromechanical model of the one degree-of-freedom (DOF) AMB system, for a number of electromagnet coils, can be subdivided into the mechanical subsystem dynamics, the magnetic force equation, and the electrical subsystem dynamics. The mechanical subsystem is governed by

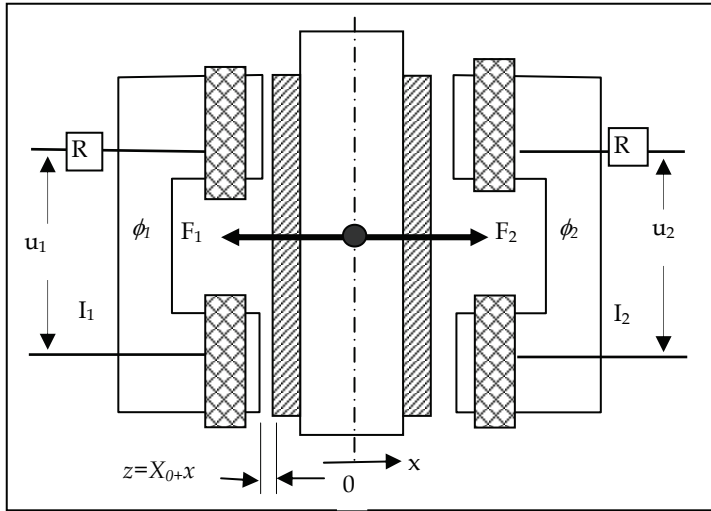


Fig. 2. Active magnetic bearing principle

$$m\ddot{x} = \sum_{i=1}^2 F_i(\Phi_i) + \sum F_D \quad (15)$$

where m is the rotor mass, x represents the position of the rotor centre, Φ_i is the magnetic flux in the i th electromagnet, F_i denotes the force produced by the electromagnet, given by

$$F_i = \frac{(-1)^{i+1} \Phi_i^2}{\mu_0 A}, \quad i=1,2 \quad (16)$$

where F_D is the load and disturbance forces.

The electrical subsystem is governed by the equations

$$N\dot{\Phi}_i + R_i I_i = v_i, \quad i=1, 2 \quad (17)$$

where X_0 is the nominal air gap, u is the input control voltage of the i th electromagnet and I_i is the current in the i th electromagnet which is related to the flux according

$$I_i = \frac{2(X_0 + (-1)^i x)\Phi_i}{\mu_0 AN}, \quad i=1, 2 \quad (18)$$

3. Backstepping based control strategy

3.1 Introduction

Since Backstepping based control strategies are model-based techniques, one of the first tasks to be carried out concerns to AMB modelling. A practical useful AMB needs at least four pairs of active magnetic coils. Nevertheless, with regard to modelling and analysis tasks, a single pair of active magnetic coils is sufficient without loss of generality. Consequently, starting from (13-14) with reference to figure 2, a strict feedback state space model is achieved, which will be used in the design procedure. The strict feedback state space model of a vertical mechanical shaft equipped with a single pair of magnetic coils, is then developed according to

$$\begin{aligned} \dot{x}_1 &= x_2 \\ \dot{x}_2 &= \frac{C}{m} F_N = \frac{C}{m} I_2^2 \frac{1}{(X_0 - x)^2} - \frac{C}{m} I_1^2 \frac{1}{(X_0 + x)^2} \end{aligned} \tag{19}$$

where a constant parameter C is being defined as $C = 0.25 \cdot \mu_0 \cdot A \cdot N^2$

3.2 Control strategy

The control objective is to determine the manipulated variables MV_1 and MV_2 to supply a stabilizing net force $F_N = F_1 - F_2$ such that the closed loop system yields a stable response under possible load disturbances with an acceptable performance. In order to manipulate a strict feedback state space model, the manipulated variables are selected such that $MV_1 = I_1^2$ and $MV_2 = I_2^2$.

Consequently, (19) is expressed as

$$\begin{aligned} \dot{x}_1 &= x_2 \\ \dot{x}_2 &= \frac{C}{m} MV_2 \frac{1}{(X_0 - x)^2} - \frac{C}{m} MV_1 \frac{1}{(X_0 + x)^2} \end{aligned} \tag{20}$$

If the effect of gravity is considered, then

$$\dot{x}_2 = \frac{C}{m} MV_2 \frac{1}{(X_0 - x)^2} - \frac{C}{m} MV_1 \frac{1}{(X_0 + x)^2} - g \text{ or } \dot{x}_2 = \frac{C}{m} F_N - g$$

According the Backstepping procedure shown by the sequence of expressions (5a) to (5i), a CLF is achieved as

$$\dot{x}_2 = \ddot{Y}_r + Z_2(P_1 + P_2) + Z_1(1 - P_2^2) \tag{21}$$

which will render GAS for the equilibrium points according definition 1 and equation (4), where

$$\begin{aligned} Z_1 &= Y_r - x_1 \\ Z_2 &= \dot{Y}_r + P_1 Z_1 - x_2 \end{aligned} \tag{22}$$

with $(P_1, P_2) > 0$ will assume real values, which must be selected according required speed and accuracy of the closed loop response. Combining (20) and (21) yields the manipulated variables MV_1 and MV_2 that satisfies the closed loop stability criteria.

$$\frac{C}{m} F_N = \frac{C}{m} MV_2 \frac{1}{(X_0 - x)^2} - \frac{C}{m} MV_1 \frac{1}{(X_0 + x)^2} = \ddot{Y}_r + Z_2(P_1 + P_2) + Z_1(1 - P_1^2) \quad (23)$$

The expression (23) establishes the stabilizing control function which depends on the net force F_N which can be generated by the two manipulated variables MV_1 and MV_2 , consisting in a squared current supplied to the coils by means of appropriate power amplifiers. According expression (23), such manipulated variables are both interdependent functions, yielding

$$\begin{aligned} MV_1 &= (X_0 + x)^2 \left[-\frac{m}{C} \dot{x}_2 + MV_2 \frac{1}{(X_0 - x)^2} \right] \\ MV_2 &= (X_0 - x)^2 \left[\frac{m}{C} \dot{x}_2 + MV_1 \frac{1}{(X_0 + x)^2} \right] \end{aligned} \quad (24)$$

where \dot{x}_2 is defined by (20).

3.3 Scheduling the backstepping controller output signal

The task of generating the stabilizing net force F_N from the manipulated variables MV_1 and MV_2 according the conventional Backstepping algorithm given by expression (24), yields a rather ambiguous results, since it provide only the net force but nothing about how to generate such stabilizing force from the availability of two unknown manipulated variables. In order to implement a deterministic control action, an output signal scheduler is proposed. In order to avoid superfluous current consumption, controller outputs must be scheduled so that only a coil of two is active at any time. Scheduling the controller outputs must be subjected to the condition by which system stability ensured by the Backstepping procedure will not be altered. In order to satisfy such condition, the Backstepping algorithm is modified with an output scheduler based on a split range procedure.

Since (21) is CLF for the controlled AMB, follows that in the setpoint position, which coincides with equilibrium point, is also GAS. As a direct consequence, from (23) and (24) follows that the net force on the shaft exerted by a set of two opposite coils is defined by the backstepping algorithm as

$$\dot{x}_2 = \frac{C}{m} \left[\frac{I_2^2}{(X_0 - x)^2} - \frac{I_1^2}{(X_0 + x)^2} \right] - g = \ddot{Y}_r + Z_2(P_1 + P_2) + Z_1(1 - P_1^2) \quad (25)$$

and hence, the net force exerted by a unique manipulated variable (NMV), defined as

$$NMV = \frac{C}{m} \left[\frac{I_2^2}{(X_0 - x)^2} - \frac{I_1^2}{(X_0 + x)^2} \right] = \ddot{Y}_r + Z_2(P_1 + P_2) + Z_1(1 - P_1^2) + g \quad (26)$$

is also GAS, where NMV is the net manipulated variable necessary to satisfy (25) which is also GAS and g is the acceleration of local gravity.

Lemma 2.

The total force necessary to stabilize the system is based on the fact by which the net force exerted by a set of two opposite coils is equivalent to the unique force exerted by feeding an independent coil with a current such that

$$\begin{aligned}
 \text{IF } NMV > 0 \rightarrow \frac{C}{m} \frac{I_{2N}^2}{(X_0 - x)^2} = NMV &= \frac{C}{m} \left[\frac{I_2^2}{(X_0 - x)^2} - \frac{I_1^2}{(X_0 + x)^2} \right] = \\
 &= \ddot{Y}_r + Z_2(P_1 + P_2) + Z_1(1 - P_1^2) + g
 \end{aligned} \tag{27}$$

which means that $I_1^2 = 0$, $\frac{I_1^2}{(X_0 + x)^2} = 0$

$$\begin{aligned}
 \text{IF } NMV < 0 \rightarrow \frac{C}{m} \frac{I_{1N}^2}{(X_0 + x)^2} = NMV &= \frac{C}{m} \left[\frac{I_2^2}{(X_0 - x)^2} - \frac{I_1^2}{(X_0 + x)^2} \right] = \\
 &= \ddot{Y}_r + Z_2(P_1 + P_2) + Z_1(1 - P_1^2) + g
 \end{aligned} \tag{28}$$

meaning that

$$I_2^2 = 0, \quad \frac{I_2^2}{(X_0 - x)^2} = 0 \tag{29}$$

where I_{iN} in (36) and (24) is the net current to the coil i , with $i = 1, 2$. Consequently, from (27) and (28) follows that

$$\text{For } NMV > 0, I_{2N}^2 = \frac{m}{C} \cdot NMV \cdot (X_0 - x)^2 \text{ with } I_1 = 0 \tag{30}$$

which yields the final result as

$$I_{2N}^2 = \frac{m}{C} \cdot [\ddot{Y}_r + Z_2(P_1 + P_2) + Z_1(1 - P_1^2) + g] \cdot (X_0 - x)^2 \tag{31}$$

$$I_{1N}^2 = \frac{m}{C} \cdot [\ddot{Y}_r + Z_2(P_1 + P_2) + Z_1(1 - P_1^2) + g] \cdot (X_0 + x)^2 \tag{32}$$

Since the range of application of I_2 and I_1 is such that

$$0 \leq I_1 \leq I_{1LIM} \quad \text{AND} \quad 0 \leq I_2 \leq I_{2LIM} \tag{33}$$

where I_{1LIM} and I_{2LIM} are the maximum allowable current to the coils, follows that the set of control outputs is restricted by

$$\begin{aligned}
 (I_1 = 0 \text{ AND } 0 < I_2 < I_{2LIM}) \text{ OR} \\
 (I_2 = 0 \text{ AND } 0 < I_1 < I_{1LIM})
 \end{aligned} \tag{34}$$

constraints that satisfy the conditions established with regard to GAS in the equilibrium point. From expressions (27-34) follows that the manipulated variables must actuate alternatively under a logic exclusive OR function, instead of actuate simultaneously in opposition to each other. Consequently, in order to schedule the manipulated variables in such a way that any active variable could not actuate in opposition to each other, it is necessary to propose and schedule the controller outputs according the following restrictions.

$$\begin{bmatrix} I_{1N}^2 \\ I_{2N}^2 \end{bmatrix} = \begin{bmatrix} NMV < 0 & NMV > 0 \end{bmatrix} \begin{bmatrix} (X_0 + x)^2 \\ (X_0 - x)^2 \end{bmatrix} \frac{C}{m} NMV \tag{35}$$

which yields definitely

$$\begin{bmatrix} I_{1N}^2 \\ I_{2N}^2 \end{bmatrix} = \begin{bmatrix} NMV < 0 & NMV > 0 \end{bmatrix} \begin{bmatrix} (X_0 + x)^2 \\ (X_0 - x)^2 \end{bmatrix} \frac{C}{m} [\ddot{Y}_r + Z_2(P_1 + P_2) + Z_1(1 - P_1^2) + g] \quad (36)$$

The amplifiers structure that satisfy the current needs to each pair of opposite coils specified by the expression (36) is depicted in figure 3.

According figure 3, when the controller output value ($V_{control}$) is positive, ($0 < V_{control} < 10 V_{cc}$), then the coil L1 is active and the coil L2 is inactive, and when $V_{control}$ is negative ($0 > V_{control} > -10 V_{cc}$), then the coil L2 is active and L1 is inactive.

The strategy of keeping active or energized only one coil at same time has the potential advantage of saving some energy. There is, however, a very serious drawback in terms of controllability since it is completely lost at zero current. In practice, the stiffness and bandwidth of the active magnetic bearing is greatly improved by activating both coils. Using only one coil at a time can achieve similar performance only if very high bandwidth, high voltage amplifiers are used to overcome the inherently high inductive impedance. Energy savings are only meaningful in the case of irrelevant disturbances. In practice, overcoming persistent, periodic disturbances such as rotor imbalance is more easily achieved by energizing both magnet coils. Consequently, in other to improve the control performance a properly selected bias current should be applied by the amplifiers. Such mentioned bias current doesn't affect obviously the rotor stability since it must be applied symmetrically to both opposite coils.

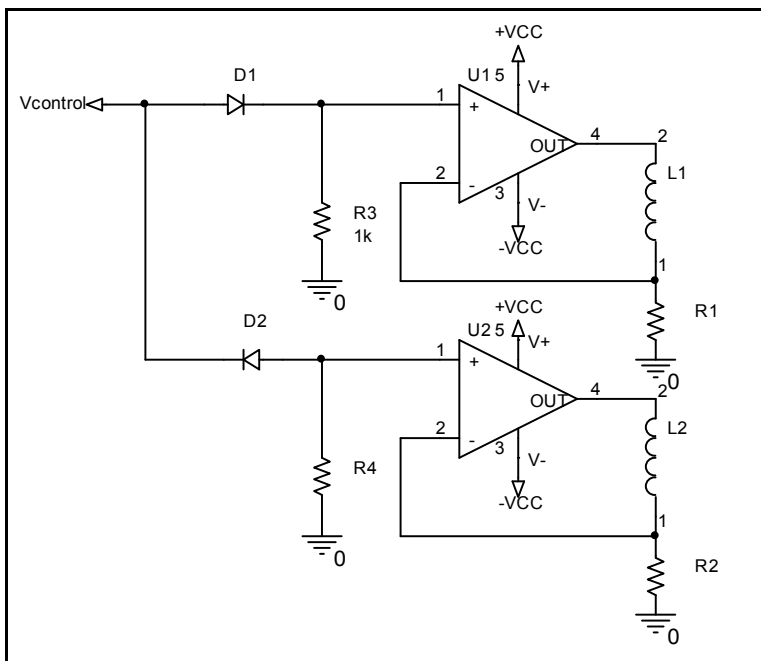


Fig. 3. The current amplifiers structure for two opposite coils

4. Implementation task

4.1 System description

AVC is studied along the work to compensate the vibration effect caused mainly by the unbalance disturbances on the machine rotor. Unbalance is considered as the unequal radial weight distribution of the rotor which consists in a condition where the mass centerline (principal inertia axis) does not coincide with the geometric centerline of the rotor. A direct consequence of unbalance in absence of some other disturbances is a vibration response of the rotor with a fundamental vibration frequency. Such fundamental vibration frequency of given amplitude should be attenuated as much as possible by means of the implemented control algorithm. In the same way, vibration frequencies near the fundamental frequency should be also attenuated.

The proposed and implemented strategy is based on the beneficial effects of conventional cascade control. While the Backstepping algorithm is responsible for the forward control loop stabilization, contributing with a robust performance yet under large load variations, the master PID controller is responsible for the fixed setpoint control.

Such proposed cascade structure is depicted in figure 4. The PID controller output variable plays the necessary role demanded by the Backstepping controller which consists in the determination and subsequent application of the reference trajectory to the Backstepping algorithm. The Backstepping controller output is then applied to the electromagnets by means of current amplifiers. Four control loops are necessary to control the shaft under two degrees of freedom, which means two control loops applied in each shaft end.

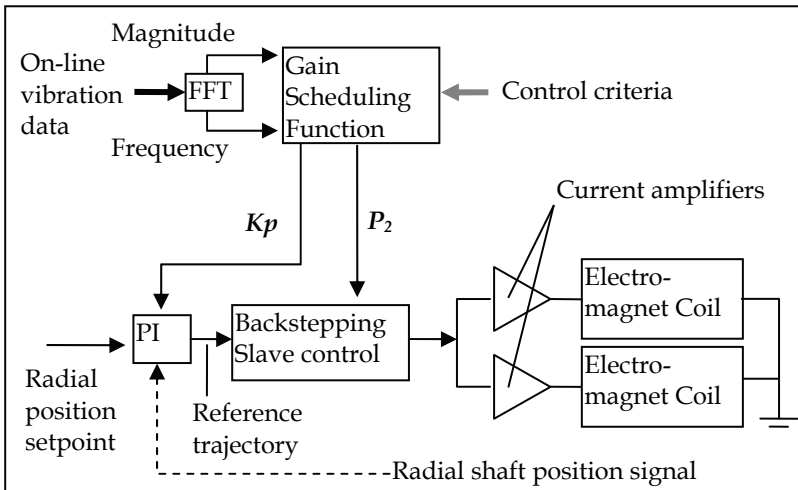


Fig. 4. The structure of the cascade strategy for a one degree of freedom control loop.

The gain scheduler based adaptive method operates with relevant information regarding to the rotor dynamics such as the magnitude and frequency of radial shaft vibration, or alternatively, with the amplitude (amplitude is on-line computed in time domain from the radial displacement measurements) and rotation speed of the shaft. Such data is applied to determine the parameters K_p and P_2 of the PID and Backstepping controllers respectively from the look-at-tables properly achieved.

Since the backstepping control algorithm is a model based technique, modelling errors are present when the values of parameters are not precisely determined. As consequence, the system control implementation must be performed under the set of selected model parameters matching the values of the test rig parameters. Such values are shown in table 1. The values selected for such set of model parameters are closely approached from the test rig data.

Large modelling error parameter values yields dramatic results in terms of rotor stabilization and active vibration control performance. Applied backstepping theory is robust under no relevant modelling errors. Consequently, the rotor mass and inertia moment as well as magnetic field parameters must be acquired and applied to the control algorithm as much accurately as possible.

Parameter/Notation	Value/Unit
Nominal air gap (X_0)	0.001m
Number of turns of each coil (n)	400
Coils resistance (R)	2 Ohms
Cross sectional area of air gap (A)	0.000625m ²
Rotor mass (m)	11 kg
Initial position of rotor (X_0)	-0.0008 m
Magnetic permeability of air gap (μ_0)	1.256E-6

Table 1. Backstepping model parameters

As shown in figure 4, the closed loop system is controlled by means of a master PID controller, followed by the slave cascade Backstepping controller. Thus, the types of disturbances for which the combination of a cascade with a PID feedback control system exhibit effectiveness, are those generated by the unbalance effect of the rotor, the impeller or turbine shaft assembled to the rotor, which operates producing an abnormal radial force. Such radial force will be accurately detected measured and compensated. Consequently, such events will be compensated by the control current scheduled by the cascade Backstepping controller.

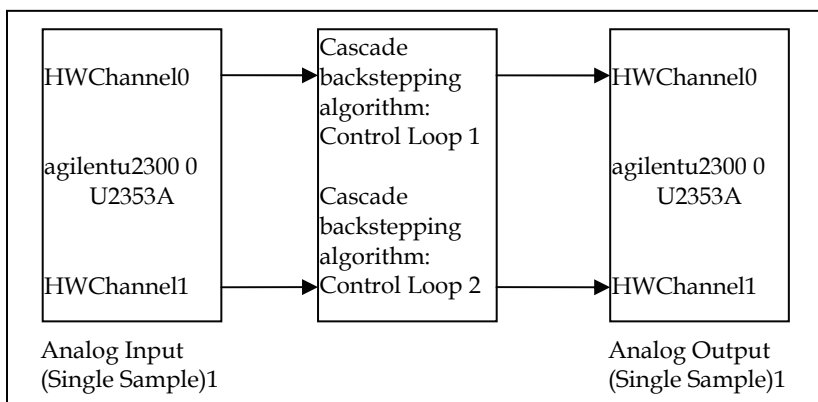


Fig. 5. The controller algorithm based on Agilent data acquisition hardware implemented under real time Matlab-Simulink software.

The implemented control type is based on a decentralized control structure (also called “side-by side” or “local” control). In such type of control structure, every degree of freedom to be controlled requires a feedback control loop. The control system applies the force commands to attenuate shaft vibration while keeping the shaft into the desired radial position, commonly symmetrically centred. The implementation of a shaft end vibration and position control scheme is shown in figure 5. It consists of Agilent Technologies based I/O hardware programmed under Matlab-Simulink.

The implemented test rig is considered as the traditional Jeffcott rotor as shown in figure 6 (a). The shaft turns around the bearing centreline and all rotating elements are concentric. This condition is depicted in detail (b) of figure 6. At very low speeds, unbalance forces are negligible. As rotor speed increases, the straight shaft will deflect into the predictable mode shape according to expression (37).

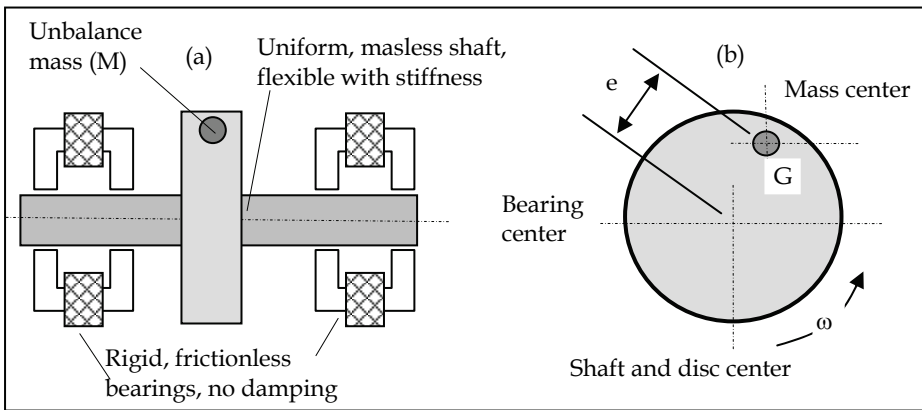


Fig. 6. The Jeffcott type rotor of the test rig: (a) rotor disk with unbalanced mass (M). (b) mass eccentricity (e) on the disc.

The only driving force in the system is the centrifugal force F_c due to the unbalance mass M , located at a radial distance e . The maximum bending deflection of the shaft is identified by r and the mass eccentricity by e . By inspection of the figure 6 it can be noted that the shaft and disk are rotating at the operating speed ω . Simultaneously, the deflected shaft is whirling in the magnetic bearings at this speed. The mechanism driving this whirl is the centrifugal force generated by the eccentric mass on the disc. As rotor speed increases, the outward force increases in accordance with the normal centrifugal force F_c equation

$$F_c = M \cdot (r + e) \cdot \omega^2 \tag{37}$$

With regard to expression (37), the total radius of the mass unbalance M is composed of the shaft bending r , and the eccentricity of the mass with respect to the shaft centreline e . Such centrifugal forces will be attenuated by the active magnetic forces developed by the control algorithm. Into the range of experimental rotating speeds, ($0 < \omega < 50$ rad/sec.) the bending deflection is considered negligible and the only centrifugal force is due to the mass eccentricity e . The unbalance characteristics for tests purposes consists of an unbalance mass M of 1 kg, radially located with an eccentricity of 0.1 m.

The general aspect of the vertical test rig is shown in figure 7. It consists of a vertical shaft supported by two radial AMB of the homopolar magnet type structure. The proposed design result is a substantial reduction of field variation around the circumference of the rotor so that the eddy current loss due to rotor rotation is considerably reduced. A detail of the homopolar type structure is depicted with figure 8.

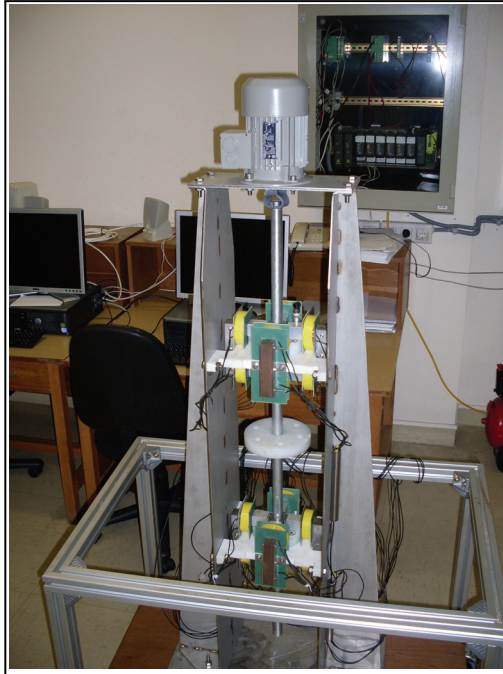


Fig. 7. The aspect of the vertical type test rig

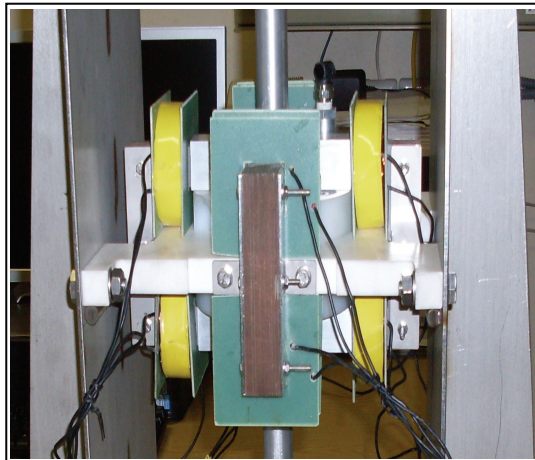


Fig. 8. Detail of the upper radial homopolar active magnetic bearing.

A detail of the upper radial magnetic bearing is shown in figure 8. The homopolar structures, being more complicated and expensive, exhibit the advantage that it produces much lower rotational losses since the rotor experiences less field variation when spinning and consequently has lower induced eddy currents. This property is of great importance in vacuum applications because any heat generated on the rotor must be removed by radiation transfer to the housing (rather than by convection as in non-vacuum AMB systems or conduction as in rolling element bearing systems): there is a high premium on rotor losses. The advantage of four-pole radial bearings, as illustrated in figures 7 and 8, is the fact that two pole pairs each can be assigned to the Cartesian coordinates x and y which are often used in mechanics.

To drive the test rig, an electric motor is assembled at the upper shaft end, driven by a variable speed drive in order to test the AVC system at different rotation speeds.

4.2 AVC performance

The implemented control algorithm under the structure depicted in figure 4 consists of a cascade control loop where the master controller is a PID and the slave is a backstepping algorithm. Such adaptive cascade structure is based in the gain scheduling technique for which two parameters are taken into account. The PID gain K_p of the master controller and the backstepping parameter P_2 shown in figures 9 and 10 respectively.

The on-line selection of such mentioned parameter values, which are applied on updating the control algorithm, obeys to the fact that the values of both parameters are sensible to rotor speed changes. For low rotating speeds, it has been experimentally determined a set of values as function of the shaft rotation speed under a satisfactory performance criterion on the basis of an accepted dynamic response of the control system at different speeds into the operational range of ($0 < \omega < 50$ rad/sec.).

In order to illustrate the dynamic performance of the vibration attenuation controller, some results among a lot of them are selected. The time response of the shaft under some tolerable unbalance is presented. The tests have been carried out at different speeds under the same conditions.

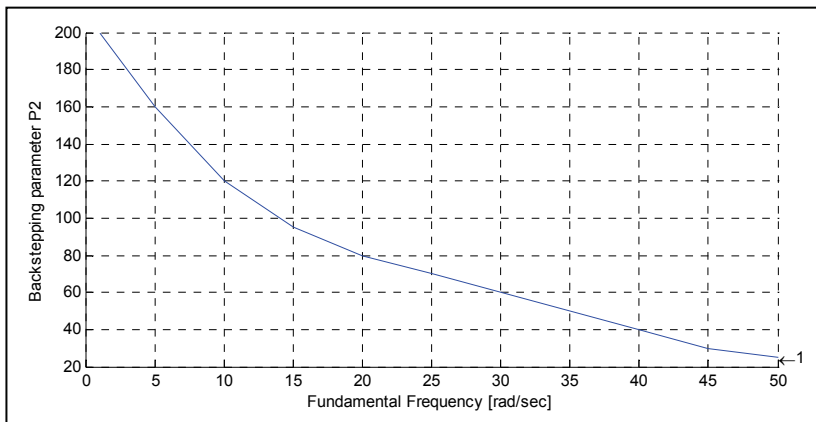


Fig. 9. The set of acceptable values for parameter P_2 of the backstepping algorithm as function of the fundamental vibration frequency located near the measured radial magnetic bearing.

Figures 11, 12 and 13 shows the control current applied to the magnetic coils scheduled by the adaptive procedure as function of the shaft rotation speed. Such control currents are scheduled by the cascade or Backstepping control algorithm. In figures 14, 15 and 16 it is shown the spectrum analyzer layout for the same rotation speeds, and in figures 17, 18 and 19 it is shown the shaft radial position as function of the rotation speed.

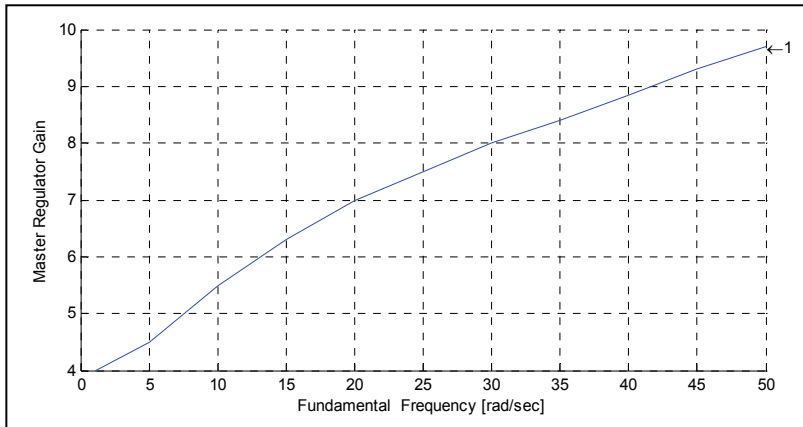


Fig. 10. The set of acceptable values for parameter K_p of the Master controller as function of the fundamental vibration frequency.

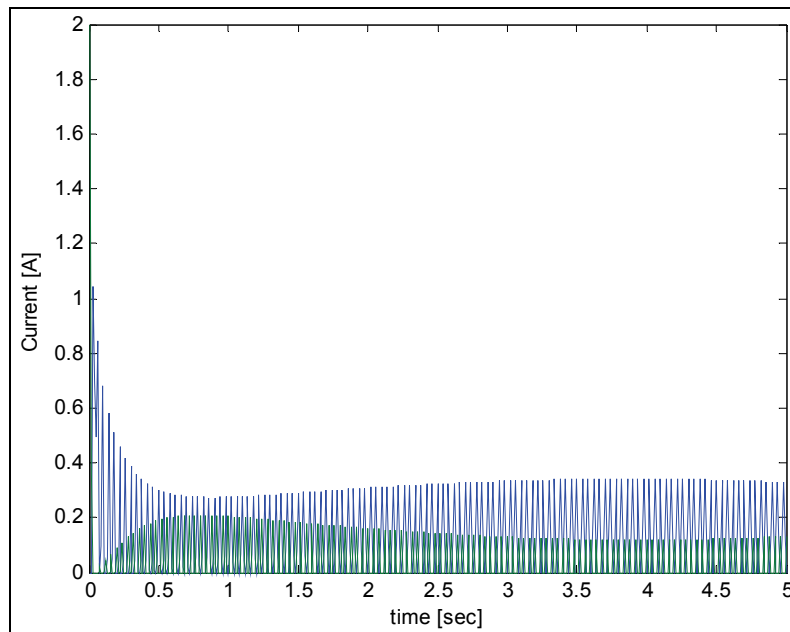
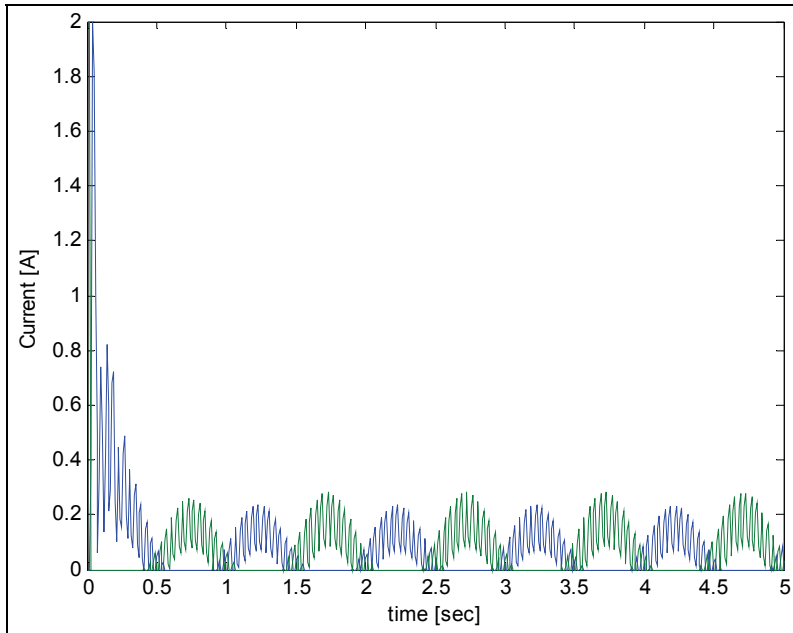
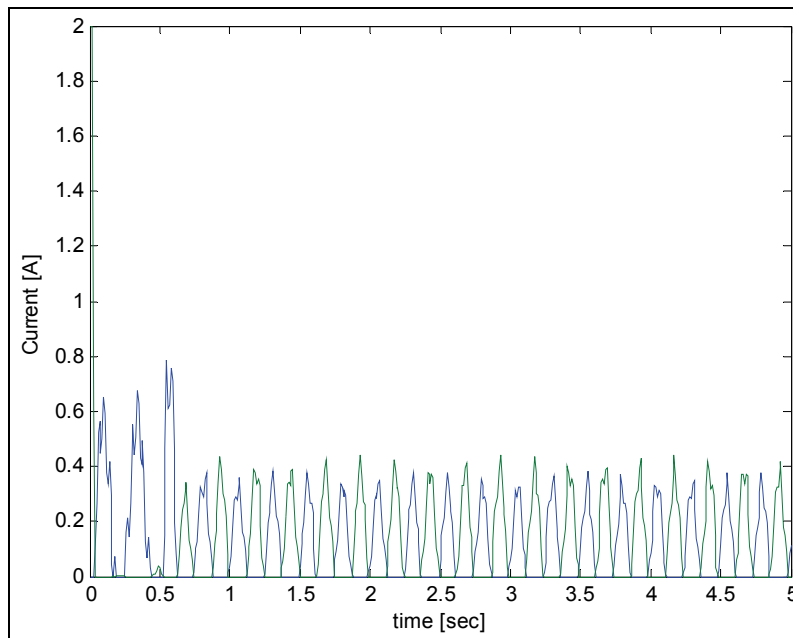


Fig. 11. Control current at $\omega=6.28$ rad/sec

Fig. 12. Control current at $\omega=25.12$ rad/secFig. 13. Control current at $\omega=50.24$ rad/sec

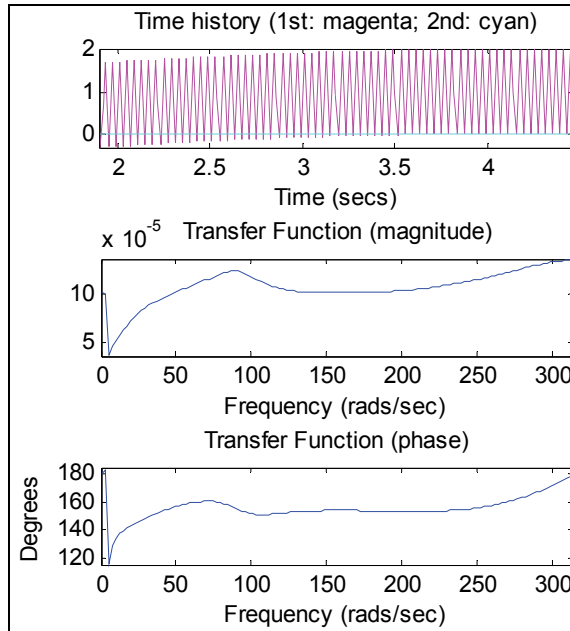


Fig. 14. Spectrum analyzer layout with $\omega=6.28$ rad/sec

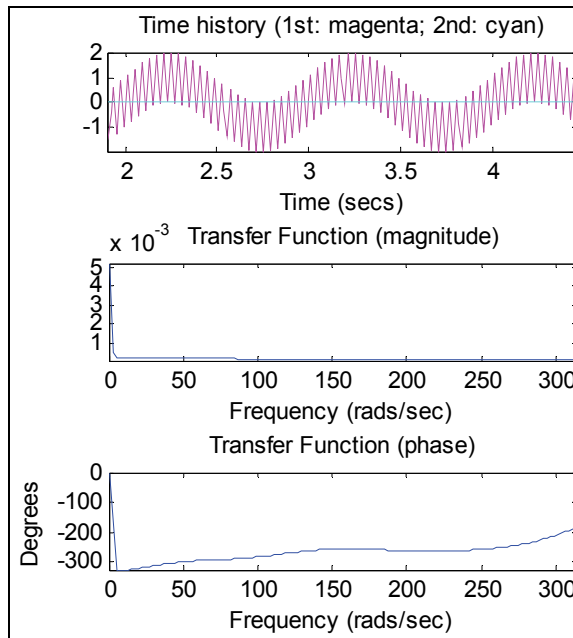


Fig. 15. Spectrum analyzer layout with $\omega=25.12$ rad/sec

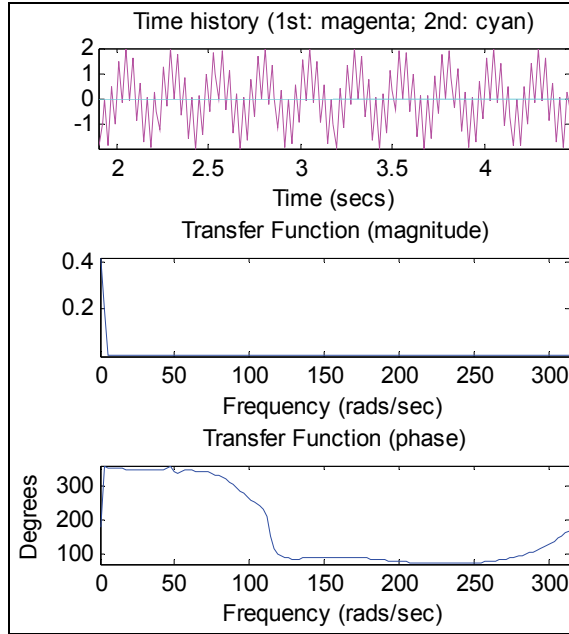


Fig. 16. Spectrum analyzer layout with $\omega=50.24$ rad/sec

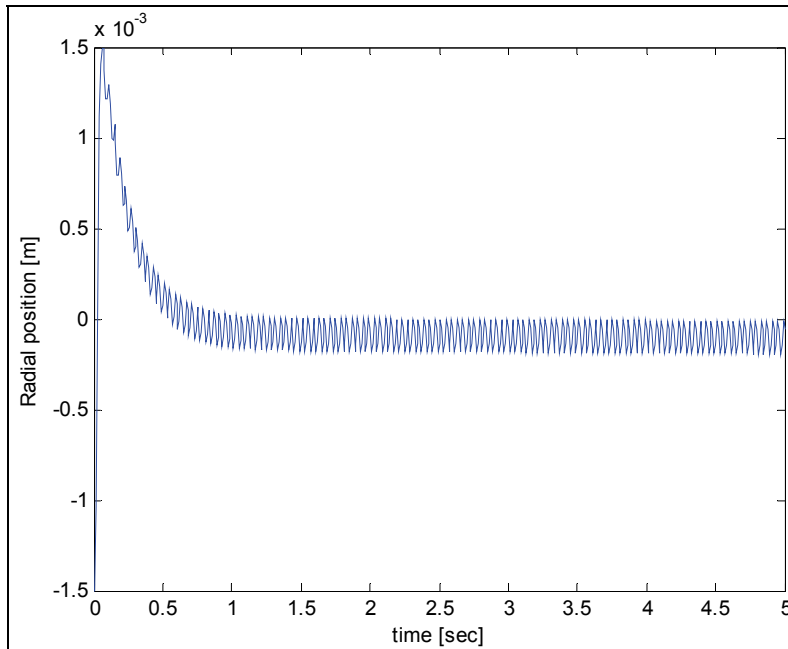


Fig. 17. Shaft radial position at $\omega=6.28$ rad/sec

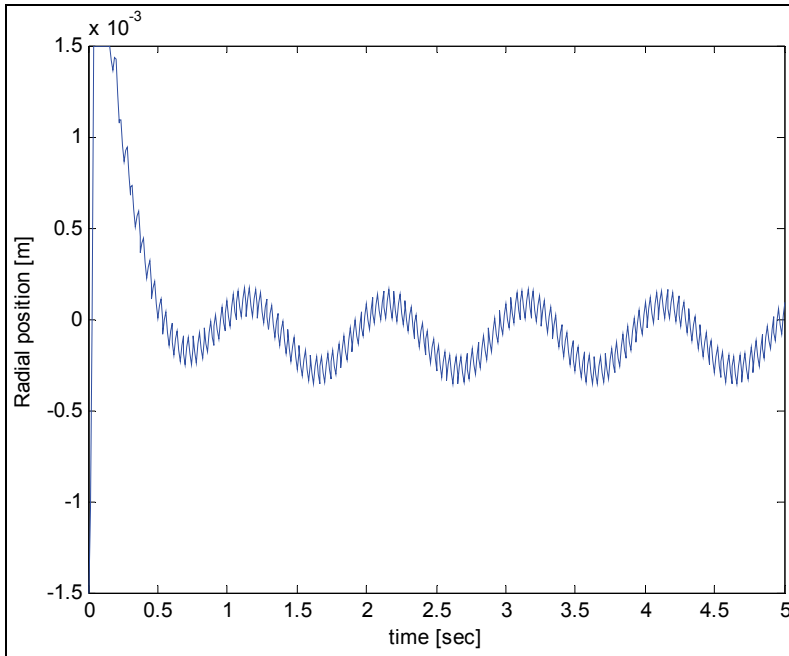


Fig. 18. Shaft radial position at $\omega=25.12$ rad/sec

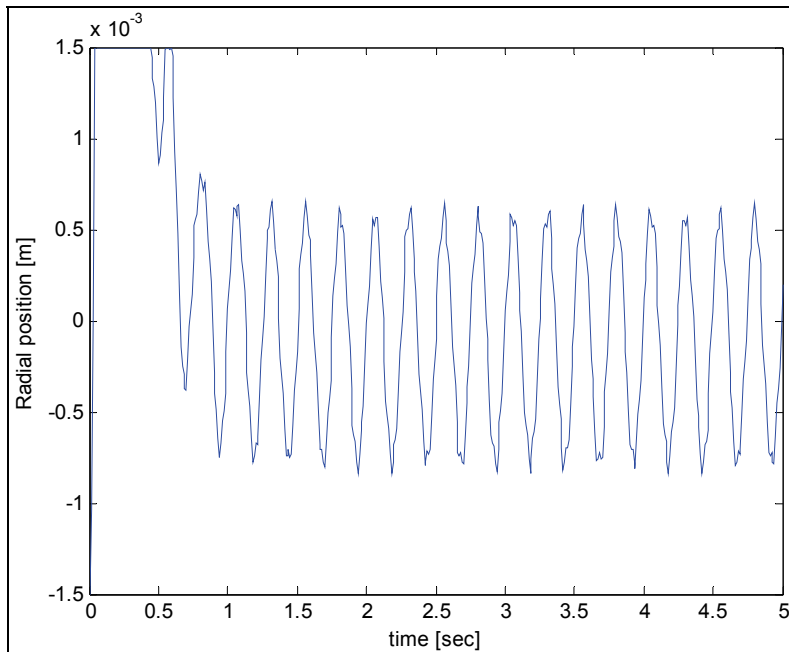


Fig. 19. Shaft radial position at $\omega=50.24$ rad/sec

4.2 Discussion of results

In spite of the fact that Backstepping design techniques has the drawbacks inherent to model based techniques, the most relevant characteristic of such control strategy is the inherent capacity to reject load disturbances under some tolerable modelling error. Furthermore, it has been shown by simple inspection of the results that the capacity of the control strategy to disturbances rejection, increases as function of the proper adjustment values of the parameter K_p at the PID controller and parameter P_2 of the Backstepping algorithm. Parameter P_1 doesn't exhibit such property. In fact, the influence on the value of P_1 on the vibration attenuation is irrelevant. On the basis of the developed work, the coupled dynamics of the test rig which includes the bed plate or platform and the Jeffcott type rotor, a robust backstepping controller for vibration isolation is derived as results of the experimental work. The results of the analysis of the achieved information show that the control strategy can effectively attenuate low frequency vibrations in two DOF. Meanwhile, to vibrations with time-varying parameters in different directions, vibration isolation performance can also be improved. The actual values of the payload through vibration isolation are greatly impacted by the parameter P_2 of the backstepping algorithm and the master controller gain K_p in the case of a cascade structure. Therefore, in order to enhance the vibration isolation performance, the gain K_p and the parameter P_2 should be carefully chosen in order to satisfy the required performance under different operating conditions. According to such idea, a gain scheduling strategy has been successfully applied. The range of useful values for K_p and P_2 experimentally determined, are such that $4 < K_p < 10$, and $25 < P_2 < 220$ as shown respectively in figures 9 and 10. The validity of such results is into the range of low rotational speeds, which for this test rig approaches a maximum speed of 50 rad/sec.

Some important influence factors of vibration isolation are considered in the cascade backstepping design procedure, such as the inclination of the test rig, the rotational speed changes, the inherent uncertainties including modelling errors and the base plate vibration conditions obviously restricted to some limits experimentally determined. Thus, the robust backstepping control method can fulfil the requirements of a vibration isolation alternative for a variety of practical applications.

4.3 Conclusions

A feedback control under a cascade structure composed by a gain scheduling based adaptive PID master controller associated to a gain scheduling based adaptive Backstepping controller has been implemented. In such a cascade control structure, the PID master controller is responsible for the reference or desired trajectory generation and the radial position, while the slave backstepping controller contributes to the rotor global stabilization and vibration suppression or attenuation.

Such a control strategy fulfils the two following objectives:

- a. Radial position control of the shaft by means of active magnetic bearings, and
- b. Vibration attenuation by active vibration control using the same actuators as for active magnetic bearing control.

With regard to the designed test rig mechanical structure, it must be taken into account that the absorbed vibration is transferred by the actuators to the base plate or stator. Consequently, in order to absorb the shaft vibration modes into the range of operational

speeds, the stator mass should be several times greater (in this case, ten times the mass of the stator bed plate) than the rotor mass.

Gain scheduling based adaptation as function of vibration frequency and amplitude contributes effectively to the vibration attenuation of rotor dynamics into the range of low rotation speeds $0 < \omega < 50$ rad/sec.

It has been shown experimentally that the vibration reduction is significant for rotors with low external damping. However, in heavy rotating machines, very large forces would be required and electromagnet based actuators under such conditions are not effective.

Gain scheduling adaptation as function of the vibration characteristics is very effective at low rotation speeds, and outside the range of resonant frequencies. Although it can be applied to attenuate resonant frequencies, obviously it is not so effective, because centrifugal forces are very large, and actuators have not been designed to compensate so large forces. To avoid resonant induced vibration, the rig structure must be designed so that resonant frequencies are outside of the operational rotation speeds.

Since a great variety of control algorithms have been applied along the last three decades of practical implementations, the experiences show that the effectiveness of a single PD or PID is comparable to sophisticated control algorithms such the backstepping one.

5. Acknowledgments

This work has been partially supported by the XUNTA DE GALICIA under the grant DPI 1 IN825N cod_web:772.

6. References

- B. Shafai, S. Beale, P. LaRocca, and E. Cusson, (1994), "Magnetic Bearing Control Systems and Adaptive Forced Balancing", *IEEE Control Systems*, Volume 14, No. 2, pp. 4-13.
- C.R. Burrows and M.N. Sahinkaya, (1983), "Vibration Control of Multi-Mode Rotor-Bearing Systems", *Proceedings of the Royal Society of London*, Vol. 386, pp. 77-94.
- C.R. Burrows, M.N. Sahinkaya, and S. Clements, (1989) "Active Vibration Control of Flexible Rotors: an Experimental and Theoretical Study", *Proceedings of the Royal Society of London*, Vol. 422, pp. 123-146.
- Francesc Pozo, Fayçll Ikhouane, Gisela Pujol, José Rodellar, (2006), "Adaptive Backstepping Control of Hysteretic Base-Isolated Structures", *Journal of Vibration and Control*. 2006; 12: 373-394
- F. Matsumura, M. Fujita, and K. Okawa, (1990), "Modeling and Control of Magnetic Bearing Systems Achieving a Rotation Around the Axis of Inertia", *Proceedings of the 2nd International Symposium on Magnetic Bearings*, July 12-14, 1990, Tokyo, Japan.
- Gerhard Schweitzer, Eric H. Maslen Editors, (2009), "Magnetic Bearings: Theory, Design, and Application to Rotating Machinery", DOI 10.1007/978-3-642-00497-1, Springer Dordrecht Heidelberg London New York
- Guang Lia, Amir Khajepour, (2005), "Robust control of a hydraulically driven flexible arm using backstepping technique", *Journal of Sound and Vibration* 280, 759 - 775

- Hassan K. Khalil (2002). *Nonlinear Systems*. Prentice-Hall, third edition, ISBN: 0-13-067389-7, Chap 4, pp 111-174.
- H. Habermann and M. Brunet, (1984), "The Active Magnetic Bearing Enables Optimum Damping of Flexible Rotors", ASME Paper 84-GT-117, 1984.
- Knospe C. R., R.W. Hope, S.J. Fedigan, and R.D. Williams, (1993), "Adaptive On-Line Rotor Balancing Using Digital Control", *Proceedings of MAG '93 Magnetic Bearings, Magnetic Drives, and Dry Gas Seals Conference*, Technomic Publishing, Lancaster, PA, July 1993.
- Krstic, M., I. Kanellakopoulos, and P. Kokotovic, (1995). *Nonlinear and Adaptive Control Design*. John Wiley & Sons, Inc. New York, NY, USA, (1995).
- Krstic M., and H. Deng (1998). *Stabilization of Nonlinear Uncertain Systems*, (Springer Verlag, Berlin).
- LaSalle J. P., (1960), "Some extensions of Liapunov's second method". *IRE Trans. Circuit Theory*, Vol. 7, pp. 520-527.
- LaSalle J. P., (1968), "Stability theory for ordinary differential equations", *Journal of Differential Equations* vol. 4, , 57-65.
- Qinglei Hu, (2009), "Robust adaptive backstepping attitude and vibration control with L2-gain performance for flexible spacecraft under angular velocity constraint", *Journal of Sound and Vibration* 327 , 285-298
- R. Larssonneur and R. Herzog, (1994), "Feedforward compensation of Unbalance: New Results", IUTAM Symposium, Bath, UK, September 1994.
- R. Larssonneur, (1998), "Design and Control of Active Magnetic Bearing Systems for High Speed Rotation", PhD Thesis, Swiss Federal Institute of Technology, ETH Zurich, Switzerland, June, 1998.
- Sontag E. D., (1989), A "universal" construction of Artstein's theorem on nonlinear stabilization". *Systems and Control Letters*, Vol.13 (2), pp.117-123, 1998.
- Sontag E.D., and Sussman, (1998) "Further comments on the stabilization of the angular velocity of a rigid body", *Systems and Control Letters*, Vol. 12, pp. 213-217, 1998.
- T. Higuchi, M. Otsuka, T. Mizuno, and T. Ide, (1990), "Application of Periodic Learning Control with Inverse Transfer Function Compensation in Totally Active Magnetic Bearings", *Proceedings of the 2nd International Symposium on Magnetic Bearings*, July 12-14, 1990, Tokyo, Japan.
- T. Higuchi, T. Mizuno, and M. Tsukamoto, (1990), "Digital Control System for Magnetic Bearings with Automatic Balancing", *Proceedings of the 2nd International Symposium on Magnetic Bearings*, July 12-14, 1990, Tokyo, Japan.
- Tao Yang, Jia Ma, Zeng-Guang Hou, Min Tan (2009), "Robust backstepping control of active vibration isolation using a Stewart platform", *2009 IEEE Int. Conf. on Robotics and Automation*, Volume , Issue , 12-17 May 2009 Page(s):1788 - 1793, 978-1-4244-2789-5/09/\$25.00 ©2009 IEEE, Digital Object Identifier:10.1109/ROBOT.2009.5152486, Kobe, Japan, May 12-17, 2009.
- V. Mañosa, F. Ikhouane, J. Rodellar, (2005), "Control of uncertain non-linear systems via adaptive backstepping", *Journal of Sound and Vibration* 280 657-680

- Yoshizawa, T., (1966), "*Stability theory in Liapunov's second method*", Mathematical Society of Japan, <http://www.ams.org/mathscinet-getitem?mr=MR0208086>
- Yoshizawa, T., (1966), "Stability and existence of a periodic solution", *J. Differential Equations*, Vol. 1 (1968), 121-129,
<http://www.ams.org/mathscinet-getitem?mr=MR0222396>

Model Independent Vibration Control

Jing Yuan

*The Hong Kong Polytechnic University
Hong Kong, P. R. China*

1. Introduction

Active vibration control (AVC) and active noise control (ANC) are closely related research areas sharing many common approaches. Feedforward control is one of the common approaches if the primary signal is available as the reference signal (Nelson & Elliott, 1992, Hansen & Snyder, 1997). Parameters of feedforward controllers can be adjusted according to path transfer functions from actuators to error sensors, to generate destructive interference at sensed locations. The filtered-x least mean squares (FxLMS) algorithm is a popular tool for such systems.

In order for the FxLMS to be stable, phase errors in the secondary path model must be less than 90° in the entire frequency range (Snyder & Hansen, 1990, Bjarnason, 1995, Vandrey et al., 2003). Since path models are sensitive to variations of loading and boundary conditions, many researchers integrate online path modeling with AVC/ANC systems to keep path models as accurate as possible. The results are model independent feedforward controllers (MIFCs), most of which inject invasive probing signals into vibration systems for accurate online path modeling (Goodwin & Sin, 1984, Eriksson & Allie, 1989, Qiu & Hansen, 2001). Some researchers try to avoid the probing signals by controller perturbations (Nowlin et al., 2000, Kim & Swanson, 2005). Unfortunately controller perturbations also cause invasive effects to noise/vibration fields.

In this chapter, a noninvasive MIFC (NMIFC) is recommended for broadband vibration control. It has two important features. F1: the NMIFC is stable without introducing any invasive effects, such as probing signals or controller perturbations, into the vibration system; and F2: the NMIFC is applicable to vibration systems with either finite impulse response (FIR) or infinite impulse response (IIR) path models.

Feature F1 of the NMIFC is intended to solve the problem of invasive effects in most existing MIFC systems. This is made possible by replacing the FxLMS with online controller optimization. The NMIFC operates two online tasks. One is online path modeling and the other is online controller optimization. Theoretical analysis is presented to discuss the convergence of the two online tasks. The coupling effects of the two online tasks make it possible for the NMIFC to be stable without introducing any invasive effects to the vibration system.

Feature F2 is targeted at the fact that some vibration systems are well-damped whose path transfer functions may be approximated by FIR filters with negligible errors; others are lightly-damped whose path transfer functions must be approximated by IIR filters. For broadband control applications in lightly-damped vibration systems, it is more difficult to implement MIFC systems, since most available MIFC systems are based on FIR path models.

Mismatches between FIR models and real IIR path transfer functions degrade control performance or even threaten closed-loop stability.

In the related ANC research, some ANC systems adopt IIR path models or IIR controllers (Eriksson, 1991, Lu et al., 2003). Adaptation of an IIR filter is a nonlinear process with multiple stationary points. There is no guarantee that an adaptive IIR filter will converge to its global optimal (Regalia, 1995). Adaptive AVCs, with FIR or IIR path models, have the same problem of depending on invasive effects as persistent excitations in vibration systems to ensure accurate parameter estimation and stable operation.

The NMIFC system is proposed to solve the above existing problems. Mathematical analysis is presented to explain the two features of the NMIFC; and how it is possible to achieve the control objectives. Experimental results are presented to verify the performance of NMIFC when it is applied to well- or lightly-damped vibration systems with FIR or IIR path models.

2. Background information

Mathematically, propagation of vibration waves in flexible structures can be described with transfer functions. When an external disturbance $f(z)$ is applied to a flexible structure at point A, its effect will propagate to other points of the structure. If one measures the vibration effect at point B and denotes the signal by $w(z)$, then there must exist a path transfer function $T(z)$, such that $w(z)=T(z)f(z)$. Propagation of vibration signals from disturbance $f(z)$ to measured signal $w(z)$ is mathematically modeled with a path model or a path transfer function $T(z)$.

2.1 Control objective

Let $P(z)$ and $S(z)$ denote, respectively, the primary and secondary path transfer functions. These are transfer functions from the primary/secondary sources to the error sensor respectively. If the primary signal, which is actually the disturbance signal, is available as the reference $r(z)$, the actuation signal $u(z)=C(z)r(z)$ can be synthesized by a controller with transfer function $C(z)$ in order to generate destructive interference at sensed locations. Mathematically, this is described by

$$e(z)=P(z)r(z)+S(z)u(z)=[P(z)+S(z)C(z)]r(z). \quad (1)$$

In a lightly-damped vibration system, path transfer functions are IIR rational functions, such as $P(z)=N_p(z)/D(z)$ and $S(z)=N_s(z)/D(z)$. These transfer functions have a common denominator polynomial $D(z)$ whose roots are eigenvalues of the vibration system (Vipperman & Burdisso, 1995). In lightly-damped vibration systems, eigenvalues represent resonant frequencies. In well-damped vibration systems, resonant effects are not significant due to strong damping effects, which implies reasonably accurate approximation of $D(z)=1$ such that path transfer functions can be approximated by FIR filters with negligible errors. It is desired that a vibration controller is able to work in either well- or lightly-damped vibration system by simply switching between a specific $D(z)=1$ and an arbitrary $D(z)$ with a conservatively estimated degree. This is feature F2 of the NMIFC system.

For broadband control applications, power spectral density (PSD) of reference $r(z)$ is almost constant in the entire frequency range. The objective of feedforward control is to minimize the norm of $P(z)+S(z)C(z)$, which requires accurate knowledge of $P(z)$ and $S(z)$. If either $P(z)$ or $S(z)$ is not available accurately, $C(z)$ may not be properly designed and the intended

destructive interference may become constructive interference to enhance vibration instead of suppressing it as the actuators keep on pumping energy into the vibration system. Unfortunately, both $P(z)$ and $S(z)$ are not available exactly in most practical applications. An important problem in feedforward controller design is to integrate online path modeling and obtain accurate estimate of at least $S(z)$, if the FxLMS algorithm is adopted for $C(z)$ tuning.

2.2 Approaches

The existing problem with FxLMS is the requirement that phase errors in the estimate of $S(z)$ must be less than 90° in the entire frequency range (Snyder & Hansen, 1990, Bjarnason, 1995, Vandrey et al., 2003). How to obtain accurate estimate of $S(z)$ with phase errors less than 90° in the entire frequency range is still not solved completely in available online path modeling algorithms. Some sort of invasive effects, either probing signals (Goodwin & Sin, 1984, Eriksson & Allie, 1989, Qiu & Hansen, 2001) or controller perturbations (Nowlin et al., 2000, Kim & Swanson, 2005), must be introduced in a MIFC system as persistent excitations to ensure accurate online estimation of path transfer functions in existing system identification techniques. The NMIFC is intended to avoid any invasive effects. It estimates both $P(z)$ and $S(z)$ simultaneously and replaces the FxLMS with an online controller optimization task. In adaptive controllers with online system identification (path modeling) tasks, parameters of transfer functions are expressed in regressions in order to be identified with the least squares (LS) methods. The NMIFC system also adopts this approach. Equation (1) is expressed in the time domain as a discrete-time regression

$$e_t = -\sum_{k=1}^{m_r} d_k e_{t-k} + \sum_{k=0}^m p_k r_{t-k} + \sum_{k=0}^m s_k u_{t-k} \tag{2}$$

where $\{d_k\}$, $\{p_k\}$ and $\{s_k\}$ are coefficients of polynomials $D(z)$, $N_p(z)$ and $N_s(z)$ to be identified with the LS methods. Using coefficient vector $\theta^T = [-d^T, p^T, s^T]$ and regression vector $\varphi_t^T = [e_{t-1}, e_{t-2}, \dots, e_{t-m_r}, r_t, r_{t-1}, \dots, r_{t-m}, u_t, u_{t-1}, \dots, u_{t-m}]^T$, one may re-write Eq. (2) as an inner product

$$e_t = \theta^T \varphi_t = -d^T x_t + p^T v_t + s^T \phi_t \tag{3}$$

where $x_t = [e_{t-1}, e_{t-2}, \dots, e_{t-m_r}]^T$, $v_t = [r_t, r_{t-1}, \dots, r_{t-m}]^T$, and $\phi_t = [u_t, u_{t-1}, \dots, u_{t-m}]^T$. If the NMIFC system is applied to well-damped vibration systems with FIR path models, there is no need to estimate $D(z)=1$ and Eq. (3) becomes

$$e_t = \theta^T \varphi_t = p^T v_t + s^T \phi_t \tag{4}$$

with a reduced data vector $\varphi_t = [r_t, r_{t-1}, \dots, r_{t-m}, u_t, u_{t-1}, \dots, u_{t-m}]^T$. The NMIFC system depends on two online tasks to ensure stability without introducing any invasive effects. Task 1 is a recursive least squares (RLS) path modeling process. Task 2 is a controller optimization process.

2.3 Online task 1

In task 1, $D(z)$, $N_p(z)$ and $N_s(z)$ are estimated as $\hat{D}(z)$, $\hat{N}_p(z)$ and $\hat{N}_s(z)$ respectively. The parameter vector is estimated as $\hat{\theta}^T = [-\hat{d}^T, \hat{p}^T, \hat{s}^T]$, where components of \hat{d} , \hat{p} and \hat{s} are coefficients of $\hat{D}(z)$, $\hat{N}_p(z)$ and $\hat{N}_s(z)$ respectively. The estimation residue is

$$\varepsilon_t = e_t - \hat{\theta}^T \varphi_t = \Delta \theta^T \varphi_t = -\Delta d^T x_t + \Delta p^T v_t + \Delta s^T \phi_t \tag{5}$$

where $\Delta\theta = \theta - \hat{\theta}$, $\Delta d = d - \hat{d}$, $\Delta p = p - \hat{p}$ and $\Delta s = s - \hat{s}$. If the NMIFC is applied to well-damped vibration systems with FIR path models and $D(z)=1$, the parameter vector is estimated as $\hat{\theta}^T = [\hat{p}^T, \hat{s}^T]$ because there is no need to estimate $D(z)$. In that case, Eq. (5) becomes

$$\varepsilon_t = e_t - \hat{\theta}^T \varphi_t = \Delta\theta^T \varphi_t = \Delta p^T v_t + \Delta s^T \phi_t, \quad (6)$$

In either case, the objective of task 1 is to drive $\varepsilon_t \rightarrow 0$, which is achievable with available system identification algorithms. A simple RLS algorithm will be adopted with convergence of $\varepsilon_t \rightarrow 0$ explained in Section 3.

2.4 Online task 2

In task 2, partial online estimates, \hat{p} and \hat{s} , are used to optimize controller transfer function $C(z)$ by minimizing $\|\hat{N}_p(z) + \hat{N}_s(z)C(z)\|_2$. In broadband noise control, power spectral density of $r(z)$ is almost constant in the entire frequency range. Minimizing $\|\hat{N}_p(z) + \hat{N}_s(z)C(z)\|_2$ is equivalent to minimizing the power spectrum of

$$\mu_t = \sum_{k=0}^m \hat{p}_k r_{t-k} + \sum_{k=0}^m \hat{s}_k u_{t-k} = \hat{p}^T v_t + \hat{s}^T \phi_t. \quad (7)$$

Several methods will be presented in Section 4 to minimize $\|\hat{N}_p(z) + \hat{N}_s(z)C(z)\|_2$. This is an important step in the NMIFC system to ensure stable operation without introducing any invasive effects into the system.

2.5 Expected results

One may use $\mu_t = \hat{p}^T v_t + \hat{s}^T \phi_t$, Eqs. (3) and (5) to derive

$$\left| e_t + \hat{d}^T x_t \right| = \left| \varepsilon_t + \mu_t \right| \leq \left| \varepsilon_t \right| + \left| \mu_t \right|. \quad (8)$$

If the NMIFC is applied to well-damped vibration systems with FIR path models and $D(z)=1$, Eq. (8) becomes

$$\left| e_t \right| = \left| \varepsilon_t + \mu_t \right| \leq \left| \varepsilon_t \right| + \left| \mu_t \right|. \quad (9)$$

Task 2 makes the NMIFC system significantly different from those MIFC systems that depend on FxLMS for controller adaptation. If the FxLMS algorithm is adopted to update controller transfer function $C(z)$, then phase errors in online estimate of $S(z)$ must be less than 90° in the entire frequency range. Invasive effects are inevitable to ensure accurate online estimation of $S(z)$ (Goodwin & Sin, 1984, Eriksson & Allie, 1989, Qiu & Hansen, 2001, Nowlin et al., 2000, Kim & Swanson, 2005). In Section 5, it will be explained why replacing the FxLMS with task 2 is able to ensure stability without introducing any forms of invasive effects.

3. Parameter adaptation

Driving the convergence of $\varepsilon_t = \Delta\theta^T \varphi_t \rightarrow 0$ is the objective of online task 1, which is achievable with available system identification algorithms. In this chapter, a simple RLS algorithm is used to explain how to estimate the parameter vector

$$\hat{\theta}_{t+1} = \hat{\theta}_t + \frac{\varepsilon_t \varphi_t}{\gamma + \varphi_t^T \varphi_t}, \quad (10)$$

where $0 < \gamma$ is a positive constant. The parameter is introduced to avoid the possibility that $\varphi_t^T \varphi_t$ may become too small at some instants to effect stable adaptation.

To see the convergence of $\varepsilon_t = \Delta \theta^T \varphi_t \rightarrow 0$, one may use positive definite function $V(t) = \Delta \theta_t^T \Delta \theta_t$. Similar to identity $a^2 - b^2 = (a-b)(a+b)$, one can see that

$$V(t+1) - V(t) = (\Delta \theta_{t+1} - \Delta \theta_t)^T (\Delta \theta_{t+1} + \Delta \theta_t). \quad (11)$$

Substituting Eq. (10) and $\Delta \theta = \theta - \hat{\theta}$, one obtains

$$\Delta \theta_{t+1} - \Delta \theta_t = \hat{\theta}_t - \hat{\theta}_{t+1} = \frac{-\varepsilon_t \varphi_t}{\gamma + \varphi_t^T \varphi_t}, \quad (12)$$

and

$$\Delta \theta_{t+1} + \Delta \theta_t = 2\theta - \hat{\theta}_t - \hat{\theta}_{t+1} = 2\Delta \theta_t - \frac{\varepsilon_t \varphi_t}{\gamma + \varphi_t^T \varphi_t}. \quad (13)$$

One may further substitute Eqs. (12) and (13) into Eq. (11) and derive

$$V(t+1) - V(t) = \frac{-\varepsilon_t \varphi_t^T}{\gamma + \varphi_t^T \varphi_t} \left(2\Delta \theta_t - \frac{\varepsilon_t \varphi_t}{\gamma + \varphi_t^T \varphi_t} \right). \quad (14)$$

Since $\varepsilon_t \varphi_t^T \Delta \theta_t = \varepsilon_t^2$, Eq. (14) is equivalent to

$$V(t+1) - V(t) = -\frac{\varepsilon_t^2 (2\gamma + \varphi_t^T \varphi_t)}{(\gamma + \varphi_t^T \varphi_t)^2} \leq -\frac{\varepsilon_t^2}{\gamma + \varphi_t^T \varphi_t} \leq 0. \quad (15)$$

It means monotonous decrease of $V(t) = \Delta \theta_t^T \Delta \theta_t$ until $\varepsilon_t \rightarrow 0$. The objective of online task 1 is therefore achievable with available RLS algorithms.

Mathematically, $\varepsilon_t = \Delta \theta^T \varphi_t \rightarrow 0$ does not mean $\Delta \theta \rightarrow 0$ unless φ_t is persistently excited (Goodwin & Sin, 1984). In those MIFC systems which depend on FxLMS to update controllers, invasive effects are introduced into the system as persistent excitations to ensure $\Delta \theta \rightarrow 0$ and accurate estimation of $S(z)$. In the NMIFC system, online task 2 is introduced to replace the FxLMS. It is an important measure to relax the phase error requirement on $S(z)$.

4. Controller optimization

In task 2, controller optimization would be a simple task if $\hat{N}_s(z)$ is minimum phase (MP) whose roots have magnitudes all less than 1. In that case, an IIR filter $C(z) = -\hat{N}_s^{-1}(z)\hat{N}_p(z)$ will achieve $\mu_t = 0$. In vibration systems, continuous-time secondary path transfer functions are sure to be MP only if the sensors collocate with the actuators. Even in case of sensor-actuator collocation, the discrete-time version of secondary transfer function and its online estimate may still be non-minimum phase (NMP). In many vibration control applications, sensors do not necessarily collocate with actuators. The secondary path transfer functions

are very likely to be NMP. Magnitudes of some roots of a NMP polynomial are equal to or larger than 1. Task 2 becomes complicated when $\hat{N}_s(z)$ is NMP with an unstable $N_s^{-1}(z)$. A stable feedforward controller $C(z)$ must be sought to cancel the effects of $\hat{N}_s^{-1}(z)$ as much as possible. The NMIFC system is prepared for the worst case when $N_s(z)$ is NMP.

4.1 Optimal IIR controller

Applying available mathematical tools, it is possible to minimize

$$\left\| \hat{N}_p(z) + \hat{N}_s(z)C(z) \right\|_2 = \left\| \hat{N}(z) \right\|_2, \quad (16)$$

to the best extent by an optimal IIR controller with even if $N_s(z)$ is NMP. The NMIFC system will check roots of $\hat{N}_s(z)$ to split $\hat{N}_s(z) = N_m(z)N_n(z)$. In this case, $N_m(z)$ is a polynomial that includes those roots of $\hat{N}_s(z)$ with magnitudes less than 1 while $N_n(z)$ is another polynomial that includes the rest roots of $\hat{N}_s(z)$. Mathematically, $N_m(z)$ is the MP part of $\hat{N}_s(z)$ such that $N_m^{-1}(z)$ is stable; $N_n(z)$ is the NMP part of $\hat{N}_s(z)$ such that $N_n^{-1}(z)$ is unstable. The strategy is to cancel the MP part and avoid the NMP part of $\hat{N}_s(z)$.

To implement this strategy, the NMIFC system obtains a MP polynomial $M(z)$ by using coefficients of $N_n(z)$ in the reversed order. It can be shown that $A(z) = N_n(z)/M(z)$ is a stable all-pass filter (Regalia, 1995) and $\|A(z)\|_2 = \text{constant}$. With the help of $\hat{N}_s(z) = N_m(z)N_n(z)$, one may express $\hat{N}_s(z)$ as a product of $A(z)$ with a MP polynomial

$$\hat{N}_s(z) = N_n(z)N_m(z) = \frac{N_n(z)}{M(z)}M(z)N_m(z) = A(z)B(z) \quad (17)$$

where $B(z) = M(z)N_m(z)$ is MP. Equation (17) is used for substitution into Eq. (16). The result reads

$$\left\| \hat{N}_p(z) + \hat{N}_s(z)C(z) \right\|_2 = \left\| \hat{N}_p(z) + A(z)B(z)C(z) \right\|_2 \quad (18)$$

The above equation may be rewritten to

$$\begin{aligned} \left\| \hat{N}_p(z) + \hat{N}_s(z)C(z) \right\|_2 &= \|A(z)\|_2 \left\| A^{-1}(z)\hat{N}_p(z) + B(z)C(z) \right\|_2 \\ &\propto \left\| A^{-1}(z)\hat{N}_p(z) + B(z)C(z) \right\|_2 \end{aligned} \quad (19)$$

where $\|A(z)\|_2 = \text{constant}$ has been substituted. The next step is to apply the long-division to Eq. (19) and obtain

$$A^{-1}(z)\hat{N}_p(z) = \frac{M(z)\hat{N}_p(z)}{N_n(z)} = \frac{N_r(z)}{N_n(z)} + N_q(z) \quad (20)$$

where $N_q(z)$ and $N_r(z)$ are the quotient and remainder polynomials. Mathematically, $N_r(z)/N_n(z)$ and $N_q(z)$, on the right hand side of Eq. (20), are orthogonal to each other in the H_2 norm sense such that Eq. (19) may be expressed as

$$\begin{aligned} \left\| \hat{N}_p(z) + \hat{N}_s(z)C(z) \right\|_2 &\propto \left\| A^{-1}(z)\hat{N}_p(z) + B(z)C(z) \right\|_2 \\ &= \left\| \frac{N_r(z)}{N_n(z)} \right\|_2 + \left\| N_q(z) + B(z)C(z) \right\|_2. \end{aligned} \tag{21}$$

Since $N_n(z)$ is the NMP part of $\hat{N}_s(z)$, $N_r(z)/N_n(z)$ is unstable and cannot be cancelled by any stable feedforward controller. The best achievable result is to cancel the stable part $\left\| N_q(z) + B(z)C(z) \right\|_2 = 0$ with an optimal IIR controller

$$C_{opt}(z) = -\frac{N_q(z)}{B(z)} = \frac{-N_q(z)}{M(z)N_m(z)}. \tag{22}$$

Any other feedforward controllers only increase the H_2 norm in Eq. (21), which is equivalent to the H_2 norm in Eq. (16), if the controller transfer functions are not given by Eq. (22).

4.2 Sub-optimal FIR controller

The optimal IIR $C(z)$, with transfer function given by Eq. (22), is very computational expensive. In each step of RLS, it involves online root-solving of a potentially high-degree polynomial $\hat{N}_s(z) = N_m(z)N_n(z)$ and many other computations in the polynomial long division of Eq. (20). To avoid heavy online computations, a sub-optimal FIR controller is recommended to minimize Eq. (16).

For simplicity, one may set the degree of $C(z)$ to m . The impulse response of Eq. (16) can be written as

$$\hat{n} = \begin{bmatrix} \hat{n}_0 \\ \hat{n}_1 \\ \vdots \\ \vdots \\ \hat{n}_{2m} \end{bmatrix} = \begin{bmatrix} \hat{p}_0 \\ \hat{p}_1 \\ \vdots \\ \hat{p}_m \end{bmatrix} + \begin{bmatrix} \hat{s}_0 & & & & \\ \hat{s}_1 & \hat{s}_0 & & & \\ \vdots & \hat{s}_1 & \ddots & & \\ \hat{s}_m & \vdots & \ddots & \hat{s}_0 & \\ & \hat{s}_m & \vdots & \hat{s}_1 & \vdots \\ & & \ddots & \vdots & \hat{s}_m \end{bmatrix} \begin{bmatrix} c_0 \\ c_1 \\ \vdots \\ c_m \end{bmatrix} = \hat{b}_p + \hat{N}_s c \tag{23}$$

where $\hat{n} = [\hat{n}_0, \dots, \hat{n}_{2m}]^T$ and $c = [c_0, \dots, c_m]^T$ are coefficient vectors of $\hat{N}(z)$ and $C(z)$. Coefficients of $\hat{N}_s(z)$ are used to construct matrix

$$\hat{N}_s = \begin{bmatrix} \hat{s}_0 & & & & \\ \hat{s}_1 & \hat{s}_0 & & & \\ \vdots & \hat{s}_1 & \ddots & & \\ \hat{s}_m & \vdots & \ddots & \hat{s}_0 & \\ & \hat{s}_m & \vdots & \hat{s}_1 & \vdots \\ & & \ddots & \vdots & \hat{s}_m \end{bmatrix}. \tag{24}$$

According to the Parseval's theorem, minimizing $\|\hat{n}\|_2^2$ is equivalent to minimizing the H_2 norm in Eq. (16). Using Eq. (23), one obtains

$$\hat{n}^T \hat{n} = (\hat{p} + \hat{N}_s c)^T (\hat{p} + \hat{N}_s c) = \hat{p}^T \hat{p} + \hat{p}^T \hat{N}_s c + c^T \hat{N}_s^T \hat{p} + c^T \Pi_s c, \quad (25)$$

where $\Pi_s = \hat{N}_s^T \hat{N}_s$ is the autocorrelation matrix of \hat{N}_s . Let $\psi = \hat{N}_s^T \hat{p}$, one can substitute $c^T \hat{N}_s^T \hat{p} = c^T \Pi_s \Pi_s^{-1} \psi$ into Eq. (25) and derive

$$\hat{n}^T \hat{n} = \hat{p}^T \hat{p} - \rho^T \Pi_s^{-1} \rho + (\Pi_s c + \rho)^T \Pi_s^{-1} (\Pi_s c + \rho). \quad (26)$$

In Eq. (26), vector c only affects $(\Pi_s c + \psi)^T \Pi_s^{-1} (\Pi_s c + \psi)$. Therefore it is possible to force $(\Pi_s c + \psi)^T \Pi_s^{-1} (\Pi_s c + \psi) = 0$ and minimize $\|\hat{n}\|_2^2$ by

$$c = -\Pi_s^{-1} \psi = -\Pi_s^{-1} \hat{N}_s^T \hat{p}. \quad (27)$$

This equation may be used to minimize the FIR controller $C(z)$ in task 2. It is less optimal than the IIR controller given by Eq. (22), but it is the best solution among all possible FIR controllers.

4.3 Economic FIR controller

In many vibration control systems, $N_p(z)$ and $N_s(z)$ are polynomials with high degrees. The dimension of Π_s is $(m \times m)$ if the degree of $C(z)$ is m . Calculation of Π_s still requires significant online computations after each step of RLS. Online solution of Eq. (27) is still expensive, though it is significantly less expensive than Eq. (22).

Alternatively, one may consider an economic FIR controller. Its coefficients are calculated by a recursive algorithm. One may use a positive definite function $O = 0.5 \hat{n}^T \hat{n}$ to study the convergence of the recursive algorithm that updates c and minimizes O . The time derivative of O is given by

$$\dot{O} = -\hat{n}^T \hat{N}_s \dot{c}, \quad (28)$$

where c is the coefficient vector of the FIR controller and Eq. (23) is used to link $d\hat{n}/dt$ to \dot{c} . The above equation suggests a very simple way to modify coefficient vector c . It is given by

$$\dot{c} = -\mu \hat{N}_s^T \hat{n}, \quad \text{or} \quad c_{t+1} = c_t - \mu \hat{N}_s^T \hat{n} \delta t, \quad (29)$$

where μ is a small positive constant and δt is the sampling interval. Combining Eqs. (28) and (29), one obtains $\dot{O} = -\mu \hat{n}^T \Pi_s \hat{n} \leq 0$. Therefore $O = 0.5 \hat{n}^T \hat{n}$ will be minimized by the recursive use of Eq. (29).

The advantage of this solution is to avoid online inverse of Π_s . The method is not able to minimize $O = 0.5 \hat{n}^T \hat{n}$ in every step of identification, though it reduces the computational cost. Mathematically, this solution is equivalent to the sub-optimal solution upon the convergence of Eq. (29).

5. Controller stability

It is time to answer the question why the NMIFC system is able to ensure stability without introducing any invasive effects into the system. Since the NMIFC is applicable to both well- and lightly-damped vibration systems, the answer is given to the respective cases when the NMIFC is applied to the two types of vibration systems.

5.1 Stability in well-damped vibration systems

If the NMIFC system is applied to well-damped vibration systems, path transfer functions are FIR filters with $D(z)=1$. There is no need to estimate $\hat{d}_i = 0$ and the control objective is described by Eq. (9).

On the right hand side of Eq. (9), $\varepsilon_t = \Delta\theta^T \varphi_t$ and $\mu_t = \hat{p}^T v_t + \hat{s}^T \phi_t$ represent two inner products. Online task 1 drives $\varepsilon_t \rightarrow 0$ and online task 2 minimizes $|\mu_t| \approx 0$ respectively. The joined effects of the two online tasks bound $|e_t| \approx 0$ from above, as suggested by Eq. (9). In the analysis of Section 3, no probing signals are required in online task 1. All available system identification algorithms are applicable to driving $\varepsilon_t \rightarrow 0$, which does not imply $\Delta\theta \rightarrow 0$ and the NMIFC system does not require $\Delta\theta \rightarrow 0$ as well. This is an important difference between the NMIFC and those feedforward controllers which are based on the FxLMS algorithm.

Figure 1 presents an inner product illustration of why the NMIFC is stable when its online path modeling process does not apply any measures to ensure $\Delta\theta \rightarrow 0$. It is assumed that online tasks in the NMIFC system have converged to a steady state where $\varepsilon_t \rightarrow 0$ and $|\mu_t| \approx 0$, but $\Delta\theta \neq 0$.

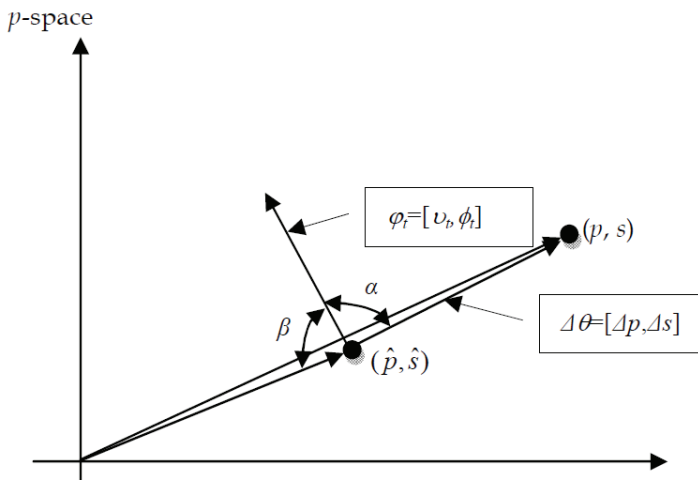


Fig. 1. Illustration of stable NMIFC without introducing invasive effects

In a FxLMS based MIFC system, $\Delta\theta \neq 0$ may cause phase errors in the estimate of secondary path transfer function to exceed 90° in some frequencies such that the closed-loop becomes unstable (Snyder & Hansen, 1990, Bjarnason, 1995, Vandrey et al., 2003). Avoiding $\Delta\theta \neq 0$ is the major issue in all FxLMS based AVC/ANC systems. Either probing signals are injected or controller perturbations are introduced as persistent excitations. Both measures introduce invasive effects to sound/vibration systems.

The NMIFC system, however, does not have such a problem at all. Online task 1 updates $\hat{\theta}^T = [\hat{p}^T, \hat{s}^T]$ to drive $\varepsilon_t = \Delta\theta^T \varphi_t \rightarrow 0$. This is enough to force φ_t and $\Delta\theta$ to be orthogonal with respect to each other such that α in Fig. 1 converges to 90° . Online task 2 optimizes controller $C(z)$. It is equivalent to adjusting $v_t = [r_t, r_{t-1}, \dots, r_{t-m}]^T$ and $\phi_t = [u_t, u_{t-1}, \dots, u_{t-m}]^T$ such that $|\mu_t| = |\hat{p}^T v_t + \hat{s}^T \phi_t| \approx 0$. This is enough to make φ_t and $\hat{\theta}^T = [\hat{p}^T, \hat{s}^T]$ almost orthogonal with respect to each other such that β in Fig. 1 becomes almost 90° .

As a result of the coupling effects of the two online tasks, φ_t and $\theta^T = [p^T, s^T]$ are almost orthogonal with respect to each other even if $\Delta\theta \neq 0$. This is not possible with FxLMS based MIFC, yet is possible with the NMIFC system. It is the ultimate objective of feedforward controllers to minimize the H_2 norm in Eq. (1), whose time domain expression becomes $e_t = \theta^T \varphi_t = p^T v_t + s^T \phi_t$ when $D(z) = 1$. Although direct minimization of $|e_t| = |\theta^T \varphi_t|$ is not possible when $\theta^T = [p^T, s^T]$ is not available accurately, indirect minimization of $|e_t| = |\theta^T \varphi_t|$ becomes possible by the NMIFC system using an imperfect $\hat{\theta}^T = [\hat{p}^T, \hat{s}^T]$ without introducing any invasive effects.

5.2 Stability in lightly-damped vibration systems

If the NMIFC system is applied to lightly-damped vibration systems with IIR path models, $\varepsilon_t \rightarrow 0$ and $|\mu_t| \approx 0$ implies $e_t + \hat{d}^T x_t \approx 0$ as suggested by Eq. (8). This means $\hat{D}(z)e(z) \approx 0$ since $\hat{D}(z) = 1 + \sum_{k=1}^{m_r} \hat{d}_k z^{-k}$ and $x_t = [e_{t-1}, e_{t-2}, \dots, e_{t-m_r}]^T$. One must prove $\hat{D}(z) \rightarrow D(z)$ to show stable minimization of $|e_t|$. Let $N(z) = N_p(z) + N_s(z)C(z)$, one can obtain an equivalent expression of Eq. (5) as

$$e_t = -\sum_{k=1}^{m_r} d_k e_{t-k} + \sum_{k=0}^{2m} n_k r_{t-k}, \tag{30}$$

where $\{n_k\}$ are coefficients of $N(z) = N_p(z) + N_s(z)C(z)$. Estimate of $N(z)$ is denoted by $\hat{N}(z)$ and defined in Eq. (16). Similar to the derivation of Eq. (3), one can obtain

$$\varepsilon_t = -\sum_{k=1}^{m_r} \Delta d_k e_{t-k} + \sum_{k=0}^{2m} \Delta n_k r_{t-k}, \tag{31}$$

where $\{\Delta d_k = d_k - \hat{d}_k\}$ and $\{\Delta n_k = n_k - \hat{n}_k\}$ are estimation errors of $D(z)$ and $N(z)$ respectively. Goodwin and Sin (1984) showed that convergence of estimation residue $\varepsilon_t = \phi_t^T \Delta\theta \rightarrow 0$ implies

$$\begin{bmatrix} e_{t-l} & e_{t-l-1} & \dots & e_{t-m_r-l+1} & r_{t-l-1} & r_{t-l-2} & \dots & r_{t-2m-l} \\ e_{t-l+1} & e_{t-l} & \dots & e_{t-m_r-l+2} & r_{t-l} & r_{t-l-1} & \dots & r_{t-2m-l+1} \\ \vdots & \vdots & \dots & \vdots & \vdots & \vdots & \dots & \vdots \\ e_{t-2} & e_{t-3} & \dots & e_{t-m_r-1} & r_{t-1} & r_{t-2} & \dots & r_{t-2m-1} \\ e_{t-1} & e_{t-2} & \dots & e_{t-m_r} & r_t & r_{t-1} & \dots & r_{t-2m} \end{bmatrix} \begin{bmatrix} \Delta d_1 \\ \Delta d_2 \\ \vdots \\ \Delta d_{m_r} \\ -\Delta n_0 \\ -\Delta n_1 \\ \vdots \\ -\Delta n_{2m} \end{bmatrix} \rightarrow 0 \tag{32}$$

where $t > l \geq m_r + 2m + 1$. If r_t contains more than $0.5(m_r + 2m + 1)$ frequency components, then the above data matrix is full rank (Goodwin & Sin, 1984). The convergence of $\varepsilon_t \rightarrow 0$ implies $\{\Delta d_k \rightarrow 0\}$ and $\{\Delta n_k \rightarrow 0\}$. As a result, $\hat{D}(z)e(z) \approx 0$ converges to $D(z)e(z) \approx 0$ in broadband control operations.

The z -transform domain version of Eq. (21) is $D(z)e(z) = N(z)r(z)$ where $D(z)$ and $N(z)$ are, respectively, the auto-regressive and moving-average parts. Analytically, one may write

$$|N(z)r| \leq |\Delta N(z)r| + \left\| \left[\hat{N}_p(z) + \hat{N}_s(z)C(z) \right] r \right\| \leq |\Delta N(z)r| + \left\| \hat{N}_p(z) + \hat{N}_s(z)C(z) \right\|_2 \|r(z)\|_2 \quad (33)$$

Since $\varepsilon_t \rightarrow 0$ implies $|\Delta N(z)r| \rightarrow 0$ and $\mu_t \approx 0$ is the result of minimizing $\left\| \hat{N}_p(z) + \hat{N}_s(z)C(z) \right\|_2$, the NMIFC system minimizes $|N(z)r|$ by the joint effects of two online tasks. The objective is also achieved without probing signals or controller perturbations.

Based on the convergence of $\{\Delta d_k \rightarrow 0\}$ and $\hat{D}(z) \rightarrow D(z)$, the closed-loop system is stable if $|N(z)r|$ is stable and minimized. In view of Eq. (30), the time domain expression of $|N(z)r|$ is also an inner product $p^T v_t + s^T \phi$. Minimization of $|N(z)r|$ can also be illustrated by Fig. 1 to explain why the NMIFC is stable without any invasive effects, when it is applied to lightly-damped vibration systems.

6. Experiments

Experiments were conducted to demonstrate advantages of the NMIFC system, with experiment setup shown in Fig. 2. Cross-sectional area of the steel beam was $50 \times 1.5 \text{ mm}^2$. The error sensor was a B&K 4382 accelerometer installed near the end of the beam. The sampling rate was 500 Hz. All signals were low-pass filtered with cutoff frequency 200 Hz. The controllers were implemented in a dSPACE 1103 board and the primary source $r(z)$ was a broadband pseudo-random signal.

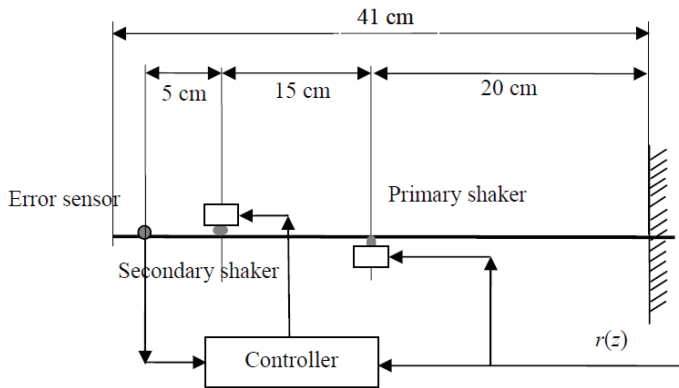


Fig. 2. Experimental setup

6.1 A well-damped beam

The first experiment was conducted to test the NMIFC in a well-damped beam shown in Fig. 2. Both actuators were shakers with shafts connected to the beam and solenoids attached to fixed bases. Damping coefficients of the shakers were different since the shakers

were made by different manufacturers. The primary shaker was one with weak damping and the secondary shaker was one with strong damping.

In the first experiment, the controller was turned off first to collect the error signal $e(z)$. Power spectral densities (PSD's) of $e(z)$ and $r(z)$ were computed with the MATLAB command "pmtm()" and denoted as $P_e = \text{pmtm}(e)$ and $P_r = \text{pmtm}(r)$ respectively. Here e and r are vectors containing data of $e(z)$ and $r(z)$. The normalized PSD of $e(z)$ is calculated as $P_{ne} = 10 \log(P_e/P_r)$ and plotted as the gray curve in Fig. 3. It is the reference for comparison. The PSD indicates a well-damped vibration system with fat resonant peaks.

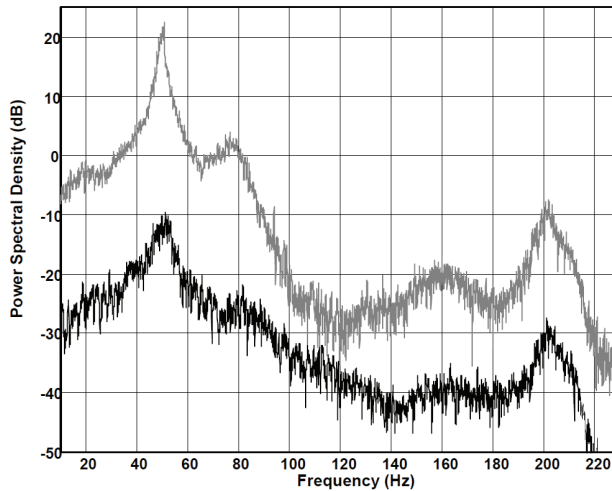


Fig. 3. Active control of a well-damped beam

Afterwards, the NMIFC was tested with $D(z)$ set to 1. The degrees of $C(z)$, $\hat{N}_p(z)$ and $\hat{N}_s(z)$ were $m=300$. The black curve in Fig. 3 represents the normalized PSD of the error signal collected after the convergence of the NMIFC system. The NMIFC was able to suppress vibration with good control performance.

6.2 A lightly-damped beam

In the second experiment, the setup was the same as in the first case. Only the secondary shaker was replaced by an inertial actuator with very weak damping. The inertial actuator was attached to the beam without other support. Its mass caused significant loading effect and reduced the fundamental frequency of the vibration system. The system sampling rate was still 500 samples/sec and all signals were low-pass filtered with cutoff frequency 200 Hz.

Again, the controllers were turned off first to collect the error signal $e(z)$. The normalized PSD of $e(z)$ is shown as the gray curve in Fig. 4. With very weak damping in both primary and secondary actuators, the system became lightly-damped. In particular, the low-frequency resonant peaks of the PSD are very narrow, which implies IIR path transfer functions.

The NMIFC system was tested in both FIR and IIR modes. When it was tested in FIR mode with $D(z)=1$, the degrees of $C(z)$, $\hat{N}_p(z)$ and $\hat{N}_s(z)$ were $m=300$. The normalized PSD of the error signal is plotted as the dashed-back curve in Fig. 4. Nose control effect is not satisfactory due to significant mismatches between FIR path models and real IIR path transfer functions. The NMIFC was also tested in IIR mode. The degrees of $C(z)$, $\hat{N}_p(z)$ and

$\hat{N}_s(z)$ was not changed. The only difference was the additional $\hat{D}(z)$ with degree $m_r=300$. The solid-black curve in Fig. 4 represents the normalized PSD of the error signal collected after the convergence of the NMIFC system. Comparing all curves in Fig. 4, one can see that the NMIFC system suppressed vibration much more significantly when it was set in IIR mode.

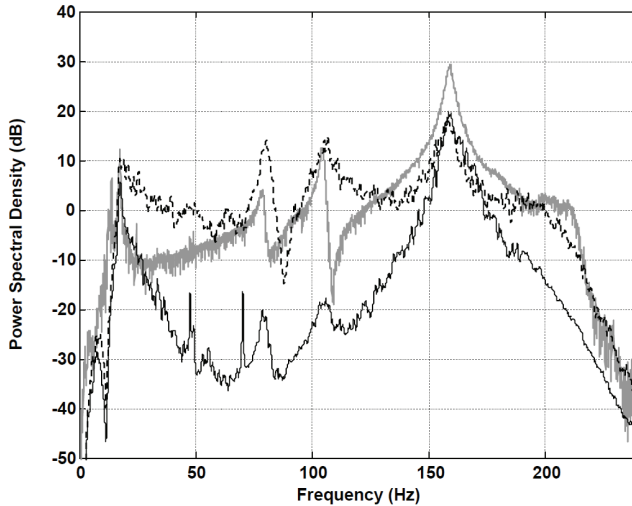


Fig. 4. Active control of a lightly-damped beam

6.3 FIR or IIR path models

In experiment 2, the beam was so lightly-damped that its vibration, if caused by an impulsive impact, would last for at least 6 seconds. The long-lasting impulse response must be modeled by a FIR filter with at least $m=3000$ taps when the sampling rate was 500 Hz. The author did not have the fast hardware to test the NMIFC with so many adaptive coefficients. Increasing FIR filter taps has other negative effects, because convergence rate and estimation accuracy of system identification algorithms are related to rank and condition number of the data matrix in Eq. (32) (Goodwin & Sin, 1984). Here the matrix had $l=m_r+2m+1=901$ columns for the NMIFC when it works in IIR mode, but at least $l=2m+1=6001$ columns for the NMIFC if the FIR path model had been increased to $m=3000$ taps. More than 6 times of columns in the data matrix of Eq. (32) would have required more than 6 times longer t to meet the necessary full rank condition. It means a much slower convergence rate. Besides, condition number of a large matrix is sensitive to quantization errors, finite word-length effects, *etc.* With a large size, the data matrix of Eq. (32) may have been analytically full rank, but numerically ill-conditioned to degrade estimate accuracy. The IIR mode is preferred with lower implementation cost, faster convergence rate and better estimation accuracy, due to a much smaller data matrix in Eq. (32). From this point of view, it is recommended to use IIR path models when the NMIFC is applied to a lightly-damped vibration system.

7. Conclusion

A NMIFC system is proposed for broadband vibration control. It has two important features. Feature F1 is that the NMIFC is stable without introducing any invasive effects, such as probing signals or controller perturbations, into the vibration system; feature F2 is

that the NMIFC is applicable to well- or lightly-damped vibration systems with either FIR or IIR path models. Mathematical analysis is presented to explain the two important features of the NMIFC; and how it is possible to achieve the intended objectives.

A significant difference between the NMIFC system and most existing MIFC systems is to replace the FxLMS algorithm with online controller optimization. The NMIFC system operates two online tasks. One is online path modeling and the other is online controller optimization. The coupling effects of the two online tasks make it possible for the NMIFC to be stable without introducing any invasive effects to the vibration system.

The NMIFC system is applicable to well- or lightly-damped vibration systems. Switching between the two kinds of systems is done by setting the degree of common denominator $D(z)$. When $D(z)=1$, the NMIFC is applicable to well-damped vibration systems with FIR path models. Otherwise, the NMIFC is applicable to lightly-damped vibration systems with IIR path models.

Experimental results are presented to demonstrate the performance of the NMIFC system when it is applied to both well- and lightly-damped vibration systems.

8. References

- Goodwin, G.C. & Sin, K.S. (1982). *Adaptive filtering, prediction and control*, Prentice-Hall, Englewood Cliffs, NJ.
- Eriksson, L.J. & Allie, M.C. (1989). Use of random noise for on-line transducer modeling in an adaptive active attenuation system, *J. Acoust. Soc. Am.*, Vol. 85, 797-802
- Snyder, S.D. & Hansen, C.H. (1990). The influence of transducer transfer functions and acoustic time delay on the LMS algorithm in active noise control systems, *J. Sound Vib.*, Vol. 140, No. 3, 409-424
- Eriksson, L.J. (1991). Development of the filtered-u algorithm for active noise control, *J. Acoust Soc Am.*, Vol. 89, 257-65
- Nelson, P.A. & Elliott, S.J. (1992). *Active Control of Sound*, Academic, London
- Regalia, P.A. (1995). *Adaptive IIR filtering in signal processing and control*, Dekker, New York
- Vipperman, J.S. & Burdisso, R.A. (1995). Adaptive feedforward control of non-minimum phase structural systems, *J. of Sound and Vib.*, Vol. 183, No. 3, 369-382
- Bjarnason, E. (1995). Analysis of the filtered-x LMS algorithm, *IEEE Trans. on Speech and Audio Process.*, Vol. 3, No. 3, 504-514
- Hansen, C.H. & Snyder, S.D. (1997). *Active Control of Noise and Vibration*, E and FN Spon, London
- Vaudrey, M.A.; Baumann, W.T. & Saunders, W.R. (2003). Stability and operation constraints of adaptive LMS-based feedback control, *Automatica*, Vol. 39, 595-605
- Nowlin, W.C; Guthart, G.S. & Toth, G.K. (2000). Noninvasive system identification for multichannel broadband active noise control, *J. Acoust. Soc. Am.*, Vol. 107, 2049-2060
- Qiu, X. & Hansen, C.H. (2001). An algorithm for active control of transformer noise with on-line cancellation path modelling based on the perturbation method, *J. Sound Vib.*, Vol. 240, No. 4, 647-665
- Lu, J.; Shen, C.; Qiu, X. & Xu, B. (2003). Lattice form adaptive infinite impulse response filtering algorithm for active noise control, *J. Acoust Soc Am.*, Vol. 113, No. 1, 327-35
- Kim, B.J. & Swanson, D.C. (2005). Linear independence method for system identification/secondary path modeling for active control, *J. Acoust. Soc. Am.*, Vol. 118, No. 3, 1452-1468

Active Vibration Control for a Nonlinear Mechanical System using On-line Algebraic Identification

Francisco Beltrán¹, Gerardo Silva², Andrés Blanco³ and Esteban Chávez⁴

¹*Universidad Politécnica de la Zona Metropolitana de Guadalajara*

²*Centro de Investigación y de Estudios Avanzados del IPN*

³*Centro Nacional de Investigación y Desarrollo Tecnológico*

⁴*Universidad Politécnica de Guanajuato
México*

1. Introduction

Many engineering systems undergo undesirable vibrations. Vibration control in mechanical systems is an important problem, by means of which vibrations are suppressed or at least attenuated. In this direction it has been common the use of passive and active dynamic vibration absorbers.

A dynamic vibration absorber is an inertia member coupled to a vibrating mechanical system by suitable linear and nonlinear coupling members (e.g., springs and dampers). For the passive case, the absorber only serves for a specific excitation frequency and stable operating conditions, but it is not recommended for variable frequencies and uncertain system parameters. An active dynamic vibration absorber achieves better dynamic performance by controlling actuator forces depending on feedback and feedforward information of the system obtained from sensors.

To cancel the exogenous harmonic vibrations on the primary system, the dynamic vibration absorber should apply an equivalent reaction force to the primary system equal and opposite to the exciting force causing the vibrations. This means that the vibration energy injected to the primary system is transferred to the absorber through the coupling elements. For more details about dynamic vibration absorber we refer to (Korenev & Reznikov, 1993) and references therein.

This chapter deals with the attenuation problem of harmonic mechanical vibrations in nonlinear mechanical systems by using active vibration absorbers and without employing vibration measurements. On-line algebraic identification is applied for the on-line estimation of the frequency and amplitude of exogenous vibrations affecting the nonlinear vibrating mechanical system. The proposed results are strongly based on the algebraic approach to parameter identification in linear systems reported by (Fliess & Sira-Ramírez, 2003), which employs differential algebra, module theory and operational calculus.

An important property of the algebraic identification is that the parameter and signal identification is not asymptotic but algebraic, that is, the parameters are computed as fast as the system dynamics is being excited by some external input or changes in its initial

conditions, in contrast to the well-known persisting excitation condition and complex algorithms required by most of the traditional identification methods (Ljung, 1987) and (Soderstrom, 1987).

The algebraic identification is combined with a certainty equivalence differential flatness based controller for asymptotic output tracking of an off-line and pre-specified output trajectory and cancellation of harmonic perturbations affecting directly the mechanical system. Numerical results show the dynamic and robust performance of the algebraic identification and the active vibration control scheme. Algebraic identification has been employed for parameter and signal estimation in linear vibrating mechanical systems by (Beltrán et al., 2010). Here numerical and experimental results show that the algebraic identification provides high robustness against parameter uncertainty, frequency variations, small measurement errors and noise.

2. Algebraic parameter identification

To illustrate the basic ideas of the algebraic identification methods proposed by (Fliess & Sira-Ramírez, 2003), it is considered the on-line parameter identification of a simple one degree-of freedom mass-spring-damper system as well as the parameters associated to an exogenous harmonic perturbation affecting directly its dynamics. The mathematical model of the mechanical system is described by the ordinary differential equation

$$m\ddot{x} + c\dot{x} + kx = u(t) + f(t) \quad (1)$$

where x denotes the displacement of the mass carriage, u is a control input (force) and $f(t) = F_0 \sin\omega t$ is a harmonic force (perturbation). The system parameters are the mass m , the stiffness constant of the linear spring k and the viscous damping c .

In spite of *a priori* knowledge of the mathematical model (1), it results evident that this is only an approximation for the physical system, where for large excursions of the mass carriage the mechanical spring has nonlinear stiffness function and close to the rest position there exist nonlinear damping effects (e.g., dry or Coulomb friction). Another inconvenient is that the information used during the identification process contains small measurement errors and noise. It is therefore realistic to assume that the identified parameters will represent approximations to equivalent values into the physical system. As a consequence the algorithms will have to be sufficiently robust against such perturbations. Some of these properties have been already analyzed by (Fliess & Sira-Ramírez, 2003).

2.1 On-line algebraic identification

Consider the unperturbed system (1), that is, when $f(t) \equiv 0$, where only measurements of the displacement x and the control input u are available to be used in the on-line parameter identification scheme. To do this, the differential equation (1) is described in notation of operational calculus (Fliess & Sira-Ramírez, 2003) as follows

$$m(s^2x(s) - sx_0 - \dot{x}_0) + c(sx(s) - x_0) + kx(s) = u(s) \quad (2)$$

where $x_0 = x(t_0)$ and $\dot{x}_0 = \dot{x}(t_0)$ are unknown constants denoting the system initial conditions at $t_0 \geq 0$. In order to eliminate the dependence of the constant initial conditions, the equation (2) is differentiated twice with respect to the variable s , resulting in

$$m \left(2x + 4s \frac{dx}{ds} + s^2 \frac{d^2x}{ds^2} \right) + c \left(2 \frac{dx}{ds} + s \frac{d^2x}{ds^2} \right) + k \frac{d^2x}{ds^2} = \frac{d^2u}{ds^2} \quad (3)$$

Now, multiplying (3) by s^{-2} one obtains that

$$m \left(2s^{-2}x + 4s^{-1} \frac{dx}{ds} + \frac{d^2x}{ds^2} \right) + c \left(2s^{-2} \frac{dx}{ds} + s^{-1} \frac{d^2x}{ds^2} \right) + ks^{-2} \frac{d^2x}{ds^2} = s^{-2} \frac{d^2u}{ds^2} \quad (4)$$

and transforming back to the time domain leads to the integral equation

$$m \left[2 \left(\int_{t_0}^{(2)} x \right) - 4 \left(\int_{t_0} (\Delta t)x \right) + (\Delta t)^2 x \right] + c \left[-2 \left(\int_{t_0}^{(2)} (\Delta t)x \right) + \left(\int_{t_0} (\Delta t)^2 x \right) \right] + k \left(\int_{t_0}^{(2)} (\Delta t)^2 x \right) = \left(\int_{t_0}^{(2)} (\Delta t)^2 u \right) \quad (5)$$

where $\Delta t = t - t_0$ and $\left(\int_{t_0}^{(n)} \varphi(t) \right)$ are iterated integrals of the form $\int_{t_0}^t \int_{t_0}^{\sigma_1} \cdots \int_{t_0}^{\sigma_{n-1}} \varphi(\sigma_n) d\sigma_n \cdots d\sigma_1$,

with $\left(\int_{t_0} \varphi(t) \right) = \int_{t_0}^t \varphi(\sigma) d\sigma$ and n a positive integer.

The above integral-type equation (5), after some more integrations, leads to the following linear system of equations

$$A(t)\theta = b(t) \quad (6)$$

where $\theta = [m, c, k]^T$ denotes the parameter vector to be identified and $A(t)$, $b(t)$ are 3×3 and 3×1 matrices, respectively, which are described by

$$A(t) = \begin{bmatrix} a_{11}(t) & a_{12}(t) & a_{13}(t) \\ a_{21}(t) & a_{22}(t) & a_{23}(t) \\ a_{31}(t) & a_{32}(t) & a_{33}(t) \end{bmatrix}, \quad b(t) = \begin{bmatrix} b_1(t) \\ b_2(t) \\ b_3(t) \end{bmatrix}$$

whose components are time functions specified as

$$\begin{aligned} a_{11} &= 2 \int_{t_0}^{(2)} x - 4 \int_{t_0} (\Delta t)x + (\Delta t)^2 x & a_{31} &= 2 \int_{t_0}^{(4)} x - 4 \int_{t_0}^{(3)} (\Delta t)x + \int_{t_0}^{(2)} (\Delta t)^2 x \\ a_{12} &= -2 \int_{t_0}^{(2)} (\Delta t)x + \int_{t_0} (\Delta t)^2 x & a_{32} &= -2 \int_{t_0}^{(4)} (\Delta t)x + \int_{t_0}^{(3)} (\Delta t)^2 x \\ a_{13} &= \int_{t_0}^{(2)} (\Delta t)^2 x & a_{33} &= \int_{t_0}^{(4)} (\Delta t)^2 x \\ a_{21} &= 2 \int_{t_0}^{(3)} x - 4 \int_{t_0}^{(2)} (\Delta t)x + \int_{t_0} (\Delta t)^2 x & b_1 &= \int_{t_0}^{(2)} (\Delta t)^2 u \\ a_{22} &= -2 \int_{t_0}^{(3)} (\Delta t)x + \int_{t_0}^{(2)} (\Delta t)^2 x & b_2 &= \int_{t_0}^{(3)} (\Delta t)^2 u \\ a_{23} &= \int_{t_0}^{(3)} (\Delta t)^2 x & b_3 &= \int_{t_0}^{(4)} (\Delta t)^2 u \end{aligned}$$

From the equation (6) can be concluded that the parameter vector θ is *algebraically identifiable* if, and only if, the trajectory of the dynamical system is *persistent* in the sense established by

(Fliess & Sira-Ramírez, 2003), that is, the trajectories or dynamic behavior of the system (1) satisfy the condition

$$\det A(t) \neq 0$$

In general, this condition holds at least in a small time interval $(t_0, t_0 + \delta]$, where δ is a positive and sufficiently small value.

By solving the equations (6) it is obtained the following algebraic identifier for the unknown system parameters

$$\left. \begin{aligned} \hat{m} &= \frac{\Delta_1}{\det A(t)} \\ \hat{c} &= \frac{\Delta_2}{\det A(t)} \\ \hat{k} &= \frac{\Delta_3}{\det A(t)} \end{aligned} \right\} \forall t \in (t_0, t_0 + \delta] \quad (7)$$

where

$$\begin{aligned} \Delta_1 &= b_1 a_{22} a_{33} - b_1 a_{23} a_{32} - b_2 a_{12} a_{33} + b_2 a_{13} a_{32} + b_3 a_{12} a_{23} - b_3 a_{13} a_{22} \\ \Delta_2 &= -b_1 a_{21} a_{33} + b_1 a_{31} a_{23} + b_2 a_{11} a_{33} - b_2 a_{13} a_{31} - b_3 a_{11} a_{23} + b_3 a_{21} a_{13} \\ \Delta_3 &= b_1 a_{21} a_{32} - b_1 a_{22} a_{31} - b_2 a_{11} a_{32} + b_2 a_{12} a_{31} + b_3 a_{11} a_{22} - b_3 a_{12} a_{21} \\ \det A(t) &= a_{11} a_{22} a_{33} - a_{11} a_{23} a_{32} - a_{12} a_{21} a_{33} + a_{12} a_{31} a_{23} + a_{21} a_{13} a_{32} - a_{13} a_{22} a_{31} \end{aligned}$$

2.2 Simulation and experimental results

The performance of the on-line algebraic identifier of the system parameters (7) is now evaluated by means of numerical simulations and experiments on a electromechanical platform (ECPTM rectilinear plant) with a single degree-of-freedom mass-spring-damper system. The physical parameters were previously estimated through several experiments with different excitation inputs (natural and forced vibrations, step and sine sweep inputs, etc.) resulting in the following set of parameters:

$$m = 2.2685[\text{kg}], \quad c = 4.1241[\text{Ns} / \text{m}], \quad k = 356.56[\text{N} / \text{m}]$$

Nevertheless, it is convenient to remark that the real system clearly exhibits nonlinear effects like nonlinear stiffness and damping functions (hard springs and Coulomb friction on the slides) that were not considered during the synthesis of the algebraic identifier.

Fig. 1 shows the simulation results using the algebraic identifier for a step input $u = 4$ [N]. Here it is clear how the parameter identification is quickly performed (before $t = 1.02$ s) and it is almost exact with respect to the real parameters. It is also evident the presence of singularities in the algebraic identifier, i.e., when the determinant $den = \det A(t)$ is zero. The first singularity, however, occurs about $t = 1.02$ s, that is too much time (more than 5 times) after the identification has been finished.

Fig. 2 presents the corresponding experimental results using the on-line algebraic identification scheme (7). In this case the actual system response is quite similar to the numerical simulation, resulting in the following (equivalent) parameters:

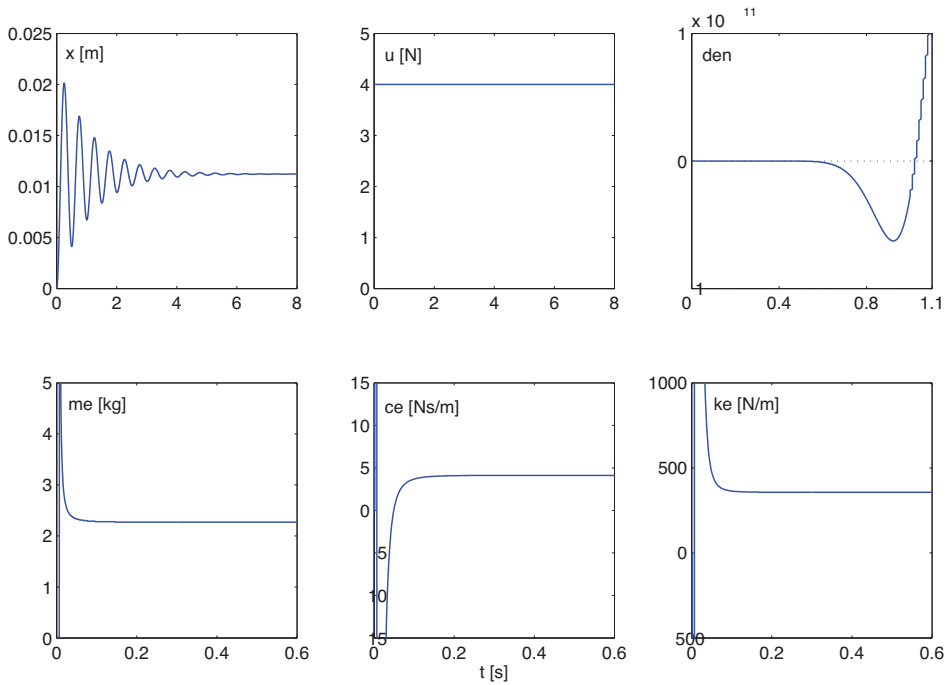


Fig. 1. Simulation results of the algebraic identifier. The subscript “*e*” denotes estimated values and $den = \det A(t)$

$$m = 2.25[\text{kg}], c = 4.87[\text{Ns} / \text{m}], k = 362[\text{Ns} / \text{m}]$$

These values represent good approximations for the real parameters. Nevertheless, the identification process starts with some irregular behavior and the estimation takes more time (about $t = 0.4$ s), which we have attributed to several factors like neglected nonlinear effects (stiffness and friction), presence of noise on the output measurements and especially the computational algorithms based upon a sampled-time system with fast sampling time $t_s = 0.000884$ s and numerical integrations based on trapezoidal rules. Some of these problems in the parameter estimation have been already analyzed by (Sagara & Zhao, 1990). Many numerical and experimental results validate the good response of the on-line algebraic identification methods of unknown parameters. In addition, it can be proved the good robustness properties of the algebraic identifiers against stochastic perturbations, noisy measurements, small parameter variations and nonlinearities, which are not included here for space limitations. Moreover, because the algebraic identification process is quickly achieved with a high-speed DSP board, then any possible singularity does not affect significantly the identification results. Otherwise, close to any singularity or variations on the system dynamics, the algebraic identifier can be restarted.

In this chapter the algebraic identification methodology is applied to estimate the parameters associated to exogenous perturbations affecting an nonlinear mechanical vibrating system.

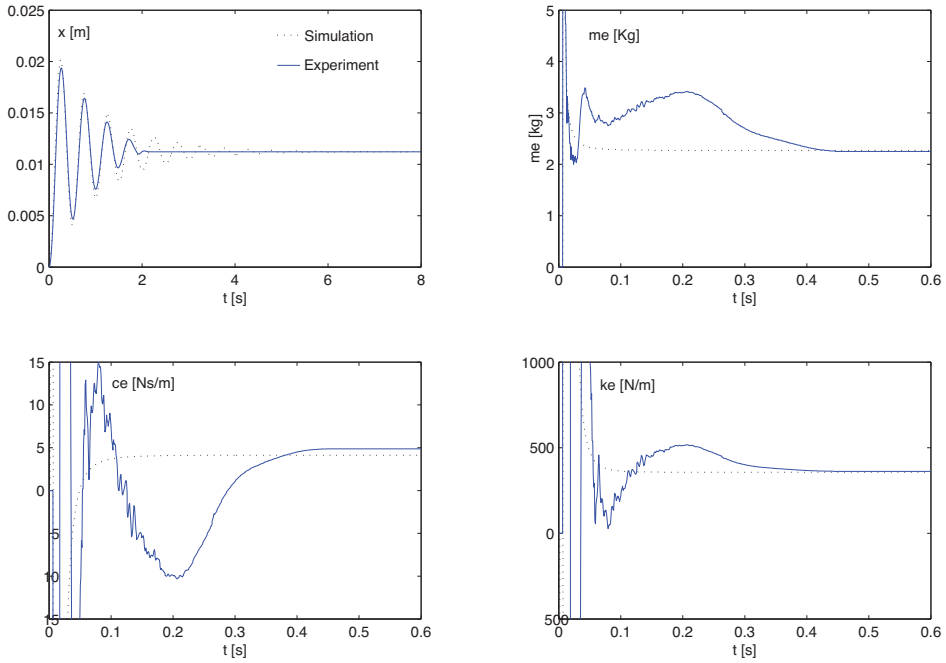


Fig. 2. Experimental results obtained on a ECPTM Rectilinear Plant using algebraic identification methods.

3. An active vibration control scheme

Consider the nonlinear vibrating mechanical system shown in Fig. 3, which consists of an active nonlinear vibration absorber (secondary system) coupled to the perturbed mechanical system (primary system). The generalized coordinates are the displacements of both masses, x_1 and x_2 , respectively. In addition, u represents the (force) control input and f an exogenous harmonic perturbation. Here m_1 and c_1 denote mass and linear viscous damping on the primary system; similarly, m_2 and c_2 denote mass and viscous damping of the active vibration absorber.

The two mechanical springs have the following nonlinear stiffness function

$$\mathcal{F}(x) = kx + k_p x^3$$

where x is the spring deformation, and k and k_p denote the linear and cubic stiffness, respectively.

The mathematical model of the two degree-of-freedom system is described by two coupled nonlinear differential equations

$$\begin{aligned} m_1 \ddot{x}_1 + k_1 x_1 + k_{1p} x_1^3 + c_1 \dot{x}_1 - k_2 (x_2 - x_1) - k_{2p} (x_2 - x_1)^3 &= f(t) \\ m_2 \ddot{x}_2 + k_2 (x_2 - x_1) + k_{2p} (x_2 - x_1)^3 &= u(t) \end{aligned} \quad (8)$$

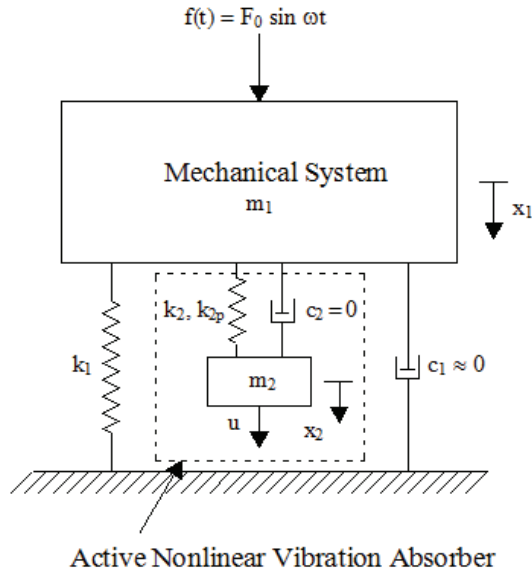


Fig. 3. Schematic diagram of the vibrating mechanical system.

where $f(t) = F_0 \sin \omega t$. In order to simplify the analysis we have assumed that $c_1 \approx 0$ and $c_2 \equiv 0$. Defining the state variables as $z_1 = x_1$, $z_2 = \dot{x}_1$, $z_3 = x_2$ and $z_4 = \dot{x}_2$, one obtains the following state space description

$$\begin{aligned}
 \dot{z}_1 &= z_2 \\
 \dot{z}_2 &= -\frac{k_1}{m_1} z_1 - \frac{k_{1p}}{m_1} z_1^3 + \frac{k_2}{m_1} (z_3 - z_1) + \frac{k_{2p}}{m_1} (z_3 - z_1)^3 + \frac{1}{m_1} f(t) \\
 \dot{z}_3 &= z_4 \\
 \dot{z}_4 &= -\frac{k_2}{m_2} (z_3 - z_1) - \frac{k_{2p}}{m_2} (z_3 - z_1)^3 + \frac{1}{m_2} u
 \end{aligned} \tag{9}$$

In what follows we will apply the algebraic identification method to estimate the harmonic force $f(t)$ and design an active vibration controller based on state feedback and feedforward information obtained from $f(t)$.

3.1 Differential flatness-based control

The system (9) is differentially flat, with flat output given by $y = z_1$ and further denoted as L . Then, all the state variables and the control input can be parameterized in terms of the flat output $L = z_1$ and a finite number of its time derivatives (Fliess et al., 1993).

Indeed, under the assumption of perfect knowledge of L , the second equation in (9) actually represents a reduced cubic algebraic equation from where the mass position of the vibration absorber z_3 can be obtained. The only real root of such a cubic equation is readily obtained as

$$z_3 = L + \frac{1}{6k_{2p}} \left[k_{2p}^2 \left(108d + 12 \sqrt{3 \frac{4k_2^3 + 27k_{2p}d^2}{k_{2p}}} \right) \right]^{1/3} - 2k_2 \left[k_{2p}^2 \left(108d + 12 \sqrt{3 \frac{4k_2^3 + 27k_{2p}d^2}{k_{2p}}} \right) \right]^{-1/3} \quad (10)$$

with $d = m_1 \ddot{L} + k_1 L + k_{1p} L^3 - f(t)$. Note that the differentially parameterized expression for z_3 , in (10), implies that its second time derivative, \dot{z}_4 , can be expressed as a function denoted by $\phi(L, \dot{L}, \ddot{L}, L^{(3)}, L^{(4)}, f, \dot{f}, \ddot{f})$. Then, from the fourth equation in (9), the control input, u , can be parameterized in terms of differential functions of L as

$$u = m_2 \dot{z}_4 + k_2 \left(z_3(L, \ddot{L}, f) - L \right) + k_{2p} \left(\phi(L, \dot{L}, \ddot{L}, L^{(3)}, L^{(4)}, f, \dot{f}, \ddot{f}) - L \right)^3 \quad (11)$$

Therefore, all system variables are expressible as differential functions of the flat output. From (11) one obtains the following differential flatness-based controller to asymptotically track a desired reference trajectory $L^*(t)$:

$$\begin{aligned} u &= m_2 \dot{z}_4 + k_2 \left(z_3(L, \ddot{L}, f) - L \right) + k_{2p} \left(\phi(L, \dot{L}, \ddot{L}, L^{(3)}, v, f, \dot{f}, \ddot{f}) - L \right)^3 \\ v &= (L^*)^{(4)}(t) - \beta_3 \left[L^{(3)} - (L^*)^{(3)}(t) \right] \\ &\quad - \beta_2 \left[\ddot{L} - \ddot{L}^*(t) \right] - \beta_1 \left[\dot{L} - \dot{L}^*(t) \right] - \beta_0 \left[L - L^*(t) \right] \end{aligned} \quad (12)$$

The use of this controller yields the following closed-loop dynamics for the trajectory tracking error $e = L - L^*(t)$ as follows

$$e^{(4)} + \beta_3 e^{(3)} + \beta_2 \ddot{e} + \beta_1 \dot{e} + \beta_0 e = 0 \quad (13)$$

Therefore, selecting the design parameters β_i , $i = 0, \dots, 3$, such that the associated characteristic polynomial for (13) be *Hurwitz*, one guarantees that the error dynamics be globally asymptotically stable.

It is evident, however, that the controller (12) requires the perfect knowledge of the exogenous signal $f(t)$ and its time derivatives up to second order, revealing several disadvantages with respect to other control schemes. Nevertheless, one can take advantage of the algebraic identification methods: *i*) to estimate the force $f(t)$ and reconstruct an estimated signal $\hat{f}(t)$, or *ii*) when the structure of the signal is well-known (e.g., harmonic force $f(t) = F_0 \sin \omega t$) to estimate its associated parameters (F_0, ω) and then reconstruct it. As a consequence, the combination of the feedback and feedforward control (12) with algebraic identification methods will improve the robustness properties against variations on the amplitude and/or excitation frequency.

4. Algebraic identification of harmonic vibrations

Consider the nonlinear mechanical system (9) with perfect knowledge of its system parameters and, that the whole set of state vector components and the control input u are

available for the identification process of the harmonic signal $f(t) = F_0 \sin \omega t$. In this case we proceed to synthesize algebraic identifiers for the excitation frequency ω and amplitude F_0 . For simplicity, we also suppose that $c_1 = c_2 \equiv 0$.

4.1 Identification of the excitation frequency ω

Consider the second equation in (9)

$$m_1 \frac{d}{dt} z_2 + \varphi = F_0 \sin \omega t \quad (14)$$

where

$$\varphi = k_1 z_1 + k_{1p} z_1^3 - k_2 (z_3 - z_1) - k_{2p} (z_3 - z_1)^3$$

In order to eliminate the presence of the amplitude F_0 , we differentiate the equation (14) twice with respect to time t , resulting

$$\frac{d^2}{dt^2} \left(m_1 \frac{d}{dt} z_2 + \varphi \right) = -F_0 \omega^2 \sin \omega t \quad (15)$$

Multiplication of (14) by ω^2 and adding it to (15), leads to

$$\omega^2 \left(m_1 \frac{d}{dt} z_2 + \varphi \right) + \frac{d^2}{dt^2} \left(m_1 \frac{d}{dt} z_2 + \varphi \right) = 0 \quad (16)$$

Multiplying (16) by the quantity t^3 and integrating the result three times with respect to time t , one gets

$$\omega^2 \left(\int_{t_0}^{(3)} t^3 \left(m_1 \frac{d}{dt} z_2 + \varphi \right) \right) + \left(\int_{t_0}^{(3)} t^3 \frac{d^2}{dt^2} \left(m_1 \frac{d}{dt} z_2 + \varphi \right) \right) = 0 \quad (17)$$

where $\left(\int_{t_0}^{(n)} \eta(t) \right)$ are iterated integrals of the form $\int_{t_0}^t \int_{t_0}^{\sigma_1} \dots \int_{t_0}^{\sigma_{n-1}} \varphi(\sigma_n) d\sigma_n \dots d\sigma_1$, with $\left(\int_{t_0} \eta(t) \right) = \int_{t_0}^t \eta(\sigma) d\sigma$ and n a positive integer.

Using integration by parts, one gets

$$\begin{aligned} & \omega^2 \left(m_1 \left(\int_{t_0}^{(3)} t^3 \frac{d}{dt} z_2 \right) + \left(\int_{t_0}^{(3)} t^3 \varphi \right) \right) + m_1 \left(\int_{t_0}^{(3)} t^3 \frac{d^3}{dt^3} z_2 \right) \\ & + \left(\int_{t_0}^{(2)} t^3 \frac{d}{dt} \varphi \right) - 3 \left(\int_{t_0}^{(3)} t^2 \frac{d}{dt} \varphi \right) = 0 \end{aligned} \quad (18)$$

where

$$\begin{aligned} \left(\int_{t_0}^{(3)} t^3 \frac{d}{dt} z_2 \right) &= \left(\int_{t_0}^{(2)} t^3 z_2 \right) - 3 \left(\int_{t_0}^{(3)} t^2 z_2 \right) \\ \left(\int_{t_0}^{(3)} t^3 \frac{d^3}{dt^3} z_2 \right) &= t^3 z_2 - 9 \left(\int_{t_0}^{(2)} t^2 z_2 \right) + 18 \left(\int_{t_0}^{(2)} t z_2 \right) - 6 \left(\int_{t_0}^{(3)} z_2 \right) \\ \frac{d}{dt} \varphi &= k_1 z_2 + 3k_{1p} z_1^2 z_2 - \left[k_2 + 3k_{2p} (z_3 - z_1)^2 \right] (z_4 - z_2) \end{aligned}$$

Finally, solving for the excitation frequency ω in (18) leads to the following on-line algebraic identifier for the excitation frequency:

$$\omega_c^2 = -\frac{N_1(t)}{D_1(t)}, \forall t \in (t_0, t_0 + \delta_0] \quad (19)$$

where

$$\begin{aligned} N_1(t) &= m_1 \left(\int_{t_0}^{(3)} t^3 \frac{d^3}{dt^3} z_2 \right) + \left(\int_{t_0}^{(2)} t^3 \frac{d}{dt} \varphi \right) - 3 \left(\int_{t_0}^{(3)} t^2 \frac{d}{dt} \varphi \right) \\ D_1(t) &= m_1 \left(\int_{t_0}^{(3)} t^3 \frac{d}{dt} z_2 \right) + \left(\int_{t_0}^{(3)} t^3 \varphi \right) \end{aligned}$$

Therefore, when the condition $D_1(t) \neq 0$ be satisfied at least for a small time interval $(t_0, t_0 + \delta_0]$ with $\delta_0 > 0$, we can find from (19) a closed-form expression for the estimated excitation frequency.

4.2 Identification of the amplitude F_0

To synthesize an algebraic identifier for the amplitude F_0 of the harmonic vibrations acting on the mechanical system (9), consider again the equation (14).

Multiplying (14) by the quantity t and integrating the result once with respect to time t , we have that

$$m_1 \int_{t_0}^t \left(t \frac{d}{dt} z_2 \right) dt + \int_{t_0}^t (t\varphi) dt = F_0 \int_{t_0}^t (t \sin \omega t) dt \quad (20)$$

By integrating by parts, the equation (20) is equivalent to

$$m_1 \left((t - t_0) z_2 - \int_{t_0}^t z_2 dt \right) + \int_{t_0}^t (t\varphi) dt = F_0 \int_{t_0}^t (t \sin \omega t) dt \quad (21)$$

At this point we assume that the excitation frequency has been previously estimated, during a small time interval $(t_0, t_0 + \delta_0]$, using (19). The estimated result is therefore $\omega_c(t_0 + \delta_0)$. After the time $t = t_0 + \delta_0$ it is started the on-line identifier for the amplitude, obtained from (21) as follows

$$F_{0e} = \frac{N_2(t)}{D_2(t)} \quad (22)$$

where

$$\begin{aligned} N_2(t) &= m_1 z_2 \Delta t + \int_{t_0 + \delta_0}^t (t\varphi - m_1 z_2) dt \\ D_2(t) &= \left(\int_{t_0 + \delta_0}^t t \sin[\omega_c(t_0 + \delta_0)t] dt \right) \end{aligned}$$

Such an estimation is valid if the condition $D_2(t) \neq 0$ holds for a sufficiently small time interval $[t_0 + \delta_0, t_0 + \delta_1]$ with $\delta_1 > \delta_0 > 0$.

5. An adaptive-like controller with algebraic identification

The differential flatness based active vibration control (12) can be combined with the online identification of harmonic vibrations (19),(22), resulting the following *certainty equivalence* feedback control law

$$\begin{aligned}
 u &= m_2 \dot{z}_4 + k_2 \left(z_3 \left(L, \ddot{L}, f_c \right) - L \right) + k_{2p} \left(\phi \left(L, \dot{L}, \ddot{L}, L^{(3)}, v, f_c, \dot{f}_c, \ddot{f}_c \right) - L \right)^3 \\
 v &= \left(L^* \right)^{(4)}(t) - \beta_3 \left[L^{(3)} - \left(L^* \right)^{(3)}(t) \right] \\
 &\quad - \beta_2 \left[\ddot{L} - \ddot{L}^*(t) \right] - \beta_1 \left[\dot{L} - \dot{L}^*(t) \right] - \beta_0 \left[L - L^*(t) \right]
 \end{aligned} \tag{23}$$

where $f_c(t) = F_0 e \sin \omega_e t$. Note that, in accordance with the algebraic identification approach, providing fast identification for the parameters associated to the harmonic vibration (ω , F_0) and, as a consequence, fast estimation of this perturbation signal, the proposed controller (23) resembles an adaptive control scheme. From a theoretical point of view, the algebraic identification is instantaneous (Fliess & Sira-Ramírez, 2003). In practice, however, there are modeling and computational errors as well as other factors that can inhibit the precise algebraic computation. Fortunately, the identification algorithms and closed-loop system are robust against such difficulties (Beltrán et al., 2010).

6. Simulation results

Some simulations were performed to show the on-line identification of harmonic vibrations and its use in an adaptive-like vibration control (23). The parameters for the ECPTM rectilinear control system are given in Table 1.

$m_1 = 10\text{kg}$	$m_2 = 2\text{kg}$
$k_1 = 1000\text{N/m}$	$k_2 = 200\text{N/m}$
$k_{1p} = 100\text{N/m}$	$k_{2p} = 50\text{N/m}^3$

Table 1. System parameters.

The controller (23) was specified such that one could observe how the active vibration absorber cancels the vibrations on the primary system and the asymptotic output tracking of an off-line and prespecified reference trajectory, towards the desired equilibrium.

The planned trajectory for the flat output $y = z_1$ is given by

$$L^*(t) = \begin{cases} 0 & \text{for } 0 \leq t < T_1 \\ \psi(t, T_1, T_2) \bar{L} & \text{for } T_1 \leq t \leq T_2 \\ \bar{L} & \text{for } t > T_2 \end{cases} \tag{24}$$

where $\bar{L} = 0.01$ [m], $T_1 = 5$ [s], $T_2 = 10$ [s] and $\psi(t, T_1, T_2)$ is a Bézier polynomial, with $\psi(T_1, T_1, T_2) = 0$ and $\psi(T_2, T_1, T_2) = 1$, described by

$$\psi(t) = \left(\frac{t-T_1}{T_2-T_1} \right)^5 \left[r_1 - r_2 \left(\frac{t-T_1}{T_2-T_1} \right) + r_3 \left(\frac{t-T_1}{T_2-T_1} \right)^2 - \dots - r_6 \left(\frac{t-T_1}{T_2-T_1} \right)^5 \right]$$

with $r_1 = 252, r_2 = 1050, r_3 = 1800, r_4 = 1575, r_5 = 700, r_6 = 126$.

In Fig. 4 is depicted the identification process of the harmonic vibrations $f(t) = 2\sin(12t)$ [N] and the dynamic behavior of the adaptive-like control scheme (23). We can observe a good and fast estimation ($t \ll 0.1s$) and how the active vibration absorber dissipates all the vibrating energy H_1 and allows that the output follows the desired reference trajectory given by (24).

The controller parameters $\{\beta_0, \beta_1, \beta_2\}$ were chosen to be in correspondence with the fourth order closed-loop tracking error dynamics characteristic polynomial:

$$\left(s^2 + 2\zeta\omega_n s + \omega_n^2 \right)^2 = s^4 + \beta_3 s^3 + \beta_2 s^2 + \beta_1 s + \beta_0$$

with $\zeta = 0.7071$ y $\omega_n = 10$.

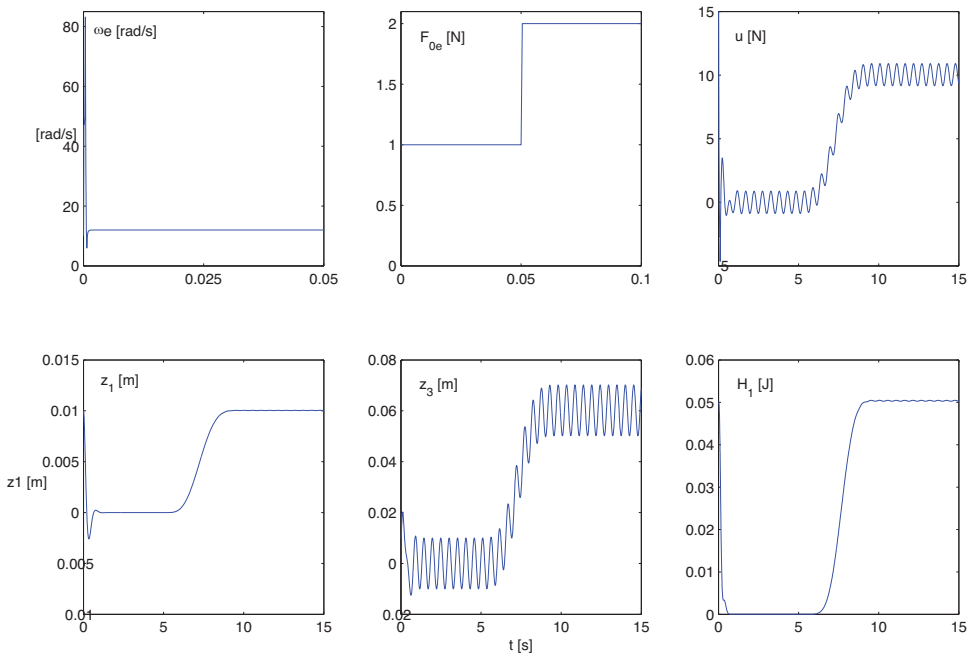


Fig. 4. Controlled system responses and identification of frequency and amplitude of $f(t) = F_0 \sin \omega t$.

7. Conclusions

The design of active dynamic vibration absorbers is performed by using feedback and feedforward control. The differential flatness property of the mechanical system is employed to synthesize an active vibration controller, simplifying the trajectory tracking problem with the application of a static state feedback controller based on linear pole placement and perturbation feedforward. Since this active controller requires information of the exogenous harmonic vibrations, an algebraic identification approach is proposed for the on-line estimation of the frequency and amplitude of vibrations affecting the mechanical system. This approach is quite promising, in the sense that from a theoretical point of view, the algebraic identification is practically instantaneous and robust with respect to parameter uncertainty, frequency variations, small measurement errors and noise. Thus the algebraic identification is combined with the differential flatness based controller to get an adaptive-like controller, which results quite precise, fast and robust against parameter uncertainty and variations on the excitation frequency and amplitude of exogenous perturbations.

8. References

- [Beltrán-Carbajal, F.; G. Silva-Navarro, H. Sira-Ramírez, A. Blanco-Ortega (2010)] Active Vibration Control Using On-line Algebraic Identification and Sliding Modes. *Computación y Sistemas*, Vol. 13, No. 3, 313-330. ISSN 1405-5546.
- [Beltrán-Carbajal, F.; G. Silva-Navarro, H. Sira-Ramírez & J. Quezada Andrade (2005)] Active vibration control using on-line algebraic identification of harmonic vibrations, *Proceedings of American Control Conference*, Portland, Oregon, pp. 4820-4825. ISSN 0743-1619.
- [Blanco-Ortega, A.; F. Beltrán-Carbajal & G. Silva-Navarro (2008)] Active Disk for Automatic Balancing of Rotor-Bearing Systems, *Proceedings of American Control Conference*, ACC2008. ISBN: 978-1-4244-2078-0.
- [Fliess, M. & H. Sira-Ramírez (2003)] An algebraic framework for linear identification, *ESAIM: Control, Optimization and Calculus of Variations*, Vol. 9, 151-168. ISSN: 1292-8119
- [Fliess, M.; J. Lévine, P. Martin & P. Rouchon (1993)] Flatness and defect of nonlinear systems: Introductory theory and examples, *Int. J. of Control*, 61(6), 1327-1361. ISSN: 0020-7179.
- [Korenev, B. G. & L. M. Reznikov (1993)] *Dynamic Vibration Absorbers: Theory and Technical Application*, Ed. John Wiley Sons, UK, pp. 320-509. ISBN-13: 978-0471928508.
- [Ljung, L. (1987)] *Systems identification: theory for the user*, Englewood Cliffs, NJ: Prentice-Hall, pp. 168-361. ISBN-13: 978-0136566953.
- [Sagara, S. & Z. Y. Zhao (1989)] Recursive identification of transfer function matrix in continuous systems via linear integral filter, *International Journal of Control*, Vol. 50, 457-477. ISSN: 0020-7179.

-
- [Sagara, S. & Z. Y. Zhao (1990)] Numerical integration approach to on-line identification of continuous systems, *Automatica*, Vol. 26, 63-74. ISSN: 0005-1098.
- [Soderstrom, T. and P. Stoica (1989)] *System Identification*, Ed. Prentice-Hall, New York, pp. 320-509. ISBN: 0-13-881236-5.

A Self-Organizing Fuzzy Controller for the Active Vibration Control of a Smart Truss Structure

Gustavo Luiz C. M. Abreu¹, Vicente Lopes Jr.¹ and Michael J. Brennan²

¹*Materials and Intelligent Systems Group – GMSINT
Universidade Estadual Paulista - UNESP, Department of Mechanical Engineering
Av. Brasil, 56, Ilha Solteira-SP,*

²*Institute of Sound and Vibration Research – ISVR
University of Southampton, Avenue Campus, Southampton,*

¹Brasil

²UK

1. Introduction

In the last two decades, the subject area of smart/intelligent materials and structures has experienced tremendous growth in terms of research and development. One reason for this activity is that it may be possible to create certain types of structures and systems capable of adapting to or correcting for changing operating conditions. The advantage of incorporating these special types of materials into the structure is that the sensing and actuating mechanism becomes part of the structure by sensing and actuating strains directly. Piezoelectric material is often suitable for this purpose. This type of material possesses direct and converse piezoelectric effects; when a mechanical force is applied to the piezoelectric material, an electric voltage or charge is generated, and when an electric field is applied to the material, a mechanical force is induced. With the recent advances in piezoelectric technology, it has been shown that the piezoelectric actuators based on the converse piezoelectric effect can offer excellent potential for active vibration control techniques, especially for vibration suppression or isolation.

A truss structure is one of the most commonly used structures in aerospace and civil engineering (Yan & Yam, 2002). Because it is desirable to use the minimum amount of material for construction, trusses are becoming lighter and more flexible which means they are more susceptible to vibration. Passive damping is not a preferred vibration control solution because it adds weight to the system, so it is of interest to study the active control of such a structure. A convenient way of controlling a truss structure is to incorporate a piezoelectric stack actuator into one of the truss members (Anthony & Elliot, 2005).

An important feature of control system in the truss structure is the collocation between the actuator and the sensor. An actuator/sensor pair is collocated if it is physically located at the same place and energetically conjugated, such as force and displacement or velocity, or torque and angle. The properties of collocated systems are remarkable; in particular, the

stability of the control loop is guaranteed when certain simple, specific controllers are used (Preumont, 2002). It requires that the control architecture be decentralized, i.e. that the feedback path include only one actuator/sensor pair, and be thus independent of others sensors or actuators possibly placed on the structure.

The choice of the actuator/sensor location is another important issue in the design of actively controlled structures. The actuators/sensors should be placed at locations so that the desired modes are excited most effectively (Lammering et al., 1994). A wide variety of optimization algorithms have been proposed to this end in the literature. Two popular examples are Simulated Annealing (Chen et al., 1991) and Genetic Algorithms (Rao et al., 1991; Padula & Kincaid, 1999). Although these methods are effective, they fail to give a clear physical justification for the choice of the actuator/sensor placement. In this chapter, a more physical method used by Preumont et al. (1992) has been chosen. It involves placing the transducer in the truss structure at the location where there is the maximal fraction of modal strain energy. At this location, the actuator will couple most effectively into this mode of vibration, i.e., there will be maximum controllability of the specific mode by the actuator.

Research on the damping of truss structures began in the late 80's. Fanson et al. (1989), Chen et al. (1989) and Anderson et al. (1990) developed active members made of piezoelectric transducers. Preumont et al. (1992) used a local control strategy to suppress the low frequency vibrations of a truss structure using piezoelectric actuators. Their strategy involved the application of integrated force feedback using two force gauges each collocated with the piezoelectric actuators, which were fitted into different beam elements in the structure. Carvalhal et al. (2007) used an efficient modal control strategy for the active vibration control of a truss structure. In their approach, a feedback force is applied to each node to be controlled according to a weighting factor that is determined by assessing how much each mode is excited by the primary source. Abreu et al. (2010) used a standard H_∞ robust controller design framework to suppress the undesired structural vibrations in a truss structure containing piezoelectric actuators and collocated force sensors.

It is difficult to implement classical controllers to systems which are complex such as truss structures. Because of this active vibration control using fuzzy controllers has received attention because of their ability to deal with uncertainties in terms of vagueness, ignorance, and imprecision. Fuzzy controllers are most suitable for systems that cannot be precisely described by mathematical formulations (Zadeh, 1965). In this case, a control designer captures the operator's knowledge and converts it into a set of fuzzy control rules.

Fuzzy logic is useful for representing linguistic terms numerically and making reliable decisions with ambiguous and imprecise events or facts. The benefit of the simple design procedure of a fuzzy controller has led to the successful application of a variety of engineering systems (Lee, 1990). Zeinoun & Khorrami (1994) proposed a fuzzy logic algorithm for vibration suppression of a clamped-free beam with piezoelectric sensor/actuator. Ofri et al. (1996) also used a control strategy based on fuzzy logic theory for vibration damping of a large flexible space structure controlled by bonded piezoceramic actuators and Abreu & Ribeiro (2002) used an on-line self-organizing fuzzy logic controller to control vibrations in a steel cantilever test beam containing distributed piezoelectric actuator patches.

In general, fuzzy logic controllers use fuzzy inference with rules pre-constructed by an expert. Therefore, the most important task is to form the rule base which represents the experience and intuition of human experts. When this rule base is not available, efficient control can not be expected.

The self-organizing fuzzy controller is a rule-based type of controller which learns how to control on-line while being applied to a system, and it has been used successfully for a wide variety of processes (Shao, 1988). This controller combines system identification and control based on experience. Therefore, only a minimal amount of information about the environment needs to be provided.

The main purpose of this chapter is to demonstrate how active vibration control of a truss structure can be achieved with the minimal input of human experts in designing a fuzzy logic controller for such a purpose. For this, the self-organizing controller is used which uses the input and output history in its rules (Abreu & Ribeiro, 2002). This controller has no rules initially, but forms rules by defining membership functions using the plant input-output data as singletons and stores them in a rule base. The rule base is updated as experience is accumulated using a self-organizing procedure. A simple method for defuzzification is also presented by adding a predictive capability using a prediction model.

The self-organizing controller is numerically verified in a truss structure using a pair of piezoceramic stack actuators. The control system consists of independent SISO loops, i.e. decentralized active damping with local self-organizing fuzzy controllers connecting each actuator to its collocated force sensor. A finite element model of the structure is constructed using three-dimensional frame elements subjected to axial, bending and torsional loads considering electro-mechanical coupling between the host structure and piezoelectric stack actuators. To simulate the effects of disturbances on the truss, an impulsive force is applied to excite many modes of vibration of the system, and variations in the structural parameters are considered. Numerical simulations are carried out to evaluate the performance of the self-organizing fuzzy controller and to demonstrate the effectiveness of the active vibration control strategy.

2. The truss structure

The truss structure of interest in this chapter is depicted in Fig. 1. It consists of 20 bays, each 75 mm long, made of circular steel bars of 5 mm diameter connected with steel joints (80g mass blocks) and clamped at the base. It is equipped with active members as indicated in the Fig. 1. They consist of piezoelectric linear actuators, each collinear with a force transducer.

2.1 Governing equations

Consider the linear structure of Fig. 1 equipped with a discrete, massless piezoelectric stack actuator. The equation governing the motion of the structure excited by a force f and controlled by a piezoelectric actuator (f_a) is

$$M\ddot{x} + C\dot{x} + Kx = bf + b_a f_a \quad (1)$$

where K and M are the stiffness and mass matrices of the structure, obtained by means of the finite element model using the three-dimensional frame elements (Kwon & Bang, 1997) (each node has six degrees-of-freedom), C is the damping matrix; b and b_a are, respectively, the influence vectors relating to the locations of the external forces (f) and the active member in the global coordinates of the truss (the non-zero components of b_a are the direction cosines of the active bar in the structure), and f_a is the force exerted by an active member.

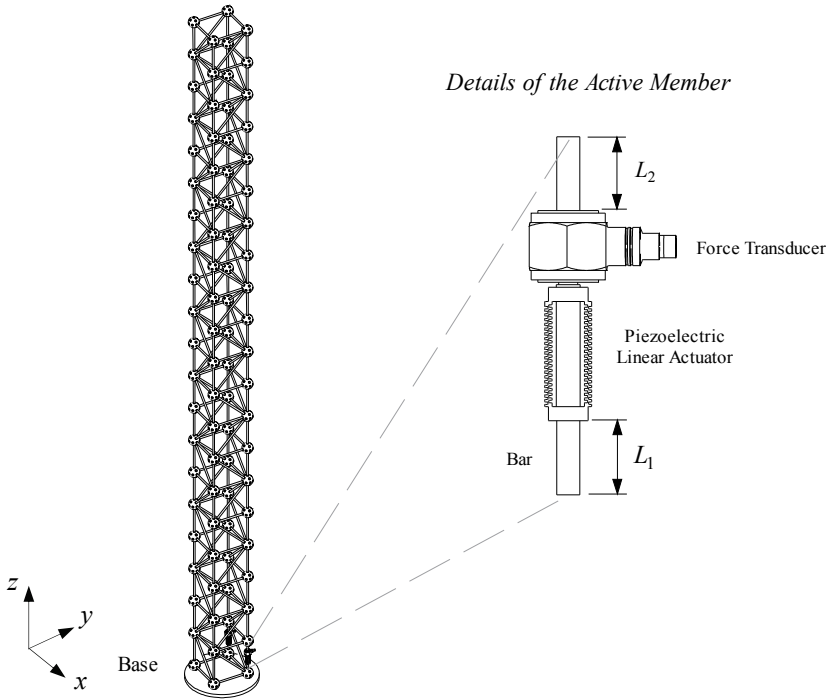


Fig. 1. Truss structure with a pair of active members.

Consider the piezoelectric linear transducer of Fig. 1 is made of n_a identical slices of piezoceramic material stacked together. Since damping is considered to be negligible, the force exerted by an active member is defined by (Leo, 2007)

$$f_a = K_{eq} (\Delta - n_a d_{33} V) \quad (2)$$

where d_{33} is the piezoelectric coefficient, V is the voltage applied to the piezo actuator, Δ is the displacement at the end nodes of the active member i.e., Δ is the sum of the free displacement of the piezoelectric actuator ($n_a d_{33} V$) and the displacement due to the blocked force of the actuator (f_a / K_a), and K_{eq} is the equivalent stiffness of the actuator, such that

$$\frac{1}{K_{eq}} = \frac{L_1 + L_2}{EA_t} + \frac{1}{K_a} \quad (3)$$

where K_a is the combined stiffness of the actuator and force sensor, and E and A_t are respectively the Young's modulus and cross-sectional area of the bar shown in Fig. 1.

The elongation Δ of each actuator is linked to the vector of structural displacements by

$$\Delta = b_a^T x \quad (4)$$

The equation governing the structure containing the active member can be found by substituting Eqs. (2) and (4) with Eq. (1). The new equation is

$$M\ddot{x} + C\dot{x} + (K - K_{eq}b_a b_a^T)x = bf - b_a K_{eq} n_a d_{33} V \tag{5}$$

where K is the stiffness matrix of the structure excluding the axial stiffness of the actuator. The equation (5) can be transformed into modal coordinates according to

$$x = \Phi \eta \tag{6}$$

where Φ is the matrix of the mode shapes, which can be determined by solving the eigenvalue problem

$$M\ddot{x} + (K - K_{eq}b_a b_a^T)x = 0 \tag{7}$$

Assuming normal modes normalized such that $\Phi^T M \Phi = I$ and introducing the modal state vector $x_n = [\eta \quad \dot{\eta}]^T$, the transformed equation of motion (5) becomes

$$\dot{q} = Aq + B_1 f + B_2 V \tag{8}$$

where

$$A = \begin{bmatrix} 0 & I \\ -\bar{K} & -\bar{C} \end{bmatrix}, B_1 = \begin{bmatrix} 0 \\ \Phi^T b \end{bmatrix} \text{ and } B_2 = \begin{bmatrix} 0 \\ -\Phi^T b_a K_{eq} n_a d_{33} \end{bmatrix} \tag{9}$$

and $\bar{K} = \text{diag}(\omega_i^2)$, $\bar{C} = \text{diag}(2\zeta_i \omega_i)$, ω_i is the i -th natural frequency of the truss and ζ_i is the associated modal damping.

Similarly to Eq. (2), the output signal of the force sensor, proportional to the elastic extension of the truss, is defined by

$$y = C_2 q + D_{22} V \tag{10}$$

Where

$$C_2 = [K_{eq} b_a^T \Phi \quad 0] \text{ and } D_{22} = -K_{eq} n_a d_{33} \tag{11}$$

3. Actuator placement

More than any specific control law, the location of the active member is the most important factor affecting the performance of the control system. Good control performance requires the proper location of the actuator to achieve good controllability. The active member should be placed where its authority in controlling the targeted modes is the greatest. It can be achieved if the transducer is located to maximize the mechanical energy stored in it. The ability of a vibration mode to concentrate the vibrational energy in the transducer is measured by the fraction of modal strain energy v_i defined by (Preumont, 2002)

$$v_i = \frac{\phi_i^T (K_{eq} b_a b_a^T) \phi_i}{\phi_i^T (K - K_{eq} b_a b_a^T) \phi_i} = \frac{K_{eq} (b_a^T \phi_i)^2}{\omega_i^2} \tag{12}$$

The Eq. (12) is the ratio between the strain energy in the actuator and the total strain energy when the structure vibrates in its i -th mode. Physically, v_i can be interpreted as a compound indicator of controllability and observability of mode i by the transducer. The best location for the transducer in the truss structure is the position which has the maximal fraction of modal strain energy of the mode to be controlled.

Here, the control objective is to add damping to the first two modes of the structure by using two active elements. The search for candidate locations where these active members can be placed is greatly assisted by the examination of the first two structural mode shapes which are shown in Fig. 2.

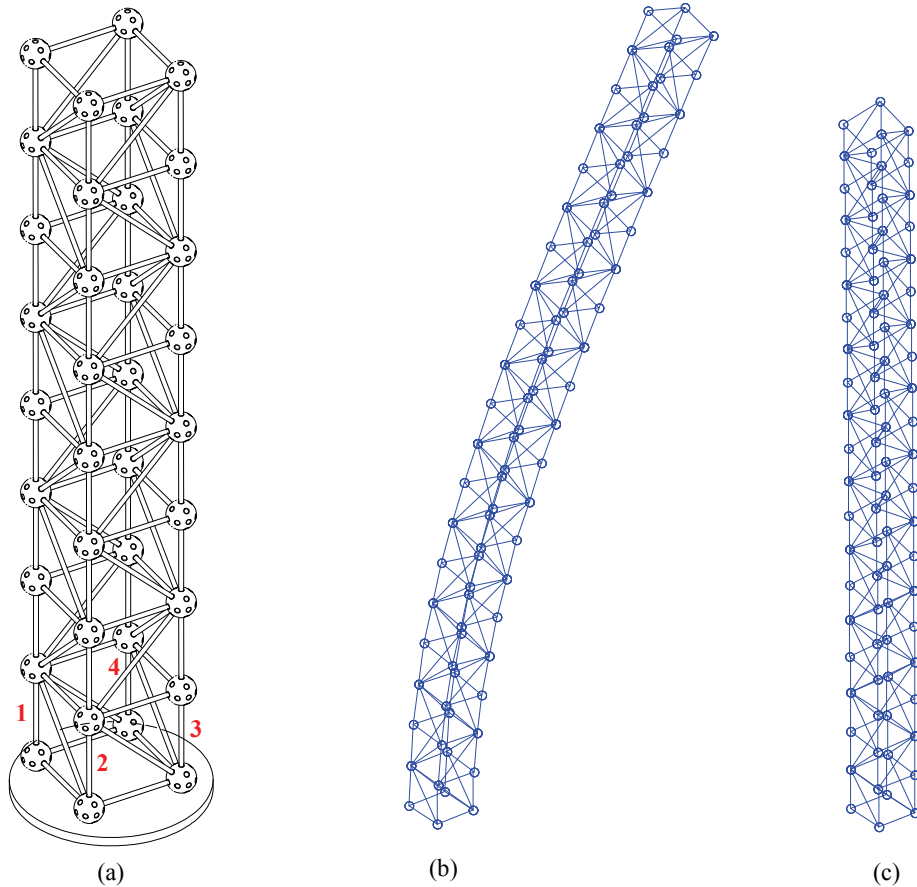


Fig. 2. a) disposition of the active elements; b) first mode shape (12.67 Hz) and c) second mode shape (12.69 Hz).

Assuming the main characteristics of both transducers as: $K_{eq} = 28 \text{ N}/\mu\text{m}$ and $n_a d_{33} = 1.12 \times 10^{-7} \text{ m/Volts}$, the fractions of modal strain energy v_i , computed from Eq. (12), are shown in Table 1, which gives the six possible combinations of the two positions of the actuators from the four candidate positions shown Fig. 2a.

Positions	v_1 (%)	v_2 (%)
1 & 2	11.22	8.79
1 & 3	16.39	0.00
1 & 4	11.08	9.46
2 & 3	1.63	3.00
2 & 4	16.93	0.04
3 & 4	14.26	15.68

Table 1. Fraction of modal strain energy in the selected finite elements.

From Fig. 2 and the Tab. 1 it can be seen that when the active members are located at positions 3 and 4, the sum of the fractions of modal strain energies v_1 and v_2 are maximal. Thus these positions are chosen for the transducers in the actual truss as shown in Fig. 1.

4. Design of the self-organizing fuzzy controller

Consider the truss structure with the active members described in Section 3. Each active member consists of a piezoelectric linear actuator collocated with a force transducer. In this section, a decentralized active damping controller is considered with a local Self-Organizing Fuzzy Controller (SOFC) connecting each actuator to its collocated force sensor (y). The control voltage (V) applied to each actuator is defined as

$$V(s) = \frac{u}{s + \varepsilon} \quad (13)$$

where s is the Laplace variable, u is the output of the SOFC and the constant ε is to avoid voltage saturation and it must be lower than the first natural frequency of the structure (Preumont et al., 1992). The integral term $1/s$ introduces a 90° phase shift in the feedback path and thus adds damping to the system (Chen et al, 1989). It also introduces a -20 dB/decade slope in the open-loop frequency response, and thus reduces the risks of spillover instability (Preumont, 2002).

Using the backward difference rule (Phillips & Nagle, 1990), Eq. (13) can be written in the time domain as

$$V_{k+1} = e^{-\varepsilon dt} V_k + u_k \varepsilon dt \quad (14)$$

where k is the sampling step and dt is the sampling time.

Based on the steps in designing a conventional Fuzzy Logic Controller (FLC), the SOFC design consists of six steps: 1) the definition of input/output variables; 2) definition of the control rules; 3) fuzzification procedure; 4) inference logic procedure, 5) defuzzification procedure, and 6) the self-organization of the rule base.

4.1 Definition of input/output variables

In general, the output of a system can be described with a function or a mapping of the plant input-output history. For a Single-Input Single-Output (SISO) discrete time systems, the mapping can be written in the form of a nonlinear function as follows

$$y_{k+1} = g(y_k, y_{k-1}, \dots, u_k, u_{k-1}, \dots) \quad (15)$$

where y_k and u_k are, respectively, the output and input variables at the k -th sampling step. The objective of the control problem is to find a control input sequence which will drive the system to an arbitrary reference point y_{ref} . Rearranging Eq. (15) for control purposes, the value of the input u at the k -th sampling step that is required to yield the reference output y_{ref} can be written as follows

$$u_k = h(y_{ref}, y_k, y_{k-1}, \dots, u_{k-1}, u_{k-2}, \dots) \quad (16)$$

which can be viewed as an inverse mapping of Eq. (15).

While a typical conventional FLC uses the error and the error rate as the inputs, the proposed controller uses the input and output history as the input terms: $y_{ref}, y_k, y_{k-1}, y_{k-2}, \dots, y_k, u_{k-1}, u_{k-2}, \dots$. This implies that u_k is the input to be applied when the desired output is y_{ref} as indicated explicitly in Eq. (16).

4.2 Definition of the control rules

In this work, the key idea behind the SOFC is not to use rules pre-constructed by experts, but forms rules with input and output history at every sampling step. Therefore, a new rule R , with the input and output history can be defined as follows

$$\begin{aligned} R^{(j)} : & \text{IF } y_k \text{ is } A_{1j}, y_{k-1} \text{ is } A_{2j}, \dots, y_{k-n+1} \text{ is } A_{nj}, \\ & \text{AND } u_{k-1} \text{ is } B_{1j}, \dots, u_{k-m} \text{ is } B_{mj}, \text{ THEN } u_k \text{ is } C_j \end{aligned} \quad (17)$$

where n and m are the number of output and input variables, $A_{1j}, A_{2j}, \dots, A_{nj}$ and $B_{1j}, B_{2j}, \dots, B_{mj}$ are the antecedent linguistic values for the j -th rule and C_j is the consequent linguistic values for the j -th rule.

4.3 Fuzzification procedure

In a conventional FLC, an expert usually determines the linguistic values $A_{1j}, A_{2j}, \dots, A_{nj}$ and $B_{1j}, B_{2j}, \dots, B_{mj}$, and C_i by partitioning each universe of discourse. In this paper, however, this linguistic values are determined from the crisp values of the input and output history at every sampling step and a fuzzification procedure for fuzzy values is developed to determine $A_{1j}, A_{2j}, \dots, A_{(n+1)j}, B_{1j}, B_{2j}, \dots, B_{mj}$, and C_i from the crisp $y_k, y_{k-1}, y_{k-2}, \dots, y_{k-n+1}, u_{k-1}, u_{k-2}, \dots, u_{k-m}$ and u_k , respectively. The fuzzification is done with its base on assumed input or output ranges. When the assumed input or output range is $[a, b]$, the membership function for crisp y_i is determined in a triangular shape

$$\mu_{A_i} = \begin{cases} 1 + (y - y_i) / (b - a) & \text{if } a \leq y < y_i \\ 1 - (y - y_i) / (b - a) & \text{if } y_i \leq y < b, \text{ for } i = 1, 2, \dots, n \\ 0 & \end{cases} \quad (18)$$

Note that all linguistic values overlap on the entire range $[a, b]$, and furthermore, every crisp value uniquely defines the membership function with the unity center or vertex value and identical slopes: $-1/(b-a)$ and $1/(b-a)$ for the right and left lines, respectively (see Fig. 3).

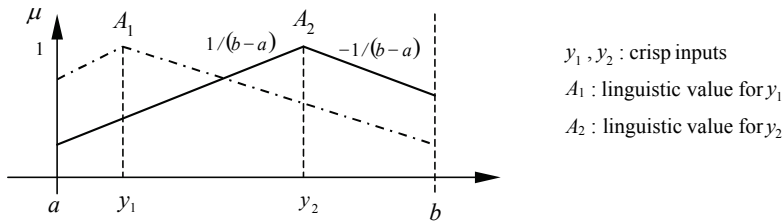


Fig. 3. Fuzzification procedure for $A_{1j}, A_{2j}, \dots, A_{nj}, B_{1j}, B_{2j}, \dots, B_{mj}$ or C_j .

The Fig. 3 shows the fuzzification procedure for crisp variables y_1 and y_2 , where A_1 and A_2 are the corresponding linguistic values (fuzzy sets) with membership functions defined in the range $[a, b]$. Thus, this fuzzification procedure requires only the minimal information in forming the membership functions.

4.4 Inference logic procedure

To attain the output fuzzy set, it is necessary to determine the membership degree (w_i) of the input fuzzy set with respect to each rule. If input fuzzy variables are considered as fuzzy singletons, the membership degree of the input fuzzy variables for each rule may be calculated by using a specific operator (AND). As with the conventional FLC, the operator used here is the *min* operator described for the i -th rule

$$w_i = \min[(A_{1i} \wedge y_1), \dots, (A_{(n+1)i} \wedge y_{n+1}), (B_{1i} \wedge u_1), \dots, (B_{mi} \wedge u_m)] \tag{19}$$

where \wedge is the AND operation.

This mechanism considers the minimum intersection degree between input fuzzy variables and the antecedent linguistic values for the example: i -th and j -th rules, as shown in Fig. 4.

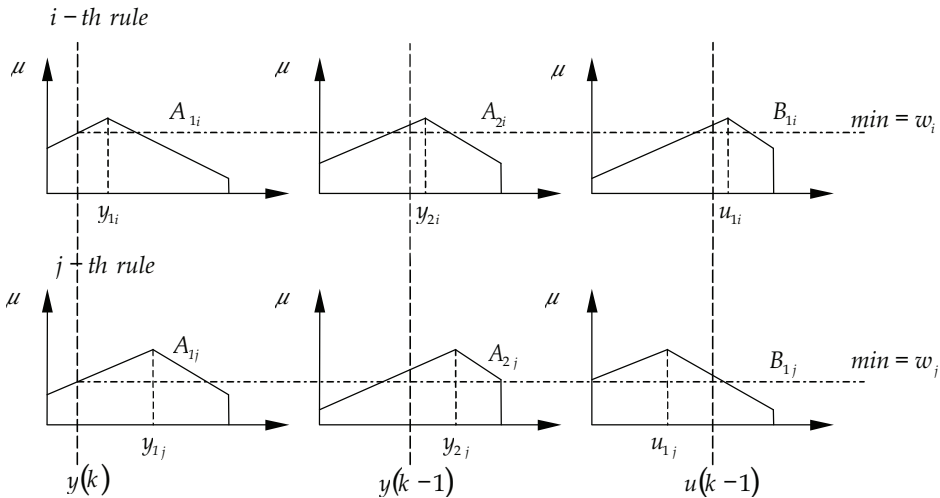


Fig. 4. Inference mechanism.

The membership degrees w_i and w_j thus defined reflect the contribution of all input variables in the i -th and j -th rules. The evaluation of the membership degree value w with three fuzzy input variables, y_k , y_{k-1} and u_{k-1} , is shown in Fig. 4, where the i -th rule is closer to the input variables than the j -th rule and thus $w_i > w_j$.

The consequent linguistic value or the net linguistic control action, C_n is calculated for taking the α -cut of C_n , where $\alpha = \max[\mu(C_n)]$. To find the control range for the example shown in Fig. 4, each operation forms the consequent fuzzy set, and the range with its membership degree is deduced as a control range for each rule, i.e., $[a, b]$ for the i -th rule, and $[c, d]$ for the j -th rule as the respective ranges. As a result of this inference, the net control range (NCR), which is the intersection of all control ranges, is determined, i.e., $[c, b]$ as shown in Fig. 5, where C_i and C_j are the consequent fuzzy sets for the i -th and j -th rules, respectively.

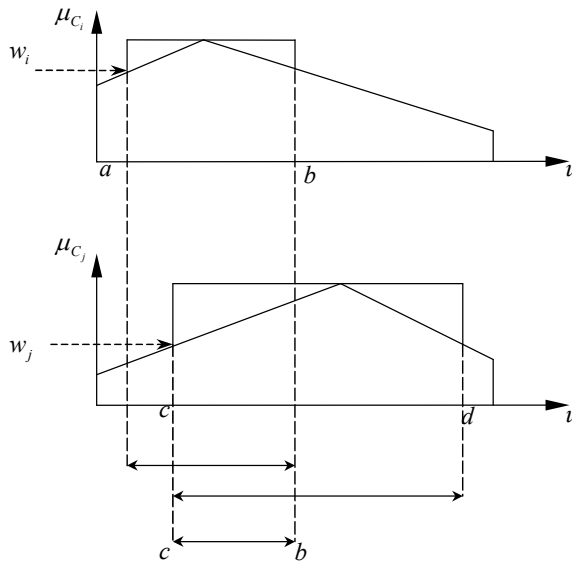


Fig. 5. The Net Control Range (NCR) with two rules.

4.5 Defuzzification procedure

Defuzzification is the procedure to determine a crisp value from a consequent fuzzy set. Methods often used to do this are the center of area and the mean of maxima (Driankov et al., 1996). Here, the purpose of defuzzification is to determine a crisp value from the NCR resulting from the inference. Any value within the NCR has the potential to be a control value, but some control values may cause overshoot while others may be too slow. This problem can be avoided by adding a predictive capability in the defuzzification. A method is presented which modifies the NCR to compute a crisp value by using the prediction of the output response. The series of the last outputs is extrapolated in the time domain to estimate y_{k+1} by the Newton backward-difference formula (Burden and Faires, 1989). If the extrapolation order is n , using the binomial-coefficient notation, the estimate \hat{y}_{k+1} is calculated as follows

$$\hat{y}_{k+1} = \sum_{i=0}^n (-1)^i \binom{-1}{i} \nabla^i y_k \tag{20}$$

where

$$\nabla^i y_k = \Delta \nabla (\nabla^{i-1} y_k), \text{ where } \nabla y_k = y_k - y_{k-1} \text{ for } i \geq 2 \tag{21}$$

Defuzzification is performed by comparing the two values, the estimate \hat{y}_{k+1} and the reference output y_{ref} or the temporary target y_{k+1}^t , generated by

$$y_{k+1}^t = y_k + \alpha (y_{ref} - y_k) \tag{22}$$

where y_{k+1}^t is the reference output or the temporary target and α is the target ratio ($0 < \alpha \leq 1$). The value α describes the rate with which the present output y_k approaches the reference output value. The value α is chosen by the user to obtain a desirable response. When the estimate exceeds the reference output, the control has to slow down. On the other hand, when the estimate has not reached the reference, the control should speed up. Two possible cases will therefore be considered: Case 1) $\hat{y}_{k+1} < y_{k+1}^t$ and Case 2) $\hat{y}_{k+1} > y_{k+1}^t$.

To modify the control range, the sign of $u_k - u_{k-1}$ is assumed to be the same as the sign of $y_{k+1}^t - \hat{y}_{k+1}$. Thus, for Case 1 the sign of $y_{k+1}^t - \hat{y}_{k+1}$, hence the sign of $u_k - u_{k-1}$, is positive, implying that u_k has to be increased from the previous input u_{k-1} .

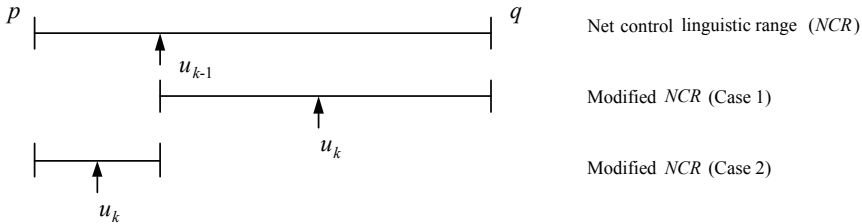


Fig. 6. The defuzzification procedure.

The final crisp control value u_k is then selected as one of the midpoints of the modified NCR as shown in Fig. 6.

$$u_k = \begin{cases} (u_{k-1} + q) / 2 & \text{for Case 1} \\ (p + u_{k-1}) / 2 & \text{for Case 2} \end{cases} \tag{23}$$

where p and q are the respective lower and upper limits of the NCR resulting from the inference mechanism (Section 4.4).

4.6 Self-organization of the rule base

The rules of the SOFC are generated at every sampling time. If every rule is stored in the rule base, two problems will occur: 1) the memory will be exhausted, and 2) the rules which are performed improperly during the initial stages also affect the later inference.

For this reason, the fuzzy *rule space* is partitioned into a finite number of domains of different sizes and only one rule, is stored in each domain. Figure 7 shows an example of the division of a rule space for two output variables y_k and y_{k-1} .

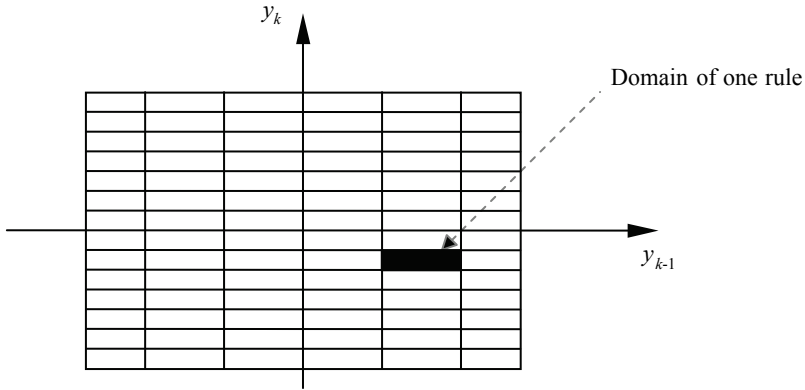


Fig. 7. Division of a two-dimensional rule space.

Figure 8 shows the rule base updating procedure. If there are two rules in the same domain, the selection of a rule is based on comparison of y_k in both rules. That is, if there is a new

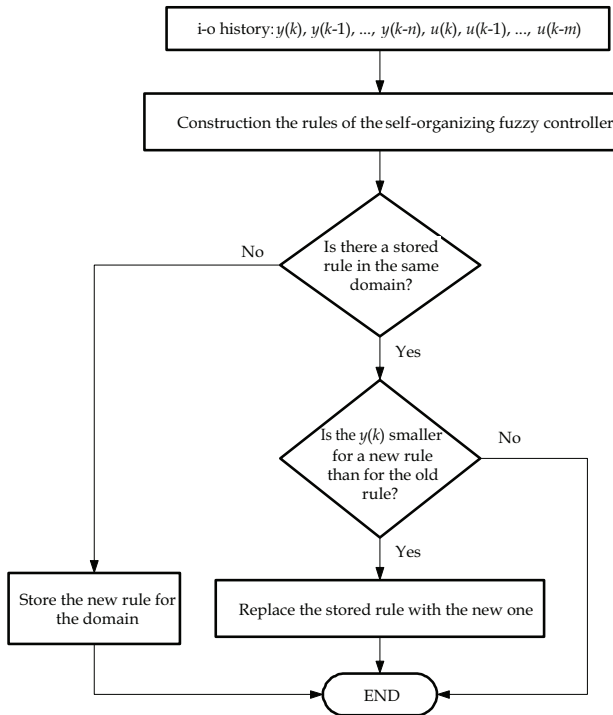


Fig. 8. The self-organization of the rule base.

rule which has an output smaller to the existing output in a given domain (*old rule*), the old rule is replaced by the new one. This updating procedure of the rule base makes the proposed fuzzy logic controller capable of learning the object plant and self-organizing the rule base. The number of rules increases as new input-output data is generated. It converges to a finite number in the steady state, however, and never exceeds the maximum number of domains partitioned in the rule space.

Figure 9 shows the architecture of the proposed FLC system. Initially, since there is no control rule in the rule base, the control input u_k for the first step is the median value of the entire input range. As time increases, the defuzzification procedure begins to determine whether the input has to be increased or decreased depending on the trend of the output. The sign of ∇u_k and the magnitude of u_k are determined in the defuzzification procedure. The self-organization of the rule base, in other words the *learning* of the system, is performed at each sampling time k .

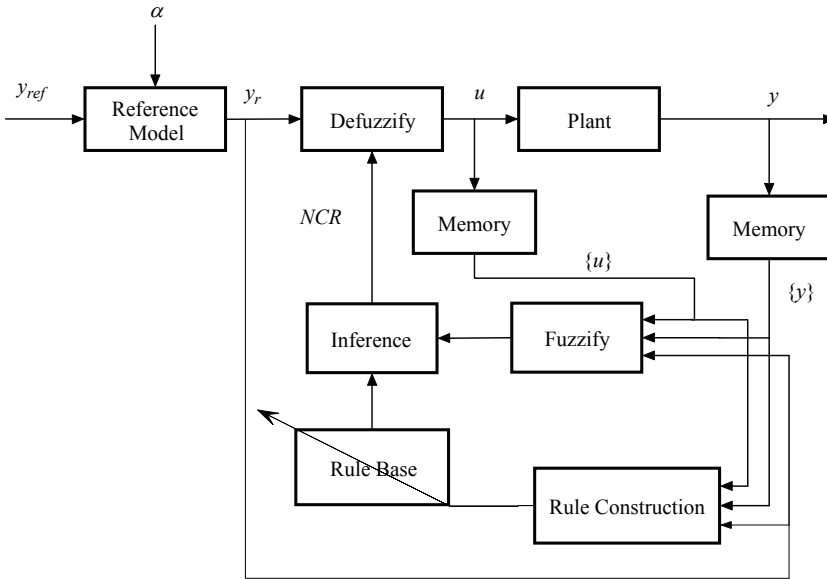


Fig. 9. The self-organizing fuzzy logic control system architecture.

5. Simulations and numerical results

Numerical simulations are presented to demonstrate the efficacy of the SOFC applied to the truss structure. The structure considered is the 20-bay truss with bays each of 75 mm. It has 244 members and 84 spherical nodes, and the nodes at the bottom are clamped (see Fig. 1). The passive members are made of steel with a diameter of 5 mm, and the damping matrix is assumed to be proportional to the stiffness and mass matrices so that $C = 10^{-1}M + 10^{-7}K$. At each node there is a centralized mass block of 80g which has six degrees of freedom (dof), translations and rotations in all directions, so the truss structure has 480 active dofs, and the state-space model consequently has an order of 960. The strategy is to control the first two modes (12.67 Hz and 12.69 Hz) by using two active members positioned in the elements

shown in Fig. 2a, and two decentralized SOFC (Eq. 14, where $\varepsilon = \omega_1 / 2$) connecting each actuator (considering $K_{eq} = 28 \text{ N}/\mu\text{m}$ and $n_d d_{33} = 1.12 \times 10^{-7} \text{ m/Volts}$) to its collocated force sensor.

5.1 Parameters of the self-organizing fuzzy controller

In the numerical simulations, y_k , y_{k-1} , and u_{k-1} , u_{k-2} were used as input variables to the SOFC and the variables y_k and y_{k-1} were divided into five segments to partition the rule space. The second-order extrapolation (Eq. 20) was performed to estimate y_{k+1} as follows

$$\hat{y}_{k+1} = 2y_k - y_{k-1} \quad (24)$$

In both controllers, the output range (y) is -0.01 to 0.01 N , input range (u) is -0.5 to 0.5 V , the target ratio α was 0.5 (determined by trial and error), y_{ref} is zero and the sampling time is set to 0.001 seconds.

5.2 Simulation results

To verify the controller performance numerically, open loop and closed loop simulations were conducted and the results are presented and discussed. Firstly, an impulsive force is applied in y direction on the node at the top of the structure (see Fig. 1). White noise excitation with a force level of 0.01 N on each force transducer was also considered. The uncontrolled and controlled responses of the force transducers 1 and 2 in the time domain for impulsive excitation are shown in Figs. 10 and 11.

This type of force is used as it will excite many modes of vibration and hence is a difficult test for the control system. From the results it can be observed that the sensor responses are reduced greatly. Figure 12 presents the corresponding control voltages.

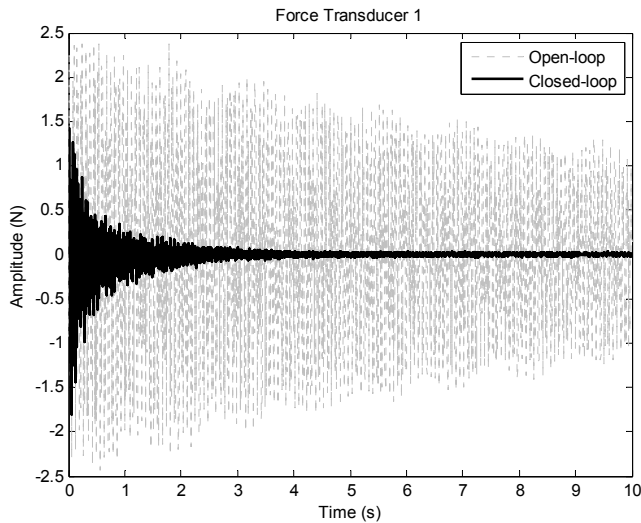


Fig. 10. Uncontrolled and controlled responses at the force transducer 1 with impulsive disturbance force.

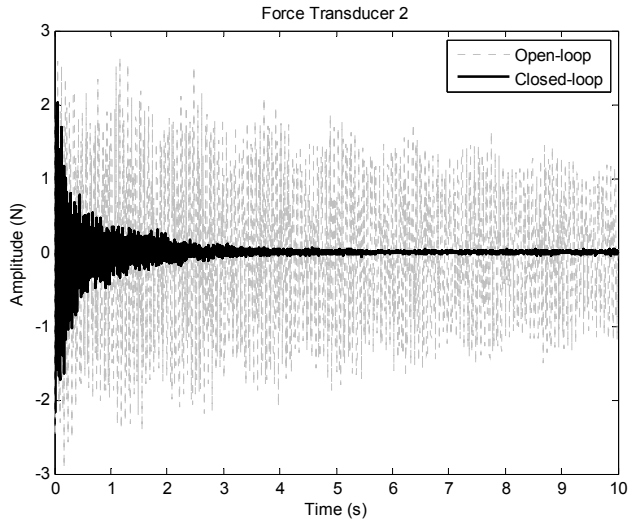


Fig. 11. Uncontrolled and controlled responses at the force transducer 2 with impulsive disturbance force.

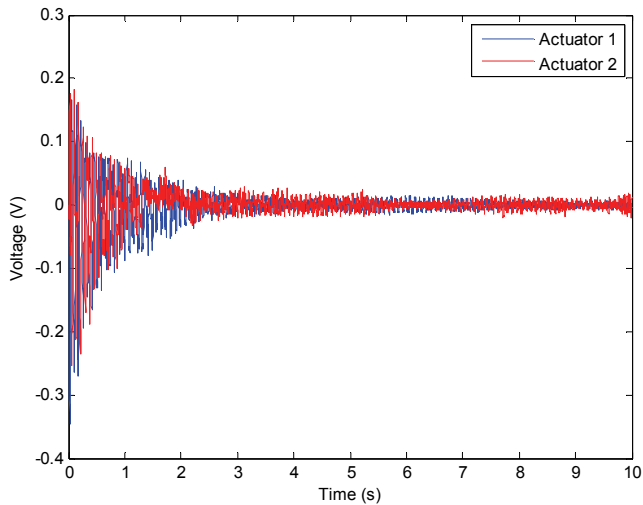


Fig. 12. Feedback control voltages applied by the piezoelectric actuators with impulsive disturbance force.

In Fig. 13, the proposed control algorithm starts with no initial rule and the number of generated rules is increased monotonically to 26 rules (each rule can be represented by Eq. 17).

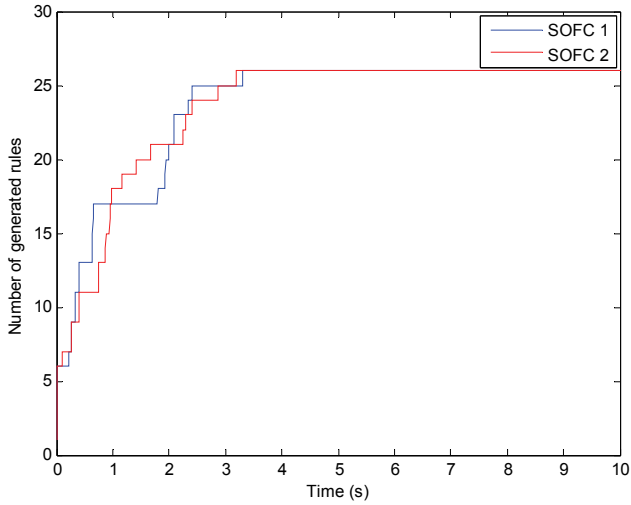


Fig. 13. Number of generated rules of SOFCs 1 and 2.

To numerically verify the robustness of the designed SOFCs in presence of modelling errors, a set of numerical tests are conducted. In the present analysis, the natural frequencies and modal damping are the uncertain parameters. To attain the presented objective, the natural frequencies and the modal damping are reduced in 20% and 60%, respectively. In this situation, the uncontrolled and controlled responses of the force transducers 1 and 2 in time domain are shown in Figs. 14 and 15. Figure 16 presents the corresponding control voltages.

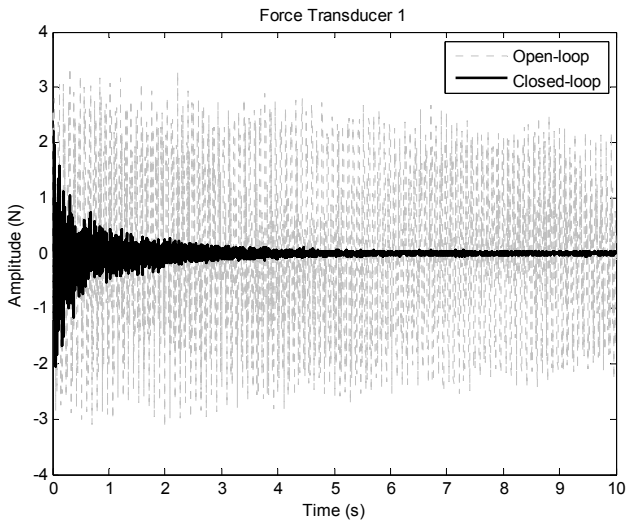


Fig. 14. Uncontrolled and controlled responses at the force transducer 1 with impulsive disturbance force in presence of modelling errors.

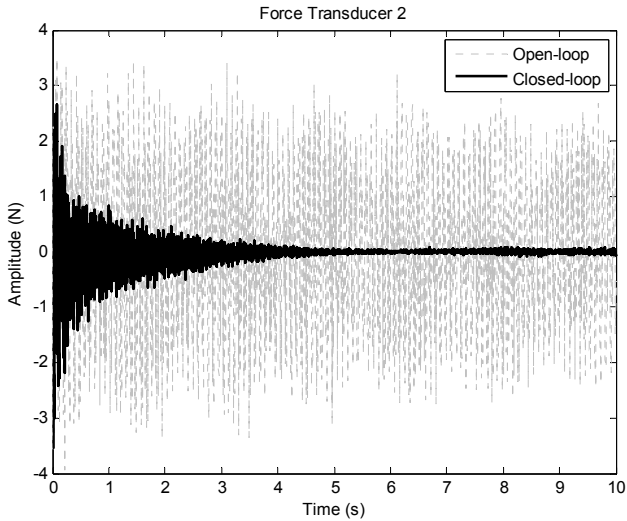


Fig. 15. Uncontrolled and controlled responses at the force transducer 2 with impulsive disturbance force in presence of modelling errors.

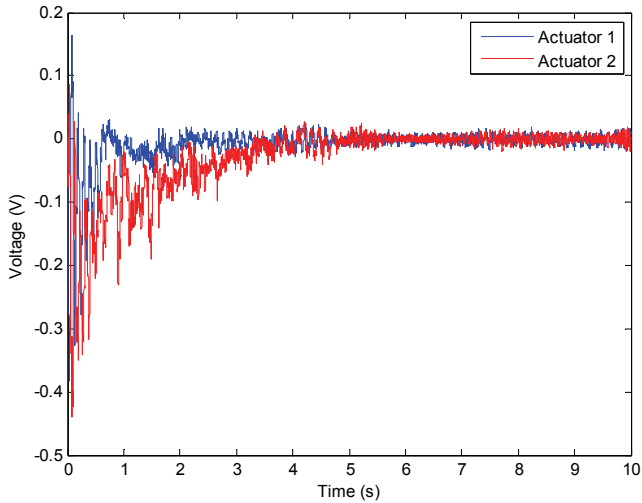


Fig. 16. Feedback control voltages applied by the piezoelectric actuators with impulsive disturbance force in presence of modelling errors.

In this case, the proposed control algorithm starts with no initial rule and the number of generated rules is increased to 26 rules (see Fig. 17).

The number of newly-generated rules is the same than the last case. This is because the system conditions for the controller are basically the same, i.e., no more rules need to be stored for a change of natural frequencies and modal damping.

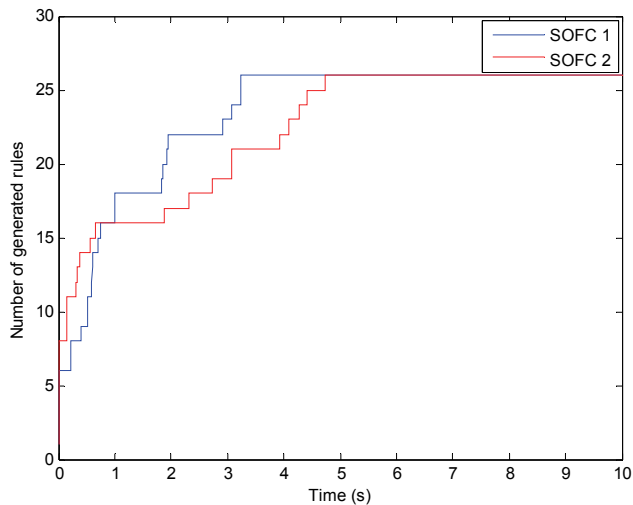


Fig. 17. Number of generated rules of SOFCs 1 and 2 in presence of modelling errors.

6. Conclusions

A self-organizing fuzzy controller has been developed to control the vibrations of the truss structure containing a pair of piezoelectric linear actuators collinear with force transducers. The procedure used for placing actuators in the structure, which has a strong intuitive appeal, has proven to be effective. The control system consists of a decentralized active damping with local self-organizing fuzzy controllers connecting each actuator to its collocated force sensor. The control strategy mimics the human learning process, requiring only minimal information on the environment. A simple defuzzification method was developed and an updating procedure of the rule was developed which makes the proposed fuzzy logic controller capable of learning the system and self-organizing the controller. A set of numerical simulations was performed, which demonstrated the effectiveness of the controller in reducing the vibrations of a truss structure. The numerical results have shown that piezoceramic stack actuators control efficiently the vibrations of the truss structure. It was also demonstrated that the fuzzy control strategy can effectively reduce truss vibration in the presence of modelling errors and under a several operating conditions.

7. Acknowledgments

The first author would like to thank the FAPESP (N° 2008/05129-3) for the financial support of the reported research.

8. References

- Abreu, G. L. C. M. and Ribeiro, J. F. (2002). A Self-Organizing Fuzzy Logic Controller for the Active Control of Flexible Structures Using Piezoelectric Actuators, *Applied Soft Computing*, Vol. 1, pp. 271-283.

- Abreu, G. L. C. M.; Lopes Jr., V. and Brennan, M. J. (2010). Robust Control of an Intelligent Truss Structure. *10th International Conference on Recent Advances in Structural Dynamics*, Southampton University, United Kingdom-UK.
- Anderson, E. H.; Moore, D. M. and Fanson, J. L. (1990). Development of an Active Truss Element for Control of Precision Structures. *Optical Engineering*, Vol. 29, No. 11, pp. 1333-1341.
- Anthony, D. K. and Elliot, S. J. (2005). On Reducing Vibration Transmission in a Two-dimensional Cantilever Truss Structure using Geometric Optimization and Active Vibration Control Techniques. *Journal of the Acoustical Society of America*, Vol. 110, pp. 1191-1194.
- Burden, R. L. and Faires, J. D. (1989). *Numerical Analysis, PWS-KENT*.
- Carvalho, R.; Lopes Jr., V. and Brennan, M. J. (2007). An Efficient Modal Control Strategy for the Active Vibration Control of a Truss Structure. *Shock and Vibration*, Vol. 14, pp. 393-406.
- Chen, G. S.; Lurie, B. J. and Wada, B. K. (1989). Experimental Studies of Adaptive Structures for Precision Performance. *SDM Conference*, pp. 1462-1472.
- Chen, G. S.; Bruno, R. J. and Salama, M., (1991). Optimal Placement of Active/Passive Members in Truss Structures using Simulated Annealing. *AIAA Journal*, Vol. 29, No. 8, pp. 1327-1334.
- Driankov, D., Hellendoorn, H. and Reinfrank, M. (1996). *An Introduction to Fuzzy Control. Springer-Verlag*, 2nd Ed.
- Fanson, J. L.; Blackwood, G. H. and Chu, C. C. (1989). Active Member Control of Precision Structures. *SDM Conference*, pp. 1480-1494.
- Kwon, Y. and Bang, H. (1997). *The Finite Element Method using Matlab. CRC Press*.
- Lammering, R.; Jia, J. and Rogers, C. A. (1994). Optimal Placement of Piezoelectric Actuators in Adaptive Truss Structure. *Journal of Sound and Vibration*, Vol. 171, pp. 67-85.
- Lee, M. (1990). Fuzzy Logic in Control Systems: Fuzzy Logic Controller - Part I and II. *IEEE Transactions on Systems, Man and Cybernetics*, Vol. 2, pp. 404-435.
- Leo, D. J. (2007). *Engineering Analysis of Smart Material Systems. John Wiley and Sons*.
- Ofri, A.; Tanchum, W. and Guterman, H. (1996). Active Control for Large Space Structure by Fuzzy Logic Controllers. *IEEE*, pp. 515-518.
- Padula, S. L. and Kincaid, R. K. (1999). Optimization Strategies for Sensor and Actuator Placement. *Technical report TM-1999-209126*, NASA Langley Research Center.
- Phillips, C. L. and Nagle, N. T. (1990). *Digital Control System Analysis and Design. Prentice Hall*, Englewood Cliffs, New Jersey.
- Preumont, A.; Dufour, J. P. and Malekian, C. (1992). Active Damping by a Local Force Feedback with Piezoelectric Actuators. *Journal of Guidance, Control and Dynamics*, Vol. 15, pp. 390-395.
- Preumont, A. (2002). *Vibration Control of Active Structures: An Introduction, Kluwer*.
- Rao, S. S.; Pan, T. S. and Venkayya, V. B. (1991). Optimal Placement of Actuators in Actively Controlled Structures using Genetic Algorithms. *AIAA Journal*, Vol. 29, No. 6, pp. 942-943.
- Shao, S. (1988). Fuzzy Self-Organizing Controller and its Application For Dynamic Processes. *Fuzzy Set and Systems*, Vol. 26, pp. 151-164.
- Yan, Y. J. and Yam, L. H. (2002). A Synthetic Analysis of Optimum Control for an Optimized Intelligent Structure. *Journal of Sound and Vibration*, Vol. 249, pp. 775-784.

Zadeh, L. A. (1965). *Information and Control*. Vol. 8, pp. 338-353.

Zeinoun, I. J. and Khorrani, F. (1994). An Adaptive Control Scheme Based on Fuzzy Logic and its Application to Smart Structures. *Smart Materials and Structures*, Vol. 3, pp. 266-276.

Semi-active Vibration Control Based on Switched Piezoelectric Transducers

Hongli Ji, Jinhao Qiu and Pinqi Xia
*Nanjing University of Aeronautics and Astronautics
China*

1. Introduction

Vibration in modern structures like airplanes, satellites or cars can cause malfunctions, fatigue damages or radiate unwanted and loud noise (Simpson & Schweiger, 1998; Wu et al., 2000; Hopkins et al., 2000; Kim et al., 1999; Zhang et al., 2001; Hagood et al., 1990). Since conventional passive damping materials have reached their limits to damp vibration because it is not very effective at low frequencies and requires more space and weight, new control designs with novel actuator systems have been proposed. These so called smart materials can control and suppress vibration in an efficient and intelligent way without causing much additional weight or cost. The vast majority of research in smart damping materials has concentrated on the control of structures made from composite materials with embedded or bonded piezoelectric transducers because of their excellent mechanical-electrical coupling characteristics. A piezoelectric material responds to mechanical force by generating an electric charge or voltage. This phenomenon is called the direct piezoelectric effect. On the other hand, when an electric field is applied to the material mechanical stress or strain is induced; this phenomenon is called the converse piezoelectric effect. The direct effect is used for sensing and the converse effect for actuation. The methods of vibration control using piezoelectric transducers can be mainly divided into three categories: passive, active, and semi-active. Passive control systems, which use the *R-L* shunting (Hagood & Crawley, 1991; Hollkamp, 1994), are simplest among the three categories, but their control performance is sensitive to the variations of the system parameters. Moreover, the passive control systems usually need large inductance in low frequency domain, which is difficult to realize. Active control systems require high-performance digital signal processors and bulky power amplifiers to drive actuators, which are not suitable for many practical applications. In order to overcome these disadvantages, several semi-active approaches have been proposed. Wang et al. (1996) studied a semi-active *R-L* shunting approach, in which an adaptive inductor tuning, a negative resistance and a coupling enhancement set-up lead to a system with damping ability. Davis et al. (1997, 1998) developed a tunable electrically shunted piezoceramic vibration absorber, in which a passive capacitive shunt circuit is used to electrically change the piezoceramic effective stiffness and then to tune the device response frequency. Clark, W. W. (1999) proposed a state-switched method, in which piezoelements are periodically held in the open-circuit state, then switched and held in the short-circuit state, synchronously with the structure motion.

Another type of semi-active control, which has been receiving much attention in recent years, is called pulse switching technique (Richard et al., 1999, 2000; Onoda et al., 2003; Makihara et al., 2005). It consists in a fast inversion of voltage on the piezoelement using a few basics electronics, which is synchronized with the mechanical vibration. In the methods proposed by Richard et al. (1999) the voltage on the piezoelectric element is switched at the strain extrema or displacement extrema of vibration. These methods are called Synchronized Switch Damping (SSD) techniques. On the other hand, in the method proposed by Onoda and Makihara the switch is controlled by an active control theory and it is called active control theory based switching technique here (Onoda et al., 2003; Makihara et al., 2005).

In this chapter, the semi-active control methods based on state-switched piezoelectric transducers and pulse-switched piezoelectric transducers are introduced (Qiu et al., 2009). The semi-active approaches have several advantages compared to the passive and active methods: it is not sensitive to the variation of the parameters of system, and its implementation is quite simple, requiring only few small electronic components. It may use inductors, but much smaller than the ones needed by passive technique. So the control system is more compact compared with active control and passive control.

2. Modeling of a structural system with piezoelectric transducers

2.1 Equivalent SDOF model

A mechanical model based on a spring-mass system having only one degree of freedom gives a good description of vibrating behavior of a structure near a resonance (Badel et al., 2006; Ji et al., 2009a). The following differential equation is established assuming that the global structure including piezoelectric elements is linearly elastic:

$$M\ddot{u} + C\dot{u} + K_E u = \sum F_i \quad (1)$$

where M represents the equivalent rigid mass, C is the inherent structural damping coefficient, K_E is the equivalent stiffness of the structural system, including the host structure and piezoelectric elements in short-circuit, u is the rigid mass displacement and $\sum F_i$ represents the sum of other forces applied to the equivalent rigid mass, comprising forces applied by piezoelectric elements. The equivalent stiffness K_E can be expressed as

$$K_E = K_s + K^{sc} \quad (2)$$

where K_s is the stiffness of the host structure and the K^{sc} is the stiffness of the piezoelectric transducer in short circuit. Piezoelectric elements bonded on the considered structure ensure the electromechanical coupling, which is described by

$$F_p = -\alpha V \quad (3)$$

$$I = \alpha \dot{u} - C_0 \dot{V} \quad (4)$$

where F_p is the electrically dependent part of the force applied by piezoelectric elements on the structure, C_0 is the blocked capacitance of piezoelectric elements, α is the force factor, and I is the outgoing current from piezoelectric elements. M , C_0 , α and K_E can be deduced from piezoelectric elements and structure characteristics and geometry.

Finally, $\sum F_i$ applied to the rigid equivalent mass comprises F_p and an external excitation force F . Thus, the differential equation governing the mass motion can be written as

$$M\ddot{u} + C\dot{u} + K_E u = F - \alpha V \quad (5)$$

The following energy equation is obtained by multiplying both sides of the above equation by the velocity and integrating it over the time variable.

$$\int_0^T F\dot{u}dt = \frac{1}{2}M\dot{u}^2\Big|_0^T + \frac{1}{2}K_E u^2\Big|_0^T + \int_0^T C\dot{u}^2dt + \int_0^T \alpha V\dot{u}dt \quad (6)$$

This equation exhibits that the provided energy is divided into kinetic energy, potential elastic energy, mechanical losses, and transferred energy. In the steady-state vibration, the terms of potential energy and kinetic energy in Eq. (6) disappear. The provided energy is balanced by the energy dissipated on the mechanical damper and the transferred energy, which corresponds to the part of mechanical energy which is converted into electrical energy. Maximizing this energy amounts to minimize the mechanical energy in the structure (kinetic + elastic).

If the frequency of excitation equals the resonance frequency of the system, the velocity of the mass, \dot{u} , can be considered to be in phase with the excitation force $F(t)$. In that case, the provided energy and the energy dissipated on mechanical damper are

$$\int_0^T F\dot{u}dt = F_M u_M \pi \quad \text{and} \quad \int_0^T C\dot{u}^2dt = C\omega_0 u_M^2 \pi \quad (7)$$

where F_M is the amplitude of the excitation force.

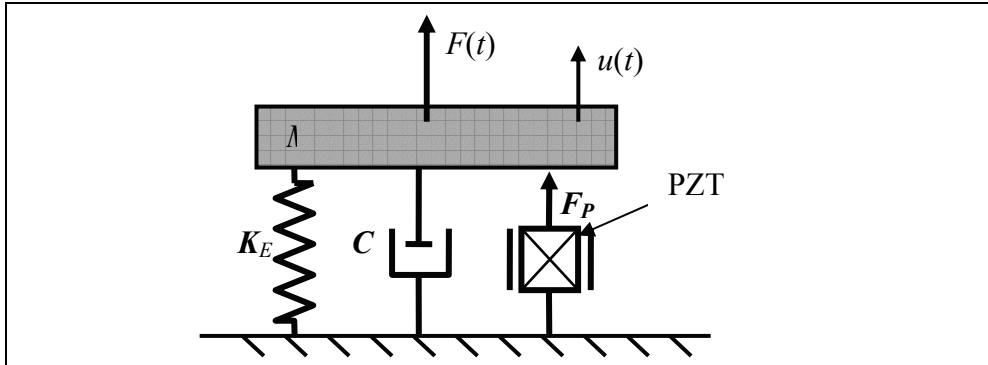


Fig. 1. A single SDOF with a piezoelectric transducer

2.2 A system with a shunt circuit

In passive control, the piezoelectric transducer in a structural system is connected to an electrical impedance (Hagood, 1991). In semi-active control, the piezoelectric transducer is usually connected to a switching shunt circuit, which is electrically nonlinear (Clark, 2000). When the piezoelectric transducer is connected to an electrical impedance Z^{su} , Eq. (4) becomes

$$\tilde{V} = \frac{s\alpha^2 Z^{su}}{sC_0 Z^{su} + 1} \tilde{u} \quad (8)$$

in the Laplace domain, where \tilde{V} and \tilde{u} are the Laplace transformation of V and u , and s is the Laplace variable. Substitution of Eq. (8) into the Laplace transformation of Eq. (5) gives the transfer function from excitation force F to displacement response u as follows

$$\tilde{u}/\tilde{F} = \frac{1}{Ms^2 + Cs + K_E + \frac{s\alpha^2 Z^{SU}}{sC_0 Z^{SU} + 1}} \quad (9)$$

where \tilde{F} is the Laplace transformation of F . In passive control, optimal control performance is achieved by tuning the electrical impedance, Z^{SU} , of the shunt circuit. However, the control performance of a passive control system deteriorates drastically when the Z^{SU} is detuned. Hence a passive control system is very sensitive to the variation of the system parameters and has low robustness.

Several semi-active approaches have been proposed to overcome the disadvantages of passive control systems. One is to adaptively tune the impedance, Z^{SU} , of the shunt circuit. The second is to switch the shunt circuit between the states with different impedances. The third is to invert the voltage on the piezoelectric transducer by synchronically pulse-switching the shunt circuit.

2.3 Different states of piezoelectric transducer

(1) Short circuit condition

In the short circuit condition, the impedance of the shunt circuit connected to the piezoelectric transducer is zero ($Z^{SU}=0$) and no electric power is dissipated, either. In the frequency domain, Equations (8) and (9) can be expressed as

$$\tilde{V} = 0, \quad \frac{\tilde{u}}{\tilde{F}} = \frac{1}{(K_E - M\omega^2 + jC\omega)} \quad (10)$$

It is assumed that at the resonance frequency the force F and the speed \dot{u} are in phase (this is a good approximation for structures with low viscous losses). The resonance angular frequency and the amplitude of the displacement are given by

$$\omega_0^{sc} = \sqrt{\frac{K_E}{M}}, \quad u_M = \frac{F_M}{C\omega_0} \quad (11)$$

where F_M is this amplitude of the driving force. In the short circuit condition, the provided energy is balanced by the mechanical loss.

(2) Open circuit condition

In the open circuit condition of the piezoelectric elements, the impedance of the shunt circuit is infinity ($Z^{SU}=\infty$) and no electric power is dissipated, either. In the frequency domain, Equations (8) and (9) can be expressed as

$$\tilde{V} = \frac{\alpha}{C_0} \tilde{u}, \quad \frac{\tilde{u}}{\tilde{F}} = \frac{1}{\left(K_E + \frac{\alpha^2}{C_0} - M\omega^2 + jC\omega \right)} \quad (12)$$

For the same reason as for the short circuit case, the resonance angular frequency and the amplitude of the displacement are given by.

$$\omega_0^{oc} = \sqrt{\frac{K_E + \frac{\alpha^2}{C_0}}{M}}, \quad u_M = \frac{F_M}{C\omega_0^{oc}}. \quad (13)$$

Obviously, the stiffness of the piezoelectric transducer in the open circuit condition is

$$K^{oc} = K^{sc} + \frac{\alpha^2}{C_0}. \quad (14)$$

The piezoelectric transducer exhibits higher stiffness in the open circuit condition and the resonance frequency of the system in open circuit condition is higher than that in the short circuit condition. The voltage on the piezoelectric transducer and the displacement and velocity of the mass are illustrated in Fig.2. In this state, the net converted energy from mechanical to electrical in a cycle of vibration is zero, that is, the last term in Eq. (6) is zero.

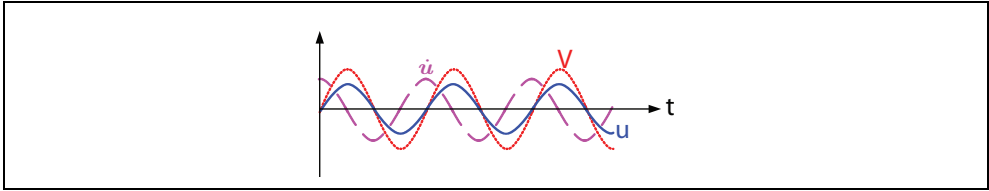


Fig. 2. Voltage, displacement and velocity in the open circuit condition

Obviously, the difference between the resonance frequency in the short circuit condition and that in the open circuit condition is due to the electro-mechanical coupling of the piezoelectric transducer in the structure. To quantitatively characterize its electro-mechanical property, the following parameter, k_{struct} , is defined as the electro-mechanical coupling factor of the structure:

$$k_{struct} = \frac{(\omega_0^{oc})^2 - (\omega_0^{sc})^2}{(\omega_0^{sc})^2}. \quad (15)$$

The resonance frequencies, ω_0^{oc} and ω_0^{sc} , of the structure with the piezoelectric transducer under open and short circuit conditions, respectively, can easily be measured experimentally. Hence the electro-mechanical coupling factor of the structure can easily be estimated from experimentally results. After k_{struct} is obtained, the force factor, α , can easily be calculated from the following equation:

$$\alpha = k_{struct} \omega_0^{sc} \sqrt{C_0}. \quad (16)$$

(3) Resistive shunt condition

When the piezoelectric transducer is shunted by a resistor R , that is, $Z^{su}=R$, Equations (8) and (9) can be expressed as

$$\tilde{V} = \frac{j\rho\omega/\omega_n}{j\rho\omega/\omega_n + 1} \cdot \frac{\alpha^2}{C_0} \tilde{u},$$

$$\frac{\tilde{u}}{\tilde{F}} = \frac{1}{\left(K_E - M\omega^2 + jC\omega + \frac{j\rho\omega/\omega_n}{j\rho\omega/\omega_n + 1} \cdot \frac{\alpha^2}{C_0} \right)} \quad (17)$$

in the frequency domain, where ω_n is an arbitrary angular frequency for non-dimensionalization and $\rho = \omega_n C_0 R$ is the non-dimensional resistance. The condition $R=0$ corresponds to short circuit and $R=\infty$ corresponds to the open circuit condition.

Resistive shunt has been widely used in passive damping based on piezoelectric transducers. An optimal resistance can be obtained by minimizing the magnitude of the transfer function from \tilde{F} to \tilde{u} at the resonance frequency of the system. In the next section the control performance of the state-switched approach is compared with that of the resistive shunt.

3. The state-switched approach

The state-switched method has been successfully used in semi-passive vibration absorbers (Cunefare, 2002) and semi-passive vibration damping using piezoelectric actuator (Clark 1999, 2000; Corr & Clark 2001). Only the state-switched approach using piezoelectric actuators is discussed in this section. In the state-switched approach using piezoelectric actuators, a piezoelectric actuator is switched between the high- and low-stiffness states using a simple switching logic to achieve vibration suppression, essentially storing energy in the high-stiffness state and dissipating a part of the that energy in the switching process between the low-stiffness state and high-stiffness state. As shown in the Section 2.3, the piezoelectric transducer has different stiffness for different electrical boundary conditions (short circuit or open circuit). Different from the pulse-switched approach introduced in the next section, this approach keeps the piezoelectric element in each of the high- and low-stiffness states for one quarter-cycle increments.

The energy loss in a state-switched system can be explained by a mass-spring system as shown in Fig. 3 (Corr & Clark, 2001). The stiffness of the spring, K^* , in the system can be switched between two states: K^{HI} and K^{LO} , with $K^{\text{HI}} > K^{\text{LO}}$. As the mass move away from its equilibrium position, the stiffness of the spring is set to K^{HI} . When the mass reaches its maximum displacement the potential energy is at a maximum:

$$U_{\max} = K^{\text{HI}} u_M^2 \quad (18)$$

At this point, the stiffness of the variable spring is changed from K^{HI} to K^{LO} . Now the potential energy of the system is less than before. The difference in energy is

$$\Delta U = \frac{1}{2} (K^{\text{HI}} - K^{\text{LO}}) u_M^2. \quad (19)$$

Hence, there is ΔU less potential energy to be converted back to kinetic energy, that is, the system has lost some of its total energy. The variable spring is left in the K^{LO} state until the mass goes back to its original equilibrium point. At this time, the variable spring is again changed to K^{HI} state and the cycle repeats itself.

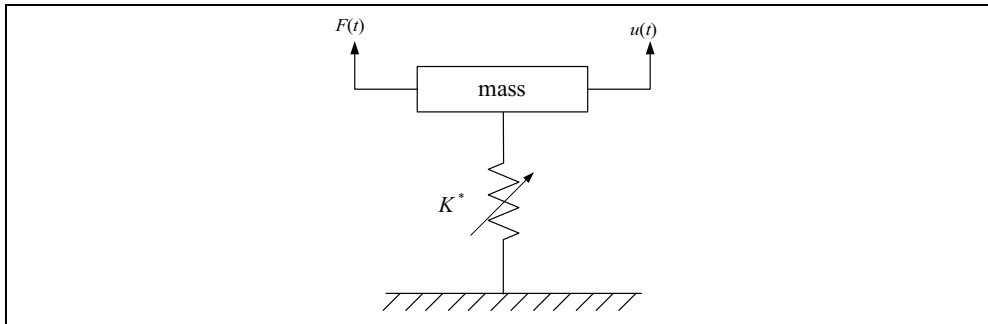


Fig. 3. A SDOF system with a variable spring

In theory, one could continuously vary the resistance in the circuit in real time to obtain a completely variable semi-active system. An alternative is to simply switch between states of the system. The two most straightforward scenarios are shown in Fig. 4(b) and 4(c), where switching occurs between the open and short circuit states (OC-SC), and between the open and resistive shunt states (OC-RS). (Note that switching between the short circuit and resistive shunt states will not be explored because neither of these states exhibits high-stiffness.) State-switching of the actuator is based on the following logic: Given the single degree-of-freedom system shown in Fig. 4, when the system is moving away from equilibrium, or

$$u\dot{u} > 0 \quad (20)$$

the circuit is switched to the high-stiffness state (open circuit), and when the system is moving toward equilibrium,

$$u\dot{u} < 0 \quad (21)$$

then the system is switched to the low-stiffness and/or dissipative state (short or resistive circuit). So during a full cycle of motion, switching occurs four times, once after each quarter cycle. At equilibrium the system is switched to a high stiffness, then at peak motion it is switched back to low stiffness and it returns to equilibrium to complete the half-cycle. At equilibrium again the system is switched to high stiffness, and the switching process repeats over the next half-cycle. This has the effect of suppressing deflection away from equilibrium, and then at the end of the deflection quarter-cycle, dissipating some of the stored energy so that it is not given back to the system in the form of kinetic energy.

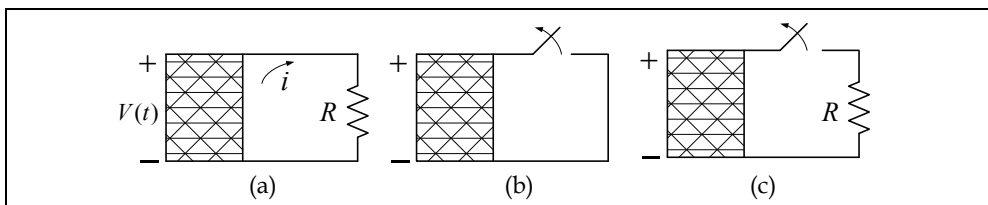


Fig. 4. Schematic of three piezoelectric configurations used in this study: (a) Passive resistive shunt; (b) State-switched: Open-circuit to short circuit; (c) State-switched: Open-circuit to resistive circuit

Now the SDOF system in Fig. 1 is considered. The mass is under excitation of a harmonic force $F(t)$ with an angular frequency of ω and its response is assumed to be a harmonic vibration of the same frequency. The piezoelectric transducer is switched between open circuit and short circuit using the switching strategy in Eqs. (20) and (21). The energy dissipated in a full cycle of vibration due to the switching actions is

$$\begin{aligned} E_{\text{cycle}}^{\text{dis}} &= \int_0^{T/4} K^{\text{oc}} u \dot{u} dt + \int_{T/4}^{T/2} K^{\text{sc}} u \dot{u} dt + \int_{T/2}^{3T/4} K^{\text{oc}} u \dot{u} dt + \int_{3T/4}^T K^{\text{sc}} u \dot{u} dt \\ &= (K^{\text{oc}} - K^{\text{sc}}) u_M^2 \\ &= \frac{\alpha^2}{C_0} u_M^2 \end{aligned} \quad (22)$$

In the open-circuit case, deflection stores energy by way of the mechanical stiffness and by the capacitance of the device, which also appears as a mechanical stiffness. When the system is then switched to the short circuit state, the charge stored across the capacitor is shunted to ground, effectively dissipating that portion of the energy, and the effective stiffness is decreased. Since the provided energy is balanced by the mechanical loss and the energy dissipated by the switched shunted circuit, the following equation holds when the system is excited at the resonance frequency:

$$F_M u_M \pi = C \omega_0 u_M^2 \pi + \frac{\alpha^2}{C_0} u_M^2. \quad (23)$$

The displacement amplitude of vibration is

$$u_M = \frac{F_M}{C \omega_0 + \frac{\alpha^2}{\pi C_0}}. \quad (24)$$

To quantitatively evaluate the damping effect of a control method, a performance index A is defined as follows

$$A = 20 \log \left(\frac{\text{vibration amplitude with control}}{\text{vibration amplitude without control}} \right). \quad (25)$$

The performance index of the state-switched control for a single-frequency vibration is given by

$$A_{\text{State-switching}} = 20 \log \left(\frac{C \omega_0}{C \omega_0 + \frac{\alpha^2}{\pi C_0}} \right). \quad (26)$$

If on the other hand, the circuit is switched to the resistive shunt, then the electrical charge is dissipated through the resistor, and the effective stiffness is also decreased (an added benefit is that additional damping is obtained while the resistor is in the circuit during the next quarter cycle, so in some cases the OC-RS system can perform better than the OC-SC system.)

The damped impulse response of the OC-SC system can be compared to that of the other two systems of interest, that is, the RS system and the OC-RS system [Clark 2000]. The resistor used in both the RS circuit and that in the OC-RS circuit are chosen to be optimal. The results are shown in Fig. 5. Note that for the impulse response, it is better to use a resistor in the circuit during state-switching. It is also shown that slightly better damping can be achieved with the passive resistive shunt circuit. The effective damping ratios were calculated for each case by logarithmic decrement and are shown in Table 1.

System	Effective Damping Ratio
Passive Resistive Shunt	0.22
State-Switched OC-SC	0.12
State-Switched OC-RS	0.19

Table 1. Effective damping ratios for passive and state-switched systems

Even though the passive resistive shunt system provides slightly better performance than the state-switched systems for the optimized cases, it is interesting to note that the results change significantly when the resistors are no longer optimized. Simulations were performed on the impulse response of the same three systems when the mass and actuator material compliance are dramatically changed but the resistance values are held at their previous optimal values. The results showed that the state-switched systems are less sensitive to the change, seeing very little change in performance, with the OC-RS case still providing slightly better performance (note that the OC-SC case can be thought of as a lower limit on damping performance), but the passive resistive shunt case is much worse than before.

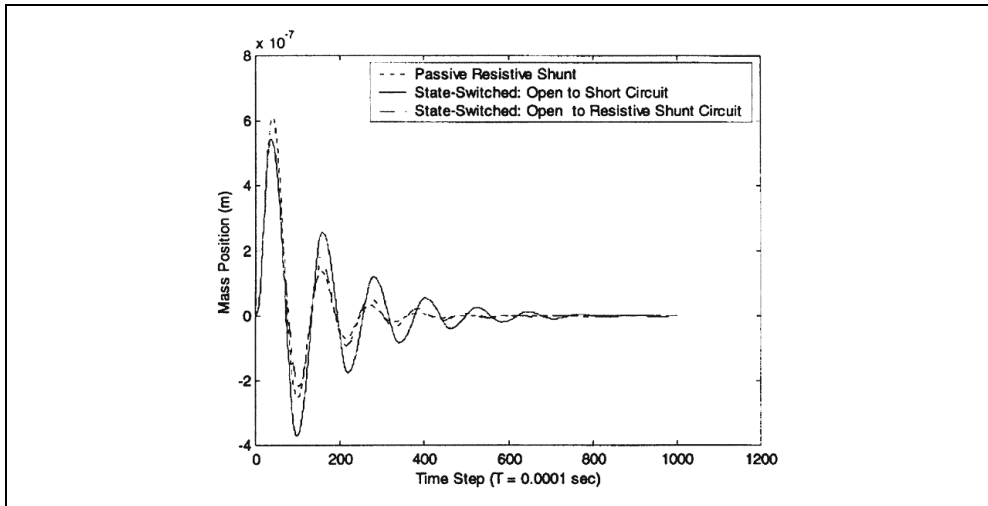


Fig. 5. Impulse response of passive resistive shunt, the OC-RS state switched, and OC-RS state-switched systems using optimal resistance

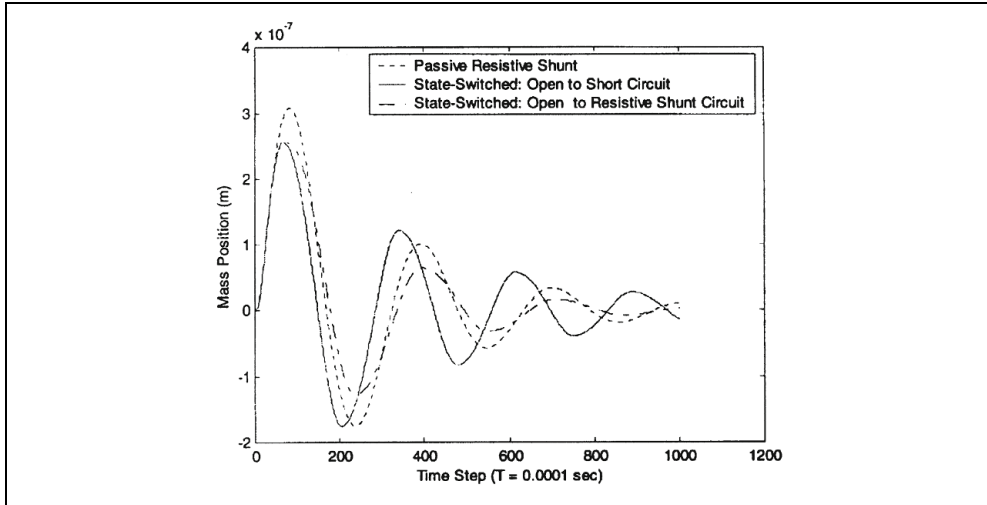


Fig. 6. Impulse response of passive resistive shunt, the OC-RS state switched, and OC-RS state-switched systems with non-optimal resistance

4. The pulse-switch methods

4.1 The Synchronized Switch Damping technique

The synchronized switch damping (SSD) method, also called pulse-switched method, consists in a nonlinear processing of the voltage on a piezoelectric actuator. It is implemented with a simple electronic switch synchronously driven with the structural motion. This switch, which is used to cancel or inverse the voltage on the piezoelectric element, allows to briefly connect a simple electrical network (short circuit, inductor, voltage sources depending on the SSD version) to the piezoelectric element. Due to this process, a voltage magnification is obtained and a phase shift appears between the strain in piezoelectric patch and the resulting voltage. The force generated by the resulting voltage is always opposite to the velocity of the structure, thus creating energy dissipation. The dissipated energy corresponds to the part of the mechanical energy which is converted into electric energy. Maximizing this energy is equivalent to minimizing the mechanical energy in the structure.

(1) The synchronized switch damping on short circuit

Several SSD techniques have been reported. The simplest is called SSDS, as shown in Figure 7(a), which stands for Synchronized Switch Damping on Short circuit (Richard et al., 1999, 2000). The SSDS technique consists of a simple switching device in parallel with the piezoelectric patch without other electric devices. The switch is kept open for most of the time in a period of vibration. It is closed when the voltage reaches a maximum (corresponding to a maximum of the strain in the piezoelectric patch) to dissipate all the electric energy in a short time (much shorter than the period of vibration) and then opened again. The voltage on the piezoelectric transducer is shown in Fig. 7(b). The maximum voltage on the piezoelectric transducer is

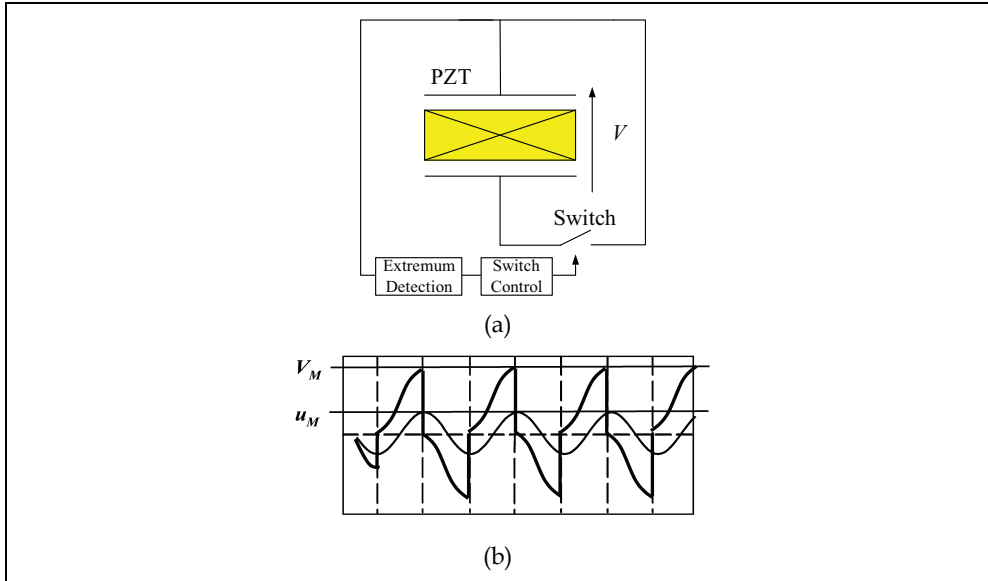


Fig. 7. The principle of SSDS technique

$$V_{Max} = \frac{2\alpha}{C_0} u_M \tag{27}$$

which is twice as large as that in the open circuit condition.

The maximum electric energy stored in the piezoelectric transducer can easily be calculated from the voltage in Eq. (27). This energy is dissipated when the voltage is discharged to zero at the maximum displacement point. In each cycle of mechanical vibration, the piezoelectric transducer is discharged twice. Hence, in the SSDS technique, the transferred energy E_t in a period of single-frequency vibration is given by

$$E_t = \frac{4\alpha^2}{C_0} u_M^2 \tag{28}$$

The performance index of the SSDS damping for a single-frequency vibration is given by

$$A_{SSDS} = 20 \log \left(\frac{C\omega_0}{C\omega_0 + \frac{4\alpha^2}{C_0\pi}} \right) \tag{29}$$

The above expressions exhibit that more energy is dissipated by the SSDS than by the state-switched shunt circuit in a single cycle of mechanical vibration and SSDS yields better control performance.

(2) The synchronized switch damping on inductor

To further increase the dissipated energy, the SSDI technique (synchronized switch damping on inductor) as shown in Fig. 8a has been developed by Richard et al. (2000),

Guyomar et al. (2001) and Petit et al. (2004). In the SSDI approach, an inductor is connected in series with the switch. Because the piezoelectric patch and the inductor constitute a L - C resonance circuit, fast inversion of the voltage on the piezoelectric patch is achieved by appropriately controlling the closing time and duration of the switch. The switch is closed at the displacement extremes, and the duration of the closed state is half the period of the L - C circuit. This leads to an artificial increase of the dissipated energy. The period of the L - C circuit is chosen to be much smaller than that of the mechanical vibration. The following relation holds between the voltage before inversion, V_M , and that after inversion, V_m ,

$$V_m = \gamma V_M, \tag{30}$$

where $\gamma \in [0,1]$ is the voltage inversion coefficient. The inversion coefficient γ is a function of the quality factor of the shunt circuit. The larger the quality factor is, the larger the voltage inversion coefficient is. A typical value of γ is between 0.6 to 0.9.

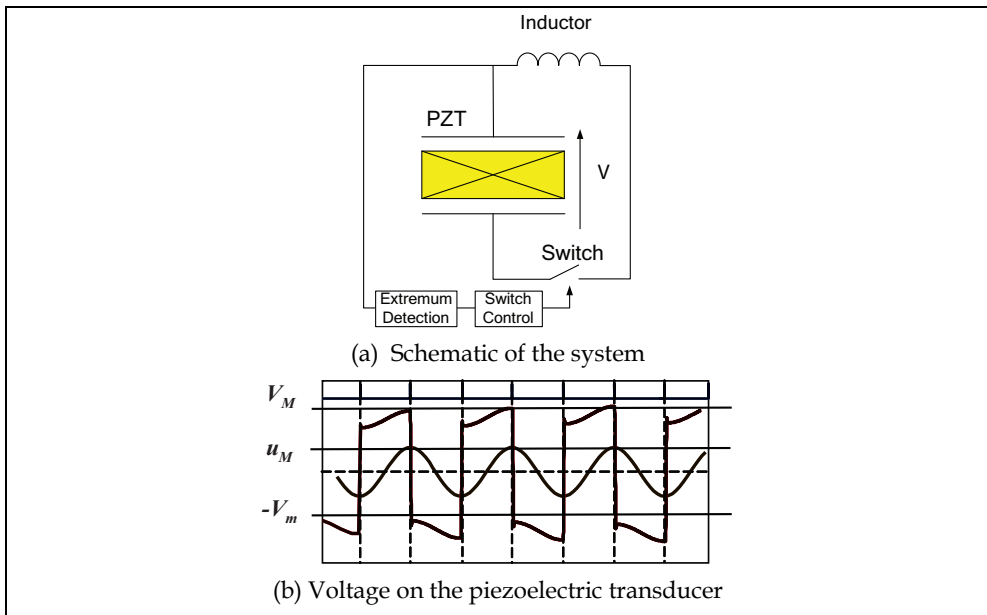


Fig. 8. The principle of SSDI technique

As shown in Fig. 8(b), in the steady-state vibration the voltage on piezoelectric transducer increases from V_m to V_M between two switching points due to mechanical strain. Hence their difference is V_{Max} given by Eq. (27). From these relationships, the absolute value of the average voltage between two switching points is

$$\frac{1}{2}(V_m + V_M) = \frac{1+\gamma}{1-\gamma} \frac{\alpha}{C_0} u_M \tag{31}$$

It indicates that the average voltage on the piezoelectric transducer has been amplified by a factor of $(1+\gamma)/(1-\gamma)$. The dissipated energy E_t during a period of single-frequency vibration is given by

$$E_t = \frac{4\alpha^2}{C_0} \frac{1+\gamma}{1-\gamma} u_M^2 \quad (32)$$

Compared with Eq. (28) the transferred energy has also been magnified by a factor of $(1+\gamma)/(1-\gamma)$ (Badel et al., 2005). If the voltage inversion coefficient is 0.9, its value is 9.5. Hence, much better control performance can be achieved with SSDI. The theoretical damping value of the SSDI technique for a single-frequency vibration is

$$A_{SSDI} = 20 \log \left(\frac{C\omega_0}{C\omega_0 + \frac{4\alpha^2}{\pi C_0} \frac{1+\gamma}{1-\gamma}} \right). \quad (33)$$

4.2 The active control theory based switching law

Onoda and Makihara proposed a new switching law based on active control method (Onoda et al., 2003; Makihara et al. 2007c). As an example, the LQR (linear quadratic regulator) control law was used in their studies. The state equation of the plant to be controlled is assumed to be

$$\dot{z} = Az + Df + BQ \quad (34)$$

where z is the state variable, A , B and C are state matrices, f is the external disturbance, and Q is the control input, which is the charges on the piezoelectric elements. A linear quadratic regulator is designed to minimized the performance index

$$J = \int (z^T W_1 z + Q^T W_2 Q) dt \quad (35)$$

where W_1 and W_2 are weight matrices. The control input can be expressed in the following form:

$$Q_T = Fz. \quad (36)$$

The regulator F is given by

$$F = W_2^{-1} B^T P \quad (37)$$

where P is a positive definite solution of

$$PBW_2^{-1} B^T P - A^T P - PA - W_1 = 0. \quad (38)$$

Usually the value of z is difficult to measure and they estimated by an observer. When the estimated value of z is used, the active control input is obtained from

$$Q_T = F\hat{z}. \quad (39)$$

where \hat{z} is the estimated value of z . Once the value of Q_T is obtained, the switch in the shunt circuit for the i th piezoelectric actuator is controlled based on Q_{Ti} , which is the i th component in the Q_T , according to the switch control law discussed below.

It should be noted that in a semi-active control system, damping effect is achieved by switching shunt circuit, not by applying the control input Q_T as in active control. In order to

obtain damping effect, a possible strategy to control the switch is to turn the switch on and off so that the charge Q_i on the i th piezoelectric element traces Q_{Ti} as closely as possible. However, in many cases, a large gain results in quick vibration damping. Therefore, the switch is controlled such a way that Q becomes as large, that is, positive, as possible when Q_T is positive, and as small, that is, negative, as possible when Q_T is negative. The study by Onoda et al. (1997) has shown that this strategy is more effective than tracing Q_T , although the difference between their performances is small.

Based on the above discussion, the following control law can be obtained for switched R shunt of a piezoelectric element: Turn on the switch when

$$Q_T V < 0, \quad (40)$$

and turn off the switch when

$$Q_T V > 0, \quad (41)$$

where V is the voltage on the piezoelectric patch.

The switch control law for a piezoelectric element with a switched L - R shunt can be expressed in the following form: Turn on the switch when

$$Q_T V < 0, \quad (42)$$

and turn it off when

$$Q_T \dot{Q} < 0. \quad (43)$$

Note that any active control theory can be used to obtain Q_T of a piezoelectric though LQR control method has been used as an example above.

5. The SSDV approach

5.1 The classical SSDV technique

In order to further increase the damping effect, a method called SSDV (SSDV stands for synchronized switch damping on voltage) as shown in Fig. 9 was proposed by Lefeuvre et al. (2006), Makihara et al. (2005), Faiz et al. (2006), and Badel et al., (2006). In the case of the SSDV, a voltage source V_{cc} is connected to the shunting branch, in series with the inductor, which can magnify the inverted voltage and hence improve the control performance. The absolute value of average voltage on piezoelectric transducer between two switching actions is (Badel, , et al., 2006)

$$V = \left(\frac{\alpha}{C_0} u_M + V_{cc} \right) \frac{1+\gamma}{1-\gamma}. \quad (44)$$

The dissipated energy during one period of vibration is a function of u_M and V_{cc} as follows:

$$E_t = \left(\frac{4\alpha^2}{C_0} u_M^2 + 4\alpha u_M V_{cc} \right) \frac{1+\gamma}{1-\gamma}. \quad (45)$$

The theoretical value of the SSDV damping is then given by

$$A_{SSDV} = 20 \log \left(\frac{C\omega_0}{C\omega_0 + \frac{4\alpha^2}{C_0\pi} \frac{1+\gamma}{1-\gamma}} \times \left(1 - \frac{4}{\pi} \frac{1+\gamma}{1-\gamma} \frac{\alpha V_{cc}}{F_M} \right) \right), \quad (46)$$

where F_M is the amplitude of excitation force F_e . The SSDV technique can achieve better vibration control performance than SSDI, but a stability problem arises due to the fact that the voltage source is kept constant. Equation (46) shows that under a given excitation force, the value of voltage source V_{cc} that theoretically totally cancels the vibration can be found. This particular value is

$$V_{cc \max} = \frac{\pi}{4\alpha} \frac{1-\gamma}{1+\gamma} F_M. \quad (47)$$

This is also the maximum voltage that can be applied in this excitation condition. Applying a voltage higher than $V_{cc \max}$ leads to instability (experimental results actually show that stability problems occur before reaching this critical value).

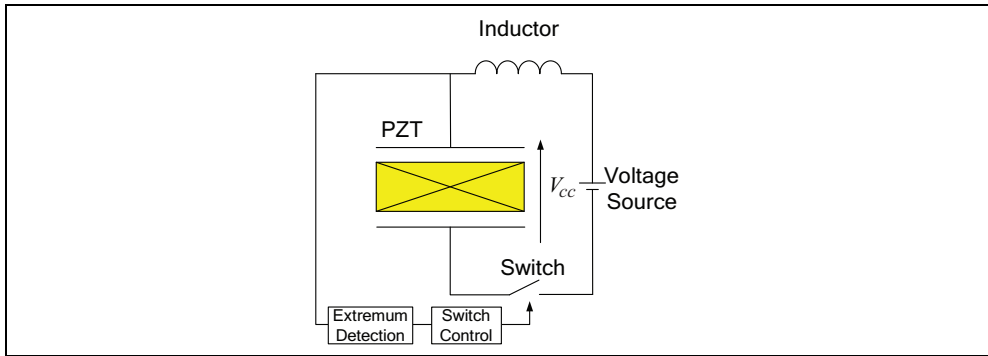


Fig. 9. The principle of SSDV technique

5.2 Adaptive SSDV techniques

Equation (47) shows that $V_{cc \max}$ is proportional to the amplitude of the excitation. Hence if the voltage is adjusted according to the amplitude of the excitation, the stability problem can be solved. Accordingly the enhanced and adaptive SSDV techniques, in which the voltage is adjusted according to the amplitude of excitation, have been developed. In a real system, the amplitude of the excitation is usually unknown, but we can measure the vibration amplitude of the structure.

(1) Enhanced SSDV

In the enhanced SSDV proposed by Badel et al. (2006) the voltage source is proportional to the vibration amplitude as shown in following equation.

$$V_{cc} = -\beta \frac{\alpha}{C_0} u_M, \quad (48)$$

where β is the mentioned voltage coefficient. In the Enhanced SSDV, the dissipated energy E_t during a period can be expressed as

$$E_t = \frac{4\alpha^2}{C_0}(1 + \beta) \frac{1 + \gamma}{1 - \gamma} u_M^2. \quad (49)$$

Compared with the classical SSDV technique, the enhanced SSDV increases the transferred energy, which results in an increase in the vibration damping. The theoretical value of damping of the enhanced SSDV is given by

$$A_{SSDV_{enh}} = 20 \log \left(\frac{C\omega_0}{C\omega_0 + \frac{4\alpha^2}{C_0\pi}(1 + \beta) \frac{1 + \gamma}{1 - \gamma}} \right). \quad (50)$$

Equation (50) shows that, for a given value of parameter β , the damping is not sensitive to the amplitude of the applied force. This is the critical point of the enhanced SSDV. But it must be noted that for large value of β , the above theoretical expressions are no longer valid because the displacement of high-order modes cannot be neglected any longer compared to the fundamental one. From the experimental results it has been found that the optimal value of the voltage coefficient β depends on many factors such as the noise level of the measured signal, the property of the switch, et al. Hence, in order to achieve optimal control performance, the voltage coefficient should be adjusted adaptively according to the vibration amplitude and other experimental conditions.

(2) Derivative-based adaptive SSDV

An adaptive enhanced SSDV technique, in which the voltage coefficient is adjusted adaptively to achieve optimal control performance, has been proposed by Ji et al. (2009a). The basic principle of the adaptive SSDV technique is that the coefficient β is adjusted based on the sensitivity of the vibration amplitude with respect to β : the more the vibration amplitude is sensitive to β , the more β is increased. If the variation of amplitude is Δu_{Mi} due to an increment of the voltage coefficient $\Delta\beta_i$, the sensitivity is defined as $\Delta u_{Mi} / \Delta\beta_i$. The increment of the voltage coefficient, $\Delta\beta_{i+1}$, in the next step is defined as

$$\Delta\beta_{i+1} = -\eta \frac{\Delta u_{Mi}}{\Delta\beta_i}, \quad (51)$$

where η is the convergence rate factor. The larger the factor η is, the faster the convergence rate is. But when η is too large, the iteration process may become unstable. The physical meaning of the algorithm defined in Eq.(51) is similar to the Newton-Raphson method in numerical analysis.

Since $\Delta u_{Mi} / \Delta\beta_i$ is an approximation of the derivative of amplitude u_M with respect to β , this approach is called derivative-based adaptive SSDV. In the real system, $\Delta\beta_i$ is not updated in each cycle of vibration because of the noise in the measured amplitude. Instead, $\Delta\beta_i$ is kept constant for n cycles and the amplitudes u_{Mk} ($k=1, \dots, n$) are recorded. A parabolic curve is then fitted from the points u_{Mk} and the slope at the final point u_{Mn} is defined as the sensitivity.

(3) LMS-based adaptive SSDV

In the derivative-based adaptive SSDV, the voltage coefficient β is optimized to achieve good damping control performance. Actually, the final goal of optimizing voltage coefficient

β is to obtain the optimal voltage. A novel adaptive SSDV method based on LMS algorithm to adjust the voltage source directly or voltage coefficient was proposed by Ji et al. (2009b). In the LMS-based adaptive SSDV, a FIR filter is used to optimize the voltage V_{cc} or the voltage coefficient β . Their values are defined at each switching point (each displacement extrema), not the discrete sampling time n . Hence the detected displacement amplitude u_M (which is used as a sensor signal to control the switch action) (Ji et al., 2009b), instead of the displacement u itself, is used as the error e to the FIR filter. The output y of the FIR filter is the voltage or the voltage coefficient β at the switching times, instead of the voltage value at each discrete time, and the calculated voltage is held constant until the next switching time so that a rectangular wave is generated automatically by the switching circuit. Hence the LMS-based system is a sub-system which is not executed at each discrete time, but triggered and executed at each detected extrema. The diagram of a LMS-based adaptive SSDV control system is shown in Fig. 10. In the case of the optimization of β , the value of β is calculated from

$$\beta(n') = \mathbf{h}(n') * \mathbf{u}_m(n' - 1) = h(1)u_m(n' - 1) + h(2)u_m(n' - 2) + \dots + h(m)u_m(n' - m) \quad (52)$$

where \mathbf{h} is an FIR filter, n' is the discrete time defined at the detected extrema. This means that $n' - 1$ represent the discrete time at the previous detected extremum. After β is calculate from Eq. (52), the voltage V_{cc} is obtained from Eq. (46). This method can be considered as an extension of the enhanced SSDV. In the case of the direct optimization of the voltage V_{cc} , the following equation is used:

$$V_{cc}(n') = \mathbf{h}(n') * \mathbf{u}_m(n' - 1) = h(1)u_m(n' - 1) + h(2)u_m(n' - 2) + \dots + h(m)u_m(n' - m). \quad (53)$$

Since the voltage is directly optimized by this method, it can be considered as an improvement to the classical SSDV, where the voltage source is fixed. The same symbol \mathbf{h} is used in Eqs. (52) and (53), but they have different values.

It should be noted that although the standard LMS algorithm has been used in this study, its implementation is not standard. The LMS-based is masked and executed only at the discrete time defined at the detected extrema, n' , at which the FIR filter is updated and the control input is calculated. Due to the non-standard implementation, the other LMS-based control laws, such as the Filtered-X algorithm, is difficult to apply in this system.

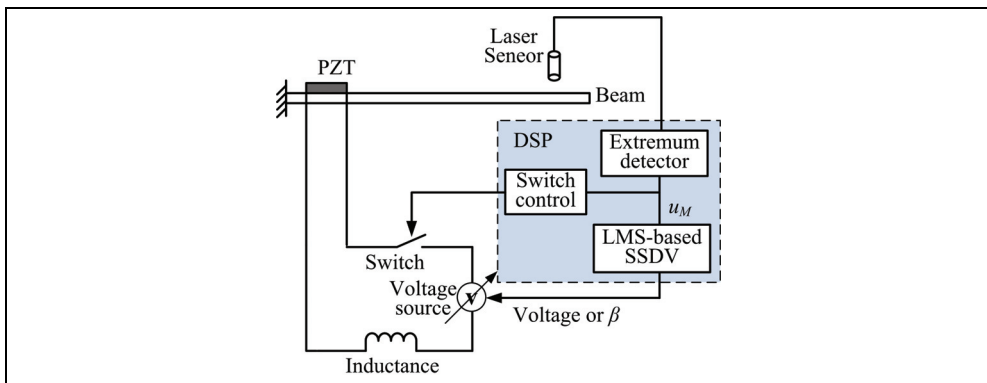


Fig. 10. The diagram of a LMS-based adaptive SSDV control system

5.3 An example of pulse-switched control

The structure used in the experiment is a cantilever GFRP (Glass Fiber Reinforced Plastics) composite beam with an embedded piezoelectric patch, as shown in Figure 11. The composite beam was made from four layers of GFRP prepreg. The GFRP prepreg and the piezoelectric patch are laminated in the following order: $0^\circ/90^\circ/90^\circ/\text{PZT}/0^\circ$, where 0° is the length direction of the beam. The beam is 150 mm long, 51 mm wide and 0.8 mm thick and its properties are given in Table 2. The piezoelectric patch is a 30 mm \times 30 mm square and its thickness is 0.2 mm. It is polarized in the thickness direction and its properties are given in Table 3. The equation of motion of the beam is a partial differential equation. The equation of motion for each mode can be obtained from a modal analysis (Ji, et al. 2008). In this study, control of the resonant vibration at the first natural frequency is considered. Hence, the amplitude of the first mode is dominant and the high-order modes can be neglected. That is, at the first resonant frequency, the structure can be simplified to a single-degree-of-freedom system, represented in Figure 1.

	GFRP
Elastic modulus E_1	1.65×10^{10} [N/m ²]
Elastic modulus E_2	3.52×10^{10} [N/m ²]
Poisson ratio	0.109
Shear modulus	1.25×10^{10} [N/m ²]
Density	1800 [kg/m ³]
Thickness	0.8×10^{-3} [m]

Table 2. Material properties of the composite beam

	PZT
Elastic modulus	59×10^9 [N/m ²]
Poisson ratio	0.345
Density	7400 [kg/m ³]
Thickness	2×10^{-4} [m]
Piezoelectric constant d_{31}	-260×10^{-12} [m/V]
Capacitance C_p	141×10^{-9} [F]

Table 3. Material properties of the piezoelectric patch

The experimental setup is shown in Fig. 11. One end of the beam is clamped and the other is free. The piezoelectric patch is located at the clamped end, where the maximum strain is induced. The clamped end is mounted on a mini-shaker, which is used to drive the vibration of the beam. The displacement at the free end of the beam is measured by a laser displacement sensor.

The control approach is implemented in a DSP environment based on the dSPACE board DS1103. The displacement signal from the laser sensor is converted to digital and sent to the DSP system. Theoretically, the maximum displacement occurrence in the time response can be detected by comparing three consecutive points. When the noise in the displacement

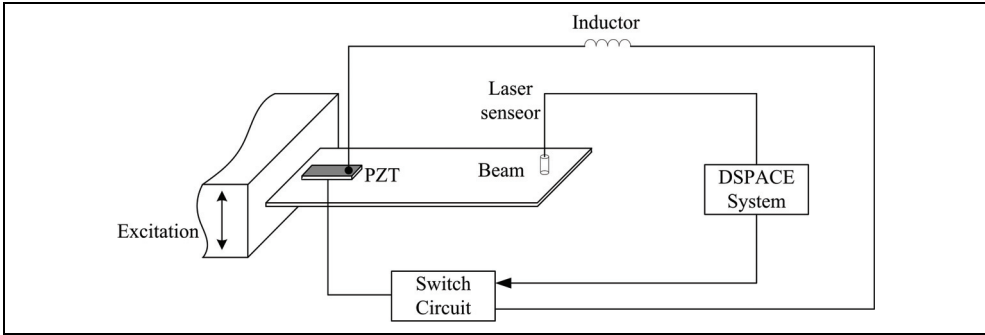


Fig. 11. Experimental setup

signal is small, this method is effective. However when the noise is relatively large, some of the obtained extrema are generated by the noise. That is, many maximum points may be obtained in a single cycle of vibration. This can lead to over-frequent switching of the circuit and induce a worsening of the control performance.

In order to prevent the system from over-frequent switching, an improved switch control algorithm has been proposed by Ji, et al. (2008). The improved algorithm turns switch to inactive state for a given period τ after each action so that no switching action can occur in this period even if extrema are detected. It can prevent the switch from over-frequent on-and-off and consequently increase the stability and performance of the control system. In this study, the improved switch control algorithm is used instead of the three-point algorithm.

The SSDI, classical SSDV, derivative-based adaptive SSDV and LMS-based adaptive SSDV methods have been used in control. Figure 12 shows the displacement curve and the voltage on the piezoelectric transducer when the voltage is not switched. The amplitude of the displacement without control is 1.6 mm and the amplitude of the voltage is 1.45 volts. Theoretically the voltage should be in phase with the displacement, but a phase difference can be observed from the figure. The phase difference may be due to the impedance of the measurement circuit connected to the piezoelectric transducer.

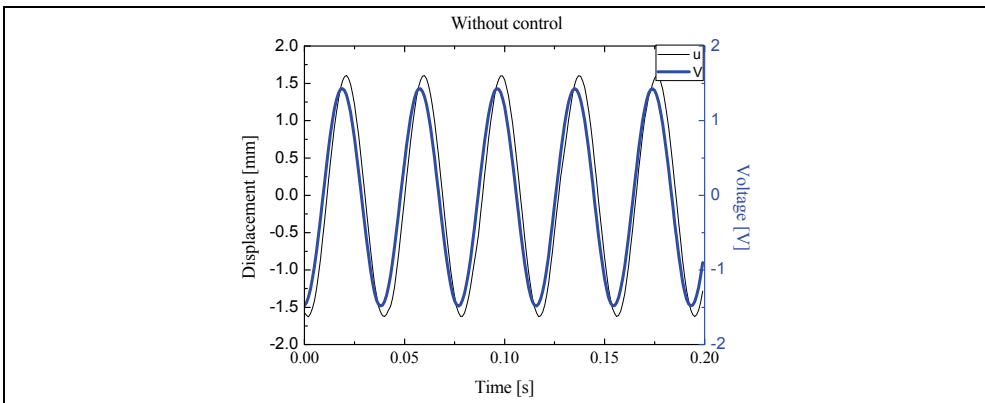


Fig. 12. Displacement of the beam and the voltage on the piezoelectric transducer

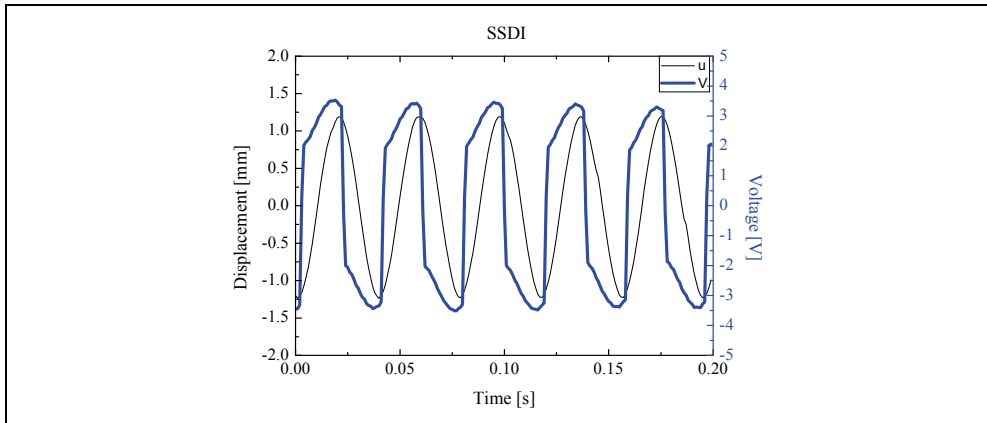


Fig. 13. Displacement of the beam and the voltage on the piezoelectric transducer with SSDI control

The result of the SSDI control is shown in Fig. 13 (Ji et al., 2008). The amplitude of voltage on the piezoelectric transducer was amplified to 3.47 volts and the displacement amplitude of vibration was reduced to 1.2 mm. It can be found that the voltage is not inverted at its extrema due to the phase difference the voltage and the displacement. The voltages before and after switching is about 3.3 volts and 1.95 volts. It means that the voltage inversion coefficient is about 0.59. For this value of inversion coefficient, the average voltage should be amplified by a factor of 2.91 when the decrease of displacement amplitude is taken into consideration. However, the average voltage was about 2.7 volts, increased only by a factor of 2.48, which corresponds to a voltage inversion coefficient of 0.43. This can be attributed to the delay of voltage inversion from its extrema.

Figure 14 shows the result of SSDV control when the voltage source V_{cc} is set to 1 volt. The amplitude of voltage on the piezoelectric transducer was raised to 5.8 volts and the

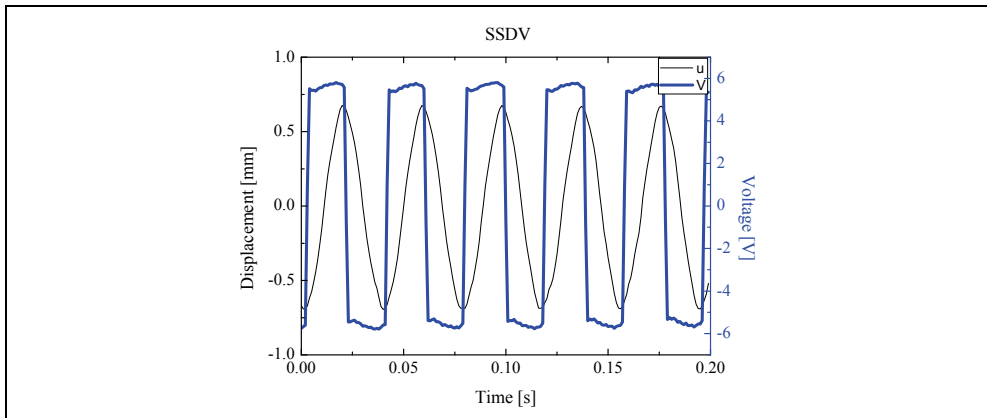


Fig. 14. Displacement of the beam and the voltage on the piezoelectric transducer with SSDV ($V_{cc} = 1$ Volt)

displacement amplitude was reduced to 0.67 mm. When the voltage inversion coefficient is 0.59 and the displacement reduction is taken into consideration, average voltage should be 6.2 volts, which is slightly larger than real value of 5.8 volts. When V_{cc} was set to 2.4 volts, the displacement amplitude of vibration was further reduced to 0.123 mm. However, the second resonance mode was excited slightly.

Figure 15(a) shows the displacement response of the beam when the derivative-based adaptive SSDV control was used (Ji et al., 2009b). In the derivative-based adaptive SSDV control, the voltage coefficient is optimized online and its variation with time is shown in Figure 15(b). It should be noted that the voltage coefficient β' in Fig. 15(b) and the following paragraphs is the ratio between the source voltage and the voltage of the displacement sensor and can be written as $\beta' = \alpha\beta / (C_0 S_0)$, where S_0 is the sensitivity of the displacement sensor expressed by the output voltage of the sensor for unit displacement. The uncontrolled displacement amplitude is 2.0 mm. The amplitude of the first resonance mode was reduced to 0.30 mm. However, the second resonance mode was excited slightly as shown in Fig. 15(a). The results of LMS-based adaptive SSDV control, in which the voltage

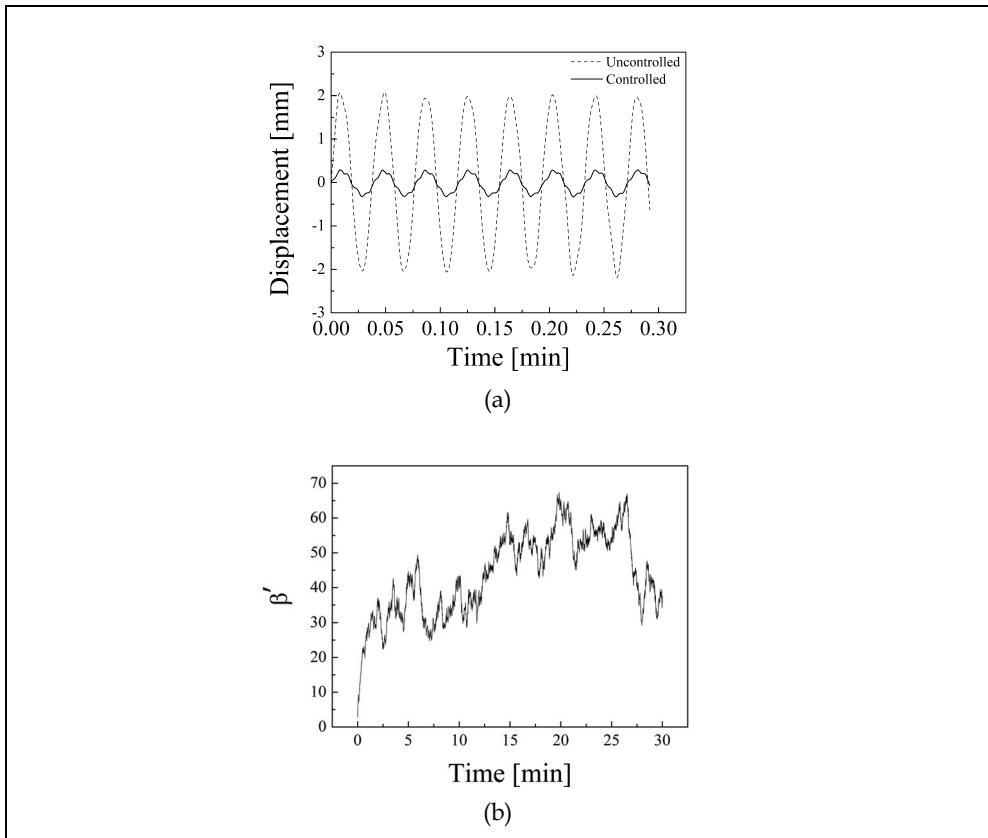


Fig. 15. Results of derivative-based adaptive SSDV (a) Displacement before and after control (b) Variation of voltage coefficient β' in thirty minutes

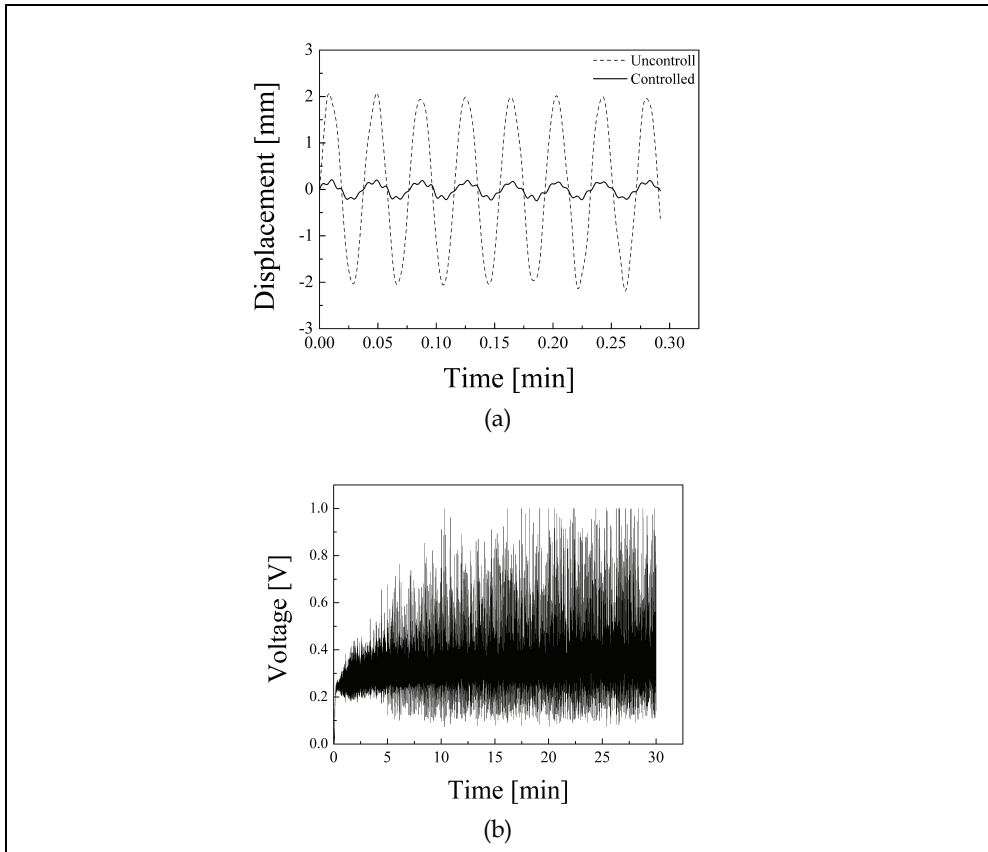


Fig. 16. Results of derivative-based adaptive SSDV (a) Displacement before and after control (b) Variation of voltage coefficient in thirty minutes

source V_{cc} was adjusted adaptively by the LMS algorithm, are shown in Fig. 16. The displacement amplitude is reduced by more than 90%, from 2.0 mm to 0.19 mm. The output of the voltage source V_{cc} varies between 0.1 and 1.0 volts, with an average value of 0.355 volts. Compared with the other methods, LMS-based adaptive SSDV methods adjusting the voltage source V_{cc} output smallest voltage, but yields almost the same control performance. This means that it consumes least energy.

The control performances of different methods, including the enhanced SSDV and the LMS-based adaptive SSDV methods adjusting the voltage coefficient, are summarized in the Table 4. Although the classical SSDV method with fixed voltage source ($V_{cc}=2.4V$) and enhanced SSDV with ($\beta'=150$) yield the best control performance, the output of the voltage source or the value of β' must be adjusted manually by a trial and error process. Since the optimal value of the voltage source or the voltage coefficient depends on many factors, slight environmental changes may cause instability in the system with a large V_{cc} or β' . For example, when a traditional switch was used, the system became unstable when β' exceeded 50. However, the system was still stable for $\beta'=150$ when the improved switch was used.

The value of voltage is also much large than the other methods, such as the LMS-based adaptive SSDV.

Control methods	Reduction (dB)
SSDI	2.58
SSDV ($V_{cc}=1V$)	7.52
SSDV ($V_{cc}=2.4V$)	22.29
Enhanced SSDV ($\beta'=150$)	22.28
Derivative-based SSDV	16.49
LMS-based SSDV (adjusting β')	20.56
Derivative-based SSDV (adjusting V_{cc})	20.25

Table 4. Comparison of different control methods

6. Semi-active control for multi-mode damping

Though most studies in semi-active so far were devoted to single-mode control, the switching laws can be used for multi-mode control. For example, in the SSD approaches the dissipated energy reaches maximum when the voltage on a piezoelectric element is switched at each extrimum of the strain if the voltage inversion is perfect. In the method proposed by Makihara et al. (2006a, 2006b, 2007a, 2007b, 2007c), switch actions are automatically generated by the control law based on active control theories. It is applicable to multi-modal control of a structure with multiple piezoelectric transducers. However, due to the energy loss during voltage inversion, these switching laws are not optimal as demonstrated by experimental results. Better control performance can be obtained by skipping some of the switching points, which are determined from these switch control laws. Hence special switch control laws are necessary for multi-modal control.

6.1 A method considering mode selection

A multi-modal control law for a piezoceramic actuator with a switched R - L shunt was developed by Corr and Clark (2003) that makes use of the concepts developed for the variable mechanical spring control laws, but is less dependent on the analytical model. They based on a multimodal approach which consists in selecting the modes to be controlled and ensuring a negative rate of energy change in the selected modes of the structure. The global extracted power is derived from the global extracted energy and is given by

$$P_s = \sum_{j=1}^N \alpha_j \dot{u}_j V. \quad (54)$$

where N is the number of modes to be controlled, u_j is modal displacement of the j th mode, and V is the voltage on the piezoelectric transducer.

If M is the set of modes to be controlled, the extracted power for the selected modes P_{SM} is given by

$$P_{SM} = \sum_{j \in M} \alpha_j \dot{u}_j V. \quad (55)$$

The technique proposed by Corr and Clark consists in inverting the voltage at each time that the sign of $\sum_{j \in M} \alpha_j \dot{u}_j$ change, so that P_{SM} remains always positive.

It can be noted that when the piezoelectric elements are open-circuited, the voltage V varies proportionally to $\sum_{j=1}^N \alpha_j u_j$, as it can be derived from

$$I = \sum_{j=1}^N \alpha_j \dot{u}_j - C_0 \dot{V} \quad (56)$$

Actually $\sum_{j=1}^N \alpha_j u_j$ is proportional to the strain in the piezoelectric elements. If all the N modes are controlled, this method then consists in processing the piezoelectric voltage at each strain extremum, which corresponds to the earlier control law proposed for the SSD technique. They showed at the same time that the original SSD control law was not optimal in the case of wide band multimodal excitation. It can also be noted that this technique requires refined filtering devices in order to select modes to be controlled. Filtering inevitably leads to time shifts that result in a lack of effectiveness (Corr & Clark, 2003).

6.2 Methods based on probability and statistics

Guyomar and Badel (2006) proposed a new multi-mode control law for the SSD techniques based on the idea of maximizing the energy dissipated in the nonlinear processing device connected to the piezoelectric elements without taking into account any information related to the different modes of the structure. It is derived from a probabilistic description of the piezoelectric voltage. The principle of this method is that the consumption of the switching device is always zero except during the voltage inversion when it is equal to the difference of the electrostatic energy on the piezoelectric elements on the voltage inversion jump. The energy dissipated in the switching device is then given by

$$\int_0^t V I dt = \frac{1}{2} C_0 \sum_k V_k^2 (1 - \gamma^2). \quad (57)$$

where V_k is the piezoelectric voltage just before the k th inversion. It appears then that maximizing the consumption of the switching device corresponds to maximizing the sum of the squared piezoelectric voltage before each inversion. In other words, optimizing the damping corresponds to finding the switch sequence that maximizes Eq. (57).

The probabilistic approach is based on the idea of letting the voltage reach a significant but statistically probable value v_{\min} before processing the voltage inversion. Since the time derivative of the extracted energy cancels when the time derivative of the strain in the piezoelectric element vanishes, the extracted energy reaches a local extremum at each extremum of the strain in the piezoelectric elements. Since strain and voltage extrema occurs at the same time, the piezoelectric voltage inversion is achieved when $V^2 > v_{\min}^2$ and V^2

reaches an extremum. v_{\min} is defined after each voltage inversion so that the probability of observing $V^2 > v_{\min}^2$ is equal to P_{SW} , where P_{SW} is a fixed probability set by the user. This can be summarized in

$$P[V^2 > v_{\min}^2] = P_{SW} = 1 - F_{V^2}(v_{\min}^2). \quad (58)$$

where v_{\min} can be determined using the cumulative distribution function $F_{V^2}(v_{\min}^2)$. The critical point of this approach consists in estimating the cumulative distribution function of the voltage after each inversion. It is then easy to determine v_{\min} . The evolution of the piezoelectric voltage after the k th inversion time can be estimated using Eq. (58) where it is assumed that the strain cumulative distribution function is a slow varying function over the estimation time interval. The strain in the piezoelectric elements after the switch is thus assumed to be similar to the strain in the piezoelectric elements before the switch. The estimation is made using an observation time T_{es} of the strain. The value of T_{es} is set by the user.

$$v_{es}(t^+) = -\gamma v_k + \frac{1}{C_0} \sum_{i=1}^N \alpha_i (u(t^-) - u_{ik}) \quad \text{with} \quad \begin{cases} t^+ \in [t_k, t_k + T_{es}] & \text{(future),} \\ t^- \in [t_k - T_{es}, t_k] & \text{(past).} \end{cases} \quad (59)$$

Experimentally, the voltage or the corresponding strain can be simply deduced from the voltage measured on an additional PZT insert left in open circuit and collocated with the principal semi-passive control PZT insert. This additional piezoelectric element is used as a strain sensor.

Recently Guyomar et al. (2007) further extended work on multi-mode vibration control based on the probability law and proposed the new control law based on a statistics. As discussed in the above, in the case of the SSD technique, the energy extracted from the structure by the piezoelectric element is proportional to $\sum v_k^2$, where v_k is the piezoelectric voltage just before the k th switching sequence. This method proposed statistical analysis to define optimization instants for the switching sequence in order to maximize the extracted energy and vibration damping. It is based on a statistical evaluation of the voltage generated by the piezoelectric elements or of the structure deflection.

6.3 A method based on a displacement threshold

Although the good control performance were achieved by using the probability and statistics method, the amount of calculation of these methods are relatively larger because the probabilistic distribution of displacement or voltage in a given period needs to be calculated for switch control. Ji et al. (2009c) proposed a simpler approach for two mode control based on a displacement threshold. In this study, the following strategy is used in controlling the switch

$$\frac{du}{dt} = 0 \quad \text{and} \quad |u| > u_{cr,k}, \quad (60)$$

where $u_{cr,k}$ is the displacement threshold for switching action at time t_k . Equation (60) means that the switching actions take place at the displacement extrema which are larger than the threshold. The physical basis of this switching strategy can be explained textually as follows.

Maximum energy conversion can be realized for the high-order mode when switching action takes place at all the extrema. However the switching frequency is too high for the first mode in this case. Hence it is necessary to skip some extrema to achieve good control performance for the first mode. Generally the extrema can be divided into two categories, those with relatively large displacement amplitude and those with relatively small displacement amplitude. The extrema with relatively large amplitude are close to the extrema of the first mode. Hence switching at these extrema will yield good control performance for the first mode. On the other hand, if switching actions take place at the extrema with relatively small displacement amplitude, the control performance will deteriorate considerably due to the phase effect.

The important issue is how to decide the displacement threshold in a real system. It should be adjusted automatically according to the vibration level and control state. In this study, the amplitude threshold is calculated from average amplitude of latest ten switching points:

$$u_{cr,k} = \lambda \times \frac{1}{10} \sum_{i=1}^{10} |u(t_{k-i})| \quad (61)$$

where t_{k-i} ($i=1, \dots, 10$) is the time of the latest ten switching points and λ ($0 < \lambda < 1$) is a parameter that can be adjusted in the experiments. The initial value of $u_{cr,k}$ is set to zero and updated after each switching action. Because $u_{cr,k}$ is the average of the displacement at latest ten switching points, it can reasonably reflect the latest vibration level. The value of λ should be smaller than 1; otherwise the displacement at the next switching point will exceed the average displacement so that the threshold will increase infinitely.

7. Future directions

Through about ten years of research, several electronic switching circuits and switch control laws have been developed for semi-active vibration control based on switched shunt circuit. However more needs to be done in the following aspects for practical applications of these methods.

The first aspect is the switch control laws for multi-modal control. As introduced above several switch control laws have been developed for multi-mode vibration control using switched shunt circuit, but more efficient control laws are required for better control performance and higher robustness of the control system. The second aspect is the design of low-power shunt circuit. The power consumed by a switched shunt circuit is usually smaller than one milli watt, but a powerful DSP for switch control can consume much higher power. Although the power consumed by a semi-active control system is much smaller than an active control system, the energy consumption of a control system can be an important issue for some application, especially in aerospace engineering. The third aspect is development of self-powered semi-active control system. Although self-powered semi-active control systems have been developed (Niederberger & Morari, 2006; Lallart et al., 2007; Richard et al., 2007; Yabu & Onoda 2005), these systems are based on analog switch control systems, which is not so efficient for multi-mode vibration control. Hence self-powered semi-active control systems with sophisticated switch control laws are expected in the future. Since more complicated switch control laws need more powerful DSP and consumes more power,

a trade-off should also be considered between control performance and energy consumption of a semi-active control system.

8. References

- Badel, A.; Sebald, G.; Guyomar, D.; Lallart, M.; Lefevre, E.; Richard, C. & Qiu, J. (2006). Piezoelectric vibration control by synchronized switching on adaptive voltage sources: Towards wideband semi-active damping. *Journal of Acoustics Society American*, Vol. 119, No. 5, 2815-2825.
- Clark, W. W. (1999). Semi-active vibration control with piezoelectric materials as variable stiffness actuators, *Proceedings of 1000 AIAA/ASME/ASCE/AHS/ASC Structures, Structural Dynamics, and Materials Conference and Exhibit*, Vol. 3672, pp. 2623-2629.
- Clark, W. W. (2000). Vibration control with state-switched piezoelectric materials. *Journal of intelligent material systems and structures*. Vol. 11, No. 4, 263-271.
- Corr, L. R. & Clark, W. W. (2001). Energy dissipation analysis of piezoceramic semi-active vibration control. *Journal of intelligent material systems and structures*, Vol. 12, No. 11, 729-736.
- Corr, L. R. & Clark, W. W. (2003). A novel semi-active multi-modal vibration control law for a piezoceramic actuator. *Transactions of the ASME*, Vol. 125, 214-222.
- Cunefare, K. A. (2002). State-switched absorber for vibration control of point-excited beams. *Journal of Intelligent Material Systems and Structures*, Vol. 13, 97-105.
- Davis, C. L.; Lesieutre, G. A. & Dosch, J. (1997). Tunable electrically shunted piezoceramic vibration absorber, *Proceedings of SPIE, Smart Structures and Materials: Passive Damping and Isolation*, pp. 51-59, San Diego, CA, 1997.
- Davis, C. L. & Lesieutre, G. A. (1998). An actively tuned solid-state piezoelectric vibration absorber, *Proceedings of SPIE, Smart Structures and Materials*, Vol. 3327, pp. 169-182.
- Faiz, A.; Guyomar, L.; Petit, L. & Buttay, C. (2006). Wave transmission reduction by a piezoelectric semi-passive technique. *Sensors and actuators*, Vol. 128, 230-237.
- Guyomar, D.; Richard, C. & Petit, L. (2001). Non-linear system for vibration damping. *142th Meeting of Acoustical Society of America*, Fort Lauderdale, USA. 2001.
- Guyomar, D. & Badel, A. (2006). Non-linear semi-passive multi-modal vibration damping: An efficient probabilistic approach. *Journal of Sound and Vibration*, Vol. 294, 249-68.
- Guyomar, D.; Richard, C. & Mohammadi, S. (2007). Semi-passive random vibration control based on statistics. *Journal of Sound and Vibration*, Vol. 30, No. 7, 818-833.
- Hagood, N. W.; Chung, W. H. & Flowtow, A.von. (1990). Modeling of piezoelectric actuator dynamics for active structural control. *Journal of Intelligent Material Systems and Structures*, Vol. 1, 327-353.
- Hagood, N. W. & Crawley, E. F. (1991). Experimental investigations of passive enhancement of damping space structures. *Journal of Guidance, Control and Dynamics*, Vol. 14, No. 6, 1100-1109.
- Hollkamp, J. J. (1994). Multimodal passive vibration suppression with piezoelectric materials and resonant shunts. *Journal of Intelligent Material Systems and Structures*, Vol. 5, 49-56.

- Hopkins, M. A.; Henderson, D. A.; Moses, R. W.; Ryall, T.; Zimcik, D. G. & Spangler, R. L. (1998). Active vibration-suppression systems applied to twin-tail buffering, *Proc. SPIE Smart Structures and Materials: Industrial and Commercial Application of Smart Structures Technologies*, Vol. 3326, pp. 27-33.
- Ji, H. L.; Qiu, J. H.; Zhao, Y. C. & Zhu, K. J. (2008). A study on semi-active vibration control using piezoelectric elements (in Chinese). *Journal of Vibration Engineering*, Vol. 21, No. 6, 614-619.
- Ji, H. L.; Qiu, J. H.; Badel, A. & Zhu, K. J. (2009a). Semi-active vibration control of a composite beam using an adaptive SSDV approach. *Journal of Intelligent Material Systems and Structures*, Vol. 20, No. 3, 401-412.
- Ji, H. L.; Qiu, J. H.; Badel, A.; Chen, Y. S. & Zhu, K. J. (2009b). Semi-active vibration control of a composite beam by adaptive synchronized switching on voltage sources based on LMS algorithm. *Journal of Intelligent Material Systems and Structures*, Vol. 20, No. 3, 939-947.
- Ji, H. L.; Qiu, J. H.; Zhu, K. J.; Chen, Y. S. & Badel, A. (2009c). Multimodal vibration control using a synchronized switch based on a displacement switching threshold. *Smart Materials and Structures*, Vol. 18, No. 3, 035016: 1-8.
- Ji, H. L.; Qiu, J. H.; Zhu, K. J. & Badel, A. (2010). Two-mode vibration control using nonlinear synchronized switching damping based on the maximization of converted energy. *Journal of Sound and Vibration*, Vol. 329, 2751-2767.
- Kim, S.; Han, C. & Yun, C. (1999). Improvement of Aeroelastic stability of hingeless helicopter rotor blade by passive piezoelectric damping, *Proc. SPIE Smart Structures and Materials: Passive Damping and Isolation*, Vol. 3672, pp. 131-141.
- Lallart, M.; Lefeuvre, E.; Richard, C. & Guyomar, D. (2007). Self-powered circuit for broadband, multimodal piezoelectric vibration control. *Sensors and Actuators A*, Vol. 143, 377-382.
- Lefeuvre, E.; Guyomar, D.; Petit, L.; Richard, C. & Badel, A. (2006). Semi-passive structural damping by synchronized switching on voltage sources. *Journal of Intelligent Material Systems and Structures*, Vol. 17, No. 8/9, 653-660 (See also the Proceedings of the First Symposium on Smart Materials for Engineering and Biomedical Applications, Suzhou, China, May 16-19, 2004, published by China Aviation Industry Press.).
- Makihara, K.; Onoda, J. & Minesugi, K. (2005). Low-Energy-Consumption hybrid vibration suppression based on an energy-recycling approach. *AIAA Journal*, Vol. 43, No. 8, 1706-1715.
- Makihara, K.; Onoda, J. & Minesugi, K. (2006a). Novel approach to self-sensing actuation for semi-active vibration suppression. *AIAA Journal*, Vol. 44, No. 7, 1445-1453.
- Makihara, K.; Onoda, J. & Minesugi, K. (2006b). Behavior of piezoelectric transducer on energy-recycling semi-active vibration suppression. *AIAA Journal*, Vol. 44, No. 2, 411-413.
- Makihara, K.; Onoda, J. & Minesugi, K. (2007a). A self-sensing method for switching vibration suppression with a piezoelectric actuator. *Smart Materials and Structures*, Vol. 16, No. 2, 455-461.

- Makihara, K.; Onoda, J. & Minesugi, K. (2007b). Using tuned electrical resonance to enhance bang-bang vibration control. *AIAA Journal*, Vol. 45, No. 2, 497-504.
- Makihara, K.; Onoda, J. & Minesugi, K. (2007c). Comprehensive assessment of semi-active vibration suppression including energy analysis. *Journal of Vibration and Acoustics, Transactions of the ASME*, Vol. 129, 84-93.
- Niederberger, D. & Morari, M. (2006). An autonomous shunt circuit for vibration damping. *Smart Material and Structure*, Vol. 15, 359-364.
- Onoda, J., Oh, H.-U., & Minesugi, K. (1997). Semiactive Vibration Suppression with Electrorheological-Fluid Dampers, *AIAA Journal*, Vol. 35, No. 12, 1844-1852.
- Onoda, J.; Makihara, K. & Minesugi, K. (2003). Energy-recycling semi-active method for vibration suppression with piezoelectric transducers. *AIAA Journal*, Vol. 41, No. 4, 711-719.
- Petit, L.; Lefeuvre, E.; Richard, C. & Guyomar, D. (2004). A broadband semi passive piezoelectric technique for structural damping, *Proceedings of SPIE International Symposium on Smart Structures and Materials: Damping and Isolation*, San Diego, CA, USA. 2004.
- Qiu, J.; Ji, H. & Zhu, K. (2009). Semi-active Vibration Control Using Piezoelectric Actuators in Smart Structures, *Frontier of Mechanical Engineering in China*, Vol. 4, No. 3, 242-251.
- Richard, C.; Guyomar, D.; Audigier, D. & Ching, G. (1999). Semi-passive damping using continuous switching of a piezoelectric device, *Proceedings of the SPIE Smart Structures and Materials Conference: Passive Damping and Isolation*, San Diego, 1999, Vol. 3672, 104-111.
- Richard, C.; Guyomar, D.; Audigier, D. & Bassaler, H. (2000). Enhanced semi passive damping using continuous switching of a piezoelectric device on an inductor, *Proceedings of SPIE International Symposium on Smart Structures and Materials: Damping and Isolation*, Vol. 3989, 288-299.
- Richard, C.; Guyomar, D. & Lefeuvre, E. (2007). Self-powered Electronic Breaker with Automatic Switching by Detecting Maxima or Minima of Potential Difference Between its Power Electrodes Patent # PCT/FR2005/003000, publication number: WO/2007/063194, 2007.
- Simpson, J. & Schweiger, J. (1998). Industrial Approach to Piezoelectric Damping of Large Fighter Aircraft Components, *Proc. SPIE Smart Structures and Materials: Industrial and Commercial Application of Smart Structures Technologies*, Vol. 3326, pp. 34-46.
- Shen, H.; Ji, H. L.; Qiu, J. H. & Zhu, K. J. (2009). A Semi-passive Vibration Damping System Powered by Harvested Energy. *International Journal of Applied Electromagnetics and Mechanics*, Vol. 31, No. 4, 219-233.
- Wu, S.; Turner, T. L. & Rizzi, S. A. (2000). Piezoelectric Shunt Vibration Damping of an F-15 Panel under High-acoustic Excitation, *Proc. SPIE Smart Structures and Materials: Damping and Isolation*, Vol. 3989, pp. 276-287.
- Wang, K. W.; Lai, J. S. & Yu, W. K. (1996). Energy-based parametric control approach for structural vibration suppression via semi-active piezoelectric networks. *Transaction of ASME, Journal Vibration and Acoustics*, Vol. 115, 505-509.

- Yabu, T. & Onoda, J. (2005). Non-power-supply semi-active vibration suppression with piezoelectric actuator (in Japanese), *Proceedings of the JSASS/JSME Structures Conference*, Vol. 47, pp. 48-50.
- Zhang, J. M.; Chang, W.; Varadan, V. K. & Varadan, V. V. (2001). Passive underwater acoustic damping using shunted piezoelectric coatings. *IOP Journal of Smart Materials and Structures*, Vol. 10, 414-420.

Self-Powered and Low-Power Piezoelectric Vibration Control Using Nonlinear Approaches

Mickaël Lallart and Daniel Guyomar

*Université de Lyon, INSA-Lyon, LGEF EA 682, F-69621, Villeurbanne
France*

1. Introduction

The constant proliferation of embedded systems as well as miniaturized devices has raised the issue of efficiently limiting the vibrations and/or providing precise positioning using a very few amount of energy. A typical application example is the damping of vibrating electronic cards, in order to limit the risk of microcracks in conductive tracks. Because of the integration constraints of these systems, the use of viscoelastic materials (*i.e.*, direct dissipation of the mechanical energy into heat (Johnson, 1995)) is not applicable. Hence, the use of energy conversion media is mandatory in this case. In particular, piezoelectric materials are good candidates for the control of embedded devices, thanks to their high power densities and integration potentials (Veley & Rao, 1996). It should be also noted that using piezoelectric elements allows achieving various functions, such as actuation, sensing and energy harvesting (Inman, Ahmadian & Claus, 2001; Qiu & Haraguchi, 2006; Guyomar et al., 2007a; Lallart et al., 2008a), making them very attractive in integrated systems.

However, the use of standard active control schemes is also prohibited when dealing with integrated systems, as their high power requirements necessitate bulky amplifiers (Gerhold, 1989). Such control schemes need a full feedback loop as well, including sensors (although some control schemes can use the transducer itself as a sensor (Qiu & Haraguchi, 2006)) and microcontrollers that may not be easily integrated.

In addition, the use of passive schemes featuring electroactive materials (*i.e.*, shunted systems (Lesieutre, 1998)) is also quite complex, as the required components are usually difficult to implement, especially in the case of using piezoelectric actuators where the required inductance for an efficient control is usually very large (several Henrys), necessitating the use of synthetic components that have to be externally powered (Fleming and Moheimani, 2003). These control techniques have limited performance as well as high sensitivity to frequency drifts caused by temperature variations or ageing, and their implementation for the control of several modes is quite complex (Wu, 1998).

Hence, the combination of passive and active control schemes has been proposed in order to combine their advantages while limiting their drawbacks. In particular, it has been shown that applying nonlinear methods can lead to significant damping abilities (Clark, 2000; Davis & Lesieutre, 2000; Cunefare, 2002; Holdhusen & Cunefare, 2003; Wickramasinghe et al., 2004; Nitzsche et al., 2005; Makihara, Onoda & Minesugi, 2007). However, the nature of these approaches is often complex, limiting their realistic application, especially in integrated systems.

Therefore, the development of effective techniques for vibration control that can be easily integrated is an issue. The purpose of this chapter is to expose several techniques addressing this problem. In order to meet the low-power and integration constraints, the proposed approaches are based on a simple nonlinear processing of the output voltage of piezoelectric elements, resulting in a magnification of the conversion abilities of the system. Hence, this increase of the coupling coefficient allows reducing the mechanical energy, leading to a damping effect in terms of mechanical vibrations.

The chapter is organized as follows. Section 2 introduces a rough but accurate model of the behavior of an electromechanical structure near one of its resonance frequencies, as well as the basic concepts of the nonlinear treatment. The direct application of this technique for vibration damping purposes is exposed in Section 3, leading to the concept of *Synchronized Switch Damping* (SSD), whose principles lie in a fast piezovoltage inversion when this latter reaches either a maximum or a minimum value. The extension of this method to a non-synchronized technique called *Blind Switch Damping* is then developed in Section 4. In Section 5 is proposed a similar concept than the SSD, but with a voltage switching on zero displacement values, allowing a control of the resonance frequency of the device. Finally, Section 6 concludes the chapter, recalling the main results and exposing a comparison of the advantages and drawbacks of the exposed techniques.

2. Modeling and nonlinear conversion enhancement

The aim of this section is to expose a simple model (developed by Badel et al. (2007)) for the description of the behavior of an electromechanical structure near one of its resonance frequencies (which correspond to the highest displacement magnitude and therefore to the cases that may be harmful to the system). This model will be used in the following sections for the theoretical developments in order to evaluate the damping abilities of the various methods.

The basic principles of the nonlinear treatment are also provided, showing the increase in terms of conversion abilities of the piezodevice.

2.1 Electromechanical structure modeling

For the sake of simplicity, it will be considered that the electromechanical structure is a simple cantilever beam, as depicted in Figure 1. However, it can be noted that the proposed model can also be applied to any structures, such as plates. In addition, it is assumed that:

- i. The strain has only two dimensions (*i.e.*, null stress along the x_2 axis).
- ii. The plane sections of the beam remain plane (Euler-Bernoulli assumption), so that no shear strain appears and the strain along the x_3 axis is null.
- iii. The dynamic deformed shape of the flexural mode is close to the static one.

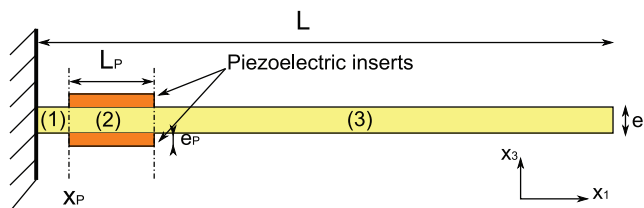


Fig. 1. Electromechanical structure

Under these conditions, the relationship between strain S_1 and stress T_1 along the x_1 axis for the beam turns to:

$$T_1 = c_B S_1, \quad (1)$$

with c_B the elastic rigidity of the structure in-plane strain, and equals $c_B = Y/(1 - \nu)$, with Y and ν the Young modulus and Poisson's ratio.

For the piezoelectric element, the constitutive equations are given by:

$$\begin{cases} S_1 = s_{11}^E T_1 + s_{12}^E T_2 + s_{13}^E T_3 + d_{13} E_3 \\ S_2 = s_{12}^E T_1 + s_{11}^E T_2 + s_{13}^E T_3 + d_{13} E_3, \\ D_3 = \epsilon_{33}^T E_3 + d_{13} T_1 + d_{13} T_2 + d_{33} T_3 \end{cases} \quad (2)$$

where D and E denote the electric displacement and electric field. s_{ij}^E , ϵ_{ii}^T and d_{ij} are given as the elastic constant under constant electric field, permittivity under constant stress and piezoelectric charge coefficient respectively.

According to the previous assumptions ($S_2 = 0$ and $T_3 = 0$), the stress-strain relationships may be simplified as:

$$S_1 = \left(s_{11}^E - \frac{s_{12}^E{}^2}{s_{11}^E} \right) T_1 + d_{13} \left(1 - \frac{s_{12}^E}{s_{11}^E} \right) E_3. \quad (3)$$

When the piezoelectric element is short-circuited ($E_z = 0$), it is therefore possible to define a rigidity in short-circuit conditions c_{PE} given by:

$$c_{PE} = \frac{s_{11}^E}{s_{11}^E{}^2 - s_{12}^E{}^2}. \quad (4)$$

Similarly, using the expression of the electric displacement gives the rigidity in open-circuit conditions ($D_3 = 0$) c_{PD} defined as:

$$c_{PD} = \left[s_{11}^E - \frac{s_{12}^E{}^2}{s_{11}^E} - \frac{d_{13}^2}{\epsilon_{33}^T - \frac{d_{13}^2}{s_{11}^E}} \left(1 - \frac{s_{12}^E}{s_{11}^E} \right)^2 \right]^{-1}. \quad (5)$$

In addition, it has been assumed that the dynamic and static flexural mode shapes are similar. Therefore, the expression of the second order derivative of the flexural displacement yields:

$$\frac{d^2 u_3}{dx_1^2} = \frac{2S_1}{e_B} = c_x I_x, \quad (6)$$

where:

$$c_x I_x = \begin{cases} c_B I_B & \text{in non-piezoelectric areas (zones (1) and (3))} \\ c_B I_B + c_{PD} I_P & \text{in piezoelectric areas (zone (2))} \end{cases}, \quad (7)$$

with I_B and I_P respectively referring to the beam and piezoelectric moments of inertia. Hence, by integrating Eq. (7) and performing an energy analysis¹, it is possible to define four stiffnesses:

$$\left\{ \begin{array}{l} K_{B1} = \frac{3C_B I_B}{L^3 - (L - x_p)^3} \quad \text{for the beam in zone (1)} \\ K_{B2} = \frac{3C_B I_B}{(L - x_p)^3 - (L - L_p - x_p)^3} \quad \text{for the beam in zone (2)} \\ K_{B3} = \frac{3C_B I_B}{(L - L_p - x_p)^3} \quad \text{for the beam in zone (3)} \\ K_{PE} = \frac{3C_{PE} I_P}{(L - L_p - x_p)^3} \quad \begin{array}{l} \text{for the piezoelectric element} \\ \text{(short-circuited) in zone (2)} \end{array} \end{array} \right., \quad (8)$$

as well as a dynamic mass M of the structure:

$$M = \frac{w}{u_3|_L^2} \left[\int_0^L (e_B \rho_B) dx + 2 \int_{x_p}^{x_p + L_p} (e_P \rho_P) dx \right], \quad (9)$$

with w the width of the beam (and piezoelectric insert) and ρ_B and ρ_P the density of the beam and of the piezoelectric element.

The piezoelectric effect in terms of electromechanical coupling may also be obtained by integrating in the space domain the time derivative of the constitutive equation giving the electrical displacement D_3 as a function of the electric field E_3 and strain S_1 , whose expression under the considered assumptions is given by:

$$D_3 = \epsilon_{33}^S E_3 + e_{33} S_3, \quad (10)$$

yielding the expression of the current I flowing out of the insert:

$$I = \alpha_p (\dot{u}_2 - \dot{u}_1) - C_{0P} \dot{V} \quad \text{with} \quad \alpha_p = -\frac{2e_{33} w L_p}{e_p} > 0 \quad \text{and} \quad C_{0P} = \frac{2\epsilon_{33}^S w L_p}{e_p}, \quad (11)$$

with \dot{u}_1 and \dot{u}_2 denoting the velocities at the length x_p and $x_p + L_p$, and V the piezovoltage. In addition, the effect of the piezoelectric element in terms of mechanical behavior may be obtained from the expression of the stress along the x_3 direction:

$$T_3 = c_{33}^E S_3 - e_{33} E_3, \quad (12)$$

leading to the expression of the force F_P exerted by the piezoelectric element:

¹ For the entire derivation, the reader may refer to Badel et al. (2007).

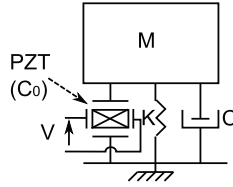


Fig. 2. SDOF model of the electromechanical structure

$$F_p = K_{pE}(u_2 - u_1) + \alpha_p V. \quad (13)$$

It is however possible to simplify the model as a Single Degree of Freedom (SDOF) electromechanically coupled spring-mass-damper system as illustrated in Figure 2, yielding the global electromechanical equation set:

$$\begin{cases} M\ddot{u} + C\dot{u} + K_E u = F - \alpha V \\ I = \alpha \dot{u} - C_0 \dot{V} \end{cases}, \quad (14)$$

with u the displacement and F the applied force at a given point and where K_E , α and C_0 are the global short-circuit stiffness, force factor and clamped capacitance:

$$\begin{cases} K_E = \frac{K_{B1}(K_{B2} + K_{pE})K_{B3}}{K_{B1}(K_{B2} + K_{pE}) + (K_{B2} + K_{pE})K_{B3} + K_{B1}K_{B3}} \\ \alpha = \frac{\alpha_p K_{B1}K_{B3}}{K_{B1}(K_{B2} + K_{pE}) + (K_{B2} + K_{pE})K_{B3} + K_{B1}K_{B3}} \\ C_0 = C_{0P} + \frac{\alpha_p^2 (K_{B1} + K_{B3})}{K_{B1}(K_{B2} + K_{pE}) + (K_{B2} + K_{pE})K_{B3} + K_{B1}K_{B3}} \end{cases}. \quad (15)$$

C is defined as the structural damping coefficient, whose value is obtained from the mechanical quality factor Q_M of the structure at the considered mode in open-circuit condition:

$$C = \frac{\sqrt{K_D M}}{Q_M}, \quad (16)$$

with K_D the open-circuit equivalent stiffness:

$$K_D = K_E + \frac{\alpha^2}{C_0}. \quad (17)$$

The global electromechanical coupling coefficient k , which gives the ability of the piezomaterial for converting the mechanical energy into electric energy (and conversely), can also be obtained from the model parameters as:

$$k^2 = 1 - \frac{f_E^2}{f_D^2} = \frac{\alpha^2}{\alpha^2 + C_0 K_E} = \frac{\alpha^2}{C_0 K_D}, \quad (18)$$

with f_E and f_D the short-circuit and open-circuit resonance frequencies.

2.2 Nonlinear conversion enhancement

From the mechanical equation of the model (Eq. (14)), it is possible to write the energy balance over a time period $[t_1; t_1 + \tau]$ as:

$$\frac{1}{2}M \left[\dot{u}^2 \right]_{t_1}^{t_1+\tau} + C \int_{t_1}^{t_1+\tau} \dot{u}^2 dt + \frac{1}{2}K_E \left[u^2 \right]_{t_1}^{t_1+\tau} = \int_{t_1}^{t_1+\tau} F \dot{u} dt - \alpha \int_{t_1}^{t_1+\tau} V \dot{u} dt, \quad (19)$$

where the left side members are respectively the kinetic energy, dissipated energy and potential energy. The left side terms correspond to the provided energy and converted energy. According to the electrical equation of Eq. (14), this latter can be decomposed into:

$$\alpha \int_{t_1}^{t_1+\tau} V \dot{u} dt = \frac{1}{2}C_0 \left[V^2 \right]_{t_1}^{t_1+\tau} + \int_{t_1}^{t_1+\tau} V I dt, \quad (20)$$

where the first term of the right side members is the electrostatic energy available on the piezoelectric element, and the second term the energy exchanged with the control system. Hence, from Eq. (19), it can be shown that in order to increase the part of converted energy, it is possible to:

1. Increase the voltage
2. Reduce the phase shift between the voltage and velocity

Both of these solutions can be achieved using a simple nonlinear treatment that does not require any external energy. The principles of this approach consist in quickly inverting the voltage when this latter reaches a maximum or a minimum value (corresponding to a maximal electrostatic energy). This inversion is however performed in an imperfect fashion - *i.e.*, the ratio of the absolute voltage values after and before the inversion is equal to γ , with $0 \leq \gamma \leq 1$.

Thanks to the continuity of the voltage ensured by the dielectric behavior of the piezoelectric element, this leads to a cumulative effect that allows a significant increase of the voltage (Figure 3). In addition, such a process also splits the voltage into two components: one that is proportional to the displacement (as in open-circuit conditions with zero initial voltage and displacement), and one created by the inversion process that is a piecewise constant function proportional to the speed². As this latter is usually much larger than the voltage produced by the open-circuit condition, the voltage is almost proportional to the speed sign. Hence, both of the conversion enhancement possibilities are met using a simple nonlinear treatment.

The way the voltage inversion can be achieved is very simple as well. It consists in using a resonant electrical network for performing the inversion process. This resonant network is composed of an inductance L and the piezoelectric capacitance (C_0). Each time the voltage reaches a maximum or minimum value, the inductance is connected to the piezoelement (that has an initial charge q_0) through a digital switch SW (Figure 4). Hence, the voltage starts oscillating around 0. In particular, after half a period of this electrical oscillation, the voltage is inverted. At this time the digital switch is opened, disconnecting the inductance from the piezoelement which is therefore in open circuit condition. The total switching time t_{sw} is thus given by:

² or, in monochromatic excitation, in phase with the speed

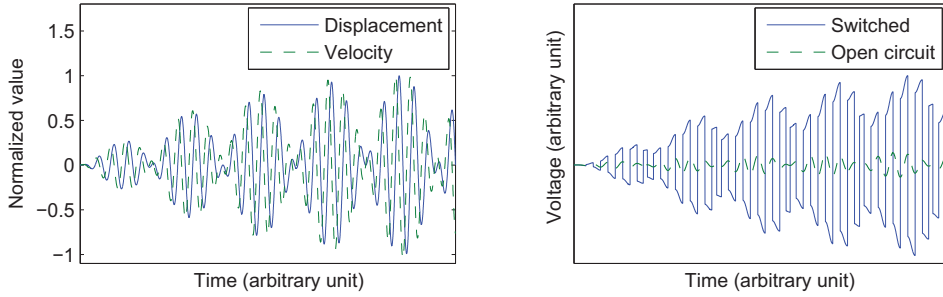


Fig. 3. Conversion enhancement principles using nonlinear approach based on voltage inversion

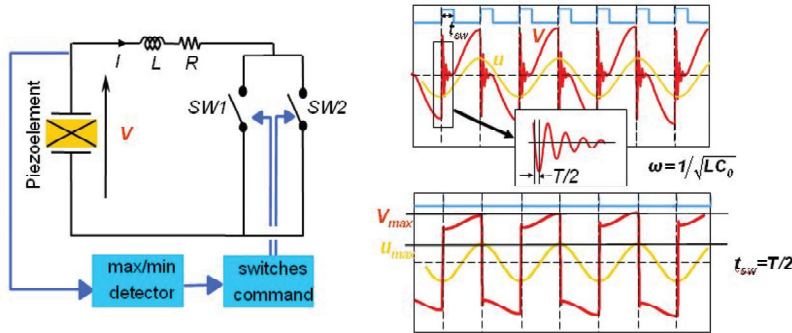


Fig. 4. Practical implementation of the voltage inversion

$$t_{sw} = \pi\sqrt{LC_0} . \tag{21}$$

However, because of losses in the switching circuit (modeled by a resistance R), the inversion is not perfect and characterized by the inversion coefficient γ defined as:

$$\gamma = e^{-R\frac{\pi}{2}\sqrt{\frac{C_0}{L}}} . \tag{22}$$

From an analysis of the maximal available electrostatic energy (given as the half product of the piezocapacitance with the squared maximal voltage), it can be shown that the electrical energy (under constant displacement magnitude) is increased by a typical factor from 12 to 200 when using such a nonlinear approach.

Many applications may benefit from this conversion ability increase, the most significant being energy harvesting from mechanical solicitations (Guyomar et al., 2005; Lefevre et al., 2006a; Lallart & Guyomar, 2008b; Lallart et al., 2008c) and vibration control (e.g., for anechoic purposes (Guyomar et al., 2006a)).

3. Synchronized Switch Damping (SSD) techniques

Now the basic modeling and nonlinear conversion enhancement exposed, it is proposed in this section to directly apply the proposed concept to damping purposes.

In addition, it will be considered that voltage sources may be added in the circuit in order to compensate the losses during the inversion process (Figure 5)³. Nevertheless, the addition of this external power supply makes the technique no longer semi-passive, as external energy is provided to active element (this energy remains nevertheless small). Hence, according to the value of the components, the different obtained techniques are summarized in Table 1 and depicted in Figure 6.

3.1 Performance under monochromatic excitation

In a first approach, it is proposed to evaluate the performance of the SSD techniques under a monochromatic excitation at one of the resonance frequencies of the system. For the sake of conciseness, the following theoretical development will be made considering all the parameters appearing in Figure 5, the damping abilities of a particular technique being obtained by replacing the parameters by those listed in Table 1.

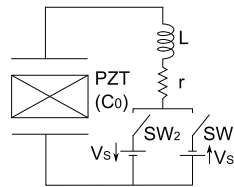


Fig. 5. General schematic for the SSD damping techniques

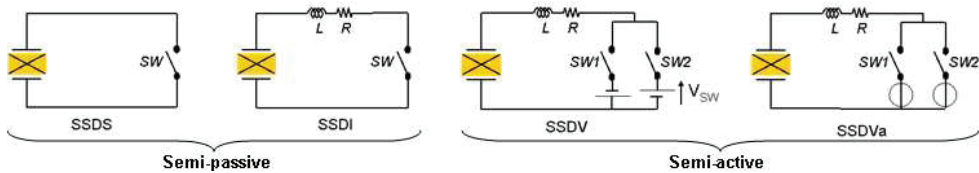


Fig. 6. SSD technique schematics

Designation		Kind	Inversion factor	Voltage source
SSDS (Richard et al., 1999)	(Synchronized Switch Damping on Short-circuit)	Semi-passive	0	0
SSDI (Richard et al., 2000; Petit et al., 2004)	(Synchronized Switch Damping on Inductor)	Semi-passive	γ	0
SSDV (Lefeuvre et al., 2006b)	(Synchronized Switch Damping on Voltage sources)	Semi-active	γ	$\pm V_s$
SSDVa ⁴ (Badel et al., 2006)	(Synchronized Switch Damping on adaptive Voltage sources)	Semi-active	γ	$\pm \beta \frac{\alpha}{C_0} u_M$

Table 1. SSD technique properties

³ In this case, the inversion is done with respect to the value of the voltage source.

⁴ β refers to the tuning coefficient and u_M to the displacement magnitude - it can be besides shown that the voltage source tuning is equivalent to an increase of the inversion factor γ .

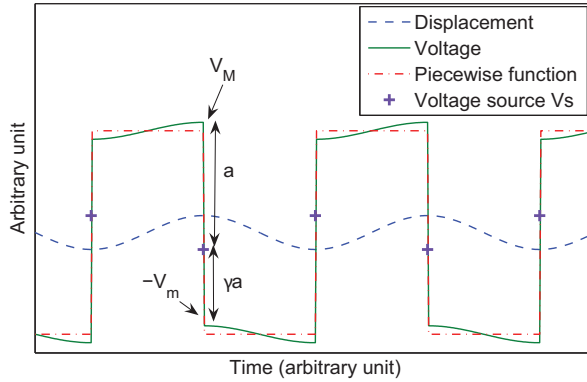


Fig. 7. Waveforms of the SSD techniques in monochromatic excitation

The theoretical performance evaluation are based on the previously exposed electromechanical model (Eq. (14)). In the case of the SSD techniques and assuming a sine excitation, the voltage may be decomposed into two voltages - one proportional to the displacement (open-circuit voltage) and one that is proportional to the sign of the speed:

$$V = \frac{\alpha}{C_0} u + H \operatorname{sign}(\dot{u}), \tag{23}$$

with H the magnitude of the voltage in phase with the speed, which can be found using the following relations (Figure 7):

$$\begin{cases} H = \frac{1}{2}(V_M + V_m) \\ V_m - V_s = \gamma(V_M + V_s) \\ V_M - V_m = 2 \frac{\alpha}{C_0} u_M \end{cases} \tag{24}$$

Hence, the amplitude of the piecewise function yields:

$$H = \frac{1 + \gamma}{1 - \gamma} \left(\frac{\alpha}{C_0} u_M + V_s \right). \tag{25}$$

Assuming that the structure filters higher harmonics, the expression of the piezovoltage may be approximated by its first harmonic, which leads to:

$$V(\omega) \approx \frac{\alpha}{C_0} U(\omega) + j \frac{4}{\pi} \frac{1 + \gamma}{1 - \gamma} \left(\frac{\alpha}{C_0} U(\omega) + V_s \right) \tag{26}$$

in the frequency domain, with $U(\omega)$ the Fourier transform of the time-domain displacement u and ω the angular frequency. From this equation, it can be seen that the effect of the SSD control is equivalent to a dry friction, as the energy cycle only depends on the displacement magnitude, and not on the frequency.

Hence, merging this expression with the motion equation of the electromechanical structure Eq. (14) yields the expression of the displacement in the frequency domain:

$$U(\omega) = \frac{F(\omega) - j\alpha \frac{4}{\pi} \frac{1+\gamma}{1-\gamma} V_S}{-M\omega^2 + j \left(C\omega + \frac{4}{\pi} \frac{1+\gamma}{1-\gamma} \frac{\alpha^2}{C_0} \right) + K_D}. \tag{27}$$

Assuming that the structure is weakly damped, the expression of the displacement magnitude at the resonance frequency is given by:

$$(u_M)_{res|_{SSD}} = \frac{F_M - \alpha \frac{4}{\pi} \frac{1+\gamma}{1-\gamma} V_S}{C\omega + \frac{4}{\pi} \frac{1+\gamma}{1-\gamma} \frac{\alpha^2}{C_0}}, \tag{28}$$

where F_m denotes the force magnitude. Hence, the obtained attenuation at the resonance frequency when using the SSD techniques yields:

$$A_{SSD} = \frac{1 - \alpha \frac{4}{\pi} \frac{1+\gamma}{1-\gamma} \frac{V_S}{F_M}}{\left(1 + \frac{4}{\pi} \frac{1+\gamma}{1-\gamma} \frac{\alpha^2}{C_0 C\omega} \right)} = \frac{1 - \alpha \frac{4}{\pi} \frac{1+\gamma}{1-\gamma} \frac{V_S}{F_M}}{\left(1 + \frac{4}{\pi} \frac{1+\gamma}{1-\gamma} k^2 Q_M \right)}. \tag{29}$$

The associated attenuation of the different SSD techniques (SSDS, SSDI, SSDV, SSDVa) are listed in Table 2, and typical frequency response functions as well as associated energy cycles are depicted in Figure 8. In the case of the SSDVa technique, the value of the voltage source is matched to the vibration magnitude such as:

$$|V_S| = \beta \frac{\alpha}{C_0} u_M. \tag{30}$$

Figure 8 demonstrates the effectiveness of the semi-passive approaches (SSDS and SSDI) for efficiently controlling the vibrations compared to the shunted approach. Especially, the addition of an inductance (SSDI approach) for performing a voltage inversion rather than a charge cancellation (SSDS technique) allows a significant enhancement of the damping abilities. In addition, the performance can be greatly improved using a few amount of external energy, as demonstrated by the transfer functions obtained in the case of

Technique	SSDS	SSDI	SSDV	SSDVa
Attenuation	$\frac{1}{1 + \frac{4}{\pi} k^2 Q_M}$	$\frac{1}{1 + \frac{4}{\pi} \frac{1+\gamma}{1-\gamma} k^2 Q_M}$	$\frac{1 - \alpha \frac{4}{\pi} \frac{1+\gamma}{1-\gamma} \frac{V_S}{F_M}}{1 + \frac{4}{\pi} \frac{1+\gamma}{1-\gamma} k^2 Q_M}$	$\frac{1}{1 + \frac{4}{\pi} \frac{1+\gamma}{1-\gamma} (1 + \beta) k^2 Q_M}$

Table 2. SSD technique attenuations at the resonance frequency

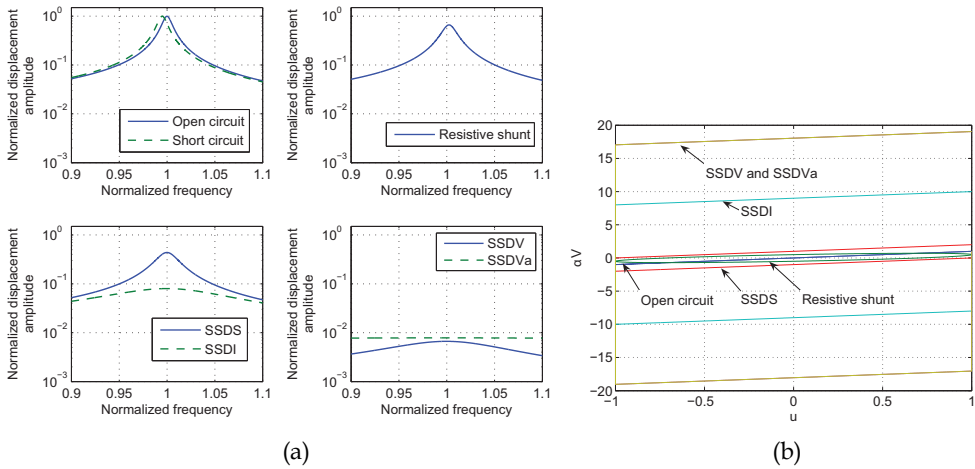


Fig. 8. (a) Frequency response functions and (b) energy cycles of SSD techniques and comparison with resistive shunt (at optimal load) ($M = 1 \text{ g}$, $K_D = 1000 \text{ N.m}^{-1}$, $C = 10^{-2} \text{ N.m}^{-2}$ ($Q_M = 100$), $\alpha = 10^{-3} \text{ N.V}^{-1}$, $C_0 = 10^{-7} \text{ F}$ ($k^2 = 10^{-2}$), $\gamma = 0.8$, $V_S = 80 \text{ V}$, $\beta = 10$)

the semi-active approaches (SSDV and SSDVa). The performance increase from the resistive shunting to the SSDVa can also be demonstrated by the energy cycle in the coordinate $(u, \alpha V)$, derived from the converted energy (Eq. (20)), where the increase in terms of area denotes the increase in terms of converted energy, and thus performance improvement. However, it should be noted that in the case of the SSDV, the attenuation expression and transfer function are negative when:

$$\alpha \frac{4}{\pi} \frac{1 + \gamma}{1 - \gamma} \frac{V_S}{F_M} > 1, \tag{31}$$

denoting the emergence of instabilities in the system (Lallart, Badel & Guyomar, 2008d), while the SSDVa, matching the value of the voltage source to the displacement magnitude, is unconditionally stable.

3.2 Broadband excitation

The previous section focused on the vibration control when only one particular mode is concerned. Thanks to the nature of the maximum and minimum detection, the adaptivity of the SSD control is ensured in the case of frequency drifts (due for example to temperature or pressure variation or ageing).

However, realistic excitation forces of structures are more likely to be random. When the structure is submitted to such forces, the nonlinear nature of the approach prevents the estimation of the system response. However, it has been shown that using a time-domain approach may help in predicting the response, by modeling the switching process as a series of step responses (Guyomar & Lallart, 2007b; Lallart et al., 2007)⁵.

⁵ This approach also permits a more accurate prediction of the response of systems featuring low mechanical quality factor (Lallart et al., 2007).

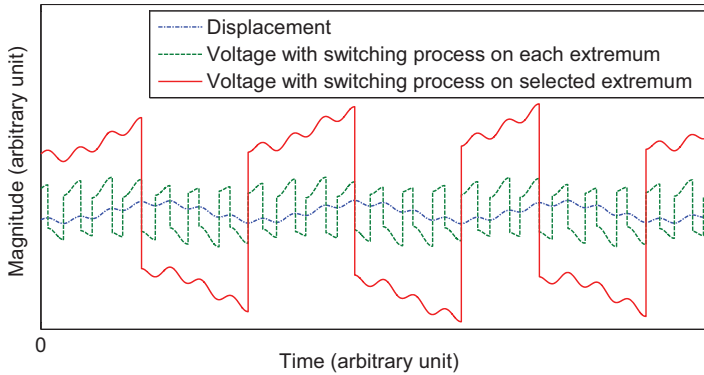


Fig. 9. SSD technique waveforms under broadband or multimodal excitation

Moreover, in the case of complex excitation, it can be shown that a trade-off exists between the voltage increase caused by the cumulative effect of the switching process itself and the number of switching events (Figure 9), as the converted energy is given by:

$$E_{conv} = \frac{1}{2}C_0V^2 + \frac{1}{2}C_0 \sum_{k=1}^n \left[(1-\gamma^2)V_k^2 - (1+\gamma)(2\gamma V_k + (1+\gamma)V_s) \right], \quad (32)$$

with V_k referring to the voltage at the k^{th} switching time instant.

Hence, if the switching process occurs on each maximum and minimum voltage values, the voltage increase would be limited due to the losses in the inversion circuit. But if the number of switching events is limited, the voltage is no longer proportional to the sign of the velocity, limiting the conversion enhancement.

In addition, Figure 9 shows that the switching process focuses on the highest mode when no particular extremum selection is performed. As higher mode are generally less coupled than first modes, this leads to moderate performance of the control.

In order to ensure the conversion gain allowed by the nonlinear process, it is therefore mandatory to properly select the voltage extrema. Several approaches can be used:

- **Probabilistic approach** (Guyomar & Badel, 2006b): This method consists in computing the cumulative distribution function of the squared displacement or voltage over a given time period. Then the switching process is enabled (*i.e.*, the inversion of the voltage will occur on the next extremum value) if the value of the squared displacement or voltage is greater than a reference value corresponding to a user-defined probability threshold.
- **Statistical approach** (Guyomar, Richard & Mohammadi, 2007c): In this approach, the switching process is enabled if the signal (squared displacement or voltage) is greater than the sum of the mean value and standard deviation weighted by a user-defined coefficient. An alternative method consists in using the RMS value rather than the mean value and standard deviation.
- **Analog approach** (Lallart et al., 2008e): This method consists in setting the threshold using analog components (typically a lossy peak detector). Although this approach is not as precise as the previously exposed techniques, the computation of the threshold is very simple, allowing the self-powered implementation of the concept.

- **Modal approach** (Harari, Richard & Gaudiller, 2009): The principles of this control consists in filtering the response of a piezoelectric element used as sensor in order to select only one mode to control. The number of required piezoelectric actuators is equal to the number of controlled mode in this case. The technique can besides be enhanced by ensuring that the switching process occurs on actual extrema.

Hence, the principles of disabling the switching process when the control signal is less than a threshold allows controlling the trade-off between voltage increase and number of switching events (Ji et al., 2009). The performance of the vibration control system are therefore increased by a typical factor of 2 compared to the simple SSDI that consists of switching on all extrema (Guyomar & Badel, 2006b; Guyomar, Richard & Mohammadi, 2007c). Such an approach also permits a simultaneous control of several modes of the structure, and automatically adapts the control to the mode featuring the highest energy.

3.3 Implementation considerations & discussion

When dealing with embeddable systems for vibration control, it is mandatory to take into account the integration potential of the envisaged technique. In the case of the SSD control, it has been shown that the required energy for the actuation is limited, and even null for the semi-passive approaches (SSDS and SSDI).

In particular, the control principles that consists in detecting minimum and maximum voltage values can be done in a simple way by comparing the voltage itself with its delayed version as depicted in Figure 10, giving the position of maximum values (the minimum positions detection is done using an additional detector but with inversed polarities).

The implementation of such a self-powered switching device is shown in Figure 11 (Richard, Guyomar & Lefeuvre, 2007). It consists in comparing the voltage (using transistor T_2) with its delayed version obtained using a diode, a resistor and a capacitor. Once the delayed version greater than the voltage, the transistor T_2 is ON, turning T_1 ON as well. Hence the inversion process is initiated. In order to ensure that the switching process stops half an oscillation period latter, a diode (D_1) is placed in the switching branch which stops the process when the current cancels (corresponding to the end of the inversion). Finally, it has to be noted that the capacitor C used both for the delay and energy storage in order to drive the transistors should be large enough to ensure a full voltage inversion but also small enough to ensure that it is discharged at the beginning of the next positive voltage value (Figure 10).

It is also important to note that such an implementation also works using the same patch both for actuation and sensing; hence no additional piezoelectric insert is required.

Such a simple implementation, that requires widely available components, can therefore be easily embedded while having a very low cost. Such a device also have a wide frequency range of operation, covering more than a decade⁶.

As stated in paragraph 3.2, the SSD technique can be improved in broadband excitation conditions by using a proper extremum selection. In particular, it is possible to slightly modify the proposed implementation in order to implement a threshold that enables the maximum detection. It consists of using an envelope detector that is compared to the piezovoltage. The detection through the peak detector is then enabled only if the piezovoltage is greater than the threshold (Lallart et al., 2008e).

⁶ It can be demonstrated that a small delay between the actual occurrence of a maximum value and the switching process does not have a significant impact on the performance of the system.

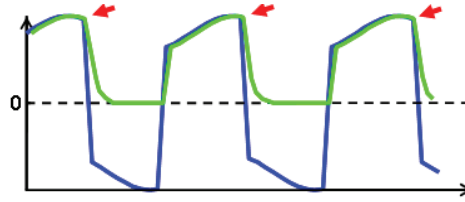


Fig. 10. Maximum detection using delayed signal

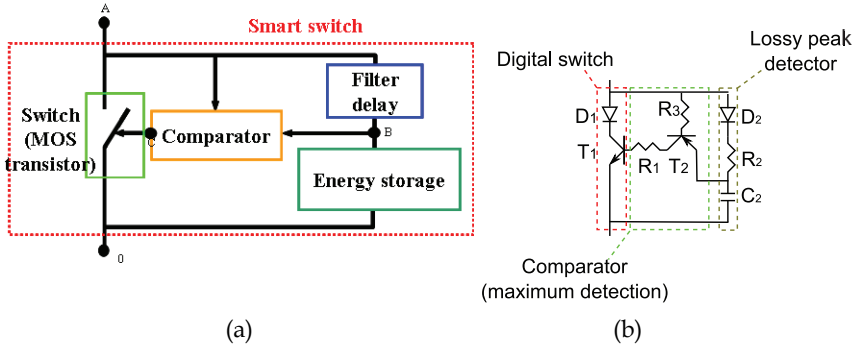


Fig. 11. Principles of the self-powered maximum detection and unipolar circuit schematic (Richard, Guyomar & Lefeuvre, 2007)

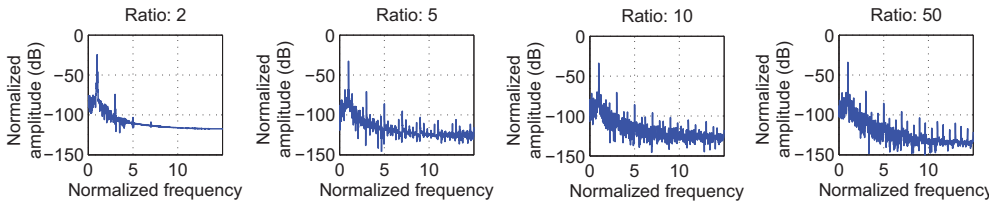


Fig. 12. Frequency response functions (normalized w.r.t. maximal magnitude of the uncontrolled system) for different switching frequencies (normalized w.r.t. vibration frequency)

An additional concern about the implementation of the SSD technique lies in the fact that the additional piecewise voltage (which is a crenel function under monochromatic excitation) leads to the appearance of odd harmonics, which may be harmful if a higher mode matches one of these harmonics, or when performing a sound wave control for comfort (as the human hearing system is more sensitive to higher frequencies). In this case, it is possible to increase the switching time period (for example by using an inductance with a higher value). This strategy hence allows a reduction of the harmonics (Petit et al., 2004) without decreasing significantly the performance of the damping system (Figure 12).

Finally, it can be noted that the switch principles are independent from the physical quantity. Hence, it is possible to extend the control to magnetic actuators (Lallart et al., 2008b) by controlling the current rather than the voltage and by operating dual transformations of the control circuit and law (*i.e.*, normally closed switch in parallel with the actuator).

4. Blind Switch Damping (BSD) approaches

The basic concept of the SSD techniques lies in switching synchronously with the structure motion. Therefore, it is mandatory to monitor the voltage or displacement (although the detection may be simply realized as shown in the previous section). The purpose of this section is to expose another nonlinear approach that allows limiting the vibrations by artificially increasing the mechanical losses without any needs of synchronization (Lallart et al., 2009). Hence no voltage or displacement sensing is required. Because of this structure-independent and non-synchronous nature, this concept is called *Blind Switch Damping on Short-circuit* (BSDS).

4.1 Principles

The principles of the BSDS technique consists in switching the piezoelectric element on short circuit (Figure 13) with a frequency $f_s n$ times higher than the vibration frequency f_0 :

$$f_s = n f_0, \quad n \in \mathfrak{R}^+ \text{ and } n \gg 1. \quad (33)$$

Hence, this intermittent short-circuit switching approach allows shaping the voltage so that this latter is in phase with the speed thanks to a low-cost differentiation process, hence leading to viscous losses and therefore reducing the vibrations.

4.2 Performance under monochromatic excitation

The principles of the BSDS technique consist in dissipating the electrostatic energy available on the piezoelectric element⁷. The expression of the piezovoltage when using the BSDS method, given as:

$$V = \frac{\alpha}{C_0} \left[u(t) - u \left(k \frac{T_0}{n} \right) \right] \text{ for } k \frac{T_0}{n} \leq t < (k+1) \frac{T_0}{n} \text{ with } k \in \mathbb{N}, \quad (34)$$

with T_0 the vibration period ($T_0 = 1/ f_0$), shows the differentiation performed by this approach. Considering that the switching coefficient n is far greater than 1 and that the electromechanical structure filters frequencies higher than its resonance frequency, the piezoelectric voltage may be approximated by its first harmonic such as:

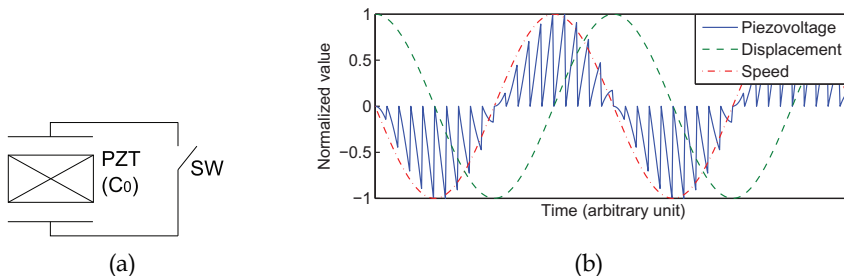


Fig. 13. (a) BSDS implementation and (b) typical waveforms

⁷ The cancellation of the piezovoltage may also be seen as a change in the initial conditions.

$$V \approx \frac{\alpha}{C_0} \frac{T_0}{\pi n} \dot{u}(t). \quad (35)$$

Hence, inserting this equation in the spring-mass-damper model obtained in Section 2.1 (Eq. (14)) leads to the motion equation when using the BSDS:

$$M\ddot{u} + \left(C + \frac{\alpha^2 T_0}{C_0 \pi n} \right) \dot{u} + K_E u = F, \quad (36)$$

which demonstrates the viscous damping effect performed by the method (while the SSD techniques are equivalent, in a mechanical point of view, to a dry friction). Hence, the attenuation at the resonance frequency permitted by the BSDS is given by⁸:

$$A_{BSDS} = \frac{1}{1 + \frac{1}{C} \frac{\alpha^2 T_0}{C_0 \pi n}} = \frac{1}{1 + \frac{2}{n} k^2 Q_M}. \quad (37)$$

From this expression it can be shown that the BSDS technique efficiency is inversely proportional to the switching coefficient n (Figure 14). Hence a trade-off appears between a correct reconstruction of the speed (high values of n) and the performance (moderate values of n).

4.3 Performance enhancement using voltage sources

As shown in the previous subsection, the performance of the BSDS technique are tightly related to the inverse switching coefficient $1/n$. As this coefficient should be large enough to ensure a proper speed reconstruction, this would lead to a moderate attenuation effect.

As the voltage is already in phase with the speed, the conversion enhancement allowing an artificial increase of the squared coupling coefficient k^2 (leading to higher damping abilities as shown in Figure 14) has to be performed by increasing the piezovoltage. Such operation may be obtained by adding voltage sources in the switching device (making the technique no longer semi-passive however) as depicted in Figure 15, leading to the concept of *Blind Switch Damping on Voltage sources* (BSDV).

The differentiation operation is still performed using short-circuit switching (through branch 1 in Figure 15(a)), but the next switching process in this case aims at magnifying the piezovoltage in order to have a higher damping ability (through branch 2 in Figure 15(a)). Hence, while the switching frequency is still given by $n f_0$ (S_1), the system intermittently switches on short-circuit and voltage source. The addition of the inductance L allows a better energy transfer from the voltage source to the piezoelectric element. In addition, the voltage source V_S is matched to the sign of the piezovoltage:

$$V_S = |V_S| \text{sign}(V). \quad (38)$$

⁸ In this section it will be considered that the uncontrolled case correspond to a short-circuited piezoelectric element. Such an assumption allows much simpler expressions while having a negligible impact on the performance evaluation.

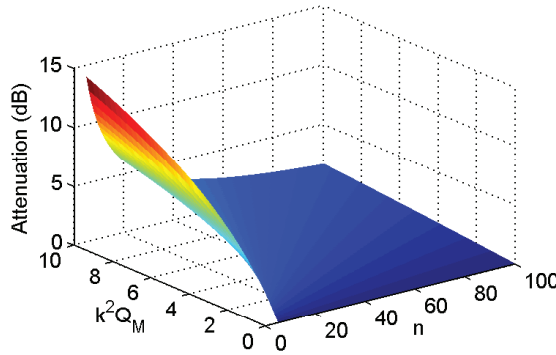


Fig. 14. Performance of the BSDS technique as a function of the product of the squared coupling coefficient by the mechanical quality factor $k^2 Q_M$ and switching coefficient n

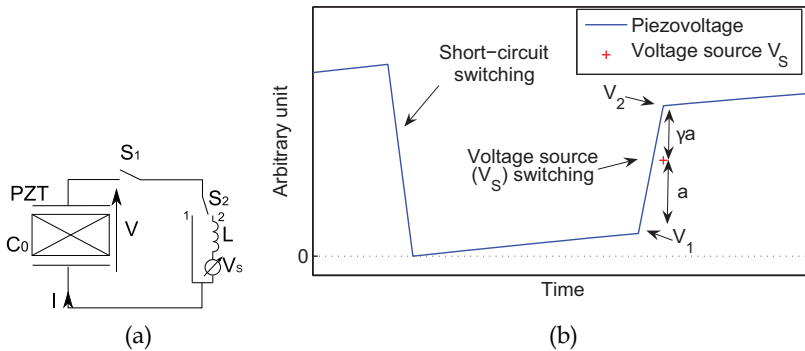


Fig. 15. (a) BSDV implementation and (b) typical waveforms

The value of the voltage V_1 before the voltage increase process is given by the differentiation performed by the short-circuit switching:

$$V_1 = \frac{\alpha}{C_0} \left[u \left((2k+1) \frac{T_0}{n} \right) - u \left(2k \frac{T_0}{n} \right) \right] \text{ with } k \in \mathbb{N}, \tag{39}$$

while the voltage after the voltage switching yields:

$$V_2 = \gamma(V_S - V_1) + V_S. \tag{40}$$

Hence, assuming that the structure filters high harmonics, the piezoelectric voltage may be approximated by:

$$\begin{aligned} V(t) &\approx \frac{\alpha}{C_0} \frac{T_0}{n} \dot{u}(t) && \text{for } 2k \frac{T_0}{n} \leq t < (2k+1) \frac{T_0}{n} && (k \in \mathbb{N}) \\ &&& \text{(short-circuit switching)} \\ V(t) &\approx \gamma \left(V_S - \frac{\alpha}{C_0} \frac{T_0}{n} \dot{u}(t) \right) + V_S && \text{for } (2k+1) \frac{T_0}{n} \leq t < 2(k+1) \frac{T_0}{n} && (k \in \mathbb{N}) \\ &&& \text{(voltage switching)} \end{aligned} \tag{41}$$

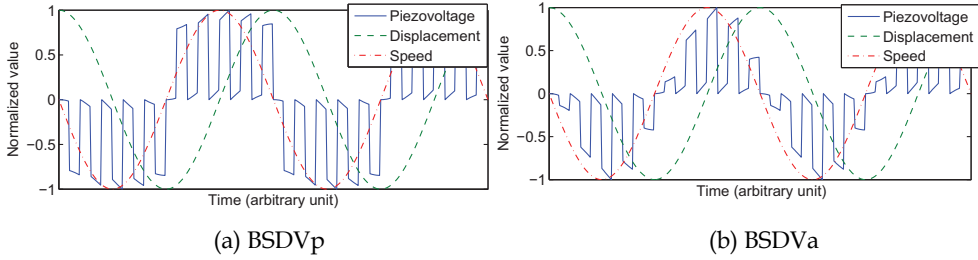


Fig. 16. BSDV typical waveforms

The value of the voltage source V_S can then be defined in several ways. In the followings, two cases will be considered:

- The voltage source V_S is proportional to the **displacement magnitude** u_M , leading to the technique called *Blind Switch Damping on piecewise constant Voltage source* (BSDVp), as the voltage source value is changed on maximum displacement only.
- The voltage source V_S is proportional to the **voltage value** V_1 just before the voltage source switching process V_1 , leading to the technique called *Blind Switch Damping on adaptive Voltage source* (BSDVa), as the voltage source continuously matches the piezovoltage (except during the inversion).

The associated waveforms to each of these approaches are depicted in Figure 16. It can be observed that the piezovoltage in the BSDVp case has an envelope that is proportional to the sign of the speed, while the envelope of the BSDVa technique is proportional to the speed, hence featuring less harmonics.

4.3.1 Blind Switch Damping on piecewise constant Voltage source (BSDVp)

In the case of the BSDVp control, the voltage source value is given as:

$$V_S = \beta \frac{\alpha}{C_0} \text{sign}(V(t)) \approx \beta \frac{\alpha}{C_0} \text{sign}(\dot{u}(t)), \quad (42)$$

leading to the expression of the voltage, assuming that $n \gg 1$ and $\beta \gg 1$:

$$\begin{cases} V(t) \approx 0 & \text{for } 2k \frac{T_0}{n} \leq t < (2k+1) \frac{T_0}{n} \quad (k \in \mathbb{N}) \\ & \text{(short-circuit switching)} \\ V(t) \approx (1+\gamma)V_S = (1+\gamma)\beta \frac{\alpha}{C_0} \text{sign}(\dot{u}(t)) & \text{for } (2k+1) \frac{T_0}{n} \leq t < 2(k+1) \frac{T_0}{n} \quad (k \in \mathbb{N}) \\ & \text{(voltage sources witching)} \end{cases} \quad (43)$$

Hence, if the structure filters higher harmonics, the motion equation turns to:

$$M\ddot{u} + \left(C + \frac{2}{\pi} \frac{\alpha^2}{C_0} \frac{1}{\omega} (1+\gamma)\beta \right) \dot{u} + K_E u = F, \quad (44)$$

with ω the angular frequency. The associated attenuation at the resonance frequency is therefore given by:

$$A_{BSDVp} = \frac{1}{1 + \frac{2}{\pi} \frac{1}{C\omega_0} \frac{\alpha^2}{C_0} (1+\gamma)\beta} = \frac{1}{1 + \frac{2}{\pi} (1+\gamma)\beta k^2 Q_M}. \quad (45)$$

This expression shows that indexing the value of the voltage on the displacement magnitude allows having an attenuation that is independent from the switching coefficient n . In addition, the BSDVp technique is close to the SSD technique, except that the crenel function is modulated by another crenel function of frequency nf_0 (Figure 16(a)). Because of this modulation (which cancels the voltage half the time), the magnitude of the first harmonic of the piezovoltage is divided by two compared to a SSD technique featuring the same voltage magnitude.

4.3.2 Blind Switch Damping on piecewise adaptive Voltage source (BSDVa)

When indexing the voltage source value V_S to the voltage V_1 just before the switching process such as:

$$V_S = \beta V_1 = \beta V \left((2k+1) \frac{T_0}{n} \right), \quad k \in \mathbb{N}, \quad (46)$$

the expression of the piezovoltage may be approximated by (assuming $n \gg 1$ and $\beta \gg 1$):

$$\left\{ \begin{array}{ll} V(t) \approx 0 & \text{for } 2k \frac{T_0}{n} \leq t < (2k+1) \frac{T_0}{n} \quad (k \in \mathbb{N}) \\ & \text{(short-circuit switching)} \\ V(t) \approx (1+\gamma)V_S = (1+\gamma)\beta \frac{\alpha}{C_0} \frac{T_0}{n} \dot{u}(t) & \text{for } (2k+1) \frac{T_0}{n} \leq t < 2(k+1) \frac{T_0}{n} \quad (k \in \mathbb{N}) \\ & \text{(voltage source switching)} \end{array} \right. \quad (47)$$

The first harmonic approximation of this voltage is then given by:

$$V \approx (1+\gamma)\beta \frac{\alpha}{C_0} \frac{T_0}{\pi n} \dot{u}(t), \quad (48)$$

yielding the transfer function of the displacement in the frequency domain and expression of the attenuation at the resonance frequency:

$$\frac{U(\omega)}{F(\omega)} = \frac{1}{-M\omega^2 + j \left(C + (1+\gamma)\beta \frac{\alpha^2}{C_0} \frac{T_0}{\pi n} \right) \omega + K_E}, \quad (49)$$

$$A_{BSDVa} = \frac{1}{1 + (1+\gamma)\beta \frac{1}{C} \frac{\alpha^2}{C_0}} = \frac{1}{1 + \frac{2}{n} (1+\gamma)\beta k^2 Q_M}. \quad (50)$$

This expression shows that the attenuation in this case is similar to the one obtained using the BSDS technique (Eq. 37), but with a value of the squared coupling coefficient artificially increase by a factor $(1+\gamma)\beta$, leading to higher damping abilities as shown in Figure 14. In addition, the voltage waveforms of the BSDVa may be seen as a modulation of a voltage

proportional to the speed (as for a simple derivative control) by a crenel function at a frequency $n f_0$.

4.4 Discussion

One of the main advantage of the BSD techniques over the SSD method is not only the non-synchronized approach (which allows a wider practical frequency range of operation), but also the possibility of controlling the reinjected harmonics through the switching coefficient n . In particular, as the switching frequency is far greater than the vibration frequency, the reinjected harmonics of the BSD techniques are far away from the first mode frequencies (contrary to the SSD case where odd harmonics appear). This is however not the case for the BSDVp as it features an envelope that is a piecewise constant voltage in phase with the speed as in the SSD case.

However, it should be noted that BSD techniques have to be semi-active in order to dispose of significant damping abilities. Nevertheless, the BSDV techniques can be made extremely low-power, by using the energy harvesting scheme described by Lefeuvre et al. (2005) during the short-circuit switching, hence allowing the recovery of most of the supplied energy during the voltage source switching process.

Among the exposed BSD methods, the BSDVa technique seems to be the most interesting one, allowing a significant damping behavior (contrary to the BSDS method that is limited), while preserving a good trade-off between performance and required energy. It can also be noted that the BSDVp technique may present instabilities for high values of n (Lallart et al., 2009).

Finally, the concept of the BSD techniques based on a low-cost differentiation of the displacement by intermittently switching the piezoelement is also well adapted to broadband control⁹, as the switching process allows the low-cost reconstruction of the speed as long as the switching frequency is much higher than the highest vibration frequency. The BSD principles may also be seen as a spreading of the converted mechanical energy on a wide frequency range (spillover) because of the switching process. Hence, as the structure filters this frequency contents, a damping effect is achieved.

5. Synchronized Switch Stiffness Control (SSSC)

The principles of the previously exposed techniques aimed at reducing the vibrations by increasing, in a mechanical point of view, the losses in the mechanical structure. However, another strategy for reducing the vibration magnitude consists in ensuring that the structure is excited out of its resonance, hence preventing the energy from entering into the structure.

5.1 Principles

The purpose of the concept exposed here is to modify the stiffness through a simple and low-cost nonlinear treatment similar to the SSD techniques. The main difference is that the switching process occurs on zero displacement (Guyomar, Lallart & Monnier, 2008), as shown in Figure 17¹⁰.

⁹ In the case of the BSDVp technique, the definition of displacement amplitude is however delicate in the case of random vibrations.

¹⁰ As the voltage is switched on zero displacement values, the use of an external voltage source is mandatory to perform a voltage inversion; hence, the SSSC technique is semi-active.

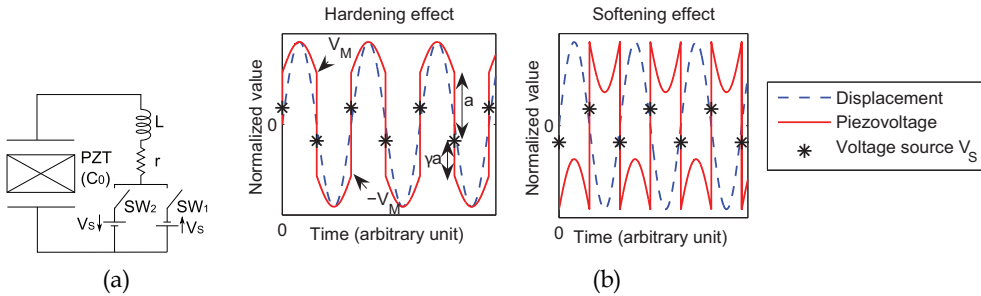


Fig. 17. (a) SSSC schematics and (b) typical waveforms

Due to the voltage switch on zero displacements, the voltage may be decomposed into one voltage proportional to the displacement, and a piecewise constant voltage in phase with the displacement which modifies the stiffness of the system. As this latter may be tuned through the voltage source V_s , its effect (and thus the equivalent stiffness of the system) may be controlled.

5.2 Performance under monochromatic excitation

In the case of a monochromatic excitation, the piezoelectric voltage in the case of the SSSC technique may be decomposed as:

$$V = \frac{\alpha}{C_0}u + V_M \text{sign}(u), \tag{51}$$

where V_M refers to the amplitude of the crenel function (Figure 17(b)), given by:

$$V_M - V_s = \gamma(V_M + V_s) \Rightarrow V_M = \frac{1 + \gamma}{1 - \gamma} V_s. \tag{52}$$

The absolute value of V_s being matched on the displacement magnitude such as:

$$|V_s| = |\beta| \frac{\alpha}{C_0} u_M. \tag{53}$$

The user-defined coefficient β may be positive or negative, according to the type of desired effect (hardening or softening effect - Figure 17(b)). Hence, using the first harmonic approximation (*i.e.*, the structure filters the higher harmonics), the piezovoltage equals to:

$$V \approx \frac{\alpha}{C_0} \left(1 + \beta \frac{4}{\pi} \frac{1 + \gamma}{1 - \gamma} \right) u. \tag{54}$$

Merging this expression in the motion equation yields the equivalent stiffness of the system:

$$K_{SSSC} = \left(K_D + \frac{4}{\pi} \frac{\alpha^2}{C_0} \frac{1 + \gamma}{1 - \gamma} \beta \right) = K_D \left(1 + \frac{4}{\pi} \frac{1 + \gamma}{1 - \gamma} \beta k^2 \right) \tag{55}$$

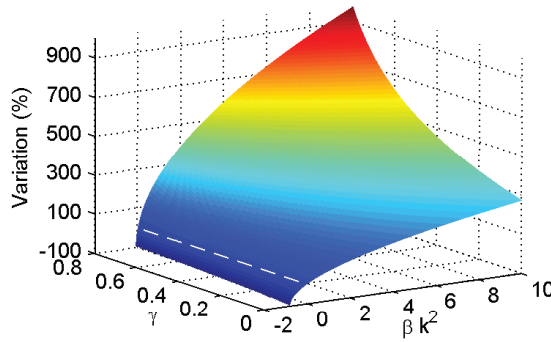


Fig. 18. Resonance frequency shift using the SSSC approach (dashed line represents null stiffness change)

It can be seen that, contrary to the previous techniques, the mechanical quality factor Q_M does not intervene in the expression of the equivalent stiffness. It is also possible to express the change operated by the SSSC technique in terms of resonance frequency and mechanical quality factor:

$$\begin{cases} (\omega_{res})_{SSSC} = \omega_{res} \sqrt{1 + \frac{4}{\pi} \frac{1+\gamma}{1-\gamma} \beta k^2} \\ (Q_M)_{SSSC} = Q_M \sqrt{1 + \frac{4}{\pi} \frac{1+\gamma}{1-\gamma} \beta k^2} \end{cases} \quad (56)$$

The performance of the system in terms of resonance frequency change is depicted in Figure 18, showing that the SSSC method allows both decreasing or increasing the resonance frequency, with a pseudo-quadratic behavior as a function of γ , while the change becomes less significant as βk^2 increases.

5.3 Energy requirements

Several techniques can be used for tuning the stiffness of a system (Wickramasinghe et al., 2004; Nitzsche et al., 2005), the most common being a proportional control. However, in the framework of embedded devices, such a control should consume a very few amount of energy. Hence, the purpose of this section is to compare the energy requirements of the SSSC method with respect to a classical proportional control.

In the latter case, the control voltage is set to be proportional to the displacement such as:

$$V_{proportional} = K_C u, \quad (57)$$

with K_C the tuning coefficient. Hence, the equivalent stiffness yields:

$$K_{proportional} = K + \alpha K_C. \quad (58)$$

When using proportional control, the main source of losses is the heat dissipated in the parallel parasitic resistance r_p of the piezoelectric element. Therefore, the dissipated power yields:

$$P_{proportional} = f_0 \int_0^{f_0} \frac{V_{proportional}^2}{r_p} dt = \frac{K_C}{2r_p} u_M^2. \quad (59)$$

In the case of the SSSC control, the losses in the parasitic resistance may be neglected facing the losses in the switching circuit (the piezoelectric element is in open-circuit most of the time). Hence, the required power for the SSSC control is given by:

$$P_{SSSC} = 2f_0 \int_{-V_M}^{V_M} C_0 V_S dV = 4f_0 \frac{1+\gamma}{1-\gamma} \frac{\alpha^2}{C_0} \beta^2 u_M^2. \quad (60)$$

Figure 19 depicts the power required for both techniques as a function of the stiffness variation. The power has been normalized with respect to the power required to have a 100% stiffness variation using the proportional control. This figure clearly demonstrates the ability of the SSSC approach for efficiently controlling the stiffness of the system without requiring high power; compared to the proportional control, the power requirement is typically 10 times less.

5.4 Application to vibration damping

The purpose of this section is the application of the SSSC technique for limiting the vibrations of the structure. Unlike the previously exposed methods whose principles are to artificially increase the mechanical losses, the concept proposed here consists in shifting the resonance frequency far away from the frequency spectrum of the input force.

The principles of such a control rely on frequency sensing (*e.g.*, based on zero crossing detection - Figure 20). Then, from the frequency information, the value of the tuning coefficient β is chosen such that the resonance frequency of the structure is out of resonance (for example, the absolute value of β may be fixed and its sign obtained from the frequency, as depicted in Figure 20(b)).

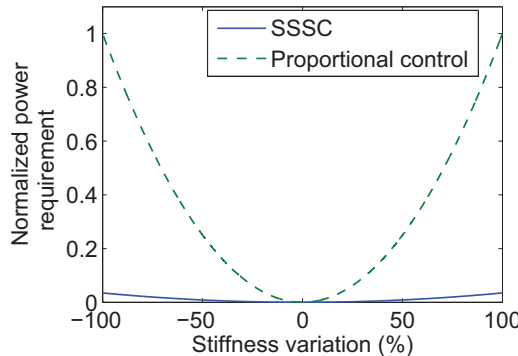


Fig. 19. Normalized power requirements for the SSSC technique ($\gamma = 0.8$) and comparison with proportional control ($1/(2\pi r_p C_0 f_0) = 0.05$) at 1 kHz) for a vibration frequency of $f_0 = 20$ Hz

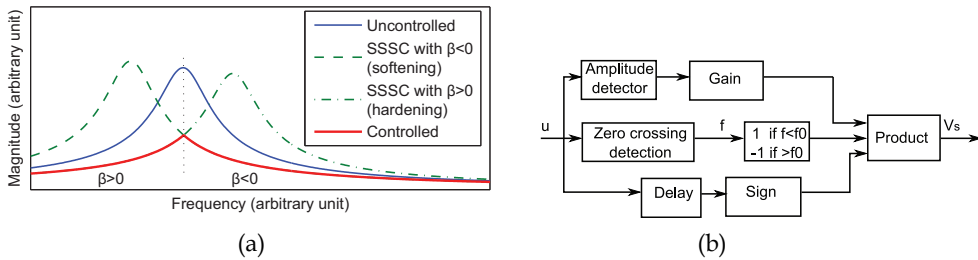


Fig. 20. SSSC technique applied to vibration damping: (a) principles; (b) implementation example

6. Conclusion

This chapter exposed energy-efficient methods for vibration control using piezoelectric elements. Based on a nonlinear approach that consists in quickly changing the voltage of piezoelectric elements, it has been shown that such a concept allows an efficient control of the vibrations while requiring a very few amount of power, therefore making the method suitable for embedded systems.

In a first step, the principles of the switching technique have been exposed, showing the conversion increase, thanks to a voltage magnification by a cumulative process as well as a reduction of the phase between the voltage and velocity.

Then this concept has been directly applied to the reduction of the vibrations, leading to the so-called *Synchronized Switch Damping* (SSD) methods. Four techniques have been exposed, whether the voltage switching is done on a short-circuit (SSDS), an inductor (SSDI), an inductor in series with constant voltage sources (SSDV), or an inductor in series with adaptive voltage sources (SSDVa); the two formers being possibly self-powered as no external energy is required for the control. The analysis of the performance under a monochromatic excitation showed that the attenuation at the resonance frequency obtained using such method is tightly related to the mechanical quality factor and squared coupling coefficient, with a typical reduction of the vibrations around 20 dB for the SSDI and 40 dB for the SSDV and SSDVa. The application of the SSD method to broadband excitations has also been discussed, showing the trade-off between voltage increase and number of switching events, that can be controlled by selecting proper switching time instants (extremum selection). Finally, the realistic implementation of the technique to integrated systems has been demonstrated, as well as the application of the concept to electromagnetic actuators.

The second part of this chapter consisted in exposing another technique for vibration damping by a non-synchronized approach called *Blind Switch Damping* (BSD). Based on a low-cost differentiation obtained by switching the piezoelectric element on a short-circuit at a frequency far greater than the vibration frequency, the technique allows reconstructing the speed with the voltage, leading to viscous damping effect. However, the performance of such a method remains modest (a few dB), and increasing the voltage is mandatory to get significant damping abilities. This voltage magnification can be obtained using voltage sources that can either be proportional to the displacement magnitude or to the value of the voltage just before the switching process. The low-cost differentiation is still obtained by connecting the piezoelectric insert on a short-circuit, but the next switching process consists in increasing the voltage, allowing damping abilities close to the SSD approach. The two

main advantages of the BSD methods are the possibility of controlling the reinjected harmonics as well as the independency from the host structure. Another interesting aspects of the BSDV methods is the possibility of working in a energy injection/energy recovery basis that dramatically limits the required power.

Finally, a third technique has been introduced. Contrary to the SSD and BSD approaches that consist in artificially increasing the mechanical losses in the structure, the proposed concept, named *Synchronized Switch Stiffness Control* (SSSC), allows tuning the stiffness in a low-cost way (typically 10 times less energy is required for the same effect compared to a proportional control). The principle of this method is to connect the piezoelectric element on a resonant electrical network featuring a voltage source each time the displacement is null. Hence, such an approach shapes a piecewise constant voltage in phase with the displacement, hence modifying the stiffness. An application to vibration reduction by ensuring that the structure is excited out of its resonance through stiffness tuning has also be exposed.

The performance comparison of all the exposed techniques is presented in Table 3. From this table, it can be seen that the SSDI featuring threshold detection is particularly interesting when no external energy is supplied to the system as it allows a self-powered broadband control with significant damping abilities, while the BSDVa approach, thanks to its harmonic reinjection control, broadband approach, effectiveness and low-power consumption, is a good option when a few amount of energy can be provided to the system. It can however be noted that the combination of several methods is possible, for example using the SSD control together with a stiffness tuning, hence allowing an increase of the global performance. Finally, the combination of active control methods with the exposed approaches for limiting the power requirements while achieving important damping if necessary (Harari, Richard & Gaudiller, 2009) may also be envisaged.














































Technique (Kind)	Efficiency	Adaptiveness	Robustness	Power requirements ¹¹	Implementation easiness
SSDS (<i>semi-passive</i>)					
SSDI (<i>semi-passive</i>)					
SSDI with threshold detection (<i>semi-passive</i>)					
SSDV (<i>semi-active</i>)					
SSDVa (<i>semi-active</i>)					
BSDS (<i>semi-passive</i>)					
BSDVp (<i>semi-active</i>)					
BSDVa (<i>semi-active</i>)					
SSSC (<i>semi-active</i>)					

Table 3. Comparison of the exposed techniques

¹¹  means that the method can be self-powered.

7. References

- Badel, A.; Sebald, G.; Guyomar, D.; Lallart, M.; Lefevre, E.; Richard, C. & Qiu, J. (2006). Piezoelectric vibration control by synchronized switching on adaptive voltage sources: Towards wideband semi-active damping. *J. Acoust. Soc. Am.*, Vol. 119, No. 5, 2815-2825.
- Badel, A.; Lagache, M.; Guyomar, D.; Lefevre, E. & Richard, C. (2007). Finite Element and Simple Lumped Modeling for Flexural Nonlinear Semi-passive Damping. *J. Intell. Mater. Syst. Struct.*, Vol. 18, 727-742.
- Clark, W. W. (2000). Vibration control with state-switching piezoelectric material, *J. Intell. Mater. Syst. Struct.*, Vol. 11, 263-271.
- Cunefare, K. A. (2002). State-switched absorber for vibration control of point-excited beams, *J. Intell. Mater. Syst. Struct.*, Vol. 13, 97-105.
- Davis, C. L. & Lesieutre, G. A. (2000). An actively Tuned Solid-State Vibration Absorber Using Capacitive Shunting of Piezoelectric Stiffness, *J. of Sound and Vibration*, Vol. 232, No. 3, 601-617.
- Fleming, A. J. & Moheimani, S. O. R. (2003). Adaptive Piezoelectric Shunt Damping, *Smart Mater. Struct.*, Vol. 12, 36-48.
- Gerhold, C.H. (1989). Active Control of Flexural Vibrations in Beams, *Journal of Aerospace Engineering*, Vol. 2, No. 3, 141-154.
- Guyomar, D.; Badel, A.; Lefevre, E. & Richard, C. (2005). Towards energy harvesting using active materials and conversion improvement by nonlinear processing, *IEEE Trans. Ultrason., Ferroelect., Freq. Contr.*, Vol. 52, 584-595.
- Guyomar, D.; Faiz, A.; Petit, L. & Richard, C. (2006a). Wave reflection and transmission reduction using a piezoelectric semipassive nonlinear technique. *J. Acoust. Soc. Am.*, Vol. 119, No. 1, 285-298.
- Guyomar, D. & Badel, A. (2006b). Nonlinear semi-passive multimodal vibration damping: An efficient probabilistic approach. *J. Sound Vib.*, Vol. 294, 249-268.
- Guyomar, D.; Jayet, Y.; Petit, L.; Lefevre, E.; Monnier, T.; Richard, C. & Lallart, M. (2007a) Synchronized Switch Harvesting applied to Self-Powered Smart Systems : Piezoactive Microgenerators for Autonomous Wireless Transmitters, *Sens. Act. A: Phys.*, Vol. 138, No. 1, 151-160. doi : 10.1016/j.sna.2007.04.009
- Guyomar, D. & Lallart, M. (2007b). Piezo-transducer Modelling with a Switched Output Voltage: Application to Energy Harvesting and Self-Powered Vibration Control. *Proceedings of the 19th International Congress on Acoustics (ICA)*, 2-7 September 2007, Madrid, Spain.
- Guyomar, D.; Richard, C. & Mohammadi, S. (2007c). Semi-passive random vibration control based on statistics. *J. Sound Vib.*, Vol. 307, 818-833.
- Guyomar, D.; Lallart, M. & Monnier, T. (2008). Stiffness Tuning Using a Low-Cost Semi-Active NonLinear Technique, *IEEE/ASME Transactions on Mechatronics*, Vol. 13, No. 5, 604- 607.
- Harari, S.; Richard, C. & Gaudiller, L. (2009). New Semi-active Multi-modal Vibration Control Using Piezoceramic Components. *J. Intell. Mater. Syst. Struct.*, Vol. 20, No. 13, 1603- 1613.
- Holdhusen , M. H. & Cunefare, K. A. (2003). Damping Effects on the State-Switched Absorber Used for Vibration Suppression, *J. Intell. Mater. Syst. Struct.*, Vol. 14, No. 9, 551-561. doi:10.1177/104538903036919

- Inman, D. J.; Ahmadian, M. & Claus, R. O. (2001). Simultaneous Active Damping and Health Monitoring of Aircraft Panels, *J. Intell. Mater. Syst. Struct.*, Vol. 12, No. 11, 775-783. doi:10.1177/104538901400438064
- Ji, H.; Qiu, J.; Zhu, K.; Y. Chen & Badel, A. (2009). Multi-modal vibration control using a synchronized switch based on a displacement switching threshold, *Smart Mater. Struct.*, Vol. 18, 035016.
- Johnson, C. D. (1995). Design of Passive Damping Systems, *J. of Mechanical Design*, Vol. 117, No. B, 171-176.
- Lallart, M.; Guyomar, D.; Petit, L.; Richard, C.; Lefeuvre, E. & Guiffard, B. (2007). Effect Of Low Mechanical Quality Factor On Non-Linear Damping And Energy Harvesting Techniques, *Proceedings of the 18th International Conference on Adaptive Structures and Technologies (ICAST)*, 3-5 October 2007, Ottawa, Ontario, Canada.
- Lallart, M.; Guyomar, D.; Jayet, Y.; Petit, L.; Lefeuvre, E.; Monnier, T.; Guy, P. & Richard, C. (2008a). Synchronized Switch Harvesting applied to Selfpowered Smart Systems: Piezoactive Microgenerators for Autonomous Wireless Receiver, *Sens. Act. A: Phys.*, Vol. 147, No. 1, 263-272. doi: 10.1016/j.sna.2008.04.006.
- Lallart, M. & Guyomar, D. (2008b). Optimized Self-Powered Switching Circuit for Non-Linear Energy Harvesting with Low Voltage Output, *Smart Mater. Struct.*, Vol. 17, 035030. doi: 10.1088/0964-1726/17/3/035030
- Lallart, M.; Garbuio, L.; Petit, L.; Richard, C. & Guyomar, D. (2008c) Double Synchronized Switch Harvesting (DSSH) : A New Energy Harvesting Scheme for Efficient Energy Extraction, *IEEE Trans. Ultrason., Ferroelect., Freq. Contr.*, Vol. 55, No. 10, 2119-2130.
- Lallart, M.; Badel, A. & Guyomar, D. (2008d). Non-Linear Semi-Active Damping Using Constant Or Adaptive Voltage Sources: A Stability Analysis. *J. Intell. Mat. Syst. Struct.*, Vol. 19, No. 10, 1131-1142. doi : 10.1177/1045389X07083612
- Lallart, M.; Lefeuvre, E.; Richard, C. & Guyomar, D. (2008e). Self-Powered Circuit for Broadband, Multimodal Piezoelectric Vibration Control. *Sens. Act. A: Phys.*, Vol. 143, No. 2, 277-382, 2008. doi : 10.1016/j.sna.2007.11.017
- Lallart, M.; Magnet, C.; Richard, C.; Lefeuvre, E.; Petit, L.; Guyomar, D. & Bouillault, F. (2008f). New Synchronized Switch Damping Methods Using Dual Transformations. *Sens. Act. A: Phys.*, Vol. 143, No. 2, 302-314. doi : 10.1016/j.sna.2007.12.001
- Lallart, M.; Harari, S.; Petit, L.; Guyomar, D; Richard, T.; Richard, C. & Gaudiller, L. (2009). Blind Switch Damping (BSD): A Self-Adaptive Semi-Active Damping Technique. *J. Sound Vib.*, Vol. 329, Nos. 1-2, 29-41.
- Lefeuvre, E.; Badel, A.; Richard, C. & Guyomar, D. (2005). Piezoelectric energy harvesting device optimization by synchronous electric charge extraction. *J. Intell. Mat. Syst. Struct.*, Vol. 16, No. 10, 865-876.
- Lefeuvre, E.; Badel, A.; Richard, C.; Petit, L. & Guyomar, D. (2006a). A comparison between several vibration-powered piezoelectric generators for standalone systems, *Sens. Act. A: Phys.*, Vol. 126, 405-416.
- Lefeuvre, E.; Badel, A.; Petit, L.; Richard, C. & Guyomar D. (2006b). Semi-passive Piezoelectric Structural Damping by Synchronized Switching on Voltage Sources. *J. Intell. Mater. Syst. Struct.*, Vol. 17, Nos. 8-9, 653-660.
- Lesieutre, G. A. (1998). Vibration Damping and Control using Shunted Piezoelectric Materials, *Shock and Vib. Digest*, Vol. 30, pp. 187-195.

- Nitzsche, F.; Harold, T.; Wickramasinghe, V. K.; Young, C. & Zimcik, D. G. (2005). Development of a Maximum Energy Extraction Control for the Smart Spring, *J. Intell. Mater. Syst. Struct.*, Vol. 16, Nos. 11-12, 1057-1066.
- Makihara, K.; Onoda, J. & Minesugi, K. (2007). A self-sensing method for switching vibration suppression with a piezoelectric actuator, *Smart Mater. Struct.*, Vol. 16, 455-461.
- Petit, L.; Lefeuvre, E.; Richard, C. & Guyomar, D. (2004). A broadband semi passive piezoelectric technique for structural damping, *Proceedings of SPIE conference on Smart Struct. Mater. 1999: Passive Damping and Isolation*, San Diego, CA, USA, March 2004, Vol. 5386, 414-425. ISBN : 0-8194-5303-X
- Qiu, J. H. & Haraguchi M. (2006). Vibration control of a plate using a self-sensing actuator and an adaptive control approach, *J. Intell. Mater. Syst. Struct.*, Vol. 17, 661-669.
- Richard, C.; Guyomar, D.; Audigier, D. & Ching, G. (1999). Semi passive damping using continuous switching of a piezoelectric device, *Proceedings of SPIE conference on Smart Struct. Mater. 1999: Passive Damping and Isolation*, Newport Beach, CA, USA, March 1999, Vol. 3672, 104-111. ISBN : 0-8194-3146-X
- Richard, C.; Guyomar, D.; Audigier, D. & Bassaler, H. (2000). Enhanced semi passive damping using continuous switching of a piezoelectric device on an inductor, *Proceedings of SPIE conference on Smart Struct. Mater. 2000: Passive Damping and Isolation*, Newport Beach, CA, USA, March 2000, Vol. 3989, 288-299. ISBN : 0-8194-3607-0
- Richard C.; Guyomar, D. & Lefeuvre, E. (2007). Self-Powered Electronic Breaker With Automatic Switching By Detecting Maxima Or Minima Of Potential Difference Between Its Power Electrodes, *patent # PCT/FR2005/003000*, publication number: WO/2007/063194, 2007.
- Veley, D. E. & Rao, S. S. (1996). A Comparison of Active, Passive and Hybrid Damping in Structural Design, *Smart Mater. Struct.*, Vol. 5, 660 - 671.
- Wickramasinghe, V. K.; Young, C.; Zimcik, D. G.; Harold, T. & Nitzsche, F. (2004). Smart Spring, a Novel Adaptive Impedance Control Approach for Active Vibration Suppression Applications, *Proceedings of SPIE Smart Materials and Structures: Smart Structures and Integrated Systems*, San Diego, CA, USA, March 2004, Vol. 5390.
- Wu, S. Y. (1998). Method for multiple shunt damping of structural vibration using a single PZT transducer, *Proceedings of SPIE conference on Smart Struct. Mater. 1998: Passive Damping and Isolation*, San Diego, CA, USA, March 1998, Vol. 3327, 159-168.

Active Vibration Control of Rotor-Bearing Systems

Andrés Blanco¹, Gerardo Silva², Francisco Beltrán³ and Gerardo Vela¹

¹*Centro Nacional de Investigación y Desarrollo Tecnológico*

²*Centro de Investigación y de Estudios Avanzados del IPN*

³*Universidad Politécnica de la Zona Metropolitana de Guadalajara
México*

1. Introduction

Rotating machinery is commonly used in many mechanical systems, including electrical motors, machine tools, compressors, turbo machinery and aircraft gas turbine engines. Typically these systems are affected by exogenous or endogenous vibrations produced by unbalance, misalignment, resonances, material imperfections and cracks.

Vibration caused by mass unbalance is a common problem in rotating machinery. Rotor unbalance occurs when the principal inertia axis of the rotor does not coincide with its geometrical axis and leads to synchronous vibrations and significant undesirable forces transmitted to the mechanical elements and supports. Many methods have been proposed to reduce the unbalance-induced vibration, where different devices such as electromagnetic bearings, active squeeze film dampers, lateral force actuators, active balancers and pressurized bearings have been developed (Blanco et al., 2008) (Guozhi et al., 2000) (Jinhao & Kwon, 2003) (Palazzolo et al., 1993) (Sheu et al., 1997) (Zhou & Shi, 2001). Passive and active balancing techniques are based on the unbalance estimation to attenuate the unbalance response in the rotating machinery. The Influence Coefficient Method has been used to estimate the unbalance while the rotating speed of the rotor is constant (Lee et al., 2005) (Yu, 2004). This method has been used to estimate the unknown dynamics and rotor-bearing system unbalance during the speed-varying period (Zhou et al., 2004). On the other hand, there is a vast literature on identification methods (Ljung, 1987) (Sagara & Zhao, 1989) (Sagara & Zhao, 1990), which are essentially asymptotic, recursive or complex, which generally suffer of poor speed performance.

This chapter presents an active vibration control scheme to reduce unbalance-induced synchronous vibration in rotor-bearing systems supported on two ball bearings, one of which can be automatically moved along the shaft to control the effective rotor length and, as an immediate consequence, the rotor stiffness. This dynamic stiffness control scheme, based on frequency analysis, speed control and acceleration scheduling, is used to avoid resonant vibration of a rotor system when it passes (run-up or coast down) through its first critical speed. Algebraic identification is used for on-line unbalance estimation at the same time that the rotor is taken to the desired operating speed. The proposed results are strongly based on the algebraic approach to parameter identification in linear systems reported (Fliess & Sira, 2003), which requires a priori knowledge of the mathematical model of the

system. This approach has been employed for parameter and signal estimation in nonlinear and linear vibrating mechanical systems, where numerical simulations and experimental results show that the algebraic identification provides high robustness against parameter uncertainty, frequency variations, small measurement errors and noise (Beltrán et al., 2005) (Beltrán et al., 2006). In addition, algebraic identification is combined with integral reconstruction of time derivatives of the output (GPI Control) using a simplified mathematical model of the system, where some nonlinear effects (stiffness and friction) were neglected; in spite of that, the experimental results show that the estimated values represent good approximations of the real parameters and high performance of the proposed active vibration control scheme, which means that the algebraic identification and GPI control methodologies could be used for some industrial applications, when at least a simplified mathematical model of the system is available (Beltrán et al., 2005).

Some numerical simulations and experiments are included to show the unbalance compensation properties and robustness when the rotor is started and operated over the first critical speed.

2. System description

2.1 Mathematical model

The Jeffcott rotor system consists of a planar and rigid disk of mass m mounted on a flexible shaft of negligible mass and stiffness k at the mid-span between two symmetric bearing supports (see figure 1(a) when $a = b$). Due to rotor unbalance the mass center is not located at the geometric center of the disk S but at the point G (center of mass of the unbalanced disk); the distance u between these two points is known as disk eccentricity or static unbalance (Vance, 1988) (Dimarogonas, 1996). An end view of the whirling rotor is also shown in figure 1(b), with coordinates that describe its motion.

In our analysis the rotor-bearing system is modeled as the assembly of a rigid disk, flexible shaft and two ball bearings. This system differs from the classical Jeffcott rotor because the effective shaft length can be increased or decreased from its nominal value. In fact, this adjustment is obtained by enabling longitudinal motion of one of the bearing supports (right bearing in figure 1.a) to different controlled positions into a small interval by using some servomechanism, which provides the appropriate longitudinal force. With this simple approach one can modify the shaft stiffness; moreover, one can actually control the rotor natural frequency, during run-up or coast-down, to evade critical speeds or at least reduce rotor vibration amplitudes. Our methodology combines some ideas on variable rotor stiffness (Sandler, 1999) and rotor acceleration scheduling (Millsaps, 1998) but completing the analysis and control for the Jeffcott-like rotor system.

The rotor-bearing system is not symmetric when the position of the right bearing changes from its nominal value, i.e., $a = b = l/2$ for the Jeffcott rotor ($\Delta l = 0$).

For simplicity, the following assumptions are considered: flexible shaft with attached disk, gravity loads neglected (insignificant when compared with the actual dynamic loads), equivalent mass for the base-bearing m_b , linear viscous damping c_b between the bearing base and the linear sliding, force actuator to control the shaft stiffness F , angular speed $\omega = \frac{d\varphi}{dt} = \dot{\varphi}$ controlled by means of an electrical motor with servodrive and local

Proportional Integral (PI) controller to track the desired speed scheduling in presence of small dynamical disturbances. The mathematical model of the four degree-of-freedom Jeffcott-like rotor is obtained using Newton equations as follows

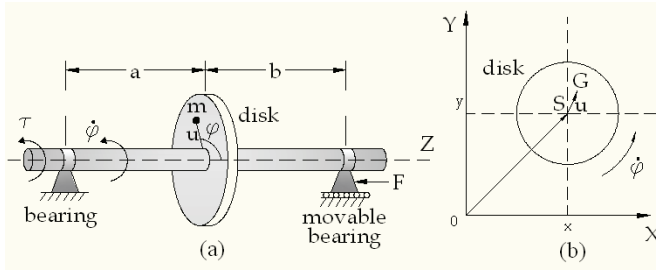


Fig. 1. Rotor-bearing system: (a) Schematic diagram of a rotor-bearing system with one movable (right) bearing and (b) end view of the whirling rotor

$$m\ddot{x} + c\dot{x} + kx = m(u\dot{\varphi} \sin \varphi + u\dot{\varphi}^2 \cos \varphi) \quad (1)$$

$$m\ddot{y} + c\dot{y} + ky = m(u\dot{\varphi}^2 \sin \varphi - u\dot{\varphi} \cos \varphi) \quad (2)$$

$$(J_z + mu^2)\ddot{\varphi} + c_\varphi\dot{\varphi} = \tau - p = m(\ddot{x}u \sin \varphi - \dot{y}u \cos \varphi) \quad (3)$$

$$m_b\ddot{b} + c_b\dot{b} = F \quad (4)$$

where k and c are the stiffness and viscous damping of the shaft, J_z is the polar moment of inertia of the disk and $\tau(t)$ is the applied torque (control input) for rotor speed regulation. In addition, x and y denote the orthogonal coordinates that describe the disk position and $\dot{\varphi} = \omega$ is the rotor angular velocity. The coordinate b denotes the position of the movable (right) bearing, which is controlled by means of the control force $F(t)$ (servomechanism). In our analysis the stiffness coefficient for the rotor-bearing system is given by (Rao, 2004)

$$k = \frac{3EI(l(a^2 - ab - b^2))}{a^3b^3} \quad (5)$$

where $l = a + b$ is the total length of the rotor between both bearings with b the coordinate to be controlled, $I = \frac{\pi D^4}{64}$ is the moment of inertia of a shaft of diameter D and E is the Young's modulus of elasticity ($E = 2.11 \times 10^{11} \text{ N/m}^2$ for AISI 4140 steel). The natural frequency of the rotor system is then obtained as follows (Rao, 2004)

$$\omega_n = \sqrt{k/m} \quad (6)$$

In such a way that, controlling b by means of the control force F one is able to manipulate ω_n to evade appropriately the critical speeds during rotor operation.

The proposed control objective is to reduce as much as possible the rotor vibration amplitude, denoted in adimensional units by

$$R = \sqrt{\frac{x^2 + y^2}{u}} \quad (7)$$

for run-up, coast-down or steady state operation of the rotor system, even in presence of small exogenous or endogenous disturbances. Note, however, that this control problem is

quite difficult because of the 8th order nonlinear model, many couplings terms, underactuation and uncontrollability properties from the two control inputs (τ, F).

3. Active vibration control

3.1 Speed control with trajectory planning

In order to control the speed of the Jeffcott-like rotor system, consider equation (3), under the temporary assumption that the eccentricity u is perfectly known and that $c \approx 0$ to simplify the analysis. Then, the following local PI controller is designed to track desired reference trajectories of speed $\omega^*(t)$ and acceleration scheduling $\dot{\omega}^*(t)$ for the rotor:

$$\begin{aligned} \tau &= J_z v_1 + c_\phi \omega + kux \sin \phi - kuy \cos \phi \\ v_1 &= \dot{\omega}^*(t) - \alpha(\omega - \omega^*(t)) - \alpha_0 \int_0^t (\omega - \omega^*(t)) dt \end{aligned} \tag{8}$$

The use of this controller yields the following closed-loop dynamics for the trajectory tracking error $e_1 = \omega - \dot{\omega}^*(t)$:

$$\ddot{e}_1 + \alpha_1 \dot{e}_1 + \alpha_0 e_1 = 0 \tag{9}$$

Therefore, selecting the design parameters $\{\alpha_1, \alpha_0\}$ so that the associated characteristic polynomial for equation (9)

$$p(s) = s^2 + \alpha_1 s + \alpha_0$$

is a *Hurwitz* polynomial, one guarantees that the error dynamics is asymptotically stable. The prescribed speed and acceleration scheduling for the planned speed trajectory is given by

$$\omega^*(t) = \begin{cases} \omega_i & 0 \leq t \leq t_i \\ \sigma(t, t_i, t_f) \omega_f & t_i \leq t < t_f \\ \omega_f & t > t_f \end{cases}$$

where ω_i and ω_f are the initial and final speeds at the times t_i and t_f , respectively, passing through the first critical frequency, and $\sigma(t, t_i, t_f)$ is a Bézier polynomials, with $\sigma(t, t_i, t_f) = 0$ and $\sigma(t, t_i, t_f) = 1$, described by

$$\sigma(t, t_i, t_f) = \left(\frac{t-t_i}{t_f-t_i} \right)^5 \left[\gamma_1 - \gamma_2 \left(\frac{t-t_i}{t_f-t_i} \right) + \gamma_3 \left(\frac{t-t_i}{t_f-t_i} \right)^2 - \dots + \gamma_6 \left(\frac{t-t_i}{t_f-t_i} \right)^5 \right] \tag{11}$$

with $\gamma_1 = 252, \gamma_2 = 1050, \gamma_3 = 1800, \gamma_4 = 1575, \gamma_5 = 700, \gamma_6 = 126$, in order to guarantee a sufficiently smooth transfer between the initial and final speeds.

The fundamental problem with the proposed feedback control in equation (8) is that the eccentricity u is not known, except for the fact that it is constant. The Algebraic identification methodology is proposed to on-line estimate the eccentricity u , which is based on the algebraic approach to parameter identification in linear systems (Fliess & Sira, 2003).

3.2 Algebraic identification of eccentricity

Consider equation (3) with perfect knowledge of the moment of inertia J_z and the shaft stiffness k , and that the position coordinates of the disk (x, y) and the control input τ are available for the identification process of the eccentricity u .

Multiplying equation (3) by t and integrating by parts the resulting expression once with respect to time t , one gets

$$\int_0^t (t\dot{\omega})dt = \frac{1}{J_z} \int_0^t t(\tau - c_\varphi\omega)dt + \frac{ku}{J_z} \int_0^t t(y \cos \varphi - x \sin \varphi)dt \quad (12)$$

Solving for the eccentricity u in equation (12) leads to the following on-line algebraic identifier for the eccentricity:

$$\hat{u} = \frac{J_z t \omega - \int_0^t (J_z \omega + t\tau - t c_\varphi \omega) dt}{k \int_0^t t(y \cos \varphi - x \sin \varphi) dt}, \forall t \in (0, \delta] \quad (13)$$

where δ is a positive and sufficiently small value.

Therefore, when the denominator of the identifier of equation (13) is different to 0, at least for a small time interval $(0, \delta]$ with $\delta > 0$, one can find from equation (13) a closed-form expression to on-line identify the eccentricity.

3.3 An adaptive-like controller with algebraic identification

The PI controller given by equation (8) can be combined with the on-line identification of the eccentricity in equation (13), resulting the following certainty equivalence PI control law

$$\begin{aligned} \tau &= J_z v_1 + c_\varphi \omega + kux \sin \varphi - k\hat{u}y \cos \varphi \\ v_1 &= \dot{\omega}^*(t) - \alpha_1(\omega - \omega^*(t)) - \alpha_0 \int_0^t (\omega - \omega^*(t))dt \end{aligned} \quad (14)$$

with

$$\hat{u} = \frac{J_z t \omega - \int_0^t (J_z \omega + t\tau - t c_\varphi \omega) dt}{k \int_0^t t(y \cos \varphi - x \sin \varphi) dt}, \forall t \in (0, \delta]$$

Note that, in accordance with the algebraic identification approach, providing fast identification for the eccentricity, the proposed controller (14) resembles an adaptive control scheme. From a theoretical point of view, the algebraic identification is instantaneous (Fliess & Sira, 2003). In practice, however, there are modeling errors and other factors that inhibit the algebraic computation. Fortunately, the identification algorithms and closed-loop system are robust against such difficulties (Beltrán et al., 2005).

3.4 Simulation results

Some numerical simulations were performed using the parameters listed in table 1.

Figure 2 shows the identification process of eccentricity and the dynamic behavior of the adaptive-like PI controller given by equation (14), which starts using the nominal value

$u = 0 \mu m$. One can see that the identification process is almost instantaneous. The control objective is to take from the rest position of the rotor to the operating speed $\omega_f = 300 \text{ rad/s}$.

$m_r = 0.9 \text{ kg}$	$D = 0.01 \text{ m}$	$a = 0.3 \text{ m}$
$m_b = 0.4 \text{ kg}$	$r_{disk} = 0.04 \text{ m}$	$c_\varphi = 1.5 \times 10^{-3} \text{ Nms/rad}$
$c_b = 10 \text{ Ns/m}$	$u = 100 \mu m$	$b = 0.3 \pm 0.05 \text{ m}$

Table 1. Rotor system parameters

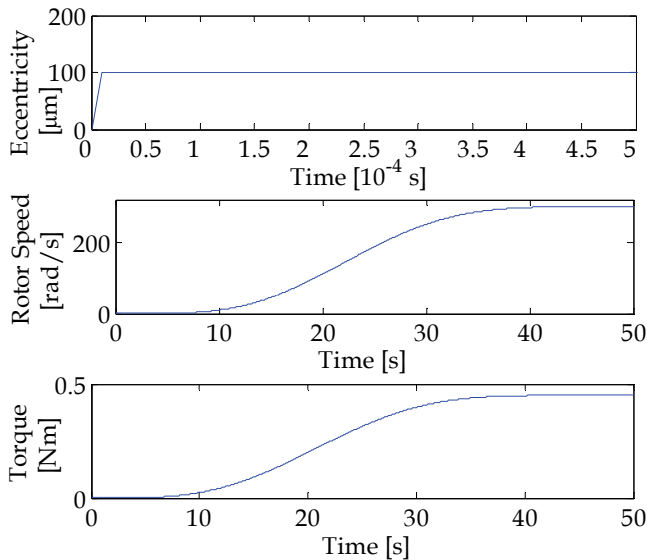


Fig. 2. Close loop system response using the PI controller: (a) identification of eccentricity, (b) rotor speed and (c) control input

The desired speed profile runs up the rotor in a very slow and smooth trajectory while passing through the first critical speed. This control scheme is appropriate to guarantee stability and tracking. The resulting rotor vibration amplitude (system response when $F = 0$) is shown in figure 3, for three different and constant positions of the right bearing (i.e., $b = 0.25 \text{ m}$, 0.30 m , 0.35 m), using the PI controller.

The purpose of these simulations is to illustrate how the position of the bearing truly affects the rotor vibration amplitudes for the desired speed profile. The nominal length of the shaft is $l = 0.60 \text{ m}$. A smaller length $l = 0.55 \text{ m}$ leads to a higher natural frequency and a bigger length $l = 0.65 \text{ m}$ leads to a smaller natural frequency (see figure 3). Hence to get a minimal unbalance response, the rotor length should start at $l = 0.55 \text{ m}$ and then abruptly change to $l = 0.65 \text{ m}$. This change of the bearing position must occur exactly when the response for $l = 0.55$ crosses the response for $l = 0.65$, in order to evade the resonance condition, because the rotor speed is different from the natural frequency of the rotor-bearing system.

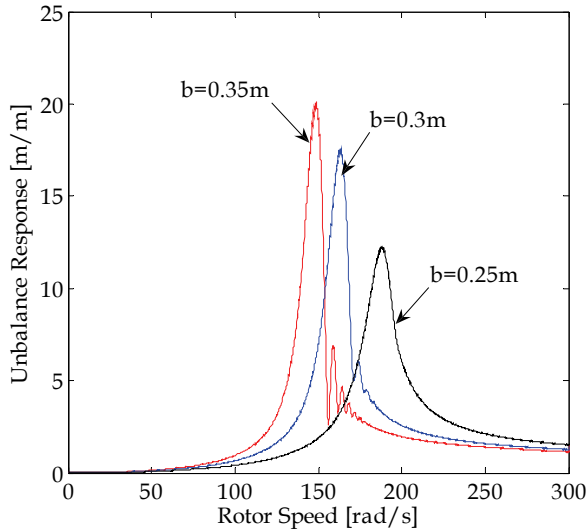


Fig. 3. Unbalance response R for different and constant positions of the movable bearing

3.5 Simulation results

It is evident from equations (5) and (6) that controlling the position of the movable (right) bearing b applying the control force F and according to a pre-specified speed profile $\omega^*(t)$ the modification of the rotor amplitude response to the unbalance is possible. As a matter of fact this methodology is equivalent to a dynamic stiffness control for the Jeffcott-like rotor system, enabling smooth changes on coordinate b .

To design a controller for position reference tracking, consider equation (4). Then, one can propose the following Generalized Proportional Integral (GPI) controller for asymptotic and robust tracking to the desired position trajectory $b^*(t)$ for the bearing position and velocity, which employs only position measurements of the bearing. For more details on GPI control see (Fliess et al., 2002).

$$F = m_b v_2 - c_b \hat{b}$$

$$v_2 = \ddot{b}^*(t) - \beta_2 \left(\hat{b} - \dot{b}^*(t) \right) - \beta_1 (b - b^*(t)) - \beta_0 \int (b - b^*(t)) dt \quad (15)$$

where \hat{b} is an integral reconstructor of the bearing velocity, which is given by

$$\hat{b} = -\frac{c_b}{m_b} b + \frac{1}{m_b} \int_0^t F(\sigma) d\sigma \quad (16)$$

The use of the GPI controller given yields the following closed-loop dynamics for the trajectory tracking error $e^2 = b - b^*(t)$:

$$e_2^{(3)} + \beta_2 \ddot{e}_2 + \beta_1 \dot{e}_2 + \beta_0 e_2 = 0 \quad (17)$$

Therefore, selecting the design parameters $\{\beta_0, \beta_1, \beta_2\}$ such that the associated characteristic polynomial for equation (17) be *Hurwitz*, one guarantees that the error dynamics be globally asymptotically stable. The desired trajectory planning $b^*(t)$ for the bearing position and velocity is also based on Bézier polynomials similar to equation (10).

3.6 Results and discussion

The proposed methodology for the active vibration control of the transient run-up or coast-down of the rotor-bearing system consists of the following steps:

1. Define the trajectory planning for the speed trajectory profile $\omega^*(t)$ to be asymptotically tracked by the use of the adaptive-like PI controller with the algebraic identifier of the eccentricity, i.e., $\lim_{t \rightarrow \infty} \omega(t) = \omega^*(t)$.
2. Establish an appropriate smooth switching on the position of the movable bearing $b^*(t)$ to be asymptotically tracked by the application of the GPI controller, i.e., $\lim_{t \rightarrow \infty} b(t) = b^*(t)$. The switching time has to be at the crossing point leading to minimal unbalance response in figure 3.

Figure 4 shows the unbalance response of the rotor-bearing system when rotor speed PI controller with algebraic identification of eccentricity and GPI control of the bearing position are simultaneously used. Note that the switching of the bearing position leads to small transient oscillations due to inertial and centrifugal effects on the overall rotor system.

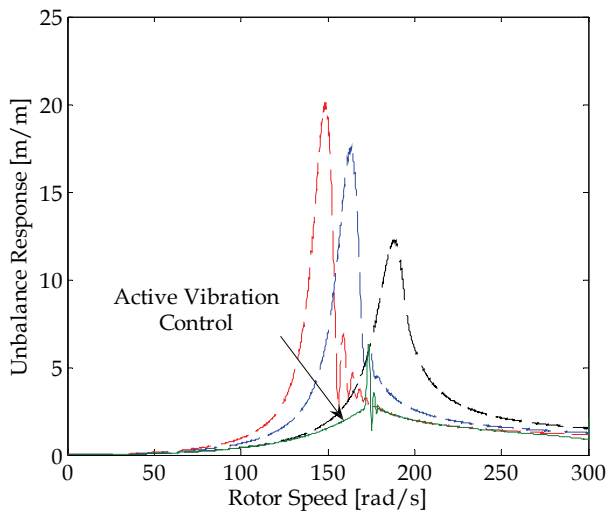


Fig. 4. Rotor vibration amplitude response using active vibration control (solid line)

First of all, the speed trajectory planning and control torque shown in figure 2 are similarly used. The smooth switching for the bearing position is implemented in such a way that the run-up of the rotor system starts with the position $b_i = 0.25 \text{ m}$ (i.e., $l = 0.55 \text{ m}$) and changes to $b_f = 0.35 \text{ m}$ (i.e., $l = 0.65 \text{ m}$) exactly at the crossing point shown in the corresponding response in figure 3. The switching time occurs when $\omega = 170.6 \text{ rad/s}$, that is, $t = 23.9 \text{ s}$. The desired position of the bearing $b(t)$ is illustrated in figure 5 together with the applied control force F . A comparison of the open-loop response and the closed-loop response in figure 4 results in important unbalance reductions about 64%.

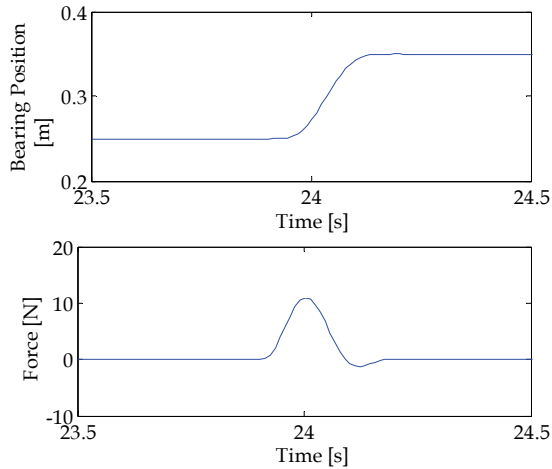


Fig. 5. Response of the bearing support using GPI controller: (a) position of the movable bearing and (b) control force

4. Conclusion

The active vibration control of a Jeffcott-like rotor through dynamic stiffness control and acceleration scheduling is addressed. The control approach consists of a servomechanism able to move one of the supporting bearings in such a way that the effective rotor length is controlled. As a consequence, the rotor stiffness and natural frequency are modified according to an off-line and smooth trajectory planning of the rotor speed/acceleration in order to reduce the unbalance response when passing through the first critical speed. The vibration control scheme results from the combination of passive and active control strategies, leading to robust and stable performance in presence of the synchronous disturbances associated to the normal operation of the rotor and some small parameter uncertainties. Since this active vibration control scheme requires information of the eccentricity, a novel algebraic identification approach is proposed for on-line estimation of the eccentricity. From a theoretical point of view, the algebraic identification is practically instantaneous and robust with respect to parameter uncertainty, frequency variations, small measurement errors and noise. The proposed active vibration control scheme, used to reduce unbalance-induced synchronous vibration, is restricted to use in small rotating machinery (e.g., tools machines, motors and generators).

5. References

- Beltrán-Carbajal, F.; H. Sira-Ramírez, G. Silva-Navarro (2006). Adaptive-like active vibration suppression for a nonlinear mechanical system using on-line algebraic identification, *Proceedings of the Thirteenth International Congress on Sound and Vibration*. Vienna, July. pp. 1-8. ISBN: 3-9501554-5-7.
- Beltrán-Carbajal, F.; G. Silva-Navarro, H. Sira-Ramírez and J. Quezada Andrade (2005). Active vibration control using on-line algebraic identification of harmonic

- vibrations, *Proceedings of American Control Conference*. Portland, Oregon, pp. 4820-4825. ISSN 0743-1619.
- Blanco-Ortega, A.; F. Beltrán-Carbajal, and G. Silva-Navarro (2008). Active Disk for Automatic Balancing of Rotor-Bearing Systems. *American Control Conference*, ACC2008. ISBN: 978-1-4244-2078-0.
- Dimarogonas, A (1996). *Vibration for Engineers*. Ed. Prentice Hall, New Jersey, pp. 533-536. ISBN: 978-0134562292.
- Fliess, M. and H. Sira-Ramírez (2003). An algebraic framework for linear identification, *ESAIM: Control, Optimization and Calculus of Variations*, Vol. 9, 151-168. ISSN: 1292-8119
- Fliess, M.; R. Marquez, E. Delaleau and H. Sira Ramírez (2002). Correcteurs proportionnels-intégraux generalizes, *ESAIM Control, Optimisation and Calculus of Variations*, Vol. 7, 23-41. ISSN: 1292-8119.
- Guozhi, Y.; Y. F. Fah, C. Guang and M. Guang, F. Tong, Q. Yang (2000). Electro-rheological multi-layer squeeze film damper and its application to vibration control of rotor system. *Journal of Vibration and Acoustics*, Vol. 122, 7-11. ISSN: 1048-9002.
- Jinhao, Q.; J. Tani and T. Kwon (2003). Control of self-excited vibration of a rotor system with active gas bearings, *Journal of Vibration and Acoustics*, Vol. 125, 328-334. ISSN: 1048-9002.
- Lee, S.; B. Kim, J. Moon and D. Kim (2005). A study on active balancing for rotating machinery using influence coefficient method, *Proceedings of International Symposium on Computational Intelligence in Robotics and Automation*. Espoo, Finland. pp. 659- 664. ISBN: 0-7803-9356-2.
- Ljung, L (1987). *Systems identification: theory for the user*. Englewood Cliffs, NJ: Prentice-Hall, pp. 168-361. ISBN-13: 978-0136566953.
- Millsaps, K. T. and L. Reed (1998). Reducing lateral vibrations of a rotor passing through critical speeds by acceleration scheduling, *Journal of Engineering for Gas Turbines and Power*, Vol. 120, 615-620. ISSN: 0742-4795
- Palazzolo, B.; S. Jagannathan, A. F. Kaskaf, G. T. Monatgue and L. J. Kiraly (1993). Hybrid active vibration control of rotorbearing systems using piezoelectric actuators, *Journal of Vibration and Acoustics*, Vol. 115, 111-119. ISSN: 1048-9002.
- Rao, S. S. (2004). *Mechanical Vibration*. Ed. Pearson Education, New Jersey, pp. 671-677, 1034.
- Sagara, S. and Z. Y. Zhao (1989). Recursive identification of transfer function matrix in continuous systems via linear integral filter, *International Journal of Control*, Vol. 50, 457-477. ISSN: 0020-7179
- Sagara, S. and Z. Y. Zhao (1990). Numerical integration approach to on-line identification of continuous systems, *Automatica*, Vol. 26, 63-74. ISSN : 0005-1098.
- Sandler, Z (1999). *Robotics: designing the mechanism for automated machinery*. San Diego, CA, Academic Press, pp. 162-164. ISBN: 978-0126185201.
- Sheu, G.; S. Yang and C. Yang (1997). Design of experiments for the controller of rotor systems with a magnetic bearing. *Journal of Vibration and Acoustics*, Vol. 119, No. 2, 200-207, ISSN: 1048-9002.
- Vance, J. M (1988). *Rotor dynamics of Turbomachinery*. Ed. John Wiley and Sons, New York, pp. 7-8, 226-231. ISBN: 9780471802587.
- Yu, X (2004). General influence coefficient algorithm in balancing of rotating machinery, *International Journal of Rotating Machinery*, Vol. 10, 85-90. ISSN: 1023-621X.
- Zhou, S.; S. Dyer, K. K. Shin, J. Shi, J. Ni. "Extended influence coefficient method for rotor active balancing during acceleration", *Journal of Dynamics Systems, Measurements and Control*, Vol. 126, 219-223. ISSN: 0022-0434.
- Zhou, S. and J. Shi (2001). Active balancing and vibration control of rotating machinery: a survey. *The Shock and Vibration Digest*, Vol. 33, 361-371. ISSN: 0583-1024.

Automotive Applications of Active Vibration Control¹

Ferdinand Svaricek¹, Tobias Fueger¹, Hans-Juergen Karkosch²,
Peter Marienfeld² and Christian Bohn³

¹*University of the German Armed Forces Munich,*

²*ContiTech Vibration Control GmbH,*

³*Technical University Clausthal
Germany*

1. Introduction

In recent years, commercial demand for comfortable and quiet vehicles has encouraged the industrial development of methods to accommodate a balance of performance, efficiency, and comfort levels in new automotive year models. Particularly, the noise, vibration and harshness characteristics of cars and trucks are becoming increasingly important (see, e.g., (Buchholz, 2000), (Capitani et al., 2000), (Debeaux et al., 2000), (Haverkamp, 2000), (Käsler, 2000), (Wolf & Portal, 2000), (Sano et al., 2002), (Mackay & Kenchington, 2004), (Elliott, 2008)).

Research and development activities at ContiTech and the UniBwM have focused on the transmission of engine-induced vibrations through engine and powertrain mounts into the chassis (Shoureshi et al., 1997), (Karkosch et al., 1999), (Bohn et al., 2000), (Svaricek et al., 2001), (Bohn et al., 2003), (Kowalczyk et al., 2004), (Bohn et al., 2004), (Kowalczyk & Svaricek, 2005) (Kowalczyk et al., 2006), (Karkosch & Marienfeld, 2010). Engine and powertrain mounts are usually designed according to criteria that incorporate trade-offs between vibration isolation and engine movement since the mounting system in an automotive vehicle has to fulfil the following demands:

- holding the static engine load,
- limiting engine movement due to powertrain forces and road excitations, and
- isolating the engine/transmission unit from the chassis.

Rubber and hydro mounts are the standard tool to isolate the engine and the transmission from the chassis. Rubber isolators work well (in terms of isolation) when the rubber exhibits low stiffness and little internal damping. Little damping, however, leads to a large resonance peak which can manifest itself in excessive engine movements when this resonance is excited (front end shake). These movements must be avoided in the tight engine compartments of today's cars. A low stiffness, while also giving good isolation, leads

¹ This is an updated version of Kowalczyk, K.; Svaricek, F.; Bohn, C. & Karkosch, H.-J.: An Overview of Recent Automotive Applications of Active Vibration Control. RTO AVT-110 Symposium "Habitability of Combat and Transport Vehicles: Noise Vibration and Motion", Prag, October 2004, Paper 24".

to a large static engine displacement and to a low resonance frequency (which would adversely affect the vehicle comfort and might coincide with resonance frequencies of the suspension system).

Classical mount (or suspension) design therefore tries to achieve a compromise between the conflicting requirements of acceptable damping and good isolation. It is clear that this, as well as other passive vibration control measures, are trade-off design methods in which the properties of the structure must be weighted between performance and comfort.

An attractive alternative that overcomes the limitations of the purely passive approach is the use of active noise and vibration control techniques (ANC/AVC). The basic idea of ANC and AVC is to superimpose the unwanted noise or vibration signals with a cancelling signal of exactly the same magnitude and a phase difference of 180° (i.e. the "anti-noise" principle of Lueg (Lueg, 1933)). In the case of ANC, this cancelling signal is generated through loudspeakers, whereas for AVC, force actuators such as inertia-mass shakers are used. Various authors have addressed the application of ANC and AVC systems to reduce noise and vibrations in automotive applications (Adachi & Sano, 1996), (Adachi & Sano, 1998), (Ahmadian & Jeric, 1999), (Bao et al., 1991), (Doppenberg et al., 2000), (Dehandschutter & Sas, 1998), (Fursdon et al., 2000), (Lecce et al., 1995), (Necati et al., 2000), (Pricken, 2000), (Riley & Bodie, 1996), (Sas & Dehandschutter, 1999), (Shoureshi et al., 1995), (Shoureshi et al., 1997), (Shoureshi & Knurek, 1996), (Sano et al., 2002), (Swanson, 1993). ContiTech has implemented prototypes of AVC systems in various test vehicles and demonstrated that significant reductions in noise and vibration levels are achievable (Shoureshi et al., 1997), (Karkosch et al., 1999), (Bohn et al., 2000), (Svaricek et al., 2001), (Bohn et al., 2003), (Kowalczyk et al., 2004), (Bohn et al., 2004), (Kowalczyk & Svaricek, 2005) (Kowalczyk et al., 2006), (Karkosch & Marienfeld, 2010). Honda has developed a series-production ANC/AVC system to reduce noise and vibration due to cylinder cutoff in combination with the engine RPM as reference signal (Inoue et al., 2004), (Matsuoka et al., 2004). A recent overview of such series-production AVC systems can be found in (Marienfeld, 2008).

Most of these approaches rely on feedforward control strategies (either pure feedforward or combined with feedback). The feedforward signal is either taken from an additional sensor (usually an accelerometer in active vibration control) or generated artificially from measurements of the fundamental disturbance frequency (Kuo & Morgan, 1996), (Hansen & Snyder, 1997), (Clark et al., 1998), (Elliot, 2001). Contrary to the major fields of application for active noise and vibration control (military and aircraft), the automotive sector is extremely sensitive to the costs of the overall system. It is therefore desirable to use an approach that requires only one sensor. Also, most approaches rely on adaptive control strategies such as the filtered-x LMS algorithm (Kuo & Morgan, 1996), (Hansen & Snyder, 1997), (Clark et al., 1998), (Elliot, 2001). This seems necessary as the characteristics of the disturbance acting upon the system are time varying. In automotive applications, for example, the fundamental frequency (engine firing frequency, which is half the engine speed in four-stroke engines) varies from 7 Hz at idle to 50 Hz at 6000 rpm. The adaptive approach will adjust the disturbance attenuation of the control system to the frequency content of the disturbance. Whereas this works well in many applications (see the references given above), some critical issues such as convergence speed, tuning of the step size in the adaptive algorithm and stability remain. Discussions between the authors and potential customers (automobile manufactures) have indicated that particularly the issues of convergence speed, tracking performance (this is related to the attenuation capability of the

algorithm during changes in engine speed such as fast acceleration) and stability are crucial. A non-adaptive algorithm might have the benefit of a higher customer acceptance.

Another advantage of a non-adaptive algorithm is that the behavior of the closed-loop system can be analysed independent of the input signals. In an adaptive algorithm, the optimal controller depends on the external signals that act upon the system; thus, it is very difficult to analyse the performance off-line.

Both kind of algorithms have been implemented in an active control system for cancellation of engine-induced vibrations in several test vehicles. The remainder will present an overview of ANC/AVC system components, control algorithms, as well as obtained experimental results.

2. System description

A schematic representation of an AVC system in a vehicle is shown in Figure 1. The disturbance force originating from the engine and transmitted into the chassis through the engine mounts is actively cancelled by an actuator force of the same magnitude but of opposite sign.

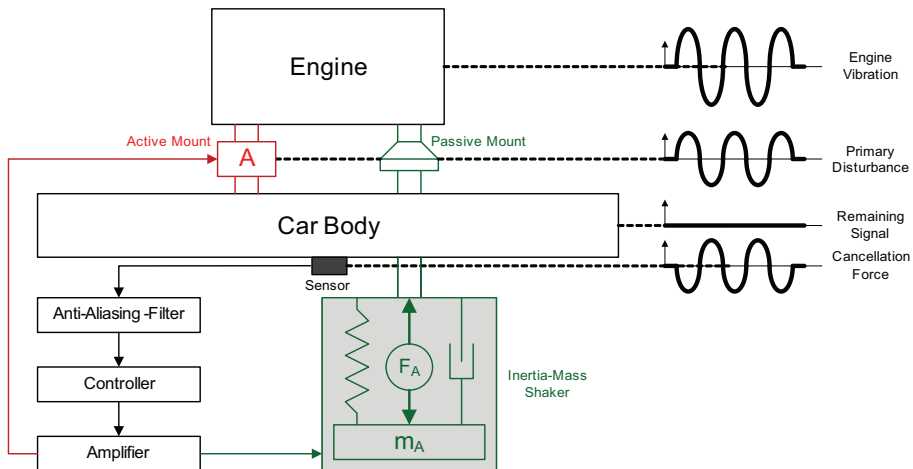


Fig. 1. Schematic representation of an AVC system with an active mount (red) or an inertia-mass shaker (green).

The basic components of the system include actuators, sensors and an electronic control unit (ECU). The electronic hardware consists of an amplifier and filter unit that contains the power amplifier and the anti-aliasing filter for the sensor signal. Figure 1 presents two alternative principles, the inertial mass actuator (green) and active mount with integrated actuator (red), whereby the ECU, sensors and the actuator's basic components can be identically used. The two principles are similar in how they function, forces are fed into the system in targeted fashion so that the resulting dynamic forces at the base of the mount (attachment point) are reduced. In this example, attachment point acceleration is measured and supplied to the controller. The countersignal calculated in the control unit powers the actuator via power amplifiers. Ideally, the superimposed forces cancel out one another so that no annoying engine vibration is disseminated via the chassis.

Generally, there are two possible ways of active vibration cancellation, the Inertial mass shakers, attached at suitable points, cancel out the disturbing vibration by a force signal of opposite phase. On the other hand, active engine mounts compensate the displacement between engine mount and the car body. Hereby the car body is kept free from the vibration forces emitted from the engine. With regard to the specifications of the AVC system the suitable system configuration has to be chosen. In (Hartwig et al., 2000), (Karkosch & Marienfeld, 2010) the electrodynamic and the electromagnetic actuator principle and the two system configurations are compared. Figure 2 shows the electrodynamic and electromagnetic actuator principles.

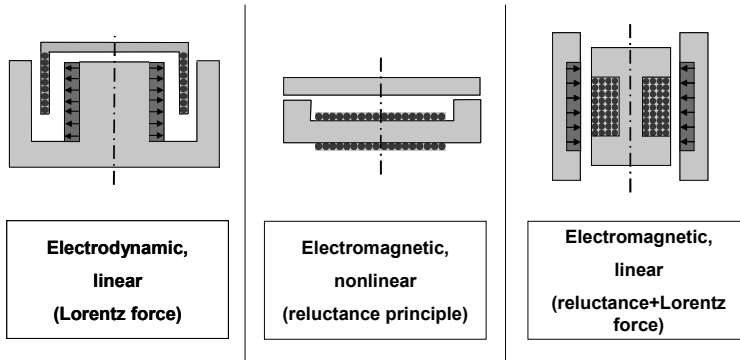


Fig. 2. Electrodynamic and electromagnetic actuator principles.

An electromagnetic actuator has the benefit to an electrodynamic actuator in higher actuator force at decreased magnet and design volume such as more cost efficient. On the other side, the electrodynamic actuator principle has the advantage in a simple design of the iron core and the absence of magnetic forces lateral to the deflection direction. A comparison between an active absorber and an active hydromount configuration is shown in Figure 3.

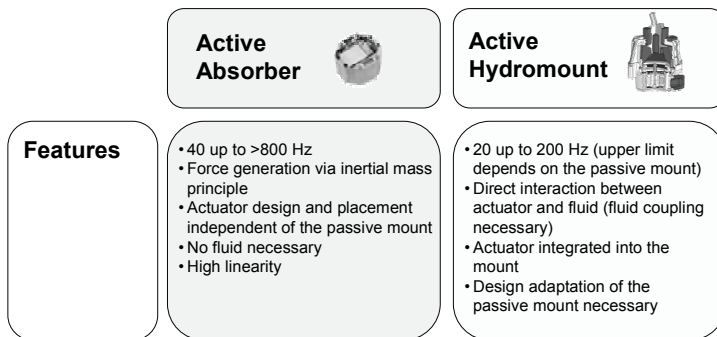


Fig. 3. Active engine mount system configurations – principle comparison.

3. Control system design

The problem of active control of noise and vibrations has been a subject of much research in recent years. For an overview see e.g. (Kuo & Morgan, 1996), (Hansen & Snyder, 1997),

(Clark et al., 1998), (Elliot, 2001) and the references therein. The main part of the published literature makes use of adaptive feedforward structures. Adaptive feedback compensation (Aström & Wittenmark, 1995), in which the feedback law depends explicitly upon the error sensor output has found little application in the active noise and vibration control field.

Feedforward control provides the ability to handle a great variety of disturbance signals, from pure tone to a fully random excitation. However, the performance of feedforward control algorithms can be degraded if disturbances are not measurable in advance (e.g. road or wind noise) or the transmission path characteristics change rapidly. Contrarily, a feedback controller can be designed to be less sensitive to system perturbations. Robustness and performance, however, are conflicting design requirements. To achieve a good attenuation of the vibrations the cancellation wave has to be very accurate, typically within ± 5 degrees in phase and ± 0.5 dB in amplitude.

3.1 FxLMS approach

The FxLMS algorithm has been originally proposed in (Morgan, 1980) and is described in detail in (Kuo & Morgan, 1996). The basic idea is to use the feedforward structure shown in Figure 4. The transfer path between the disturbance source and the error sensor is called *primary path*. The *secondary path* is the transfer path between the output of the controller and the error sensor. The aim in the control loop is to minimise the output signal (error signal).

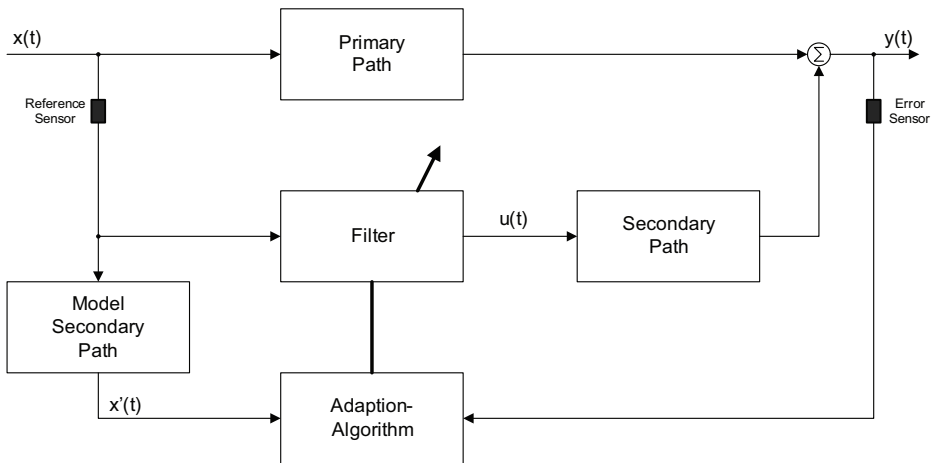


Fig. 4. Block diagram of FxLMS algorithm.

The adaptive filter has to approximate the dynamics of the primary path and the inverse dynamics of the secondary path. For the on-line adaptation of a FIR-filter (finite-impulse-response filter), two signals are used: error signal and reference signal filtered with the model of the secondary path (filtered-x).

The discrete-time transfer function of a FIR-filter has the form

$$F(z) = \frac{U(z)}{X(z)} = \frac{w_0 z^m + w_1 z^{m-1} + \dots + w_m}{z^m}, \quad (1)$$

whereas the filter coefficients w_i , $i=1, \dots, m$ can be represented as a vector:

$$w(k) = [w_0(k) \quad w_1(k) \quad \dots \quad w_m(k)]^T. \quad (2)$$

The adaptation of the filter weights w_i is performed through the well-known LMS (least mean square) algorithm originally proposed in (Widrow & Hof, 1960). A performance index J is built from the sum of squares of the sampled error signal:

$$J = \frac{1}{N} \sum_{i=1}^N y^2(i). \quad (3)$$

This performance function depends on the filter coefficients and can be described through a hyperparaboloid as shown in Figure 5. The optimal values for the adaptive filter coefficients are located in the deepest point of the performance surface. The LMS-algorithm is searching on-line for the coordinates of the deepest point. The control signal is generated as the output of the adaptive filter.

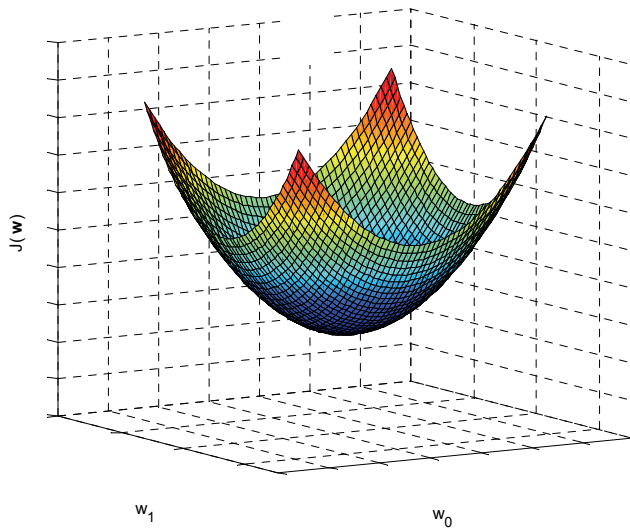


Fig. 5. Example of a performance surface for a two-weight system.

3.2 Disturbance observer approach

This method is based on state observer and state feedback and has been proposed in (Bohn et al., 2003), (Kowalczyk et al., 2004), (Bohn et al., 2004), (Kowalczyk & Svaricek, 2005). It is assumed that the disturbance enters at the input of the plant S , see Figure 6.

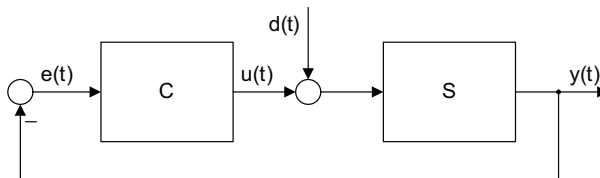


Fig. 6. Control loop with a plant S and a controller C .

The disturbance is modelled as a sum of a finite number of sine signals, which are harmonically related:

$$d(t) = \sum_{i=1}^N A_i \sin(2\pi f_i t + \varphi_i). \quad (4)$$

This disturbance is time-varying and needs frequency measurements to be fed into the model. The disturbance attenuation is achieved through producing an estimate of the disturbance d and using this estimate, with a sign reversal, as a control signal u . To generate the estimate, a disturbance observer is used. The observer is designed off-line assuming time-invariance and investigating the property of robustness over a certain frequency region for a single observer. Later on, a gain-scheduling is implemented to cover the whole frequency region of interest by a stable observer. This provides a non-adaptive approach, where the frequency is used as a scheduling variable.

The transfer function of the controller C has infinite gain at the frequencies included in the disturbance model. The controller poles show up as zeros in the closed-loop transfer function. Figure 7 shows the frequency response magnitude of the sensitivity function $1/(1+CS)$.

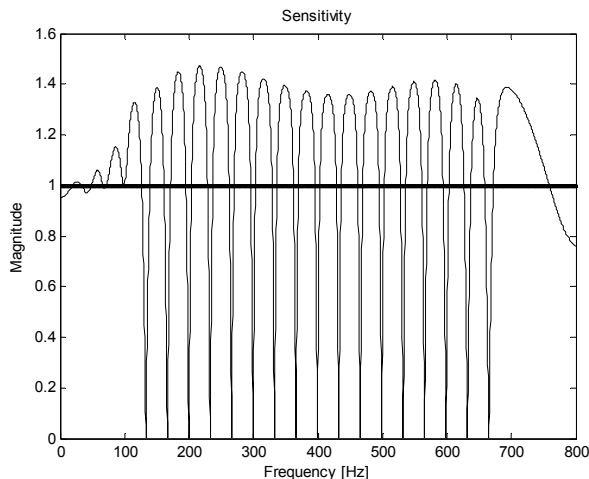


Fig. 7. Frequency response magnitude of the sensitivity function.

It can be seen that the magnitude of the sensitivity function is zero for the frequencies specified in the disturbance model, which corresponds to complete disturbance cancellation. The improvement of the disturbance attenuation for these frequencies leads to some disturbance amplification between these frequencies. This effect is in accordance with Bode's well-known sensitivity integral theorem and is called *waterbed effect* (Hong & Bernstein, 1998). For more details on this algorithm, see (Bohn et al., 2004).

Finally, both approaches can be combined to give a two-degree-of-freedom control structure, which is referred to as a hybrid approach in the ANC/AVC literature (Shoureshi & Knurek, 1996), (Hansen & Snyder, 1997). The implementation of all control algorithms is usually done on digital signal processing hardware.

Due to a large number of influence parameters, no definite statements can be made with regard to which control scheme will give a better performance. Rather, control strategies have to be chosen with regard to the characteristics of the vibration problem to be addressed, such as available sensor signals (e.g., costs associated with additional feedforward sensors, possible use of existing sensors), Type of excitation (periodic, e.g. engine vibrations, or stochastic, e.g. road excitations), Frequency range of interest (e.g. 25 – 30 Hz for idling speed or 25 – 300 Hz for the whole engine speed range), Spectral characteristics of excitation (narrowband, e.g. distinct frequencies, or broadband; e.g. fixed/varying frequencies).

The decision for one particular control strategy and the determination of suitable controller settings is a very important step in the development of ANC/AVC schemes. Therefore, simulation studies and real-time experiments on vehicles are carried out to identify a suitable strategy for a given noise and vibration problem. For the real-time experiments, the control strategies, together with auxiliary function such as signal conditioning and monitoring routines, are implemented on a rapid prototyping system.

4. Experimental results

In the last years, several vehicles – with different problems – have been equipped with active absorber systems to attenuate the transmission of the engine vibrations into the vehicle cabin. As mentioned earlier, the control algorithms have to be chosen with regard to the particular problem of the considered vehicle. ContiTech has equipped a test vehicle with an AVC system with inertia-mass shaker attached on the transmission cross-member. Figure 8 shows the location of the system components on the transmission cross-member in the test vehicle.

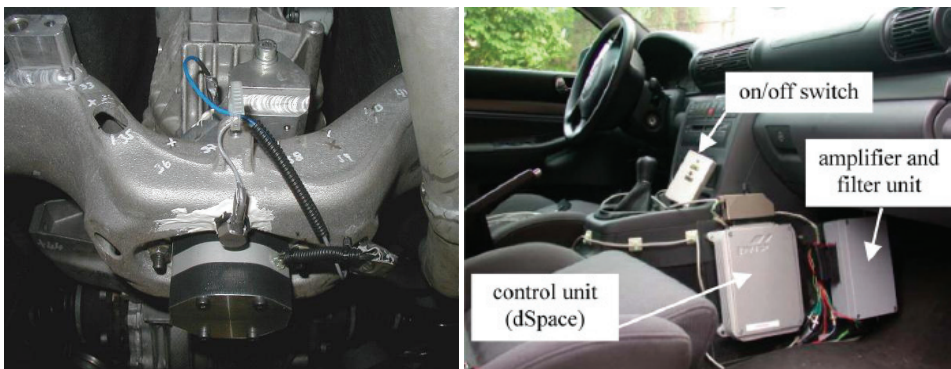


Fig. 8. Location of the AVC components in the test vehicle.

The control algorithm is implemented on a rapid prototyping unit, the dSPACE MicroAutoBox. The electronic hardware consists of an amplifier and filter unit that contains the power amplifier and the anti-aliasing filter for the sensor signal, and the electronic control unit. A remote control on/off switch is used to turn the control algorithm on and off during vehicle tests (Kowalczyk et al., 2006).

In control engineering terms, the transfer function from the amplifier input to the (filtered) sensor output is the transfer function of the plant to be controlled (assuming linearity and

time invariance). In accordance with the active noise and vibration control literature (Kuo & Morgan, 1996), (Hansen & Snyder, 1997), (Clark et al., 1998) this is called the secondary path *S*. To design a control algorithm, a model for the secondary path is required. Quite often models for vibration control systems are derived from physical principles (Preumont, 1997), from finite-element models or through experimental techniques such as modal analysis (Heylen et al., 1997). Physical principles are mostly applied to fairly simple mechanical structures such as beams or plates for which analytical solutions can be found. Finite-element models or models derived from modal analysis will give a model of the structure only, that is, without the dynamics of the electrical and electromechanical components (amplifier, actuator, sensor). The approach taken here is to excite the system with a test signal and record the response. Any of the discrete-time black-box system identification techniques (such as the least squares approach for equation-error models) can then be used to identify a model (Ljung & Söderström, 1983). Figure 9 shows the amplitude and phase responses of an identified system transfer function. The amplitude response would be dimensionless, since it corresponds to the output voltage, i.e. the filtered sensor signal, over the input voltage of the amplifier. However, for interpretability, the output signal has been scaled to acceleration (m/s^2 , using the sensor sensitivity) and the input signal to current (A, using the amplifier gain). Such models are used for the subsequent controller design and for simulation studies.

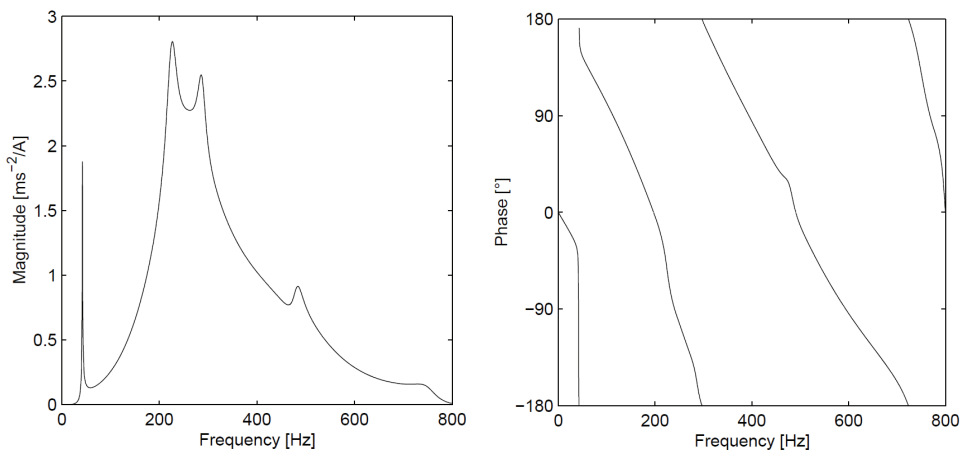


Fig. 9. Amplitude and phase plots of an identified system transfer function (actuator current to filtered sensor output; the first peak corresponds to the resonance of the inertia-mass actuator).

For instance, the stationary behavior of the controlled system is of interest when the comfort under idling speed conditions should be improved.

A typical real-time result for such a problem is given in Figure 10. Here, a comparison of the error signals (measured accelerations at the frame) is shown for control off and on. It can be seen that the engine orders 2, 4 and 6 are predominant at idling speed without active control. However, a significant reduction (up to 37 dB) of these engine orders can be achieved by using an AVC system.

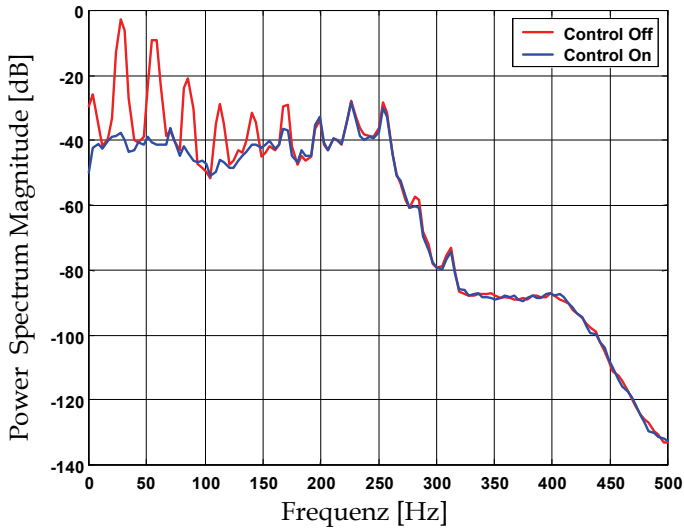


Fig. 10. Power spectrum of the measured frame vibrations at idle.

In other applications, the active system should work over a wide engine speed range. For such applications the tracking behavior of the active system must be considered. Figure 11 gives an impression of the dynamic behavior of the adaptive FxLMS algorithm. To illustrate the adaptation of the controller, the decrease in the measured frame vibrations after switching on the control algorithm at $t=1$ [s] is shown.

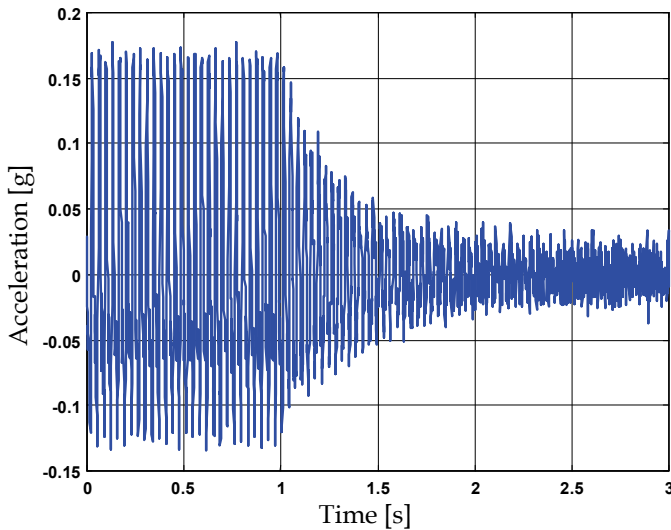


Fig. 11. Adaptation behavior of the FxLMS algorithm.

It is well-known that parts of the transmitted vibration energy through the mounts pass through the chassis and emanate in the vehicle passenger compartment in the form of structure-borne noise. Figure 12 shows an order analysis of a sound pressure level measurement at the passenger's left ear of a test vehicle that has acoustic problems in the frequency range between 200 and 300 Hz.

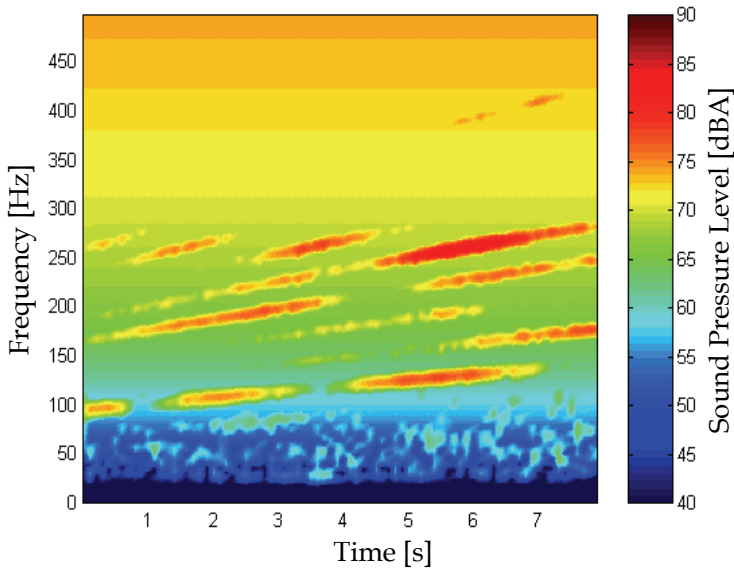


Fig. 12. Order analysis of sound pressure level (passenger's left ear) of a road test (acceleration from 1800 to 4500 rpm, full throttle, 3rd gear, control off).

Here a lot of engine orders (2.5, 3, 3.5, ...) are visible since the transmission mount is the major path for this engine-induced noise. The improvement with control on is shown in Figure 13. The sound pressure level measurement at the passenger's left ear points out a significant reduction in sound for frequencies higher than 120 [Hz].

Due to the fact that the measured vibrations at the transmission are well correlated to the cross member vibrations a classical FxLMS algorithm has been chosen for this application. An impressive reduction of the sound pressure level, achieved by the small (weight about 0.6 kg) active absorber at the transmission mount, can be registered in Figure 13. The remaining 2nd order line is a result of the vibrations that are still transmitted through the two front engine mounts.

The active absorber system has not only a great impact on the interior noise of the vehicle but also on vibrations at comfort relevant points. Such an interior comfort improvement for the passengers can be observed from a control on/off comparison of the power spectrum of the measured acceleration signal at the steering wheel, see Figure 14.

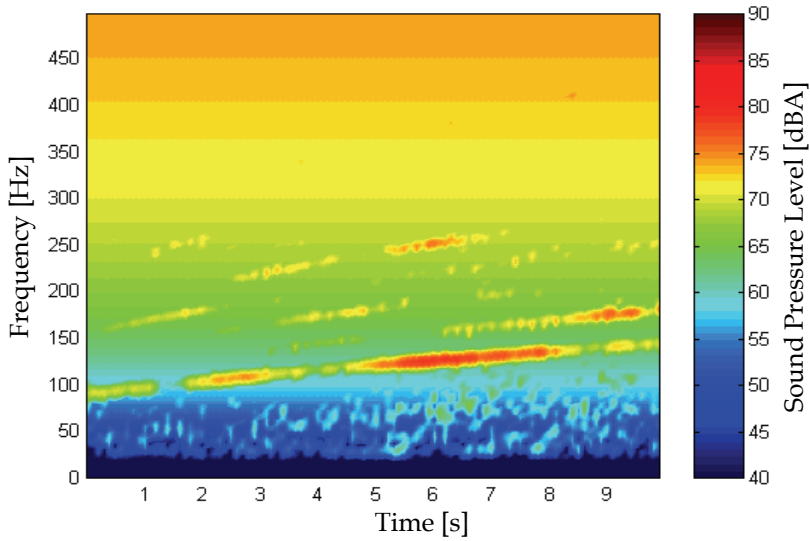


Fig. 13. Order analysis of sound pressure level (passenger's left ear) of a road test (acceleration from 1800 to 4500 rpm, full throttle, 3rd gear, control on).

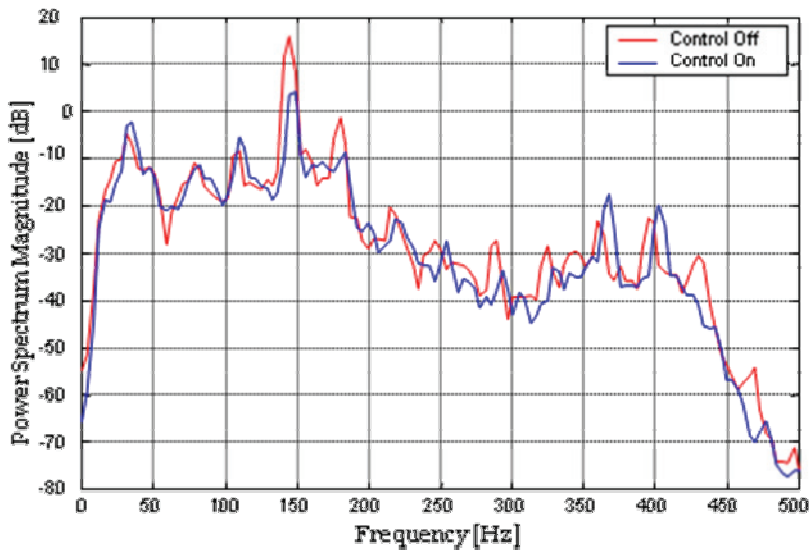


Fig. 14. Power spectrum comparison of the measured steering wheel acceleration for constant drives with 4400 RPM.

5. Conclusion

This chapter has given an overview of recent research and development activities in the field of active noise and vibration control in automotive applications. The design of an ANC/AVC system with its components is described in general such as two control approaches, a feedforward and a feedback approach, are presented in detail. Experimental results from a test vehicle, equipped with an AVC system with inertial-mass shaker and a dSpace MicroBox, were discussed.

Recent advances in NVH (Noise Vibration Harshness) design and analysis tools, development of low cost digital signal processors, and adaptive control theory, have made active vibro-acoustic systems a viable and economically feasible solution for low frequency problems in automotive vehicles.

Further experimental results and a comparison of the presented control approaches can be found in (Kowalczyk et al., 2004) and (Kowalczyk & Svaricek, 2005).

6. References

- Adachi, S. & Sano, H. (1996). Application of a two-degree-of-freedom type active noise control using IMC to road noise inside automobiles. *Proceedings of the 35th IEEE Conference on Decision and Control*, pp. 2794-2795, Kobe
- Adachi, S. & Sano, H. (1998). Active noise control system for automobiles based on adaptive and robust control. *Proceedings of the 1998 IEEE International Conference on Control Applications*, pp. 1125-1128, Trieste
- Ahmadian, M. & Jeric, K.M. (1999). The application of piezoceramics for reducing noise and vibration in vehicle structures. SAE Technical Paper 1999-01-2868. *Proceedings of the International Off-Highway and Powerplant Congress and Exposition*, Indianapolis
- Aström, K.J. & Wittenmark, B. (1995). *Adaptive Control*, Addison-Wesley, Reading
- Bao, C.; Sas, P. & Van Brussel, H. (1991). Active control of engine-induced noise inside cars. *Proceedings of the International Conference on Noise Control Inter-noise 91*, pp. 525-528, Sydney
- Bohn, C.; Karkosch, H.-J.; Marienfeld, P.M. & Svaricek, F. (2000). Automotive applications of rapid prototyping for active vibration control. *Proceedings of the 3rd IFAC Workshop Advances in Automotive Control*, pp. 191-196, Karlsruhe, Germany
- Bohn, C.; Cortabarría, A.; Härtel, V. & Kowalczyk, K. (2003). Disturbance-observer-based active control of engine-induced vibrations in automotive vehicles. *Proceedings of the 10th Annual International Symposium on Smart Structures and Materials*. Paper 50, pp. 49-68, San Diego, USA
- Bohn, C.; Cortabarría, A.; Härtel, V. & Kowalczyk, K. (2004). Active control of engine-induced vibrations in automotive vehicles using disturbance observer gain scheduling. *Control Engineering Practice* 12, 1029-1039.
- Buchholz, K. (2000). Good vibrations. *Automotive Engineering*, 108, (August 2000) 85-89
- Capitani; Citti, R.P.; Delogu, M.; Mascellini, R. & Pilo, L. (2000). Experimental validation of a driveline numerical model for the study of vibrational comfort of a vehicle. *Proceedings of the 33rd ISATA Electric, Hybrid, Fuel Cell and Alternative Vehicles/Powertrain Technology*, pp. 521-530, Dublin
- Clark, R.L.; Saunders, W.R. & Gibbs, G.P. (1998). *Adaptive Structures: Dynamics and Control*, John Wiley and Sons, New York

- Debeaux, E.; Claessens, M. & Hu, X. (2000). An analytical-experimental method for analysing the low-frequency interior acoustics of a passenger car. *Proceedings of the 2000 International Conference on Noise and Vibration Engineering ISMA 25*, pp. 1331-1338, Leuven
- Dehandschutter, W. & Sas, P. (1998). Active control of structure-borne road noise using vibration actuators. *Journal of Vibration and Acoustics* 120:517-523
- Doppenberg, E.J.J.; Berkhoff, A.P. & van Overbeek, M. (2000). Smart materials and active noise and vibration control in vehicles. *Proceedings of the 3rd IFAC Workshop Advances in Automotive Control*, pp. 205-214, Karlsruhe, Germany
- Elliott, S.J. (2001). *Signal Processing for Active Control*, San Diego, Academic Press
- Elliott, S.J. (2008). *A Review of Active Noise and Vibration Control in Road Vehicles*. ISVR Technical Memorandum No. 981, University of Southampton
- Fursdon, P.M.T.; Harrison, A.J. & Stoten, D.P. (2000). The design and development of a self-tuning active engine mount. *Proceedings of the European Conference on Noise and Vibration 2000*, pp. 21-32, London
- Hansen, C.H. & Snyder, S.D. (1997). *Active Control of Noise and Vibration*, E & FN, London
- Hartwig, C.; Haase, M.; Hofmann, M. & Karkosch, H.-J. (2000). Electromagnetic actuators for active engine vibration cancellation. *Proceedings of the 7th International Conference on New Actuators ACTUATOR 2000*, Bremen, June 2000
- Haverkamp, M. (2000). Solving vehicle noise problems by analysis of the transmitted sound energy. *Proceedings of the 2000 International Conference on Noise and Vibration Engineering ISMA25*, pp.1339-1346, Leuven
- Heylen, W.; Lammens, S. & Sas, P. (1997). *Modal Analysis Theory and Testing*, Katholieke Universiteit Leuven Departement Werktuigkunde, Leuven
- Hong, J. & Bernstein, D.S. (1998). Bode integral constraints, colocation, and spillover in active noise and vibration control. *IEEE Transactions on Control Systems Technology* 6, 111-120
- Inoue, T.; Takahashi, A.; Sano, H.; Onishi, M. & Nakamura, Y. (2004). NV Countermeasure Technology for a Cylinder-On-Demand Engine- Development of Active Booming Noise Control System Applying Adaptive Notch Filter. SAE-Paper 2004-01-0411. *Noise and Vibration 2004 SP-1867*. 131-138
- Käsler, R. (2000). Development trends and vibro-acoustic layout criteria for powertrain mounting systems. *Proceedings of the International Congress Engine & Environment 2000*, pp. 155-172, Graz
- Karkosch, H.-J.; Svaricek, F.; Shoureshi, R.A. & Vance, J.L. (1999). Automotive applications of active vibration control. *Proceedings of the European Control Conference*, Karlsruhe
- Karkosch, H.-J. & Marienfeld, P.M. (2010). Use of Active Engine Mounts to Optimize Comfort in Cars with Innovative Drives. *Proceedings of the 12th International Conference on New Actuators ACTUATOR 2010*, Bremen, June 2010
- Kowalczyk, K.; Svaricek, F. & Bohn, C. (2004). Disturbance-observer-based active control of transmission-induced vibrations. *Proceedings IFAC Symposium Advances in Automotive Control*, pp. 78-83, Salerno, Italy
- Kowalczyk, K. & Svaricek, F. (2005). Experimental Robustness of FXLMS and Disturbance-Observer Algorithms for Active Vibration Control in Automotive Applications. In *Proceedings of the 16th IFAC World Congress*, Prag

- Kowalczyk, K.; Karkosch, H.-J.; Marienfeld, P.M. & Svaricek, F. (2006). Rapid Control Prototyping of Active Vibration Control Systems in Automotive Applications. Proceedings of the 2006 IEEE International Conference on Computer Aided Control Systems Design, Munich, pp. 2677-2682
- Kuo, S.M. & Morgan, D.M. (1996). *Active Noise Control Systems*, John Wiley and Sons, New York
- Lecce, L.; Franco, F.; Maja, B.; Montouri, G. & Zandonella-Necca, D. (1995). Vibration active control inside a car by using piezo actuators and sensors. 28th International Symposium on Automotive Technology and Automation. *Proceedings for the Dedicated Conference on Mechatronics - Efficient Computer Support for Engineering, Manufacturing, Testing and Reliability*. Croydon, pp. 423-432, UK
- Ljung, L. & Söderström, T. (1983). *Theory and Practice of Recursive Identification*, MIT Press, Cambridge
- Lueg, P. (1933). Process of silencing sound oscillations. US Patent No 2,043,416. Filed: March 8, 1934. Patented: June 6, 1936. Priority (Germany): January 1933
- Mackay, A.C. and Kenchington, S. (2004). Active control of noise and vibration - A review of automotive applications. *Proceedings ACTIVE 2004, Williamsburg*
- Marienfeld, P. (2008). Übersicht über den Serieneinsatz mechatronischer Systeme im Bereich der Aggregatelagerung. *Tagung „Geräusch- und Schwingungskomfort von Kraftfahrzeugen“*, Haus der Technik, Munich
- Matsuoka, H. ; Mikasa, T. & Nemoto, H. (2004). NV Countermeasure Technology for a Cylinder-On-Demand Engine- Development of Active Control Engine Mount. SAE-Paper 2004-01-0413. Noise and Vibration 2004 SP-1867
- Morgan, D.R. (1980). An Analysis of Multiple Correlation Cancellation Loops with a Filter in the Auxiliary Path. *IEEE Trans. Acoust., Speech, Signal Processing* 28, 454-467
- Necati, G.A.; Doppenberg, E.J.J. & Antila, M. (2000). Noise radiation reduction of a car dash panel. *Proceedings of the 2000 International Conference on Noise and Vibration Engineering ISMA25*, pp. 855-862, Leuven
- Preumont, A. (1997). *Vibration Control of Active Structures*, Kluwer Academic Publishers, Dordrecht, The Netherlands
- Pricken, F. (2000). Active noise cancellation in future air intake systems. SAE-Paper 2000-01-0026. Powertrain Systems NVH. SAE Special Publication SP-1515. 1-6
- Riley, B. & Bodie, M. (1996). An adaptive strategy for vehicle vibration and noise cancellation. *Proceedings of the IEEE 1996 National Aerospace and Electronics Conference NAECON 1996*, pp. 836-843, Dayton
- Sano, H.; Yamashita, T. & Nakamura, M. (2002). Recent application of active noise and vibration control to automobiles. *Proceedings ACTIVE 2002*, pp. 29-42, Southampton, UK
- Sas, P. & Dehandschutter, W. (1999). Active structural and acoustic control of structure-borne road noise in a passenger car. *Noise & Vibration Worldwide* 30, 17-27
- Shoureshi, R.A.; Alves, G.; Knurek, T.; Novotry, D.; Ogundipe, L. & Wheeler, M. (1995). Mechanically-based vibration and noise control in automotive systems. 28th International Symposium on Automotive Technology and Automation. *Proceedings for the Dedicated Conference on Mechatronics - Efficient Computer Support for Engineering, Manufacturing, Testing and Reliability*, pp. 691-698, Croydon, UK

- Shoureshi, R. & Knurek, T. (1996). Automotive applications of a hybrid active noise and vibration control. *IEEE Control Systems Magazine* 16, 72-78
- Shoureshi, R.A.; Gasser, R. & Vance, J.L. (1997). Automotive applications of a hybrid active noise and vibration control. *Proceedings of the IEEE International Symposium on Industrial Electronics*, pp. 1071-1076, Guimaraes, Portugal
- Shoureshi, R.A.; Vance, J. L.; Ogundipe, L.; Schaaf, K.; Eberhard, G. & Karkosch, H.-J. (1997). Active vibro-acoustic control in automotive vehicles. *Proceedings of the 1997 Noise and Vibration Conference*, pp. 131-136, Traverse City, MI
- Svaricek, F.; Bohn, C.; Karkosch, H.-J. & Härtel, V. (2001). Aktive Schwingungskompensation im Kfz aus regelungstechnischer Sicht. *at - Automatisierungstechnik* 49, 249-259. (Active vibration cancellation in automotive vehicles from a control engineering point of view, in German)
- Swanson, D.A. (1993). Active engine mounts for vehicles. SAE Technical Paper 932432. *Proceedings of the 1993 International Off-Highway and Powerplant Congress and Exposition*, Milwaukee
- Widrow, B. & Hof, M.E. (1960). Adaptive Switching Circuits. *IRE WESCON Conv. Rec.* 96-104
- Wolf, A. & Portal, E. (2000). Requirements to noise reduction concepts and parts in future engine compartments. *SAE-Paper 2000-01-0027*. Powertrain Systems NVH. SAE Special Publication SP-1515, pp. 7-12

Neural Network Control of Non-linear Full Vehicle Model Vibrations

Rahmi Guclu and Kayhan Gulez
*Yildiz Technical University
Turkey*

1. Introduction

Vehicle suspension serves the basic function of isolating passengers and the chassis from the roughness of the road to provide a more comfortable ride. In other words, very important role of the suspension system is the ride control. Due to developments in the control technology, electronically controlled suspensions have gained more interest. These suspensions have active components controlled by a microprocessor. By using this arrangement, significant achievements in vehicle response can be carried out. Selection of the control method is also important during the design process. In this study, Neural Network (NN) controllers parallel to McPherson strut-type independent suspensions are used. The major advantages of this control method are its success, robust structure and the ability and adaptation of using these types of controllers on vehicles. To simplify models, a number of researchers assumed vehicle models to be linear. However, such models ignore non-linearities present in the system. By including non-linearities such as dry friction on dampers, the results become more realistic.

During the last decade, many researchers applied some linear and non-linear control methods to vehicle models. Due to simplicity, quarter car models were mostly preferred. (Redfield & Karnopp, 1998) examined the optimal performance comparisons of variable component suspensions on a quarter car model. (Yue et al., 1989) also applied LQR and LQG controller to a quarter car model.

(Stein & Ballo, 1991) designed a driver's seat for off-road vehicles with active suspensions. Hac (Hac, 1992) applied optimal linear preview control on the active suspensions of a quarter car model. (Rakheja et al., 1994) added a passenger seat in their analysis. A passenger seat suspension system was described by a generalized two degrees of freedom model and with non-linearities such as shock absorber damping, linkage friction and bump stops. Since the quarter car model is insufficient to give information about the angular motions of a vehicle, some researchers used more complex models like half and full car models. These models give information about the pitch, roll and bounce motions of a vehicle body. (Crolla & Abdel Hady, 1991) compared some active suspension control laws on a full car model. Integrated or filtered white noise was taken as the road input. The same researchers applied linear optimal control law to a similar model in 1992. (Hrovat, 1993) compared the performances of active and passive suspension systems on quarter, half and full car models using linear quadratic optimal control.

Dry friction on dampers is one of the main factors affecting ride comfort. For a vehicle traveling on a relatively smooth road at low speeds, the effect of road input cannot overcome dry friction force and, therefore, the suspensions are almost locked, which is known as Boulevard Jerk, and an uncomfortable vibration mode becomes effective due to reduced degrees of freedom (Silvester, 1966). Control of vibrations using non-linearity on active suspensions was achieved. (Alleyne et al., 1993) compared sliding mode controlled active suspensions with PID controlled active suspensions for a quarter car active suspension system. As the conclusion, the paper shows that sliding mode controller is better than PID one.

(Park & Kim, 2000) designed a decentralized variable structure controller for active suspension systems of vehicles. (Yokoyama et al., 2001) examined a new SMC for semi-active suspension systems with magneto-rheological (MR) dampers which have undesirable non-linear properties. (Yoshimura et al., 2001) showed the construction of an active suspension system for a quarter car model using the concept of sliding mode control. (Al-Holou et al., 2002) examined the development of a robust intelligent non-linear controller for active suspension systems based on a comprehensive and realistic non-linear model. (Guclu, 2004), (Guclu, 2005), (Guclu & Gulez, 2008) applied fuzzy logic controlled active suspensions on a non-linear four and eight degrees of freedom vehicle model without suspension-gap degeneration.

(Otten et al., 1997) applied for linear motors of a learning feed-forward controller.

2. Vehicle model

The non-linear full car model used in this study is shown in Figure 1. This full car model has eight degrees of freedom, namely vertical translations $x_1, x_2, x_3, x_4, x_5, x_6$ and angular rotations $x_7 = \theta, x_8 = \alpha$. These are the motion of the right front axle, the motion of the left front axle, the motion of the right rear axle, the motion of the left rear axle, the bounce motion of the passenger seat, the bounce motion of the vehicle body, the pitch motion of the vehicle body and the roll motion of the vehicle body, respectively. A passenger seat is included in the vehicle model to predict the response of the passenger due to a road disturbance. The common application in modeling the vehicle with a passenger seat is to add only one passenger seat preferably in the driver seat position though considering only one suspended seat implies that other seats are assumed to be fixed rigidly to the chassis (Baumal et al., 1998).

$f(Vr_i)$ is dry friction force. Namely, z_i ($i = 1, \dots, 4$) in Figure 2 is road excitation and is given in Figure 7 in detail. $y_i - x_i$ ($i=1, \dots, 5$) represents relative displacements of the suspension systems and controllers. y_i is given in the Appendix. The equation of the linear motor is

$$R I + K_e (\dot{y}_i - \dot{x}_i) = v \quad i = (1, \dots, 5) \quad (1)$$

where v and I are the control voltage and current of the armature coil, respectively. R and K_e are the resistance value and induced voltage constant of the armature coil. The current of the armature coil (I) and control force (u) has the following relation:

$$u = K_f I \quad (2)$$

K_f is the thrust constant. The inductance of the armature coil is neglected.

In general, the state-space form of a non-linear dynamic system can be written as follows:

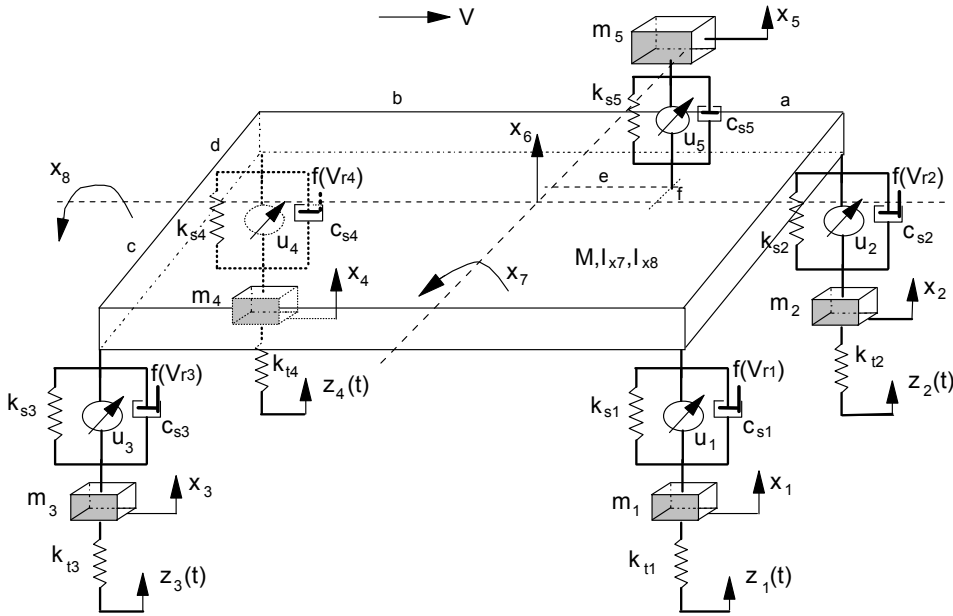


Fig. 1. The non-linear full car model with a passenger seat.

$$\dot{x} = f(x) + [B]u \tag{3}$$

Here, for the eight degree-of-freedom system considered in this study, $x = [x_1 \ x_2 \ x_3 \ \dots \ x_{16}]^T$ where $x_9 = \dot{x}_1 = f_1(x)$, $x_{10} = \dot{x}_2 = f_2(x)$ and so on. $f(x)$ is vector functions composed of first order differential equations that can be non-linear, $[B]$ is the controller coefficient matrix and $u = [u_1 \ u_2 \ u_3 \ u_4 \ u_5]^T$ is the control input vector written for the most general case in this study. $f(x)$ and $[B]$ are given in the Appendix along with the nomenclature of vehicle parameters. Mathematically, u_1 , u_2 , u_3 and u_4 do not have to exist together. In order to control vehicle body motions, three controller forces are sufficient since the body has three degrees of freedom in this study. These are bounce, pitch and roll motions. But, for practical reasons, four controllers parallel to the suspensions are introduced. The yaw motion is neglected. Finally, five controllers are used including the one under the passenger seat.

As mentioned before, the major non-linearity of the model comes from dry friction on the dampers. Geometric non-linearity has also been included. Dry friction on the dampers depends on the relative speed (V_r) between related damper ends. Experiments show that the dry friction model (Figure 2) has a viscous band character rather than being of a classical bang-bang type. The band ε is very small, and this prevents the complete locking of the suspension ends. For vehicle traveling with a low speed on a road with relatively low roughness generate dry friction force $f(V_r)$ around $\pm R$ that practically locks the suspension generating a high equivalent viscous friction effect. Dry friction parameters are $R=22$ N and $\varepsilon=0.0012$ m/s.

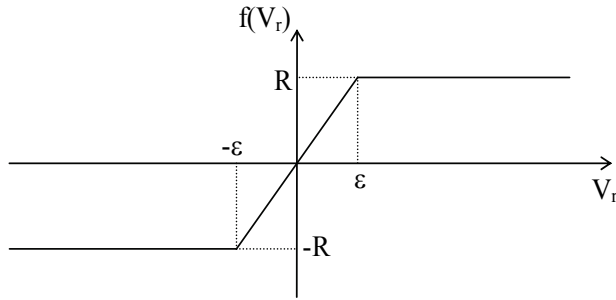


Fig. 2. Dry friction model

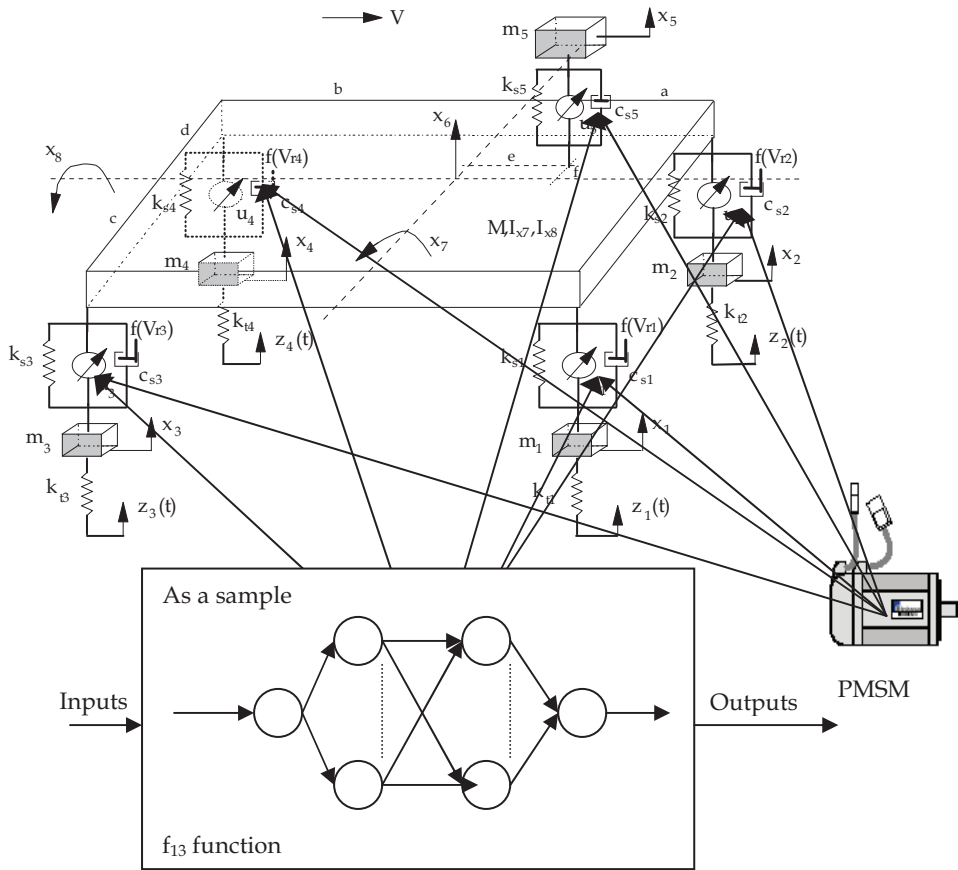


Fig. 3. The adaptation of NN controller closed form to the non-linear full vehicle model. Fast Back-propagation Algorithm (FBA) which is proposed by (Karayiannis & Venetsanopoulos, 1993) is used in the study.

3. Neural Network (NN) controller design

The Neural Network control is basically non-linear and adaptive in nature, giving robust performance under parameter variation and load disturbance effect. The main idea behind proposing a neural network controller on vehicles is its simplicity, satisfactory performance and the ability. Neural Networks are successfully used in variety applications areas such as control and early detection of machine faults. The feed-forward neural network is usually trained by a back-propagation training algorithm first proposed by (Rumelhart et al, 1986). This was the starting point of the effective usage of NNs after the 1980s. With the advantage of high speed computational technology, NNs are more realistic, easily updateable and implementable today. The distributed weights in the network contribute to the distributed intelligence or associative memory property of the network. The actual output pattern is compared with the desired output pattern and the weights are adjusted by the supervised back-propagation training algorithm until the pattern matching occurs, i.e., the pattern errors become acceptably small.

The impressive advantages of NNs are the capability of solving highly non-linear and complex problems and the efficiency of processing imprecise and noisy data.

Figure 3 shows the adaptation of the closed form of NN controller to the non-linear full car model with a passenger seat. The control forces are produced by PMSM.

4. Simulation part

In this study, the code of the tool written in C++ and Matlab with Simulink are used. The aim of the neural network control system for the vehicle system uses the functions from f_1 to f_{16} in the vehicle motions as the output variable while the variables of the other side of the equations of f_1 - f_{16} in the Appendix are their inputs. Figure 4 shows the general operating block diagram of a NN algorithm.

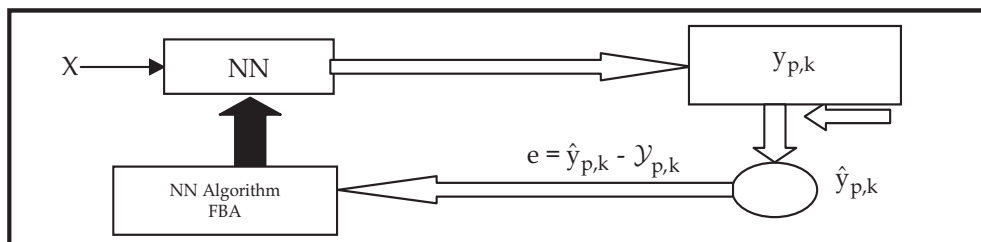


Fig. 4. Closed loop general block diagram of a neural network algorithm.

In this study, the FBA is used in the NN structure. The Neural Network input and output functions for the full vehicle system with passenger seat are given in Figure 5. The controllers have the following structures in Table 1.

In this study, NN controller is applied to a non-linear full vehicle model including Figure 5.

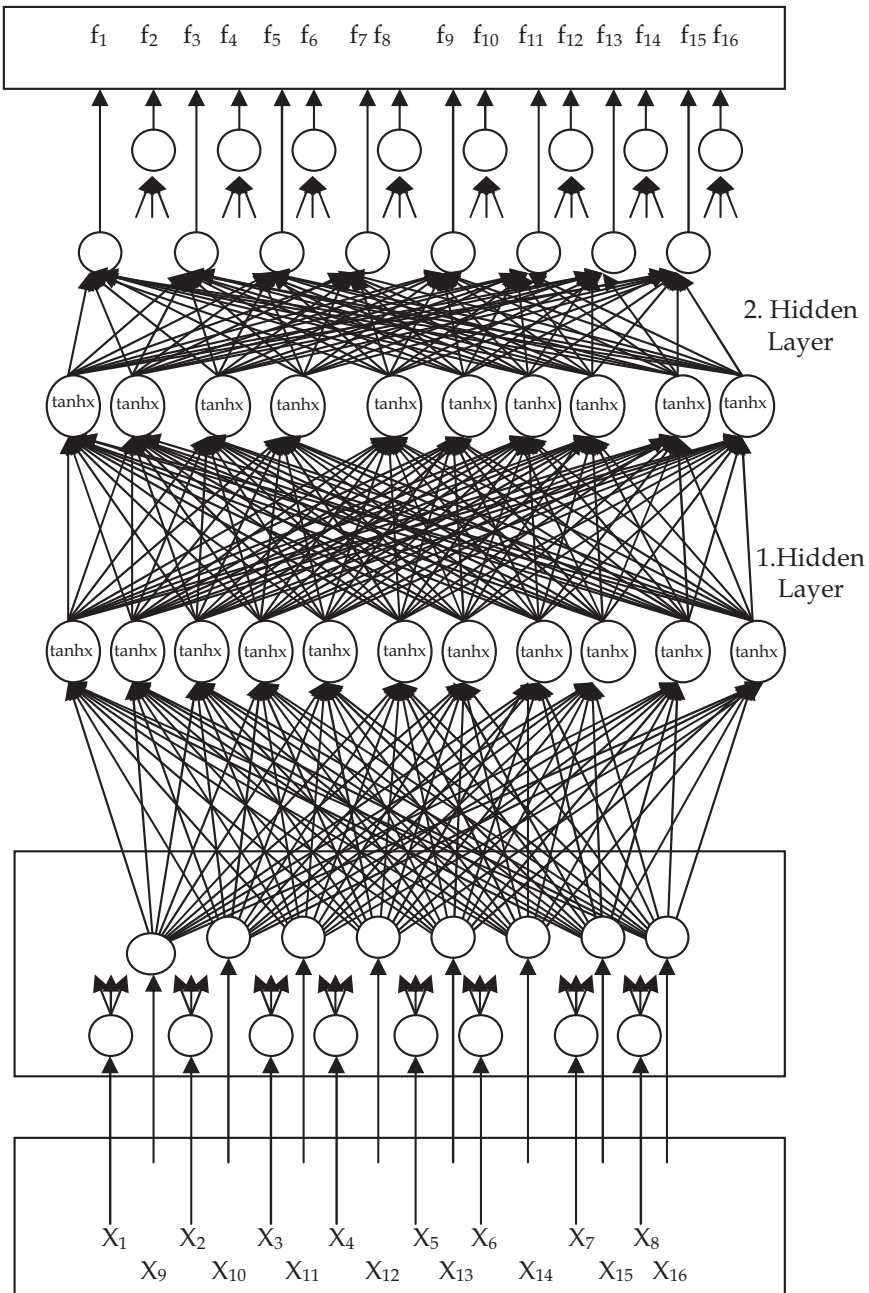


Fig. 5. Neural Network structure for the full vehicle control.

The Corresponding Variable	Number of Inputs	Number of Nodes in Hidden Layer-1	Number of Nodes in Hidden Layer-2	Number of Outputs	Generalized System Error (%)
f ₁	1	4	3	1	0
f ₂	1	4	3	1	0
f ₃	1	4	3	1	0
f ₄	1	4	3	1	0
f ₅	1	4	3	1	0
f ₆	1	4	3	1	0
f ₇	1	4	3	1	0
f ₈	1	4	3	1	0
f ₉	7	10	9	1	0
f ₁₀	7	10	9	1	0
f ₁₁	8	11	10	1	0
f ₁₂	8	11	10	1	0
f ₁₃	6	9	8	1	0
f ₁₄	15	18	17	1	0
f ₁₅	15	18	17	1	0
f ₁₆	15	18	17	1	0

Table 1. The structures of NN controllers for each function.

4.1 Time response of the non-linear vehicle model

In the simulation stage, first the non-linear model is used in order to obtain time responses. Second, for the frequency responses, the non-linear dry friction model is linearized using a describing function method. Accelerometers are used as sensors. These sensors are placed only to measure the states to be controlled. The data provided by these sensors are processed by micro-controllers having the NN algorithms designed. Here, the vehicle is assumed to travel over the bump road surface (Figure 6). The road bump parameters are $h = 0.035$ m and $L = 0.025$ m.

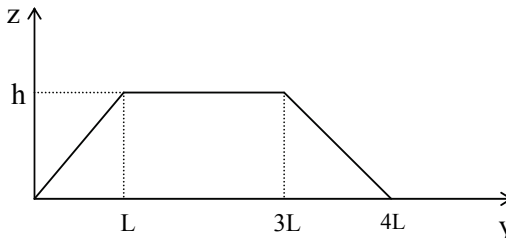


Fig. 6. Road disturbance.

There is a time delay between the front and rear wheel inputs. This time delay is as follows:

$$\delta(t) = (a + b)/V \tag{4}$$

where $(a + b)$ is the distance between the front and rear axles and V is the velocity of the vehicle. Table 2 gives the NN test phase results for all functions, separately. Comparison diagrams of NN controller results and uncontrolled values are depicted in Figure 7. As to be seen from Table 2, all of the NN test phase results in Figure 7 are very good harmony with

the uncontrolled ones. The momentum and learning rates are 0,7 and 0,9 respectively. The number of iteration for training phase is 3000000, and the number of hidden layer is 2. The

$f_1(x'_1)$	f_1	$f_2(x'_2)$	f_2	$f_3(x'_3)$	f_3	$f_4(x'_4)$	f_4
Uncontrolled Values	NN Results	Uncontrolled Values	NN Results	Uncontrolled Values	NN Results	Uncontrolled Values	NN Results
-0.2	-0.204308	-0.35	-0.3482	-0.0052	-0.004826	0.004	0.003139
0	0	-0.01	-0.010068	-0.0041	-0.003805	-0.0018	-0.001855
0	0	0	0	-0.0026	-0.002412	-0.0013	-0.001425
0	0	0	0	-0.0029	-0.002691	0.0018	0.001244
0	0	0	0	-0.0029	-0.002691	-0.0031	-0.002974
0	0	0	0	-0.0027	-0.002505	-0.002	-0.002027
0	0	0	0	0.001	0.00093	-0.0019	-0.001941

$f_5(x'_5)$	f_5	$f_6(x'_6)$	f_6	$f_7(\theta')$	f_7	$f_8(\alpha')$	f_8
Uncontrolled Values	NN Results	Uncontrolled Values	NN Results	Uncontrolled Values	NN Results	Uncontrolled Values	NN Results
0.017	0.016104	-0.028	-0.02744	0.1	0.098095	-0.006	-0.00573
0.007	0.006631	-0.001	-0.00098	-0.002	-0.001966	-0.004	-0.003822
0.012	0.011368	-0.001	-0.00098	-0.001	-0.000983	-0.001	-0.000959
-0.0025	-0.002371	0	0	0	0	0	-0.000004
0.0009	0.000851	0	0	0	0	0.001	0.00095
0	-0.000002	0	0	0	0	0	-0.000004
0	-0.000002	0	0	0	0	0	-0.000004

$f_9(x''_1)$	f_9	$f_{10}(x''_2)$	f_{10}	$f_{11}(x''_3)$	f_{11}	$f_{12}(x''_4)$	f_{12}
Uncontrolled Values	NN Results	Uncontrolled Values	NN Results	Uncontrolled Values	NN Results	Uncontrolled Values	NN Results
-49.99911	-50	-15.01661	-15	-0.4	-0.399975	0.37	0.370004
-9.947977	-10	-7.896958	-8	-0.2	-0.199977	-0.3	-0.300001
-0.920222	0	-0.581933	0	0.63	0.688073	-0.56	-0.622842
-0.324225	0	-0.182448	0	-0.6	-0.613647	0.52	0.447904
-0.197652	0	-0.323465	0	-0.5	-0.541713	0.59	0.512811
-0.336008	0	-0.230341	0				

$f_{13}(x''_5)$	f_{13}	$f_{14}(x''_6)$	f_{14}	$f_{15}(\theta'')$	f_{15}	$f_{16}(\alpha'')$	f_{16}
Uncontrolled Values	NN Results	Uncontrolled Values	NN Results	Uncontrolled Values	NN Results	Uncontrolled Values	NN Results
0.13	0.13	-0.8	-0.8	-0.1	-0.099969	-0.25	-0.249997
-0.15	-0.15	-0.5	-0.499998	-0.05	-0.049979	0	0.000003
0.02	0.003019	0	-0.031477	0.1	0.081286	0.1	0.121414
0.01	0.00281	0	-0.000726	-0.001	-0.012811	0.02	0.02012
0	-0.01114	-0.001	0.000546	-0.0012	-0.002351	-0.001	0.001679
		-0.001	0.000443	-0.0012	0.000695	-0.0013	-0.005978
		-0.001	0.00035	-0.0012	-0.000332	-0.0013	0.001662

Table 2. The NN test phase results for all functions

number of hidden nodes in hidden layers are given in Table 1, respectively. The level of error shows that NN controller has a good approximation to control the system parameter and functions, since the generalized system error for all variables in Table 1 is % 0.

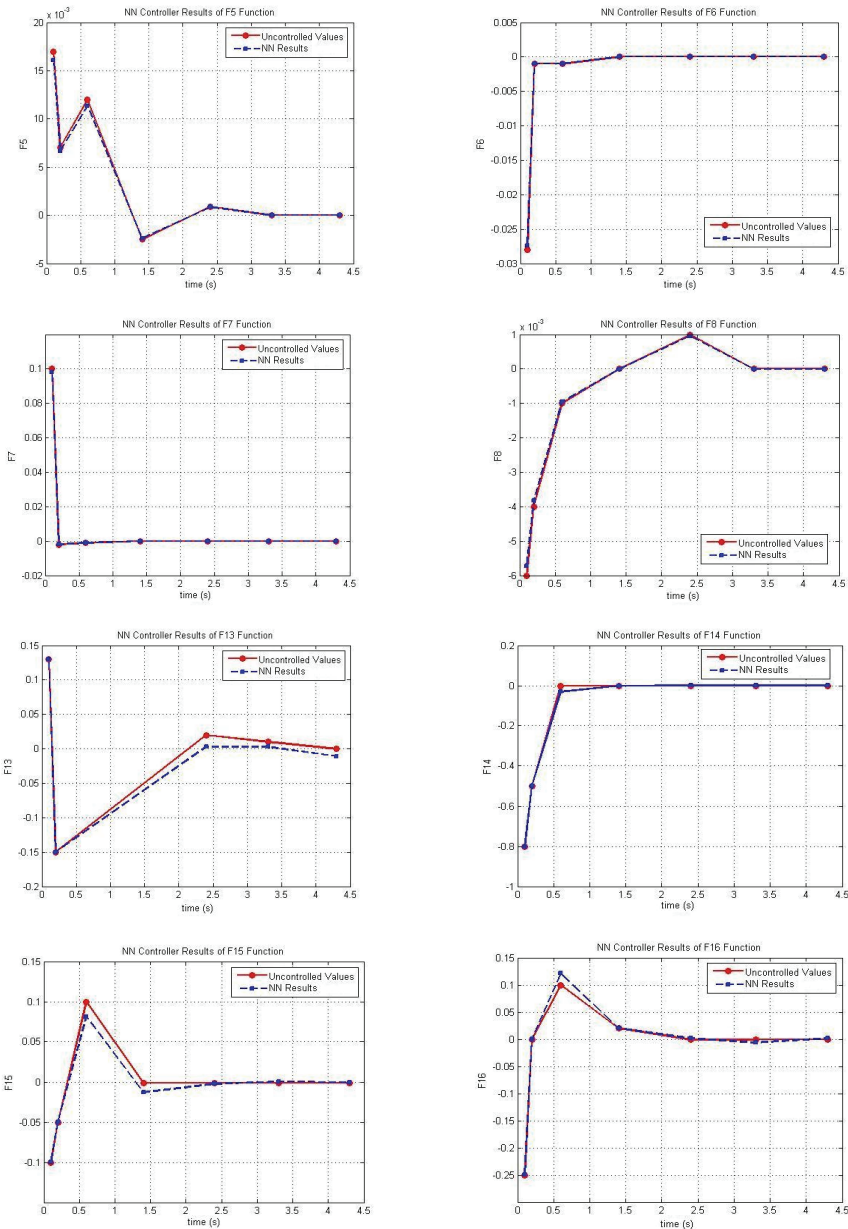


Fig. 7. Neural Network (NN) Controller results comparing with uncontrolled values.

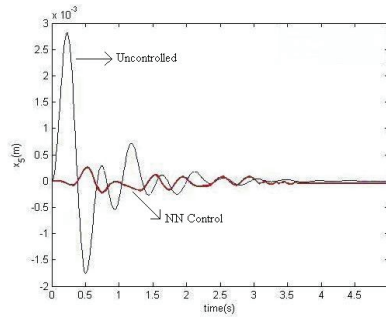


Fig. 8. Neural Network (NN) Controller results of passenger seat displacement for $u_5=0$.

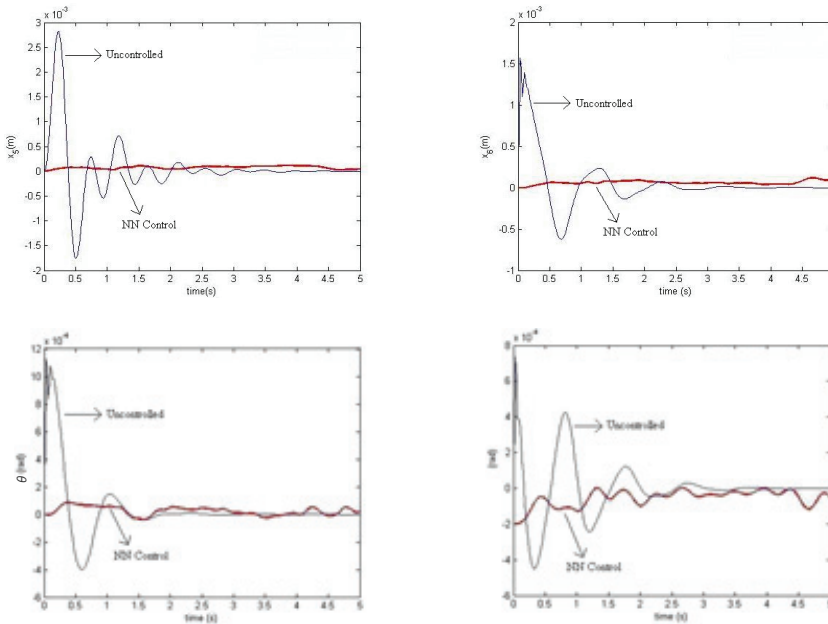


Fig. 9. Time responses of passenger seat and vehicle body displacements, pitch and roll angular displacements for controlled and uncontrolled cases.

“Figure 8 shows plot of x_5 without passenger seat controller ($u_5=0$). Since the other controllers are active, u_5 controller force of 9 N for the passenger seat is enough. If the seat controller is eliminated ($u_5=0$) and other controllers are kept, the results changes as in Figure 8.” The time responses of passenger seat and vehicle body displacements, pitch and roll angular displacements for NN controlled and uncontrolled cases of the non-linear vehicle are shown in Figure 9. The maximum displacements of the active system are less than those of the passive system, and the active system returns to rest faster. All displacements are successfully controlled by the proposed NN controller as well. The stick-slip effect of dry friction non-linearity having an offset in Figure 9 is observed for the uncontrolled case. This undesired effect is considerably overcome by NN controller as shown in the same figure.

“The passenger is almost isolated from the disturbance, since the all controllers are active. Here, maximum displacements of passenger seat for uncontrolled and NN controlled cases are $2,8 \cdot 10^{-3}$ m and $0,2 \cdot 10^{-3}$ m, respectively.”

The vertical acceleration of the passenger is also an important criterion, which mainly affects ride comfort since the force generated by the inertia of the passenger creates disturbances. In other words, minimizing the vertical displacement may not mean an improvement in itself alone, as an improvement in the acceleration is also obtained. In Figure 10, the acceleration of the passenger in the non-linear vehicle model is shown. The NN controller decreases the amplitude of the acceleration when compared with the uncontrolled one.

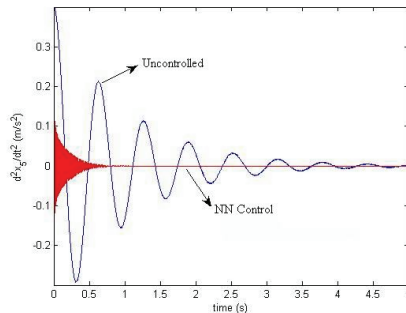


Fig. 10. Time responses of passenger seat vertical acceleration.

Another criterion is the control forces used since it is directly related with the cost of the controller. Figure 11 shows the controller force inputs. The front and rear suspensions apply a maximum force of about 4000 N. The amount of force applied to the passenger seat decreases since the body is controlled and the passenger seat is slightly isolated. A 9 N maximum force in addition to the other controller forces is sufficient to bring the passenger to the reference value of zero displacement.

4.2 Frequency response of the vehicle model

Frequency response analysis is the main tool in interpreting the dynamic behavior of vehicles. Since the frequency response plot of a non-linear system is dependent on input and is not unique, the dry friction model is linearized in frequency response analysis. Linearization without ignoring non-linearity is achieved by using the describing function method for dry friction on dampers and assuming that the vehicle body angular motions are small. In this technique, the effect of a non-linear dry friction model is replaced by a linear equivalent damping coefficient (C_e) obtained by the describing function method (Appendix). The frequency responses of the uncontrolled condition are compared with NN controller frequency response of the frame. In Figure 12, the frequency response plots of the passenger seat displacements and accelerations are considered. Two visual groups of displacement resonance frequencies in the uncontrolled case at approximately 2 and 15 Hz are observed in logarithmic plots. These frequencies belong to the vehicle system. In the NN controlled cases, the amplitudes of resonance frequencies of the vehicle system decrease. Actually, the vehicle model has eight resonance frequencies. The values of the related natural frequencies are obtained by solving the eigenvalue problem using Matlab. These values are 0.975, 1.183, 1.396, 2.202, 12.261, 12.264, 16.387 and 16.388 Hz. Since the natural frequencies are very close

to each other, only two visual groups are seen in Figure 12. Using controllers under the vehicle body and passenger seat gives the maximum displacement and acceleration isolation for the passenger as shown in the figures.

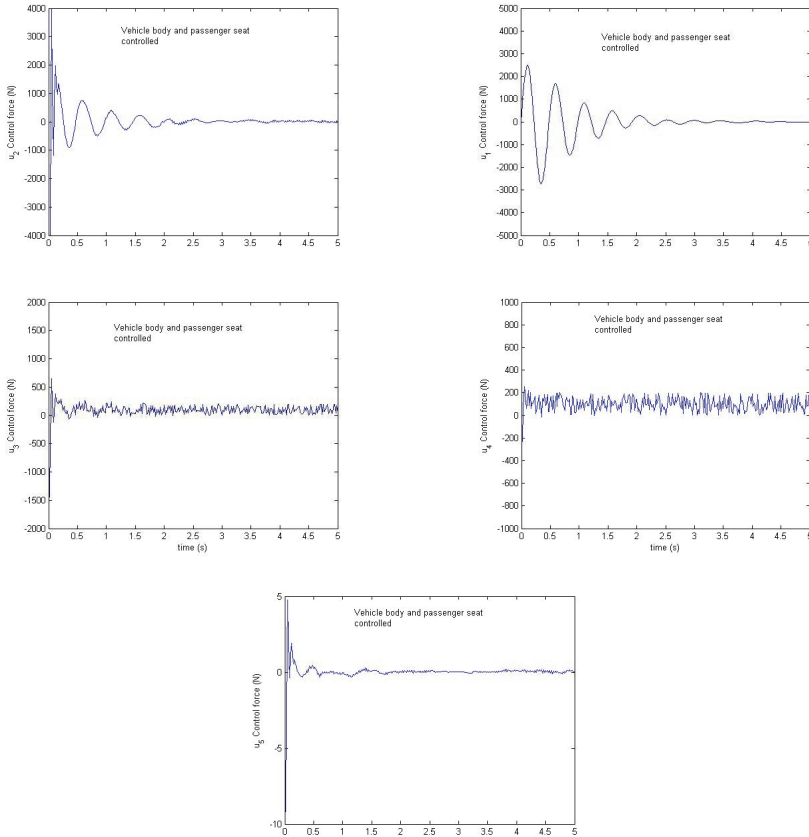


Fig. 11. NN Control force inputs.

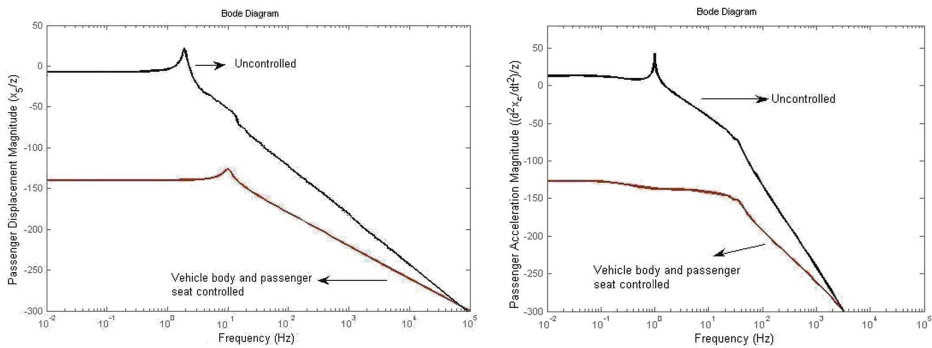


Fig. 12. Frequency response plots of passenger displacements and accelerations.

5. Conclusions

The aim of this study was the development of a Neural Network (NN) based controller for vibrations of a non-linear eight-degree-of-freedom vehicle model with active suspensions. This controller, which had a very good performance for the results both in time and frequency responses, has been applied to the vehicle. Only having controllers under the vehicle body without u_5 does not provide a good control over passenger comfort. The simulation results prove that, using controllers under the vehicle body and passenger seat provided excellent ride comfort. Therefore, this strategy should be taken into account by considering the control of the vehicle body and passenger seat together. Using this strategy, the bounce motion of the passenger reduces with an extra controller that applies very small force input, since the other controllers are active. If the passenger seat controller is eliminated and only other controllers are kept, the vibrations increase. A successful improvement has also been obtained in the isolation of the vertical acceleration of passengers. Frequency response plots of a passenger for this strategy support the results obtained. In conclusion, adding a controller under the passenger seat in addition to the other controllers improves ride comfort considerably. The decrease in vibration amplitudes and the excellent improvement in resonance values support this result.

6. Nomenclature

Vehicle variables

a, b	distances of axle to the center of gravity of the vehicle body (m)
c, d	distances of unsprung masses to the center of gravity of the axles (m)
e, f	distances of passenger seat to the center of gravity of the vehicle body (m)
c_{si}	i th damping coefficient of suspension (Ns/m)
c_{s5}	damping coefficient of passenger seat (Ns/m)
$f(V_{ri})$	i th dry friction force (N)
k_{si}	i th spring constant of suspension (N/m)
k_{s5}	spring constant of passenger seat (N/m)
k_{ti}	i th stiffness coefficient of tire (N/m)
m_i	i th mass of axle (kg)
m_5	mass of the passenger (kg)
x_i	i th state variable (m)
$z_i(t)$	i th road excitation (m)
I_{x7}	mass moment of inertia of the vehicle body for pitch motion (kgm ²)
I_{x8}	mass moment of inertia of the vehicle body for roll motion (kgm ²)
M	mass of the vehicle body (kg)

7. Appendix

The parameters of the vehicle:

$M = 1100$ kg
$I_{x7} = 1848$ kg.m ²
$I_{x8} = 550$ kg.m ²
$m_1 = m_2 = 25$ kg
$m_3 = m_4 = 45$ kg
$m_5 = 90$ kg

$$k_{s1} = k_{s2} = 15000 \text{ N/m}$$

$$k_{s3} = k_{s4} = 17000 \text{ N/m}$$

$$k_{s5} = 15000 \text{ N/m}$$

$$c_{s1} = c_{s2} = c_{s3} = c_{s4} = 2500 \text{ N.s/m}$$

$$c_{s5} = 150 \text{ N.s/m}$$

$$k_{t1} = k_{t2} = k_{t3} = k_{t4} = 250000 \text{ N/m}$$

$$a = 1.2 \text{ m}$$

$$b = 1.4 \text{ m}$$

$$c = 0.5 \text{ m}$$

$$d = 1.0 \text{ m}$$

$$e = 0.3 \text{ m}$$

$$f = 0.25 \text{ m}$$

Dry friction force and linear equivalent damping coefficient:

$$f(V_{r_i}) = C e_i (\dot{y}_i - \dot{x}_i) \quad (i = 1 \dots 5)$$

$$C e_i = \begin{cases} n & \text{if } \left| \dot{y}_i - \dot{x}_i \right| < \varepsilon \\ \frac{n}{\pi} (2\theta_i - \sin 2\theta_i) + \frac{4R}{\pi \left| \dot{y}_i - \dot{x}_i \right|} \cos \theta_i & \text{else} \end{cases}$$

$$\theta_i = \sin^{-1} \frac{\varepsilon}{\left| \dot{y}_i - \dot{x}_i \right|}$$

$$y_1 = x_6 + a \sin x_7 - c \sin x_8$$

$$y_2 = x_6 + a \sin x_7 + d \sin x_8$$

$$y_3 = x_6 - b \sin x_7 - c \sin x_8$$

$$y_4 = x_6 - b \sin x_7 + d \sin x_8$$

$$y_5 = x_6 + e \sin x_7 + f \sin x_8$$

State equations excluding control inputs:

$$f_1(x) = x_9, \quad f_2(x) = x_{10}, \quad f_3(x) = x_{11}, \quad f_4(x) = x_{12}$$

$$f_5(x) = x_{13}, \quad f_6(x) = x_{14}, \quad f_7(x) = x_{15}, \quad f_8(x) = x_{16}$$

$$f_9(x) = 1/m_1 \{ -(k_{s1} + k_{t1})x_1 + k_{s1}x_6 + a k_{s1} \sin x_7 - c k_{s1} \sin x_8 - c_{s1}x_9 + c_{s1}x_{14} \\ + a c_{s1} \cos x_7 x_{15} - c c_{s1} \cos x_8 x_{16} + k_{t1}z_1 + f(V_{r1}) - u_1 \}$$

$$f_{10}(x) = 1/m_2 \{ -(k_{s2} + k_{t2})x_2 + k_{s2}x_6 + a k_{s2} \sin x_7 + d k_{s2} \sin x_8 - c_{s2}x_{10} + c_{s2}x_{14} \\ + a c_{s2} \cos x_7 x_{15} + d c_{s2} \cos x_8 x_{16} + k_{t2}z_2 + f(V_{r2}) - u_2 \}$$

$$f_{11}(x) = 1/m_3 \{ -(k_{s3} + k_{t3})x_3 + k_{s3}x_6 - b k_{s3} \sin x_7 - c k_{s3} \sin x_8 - c_{s3}x_{11} + c_{s3}x_{14} \\ - b c_{s3} \cos x_7 x_{15} - c c_{s3} \cos x_8 x_{16} + k_{t3}z_3 + f(V_{r3}) - u_3 \}$$

$$f_{12}(x) = 1/m_4 \{ -(k_{s4} + k_{t4})x_4 + k_{s4}x_6 - b k_{s4} \sin x_7 + d k_{s4} \sin x_8 - c_{s4}x_{12} + c_{s4}x_{14} \\ - b c_{s4} \cos x_7 x_{15} + d c_{s4} \cos x_8 x_{16} + k_{t4}z_4 + f(V_{r4}) - u_4 \}$$

$$f_{13}(x) = 1/m_5 \{ -k_{s5}x_5 + k_{s5}x_6 + e k_{s5} \sin x_7 + f k_{s5} \sin x_8 - c_{s5}x_{14} + c_{s5}x_{14} \\ + e c_{s5} \cos x_7 x_{15} + f c_{s5} \cos x_8 x_{16} + u_5 \}$$

$$f_{14}(x) = 1/M \{ k_{s1} x_1 + k_{s2} x_2 + k_{s3} x_3 + k_{s4} x_4 + k_{s5} x_5 - (k_{s1} + k_{s2} + k_{s3} + k_{s4} + k_{s5}) x_6 \\ - (a(k_{s1} + k_{s2}) - b(k_{s3} + k_{s4}) + e k_{s5}) \text{Sin} x_7 - (d(k_{s2} + k_{s4}) - c(k_{s1} + k_{s3}) + f k_{s5}) \text{Sin} x_8 \\ + c_{s1} x_9 + c_{s2} x_{10} + c_{s3} x_{11} + c_{s4} x_{12} + c_{s5} x_{13} - (c_{s1} + c_{s2} + c_{s3} + c_{s4} + c_{s5}) x_{14} \\ - (a(c_{s1} + c_{s2}) - b(c_{s3} + c_{s4}) + e c_{s5}) \text{Cos} x_7 x_{15} - (d(c_{s2} + c_{s4}) - c(c_{s1} + c_{s3}) + f c_{s5}) \text{Cos} x_8 x_{16} \\ - f(V_{r1}) - f(V_{r2}) - f(V_{r3}) - f(V_{r4}) + u_1 + u_2 + u_3 + u_4 - u_5 \}$$

$$f_{15}(x) = 1/I_{x7} \{ a k_{s1} x_1 + a k_{s2} x_2 - b k_{s3} x_3 - b k_{s4} x_4 + e k_{s5} x_5 - (a(k_{s1} + k_{s2}) - b(k_{s3} + k_{s4}) + e k_{s5}) x_6 \\ - (a^2(k_{s1} + k_{s2}) + b^2(k_{s3} + k_{s4}) + e^2 k_{s5}) \text{Sin} x_7 - (d(a k_{s2} - b k_{s4}) - c(a k_{s1} - b k_{s3}) + e f k_{s5}) \text{Sin} x_8 \\ + a c_{s1} x_9 + a c_{s2} x_{10} - b c_{s3} x_{11} - b c_{s4} x_{12} + e c_{s5} x_{13} - (a(c_{s1} + c_{s2}) - b(c_{s3} + c_{s4}) + e c_{s5}) x_{14} \\ - (a^2(c_{s1} + c_{s2}) + b^2(c_{s3} + c_{s4}) + e^2 c_{s5}) \text{Cos} x_7 x_{15} - (d(a c_{s2} - b c_{s4}) - c(a c_{s1} - b c_{s3}) + e f c_{s5}) \text{Cos} x_8 x_{16} \\ - a f(V_{r1}) - a f(V_{r2}) + b f(V_{r3}) + b f(V_{r4}) + a(u_1 + u_2) - b(u_3 + u_4) - e u_5 \} \text{Cos} x_7$$

$$f_{16}(x) = 1/I_{x8} \{ -c k_{s1} x_1 + d k_{s2} x_2 - c k_{s3} x_3 + d k_{s4} x_4 + f k_{s5} x_5 - (d(k_{s2} + k_{s4}) - c(k_{s1} + k_{s3}) + f k_{s5}) x_6 \\ - (d(a k_{s2} - b k_{s4}) - c(a k_{s1} - b k_{s3}) + e f k_{s5}) \text{Sin} x_7 - (d^2(k_{s2} + k_{s4}) + c^2(k_{s1} + k_{s3}) + f^2 k_{s5}) \text{Sin} x_8 \\ - c c_{s1} x_9 + d c_{s2} x_{10} - c c_{s3} x_{11} + d c_{s4} x_{12} + f c_{s5} x_{13} - (d(c_{s2} + c_{s4}) - c(c_{s1} + c_{s3}) + f c_{s5}) x_{14} \\ - (d(a c_{s2} - b c_{s4}) - c(a c_{s1} - b c_{s3}) + e f c_{s5}) \text{Cos} x_7 x_{15} - (d^2(c_{s2} + c_{s4}) + c^2(c_{s1} + c_{s3}) + f^2 c_{s5}) \text{Cos} x_8 x_{16} \\ - c f(V_{r1}) + d f(V_{r2}) - c f(V_{r3}) + d f(V_{r4}) - c(u_1 + u_3) + d(u_2 + u_4) - f u_5 \} \text{Cos} x_8$$

The controller force matrix:

$$[B] = \begin{bmatrix} 0 & 0 & 0 & 0 \\ 0 & 0 & 0 & 0 \\ 0 & 0 & 0 & 0 \\ 0 & 0 & 0 & 0 \\ 0 & 0 & 0 & 0 \\ 0 & 0 & 0 & 0 \\ 0 & 0 & 0 & 0 \\ 0 & 0 & 0 & 0 \\ \frac{bd}{(a+b)(c+d)m_1} & \frac{d}{(a+b)(c+d)m_1} & \frac{1}{(c+d)m_1} & \frac{-d(b+e)+f(a+b)}{(a+b)(c+d)m_1} \\ \frac{bc}{(a+b)(c+d)m_2} & \frac{c}{(a+b)(c+d)m_2} & \frac{1}{(c+d)m_2} & \frac{-c(b+e)-f(a+b)}{(a+b)(c+d)m_2} \\ \frac{ad}{(a+b)(c+d)m_3} & \frac{d}{(a+b)(c+d)m_3} & 0 & \frac{d(a-e)}{(a+b)(c+d)m_3} \\ \frac{ac}{(a+b)(c+d)m_4} & \frac{c}{(a+b)(c+d)m_4} & 0 & \frac{c(a-e)}{(a+b)(c+d)m_4} \\ 0 & 0 & 0 & \frac{1}{m_5} \\ \frac{1}{M} & 0 & 0 & 0 \\ 0 & \frac{1}{I_{x7}} & 0 & 0 \\ 0 & 0 & \frac{1}{I_{x8}} & 0 \end{bmatrix}$$

8. References

- Redfield, R.C. & Karnopp, D.C. (1988). Optimal performance of variable component suspensions, *Vehicle System Dynamics* 17, pp 231-253.
- Yue, C.; Butsuen, T. & Hedrick, J.K. (1989). Alternative control laws for automotive active suspensions, *Journal of Dynamic Systems, Measurement and Control* 111, pp. 286-291
- Stein, G.J. & Ballo, I. (1991). Active vibration control system for the driver's seat for off-road vehicles, *Vehicle System Dynamics* 20, pp. 57-78.
- Hac, A. (1992). Optimal linear preview control of active vehicle suspension, *Vehicle System Dynamics* 21, pp. 167-195.
- Rakheja, S., Afework, Y. & Sankar, S. (1994). An analytical and experimental investigation of the driver-seat-suspension system, *Vehicle System Dynamics* 23, pp. 501-524.
- Crolla, D.A. & Abdel Hady, M.B.A.,(1991). Active suspension control; Performance comparisons using control laws applied to a full car model, *Vehicle System Dynamics* 20, pp. 107-120.
- Hrovat, D. (1993). Applications of optimal control to advanced automotive suspension design, *Journal of Dynamic Systems, Measurement, and Control* 115, 328-342.
- Silvester, B.C. (1966). Vibration reduction in motor cars, *Soc. Environmental Engineers* 4.
- Alleyne, A.; Neuhaus, P.D. & Hedrick, J.K. (1993). Application of non-linear control theory to electronically controlled suspensions, *Vehicle System Dynamics* 22, pp. 309-320.
- Park, J.H. & Kim, Y.S. (2000). Decentralized variable structure control of vehicle active suspensions, *JSME Mech. Systems, Machine Elements, Manufacturing* 43(1), pp. 73-79.
- Yokoyama, M.; Hedrick, J.K. & Toyama, S.(2001). A model following sliding mode controller for semi-active suspension systems with MR dampers, in *Proceedings of the American Control Conference*, pp. 2652-2657, Arlington, VA, 4, June 25-27.
- Yoshimura, T.; Kume, A.; Kurimoto, M. & Hino, J. (2001). Construction of an active suspension system of a quarter car model using the concept of sliding mode control, *Journal of Sound and Vibration* 239(2), pp. 187-199.
- Al-Holou, N.; Lahdhiri, T.; Joo, D.S.; Weaver, J. & Al-Abbas, F. (2002). Sliding mode neural network inference fuzzy logic control for active suspension systems, *IEEE Transactions on Fuzzy Systems* 10(2), pp. 234-246.
- Guclu, R. (2004). The Fuzzy Logic control of active suspensions without suspension-gap degeneration, *Strojnicki Vestnik*, 50, pp. 462-468.
- Guclu, R. (2005) Fuzzy Logic control of seat vibrations of a non-linear full vehicle model, *Nonlinear Dynamics*, 40, pp. 21-34.
- Guclu, R., Gulez K. (2008). Neural Network Control of Seat Vibrations of a Non-linear Full Vehicle Model using PMSM, *Mathematical and Computer Modelling*, 47(11-12), pp.1356-1371.
- Otten, G.; de Vries, T.J.A.; Rankers, A.M. & Gaal, E.W. (1997). Linear motor motion control using a learning feedforward controller, *IEEE Transactions on Mechatronics*, 2(3).
- Baumal, A.E.; McPhee, J.J. & Calamai, P.H. (1998). Application of genetic algorithms to the design optimization of an active vehicle suspension system, *Computer Methods in Applied Mechanics and Engineering* 163, pp. 87-94.
- Rumelhart, D. E.; Hinton, G. E & Williams, R. J. (1986). Learning representations by back-propagation errors, *Nature* 323, pp. 533-536.
- Karayiannis, N.B. & Venetsanopoulos A.N. (1993). In: *Artificial Neural Networks- Learning Algorithms, Performance Evaluation and Applications*, Kluwer Academic Publishers.

Robust Active Vibration Control of Flexible Stewart Isolators

Liu Lei, Wang Pingping, Kong Xianren and Wang Benli
School of Astronautics, Harbin Institute of Technology, Harbin 150080, China

1. Introduction

There are increasing needs of precision pointing and extreme stability for current and future spacecrafts. The James Webb space telescope, terrestrial planet finder, space based laser, space-based interferometer and deep-space laser communication are such examples where the micro-radian pointing and nanometer level of motion stability are required by (Ford, et al, 2005), (Chen, et al, 2004) and (Winthrop, et al 2003). On the other hand, the space systems may contains many vibration sources. A satellite may contain multiple instruments; some of them may use reaction wheels, cryogenic coolers, control moment gyroscopes, solar array drives, stepper motors, and other motion devices. These devices will transmit vibrations.

Passive isolation presents a reliable, low cost solution that is effective for attenuating high frequency vibrations, but it is in general not suitable for low frequency vibration isolation, and especially, passive isolation can not provide good trade-off between resonant peak and high frequency attenuation and the trade-off between pointing command keeping and disturbance rejection. (Winthrop, et al 2003) indicates the active vibration control can overcome these limitations.

In order to achieve multi-DOF vibration isolation in broadband and precision pointing, the Stewart platform (or hexapod), especially the cubic one, has become one of the most popular approaches as in (Anderson, et al, 2000) and (Thayer, et al, 2002), as shown in Fig.1. The cubic hexapod simplifies the control topologies to allow the decoupled controller designs to be identical for each strut. In order to eliminate the micro dynamics (friction and backlash), flexure joints are generally used as in (Hanieh, 2003).

Jet Propulsion Laboratory, Air Force Research Laboratory, Naval Postgraduate School, University of Washington, Free University of Brussels, University of Wyoming, CSA Engineering Inc are very active in this research. Classic control, adaptive control, LQG control, neural control, simple robust control and other control approaches were studied by (Gawronski, et al, 2004), (Joshi, et al, 2005) and (Liu et al, 2008). In this chapter, H_∞ and μ controllers are designed for the struts of Stewart platforms, suppressing the overshoot in the neighborhood of resonance frequencies. Then the dynamic model of Stewart isolator is derived, and D-K iteration is used to solve the robust controller, finally, the time domain responses to suppress disturbance are also presented.

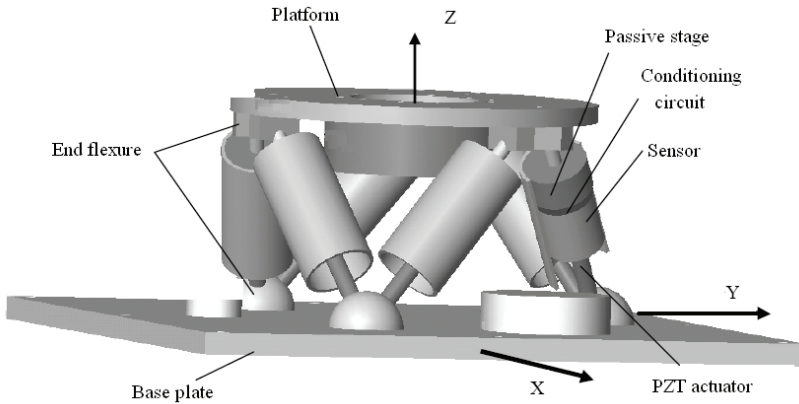


Fig. 1. Stewart platform with flexure joints

2. Dynamic model of active struts

The hexapod can be decoupled into six single-axis systems. Fig.2 shows a spring-mass model of a single strut, which can be represented as shown by equation (1-2), and the measuring output for control is the force of the strut on the side of payload. But the force due to the parasitic stiffness and damping, which represent the coupling between 6 struts, is not contained in the measuring output as in (Thayer, et al, 2002).

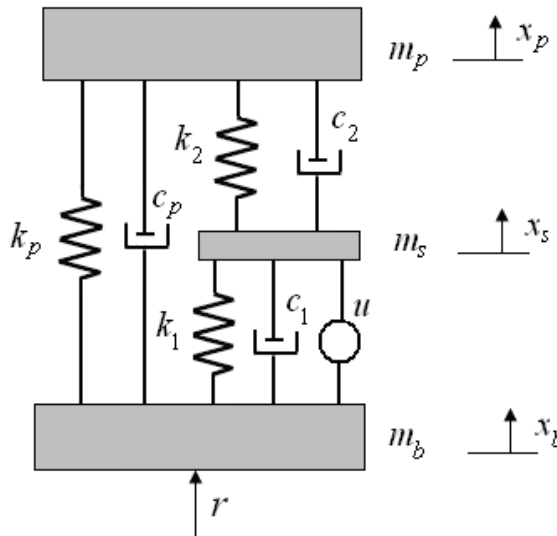


Fig. 2. Block diagram of the strut with PZT actuator

Where mass of base $m_b = 200\text{kg}$, mass of strut $m_s = 0.254\text{kg}$, Mass of payload $m_p = 20\text{kg}$, parasitic stiffness and damping $k_p = 760\text{N/m}$, $c_p = 2\text{kg/s}$; axis stiffness and damping of flexible joints $k_2 = 800000\text{N/m}$, $c_2 = 100\text{kg/s}$; stiffness and damping of the actuator

$k_1 = 80000000$ N/m, $c_1 = 100$ kg/s. u is the output of actuators, and r is the attitude control signal in addition with disturbance.

$$M\ddot{q} + D\dot{q} + Kq = f \quad (1)$$

$$y = C_q q + C_v \dot{q} \quad (2)$$

Where

$$\begin{aligned} q &= (x_b, x_s, x_p)^T \\ M &= \text{diag}([m_b, m_s, m_p]) \\ f &= \begin{pmatrix} 1 & 0 & 0 \\ 1 & -1 & 0 \end{pmatrix}^T \cdot \begin{bmatrix} r \\ u \end{bmatrix} \\ C_q &= [0 \quad -k_2 \quad k_2] \\ C_v &= [0 \quad -c_2 \quad c_2] \\ D &= \begin{pmatrix} c_1 + c_p & -c_1 & -c_p \\ -c_1 & c_1 + c_2 & -c_2 \\ -c_p & -c_2 & c_p + c_2 \end{pmatrix} \\ K &= \begin{pmatrix} k_1 + k_p & -k_1 & -k_p \\ -k_1 & k_1 + k_2 & -k_2 \\ -k_p & -k_2 & k_2 + k_p \end{pmatrix} \end{aligned}$$

Introducing the K and M in equation $\det(K - \omega^2 M) = 0$, the modal frequency matrix $\Omega = \text{diag}([w_1, w_2, w_3])$ is found as follows:

$$\Omega = \begin{pmatrix} 0 & 0 & 0 \\ 0 & 207.8 & 0 \\ 0 & 0 & 11670 \end{pmatrix} \quad (3)$$

Substituting Ω into $(K - \Omega^2 M)\Phi = 0$

$$\Phi = \begin{pmatrix} -0.5774 & -0.0015 & -0.0991 \\ -0.5774 & -0.9999 & -0.0777 \\ -0.5774 & 0.0003 & 0.9920 \end{pmatrix} \quad (4)$$

Introducing modal matrix Φ into equation (2), a modal equation is gotten, as shown in Equation (5). The symbols q_m , M_m , D_m and K_m are modal displacement, modal mass matrix, modal damping matrix and modal stiffness matrix.

$$\begin{cases} M_m \ddot{q}_m + D_m \dot{q}_m + K_m q_m = \Phi^T f \\ y = C_q \Phi q_m + C_v \Phi \dot{q}_m \end{cases} \quad (5)$$

Where

$$q_m = \Phi^{-1}q, D_m = \Phi^T D \Phi$$

$$M_m = \Phi^T M \Phi, K_m = \Phi^T K \Phi$$

It is seen that the first mode is a rigid mode, and the corresponding natural frequency is zero (in Ω). On the other hand, the singular value plot for the nodal model with parametric (stiffness and damping) uncertainty, as illustrated in Fig.3, a rigid mode can be found.

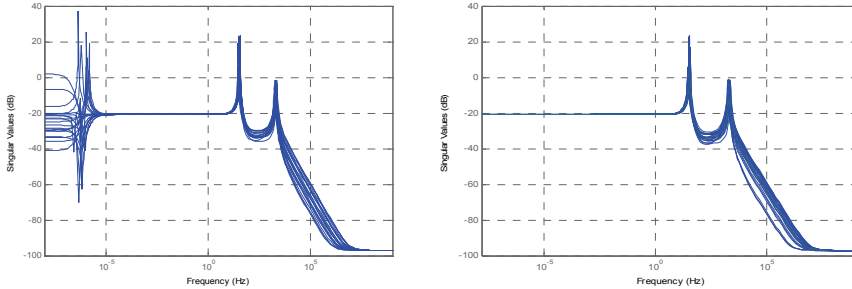


Fig. 3. Singular value plot for struts with and without rigid mode

The structures with rigid mode are unstable, but the rigid mode is the one that allows a controller to move the structures or track a command. So the rigid mode is removed when active vibration isolation controller is design. The singular value response for the dynamic model without rigid mode is shown in Fig.3, where the parametric uncertainty is also contained.

3. Robust synthesis controller design

The active vibration controller should be robust to the modeling uncertainty and parametric uncertainty, for the complex dynamic environment and model error. Robust H_∞ synthesis and μ synthesis are presented in this section, and the dynamic uncertainty is contained in the model, but the parameter uncertainty is also contained in the robust stability and performance test.

3.1 performance and system interconnection

The performance objective of this chapter is based on the strict requirements of future precision spacecrafts. The low frequency pointing signals must be fully transfer through the Stewart platform, but the high frequency disturbance (both harmonic and broadband), which will disturb the precision instruments, should be isolated. So the two strict requirements are as follows:

REQ1: Low frequencies pointing command (0-5Hz)

Keep pointing attenuation within ± 0.2 dB.

REQ2: Disturbance (>15Hz) and noise

Isolate the overshoot in the neighborhood of resonance frequencies 25dB, known as active damping, and isolate the noise 10dB.

The structure of closed-loop system is seen in Fig.4, G is the dynamic model without rigid mode, K is the controller to be designed, the weights describe the magnitude, relative

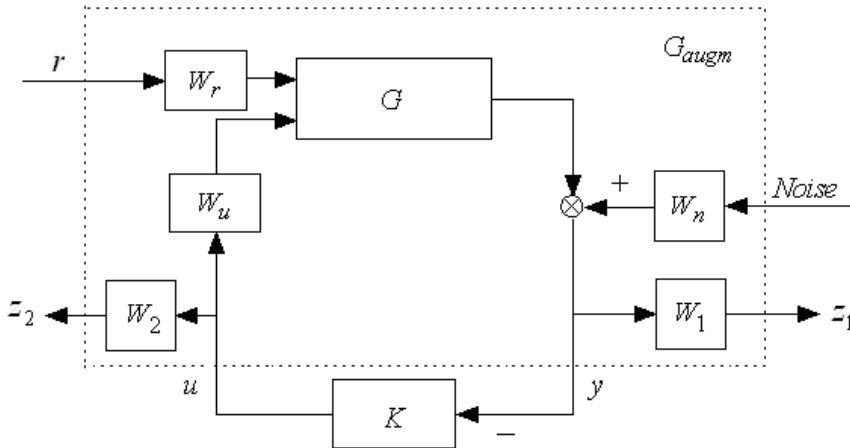


Fig. 4. Closed-loop system structure in robust design

importance and frequency content of inputs and outputs as in (Skogestad, etal, 2005). The performance weighting function W_1 reflects the relative significance of performance requirements over difference frequency ranges, because the maximum peak of G is 23 dB, so the maximum of W_1 should be more than 0dB to satisfy REQ1; the control weighting function W_2 avoids saturation of the PZT actuator and suppresses the high and low frequency gains, because the maximum force of actuators is 400N, the W_2 should be more than -52dB (1/400); the noise weighting function W_n is less than 0.3N in low frequency (<300Hz), but is 1N in high frequencies (>1000Hz); $W_n = 10$ is the disturbance weighting function. The weighting functions are selected as follows:

$$\begin{aligned}
 W_1 &= \frac{0.000445s^2 + 70s + 0.00022}{s^2 + 64.4s + 98.7} \\
 W_2 &= \frac{0.3s^2 + 154.2s + 18850}{s^2 + 62830s + 314.2} \\
 W_n &= \frac{s + 942.5}{s + 9425}
 \end{aligned}
 \tag{6}$$

The augmented plant G_{augm} is given by equation (7):

$$\begin{aligned}
 \dot{x} &= Ax + B_1w + B_2u \\
 z &= C_1x + D_{11}w + D_{12}u \\
 y &= C_2x + D_{21}w + D_{22}u
 \end{aligned}
 \tag{7}$$

Where $z = [z_1, z_2]^T$, $w = r$

The PZT stacks are very precision actuators, but they are typically not highly linear, for the nonlinear factors, such as hysteresis, creep and temperature effects, and in low frequencies the error can be 10%-15% of the full scale in open loop. And so the output uncertainty of the PZT stack is represented by W_u , as seen in equation (8)

$$W_u = 1 + \frac{1}{10} \cdot \frac{2094s + 10^6}{12.6s + 10^6} \cdot \Delta \quad (8)$$

Where is Δ the complex perturbation.

3.2 Controller design

The H_∞ synthesis is a mixed sensitivity H_∞ suboptimal control, based on DGKF method, and μ synthesis is based on $D - K$ iteration in (Skogestad, 2005). The following criterion is used for H_∞ synthesis:

$$\left\| \begin{array}{l} w_1(s)S(s) \\ w_2(s)T(s) \end{array} \right\|_{H_\infty} < \gamma \quad (9)$$

Where $S(s)$ and $T(s)$ are the sensitivity function and complementary sensitivity function respectively.

The $D - K$ iteration μ synthesis method is based on solving the following optimization problem, for a stabilizing controller K and a diagonal constant scaling matrix D .

$$K(s) = \arg \min_{K(s) \in \mathcal{K}_s} \sup_{\omega \in \mathbb{R}} \inf_{D(s) \in \mathcal{D}} \left\{ \bar{\sigma} \left(D(s)F_l(P, K)D^{-1}(s) \right) \right\} \quad (10)$$

Where P is the open loop interconnected transfer function matrix of the system.

The $D - K$ iteration procedure can be formulated as follows:

Step 1. Start with an initial guess for D , usually set $D = I$

Step 2. Fix D and solve the H_∞ sub-optimal $K(s)$

$$K(s) = \arg \min_{K(s) \in \mathcal{K}(s)} \|F_l(P, K)\|_{H_\infty} \quad (11)$$

Step 3. Fix $K_i(s)$ and solve the convex optimal problem for D^* at each frequency over a selected frequency range.

$$D^*(j\omega) = \arg \min_{D(s) \in \mathcal{D}} \left\{ \bar{\sigma} \left(D(s)F_l(P, K)D^{-1}(s) \right) \right\} \quad (12)$$

Step 4. Curve fit $D^*(j\omega)$ to get a stable, minimum phase D^* , and compare D^* and D , stop if they closed in magnitude, otherwise go to step 2 until the tolerance is achieved.

The achieved H_∞ norm γ is found to be 0.9932, and a 10th order controller is obtained. Correspondingly, the structured singular value μ is found to be 0.993, and a 12th order controller is obtained, and the bode magnitude of two controllers is in the Fig.5. During the control synthesis process, the weighting function W_1 and W_2 are adjusted repeatedly, a few trials are needed, and the final results are Equation (6).

The closed loop structure without performance weighting functions is shown in Fig.6, where G contains rigid mode.

The singular value plots for closed loops are shown in left Fig. 7, from which it can be seen that H_∞ and μ controllers isolate high frequency disturbance and noise, in the neighborhood of resonance frequencies. The disturbance and noise isolated by H_∞ controller is more than 27dB, and 21dB by μ controller. Right Fig. 7 shows that low frequency pointing fully transfer with attenuation less than 0.2dB. The nominal performance for H_∞ synthesis controller is better than μ synthesis controller at resonance, but worse in high frequencies.

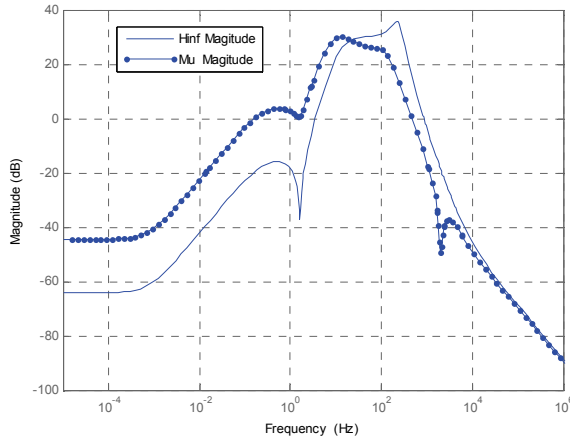


Fig. 5. Bode magnitude of the controllers

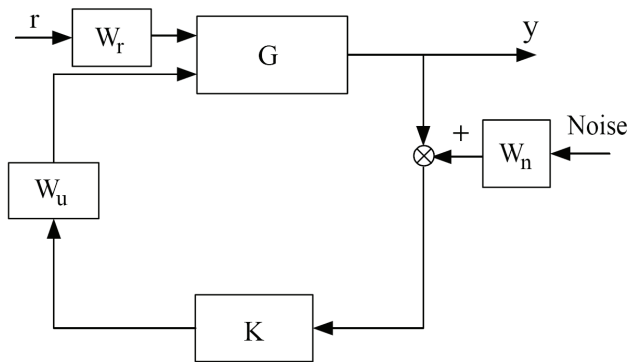


Fig. 6. Closed-loop system structure for frequency responses

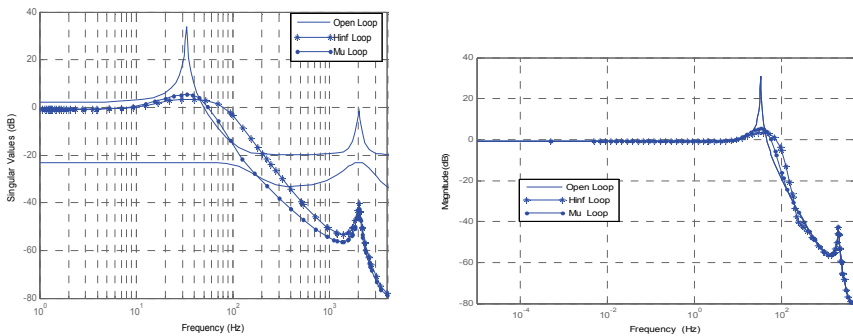


Fig. 7. Comparison of open loop and closed loop, Bode diagram from r to y

3.3 Robust stability analysis and controller reduction

Robust stability is very important due to various uncertainties^[22] and this section will give the robust stability margins of the uncertain closed loop. By calculating, the robust stability margin for H_∞ closed loop is 1.56, and the destabilizing frequency is 625.9rad/s, and the corresponding values are 6.29 and 346rad/s for μ closed loop. Their stability robustness margins greater than 1 means that the uncertain system is stable for all values of its modeled uncertainty. On the other hand, parametric uncertainty, which is 30% change in stiffness and 80% change in damping, is considered with modeling uncertainty in order to test the robust stability and robust performance further. Fig. 8 show the singular value plots for H_∞ and μ closed loop, from which it can be seen that robust stability and robust performance for H_∞ closed loop is worse than μ closed loop in presence of large uncertainty.

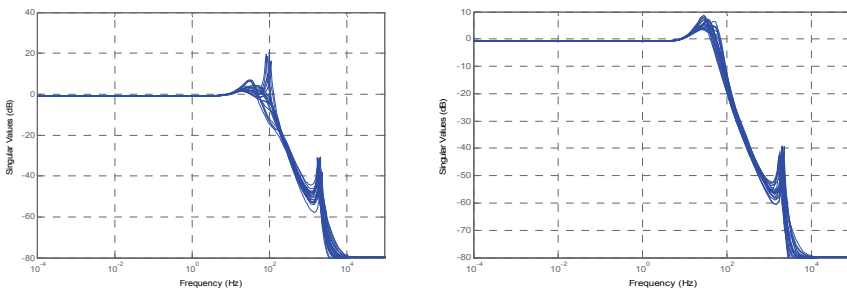


Fig. 8. Singular value plot for H_∞ closed loop and μ closed loop

As shown in section 3.2, the order of H_∞ controller is 10, and 12 of μ controller. Square root balanced model truncation, is used to reduce the order of controllers. Fig.9 shows the Bode diagrams for 6th order H_∞ controller and 8th order μ controller with their original controller.

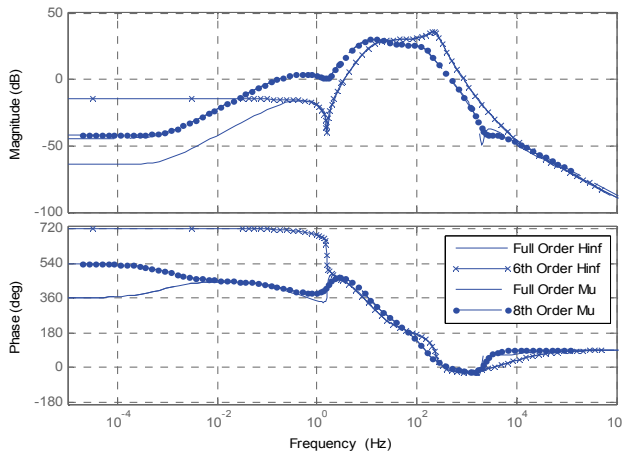


Fig. 9. Bode diagram for full and reduced controllers

The stability robustness margin is 1.56 of reduced H_∞ closed loop, and 6.3 for μ closed loop, so the reduced controllers are robust stability.

4. Robust control simulations of flexible struts

The frequency responses of the open and closed loop system are shown in section 2.2 and 2.3, and this section will give the corresponding transient response for reduced order μ controller and a PI controller that is shown in Equation (13), the nominal closed loop system structure for time domain responses shown in Fig.10

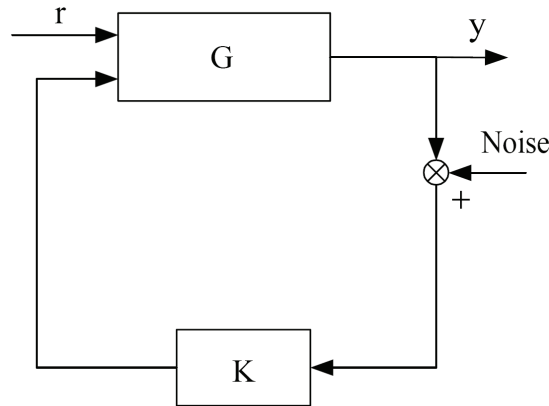


Fig. 10. Nominal closed-loop system structure

The input signal r can contain three parts: tracking signal r_0 , sinusoid disturbance $dist$, and random stochastic disturbance which is Gaussian white noise with mean zero and standard deviation 0.6

$$K_{pi} = \frac{20}{s} + 32 \quad (13)$$

$$r_0 = 10 \sin(t) \quad (14)$$

$$dist = 0.1 \sin(33 \times 2\pi) \quad (15)$$

Figs.11 and 12 present the transient response to a harmonic disturbance input, and from the figures it can be seen that the μ controller or PI controller can effectively isolate the harmonic disturbance located at 33 Hz more than 25.2dB (94.5%).

For comparison, Fig.13 shows open response to the random disturbance, normally distributed Gaussian white noise with mean zero and standard deviation 0.60. Simultaneously, the sensor noise is also contained, which is 2% of random disturbance. Figs.14 and 15 shows the corresponding μ and PI closed loop response to the random disturbance and sensor noise. From the figures, it can be seen that the standard deviations are attenuated 11dB (70%) by μ controller, but the random disturbance is magnified to 132% by PI controller.

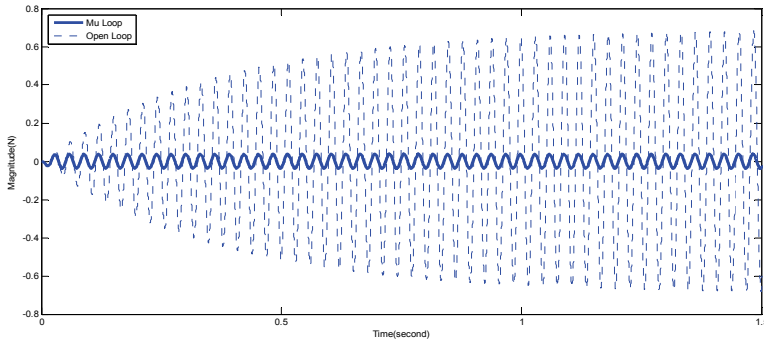


Fig. 11. Open loop and μ closed loop response to sinusoid disturbance in 33 Hz

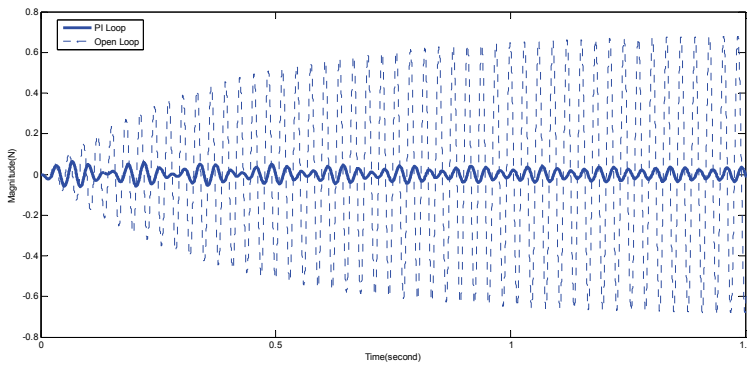


Fig. 12. Open loop and PI closed loop response to sinusoid disturbance in 33 Hz

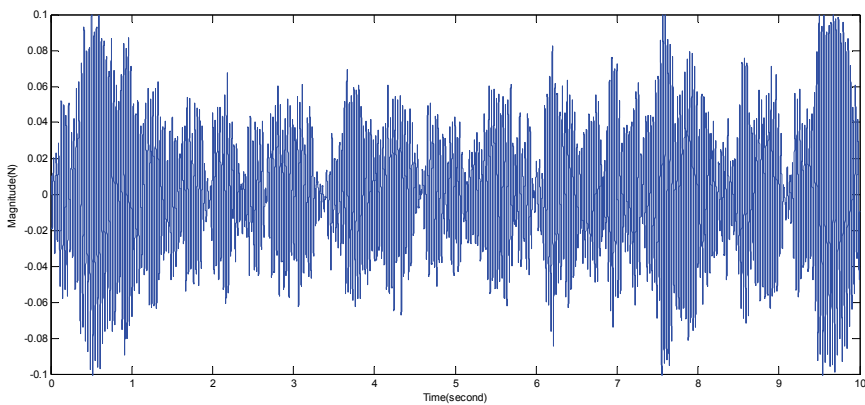


Fig. 13. Open loop response to stochastic disturbance

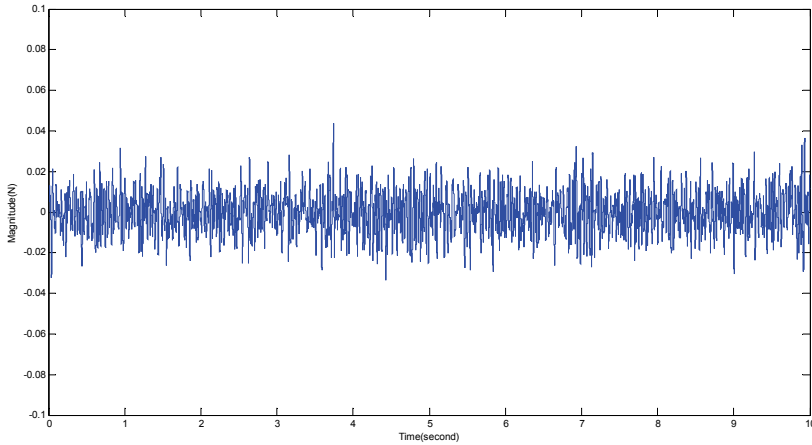


Fig. 14. μ Closed loop response to stochastic disturbance

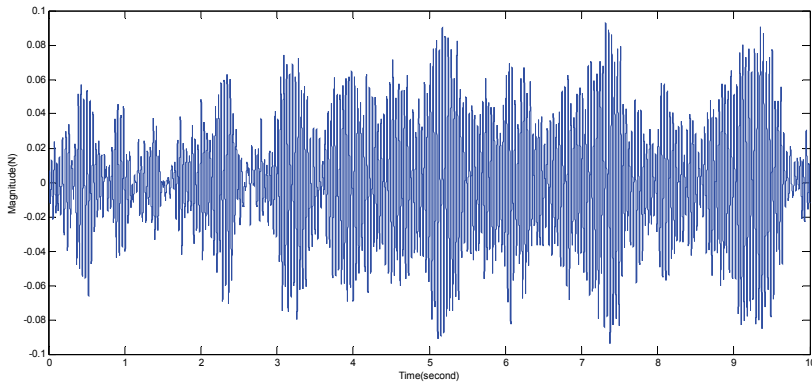


Fig. 15. PI Closed loop response to stochastic disturbance

The magnitude of PI and μ are shown in Fig.16, respectively, if the input r is a sinusoid tracking force r_0 , from which it can be seen that the magnitude of PI is much larger than that of μ , and the PI maybe destroy r_0 , additionally, the PZT actuators are easily saturated for the large gain.

In order to verify the two requirements of μ , another input signal is selected which is made up of tracking signal r_0 , sinusoid disturbance $dist$, random disturbance and the sensor noise. The open loop response is shown in left Fig.17, from which it can be seen that the tracking signal is destroyed by the relatively small disturbance (5% of tracking signal). But the μ closed loop response, as shown in right Fig.17, gives very good result.

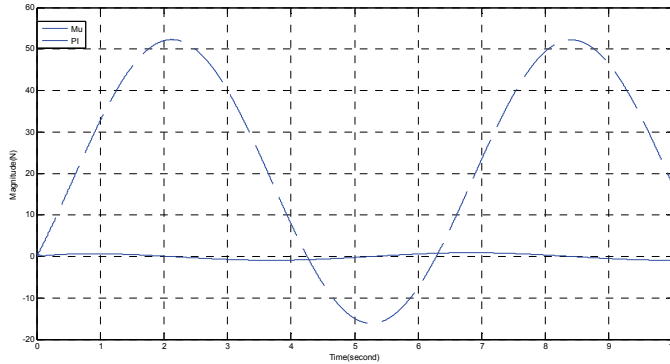


Fig. 16. The magnitude of PI and μ with input r_0

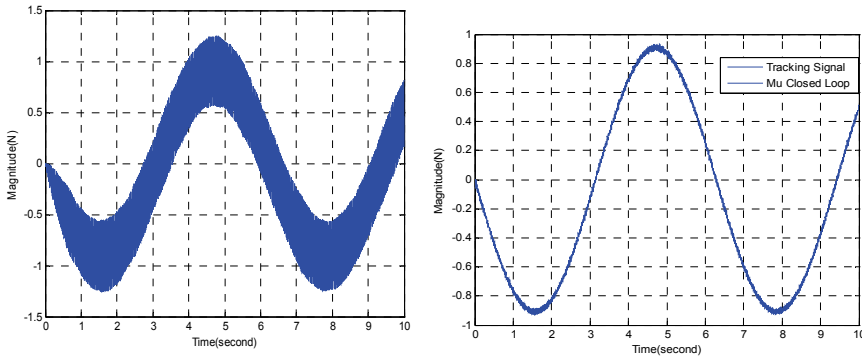


Fig. 17. Open and μ closed loop response to tracking signal with sinusoid and stochastic disturbance

5. Dynamic modeling and robust control of Stewart platforms

The Stewart isolator is used to suppress vibrations, as shown in Fig.18. It can be seen that there are 6 PZT actuators, $\{U\}$, $\{B\}$, $\{P\}$ denotes the inertial frame, base frame, payload frame, respectively. A_i is the joint connecting the payload with the strut i , the mass center of the payload is \vec{p} which is also the origin of the payload frame, \vec{x}_p is the vector representing the origin of payload frame in the base frame.

\vec{A}_i can be represented in the base frame as in equation (16)

$$\vec{A}_i = \vec{p} + \vec{x}_p \tag{16}$$

Then the inertial velocity of \vec{A}_i is given in equation (17)

$$\vec{v}_i = \vec{v} + \vec{\omega} \times \vec{p}_i \tag{17}$$

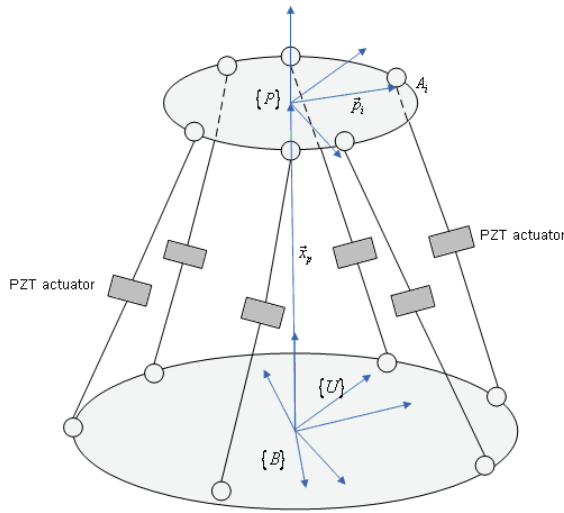


Fig. 18. Stewart isolators

The component of \vec{v}_i projecting on the strut i is shown in equation

$$\vec{q}_i = \vec{1}_i \cdot (\vec{v} + \vec{\omega} \times \vec{p}_i) \tag{18}$$

Then, it can be written in matrix form equation (19)

$$\dot{q}_i = \mathbf{1}_i^T \mathbf{v} - \mathbf{1}_i^T \mathbf{p}_i^* \boldsymbol{\omega} \tag{19}$$

Thus, equation 19 of 6 struts can be written as equation (20)

$$\dot{\mathbf{q}} = \begin{pmatrix} \dots & \dots \\ \mathbf{1}_i^T & -\mathbf{1}_i^T \mathbf{p}_i^* \\ \dots & \dots \end{pmatrix} \begin{pmatrix} \mathbf{v} \\ \boldsymbol{\omega} \end{pmatrix} = \mathbf{J} \dot{\boldsymbol{\chi}} \tag{20}$$

Where \mathbf{J} is the Jacobi matrix describing the motion transformation between the struts and the payload, \mathbf{J} can be assumed as a constant in vibration isolation.

According to Euler equation of the payload is given in equation (21)

$$\mathbf{r}_c \times \mathbf{a}_p m_p + \mathbf{J} \cdot \dot{\boldsymbol{\omega}} + \boldsymbol{\omega} \times \mathbf{J} \cdot \boldsymbol{\omega} = \mathbf{T} \tag{21}$$

Where \mathbf{r}_c is the vector of the mass center of the payload in the payload frame, $\boldsymbol{\omega}$ is its inertial angular velocity.

Assuming the mass center of the payload is the origin of payload frame, i.e. $\mathbf{r}_c = 0$, Newton-Euler equation can be written as matrix equation (22)

$$\begin{bmatrix} m\mathbf{I}_3 & \mathbf{0}_{3 \times 3} \\ \mathbf{0}_{3 \times 3} & \mathbf{J}_{3 \times 3} \end{bmatrix} \ddot{\boldsymbol{\chi}} + \begin{bmatrix} \mathbf{0}_{3 \times 1} \\ \boldsymbol{\omega} \times \mathbf{J}_{3 \times 3} \boldsymbol{\omega} \end{bmatrix} = \begin{bmatrix} \mathbf{F} \\ \mathbf{T} \end{bmatrix} \tag{22}$$

Let $M = \begin{bmatrix} mI_3 & 0_{3 \times 3} \\ 0_{3 \times 3} & J_{3 \times 3} \end{bmatrix}$, $c(\omega) = \begin{bmatrix} 0_{3 \times 1} \\ \omega \times J_{3 \times 3} \omega \end{bmatrix}$

Then

$$M\ddot{\chi} + c(\omega) = J^T f \tag{23}$$

The dynamic model sketch can be shown in Fig. 19. Thus the equation (24) of the active struts can be obtained

$$m_s \ddot{x}_2 + (c_1 + c_2) \dot{x}_2 + (k_1 + k_2)x_2 - c_3 \dot{l} - k_2 l = (c_1 + c_3) \dot{x}_1 + (k_1 + k_2)x_1 + u \tag{24}$$

$m_s = \text{diag}([m_{s1}, m_{s2}, \dots, m_{s6}])$, $l = \text{diag}([l_1 \ l_2 \ \dots \ l_6])$, $k_1 = \text{diag}([k_{11}, k_{21}, \dots, k_{61}])$,
 $k_2 = \text{diag}([k_{12}, k_{22}, \dots, k_{62}])$, $k_3 = \text{diag}([k_{13}, k_{23}, \dots, k_{63}])$, $c_1 = \text{diag}([c_{11}, c_{21}, \dots, c_{61}])$,
 $c_2 = \text{diag}([c_{12}, c_{22}, \dots, c_{62}])$, $c_3 = \text{diag}([c_{13}, c_{23}, \dots, c_{63}])$

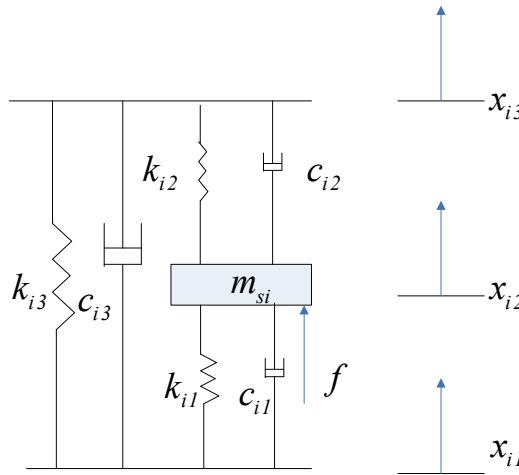


Fig. 19. The spring-mass model of struts

The force of payload subject to active struts is represented in equation (25)

$$f = -(k_2 + k_3)l - (c_2 + c_3)\dot{l} - k_2x_1 - c_2\dot{x}_1 \tag{25}$$

The dynamic model of the payload can be given as (26)

$$M {}^U J^{-1} \ddot{l} + (M {}^U_B R J^{-1} + {}^U J^T (c_2 + c_3)) \dot{l} + {}^U J^{-1} (k_2 + k_3) l = -M J_C J_B^{-1} \ddot{x}_1 - {}^U J^T c_2 \dot{x}_1 - {}^U J^T k_2 x_1 + (M J_C J_B^{-1} c_B - M c_{BP} - c(\omega)) \tag{26}$$

Where $J_B = \begin{bmatrix} {}^U 1_1^T & ({}^U_B R {}^B q_i \times {}^U 1_i^T) \\ \vdots & \vdots \\ {}^U 1_6^T & ({}^U_B R {}^B q_i \times {}^U 1_i^T) \end{bmatrix}$, $J_C = \begin{bmatrix} I & -({}^U_B R {}^B x_p)^* \\ 0 & I \end{bmatrix}$

$$C_{BP} = \begin{bmatrix} 2\omega_B \times {}^U_B R^B \dot{x}_p + \omega_B \times (\omega_B \times {}^U_B R^B x_p) \\ \omega_B \times {}^U_B R^B \omega \end{bmatrix}$$

$$C_B = \begin{bmatrix} {}^U 1_1^T (\omega_B \times (\omega_B \times {}^U_B R^B q_1) + 2\omega_B \times {}^U_B R^B \dot{q}_1) \\ \vdots \\ {}^U 1_6^T (\omega_B \times (\omega_B \times {}^U_B R^B q_6) + 2\omega_B \times {}^U_B R^B \dot{q}_6) \end{bmatrix}$$

Assuming that the velocity \dot{x}_2 can be measured

$$y_v = \dot{x}_2 \quad (49)$$

Considering micro vibration in space, where disturbance force is from micro Newton to several Newton, ω_B and ${}^B_P \omega$ are small variables, such that C_B and C_{BP} can be neglected.

Using the following parameters of Stewart isolator as following;

The coordinates of 6 Joints A_i connecting strut and the payload are $[\frac{\sqrt{2}}{2} \quad -\frac{\sqrt{6}}{6} \quad \frac{\sqrt{3}}{3}]$, $[0 \quad \frac{\sqrt{6}}{3} \quad \frac{\sqrt{3}}{3}]$, $[-\frac{\sqrt{2}}{2} \quad -\frac{\sqrt{6}}{6} \quad \frac{\sqrt{3}}{3}]$ m, respectively, where two joints share the same coordinates.

The corresponding base joints are $[0 \quad -\frac{\sqrt{6}}{3} \quad 0]$, $[\frac{\sqrt{2}}{2} \quad \frac{\sqrt{6}}{6} \quad 0]$, $[-\frac{\sqrt{2}}{2} \quad \frac{\sqrt{6}}{6} \quad 0]$ m, respectively.

The moment inertia of payload is $I = \begin{bmatrix} 20 & 2 & 2 \\ 1.5 & 2 & 1.5 \\ 1.5 & 1.5 & 2 \end{bmatrix}$ kgm²

The mass of payload $m = 15$ Kg, and it has uncertainty 2%. The stiffness $k_1 = 800000 I_{6 \times 6} N / m$, $k_2 = 800000 I_{6 \times 6} N / m$

Damping $c_1 = 100 I_{6 \times 6}$ Ns/m, $c_2 = 200 I_{6 \times 6}$ Ns/m, $c_3 = 10 I_{6 \times 6}$ Ns/m

Choosing the performance weighting function and control weighting function as following

$$W_1 = 20400 \times \frac{(s+0.2)(s+10^6)}{(s+20)(s+10^4)} I_6 \quad (50)$$

$$W_2 = 80 \times \frac{(s+1)(s+2000)}{(s+0.01)(s+20000)} I_6 \quad (51)$$

The robust controller is solved using D-K iteration, the singular values of controller can be seen in left Fig.20. The comparison of open loop (i.e. passive isolation) and closed loop with robust controller (i.e. active isolation) is shown in right Fig.20

The robust controller can suppresses vibrations from 0.3Hz to 2000Hz, and the vibrations in frequency 3Hz-800Hz is isolated more than 25dB.

6. Simulations of the robust control of Stewart isolators

Assuming Stewart isolator is excited by the disturbance force 0.1 N in 10Hz and the magnitude of x_1 is 3.93×10^{-6} m/s. The open loop response of the Stewart isolator, i.e. the passive isolation, is shown in Fig. 21. However, the closed loop response (active isolation) of Stewart isolator is shown in Fig.22. The velocity of the payload is very small, such that the second terms can be neglected, indicating the assuming of the Stewart isolator is correct.

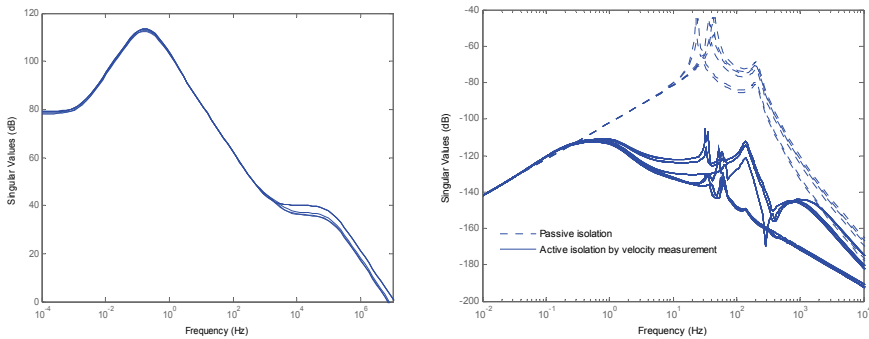


Fig. 20. The comparison of open loop and closed loop with robust controller

The maximal translation velocity of the center of payload under passive isolation is 8.8×10^{-6} (m/s), obviously, it is amplified to 124%, in other words, the Stewart isolator is a amplifier for the disturbance in 10Hz. The maximal translation velocity of the center of payload after the active isolation by robust controller is 3.4×10^{-8} (m/s), which is reduced by 99.13% (equals to 41.3dB) with respect to the input velocity, moreover, the angular velocity of the payload can be reduced by 99.13%(46.4dB) with respect to passive isolation.

Assuming the Stewart isolator is excited by white noise disturbance as shown in Fig.23, The maximal RMS velocity of input disturbance is 0.0036 (m/s), and the maximal RMS force of input disturbance is 0.1N.

With passive isolation (open loop), the RMS of the payload translation velocity is 5.74×10^{-5} (m/s), and the RMS of payload angular velocity is 3.5×10^{-3} (deg/s), indicating that the translation vibrations of the payload can be reduced by 98.4%, 35.9dB; With active isolation by robust controller, the RMS of the payload translation velocity is RMS 1.3×10^{-6} (m/s), reduced by 99.96% (68.8dB) with respect to disturbance velocity, however, the RMS of payload angular velocity is 8.4×10^{-5} (deg/s), reduced by 97.6% (32.4dB) with respect to the passive isolation.

The control signal is shown in Fig.26, the RMS of the maximal control force is 0.2N, and the maximal displacement of the PZT is less than 0.02 μm , which is far smaller than the length of the active strut.

7. Conclusions

This chapter presents multi objective robust H_∞ and μ synthesis for active vibration control of the flexure Stewart platform. The robust H_∞ and μ synthesis control of flexible struts are given considering the noise of sensors. The simulation indicates that the reduced controllers, by square root balanced model truncation, can keep the robust stability compared with the original controllers. Finally, dynamic model and robust control of Stewart isolators is given, and the robust controller can reduce vibrations in 3Hz-800Hz more than 96%.

8. References

Anderson H.; Fumo P, Ervin S. (2000). Satellite ultra-quiet isolation technology experiment (SUITE), *proceeding of IEEE aerospace conference* 4: 219-313

- Chen J., Hospodar E, & Agrawal B. (2004). Development of a hexapod laser-based metrology system for finer optical beam pointing control, *AIAl Paper*, 2004-3146
- Ford V. (2005). Terrestrial planet finder coronagraph observatory summary, *NASA report* document ID: 20060043653
- Gawronski K. (2004). *Advanced structural dynamics and active control of structures*, New York: Springer
- Gu D-W., Petkov P., Konstantinov M. (2005). *Robust control design with MATLAB*, London: SpringerVerlag
- Hanieh A. (2003). *Active isolation and damping of vibration via Stewart platform*, PhD thesis, Free University of Brussels
- Joshi A, Kim W. (2005). Modeling and multivariable control design methodologies for hexapod-based satellite vibration isolation, *Journal of Dynamic Systems, Measurement, and Control*, 127(4): 700-704
- Liu L, Wang B. (2008). Multi objective robust active vibration control for flexure jointed struts of Stewart platforms via H_∞ and μ Synthesis, *Chinese Journal of Aeronautics*, 21(2): 125-133
- M. McMickell, T. Kreider, E. Hansen, et al, (2007). Optical Payload Isolation using the Miniature Vibration Isolation System (MVIS-II), *In Proc. of SPIE Vol.6527, Industrial and Commercial Applications of Smart Structures Technologies*, No.652703
- Skogestad S, Postlethwaite I. (2005). *Multivariable feedback control: design and analysis*, 2nd edition, Chichester: John Wiley & Sons Ltd
- Thayer D, Campbell C. (2002). Six-axis vibration isolation system using soft actuators and multiple sensors, *Journal of Spacecraft and Rockets*, 39(2):206-212
- Winthrop M, Cobb R. (2003). Survey of state of the art vibration isolation research and technology for space applications, *proceeding of SPIE on 2003 Smart Structures and Materials*, 5052:13-26

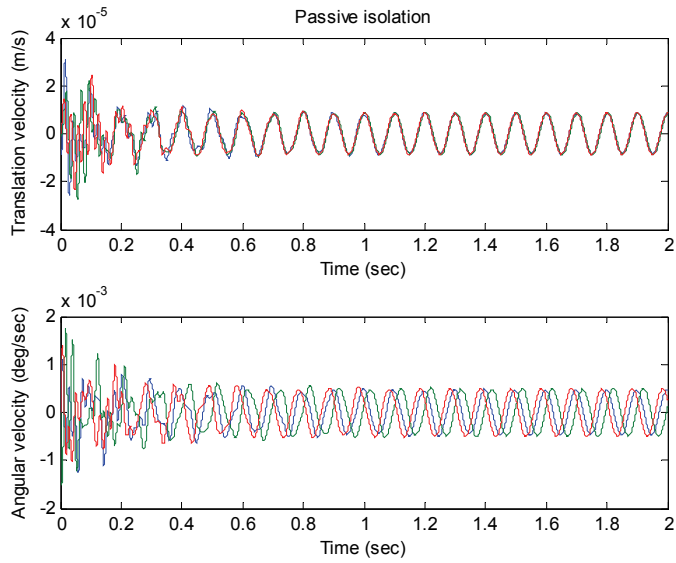


Fig. 21. the velocity of the payload under passive isolation(open loop)

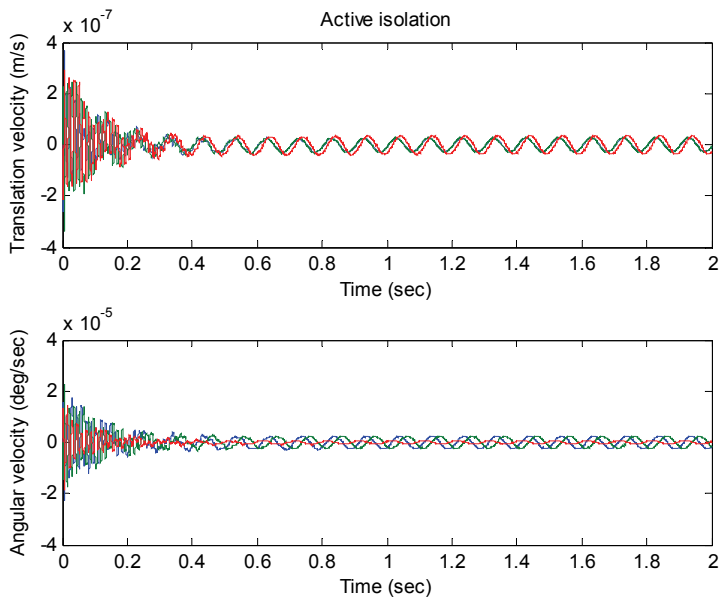


Fig. 22. The velocity of the payload under active isolation(close loop)

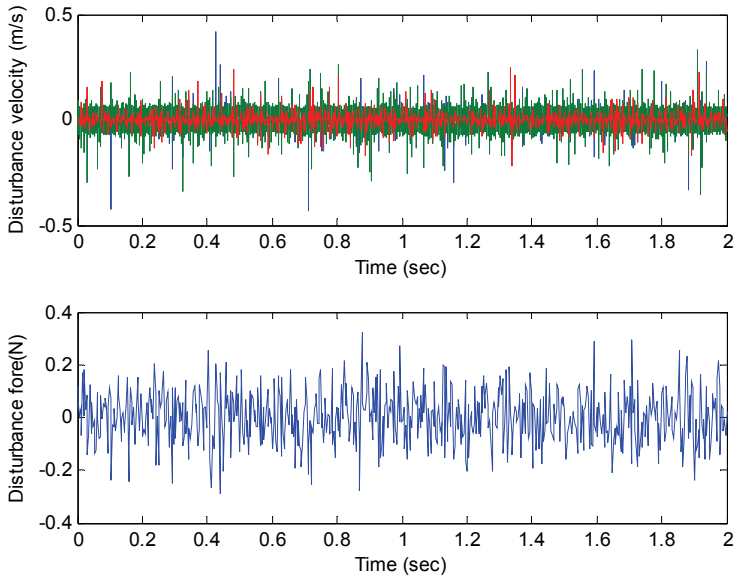


Fig. 23. The velocity and force of disturbance of Stewart isolator

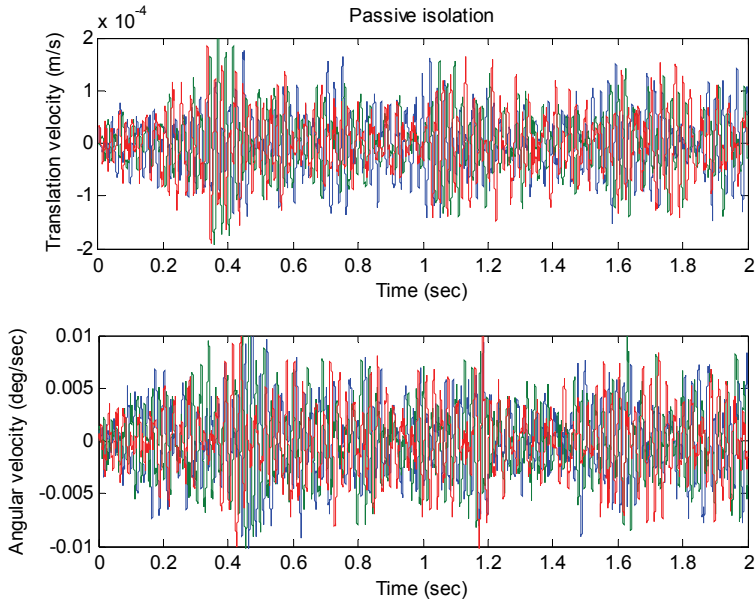


Fig. 24. The velocity of the payload under passive isolation(open loop)

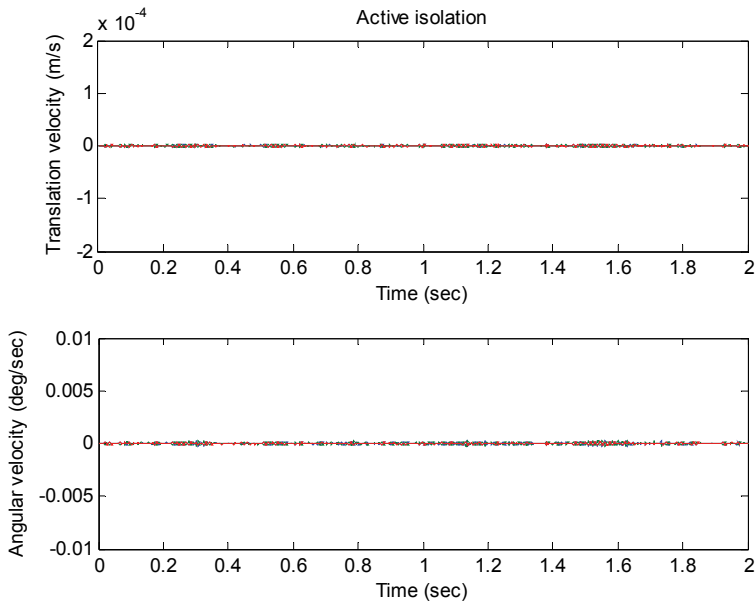


Fig. 25. The velocity of the payload under active isolation (close loop)

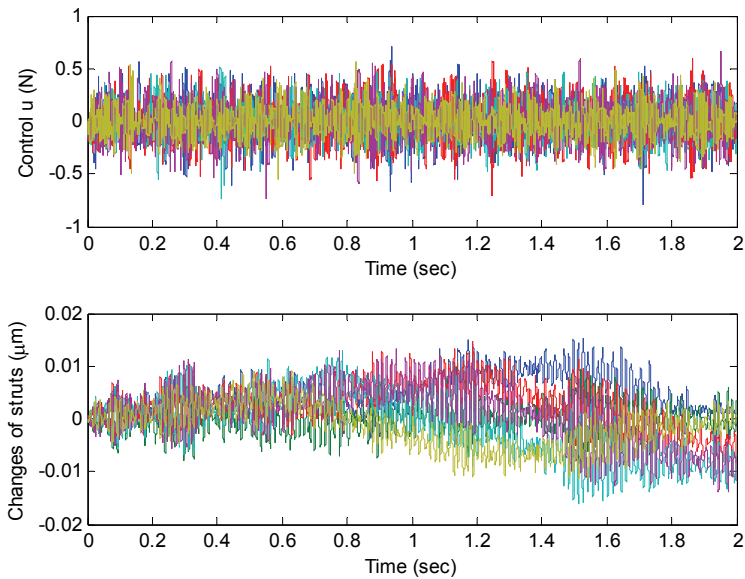


Fig. 26. The control signal and variances of 6 struts

Vibration Control

Ass. Prof. Dr. Mostafa Tantawy Mohamed
Mining and Metallurgical Department
Faculty of Engineering
Assiut University
Egypt

1. Introduction

One of the most troublesome and controversial issues facing mining and other industries related to blasting is that of ground vibration and air blast produced from blasts. It goes without saying that huge mutation in the field of industries and buildings happened in all over the world, have to be accompanied with a same amount of progress in the field of rocks and minerals excavation by blasting, which is considered the backbone of this industrial prosperity. For that, accurate control must to be serious restricted to minimize blasting effect on people and environment. When a blast is detonated, some of the explosive energy not utilized in breaking rock travels through the ground and air media in all direction causing air and ground vibrations. Air and ground vibration from blasting is an undesirable side effect of the use of explosives for excavation. The effects of air and ground vibrations associated with blasting have been studied extensively. Particular attention has focused on criteria to control the vibration and prevent damage to structures and people.

There are many variables and site constants involved that collectively result in the formation of a complex vibration waveform. Many parameters controlled and uncontrolled influence the amplitude of ground vibrations such as distance away from the source; rock properties; local geology; surface topography; explosive quantity and properties; geometrical blast design; operational parameters (initiation point and sequence, delay intervals patterns, firing method). The propagation of ground vibration waves through the earth's crust is a complex phenomenon. Even over small distances, rocks and unconsolidated material are anisotropy and non-homogeneous. Close to the rock/air interface at the ground surface, complex boundary effects may occur. These difficulties restrict theoretical analysis and derivation of a propagation law, and consequently research workers have concentrated upon empirical relationships based on field measurements.

Human are quite sensitive to motion and noise that accompany blast-induced ground and air vibrations. Complaints and protest resulting from blast vibration and air overpressure, to a large extent, are mainly due to the annoyance effect, fear of damage, and the starting effect rather than damage. The human body is very sensitive to low vibration and air blast level, but unfortunately it is not reliable damage indicator. In this regard psychophysiological perception of the blast is more important than the numerical values of the ground vibration and air vibrations. Generally speaking, the key factor that controls the amount and type of blast vibration produced is energy of explosives and the distance of the structure from the blast location.

In order to control and protect the structures from deleterious effect of ground and air vibrations, regulations have been formulated in different countries. These regulations vary from country to country depending on the type and the construction material used. Many damage criteria and propagation equations have been established and fulfilled with varying of degree of success. Its development begins from Rockwell's vibration energy prediction formula in 1934 to OSM regulations (1983) and Indian criteria (DGMS 1997). In recent years, there has been an increasing interest in the utilization of unconventional control strategies such as neural networks (NN), fuzzy logic, and genetic algorithm (GA) etc. to predict and control the air and ground vibrations.

2. The nature of ground vibrations from blasting and types of elastic waves:

In blasting operations, the potential energy, contained in an explosive is suddenly released, normally with the primary intention of fragmenting rock. A secondary, and undesirable result of explosive detonation is that the surface of the ground in the vicinity of the blast undergoes displacement, the amplitude of which depends upon, distance from the blast, the energy released in the explosion and the local geological conditions.

When an explosive is detonated, rock in the immediate vicinity is crushed and shattered and an oscillatory wave is propagated through the rock mass causing particles along its path to move backwards and forwards longitudinally along the lines of advance of this primary wave, which is normally designated the P-wave. Where the P-wave strikes a free surface or change of material at any angle other than 90° , complex displacements occur which give rise to secondary or shear waves usually termed S-waves.

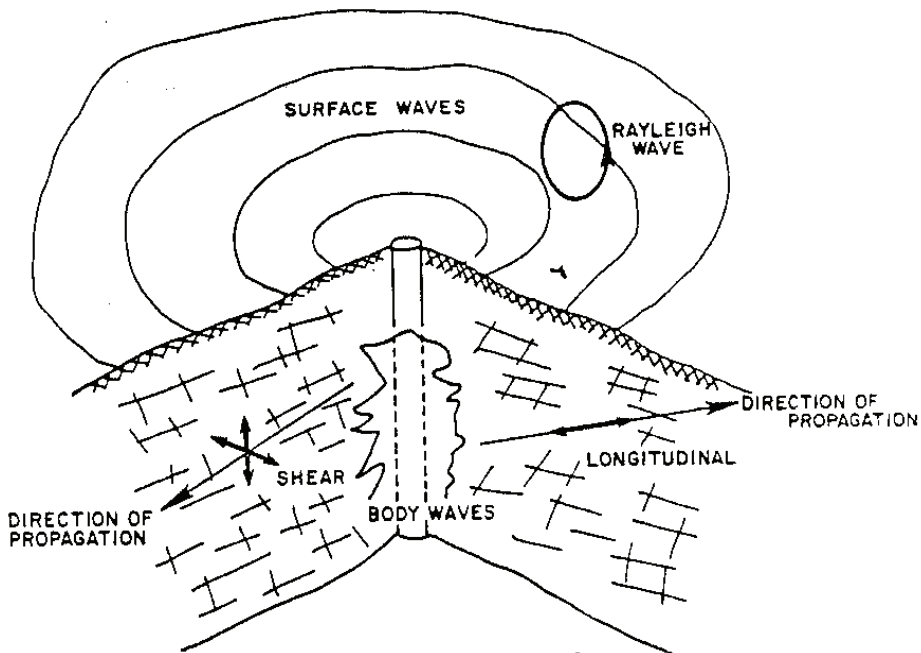
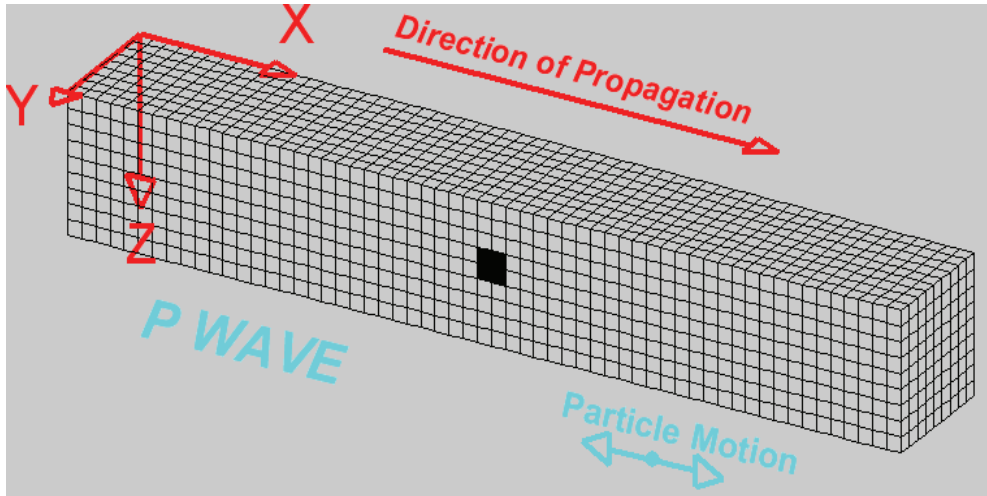
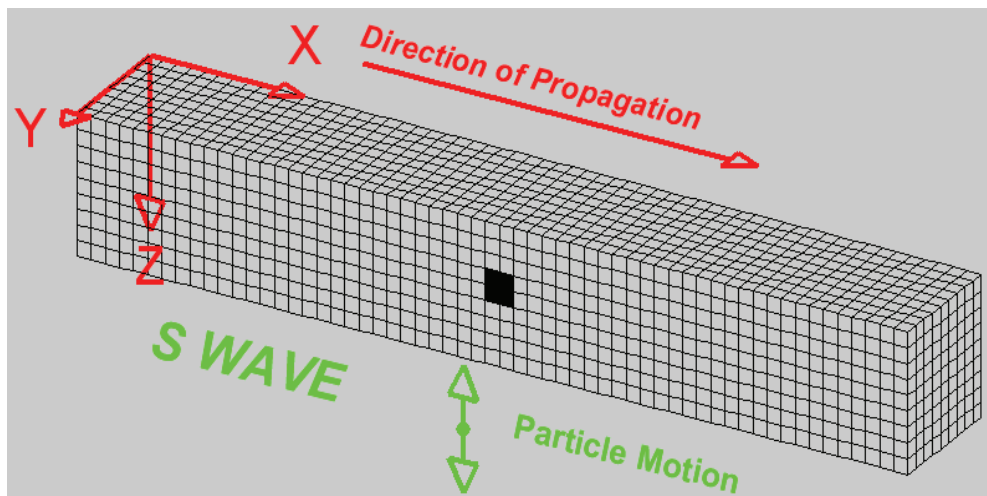


Fig. 1. Common types of elastic waves induced by blasting

The P- and S-waves are called body waves because they travel through the body of the materials, which transmit them. At the free surface between ground and air, the body waves generate a number of surface waves, each of which is characterized by the motion through which a particle in its path goes as the wave passes. Common types of elastic waves (body and surface waves) induced by blasting are illustrated in figure 1 and table [1], the direction of propagation and particle motion for body and surface waves are shown in figures (2, 3).

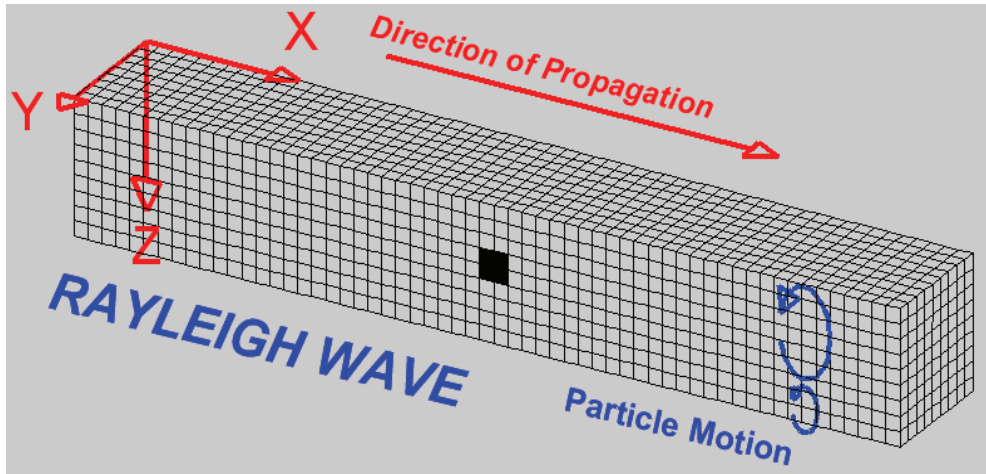


Compressional wave

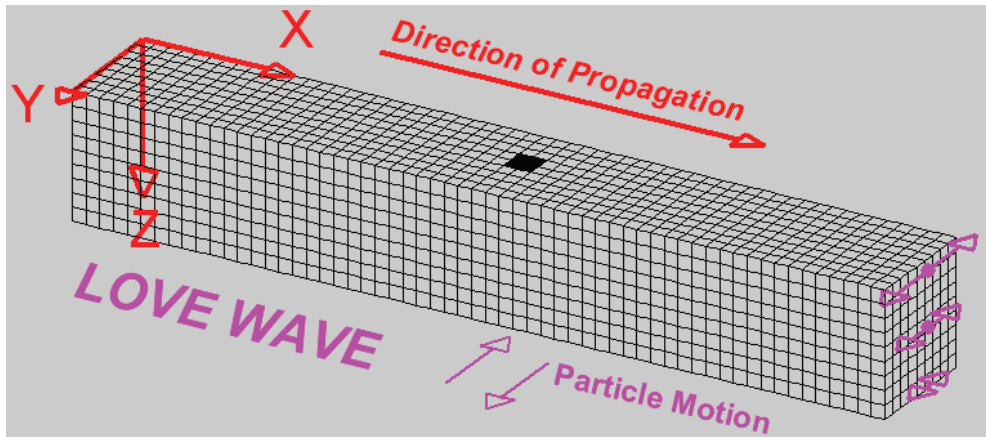


Shear wave

Fig. 2. Body waves motions (compressional and shear).



Rayleigh wave



Love wave

Fig. 3. Surface waves motion (Rayleigh and Love)

The particle motions associated with each of the major surface waves are illustrated in Figure 4. The Rayleigh or R-wave is longitudinal and causes mainly vertical retrograde motion. It is the most commonly observed surface wave, carries the major part of the surface ground energy and consequently is most likely to cause damage. The love or Q-wave (from the German *querwellen*) causes transverse vibration in the horizontal plane with no vertical displacement. The displacement of particles by coupled or C-waves is elliptical and inclined, having components in both vertical and horizontal directions. The use of the term coupled implies combined P-and S-type motions. The H-wave moves particles in an elliptical orbit similar to the R-wave but in the reverse direction. It has only been detected in nuclear blasting. P-waves have the highest velocity, usually in the order of 3000 - 6000 m/s (10000 - 20000 ft/s) in hard rock formations. For surface waves the following order generally obtains:

Wave Type and names	Particle Motion	Typical Velocity	Other Characteristics
P, Compressional, Primary, Longitudinal	Alternating compressions (“pushes”) and dilations (“pulls”) which are directed in the same direction as the wave is propagating (along the ray path); and therefore, perpendicular to the wavefront.	VP~ 5-7km/s in typical Earth’s crust >~8 km/s in Earth’s mantle and core; ~1.5 km/s in water; ~0.3 km/s in air.	P motion travels fastest in materials, so the P-wave is the first-arriving energy on a seismogram. Generally smaller and higher frequency than the S and Surface-waves. P waves in a liquid or gas are pressure waves, including sound waves.
S, Shear, Secondary, Transverse	Alternating transverse motions (perpendicular to the direction of propagation, and the ray path); commonly approximately polarized such that particle motion is in vertical or horizontal planes.	VS ~3-4 km/s in typical Earth’s crust; >~4.5 km/s in Earth’s mantle; ~2.5-3 km/s in (solid) inner core.	S-waves do not travel through fluids, so do not exist in Earth’s outer core (inferred to be primarily liquid iron) or in air or water or molten rock (magma). S waves travel slower than P waves in a solid and, therefore, arrive after the P wave.
L, Love, Surface waves, Long waves	Transverse horizontal motion, perpendicular to the direction of propagation and generally parallel to the Earth’s surface.	VL ~ 2-4.4 km/s in the Earth depending on frequency of the propagating wave, and therefore the depth of penetration of the waves. In general, the Love waves travel slightly faster than the Rayleigh waves.	Love waves exist because of the Earth’s surface. They are largest at the surface and decrease in amplitude with depth. Love waves are dispersive, that is, the wave velocity is dependent on frequency, generally with low frequencies propagating at higher velocity. Depth of penetration of the Love waves is also dependent on frequency, with lower frequencies penetrating to greater depth.
R Rayleigh, Surface waves, Long waves, Ground roll	Motion is both in the direction of propagation and perpendicular (in a vertical plane), and “phased” so that the motion is generally elliptical – either prograde or retrograde.	VR~ 2-4.2 km/s in the Earth depending on frequency of the propagating wave, and therefore the depth of penetration of the waves.	Rayleigh waves are also dispersive and the amplitudes generally decrease with depth in the Earth. Appearance and particle motion are similar to water waves. Depth of penetration of the Rayleigh waves is also dependent on frequency, with lower frequencies penetrating to greater depth.

Table 1. Types of seismic waves

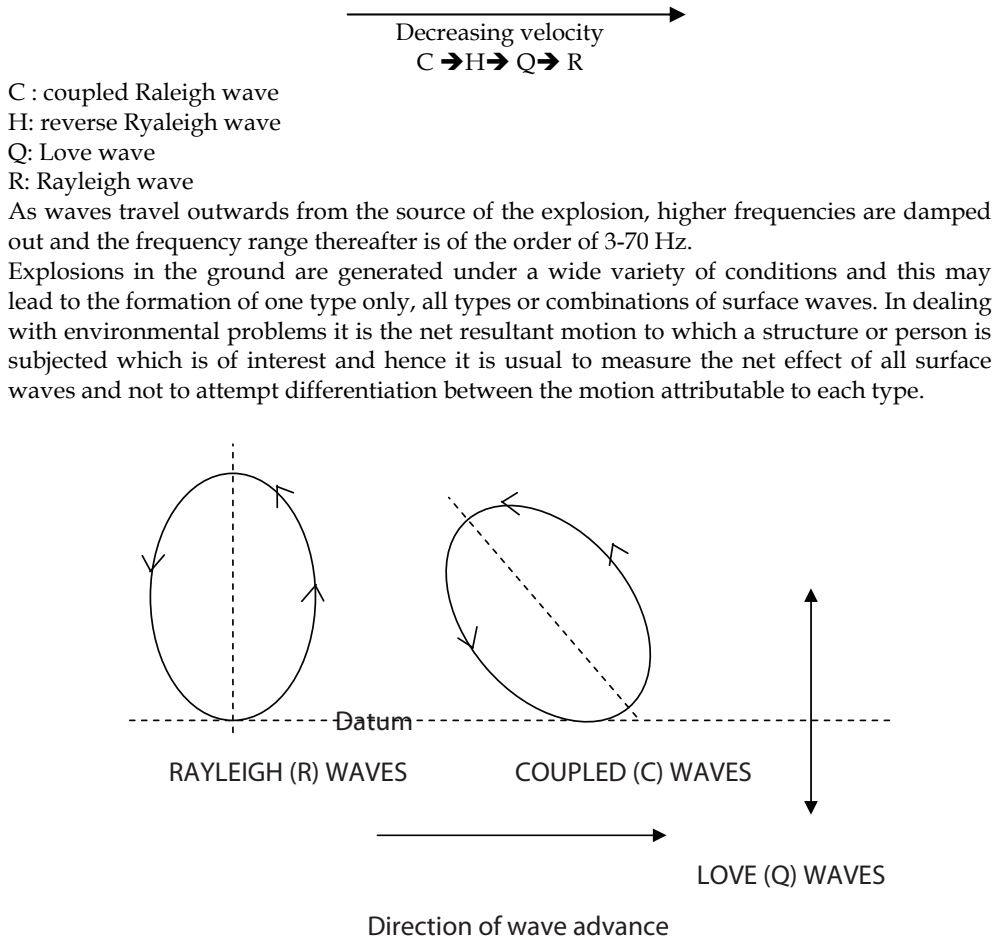


Fig. 4. Particle motions associated with R, C and Q surface waves

The material involved in the transmission of surface waves is a zone about one wave length in thickness.

All surface waves are generated at approximately the same time and, in the immediate vicinity of the blast, the total surface displacement is controlled by the total energy contained within the waves. However, as the waves travel outwards at differing velocities, they quickly separate and maximum ground motion is then controlled by the energy contained within each individual wave. Hence maximum displacement decreases very rapidly at first but then diminishes more slowly as individual waves die out from loss of energy and dispersion. The rate at which the waves die out is dependent upon the nature of the materials through which they pass. The wave forms are elastic and are more readily transmitted through competent rock which has a relatively high elasticity, than through clays, sand and similar unconsolidated material which rapidly convert wave energy into heat by friction.

Makano in 1925 presented the point of Rayleigh wave development (E) on surface as follows, (Fig. 5).

$$E = V_r \cdot d / (V_p^2 - V_r^2)^{1/2}$$

Where:

V_r = the Rayleigh wave velocity.

V_p = Compressional wave velocity.

d = the depth of the disturbance.

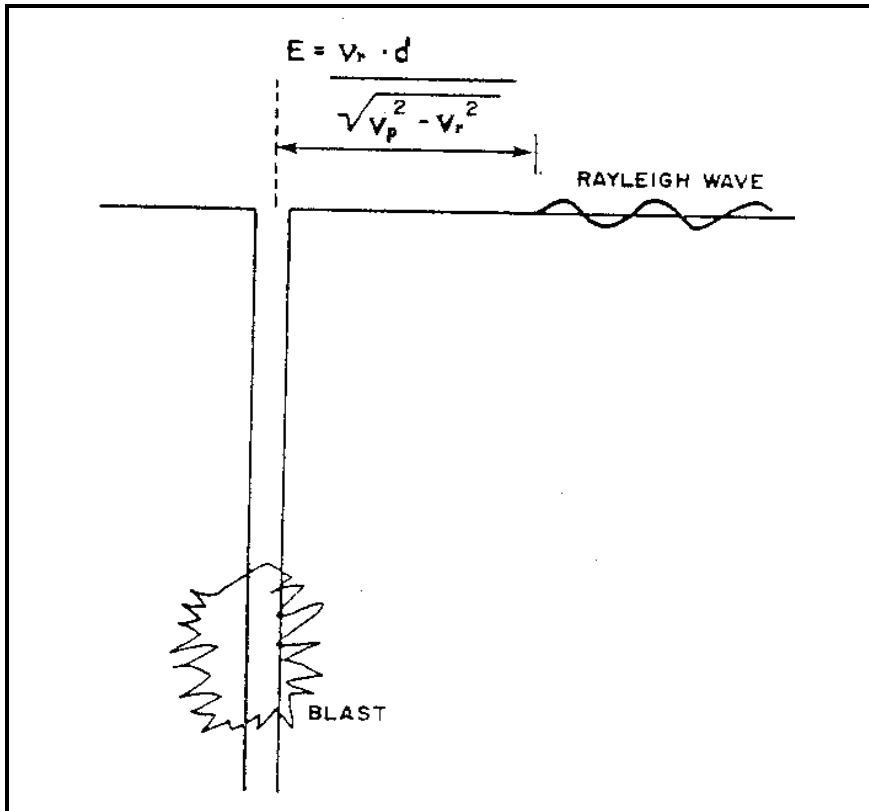


Fig. 5. Epicentral distance (E) from the charge to the point of Rayleigh wave development.

3. Effect on structures

When defining damage to residential type structures the following classifications are used:

Cosmetic or threshold damage - the formation of hairline cracks or the growth of existing cracks in plaster, drywall surfaces or mortar joints.

Minor damage - the formation of large cracks or loosening and falling of plaster on drywall surfaces, or cracks through bricks/concrete blocks.

Major or structural damage - damage to structural elements of a building.

BS 7385 1993 gives guide values with respect to all 3 of these damage classifications for residential structures in terms of peak particle velocity and frequency. These values are based on the lowest vibration levels above which damage has been credibly demonstrated.

In terms of cosmetic damage, at a frequency of 4 Hz the guide value is 15mm/s peak particle velocity, increasing to 20mm/s at 15 Hz and 50mm/s at 40 Hz and above. Minor damage is possible at vibration magnitudes that are greater than twice those given for the possible onset of cosmetic damage with major damage to a building structure possible at values greater than four times the cosmetic damage values. These values apply even when a structure experiences repeated vibration events.

Although damage or the fear of damage is the major concern for neighbors of surface mineral workings the reality is that vibration levels at adjacent residential properties rarely if ever even approach the levels necessary for even the most cosmetic of plaster cracking. Engineered structures such as industrial and heavy commercial buildings and underground constructions are able to sustain higher levels of vibration than those applicable to residential type properties by virtue of their more robust design.

4. Damage criteria and regulations

Many damage criteria have been established and fulfilled with varying of degree of success. Its development stretches from Rockwell's vibration energy formula in 1934 to the present-day OSM regulations Indian criteria (DGMS 1997). A short account review of each is as follow:

- Rockwell's Energy Formula, 1934;
- USBM's Acceleration Criterion, 1935-1940;
- USBM's Formula, 1942;
- Crandell's Energy Ratio, 1949;
- Langefor's Particle Velocity Criterion, 1958;
- Edwards and Northwood's Particle Velocity, 1959;
- USBM's Particle Velocity Criterion, 1969-1971;
- Medearis's Particle Velocity and Frequency, 1976;
- Bauer's Particle Velocity Criterion, 1977;
- USBM's Variable Particle Velocity Versus Frequency, 1980;
- OSM's Current Federal Regulations, 1983;
- Indian criteria (DGMS 1997).

In 1934, Rockwell stated that vibration energy caused by blasting was proportional to frequency (f) and amplitude (A) (is proportional to $f^2 A^2$). Field studies from 1935 to 1940 by the USBM in the frequency range 4-40 Hz and amplitude range 0.0025-12 mm related damage to acceleration have been fulfilled. These studies found that, no damage with acceleration of lower than 0.1g, minor damage (fine plaster cracks) with acceleration ranges from 0.1 to 1.0g, but major damage (fall of plaster) when acceleration is above 1.0g.

In 1942, USBM combined the effect of charge quantity, ground character and distance. This formula was found to be inadequate in view of the more complex blasting designs.

In 1949 Crandell developed the concept of energy ratio which is defined as the ratio of the square of the acceleration to the square of the frequency ($ER = a^2/f^2$). Crandell's damage criteria were based on pre- and post-blast investigations of over 1000 residential structures, He recommended that the threshold level at which minor damage occurs is about 3 while above 6 is more danger.

In 1958 A report by Langefors et al. described the relationship between ground vibrations from blasting and structural damage during a reconstruction project in Stockholm. Frequencies measured ranged from 50 to 500 Hz and amplitudes from 0.02 to .5 mm. They concluded that particle velocity gave the best guide to damage potential and derived the results as shown in table (2).

In 1959 investigations by Edwards and Northwood for the frequency range 3-30 Hz and amplitude range 0.25-9 mm concluded that damage was more closely related to velocity than displacement or acceleration. And minor damage was likely to occur with a peak particle velocity of 100-125 mm/s, table (3) presents these damage levels.

In 1971, USBM has been set damage criteria of peak particle velocity of less than 2 in/sec would result in a low probability of structural damage to residential dwellings, see table (4).

In 1976, Medearis reported that specifying a peak ground particle velocity alone, did not take into account two very significant parameters, namely the predominant frequencies of the ground motion and the structure being existing. He concluded that Pseudo Spectral Response Velocity (PSRV) was deemed to be the best predictor of damage due to blast vibrations. For a predicted PSRV of 1.5 in/sec, the probability of damage ranged from 0 to 1 %.

In 1977, Bauer et al. has been established damage for equipment and structures depending on peak particle velocity criterion as shown in table (5). In 1980, Siskind et al. Published the results of comprehensive study of ground vibration produced by blasting on 76 homes from 219 production blasts in RI 8507. the main conclusions are peak particle velocity is still the best single ground descriptor. Also, practical safe criteria for blasts that generate low-frequency ground vibrations are 0.75 in/sec for modern gypsum board houses and 0.5 in/sec for plaster-on-lath interiors. For frequencies above 40 Hz, a safe peak particle velocity of 2 in/sec is recommended for all houses.

In 1983, the United States Office of Surface Mine (OSM) published its final regulations concerning the use of explosives for the control of ground vibrations and air blast. These regulations applied only to surface coal mining operations and designed to control blasting effects. Many non-coal surface mining operations have opted to comply with these regulations as operating guidelines. The office of OSM regulations were designed to offer more flexibility in meeting performance standards and to prevent property damage. The operator has the choice of employing any one of the the methods as in table (6) to satisfy the OSM regulations.

Particle Velocity	Damage
2.8 in/sec	No noticeable damage
4.3 in/sec	Fine cracks and fall of plaster
6.3 in/sec	Cracking of plaster and masonry walls
9.1 in/sec	Serious cracking

Table 2. Selected particle velocity damage criteria are listed as follows (Lagefors, Kihlstrom, and Westerber (1957)).

Particle Velocity	Damage
≤ 2 in/sec	Safe no damage
2.4 in/sec	Caution
> 4 in/sec	Damage

Table 3. Edwards and Northwood based their criteria in connection with the St. Lawrence project in Canada (1959).

Particle Velocity	Damage
< 2.0 in/sec	No damage
2.0-4.0 in/sec	Plaster cracking
4.0-7.0 in/sec	Minor damage
> 7.0 in/sec	Major damage to structures

Table 4. USBM (1971).

Type of structure	Type of damage	Particle velocity at which damage starts
Rigidity mounted mercury switches	Trip out	0.5 in/sec
Houses	Plaster cracking	2 in/sec
Concrete blocks in a new home	Cracks in block	8 in/sec
Cased drill holes	Horizontal offset	15 in/sec
Mechanical equipment pumps compressors	Shafts misaligned	40 in/sec
Prefabricated metal building on concrete pads	Cracked pads building twisted and distorted	60 in/sec

Table 5. Equipment and Structure Damage Criteria (Canmet, Bauer and Calder 1977).

- *Method 1*- Limiting particle velocity criterion: requires that each blast be monitored by a seismograph capable of monitoring peak particle velocity. Providing the maximum particle velocity stays below the levels specified in table (6).
- *Method 2*- Scaled distance equation criterion: requires the operator to design shots in accordance with table (6), which specifies a scaled distance design factor for use at various distances between a dwelling and blast site. No seismic recording is necessary. Providing that scaled distance in table (6) is observed.
- *Method 3*- Blast level chart criterion: This method allows an operator to use particle velocity limits that vary with frequency as illustrated in Figure 6. This method requires frequency analysis of the blast-generated ground vibration wave as well as particle velocity measurements for each blast. This method may represent the best means evaluating potential damage to residential structures as well as human annoyance from blasting. Any seismic recordings for any component (longitudinal, transverse, or vertical) for the particle velocity at a particular predominant frequency that fall below any part of the solid line graph in Figure 6 are considered safe. And any values that fall above any part of the solid line graph will increase the likelihood of residential damage and human annoyance. An investigation of the impact of surface mining blasting on a domestic building at Gilfach Lags open-cast site at U.K. was done by Rob Farufields research project. The research concluded that there is no damage below 24.1 mm/sec peak particle velocity. Djordjevic stated that a maximum ground vibration velocity of 5mm/sec has been set in

Distance from blast site (ft)	Method 1 Maximum allowed peak particle velocity (in./sec)	Method 2 Scaled distance factor to be used without seismic monitoring
0 to 300	1.25	50
301 to 5000	1.00	55
5001 and beyond	0.75	65

Table 6. Maximum permitted particle velocities (method 1 and scaled distance factors permitted to various distances from blast method 2)

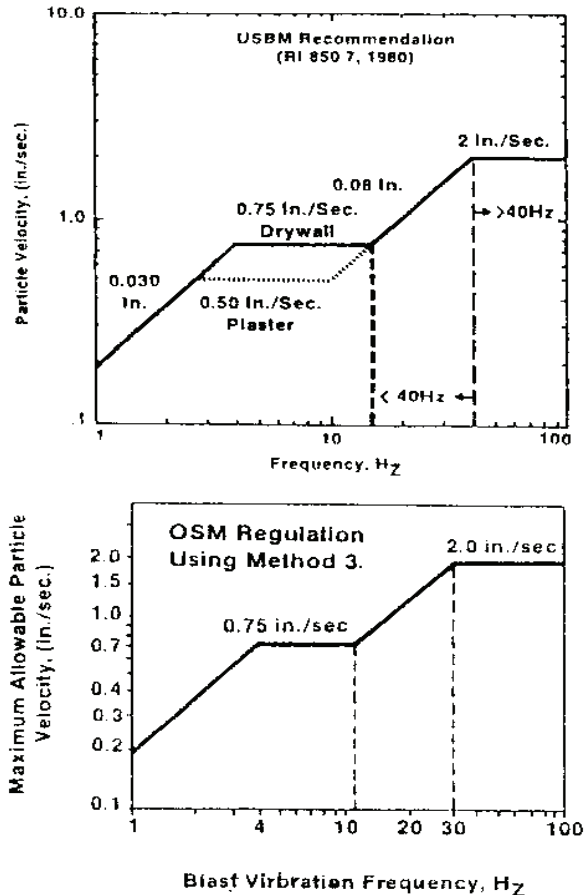


Fig. 6. Recommended safe levels of blasting vibrations by USBM and OSM

Australian Environmental Council Standard. The Australian "SSA explosive code AS 2187" has been presented as in table (7) the recommend maximum limits for the level of ground vibration in soil near the foundation buildings. Some standards of damage for some countries are shown in tables (8), (9), (10), (11), (12), and (13). The apparent discrepancies of damage standards as mentioned before result in the response of a structure to ground

vibrations depends mainly upon the nature of the building, soil and rock geology, as well as the characteristics of vibration.

Peak Particle velocity (mm/sec)	Type of building or structure
25	Commercial and industrial building or structure of reinforced concrete or steel construction
10	Houses and low - rise residential buildings : commercial buildings not included in the third category, below.
2	Historical building or monuments and buildings of special value or significance

Table 7. Peak Particle Velocity (PPV) criteria from AS 2187.

Buildings Class	Maximum resultant of the particle velocities Vr (mm/s)	Estimated maximum vertical particle velocity Vz (mm/sec)
I. Residential Building, offices and others similarly built in the conventional way and being in normal condition	8	4.8 - 8
II. Stall building in normal condition	30	18 - 30
III. Other building and historical monuments	4	2.4 - 44

Table 8. German Din 4150 Standard.

Structural type	Peak particle velocity (mm/s)		
	<10Hz	10-50Hz	50-100Hz
Commercial	20	20-40	40-50
Residential	5	5-15.0	15-20
Sensitive	3	3-8.0	8-10.0

Table 9. German Standards.

Structural type	Peak particle velocity (mm/s)		
	4-8Hz	8-30Hz	30-100Hz
Resistant	8	12	15
Sensitive	6	9	12
Very sensitive	4	6	9

Table 10. French Standards.

Subsoil	Vibration (mm/s)
Unconsolidated strata of moraine sand, gravel, clay.	18
Unconsolidated strata of moraine slate, soft limestone.	35
Granite, gneiss, hard limestone, quartzitic sandstone, diabase.	70

Table 11. Swedish Standards.

Seismic intensity categories	Effects induced on the structures	Particle velocity cm/s	
		Allowed	Limit
IV	Possible damages for village-type buildings, under pressure pipes, gas and petrol wells, mine shaft, and very fragile structures.	0.5	1.0
V	The painting is falling down, small and thin cracks appear in mortar plaster in rural and urban buildings. Possible minor damages for industrial constructions.	1.1	2.0
VI	Cracks in mortar (plaster) on the walls and pieces of mortar start to fall down in rural and urban buildings. Also minor damage for industrial constructions.	2.1	4.0
VII	Significant fractures are occurring in the basic elements of the rural buildings, great pieces of mortar are falling down in urban buildings and cracks are appearing in industrial constructions. Possible damage for pipes jointing system and fixed-mounted equipment.	4.1	8.0
VIII	Major fractures occur in the resistance elements of rural and urban buildings. Cracks are produced in the resistance elements of industrial constructions.	8.1	16.0
IX	Crumbing (collapse, falling down) of some joint elements of rural and urban buildings can occur. Fractures can take place in industrial structures. Dams and underground pipes can be damaged.	16.1	32.0
X	Rural buildings are destroyed, urban constructions are seriously damaged and industrial structures are affected seriously by fracturing and dislocation of resistance elements.	32.1	64.2

Table 12. Romanian Standards.

Type of Structure	Dominant frequency, Hz		
	< 8 Hz	8-25 Hz	>25 Hz
(A) Buildings/structures not belong to the owner			
i) Domestic houses /structures (Kuchha brick and cement)	5	10	15
ii) Industrial buildings (RCC and framed structures)	10	20	25
iii) Objects of historical importance and sensitive structures	2	5	10
(B) Building belonging to owner with limited span of life			
i) Domestic houses /structures (Kuchha brick and cement)	10	15	25
ii) Industrial buildings (RCC and framed structures)	15	25	50

Table 13. Indian Standard

5. Air blast

Air vibrations are generated by the blast and propagated outward through the air under the influence of the existing topographic and atmospheric conditions. Four mechanisms are usually responsible for the generation of air blast vibrations: the venting of gases to the atmosphere from blown-out unconfined explosive charges, release of gases to the atmosphere from exposed detonating fuse (initiation system), ground motions resulting from the blast, and the movement of rock at the bench face. Audible air blast is called noise while air blasts at frequencies below 20 Hz and inaudible to the human ear are called concussions. This is measured and reported as an "overpressure" it means air pressure over and above atmospheric pressure. The noise can either be continuous (lasts more than 1 second) or be of impulsive nature such as a shock from explosions. Overpressure is usually expressed in pounds per square inch (psi), Pascal or Kilopascal (Pa, kpa), or in decibels (dB). Peak pressures are reported in terms of decibels, which are defined as:

$$\text{dB} = 20 \log_{10} (P/P_0)$$

where P is the measured peak sound pressure and P_0 is a reference pressure of 2.9×10^{-9} psi (20×10^{-6} pa).

Energy transmitted in acoustic waves behaves in the same manner as seismic energy. Air blast overpressures are greatly affected by atmospheric conditions, direction and strength of wind, temperature, humidity, and cloud cover. Like ground vibrations, the peak overpressure level is controlled by the charge weight of explosive per delay and the distance from the blasthole. Unlike ground motions, air pressure can be described completely with only one transducer, since at any one point, air pressure is equal in all three orthogonal directions.

The pressure developed by noise and shock waves is the primary cause of window rattling. Nicolls et al, through the Bureau of Mines conducted extensive research in blasting and concluded that overpressure less than 0.75 psi would not result in any window damage and overpressure of 1.5 psi or more would definitely produce window damage. Maximum value recommended by Nitro Consult and generally accepted for sound pressure is equal and less than 142 dB (250 pa). Figure 7 illustrates overpressure equivalence for both types of units (dB and psi). In order to understand the overpressure levels, 0.01 psi is comparable to the maximum found in a boiler shop or to the pressure level present 4 ft from a large pneumatic riveter.

6. Human response

Human response to blast induced ground vibration is a relatively complex phenomenon and is dependent upon a range of factors of which the actual vibration magnitude is only one and not necessarily the most important. It is well recognized that the human body is very sensitive to the onset of vibration albeit very poor at distinguishing relative magnitudes. Although sensitivity to vibration varies significantly between individuals, a person will generally become aware of blast induced vibration at levels of around 1.5mms⁻¹ peak particle velocity, and under some circumstances at levels as low as 0.5mms⁻¹.

Once a received vibration is greater than an individual's perception threshold then it is possible for concern to be expressed about the blasting. Such concern normally relates to the vibration's potential for causing damage to the complainant's property. Concern may be

180	3.0	← Structural damage
170	0.95	← Most windows break
160	0.30	
150	0.095	← Some windows break
140	0.030	← OSHA* maximum for impulsive sound
130	0.0095	← USBM TPR 78 maximum
		← USBM TPR 78 safe level
120	0.0030	← Threshold of pain for continuous sound
110	0.00095	← Complaints likely
100	0.00030	OSHA maximum for 15 minutes
90	0.000095	
80	0.000030	← OSHA maximum for 8 hours

* Occupational Safety and Health Administration

Fig. 7. Overpressure unit conversion (dB and psi) and effects on human annoyance and structural damage.

expressed that damage has already occurred due to the recent discovery of cracking that may have been present for some time or have been caused by natural processes. More often, however, concerns are based on the fear that damage will be caused at some time in the future as a result of repeated vibration.

The degree of concern and whether or not it leads to complaints is governed by many factors. Perhaps the most obvious is the vibration itself in terms of its magnitude, duration and frequency. However, the vibration magnitude at which complaints arise varies greatly from site to site such that no common complaint threshold exists. This is considered to be in part a reflection of the fact that individuals are very poor at distinguishing between vibrations of differing magnitudes.

The susceptibility of individuals to vibration will vary from person to person depending on factors such as age, health and, to a large extent, previous exposure. It is usually the case that adverse comments are less likely once a neighbor has become accustomed to the perceived effects of blasting. An explanation of the need to blast and the significance of the vibration levels being received by a site's neighbors are paramount as is an understanding and sympathetic attitude from the operator.

Human are quite sensitive to motion and noise that accompany blast-induced ground and air born disturbances. Complaints resulting from blast vibration and air overpressure, to a large extent, are mainly due to the annoyance effect, fear of damage, and the startling effect rather than damage. The human body is very sensitive to low vibration and air blast level, but unfortunately it is not reliable damage indicator. With air overpressure blast generally levels of over 120 dB will produce some annoyance and fright throughout excite wall and rattle dishes, and together tend to produce more noise inside a structure than outside. In most cases, personal contact, assurance, and a good public relations program with the residential owners in question should alleviate the problem, assuming no structural damage. In this regard psychophysiological perception of the blast is generally more important than the numerical values of the ground vibration and air overpressure.

7. Attenuation analysis by scaled distance

The attenuation of ground vibrations in terms of the peak velocity component and airblast intensities is evaluated based on scaled distance, generally referred to as SD. The scaled distance factors for ground motions and airblast are given, respectively, by the following:

$$\text{Square-root scaled distance SRSD} = R/W^{1/2}$$

$$\text{Cube-root scaled distance CRSD} = R/W^{1/3}$$

Where R is the shot-to-seismograph distance and W is the maximum charge weight detonated within any 8 ms time period (referred to as one delay time period). Scaled distance is a means of incorporating the two most important factors contributing to the intensity of ground motion and airblast as intensity decreases proportionally with distance and inversely with the explosive weight detonated on one time delay. In the case of ground motion, the SRSD is used (commonly referred to as simply SD) as ground motion has been shown to correlate with the square root of the charge weight. In the airblast case, air pressures correlate best with the cube-root of the charge weight (CRSD).

7.1 Vibration prediction

The prediction of ground vibration waves through the earth's crust is a complex phenomenon. Even over small distances, rocks and unconsolidated material are anisotropy and non-homogeneous. Close to the rock/air interface at the ground surface, complex boundary effects may occur. These difficulties restrict theoretical analysis and derivation of a propagation law that predict the ground vibration, and consequently research workers have concentrated upon empirical relationships based on field measurements.

Many researchers, over the world, have studied ground vibrations originating from blasting and theoretical empirical analyses have been developed to explain the experimental data. At a given location, peak particle velocity (PPV) depends mainly on the distance from the blast and the maximum charge per delay. Scaled distance The scaled-distance concept vs. particle velocity and air overpressure is generally used for blast vibration prediction. Currently the most widely accepted propagation equation for ground and air vibration considering the damage to structures is of the form.

$$V = K \left(R/W^\beta \right)^{-\alpha}$$

Traditional empirical equations prediction:

In 1949, Grandell developed the concept of energy ratio as mentioned before:

$$ER = a^2/f^2$$

Also, he suggested the following propagation equation:

$$ER. = k Q^2 (50/D)^2$$

Where: ER = energy ratio;

a = acceleration, ft/sec² ;

f = frequency, Hz;

k = site constant;

Q = quantity of explosives, lb;

D = distance from measuring point to blast point, ft.

In 1950, studies on wave propagation phenomena were concluded by Morris. He propounded that the amplitude (A) of particle displacement is direct proportional to the square root of the weight of the charge (Q) and inversely proportional to the distance from the blast. That is:

$$A = k(Q^{1/2})/D$$

Where k = the site constant and was found to vary from 0.05 for hard competent rock to 0.30 for clay up to 0.44 or 0.5 for completely unconsolidated material.

A = maximum amplitude, in;

Q = quantity of explosives, lb,

Habberjam and Whetton (1952) suggested a higher power for the charge weight in their formula:

$$A \propto Q^{0.085}$$

Langefors, Kihlstrom and Westerberg (1958) suggested the following relationship:

$$V = k(\sqrt{Q}/D^{1/2})^B$$

Where k and B = site constants;

V = mm/sec or in/sec;

Q = Weight of explosives, kg or lb;

D = distance from point of blast to measuring point, m or ft.

Assuming cylindrical explosive geometry for long cylindrical charge, Duvall and Petkof (1959); Duvall and Fogelson (1962); Duvall et al. (1963); and Daemen et al. (1983) concluded that any linear dimension should scale with the square root of the charge weight. The corresponding relationship assumes the form:

$$V = k(Q/D^{1/2})^{-B}$$

For spherical symmetry, the U.S. Bureau of Mines investigators suggested that any linear dimension should be scaled to the cube root of the charge size and it's supported by Ambraseys and Hendron in India. An inverse power law was suggested to relate amplitude of seismic waves and scaled distance to obtain the following relationship:

$$V = k(Q/D^{1/3})^{-B}$$

In 1965, Attewell et al., proposed the following shape of propagation equation:

$$V = k(Q/D^2)^n$$

Where n = constant depending on site conditions = 0.64 to 0.96;

K = site constant, ranges from 0.013 to 0.148 (increasing constant for softer Rock)

The Romanian method, which was proposed by Enesco in 1968 to evaluate the seismic effect of blasting based on the determination of apparent magnitude "Ma" with the following empirical relationship:

$$Ma = 0.67(\log V^2_{\max} * T + \log r + 4 \log 4 \rho V - 11.8)$$

Where: V_{\max} = the maximum oscillation particle velocity, cm/sec;

T = oscillation period;

V = propagation velocity of elastic waves, m/sec;

ρ = the density of rock in which the seismic wave propagate, gm/cm³;

r = distance from the shot point to measuring point, m.

This method presumes the assessment of the so-called "acceptable intensity" for construction. Through field test and using the above relationship, the safe distance corresponding to "Ma" and consequently to a certain quantity of explosive is determined. The Russian method was suggested by Medvedev in 1968 to assess the safe distance "r" as follows:

$$r = K_e * K_t * K_c * R_{\text{red}} * Q^{1/3}$$

Where: K_e = coefficient depending on the method of firing (instantaneous or delayed time) and the mining conditions (underground, open-pit or combined);

K_t = Coefficient depending on the characteristics of media in which the waves propagate;

K_c = coefficient depending on the type of construction (more or less damaged);

R_{red} = reduced distance depending on the function of the admissible intensity of vibration;

Q = explosive quantity (equivalent TNT).

Also, Sadovski in Russia has computed the non-dangerous explosive quantity by the following relationship:

$$V = k/D (Q/D)^{1/3} f(n)$$

Where: V = admissible particle velocity for construction, cm/sec;

k = global coefficient depending on the blasting and propagation conditions;

R = distance from the blasting point to construction, m;

Q = explosive quantity, (equivalent TNT);

$F(n)$ = function for diminishment of seismic effect depending on firing system. It means on the number of blasting rows "n" and delay time between them.

" Δt ", the conditions are as follow:

i. For $n \Delta t < 0.15$ sec, $f(n) = 1 - 12.9 (n \Delta t)^2$.

ii. For $n \Delta t > 0.15$ sec, $f(n) = 0.275 / n \Delta t$.

iii. For instantaneous blasting, $f(n) = 1$.

The empirical relationship suggested by the Indian Standard (1973) used the concept in which blast is scaled to the equivalent distance, the relation is expressed as:

$$V = k (Q^{2/3}/D)^{-B}$$

Swedish Detonic Research Foundation has worked out an empirical formula to predict the vibration velocity as follows:

$$V = 700 Q^{0.7}/D^{1.5}$$

Davis et al., (1964), Daemen et al., (1983) and others investigators considered no particular charge symmetry. They proposed the most widely general formula is of the type:

$$V = k Q^A D^{-B}$$

Ghosh and Daemen (1983) reformulated the propagation equation of U.S. Bureau of Mines and Ambraseys and Hendron by incorporating the inelastic attenuation factor e^{-pD} . The modified equations are:

$$V = k (Q/D^{1/2})^{-B} e^{-pD}$$

and

$$V = k (Q/D^{1/3})^{-B} e^{-pD}$$

Where k , B , and p are empirical constants; p is called the inelastic attenuation factor.

In 1991, Central Mining Research Station (CMRS) in India has also established an efficient blast vibration predictor. The equation considers only geometrical spreading as the cause of the decrease in amplitude of ground vibrations:

$$V = n + k (Q/D^{1/2})^{-1}$$

But in practical situation, the value of "n" is always negative, then the equation will be:

$$V = -n + k (Q/D^{1/2})^{-1}$$

Where n is the damping factor influenced by rock properties and geometrical discontinuities.

Propagation law of blast-induced air overpressures has been studied by numerous investigators and is generally reported with cube-root rather than square-root scaled distances. Following equations are commonly used for overpressure prediction:

$$dBL = 164.4 - 241 \log (D/ W^{1/3})$$

or alternatively:

$$P_{over} = 3300 (D/ W^{1/3})^{-1.2}$$

Where dBL is the overpressure decibel level, D is the distance from the blasthole (m), W is the weight of explosive detonated per delay (kg) and P_{over} is the overpressure level (pa). According to Nito-Consult AB the air overpressure propagation equation is estimated as follows:

$$P = 70 \times (0.6 Q)^{1/3} / R \text{ kpa}$$

Where: Q is charge weight in kg and R distance in m.

Model for prediction of Threshold Value of PPV:

The model for determination of the allowed peak particle velocity has its origin in the Norwegian practice for prudent blasting in the last 30 -40 years.

The peak particle value is calculated by:

$$V = V_o * F_k * F_d * F_t$$

V_o = Uncorrected max. value of vertical particle velocity measured in mm/s.

V_o is dependent on the kind of geological material of the ground, see table [14].

F_k = construction coefficient = $F_b * F_m$

F_b = building factor, see table [15].

F_m = material factor, see table [16].

F_d = distance coefficient, which takes into consideration the distance between the blasting site and the critical object (.5 and 1 for distance 200 and 5).

F_t = time coefficient, which takes into consideration how long the construction is exposed for blast vibration, see table [17].

Ground conditions	Vertical uncorrected particle velocity mm/s			
	No cracks	Minor cracks	Major cracks	Danger cracks
Very soft soils/ soft clays	Separate valuation	-	-	-
Loose layered moraine, sand, gravel, clay (seismic velocity <2000 m/s).	18	30	40	60
Hard layered moraine, schist, soft limestone and corresponding rock (seismic velocity 2000-4000 m/s).	35	55	80	115
Granite, gneiss, hard limestone, quartzite, diabase and corresponding rock (seismic velocity >4000 m/s).	70	110	160	230

Table 14. Vertical uncorrected particle velocity V_o at different ground condition.

Class	Type of structure	Building coef. F_b
1	Heavy constructions like bridge, quays, military defense works etc.	1.70
2	Industrial- and office buildings.	1.20
3	Ordinary houses.	1.00
4	Particularly sensitive buildings, such as museums, buildings with high and arch shaped roofs or constructions with large spans.	0.65
5	Historical buildings and ruins in particular sensitive condition.	0.50

Table 15. Building coefficient for different types of constructions.

Class	Material	Material coef. F_m
1	Armored concrete, steel, wood.	1.2
2	Unarmed concrete, brick, brickwork, hollow concrete, stones, light weight concrete.	1.00
3	Porous concrete (gassed concrete).	0.75
4	Mixed bricks.	0.65

Table 16. Material coefficient for different construction material.

Duration of blasting work	Time coef. F_t
Less than 12 months.	1
More than 12 months.	0.75

Table 17. Time coefficient.

Artificial intelligence prediction:

If an unusual noise or uncertainties exists in the measured data of vibrations, statistical models have difficulty in making accurate predictions. So, the use of neural networks from a branch of artificial intelligence is very important to predict the air vibration and peak particle velocity efficiently. Artificial neural network and fuzzy logic are the two most important concepts of artificial intelligence. They are useful in modeling or prediction of one or more variables.

7.2 Artificial Neural Network (ANN)

Neural networks first became popular in the late 1980s and, more recently, in the 1990s. Compared to traditional statistical methods, neural network analysis has been found to be very useful in diverse, real-world applications. An artificial neural network can be defined as a data processing system consisting of a large number of simple, highly interconnected processing elements (artificial neurons) in an architecture inspired by the structure of the cerebral cortex of the brain (Tsoukalas & Uhrig, 1996). These processing elements are usually organized into a sequence of layers or slabs with full or random connections between the layers. The input layer is a buffer that presents data to the network. The following layer(s) is called the hidden layer(s) because it usually has no connection to the outside world. The output layer is the following layer in the network, which presents the output response to a given input. Typically the input, hidden, and output layers are designated the i th, j th, and k th layers, respectively. A typical neural network is "fully connected," which means that there is a connection between each of the neurons in any given layer with each of the neurons in the next layer.

Artificial neural networks (ANNs) are a form of artificial intelligence that has proved to provide a high level of competency in solving many complex engineering problems that are beyond the computational capability of classical mathematics and traditional procedures. Back-propagation artificial neural network a Feed-forward network is considered the most popular, effective and easy-to-learn model for complex, multi-layered networks of the supervised learning techniques. The typical back-propagation network has an input layer, an output layer, and at least one hidden layer. Each layer is fully connected to the

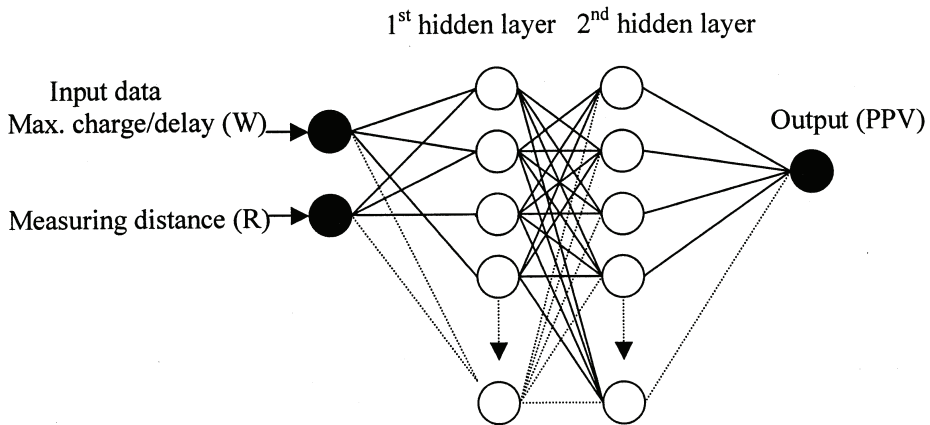


Fig. 8. Back propagation training ANN

succeeding layers, as shown in Figure 8. In the back propagation training, the connection weights are adjusted to reduce the output error. In the initial state, the network begins with a small random set of connection weights. In order for the network to learn, a set of inputs is presented to the system and a set of outputs is calculated. A difference between the actual outputs and desired outputs is calculated and the connection weights are modified to reduce this difference.

Fuzzy logic system:

Fuzzy logic is preferable when the mathematical problem is hard to derive, and when decisions have to be made with estimated values under incomplete information. Fuzzy models can be seen as logical models which use "if-then" rules to establish qualitative relationships among the variables in the model. Fuzzy set theory enables the processing of imprecise information by means of membership functions, in contrast to the classical set theory. The classical set (called crisp set) takes only two values: one, when an element belongs to the set; and zero, when it does not. In fuzzy set theory, an element can belong to a fuzzy set with its membership degree ranging from zero to one. The basis of fuzzy logic is to consider the system states in the form of subsets or fuzzy sets, each of which is labeled with words such as "low," "medium," "big," etc. A general fuzzy inference system basically consists of; fuzzification, knowledge base, a decision-making unit, and finally a defuzzification, the fuzzy system is shown in figure 9.

8. Measurement

There are four interrelated parameters that may be used in order to define ground vibration magnitude at any location. These are:

Particle Displacement - the distance that a particle moves before returning to its original position, measured in millimeters (mm).

Particle Velocity - the rate at which particle displacement changes, measured in millimeters per second (mms⁻¹).

Particle Acceleration - the rate at which the particle velocity changes, measured in millimeters per second squared (mms⁻²) or in terms of the acceleration due to the earth's gravity (g).

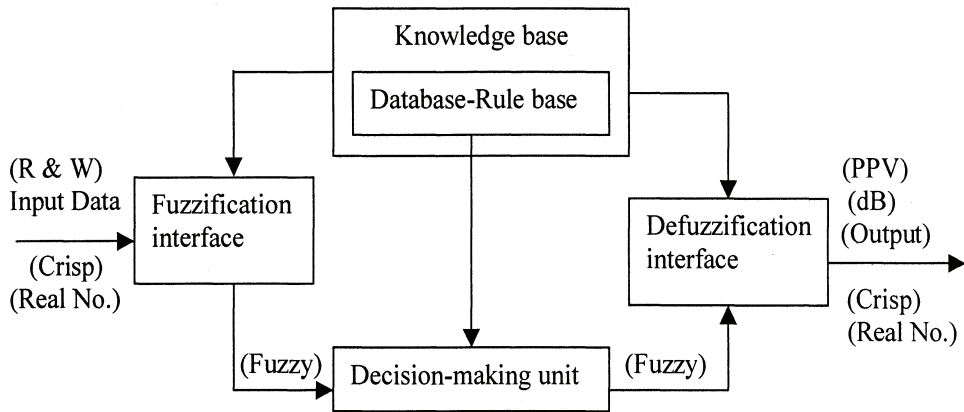


Fig. 9. A typical Fuzzy System for Fuzzy Logic Modeling Process

Frequency - the number of oscillations per second that a particle undergoes measured in Hertz (Hz).

In all standards the preferred parameter of measurement is peak particle velocity (ppv). The measurement of particles by vibration waves is usually measured in 3 mutually perpendicular directions, as particles will be oscillating in 3 dimensions, these are:

Longitudinal (sometimes termed radial) - back and forth particle movement in the same direction that the vibration wave is traveling.

Vertical - up and down movement perpendicular to the direction the vibration wave is traveling.

Transverse - left and right particle movement perpendicular to the direction the vibration wave is traveling.

9. How to control vibrations

9.1 Ground vibration

The ground vibration can be affected by certain blast design parameters:-

1. The maximum instantaneous charge or MIC is the amount of explosives fired at the same moment in time.
2. The number and frequency of delays.
The introduction of a delay sequence can reduce the size of the maximum wave produced.
3. The height of the working bench and therefore the length of borehole.
4. The number of "decks" or layers of explosives and detonators in each hole.
5. The spacing, burden and number of holes, in the blast ratio.
6. The diameter of the shot hole, which will affect the amount of explosives used.

There are several steps an operator can take to reduce ground vibrations:

Blast design

Use a blast design that produces the maximum relief practical in the given situation. Explosions in blastholes which have good relief - i.e. those having nearby free faces - produce less ground vibration. The use of delay blasting techniques establishes internal free

faces from which compressional waves produced later in the blast can delay patterns, maximum relief can be retained.

In general, when blasting multiple row patterns, greater relief can be obtained by using a longer delay between rows than between the holes within a single row. A delay of at least 2–3 ms/m of burden between the holes within a row is recommended for the necessary relief and best fragmentation.

Use a spacing/burden ratio greater than one. The presence of weak seams or irregular back break may dictate the local use of a spacing/burden ratio close to one.

Hole straightness

Control drilling of blast holes as closely as possible. Establish bench marks for use in setting out the hole locations for the next blast before each blast in order to help avoid possible errors due to irregular back break.

Subdrilling

Restrict the amount of sub drilling to the level required to maintain good floor conditions. Typical sub drilling for holes inclined 3:1 is 30% of the burden at floor level. Tape each drill hole and match it to the face height. If hole depth is greater than intended, backfill with drill cuttings or crushed stone. Excessive sub drilling can increase vibration because of the lack of a nearby free face to create reflection waves.

Charge per delay

Use the following techniques to reduce charge weight per delay and, therefore, peak particle velocity.

- reduce hole depths with lower bench heights and increase specific drilling,
- use smaller diameter holes,
- subdivide explosive charges in holes by using inert decks and fire each explosive deck with initiators using different delays,
- Use electronic or mechanical timers to increase the available number of periods of delay electric blasting caps and to increase timing flexibility. Non electric delays coupled with surface delay connectors can provide similar flexibility.

Explosives

Eliminate or reduce hole-to-hole propagation between charges intended to detonate at different delay periods. Use explosive, such as water gels, which are much less sensitive than dynamite to hole -to-hole propagation. Hole-to-hole propagation occurs when the explosive charges or blastholes are only a few feet apart, as in trenching, decked holes, or underwater excavations, or at greater distances when blasting interbedded soft and hard layer rock, such as coral or mud-seamed rock, that is saturated with water.

Using NONEL blasting system

Use NONEL blasting system can reduce the wave superposition by increasing delay time among shots. In addition to reduce the air vibration by using NONEL shock tube instead of detonating cord.

9.2 Air overpressure

There are five principal sources of air overpressure from blasting at surface mineral workings:

1. The use of detonating cord which can produce high frequency and hence audible energy within the air overpressure spectrum.
2. Stemming release, seen as a spout of material from the boreholes, gives rise to high frequency air overpressure.
3. Gas venting through an excess of explosives leading to the escape of high-velocity gases, give rise to high frequency air overpressure.
4. Reflection of stress waves at a free face without breakage or movement of the rock mass. In this case the vertical component of the ground-vibration wave gives rise to a high-frequency source.
5. Physical movement of the rock mass, both around the boreholes and at any other free faces, which gives rise to both low and high-frequency air overpressure.

The steps to reduce air vibrations:

Detonating cord should be used as sparingly as possible, and any exposed lengths covered with as much material as possible. Just a few feet of exposed cord can lead to significant amounts of audible energy and, hence, high air overpressure levels. Stemming release can be controlled by detonation technique, together with an adequate amount of good stemming material. Drill fines, while readily available, do not make good stemming material. The use of angular chippings is better. It should be noted however that detonation cord and stemming release have been virtually eliminated with the use of in hole initiation techniques.

Gas venting results from overcharging with respect to burdens and spacings or, perhaps, a local weakness within the rock, and is also typified by the occurrence of fly rock. Its control is essential for economic and safe blasting, and is considerably aided by accurate drilling and placement of charges, together with regular face surveys.

The controllable parameters such as geology, Topography, and Meteorological Conditions can be controlled to some extent by adjustment of blast pattern and blaster in charge judgment for blasting operation.

10. References

- [1] Atlas of Powder Company, "Explosives and Rock Blasting", Text Book, Dallas, Texas USA, 1987.
- [2] Olofsson S. O., "Applied Explosives Technology for Construction and Mining", Nitro Nobel Hand Book, Arla, Sweden, pp. 59-61, June 1990.
- [3] Dowding C. H., "Blast Monitoring for Rock Engineering", Comprehensive Rock Engineering Practice and Projects Excavation, Support and Monitoring, Vol. 4, Pergamon Press Ltd, Headington Hill Hall, Oxford, England, 1993.
- [4] Siskind D. E., Stagg M. S., Kopp J. W., and Dowding C. H., "Structure Response and Damage Produced by Ground Vibration from Surface Mine Blasting", RI 8507, Bureau of Mines, Report of Investigations, 1980
- [5] Bollinger, G.A., "Blast Vibration Analysis", Southern Illinois University Press, USA, 1971.
- [7] Eugene P. Peleider "Surface Mining" Text Book - New York, 1972.
- [8] Tamrock, "Surface Drilling and Blasting", Tamrock Hand Book, Tamrock Publisher, Finland, 1987.

-
- [9] Sever c., "Artificial Neural Networks and Fuzzy Logic Applications in Modeling the Compressive Strength of Portland Cement", M.Sc. thesis, Izmir Institute of Technology, Izmir, Turkey, December, 2004.
- [10] Ross TJ., "Fuzzy logic with Engineering Applications", Second Edition. England: John Wiley & Sons, 2004.
- [11] J. Grznar, S. Prasad, and J. Jasmine, "Neural Networks and Organizational System: Modeling Non-linear Relationships", European Journal of Operational Research, Vol. 181, 2007.